NASA Contractor Report 144881

THE DEVELOPMENT OF THE DAST I REMOTELY PILOTED RESEARCH VEHICLE FOR FLIGHT TESTING AN ACTIVE FLUTTER SUPPRESSION CONTROL SYSTEM

David L. Grose

University of Kansas
Lawrence, Kansas

February 1979

Prepared for

NATIONAL AERONAUTICS AND SPACE ADMINISTRATION
Dryden Flight Research Center
Edwards, California 93523

1. Report No.	2. Government Accession No.	3. Recipient's Catalog No.
NASA CR-144881		

4. Title and Subtitle	5. Report Date
THE DEVELOPMENT OF THE DAST I REMOTELY PILOTED RESEARCH VEHICLE FOR FLIGHT TESTING AN ACTIVE FLUTTER SUPPRESSION CONTROL SYSTEM	February 1979
	6. Performing Organization Code
7. Author(s) David L. Grose	8. Performing Organization Report No.
	10. Work Unit No.
9. Performing Organization Name and Address University of Kansas Lawrence, Kansas 66045	11. Contract or Grant No. NAS1-4007
	13. Type of Report and Period Covered Contractor Report - Final
12. Sponsoring Agency Name and Address National Aeronautics and Space Administration Washington, D.C. 20546	14. Sponsoring Agency Code H-1083

15. Supplementary Notes

NASA Technical Monitor: Dwain A. Deets, Dryden Flight Research Center

This report was prepared in partial fulfillment of the requirements for the degree of Doctor of Engineering at the University of Kansas.

16. Abstract

The development of the DAST I (Drones for Aerodynamic and Structural Testing) remotely piloted research vehicle is described. The DAST I is a highly modified BQM-34E/F Firebee II Supersonic Aerial Target incorporating a swept supercritical wing designed to flutter within the vehicle's flight envelope. The predicted flutter and rigid body characteristics are presented. A description of the analysis and design of an active flutter suppression control system (FSS) designed to increase the flutter boundary of the DAST wing (ARW-1) by a factor of 20% is given. The design and development of the digital remotely augmented primary flight control system and on-board analog backup control system is presented. An evaluation of the near real-time flight flutter testing methods is made by comparing results of five flutter testing techniques on simulated DAST I flutter data. The development of the DAST ARW-1 state variable model used to generate time histories of simulated accelerometer responses is presented. This model uses control surface commands and a Dryden model gust as inputs. The feasibility of the concept of extracting open loop flutter characteristics from closed loop FSS responses was examined. It was shown that open loop characteristics can be determined very well from closed loop subcritical responses. Some open loop aircraft modes are identifiable in the closed loop supercritical responses, but the wing bending and torsion modes involved in flutter are obscured. Existing flutter testing methods appear satisfactory for the FSS experiment. Flight testing is to begin in March 1979. It is a scheduled six flight program.

17. Key Words (Suggested by Author(s))	18. Distribution Statement
Active controls technology Remotely piloted vehicles Active flutter control	Unclassified-Unlimited STAR Category: 05

19. Security Classif. (of this report)	20. Security Classif. (of this page)	21. No. of Pages	22. Price*
Unclassified	Unclassified	366	

*For sale by the National Technical Information Service, Springfield, Virginia 22161

FOREWORD

This work was made possible by a National Aeronautics and Space Administration grant NAS1-4007 to the University of Kansas.

I would like to express my thanks to the many people at the NASA Dryden Flight Research Center for their help and cooperation.

The support extended by Dr. Jan Roskam and Dr. Kenneth Lenzen from the University of Kansas is greatly appreciated.

A special acknowledgment is extended to Dwain Deets at the NASA Dryden Flight Research Center whose advice and patience made this work possible.

I would also like to thank my wife, Karen, whose constant support was truly invaluable.

TABLE OF CONTENTS

LIST OF ACRONYMS

ACT - Active Controls Technology

ADC - Analog to Digital Converter

AMP - Amplitude Ratio

AP - Autopilot

ARW-1 - Aeroelastic Research Wing 1

BWC - Boeing Wichita Company

CAS - Command Augmentation System

CCV - Controlled Configured Vehicle

CD - Computer Direct

CG - Center of Gravity

Co - Coincidence (In-Phase)

DAC - Digital to Analog Converter

DAST - Drones for Aeroelastic and Structural Testing

DFRC - Dryden Flight Research Center

FFT - Fast Fourier Transform

FSS - Flutter Suppression System

GVT - Ground Vibration Test

LaRC - Langley Research Center

MAC - Mean Aerodynamic Chord

MARS - Mid-Air Recovery System

NASA - National Aerodynamics and Space Administration

PCM - Pulse Code Modulation

PSD - Power Spectral Density

QUAD - Quadrature (Out-of-Phase)

RAV - Remomely Augmented Vehicle

RD - Rate Damped

RMS - Root Mean Square

RPM - Revolutions Per Minute

RPRV - Remotely Piloted Research Vehicle

SCW - Super Critical Wing

TM - Telemetry

WBL - Wing Buttocks Line

LIST OF FIGURES

LIST OF TABLES

LIST OF SYMBOLS

Symbol	Definition	Usual Dimension
$[A]$	State matrix	
$[A_I]$	Aerodynamic influence coefficient matrix	
AR	Aspect ratio	
b	Wing span	
$[B]$	Control distribution matrix	
B_i	Aerodynamic lag terms	
$[C]$	Coefficient matrix	
$\bar{c}$	Mean aerodynamic (geometric) chord	
$C_D = \frac{D}{\bar{q}S}$	Drag coefficient	
$C_{D_u} = \frac{\partial C_D}{\partial (\frac{u}{u_1})}$	Variation of drag coefficient with speed	
$C_{D_\alpha} = \frac{\partial C_D}{\partial \alpha}$	Variation of drag coefficient with angle of attack	rad^{-1}
$C_{D_{\delta_E}} = \frac{\partial C_D}{\partial \delta_E}$	Variation of drag coefficient with elevator angle	deg^{-1} rad^{-1}
$C_\ell = \frac{L}{\bar{q}Sb}$	Rolling moment coefficient	
$C_L = \frac{L}{\bar{q}S}$	Lift coefficient	

Symbol	Definition	Usual Dimension
$C_{\ell_p} = \frac{\partial C_\ell}{\partial (\frac{pb}{2U_1})}$	Variation of rolling moment coefficient with roll rate	
$C_{L_q} = \frac{\partial C_D}{\partial (\frac{q\bar{c}}{2U_1})}$	Variation of lift coefficient with pitch rate	
$C_{\ell_r} = \frac{\partial C_\ell}{\partial (\frac{rb}{2U_1})}$	Variation of rolling moment coefficient with roll rate	
$C_{L_u} = \frac{\partial C_L}{\partial (\frac{u}{U_1})}$	Variation of lift coefficient with speed	
C_{L_o}	Effective lift curve slope intercept	
$C_{L_\alpha} = \frac{\partial C_L}{\partial \alpha}$	Variation of lift coefficient with angle of attack	rad^{-1}
$C_{L_{\dot{\alpha}}} = \frac{\partial C_L}{\partial (\frac{\dot{\alpha}c}{2U_1})}$	Variation of lift coefficient with rate of change of angle of attack	
$C_{\ell_\beta} = \frac{\partial C_\ell}{\partial \beta}$	Variation of rolling moment coefficient with sideslip angle	rad^{-1}
$C_{\ell_{\delta_A}} = \frac{\partial C_\ell}{\partial \delta A}$	Variation of rolling moment coefficient with aileron angle	$\frac{deg^{-1}}{rad^{-1}}$
$C_{L_{\delta_E}} = \frac{\partial C_L}{\partial \delta_E}$	Variation of lift coefficient with elevator angle	$\frac{deg^{-1}}{rad^{-1}}$
$C_{L_{\delta_R}} = \frac{\partial C_\ell}{\partial \delta_R}$	Variation of rolling moment coefficient with rudder angle	$\frac{deg^{-1}}{rad^{-1}}$

Symbol	Definition	Usual Dimension
$C_m = \frac{M}{\bar{q}S\bar{c}}$	Pitching moment coefficient	
$C_{m_q} = \frac{\partial C_m}{\partial(\frac{qc}{\partial U_1})}$	Variation of pitching moment coefficient with pitch rate	
$C_{m_u} = \frac{\partial C_m}{\partial(\frac{u}{U_1})}$	Variation of pitching moment coefficient with speed	
C_{m_o}	Effect pitching moment curve slope intercept	
$C_{m_\alpha} = \frac{\partial C_m}{\partial \alpha}$	Variation of pitching moment coefficient with angle of attack	rad^{-1}
$C_{m_{\dot{\alpha}}} = \frac{\partial C_m}{\partial(\frac{\dot{\alpha}\bar{c}}{\partial U_1})}$	Variation of pitching moment coefficient with elevator angle	deg^{-1} rad^{-1}
$C_n = \frac{N}{\bar{q}Sb}$	Yawing moment coefficient	
$C_{n_p} = \frac{\partial C_n}{\partial(\frac{pb}{\partial U_1})}$	Variation of yawing moment coefficient with roll rate	
$C_{n_r} = \frac{\partial C_n}{\partial(\frac{rb}{\partial U_1})}$	Variation of yawing moment coefficient with yaw rate	
$C_{n_\beta} = \frac{\partial C_n}{\partial \beta}$	Variation of yawing moment coefficient with sideslip angle	rad^{-1}

Symbol	Definition	Usual Dimension
$C_{n_{\delta_A}} = \frac{\partial C_n}{\partial \delta_A}$	Variation of yawing moment coefficient with aileron angle	deg^{-1} or rad^{-1}
$C_{n_{\delta_R}} = \frac{\partial C_n}{\partial \delta_R}$	Variation of yawing moment coefficient with rudder angle	deg^{-1} or rad^{-1}
$C_Y = \frac{Y}{\bar{q}Sb}$	Side force coefficient	
$C_{Y_p} = \frac{\partial C_Y}{\partial (\frac{pb}{\partial U_1})}$	Variation of side force coefficient with roll rate	
$C_{y_r} = \frac{\partial C_y}{\partial (\frac{rb}{\partial U_1})}$	Variation of side force coefficient with yaw rate	
$C_{y_\beta} = \frac{\partial C_y}{\partial \beta}$	Variation of side force coefficient with sideslip angle	rad^{-1}
$C_{y_{\delta_A}} = \frac{\partial C_y}{\partial \delta_A}$	Variation of side force coefficient with aileron angle	deg^{-1} or rad^{-1}
$C_{y_{\delta_R}} = \frac{\partial C_y}{\partial \delta_R}$	Variation of side force coefficient with rudder angle	deg^{-1} or rad^{-1}
$C_T = \frac{T}{\bar{q}S}$	Thrust coefficient	

Symbol	Definition	Usual Dimension
$C_{T_u} = \frac{\partial C_T}{\partial(\frac{u}{U1})}$	Variation of thrust coefficient with speed	
C_w	Linearized boundary condition	
C_z	Linearized boundary condition coefficients	
C_θ	Linearized boundary condition coefficients	
d	Distance from thrust line to vertical center of gravity	
D	Drag	N
$\{D_i\}$	Aerodynamic lag coefficient matrix	
f	Force	$Kg\text{-}m/sec^2$
F_f	Fourier transform of f	
$\bar{F}_f$	Complex conjugate of the Fourier transform of f	
g	Acceleration of gravity	m/sec^2
G_i	Aerodynamic lag terms due to gust	
$G_o(s)$	Zero Order Hold	
$\ddot{h}$	Vertical acceleration	m/sec^2
H_z	Frequency response function	
I_{xx}	Moments of inertia about X axis	$Kg\text{-}m^2$
I_{yy}	Moments of inertia about Y axis	$Kg\text{-}m^2$
I_{zz}	Moments of inertia about Z axis	$Kg\text{-}m^2$

Symbol	Definition	Usual Dimension
K	gain constant	
m	mass	Kg
M	Pitching moment	N - m
M	Mach number	
p	Perturbed roll rate	rad/sec
q	Generalized coordinate	
q	Perturbed pitch rate	rad/sec
$\bar{q}$	Dynamic pressure	N/m^2
r	Perturbed yaw rate	rad/sec
$[R_i]$	Aerodynamic lag coefficient matrix for vertical gust	
$[R_o]$	Aerodynamic stiffness coefficients for vertical gust	
s	Laplace variable	sec^{-1}
S	Reference area	m^2
T_{2_p}	Time to double the amplitude in phugoid mode	sec

Symbol	Definition	Usual Dimension
T_{γ_1}	Numerator time constant in the γ/δ_E transfer function	sec
u	Perturbed forward velocity	m/sec
U_o, U_1	Freestream velocity	m/sec
V	Velocity	m/sec
V_H	Volume coefficient	m/sec
w	Weight	Kg
w_g	Vertical gust velocity	m/sec
$\{X\}$	State vector	
$\{\dot{X}\}$	State Derivative vector	
$\bar{X}_{cg} = \frac{X_{cg}}{\bar{c}}$	Nondimension center of gravity location	
$\ddot{\gamma}_f$	Acceleration due to force f	
$\ddot{\gamma}_n$	Acceleration due to random force (noise)	

Greek Symbols	Definitions	Usual Dimensions
α	Angle of attack	rad deg
α_1	Trimmed angle of attack	rad deg
β	Prandtl-Glauert transformation	
β	Sideslip angle	rad deg
ϕ	Bank angle, spectral density	rad deg
ν	Real part of z-plane complex root	
μ	Imaginary part of z-plane complex root	
ω	Frequency, rotational velocity	rad/sec hertz
ω_n	Undamped natural frequency	rad/sec hertz
ω_d	Damped frequency	rad/sec hertz
Λ	Sweep angle	rad deg
δ_A	Actuator command	deg rad
δ_D	Differential tail deflection	
δ_E	Elevator angle	deg rad
δ_R	Rudder angle	rad deg

Symbol	Definition	Usual Dimension
δ_S	Surface deflectionangle	rad deg
δ_T	Thrust command	% rpm
$\eta_H = \frac{\bar{q}_H}{\bar{q}}$	Dynamic pressure ratio at horizontal tail	
ρ	Air density	Kg/m^3
γ	Flight path angle	rad
θ	Pitch attitude angle	rad
ζ	Damping ratio	
σ_w	Mean square value of vertical gust velocity	m/sec

Subscripts

A	Actuator
T	Thrust
i	ith component or row
j	jth component or column
1	Trimmed
M	Mach number

Subscript	Definition
wb	Wing body
ref	Reference
H	Horizontal tail
d	Differential tail
ac	Aerodynamic center
cg	Center of gravity
$.25\bar{c}$	Quarter chord point
E	Elevator
P	Phugoid
sp	Short period
s	Stability axis
R	Roll
S	Spiral
D	Dutch roll

Computer Plot Labels	Definition	Usual Dimensions
THADDOT = $\ddot{\theta}$	Rigid body pitch mode acceleration	g's
Q1DDOT = $\ddot{q}_1$	First wing structural mode acceleration	g's
Q2DDOT = $\ddot{q}_2$	Fuselage structural mode acceleration	g's
Q3DDOT = $\ddot{q}_3$	Second wing structural mode acceleration	g's
Q4DDOT = $\ddot{q}_4$	Third wing structural mode acceleration	g's

Computor Plot Labels	Definition	Usual Dimension
Q6DDOT = $\ddot{q}_6$	Fourth wing structural mode acceleration	g's
Q8DDOT = $\ddot{q}_8$	Fifth wing structural mode acceleration	g's
DS	Wing control surface deflection	rad
ALPGUST = $\frac{w_g}{U_o}$	Gust angle of attack	rad
DA	Wing actuator command	rad
REAL	Real part of frequency response transfer function	
IMAGINARY	Imaginary part of frequency response transfer function	
PSD	Power Spectral density	
HDDOT = $\ddot{h}$	Total acceleration	g's

CHAPTER I

INTRODUCTION

The increasing cost of fuel is exerting great pressure on aircraft manufacturers to develop more energy efficient aircraft. Many of the refinements and improvements necessary in achieving more efficient aircraft will be by applications of Active Controls Technology (ACT). In this concept aircraft efficiency improvements are made by the increased dependence on augmentation control systems.

The largest benefit of active controls will occur when the design process incorporates ACT concepts into airplane configurations at the preliminary design stage. However, this change in design philosophy is not likely to occur until much more reliability is achieved in predicting aerodynamic and structural characteristics accurately. The aircraft industry is relying on government and military funded research to advance the technology needed to enable reliable predictions of aerodynamic, structural, and control system behavior.

Of all ACT concepts, flutter suppression has the highest technical risk. The consequences of a design error from a safety standpoint are catastrophic. The National Aeronautics and Space Administration (NASA) is actively pursuing applications of active controls in a technology development program that will provide the data which will

lead to a better understanding of unsteady aerodynamics and structural dynamics required to alleviate some of the risk in flutter suppression designs. Flight test evaluations of active flutter suppression controls will be performed in a program called DAST (Drones for Aeronautic and Structural Testing) which utilizes a highly modified BQM-34E/F Firebee II supersonic target drone as a testbed.

Flutter Suppression Systems (FSS) have been demonstrated on exisiting aircraft such as the B-52 CCV (reference 1) but these have had known and well defined flutter modes. What makes the DAST program unique is the fact that the FSS is designed to suppress a flutter mode whose characteristics have only been predicted analytically.

The objectives of the flight test activity for the flutter suppression experiment, known as DAST I, are:

- Validate active controls technology for flutter suppression,
- Enhance and verify transonic flutter prediction techniques.

A secondary objective is to provide a data base for transonic aerodynamic loads prediction techniques for elastic structures.

The validation of ACT for flutter suppression will be accomplished by demonstrating in flight a 20 per cent increase in the flutter speed of a transonic flutter critical wing and correlate the results with theoretical data.

Only in the relatively recent past have attempts been made to analytically predict flutter characteristics in the transonic speed range. The flight test activity of the DAST program will provide the data needed for evaluation of the developing transonic flutter prediction techniques.

This report will describe the development of the DAST I aircraft and some of the unique aspects of testing this vehicle.

Chapter 2 will provide a description of the DAST I remotely piloted research vehicle (RPRV) and the support requirements for flight operations. In Chapter 3 the predicted flutter and rigid body flight characteristics are presented. The synthesis of the flutter suppression control system, the primary flight control system, and the back-up autopilot are described in Chapter 4. Chapter 5 describes the hardware and software implementation of the DAST I vehicle systems.

The preparation for the flight testing phase of the DAST program is presented in Chapter 6. This includes a discussion of testing philosophy and methods. A simulation of the flexible and rigid body modes of the DAST I aircraft is used to evaluate the near-real time testing procedures that will be used for the FSS flight experiment.

The conclusions of this report are presented in Chapter 7 along with recommendations for further study.

Numerous individuals from several organizations support the DAST program. Those supplying information and support in the preparation of this report are acknowledged below:

Mr. Harold N. Murrow, NASA, Langley Research Center (LaRC), Program Manager: DAST I supercritical wing design and project support.

Mr. Donald H. Gatlin, NASA Dryden Flight Research Center (DFRC), DFRC Program Manager: Flight Operations.

Mr. Dwain A. Deets, NASA DFRC, Chief, Systems Analysis Branch: Technical monitor on this project report.

Dr. John W. Edwards, NASA DFRC: Flutter suppression system flight test requirements.

Mr. Larry W. Abbott, NASA DFRC: RPRV electronics design.

Mr. Gary Hodges, Boeing Wichita Company (BWC): Flutter suppression system design.

The author, David L. Grose, participated in the DAST program at NASA DFRC as Doctor of Engineering candidate from the University of Kansas. The following responsibilities reflect his involvement in the DAST program:

- Development of the DAST ARW-1 rigid body characteristics and their adaptation into the real-time simulator.
- Design and development of the control laws of the primary digital flight and analog backup control system.
- Development of a state variable aeroelastic representation of the DAST ARW-1 and flutter suppression system to generate simulated accelerometer responses.
- Investigation of candidate flight flutter testing technique using the simulated flutter data.

Flight testing of the DAST I is scheduled to begin in the spring of 1979. It is a scheduled six flight program.

CHAPTER 2

OPERATIONAL APPROACH

A description of the DAST I vehicle and its support requirements are presented in this chapter. The vehicle's estimated operating envelope is defined and a description of the remotely augmented control mode is given. The basic elements involved in flight testing this aircraft are presented.

2.1 Test Vehicle Description - The flight testing phase of the DAST I program will involve a highly modified BQM-34E/F supersonic target drone shown in figure 2.1. This vehicle has a supercritical wing (SCW), designed to flutter within the operating envelope of the aircraft, in place of the standard drone wing. The wing, called ARW-1 (Aeroelastic Research Wing - 1), is a 3/8 scale of the F-8 SCW (reference 2) which is representative of possible transport aircraft wings designed to cruise at near sonic velocity. Small control surfaces on the trailing edge of the wing near the tip are utilized in the active flutter suppression system.

No external modification to the DAST fuselage was required, however, extensive internal changes for the new avionics and other systems have been made. The internal system changes are listed below:

- Addition of FSS electronic and hydraulic

WING
GROSS AREA 2.79 SQUARE METERS
AIRFOIL SUPERCRITICAL T/C 11% ROOT 7% TIP
ASPECT RATIO 6.6
TAPER RATIO 0.38

TAIL-HORIZONTAL
GROSS AREA 0.845 SQUARE METERS(0.511 EXPOSED)
AIRFOIL NACA-65003.5 (MODIFIED) TIP
NACA-65006 (MODIFIED) ROOT
ASPECT RATIO 3.6
TAPER RATIO 0.40
INCIDENCE ALL-MOVEABLE
STABILIZER HINGE AXIS XF=369.56

TAIL-VERTICAL
GROSS AREA 0.804 SQUARE METERS
AIRFOIL NACA 66-003 (MODIFIED)
ASPECT RATIO (GEOMETRIC) 1.2
TAPER RATIO 0.30
RUDDER HINGE AXIS 65% CHORD
RUDDER AREA 0.67 SQUARE METERS

POWER PLANT
CONTINENTAL(YJ69-T-6 CAE MODEL 356.34)
RATED THRUST 8184.73 NEWTONS SEA LEVEL STATIC

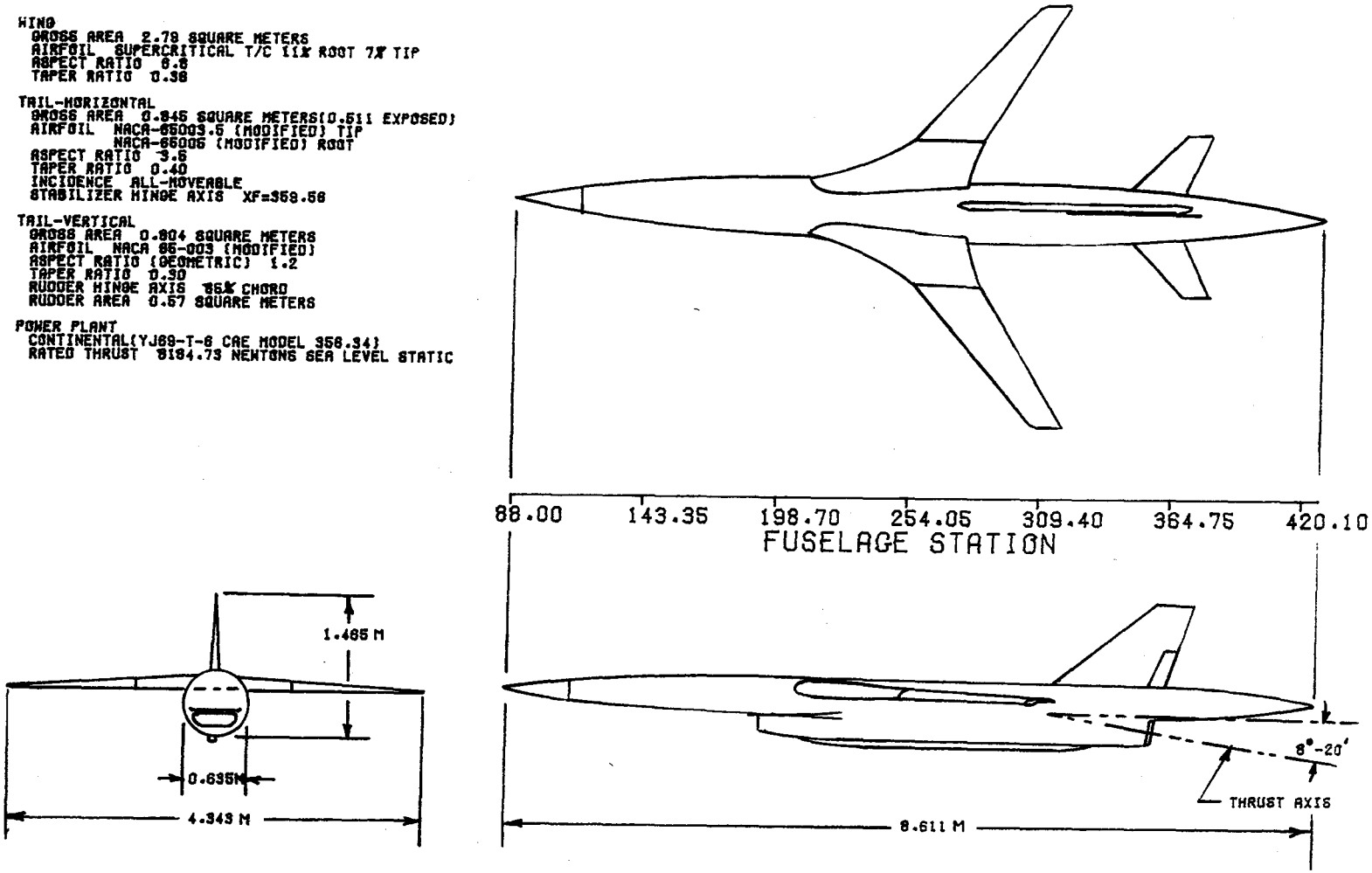

FIGURE 2.1 BQM-34E/F DRONE THREE VIEW WITH SUPERCRITICAL WING (DAST I)

systems.

- Replacement of the wing tip antennas with wrap-around nose cone antenna.
- Replacement of the standard drone discrete autopilot with a simplified analog proportional system.
- The addition of avionics for primary digital proportional remotely augmented control system.
- Replacement of standard vehicle sensors with new instruments and PCM systems.

Further details on these hardware changes are presented in Chapter 5.

The DAST I estimated flight envelope is seen in figure 2.2. This performance envelope is based on the engine capabilities defined in reference 3 and drag characteristics estimated from wind tunnel tests of a 1/6 scale DAST I model. Drag information at Mach numbers greater than 0.98 are based on data from the F-8 SCW aircraft (reference 2). The 80 per cent throttle operating minimum seen in figure 2.2 is a placard based on safe continuous engine operating conditions. An unsteady pitch-up occuring at high angles of attack will occur above the placard also indicated in figure 2.2. Although the DAST I has the capability to fly supersonically, no plans exist to fly the aircraft at speeds greater than M = 0.98.

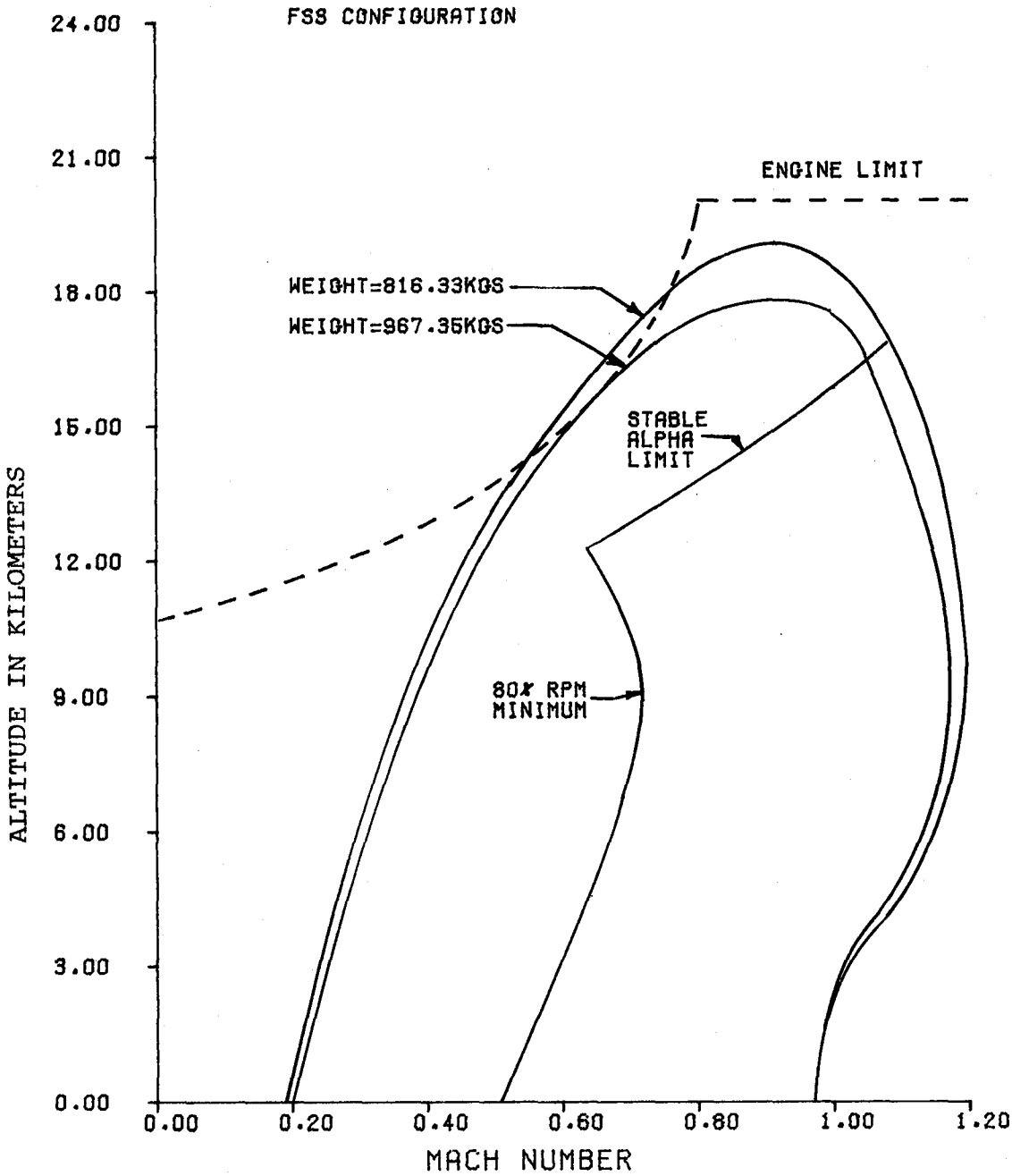

FIGURE 2.2 DAST I ESTIMATED OPERATING ENVELOPE

The vehicle can carry 138.32 kilograms of fuel which gives it a flight time duration of approximately one hour at high altitudes. The fuel consumption rates increase dramatically at altitudes below 7,600 meters, however, and flight time duration at 3048 meters and M = 0.98 is only approximately 13 minutes.

2.2 Description of RPRV Operations - The support requirements to operate the DAST I as a RPRV at NASA DFRC are listed below:

- RPRV launch aircraft
- RPRV ground facility
- Secondary command station
- RPRV recovery vehicle

Each of these elements are described in Sections 2.2.1 through 2.2.4.

The advantages of the RPRV testing technique are demonstrated in high risk experiments such as the DAST I program. The development costs of full scale manned aircraft are eliminated by building simplified subscale RPRV's which if destroyed, neither risk the pilot nor result in a large financial loss. Public safety is not jeopardized because of the remote testing site at NASA DFRC in the Mojave Desert in California. Flexibility in critical flight systems is achieved by utilizing the facilities already developed in the remote augmented vehicle (RAV) concept.

2.2.1 RAV Concept - The primary flight control system for the DAST I will be by remote augmentation. In this concept the control laws which augment the flying characteristics of the aircraft are programmed in FORTRAN in a general purpose computer on the ground. Closed loop operation is achieved by a telemetry uplink/downlink between the vehicle and the ground facility. This operation is illustrated in figure 2.3. The pilot has a full instrument display in the ground cockpit and plot boards indicating the vehicle's flight pattern and altitude are available to indicate deviations in the flight plan. The details of the mechanization of the primary control system are given in sections 5.4 and 5.5.

The RAV concept has been successfully demonstrated on a 3/8 F-15 RPRV (reference 4) and as part of the F-8 Digital Fly-By-Wire aircraft presently being flown at NASA DFRC.

2.2.2 F-104 Secondary Command Station - Air Force requirements at the Edwards, California test range specify that all powered RPRV's need a secondary and independent command station in the event of a loss in the telemetry link between the ground station and the test vehicle. For the DAST program this function will be performed by a 2-seat F-104 chase aircraft. In the rear seat of the F-104 a small control panel is installed from which the chase aircraft can command the DAST in much the same manner as the ground facility. However, only an uplink signal to the

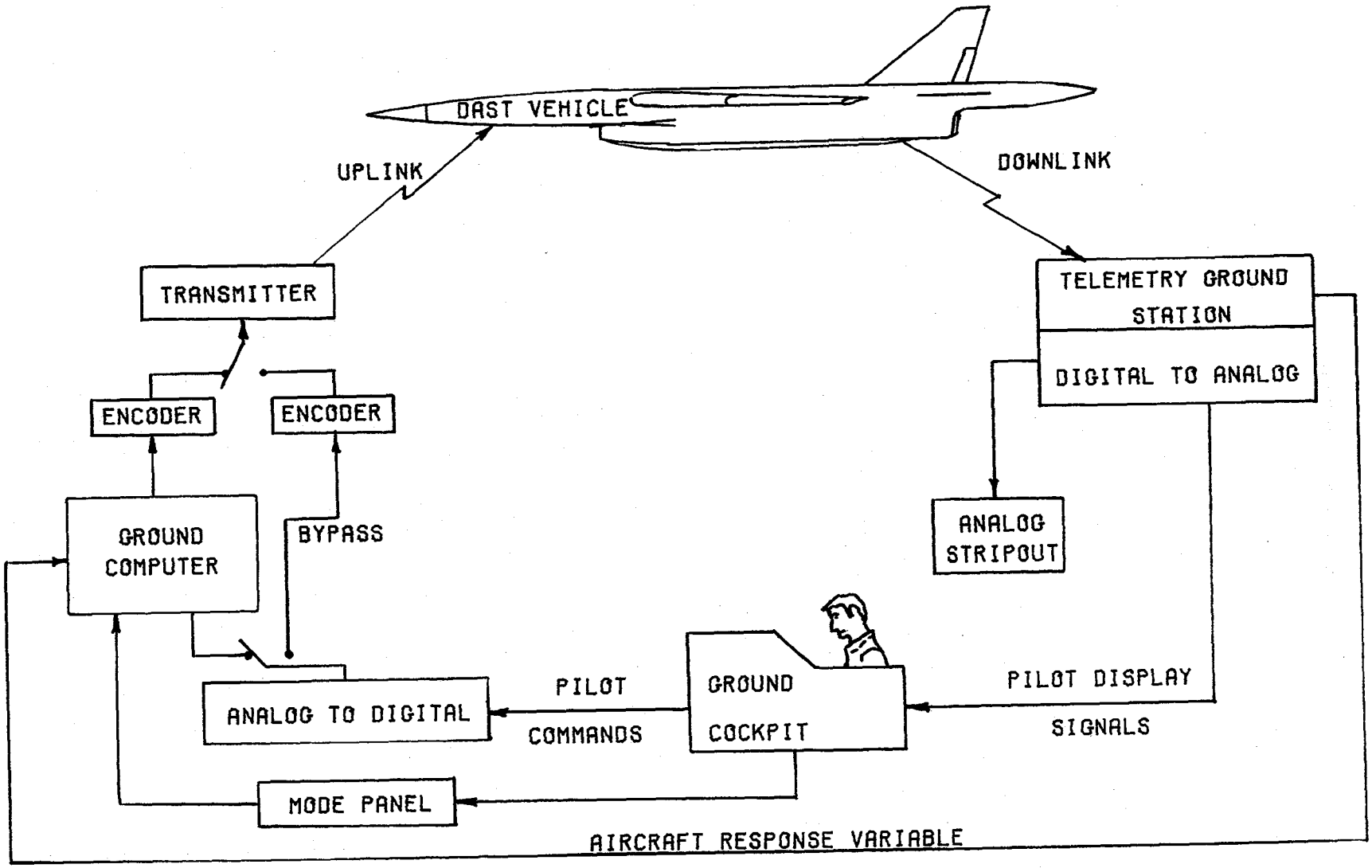

FIGURE 2.3 REMOTELY AUGMENTED VEHICLE CONCEPT

DAST is active. Stability augmentation is supplied by an on-board autopilot in the RPRV.

Figure 2.4 shows the range capability of the F-104 transmitter. Oil is ejected into the jet exhaust of the DAST to enhance visable tracking of the vehicle in the occurance that the chase plane loses sight of the DAST vehicle . The secondary command station will fly the RPRV to a recovery area since the loss of the telemetry command link terminates reception of the test data also.

2.2.3 B-52 Launch Aircraft - The basic drone was designed to be air launched from an aircraft or ground launched using jato rockets. The ARW-1 was not designed to withstand the stresses of ground launch so the DAST 1 will be air launched from a Boeing B-52 aircraft. This B-52 air launch capability was demonstrated with a basic Firebee vehicle. The basic Firebee vehicle is shown in figure 2.5 on the B-52 pylon just prior to launch.

A launch panel operator in the B-52 monitors the RPRV's systems and starts the drone's engine before the B-52 climbs above 3000 meters. When the RPRV has satisfied system checks performed by the ground facility, F-104 chase aircraft, and launch panel operator, the B-52 flies to the designated drop zone for launch. Before the vehicle is released from the pylon, the RPRV's fuel tanks are "topped off" to insure that the vehicle is released with full tanks.

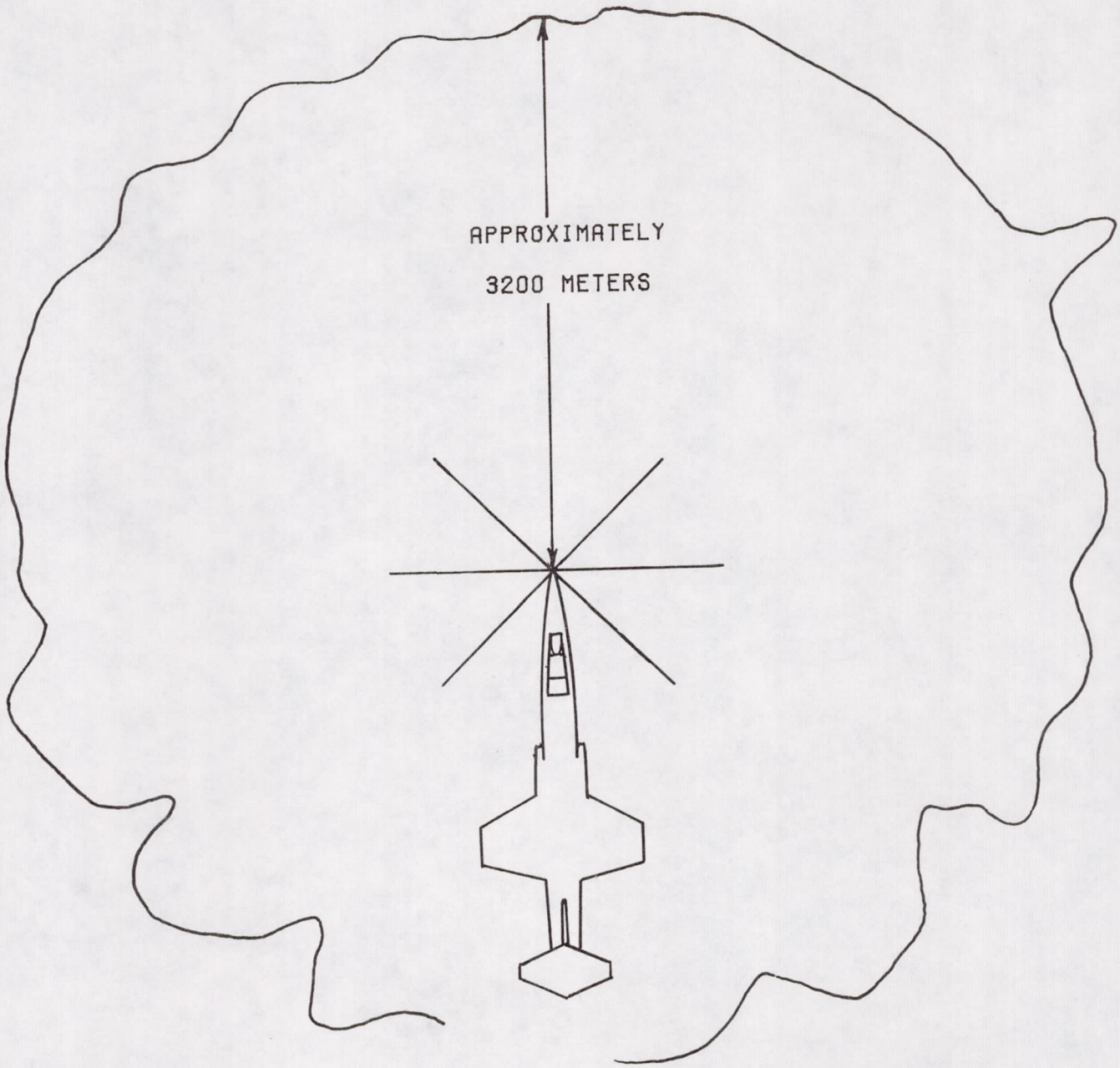

FIGURE 2.4 F-104 SECONDARY COMMAND STATION RANGE

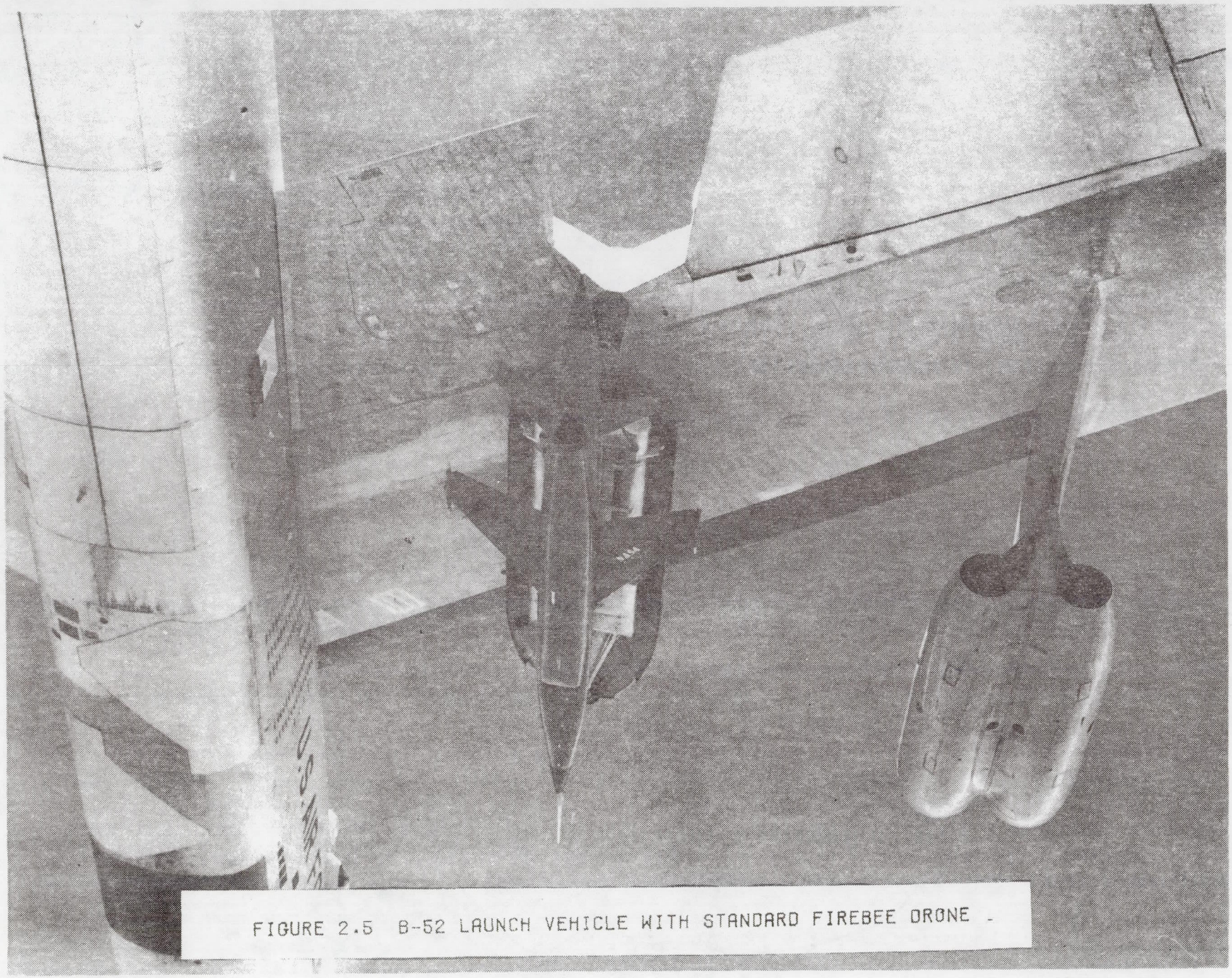

FIGURE 2.5 B-52 LAUNCH VEHICLE WITH STANDARD FIREBEE DRONE

The RPRV is launched with its tail surfaces locked in a nose down command for the first three seconds after release. This precaution is to guarantee adequate separation from the B-52.

2.2.4 Mid-Air Recovery - The DAST I flights will terminate in a mid-air recovery (MARS) of the vehicle by helicopter. At the end of a flight or if an emergency occurs the vehicle's recovery mode is activated. This starts the sequence listed below:

1. Vehicle is transferred to autopilot control.
2. Engine shutdown.
3. The vehicle begins a moderate climb.
4. Drogue chute deployment and systems shutdown.
5. Main chute deployment.
6. Helicopter capture of the drogue chute tow line.

This procedure is illustrated in figure 2.6. Events 1 and 3 serve the purpose of starting internal timers and slowing down the aircraft. If speed requirements have been met ($M < .94$) at the expiration of the drogue chute timer, the drogue chute is deployed and the vehicle's systems are turned off. Main chute deployment occurs when a second timer expires and the vehicle descends below 4570 meters.

If a safety timer expires and events 4 or 5 have not taken place, the command to deploy the chutes is given regardless of flight conditions. Air Force experience with MARS technique has demonstrated an 80 percent success rate.

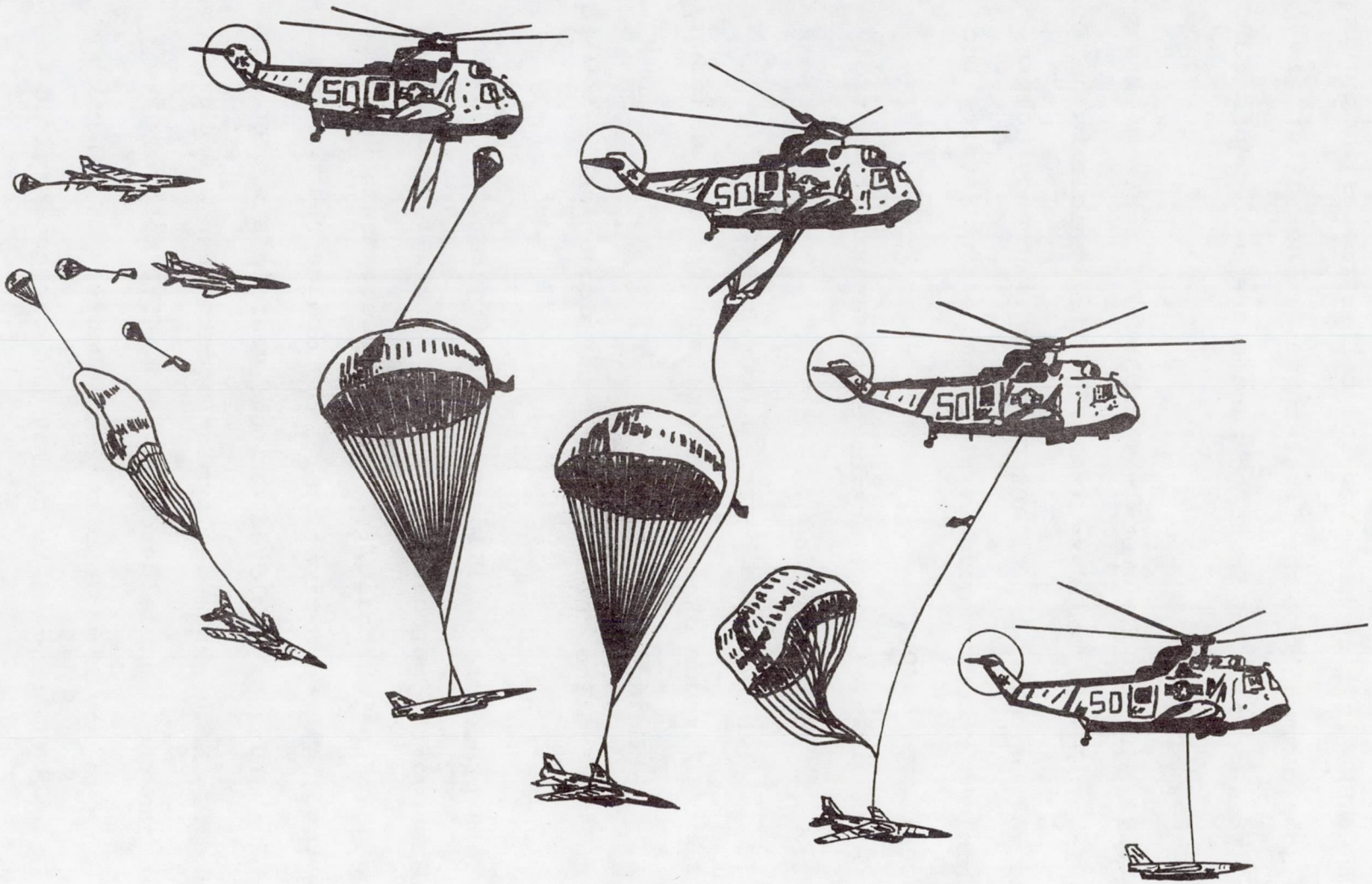

FIGURE 2.6 MID-AIR RECOVERY SEQUENCE

CHAPTER 3

PREDICTED UNAUGMENTED CHARACTERISTICS

This chapter presents the information defining the predicted flutter and rigid body characteristics of the DAST I vehicle. These estimates have increased signifiance in the DAST flight test program since the active controls and flight controls were designed for these predicted characteristics. The planning for the flight tests will be done under the assumption that the estimated characteristics are accurate enough to preclude the requirement for further definition.

3.1 ARW-1 Flutter Characteristics - Flutter is an aeroelastic phenomena characterized by a dynamic instability occuring in flight when the elasticity of the structure plays an essential part in the instability. The DAST I wing has been designed so that flutter will occur within its operating envelope. The problem of predicting the flutter characteristics and designing the FSS involves an accurate determination of the ARW-1 structural and unsteady aerodynamic characteristics.

The development of the analytical model of the unsteady airloads and equations of motion are described in section 4.1.1. The representation of the DAST I structure used in the analysis is described below.

3.1.1 Structural Dyanmics - The DAST I wing structure

consists of two machined steel spars, formed aluminum ribs spaced 30.84 centimeters apart, and fiberglass skins. A more detailed description of the wing is given in section 5.1.

The vibration model for this wing that was used in the analysis was a NASA supplied NASTRAN model of the wing and wing center section structure. The ARW-1 idealization included:

1. The removeable leading and trailing edge fiberglass structure, constructed of elements providing stiffness only for translational degrees of freedom.
2. The ARW-1 skins were modeled as shear elements with axial rods added to supply the membrane stiffness.
3. The wing center section was modeled as horizontal beam and plate elements.
4. The fuselage and empennage were modeled as beam elements with body mass represented as lumped masses.

An illustration of this DAST structural model is shown in figure 3.1. The NASTRAN data for ARW-1 is found in reference 5. However, several changes were required to this NASTRAN model to more accurately describe the actual vehicle. The fuselage attachment of the wing was improved and places where the wing was very thin, foam core was

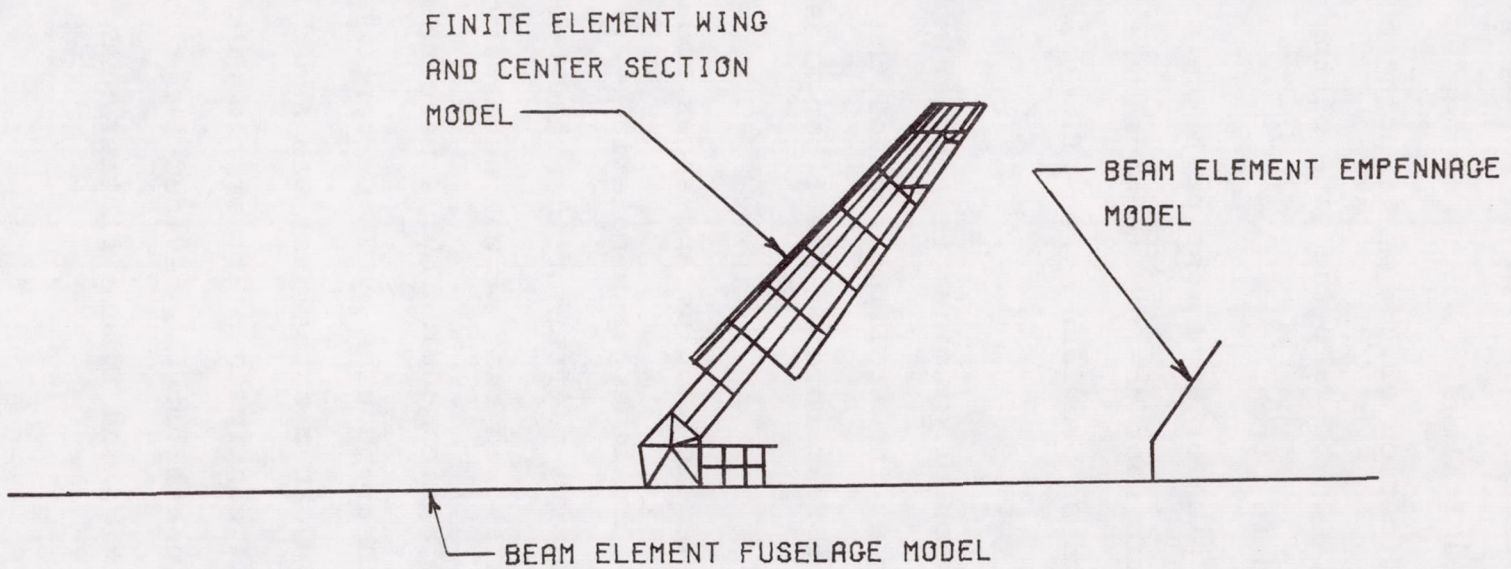

FIGURE 3.1 DAST I STRUCTURAL MODEL

added to provide stiffness. A summary of improvements made in the NASTRAN model follows:

1. Modification of the multi-point constraint equations to make the side of the fuselage rigid in pitch.
2. Extension of spar webs past the solid aluminum rib near the tip to model the vertical stiffness provided by the fiberglass tip's foam core.
3. Addition of aluminum triangular membrane elements at the trailing edge of the ribs to model the foam core of the fiberglass trailing edge.
4. The elastic modulus and shear modulus of the wing skin fiberglass material was found to be considerably different than had been estimated. Tests showed that it was necessary to decrease the elastic modulus by 14 percent and increase the shear modulus by 26 percent.
5. A 0.907 Kg mass ballast was added approximately 8.4 centimeters aft of the wing tip rib to compensate for the revised fiberglass characteristics and insure flutter within the flight envelope.

Vibration solutions for three rigid body modes and ten elastic modes were found for both symmetric and antisymmetric

conditions. The predicted vibration modes are presented in Table 3.1 and 3.2. These values are compared to the preliminary results of a ground vibration test (GVT) conducted at NASA LaRC. Reasonable agreement exists between the ARW-1 modes but considerable discrepancies occurred in the fuselage modes. The fuselage used in the GVT was that of the basic drone with standard equipment. The measured fuselage modes were also in considerable disagreement with GVT tests done on numerous standard drones for the military. For this reason, no modifications to the fuselage structural model will be done until further testing determines the source of discrepancies in the LaRC GVT.

3.1.2 Flutter Boundary - The flutter mechanism of ARW-1 is a coalesence of the first and second wing modes. Both symmetric and anti-symmetric flutter modes exist with ARW-1. Root contours showing the two wing modes involved in the flutter are shown in figures 3.2 and 3.3. The symmetric flutter mode locus also shows a vertical bending fuselage mode at approximately 20 hertz. It was included in the flutter analysis due to its correspondence to the flutter frequency. Figure 3.2 shows that the fuselage mode is slightly de-stabilized but does not become divergent before the wing flutter mode.

The ARW-1 flutter characteristics are described as explosive in nature. This is evident in figure 3.2 when the de-stabilizing movement of the wing roots are compared

TABLE 3.1 MODE DESCRIPTION - SYMMETRIC

ELASTIC MODE	FREQUENCY - HZ		DESCRIPTION
	ANALYSIS	GVT	
1	9.1	9.8	WING VERTICAL BENDING
2	19.3	16.6	FUSELAGE BENDING
3	29.9	30.9	WING
4	34.1		WING
5	46.1		FUSELAGE BENDING
6	48.9	49.2	WING VERTICAL BENDING AND TORSION
7	65.6	43.1	STABILIZER VERTICAL BENDING
8	77.0		WING TORSION
9	79.8		MIXED
10	112.7		MIXED

TABLE 3.2 - MODE DESCRIPTION - ANTISYMMETRIC

ELASTIC MODE	FREQUENCY - HZ		DESCRIPTION
	ANALYSIS	GVT	
1	12.5	14.2	WING VERTICAL BENDING
2	26.5	20.0	FUSELAGE BENDING
3	31.7	33.3	WING
4	34.6		FIN BENDING AND FUSELAGE TORSION
5	36.3	27.8	FIN BENDING
6	49.7	50.9	WING
7	54.5		STABILIZER VERTICAL BENDING
8	62.8		FUSELAGE BENDING
9	79.2		EMPENNAGE
10	81.2		MIXED

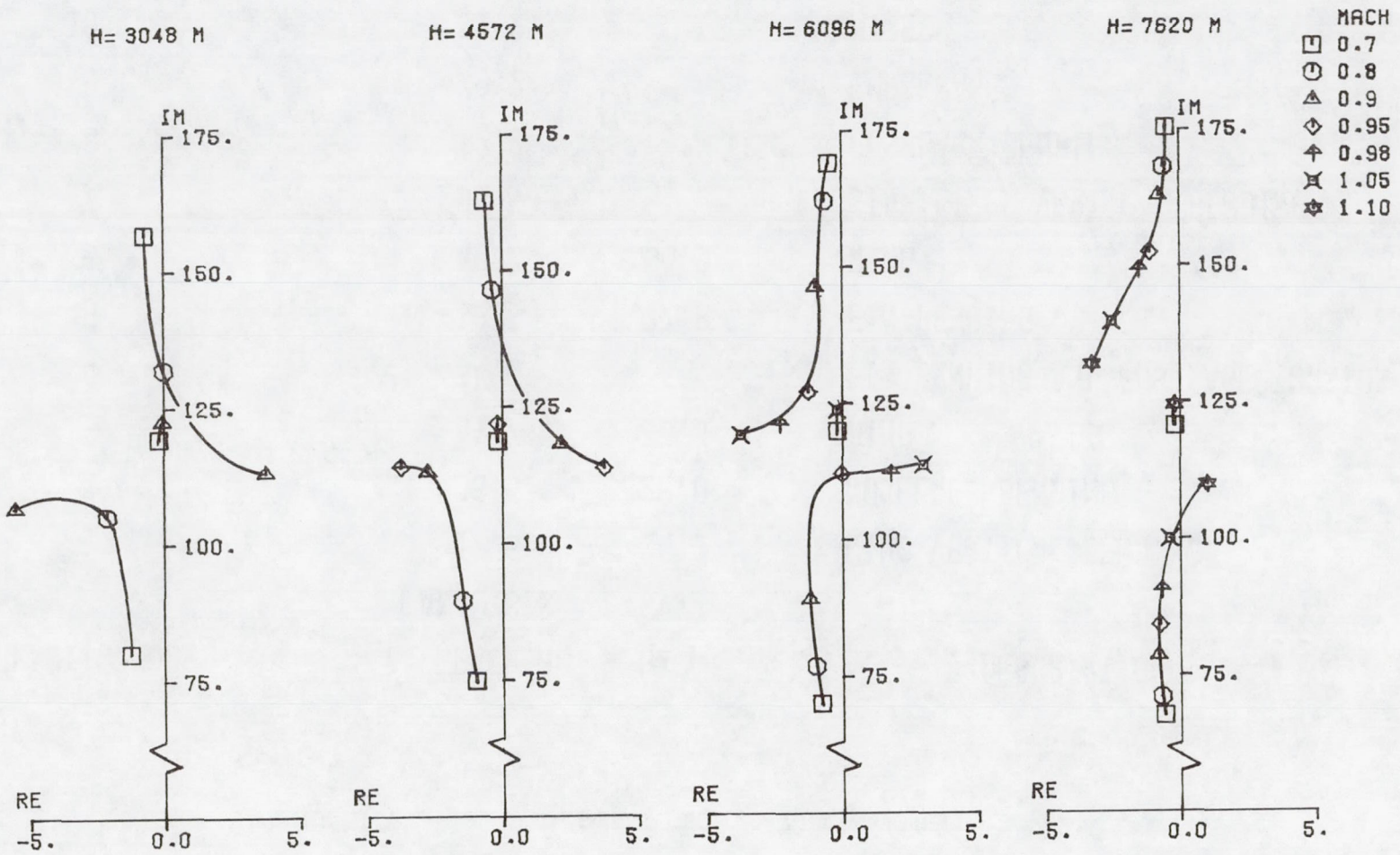

FIGURE 3.2 DAST I SYMMETRIC FLUTTER MODE LOCUS

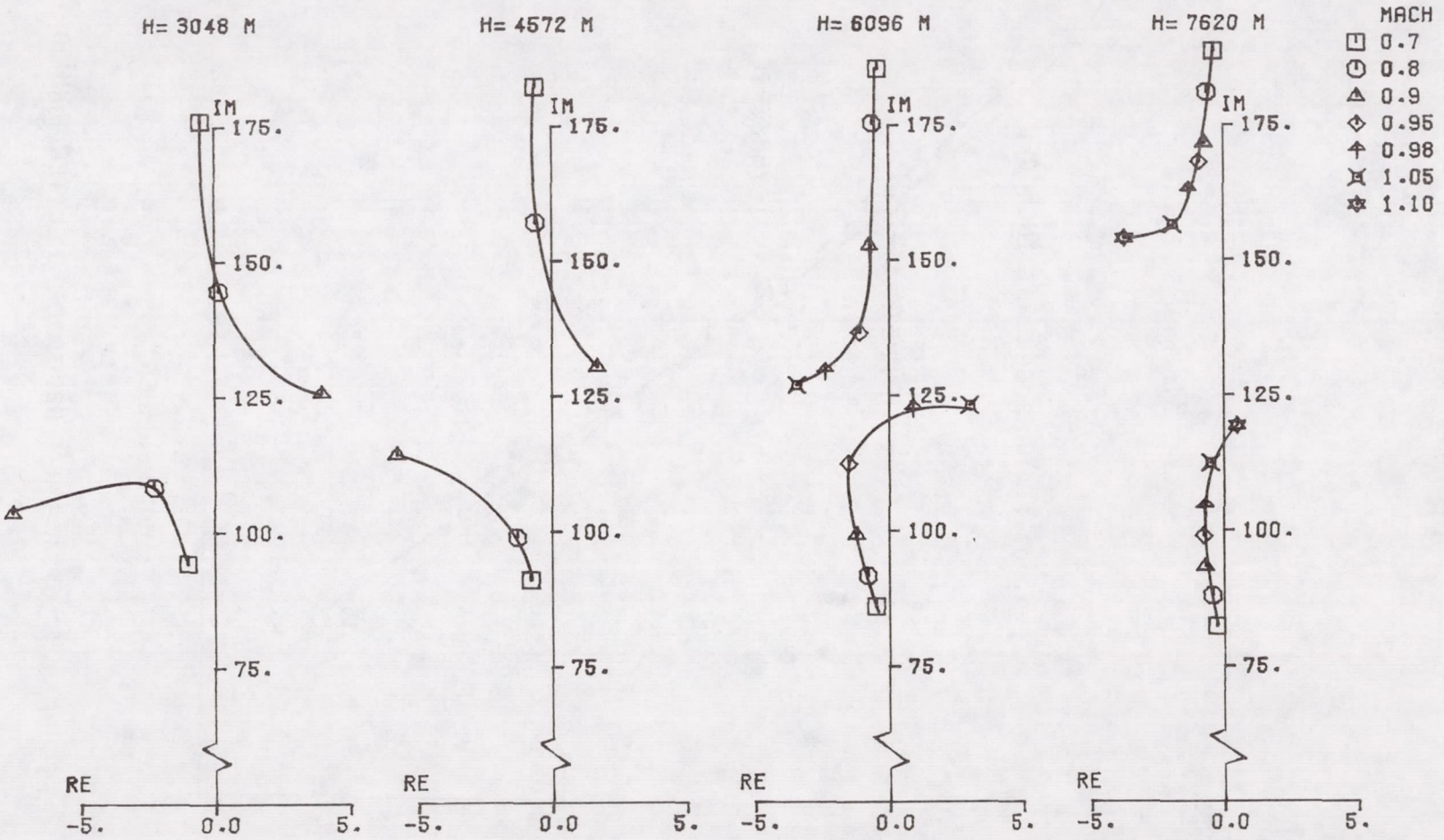

FIGURE 3.3 DAST I ANTI-SYMMETRIC FLUTTER MODE LOCUS

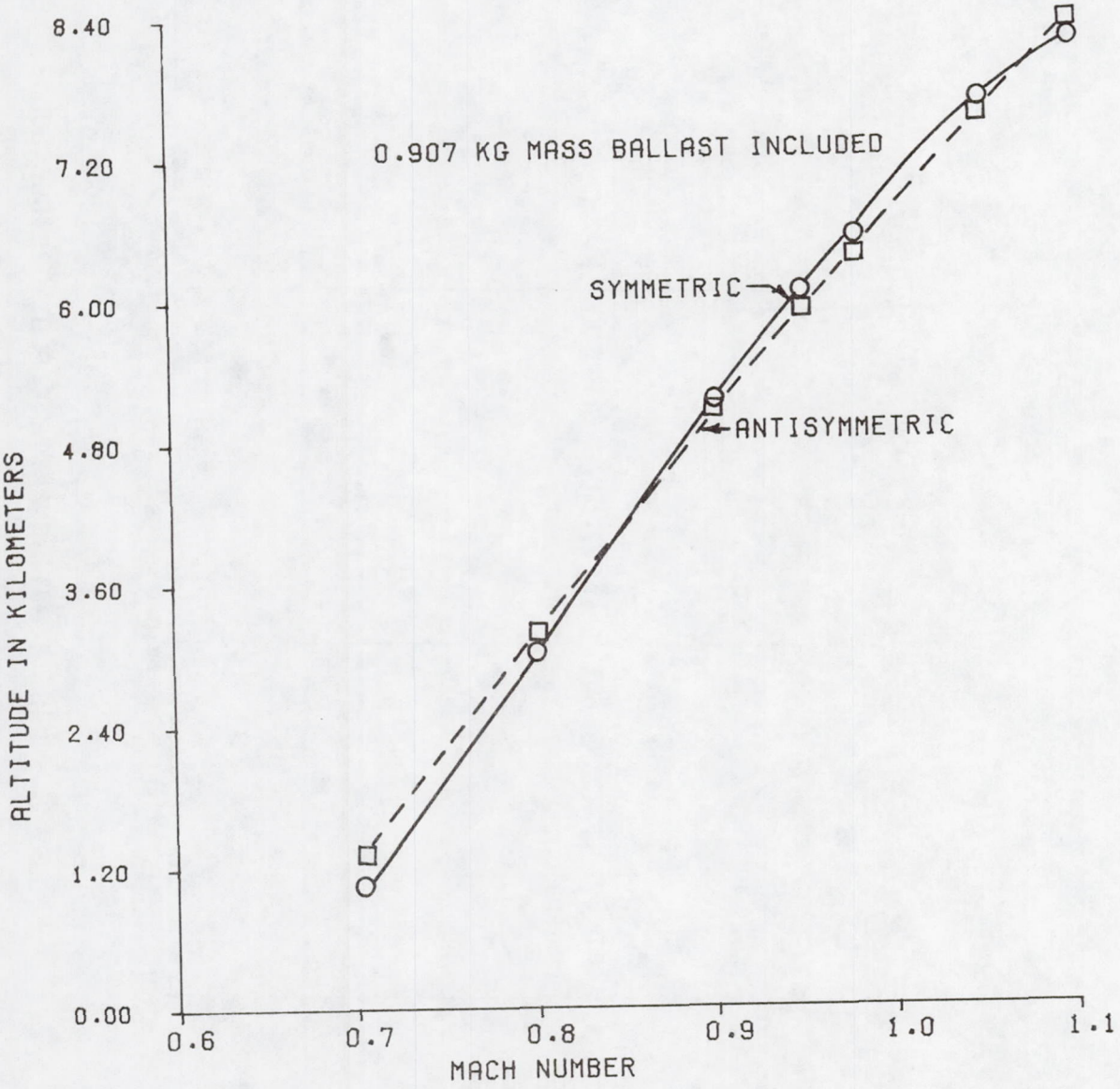

FIGURE 3.4 DAST ARW-1 PREDICTED FLUTTER BOUNDARY

to changes in Mach number. Small changes in Mach number result in large changes in the real and imaginary components of the elastic modes. Both the symmetric and anti-symmetric flutter characteristics are explosive in nature with the symmetric flutter occuring first at altitudes above 4270 meters and the anti-symmetric mode fluttering first below 4270 meters. This can be observed in figure 3.4.

It is interesting to note from figures 3.2 and 3.3 that at lower altitudes the second wing mode is the one which goes unstable while at the higher altitudes the wing bending mode encounters the instability. No instabilities in the higher frequency modes were predicted from the analysis .

3.2 DAST I Rigid Body Characteristics - The modification of the basic Firebee II flight simulator at NASA DFRC to account for the ARW-1 aerodynamics is described in this section. The digital six degree of freedom simulation required rigid body aerodynamic coefficients in a format defined by angle of attack and Mach number break points. This format allows for non-linear characteristics to be included. The data described in section 3.2.1 was used in the flight planning simulator and the flight controls system analysis of sections 4.2 and 4.3.

3.2.1 Aerodynamic Derivative Generation - The rigid body aerodynamic data for DAST I was generated from wind tunnel tests and Air Force DATCOM methods (reference 6).

Data on the F-8 SCW aircraft (reference 2) and the basic Firebee II drone (reference 3) were compared to the DAST I estimated values where applicable to generate confidence in the estimates. No flight manuevers are planned to collect performance or stability and control data unless significant discrepancies are encountered.

The 1/6 scale DAST I wind tunnel mode is shown in figure 3.5. Static derivatives from M = 0.4 to M = 0.98 were determined from tests on this model in the NASA LaRC 8-foot Transonic Dynamics Tunnel. The static derivative values were extended to M = 1.2 by extrapolating from trends observed in the F-8 SCW flight test results.

The static longitudinal data is presented in Appendices A.1.1 through A.1.3. Some general observations about the static longitudinal derivatives are summarized below:

1. The lift, drag, and pitching moment coefficients are non-linear in both angle of attack and Mach number.
2. The value of C_{L_α} can exceed 7.7 per radian at small angles of attack in the vicinity of M = 1.0.
3. A severe pitch-up characteristic can be expected because of a large positive value for C_{m_α} above approximately seven degree angle of attack.

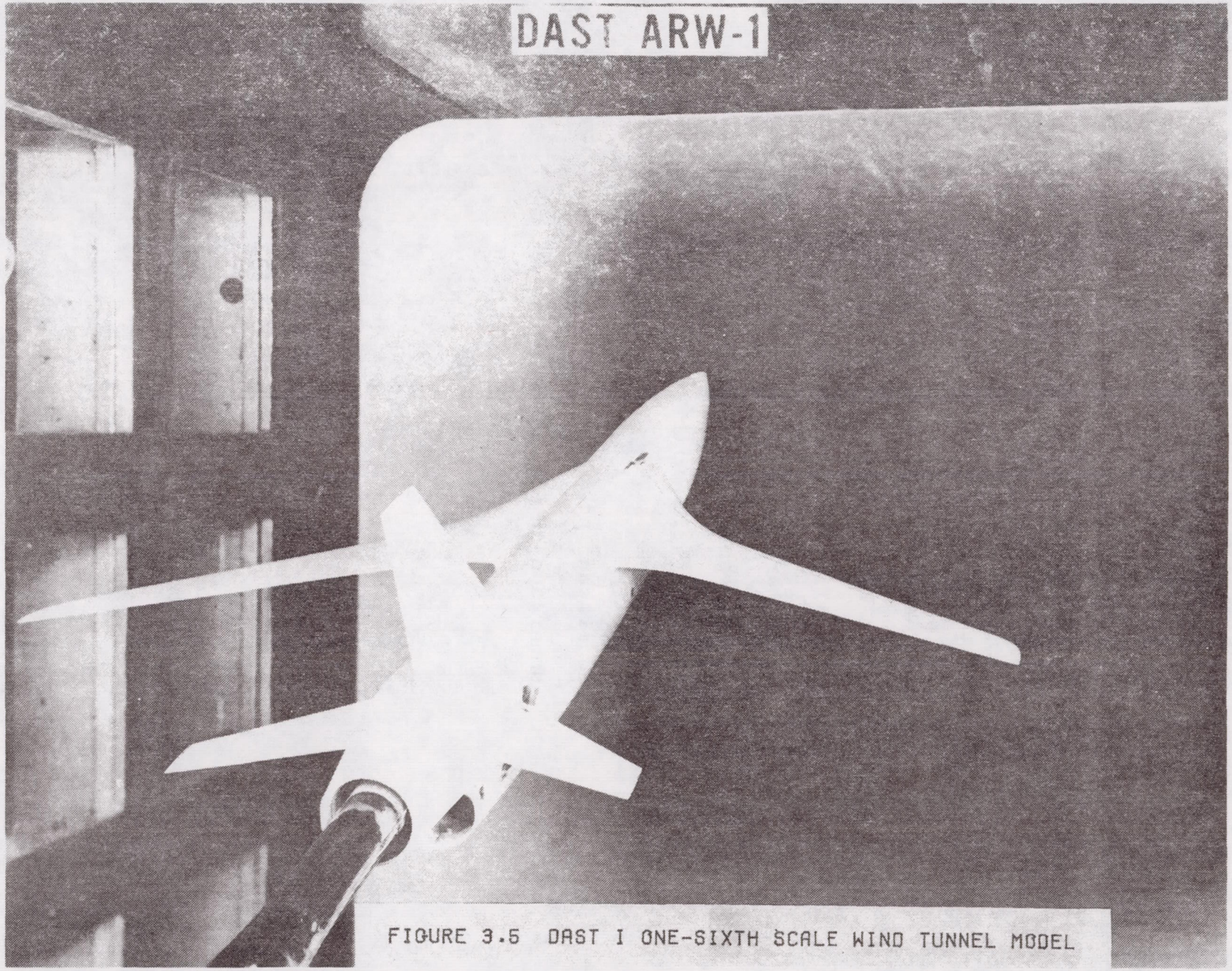

FIGURE 3.5 DAST I ONE-SIXTH SCALE WIND TUNNEL MODEL

4. The control surface effectiveness in the pitch axis at high Mach numbers is approximately twice the value seen on the basic drone configuration.

Some general comments on the static lateral-directional derivatives found in Appendices A.1.4 through A.1.6 are:

1. The yawing moment coefficient, C_n, is non-linear with respect to sideslip angle.
2. The rolling moment coefficient, C_ℓ, experiences rather large non-linearities at high angles of attack (above M = .80).
3. Non-linearities with angle of attack exist in C_n.
4. Significant non-linearities exist in both Mach number and angle of attack for:
   - C_{n_β}, C_{ℓ_β}
   - $C_{\ell_{\delta_R}}$
   - $C_{y_{\delta_a}}$, $C_{n_{\delta_a}}$
5. Derivatives non-linear with Mach number alone are:
   - $C_{y_{\delta_R}}$, $C_{n_{\delta_R}}$

The generation of the dynamic derivative estimates were accomplished using Air Force DATCOM procedures. The limiting Mach number for which the estimates are valid is M = .90.

The higher Mach number values were extrapolated from F8-SCW and Firebee II trends. The static derivative values generated in the wind tunnel tests were used in the DATCOM equation whenever appropriate.

The estimated dynamic derivatives and the equations used to determine them are presented in Appendix A.2.

General comments observed in this simulated data are:

1. Because the static derivatives were non-linear in either Mach number or angle of attack (or both), these trends appear in the dynamic derivatives as well.
2. The higher aspect ratio ARW-1 and increased sweep angle of the wing causes a considerable improvement in the longitudinal dynamic derivatives compared to the basic Firebee II.
3. Those lateral-directional derivatives where the vertical tail is the dominant contributor are very similar to the Firebee II values as should be expected.
4. The derivatives C_{n_p} and C_{ℓ_p} show considerable improvement from the Firebee II values due to the increased aspect ratio.
5. Yaw damping, C_{n_r}, is considerably decreased in comparison to the Firebee II, again due to the increased aspect ratio of ARW-1.
6. The variation in C_{ℓ_r} with angle of attack is

much greater for the DAST I than for the Firebee II.

Some confidence is obtained from these estimates when it is observed that the non-linearities that are evident in the DAST data were also observed in the F8-SCW.

3.2.2 Stability and Control Characteristics - The open loop flying characteristics for DAST I were defined based on the data presented in the previous section. The equations used in the longitudinal analysis were:

$$[C]\left\{\dot{X}\right\} = [A]\left\{X\right\} + [B]\left\{U\right\} \tag{3.1}$$

where

$$C = \begin{bmatrix} 1 & 0 & 0 & 0 \\ 0 & 1 - \frac{\bar{q}S\bar{c}W}{2gV^2} C_{L_\alpha} & 0 & 0 \\ 0 & -\frac{\bar{q}S\bar{c}^2}{2VI_{yy}} C_{m_\alpha} & 1 & 0 \\ 0 & 0 & 0 & 1 \end{bmatrix} \tag{3.2}$$

$$[A] = \begin{bmatrix} -\frac{\bar{q}Sg}{wV}\left[\left(C_{D_u} + 2C_D\right) - \left(C_{T_u} + 2C_T \cos\delta_T\right)\right] & \frac{-\bar{q}Sg}{w}\left(C_{D_\alpha} - C_L\right) & 0 & -g\cos\alpha_1 \\ -\frac{\bar{q}Sg}{wV^2}\left[\left(C_{Lu} + 2C_L\right) - \left(C_{T_u} + 2C_T \sin\delta_T\right)\right] & -\frac{\bar{q}Sg}{wV}\left(C_{L_\alpha} + C_D\right) & 1 - \frac{\bar{g}Sg\bar{c}}{2wV^2} C_{L_q} & -\frac{g\sin\alpha_1}{V} \\ \frac{\bar{q}S\bar{c}}{VI_{yy}}\left(C_{m_u} - C_{T_u}\frac{d}{\bar{c}}\right) & \frac{\bar{q}S\bar{c}}{I_{yy}} C_{m_\alpha} & \frac{\bar{q}S\bar{c}^2}{2VI_{yy}} C_{m_q} & 0 \\ 0 & 0 & 1 & 0 \end{bmatrix} \tag{3.3}$$

$$\left[B\right] = \begin{bmatrix} -\frac{\bar{q}Sg}{w} C_{D_{\delta_E}} \\ -\frac{\bar{q}Sg}{Vw} C_{L_{\delta_E}} \\ \frac{\bar{q}S\bar{c}}{I_{yy}} C_{m_{\delta_E}} \\ 0 \end{bmatrix} \tag{3.4}$$

$$\left\{X\right\}^T = \left\lfloor u \ \alpha \ q \ \theta \right\rfloor \tag{3.5}$$

The equations for the lateral-directional analysis are:

$$\left[C\right] = \begin{bmatrix} 1 & -I_{xz_s}/I_{xx_s} & 0 & 0 \\ -\frac{I_{xz_s}}{I_{zz_s}} & 1 & 0 & 0 \\ 0 & 0 & 1 & 0 \\ 0 & 0 & 0 & 1 \end{bmatrix} \tag{3.6}$$

$$\left[A\right] = \begin{bmatrix} \frac{\bar{q}Sb^2}{2VI_{xx_s}} C_{\ell_p} & \frac{\bar{q}Sb^2}{2VI_{xx_s}} C_{\ell_r} & \frac{\bar{q}Sb}{I_{xx_s}} C_{\ell_\beta} & 0 \\ \frac{\bar{q}Sb^2}{2VI_{zz_s}} C_{n_p} & \frac{\bar{q}Sb^2}{2VI_{zz_s}} C_{n_r} & \frac{\bar{q}Sb}{I_{zz_s}} C_{n_\beta} & 0 \\ \frac{\bar{q}Sgb}{2wV^2} C_{Y_p} & \frac{\bar{q}Sgb}{2wV^2} C_{Y_r} - 1 & \frac{\bar{q}Sg}{wV} C_{Y_\beta} & g/V \cos \alpha_1 \\ 1 & 0 & 0 & 0 \end{bmatrix} \tag{3.7}$$

$$\left[B\right] = \begin{bmatrix} \frac{\bar{q}Sb}{I_{xx_s}} C_{\ell_{\delta_A}} & \frac{\bar{q}Sb}{I_{xx_s}} C_{\ell_{\delta_R}} \\ \frac{\bar{q}Sb}{I_{zz_s}} C_{n_{\delta_A}} & \frac{\bar{q}Sb}{I_{zz_s}} C_{n_{\delta_R}} \\ \frac{\bar{q}Sg}{wV} C_{Y_{\delta_A}} & \frac{\bar{q}Sg}{wV} C_{Y_{\delta_R}} \\ 0 & 0 \end{bmatrix} \tag{3.8}$$

$$\left\{X\right\}^T = \begin{bmatrix} p & r & \beta & \phi \end{bmatrix} \tag{3.9}$$

The following center of gravity corrections have been included in equations (3.3), (3.4), (3.7), and (3.8). The prime terms represent the correct values:

$$C^1_{m_o} = C_{m_o} + C_{L_o}\left(\bar{X}_{cg} - .25\right)$$

$$C^1_{m_\alpha} = C_{m_\alpha} + C_{L_\alpha}\left(\bar{X}_{cg} - .25\right) \tag{3.10}$$

$$C^1_{m_{\delta_E}} = C_{m_{\delta_E}} + C_{L_{\delta_E}}\left(\bar{X}_{cg} - .25\right)$$

$$C^1_{m_q} = C_{m_q} - 2C_{m_\alpha}\left(\bar{X}_{cg} - .25\right)$$

$$C^1_{n_r} = C_{n_r} + \frac{2\bar{c}}{b}\left(\bar{X}_{cg} - .25\right)\left(C_{n_\beta} + \tfrac{1}{2}C_{Y_r} + C_{Y_\beta}\left(\bar{X}_{cg} - .25\right)\bar{c}/b\right)$$

$$C^1_{Y_r} = C_{Y_r} + \frac{2\bar{c}}{b}\left(\bar{X}_{cg} - .25\right)C_{Y_\beta}$$

$$
\begin{aligned}
C^{1}_{\ell_r} &= C_{\ell_r} + \frac{2\bar{c}}{b}\left(\bar{X}_{cg} - .25\right) C_{\ell_\beta} \\
C^{1}_{n_p} &= C_{n_p} + \frac{\bar{c}}{b}\left(\bar{X}_{cg} - .25\right) C_{y_p} \\
C^{1}_{n_\beta} &= C_{n_\beta} + \frac{\bar{c}}{b}\left(\bar{X}_{cg} - .25\right) C_{y_\beta} \\
C^{1}_{n_{\delta_R}} &= C_{n_{\delta_R}} + \frac{\bar{c}}{b}\left(\bar{X}_{cg} - .25\right) C_{y_{\delta_R}} \\
C^{1}_{n_{\delta_A}} &= C_{n_{\delta_A}} + \frac{\bar{c}}{b}\left(\bar{X}_{cg} - .25\right) C_{y_{\delta_A}}
\end{aligned}
\qquad (3.10)\ \text{(Continued)}
$$

The transformations listed above were exercised whenever the center of gravity differed from the 25 percent MAC that the aerodynamics were referenced to in the wind tunnel tests.

The lateral-directional analysis was done in the stability axis system. The lateral-directional aerodynamics in the appendix are referenced to the body axis coordinate system. The axis transformation equations found in Appendix A of reference 7 were used to place the inertias and derivatives into the stability axes.

The center of gravity envelope for DAST I is shown in figure 3.6. This plot shows the movement in the center of gravity with fuel burn-off. The forward and aft center of gravity limits are based on recommendations in reference 5. If the center of gravity of DAST I remains within this range, the loads produced by the horizontal tail will be

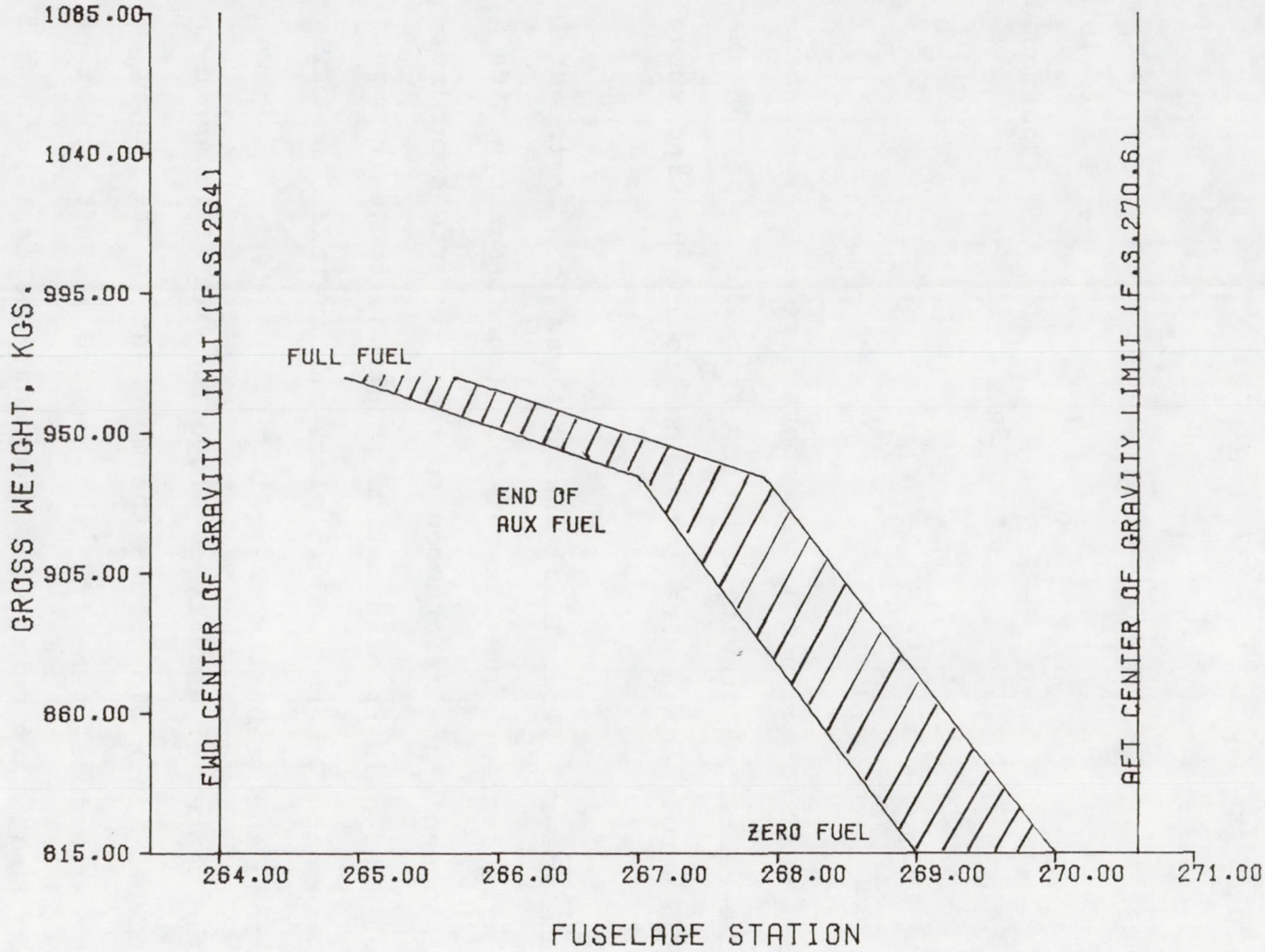

FIGURE 3.6 RECOMMENDED CENTER OF GRAVITY ENVELOPE

within the range of those produced with the basic Firebee II drone. The target zero weight center of gravity is recommended to fall between fuselage station 269.0 and 270.0. This allows a margin of safety at the full fuel and zero fuel extremes.

The predicted inertias and engine moment arm in pitch are shown in Table 3.3. These estimates are based on information in reference 5. The engine moment arm is a measure of distance between the vertical center of gravity and the engine thrust line.

Trim conditions at various locations in the flutter testing region were established in order to determine the rigid body open loop roots. Requirements for throttle setting, elevator deflection, and trimmed angle of attack throughout the testing region are shown in figure 3.7. These estimates indicate that the angle of attack throughout the flutter testing region will not exceed four degrees which is well below the pitch-up condition. Trim elevator requirements also will remain relatively small. Based on the engine model used, excess thrust is still available at the low altitude, high Mach number extreme of h = 3048 meters and M = 0.98. However, the 80 percent minimum throttle setting prevents some low speed testing at lower altitudes. Operation of the engine below the 80 percent setting is avoided because of engine overheating.

TABLE 3.3

ESTIMATED INERTIAS AND CG LOCATIONS

	Full Fuel	Zero Fuel
I_{xx}	259.51	186.37
I_{yy}	3277.89	3105.83
I_{zz}	4194.62	3266.49
I_{xz}	19.54	16.55
$\bar{X}_{cg}$	13.4	28.7
$\bar{Z}_{cg}$	.074	.146

* Inertias are in Kgs - m^2

cg's are in percent MAC

MAC = .68707 meters

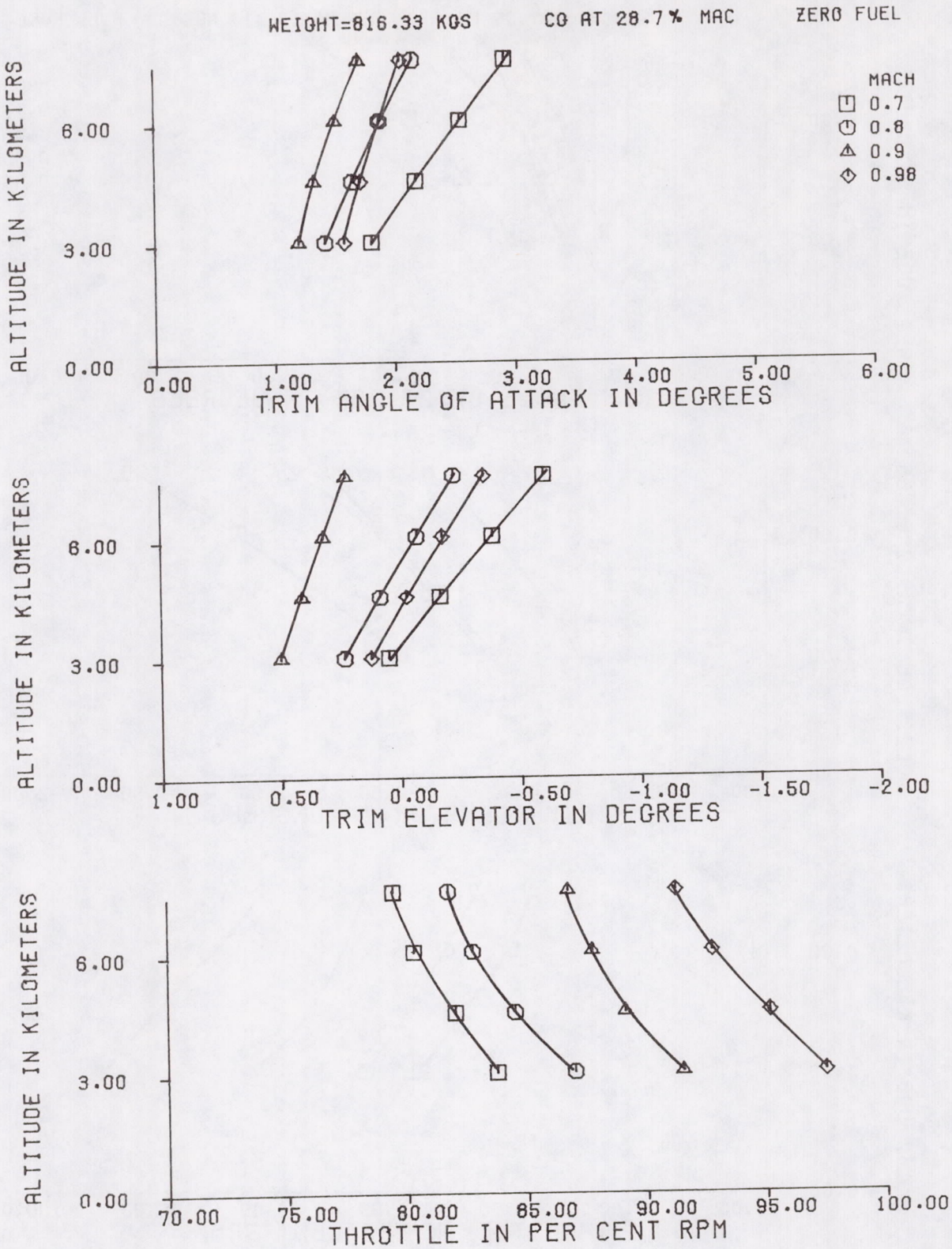

FIGURE 3.7 TRIMMED FLIGHT REQUIREMENTS (PAGE 1 OF 2)

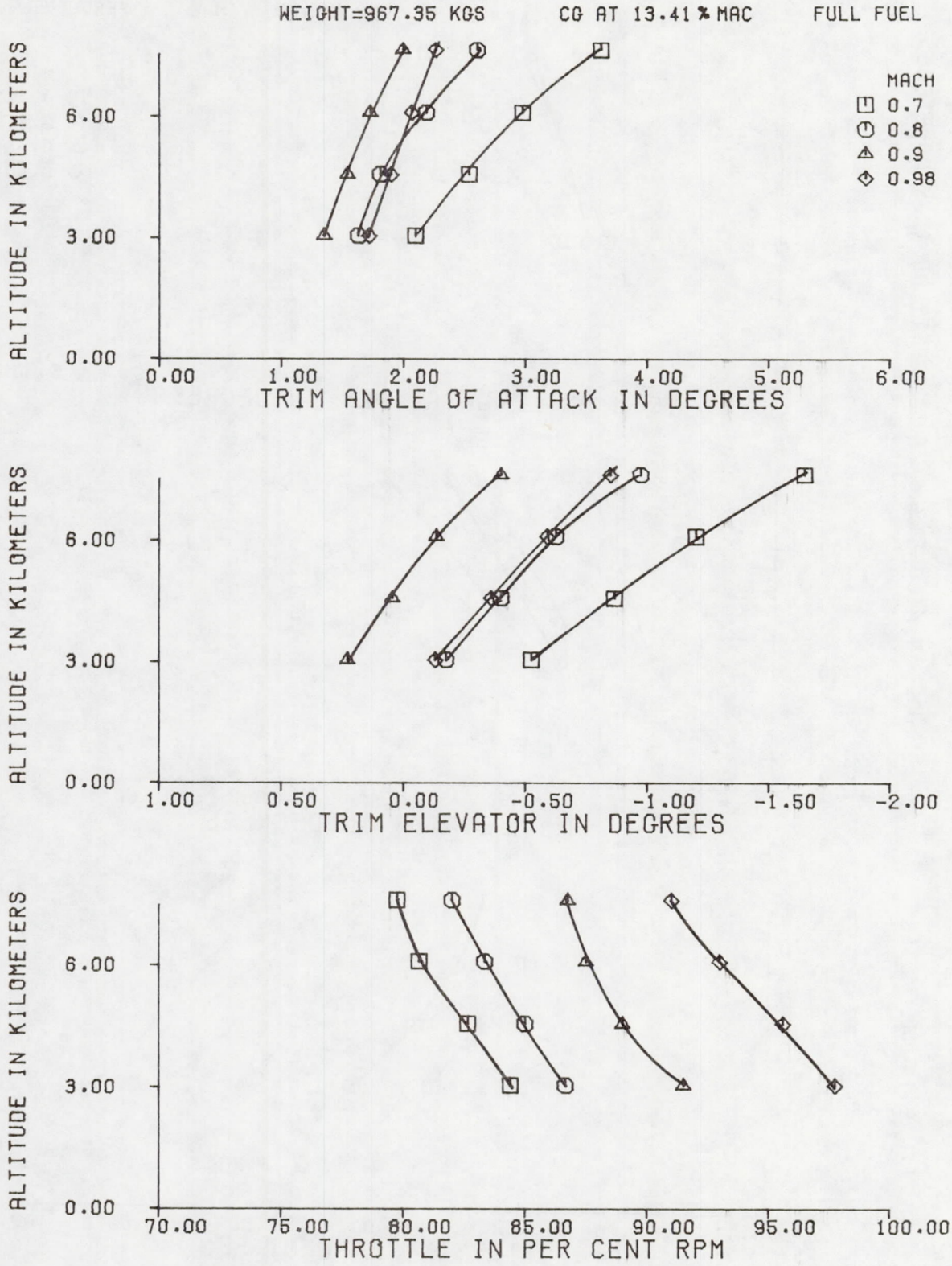

FIGURE 3.7 (CONCLUDED) (PAGE 2 OF 2)

The unaugmented aircraft roots were determined by implementing the DAST rigid body equations of motion in the CONTROL computer program of reference 8. The short period mode locus is shown in figure 3.8. From figure 3.8 the worst and best short period characteristics can be determined. The worst condition occurs at an altitude of 7620 meters and M=0.98. Here the short period damping ratio, ζ_{sp}, is .15 with a natural frequency, $\omega_{n_{sp}}$, of 8.19 rad/sec. This is at the full fuel condition. The best characteristics occur at h=3048 meters and M=0.9 with no fuel left. At these conditions, ζ_{sp}=.372 and $\omega_{n_{sp}}$=5.48 rad/sec. The short period frequency increases rather substantially between M=0.9 and M=0.98 due to large increases in C_{m_α}.

The phugoid mode locus is presented in figure 3.9. Here it can be seen that the worst case condition occurs with no fuel at M=0.8 and h=3048 meters. Under these circumstances, the phugoid natural frequency is .0473 rad/sec with a damping ratio of -.0173. This corresponds to a time to double the amplitude in the phugoid mode of T_{2_p}=847 seconds. The best phugoid mode characteristics occur at an altitude of 3048 meters and M=0.98, again with no fuel on board. At these conditions ω_{n_p}=.0302 rad/sec and ζ_p=.0484. The changes in the phugoid mode characteristics with increasing Mach number are due to a change in sign of C_{D_u} from negative to positive.

In the lateral-directional case, the dutch roll mode locus is plotted in figure 3.10. Minimum damping in this mode occurs at the conditions of full fuel, h=3048 meters,

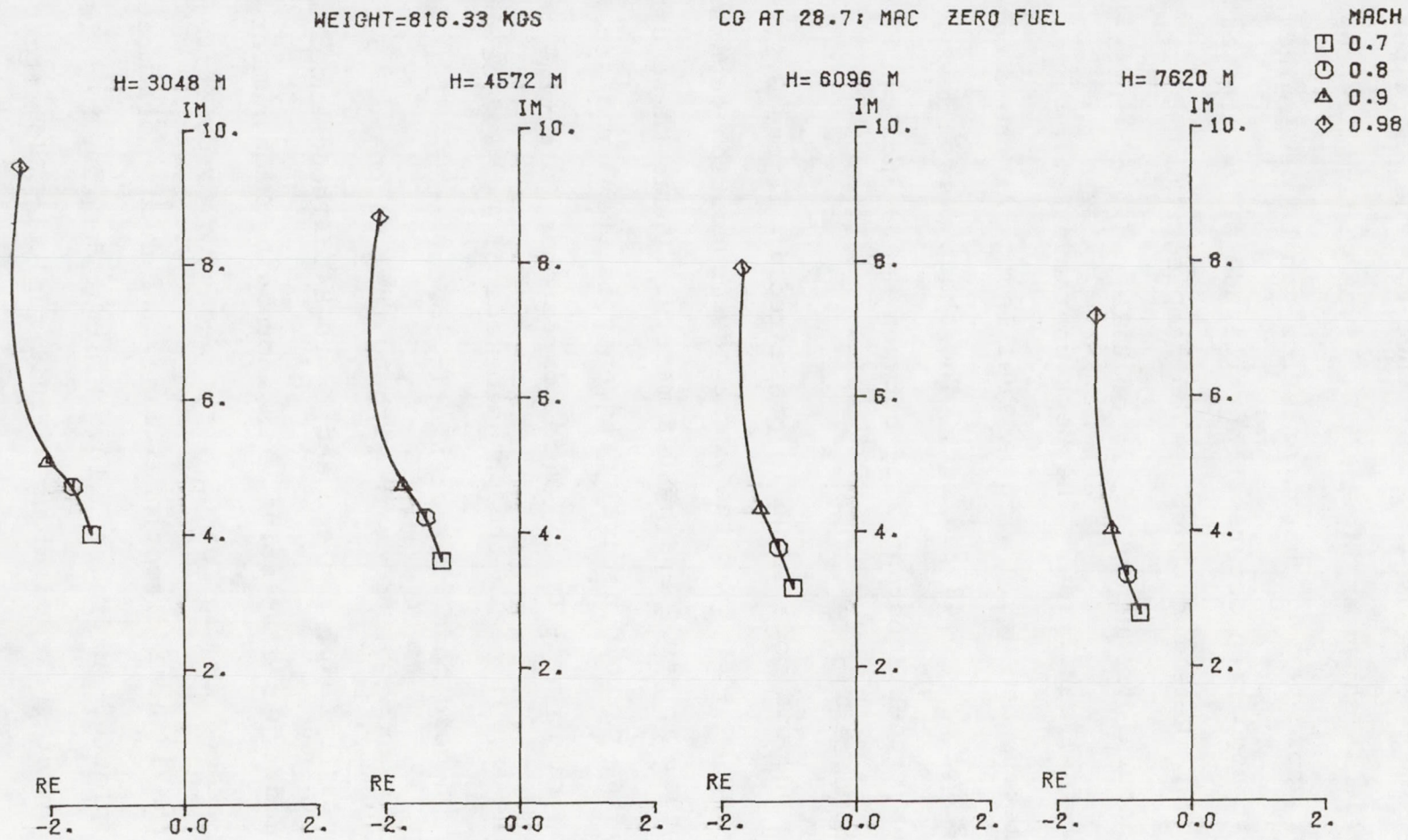

FIGURE 3.8 DAST I SHORT PERIOD MODE LOCUS (PAGE 1 OF 2)

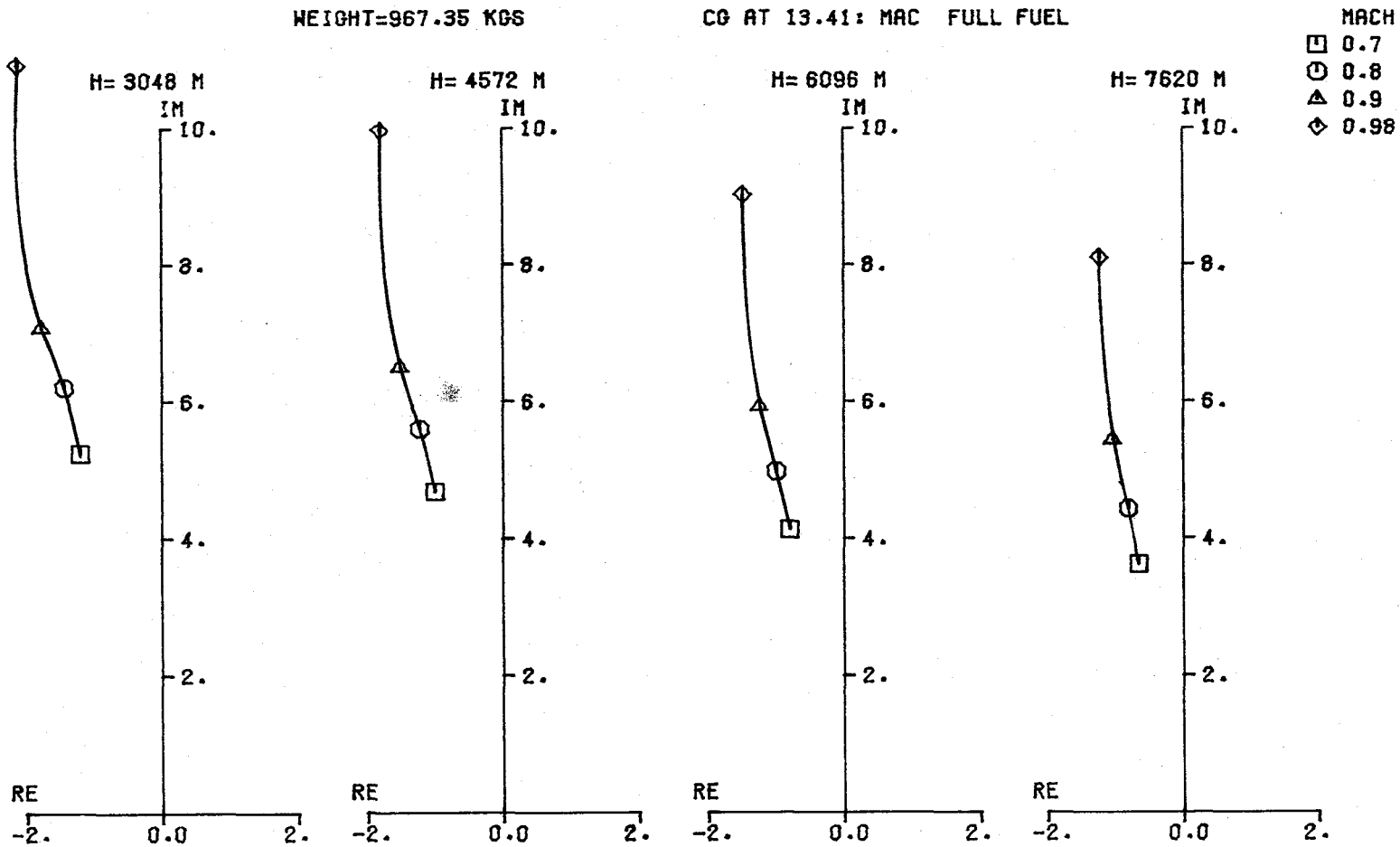

FIGURE 3.8 (CONCLUDED) (PAGE 2 of 2)

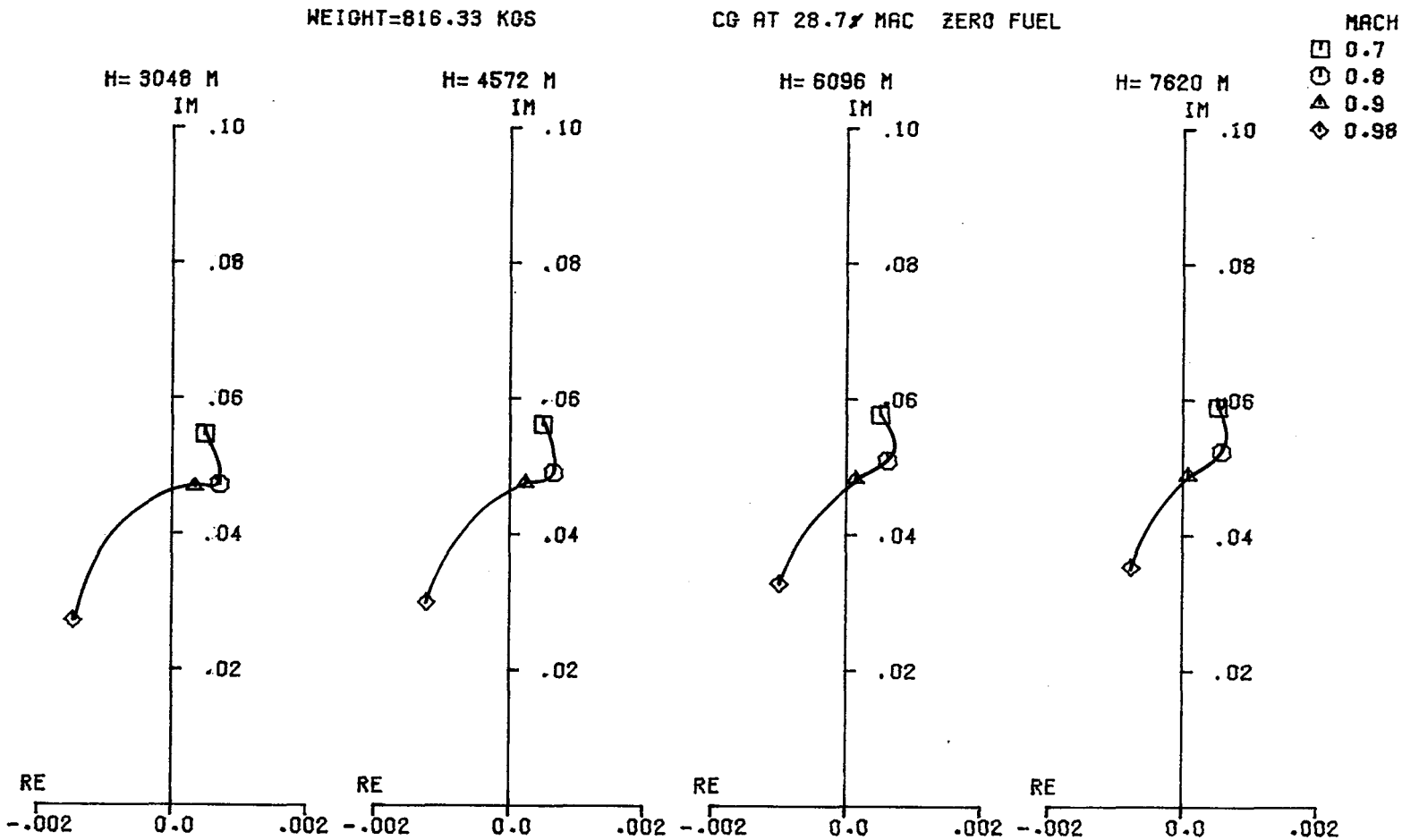

FIGURE 3.9 DAST I PHUGOID MODE LOCUS (PAGE 1 OF 2)

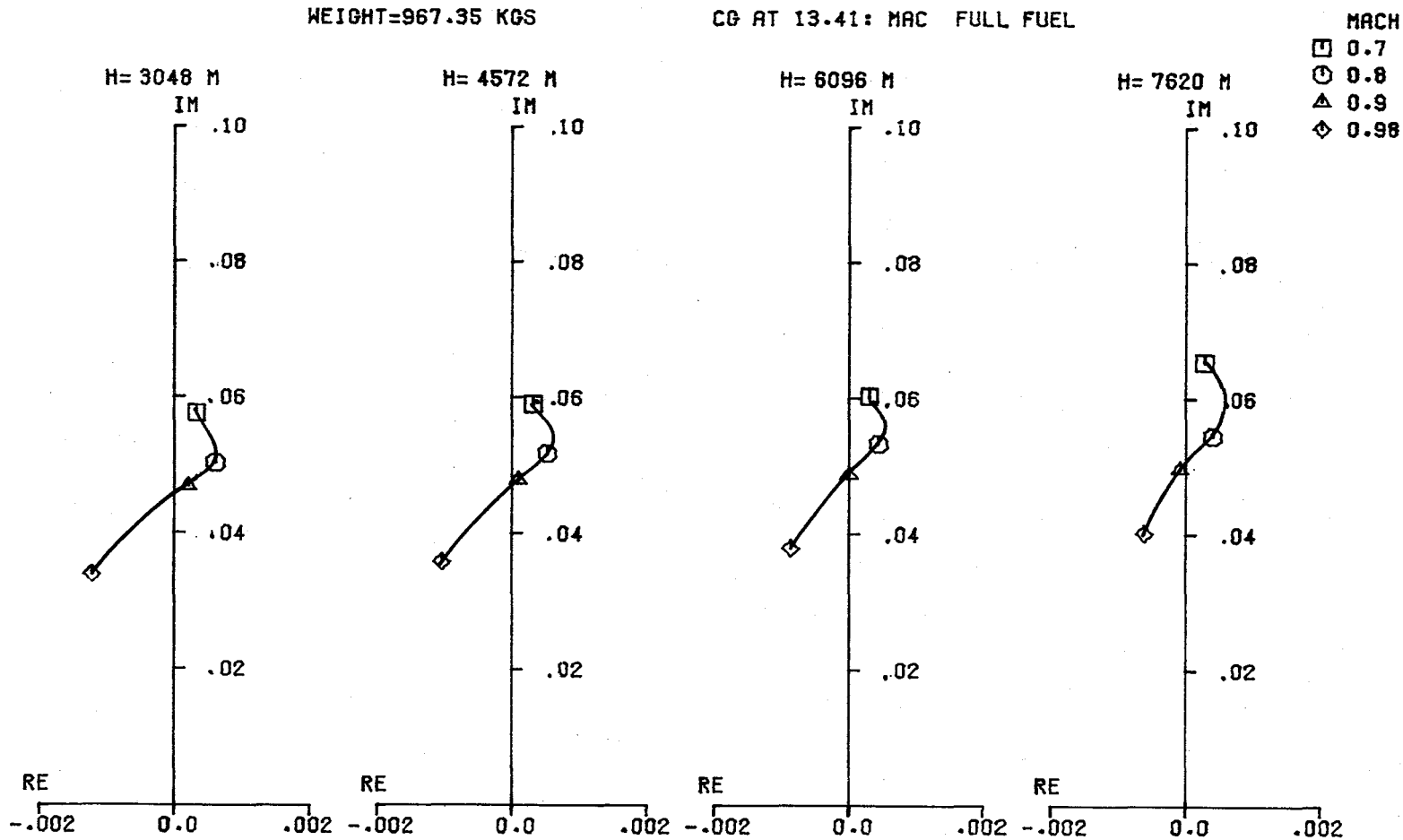

FIGURE 3.9 (CONCLUDED) (PAGE 2 OF 2)

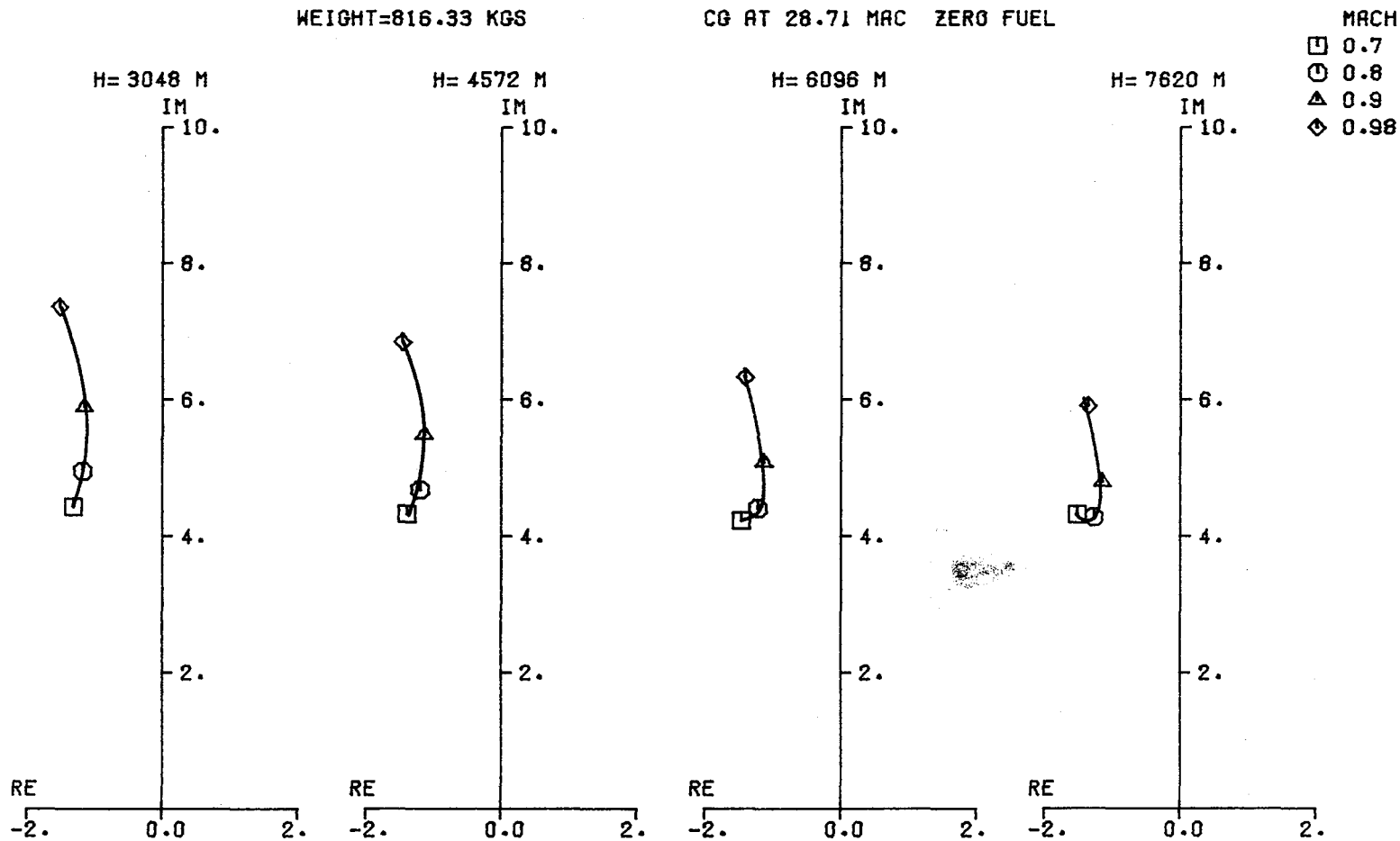

FIGURE 3.10 DAST I DUTCH ROLL MODE LOCUS (PAGE 1 OF 2)

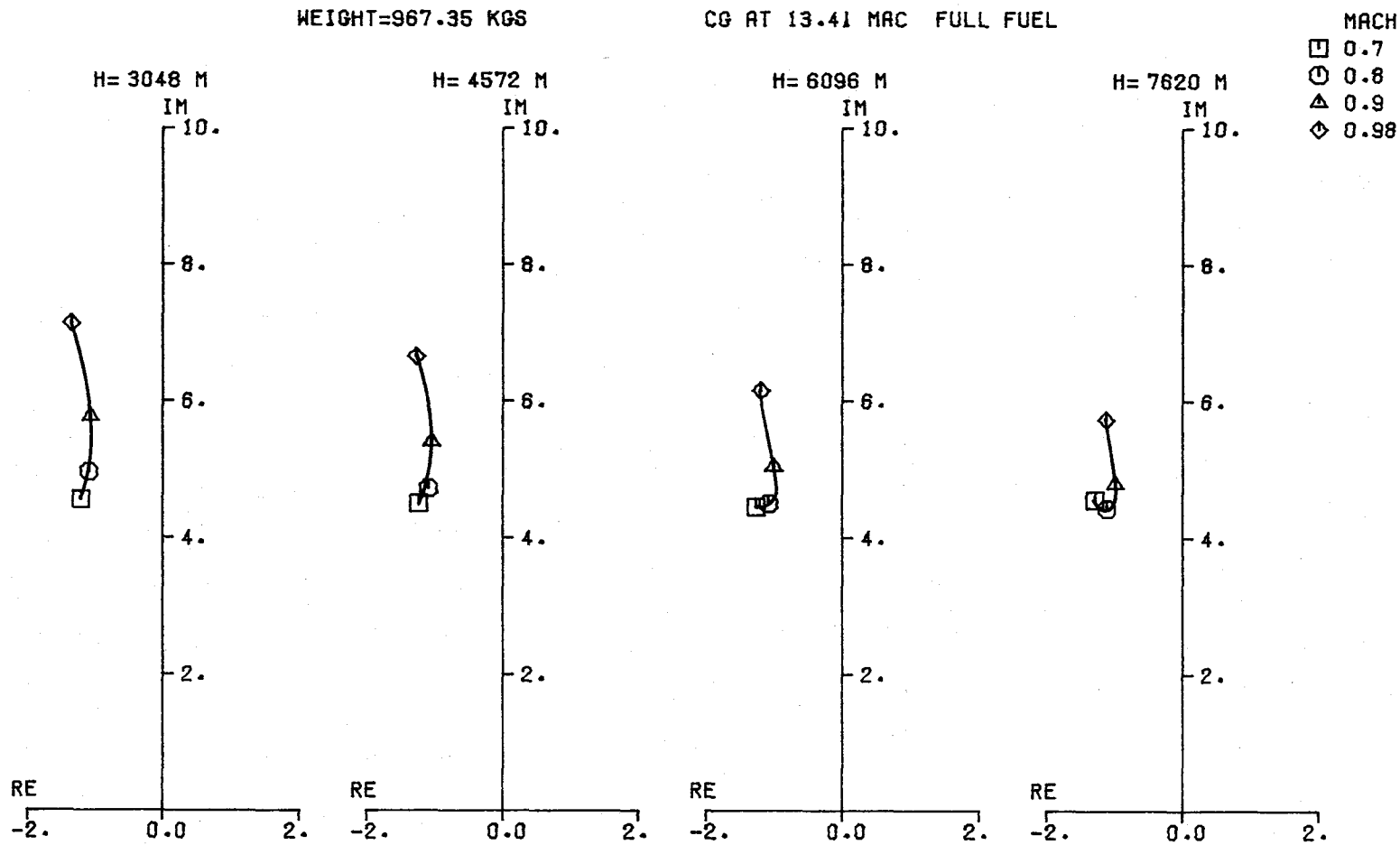

FIGURE 3.10 (CONCLUDED) (PAGE 2 OF 2)

and M=0.9. At this flight condition, ω_{n_D}=5.85 rad/sec and ζ_D=0.181. The best dutch roll mode characteristics are exhibited at zero fuel, h=7620 meters, and M=0.7. The natural frequency is 4.576 rad/sec with ζ_D= .332.

The roll and spiral mode loci are shown in figure 3.11. For the roll mode, the worst case condition is at full fuel, h = 7620 meters, and M = 0.7. The roll mode time constant, T_R, is .741 seconds at this condition. When the aircraft is at the zero fuel condition at M=0.98 and h = 3048 meters, then T_R= .106 seconds for the best characteristics.

With the DAST I in the empty fuel configuration, there are flight conditions where the spiral mode is stable. The most stability is achieved at M = 0.8 at h = 3048 meters. The spiral mode time constant, T_S, is 357.14 seconds at this flight condition. The spiral mode is unstable at all flight conditions with full fuel. When M = 0.98 and h = 7620 meters, the worst case occurs with T_S= -84.03 seconds with a time to double the amplitude of 58.25 seconds.

To place the unaugmented characteristics of the DAST I in their proper perspective, the aircraft was defined as a Class II (reference 9) vehicle which will perform Category B flight phase type manuevers. This corresponds to transport aircraft requirements of gradual manuevers with accurate flight path control.

Under this criterion the DAST I possesses the following unaugmented flying qualities according to reference 9.

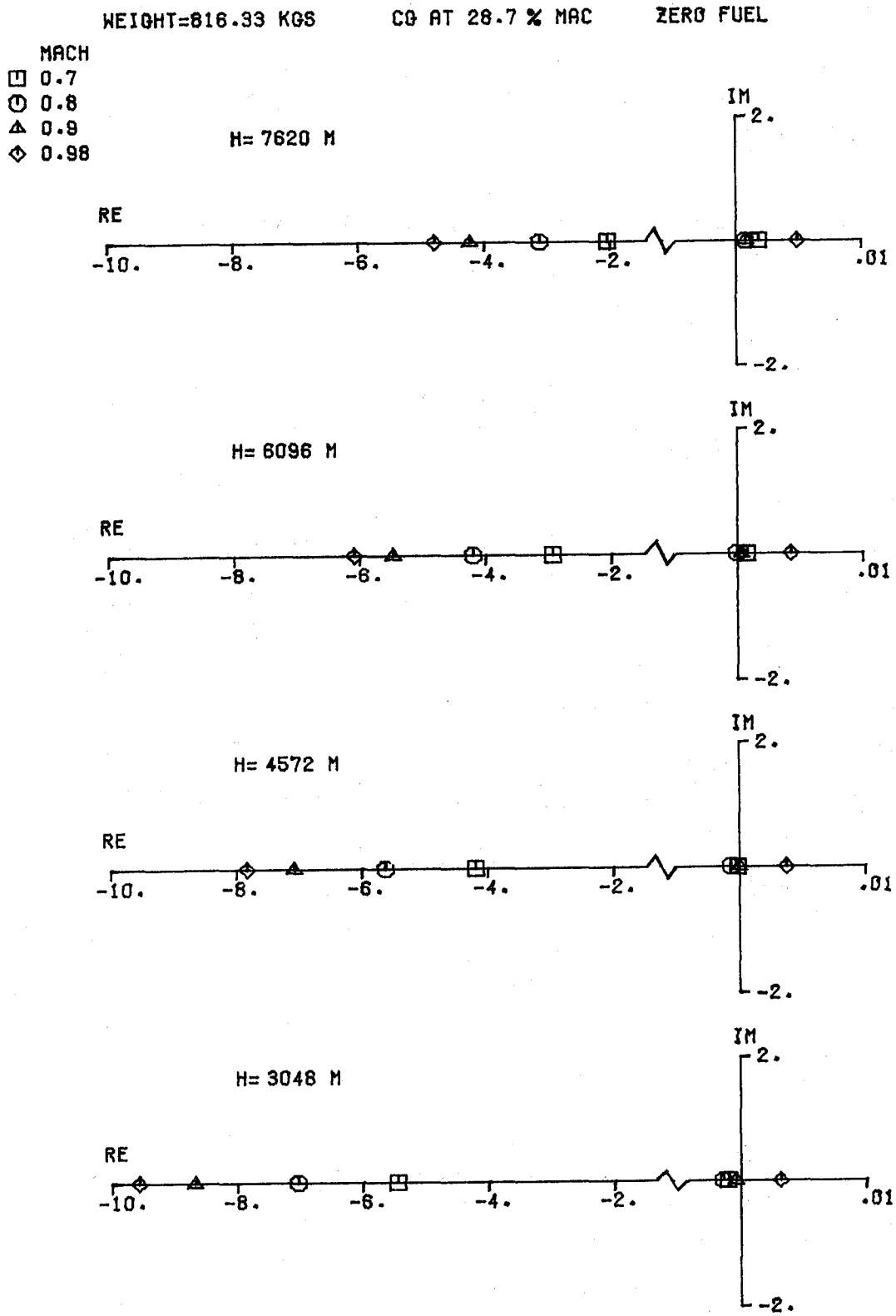

FIGURE 3.11 SPIRAL AND ROLL MODE LOCUS
(PAGE 1 OF 2)

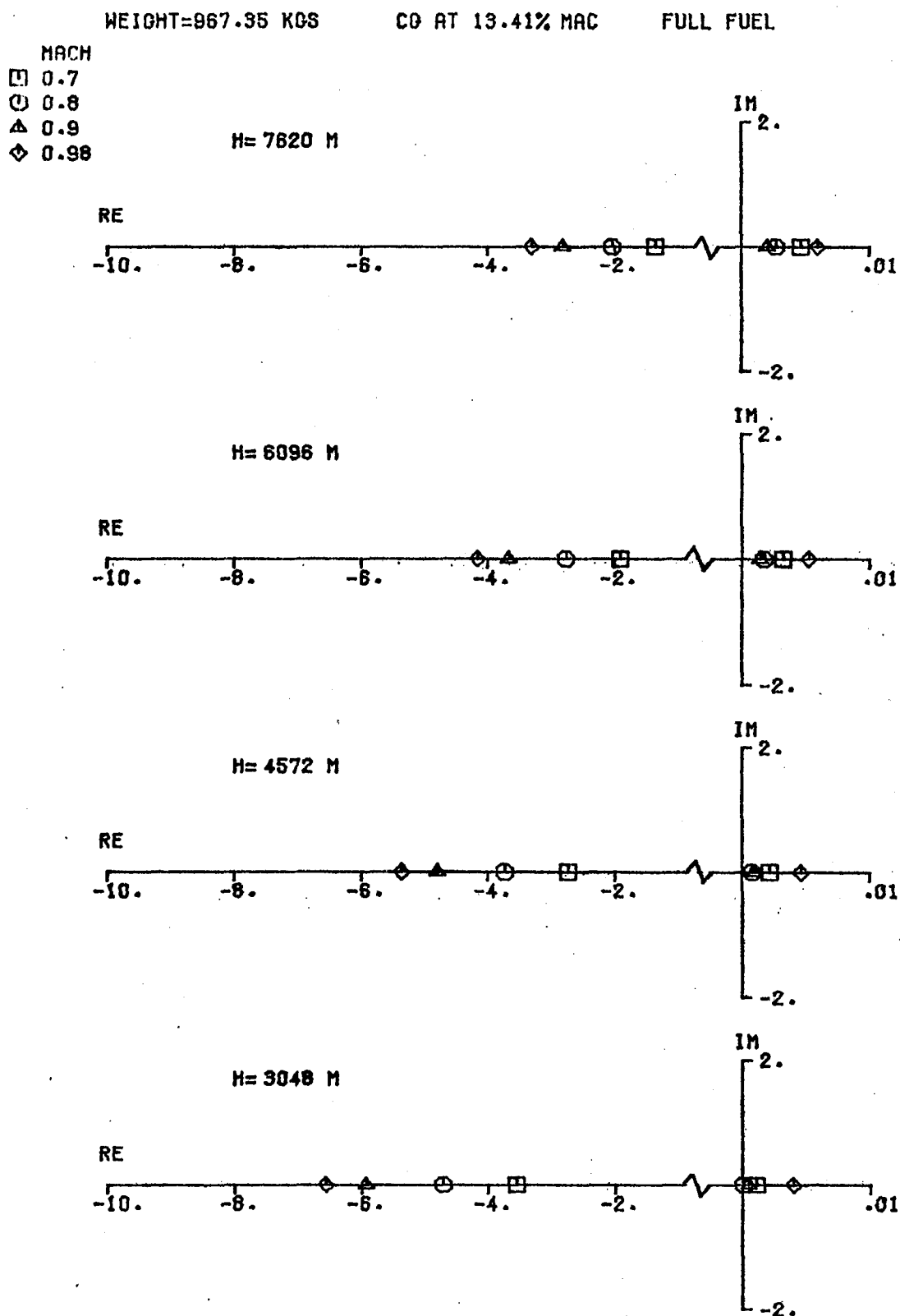

FIGURE 3.11 (CONCLUDED) (PAGE 2 OF 2)

	Worst	Best
Short period mode:	Level 3	Level 1
Phugoid mode:	Level 3	Level 1
Dutch roll mode:	Level 1	Level 1
Roll mode:	Level 1	Level 1
Spiral mode:	Level 1	Level 1

CHAPTER 4

CONTROL SYSTEMS SYNTHESIS

This chapter will describe the augmentation control systems developed for the DAST I. A description of Boeing's analysis for the FSS design is presented first. The development of the primary RAV flight control system is presented second. The backup autopilot system is described third with some special requirements for launch and recovery examined.

4.1 Flutter Suppression System - In the scheme called flutter suppression, an augmentation control system generates artifical stiffness in a system, such as ARW-1, by producing forces which oppose motion in the system. Divergent motion of the wing due to flutter is designed to be suppressed by the FSS as long as that control system operates properly.

The design of the FSS was conducted by the Boeing Wichita Company under contracts NAS1-14675 and 14028 from NASA LaRC. The major contract requirement was to provide a flutter suppression system to extend the flutter boundary of DAST I by twenty percent. Additional detail on the information presented in the next section can be found in reference 10.

4.1.1 Equations of Motion - Through the design cycle, vibration solutions for the structural model described in section 3.1.1 were obtained. For each solution, structural reference points were added at the midpoint of the front

and rear spars at each rib and on the hinge line of the control surface. The points, also called co-location points, contain the motion for the six degrees of freedom and are used to obtain the motion of the aerodynamic panels in the aerodynamic analysis.

The flutter analysis sequence is illustrated in figure 4.1. The unsteady aerodynamics forces on the wing and horizontal and vertical tail were generated using a BWC developed three-dimensional plate doublet finite element solution. The theory accounts for Mach number and finite span effects, and includes the aerodynamic coupling between all the components of the aircraft. The finite element wing aerodynamic model is illustrated in figure 4.2. The unknown pressure distribution for each aircraft mode is determined by assuming the pressure to be constant over a given aerodynamic panel and solving for the pressure based on a specified Mach number and reduced frequency. The primary lifting surfaces are modeled with trapezoidal elements arranged in strips parallel to the free stream.

The equations of motion for the flutter analysis were initially formed using complex oscillatory aerodynamic coefficients determined for specific values of reduced frequency, ω/U_o. The final form of the equations of motion were formulated in terms of real matrices through introduction of an approximating function.

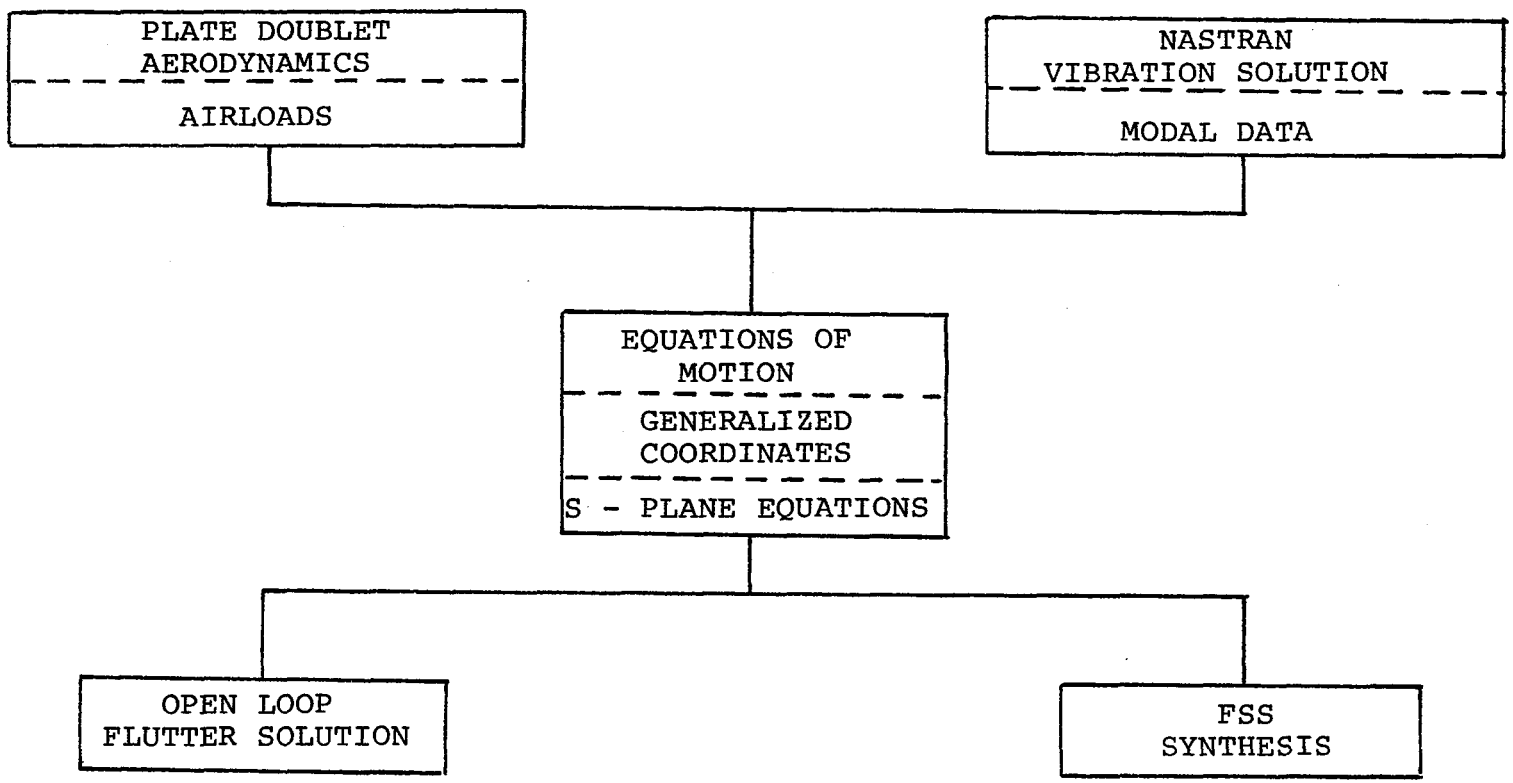

FIGURE 4.1 FLUTTER ANALYSIS SEQUENCE

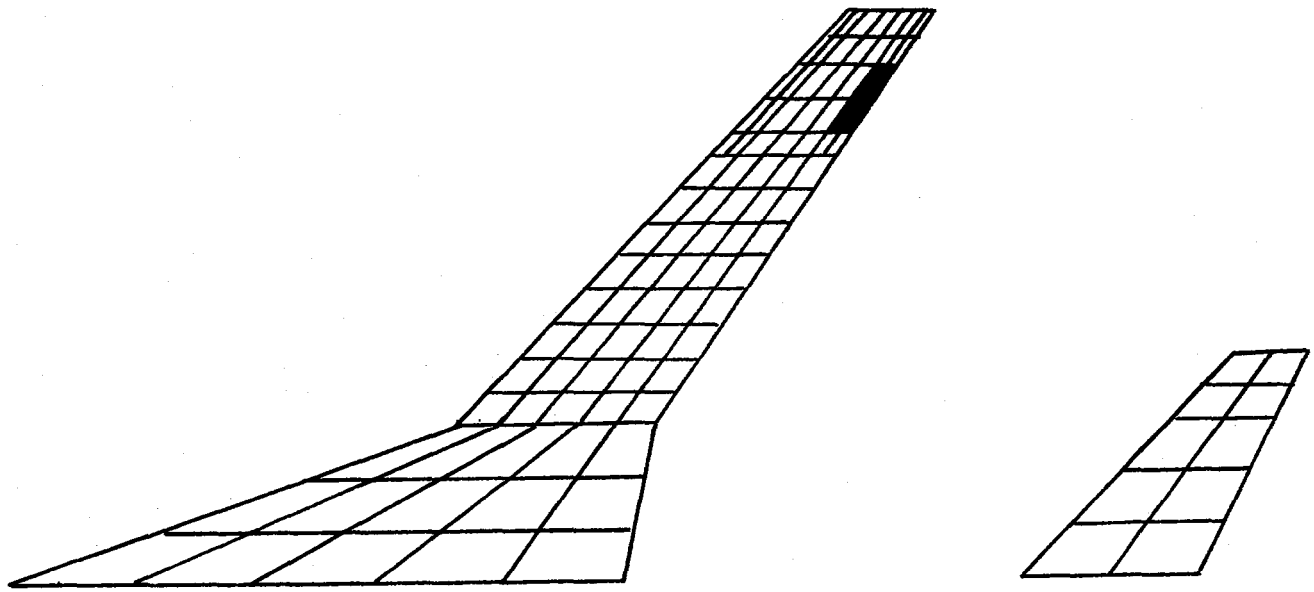

FIGURE 4.2 DAST ARW-1 AERODYNAMIC MODEL

From reference 10 the original equations in standard form were:

$$\left(-(j\omega)^2\left[M\right] + (j\omega)\left[Z\right] + \left[K\right]\right)\left\{q(j\omega)\right\} + \rho u_o^2\left[A_I\left(\frac{j\omega}{U_o}\right)\right]\left(\left[C_\theta\right]\left\{q(j\omega)\right\} + \frac{j\omega}{U_o}\left[C_z\right]\left\{q(j\omega)\right\} + \frac{1}{U_o}\left[C_w\right]\left\{w_g\,(j\omega)\right\}\right) = 0 \tag{4.1}$$

where

q	=	generalized modal coordinate
A_I	=	aerodynamic influence coefficient matrix
C_θ, C_z, C_w	=	the linearized boundary conditions
U_o	=	free stream velocity
w_g	=	vertical gust velocity

Only the symmetrical equations will be examined in this report. The anti-symmetrical equations will be of the same form and can be assertained from reference 10.

The approximating functions were developed by plotting particular elements of the complex matrix A_I at various values of ω from 0 to 400 radians/second. This is illustrated in figure 4.3. The solid line in figure 4.3 is an approximating function, chosen as a rational polynomial function of the complex variable s. The use of the approximating function allows accurate approximation of the time delays inherent in the unsteady aerodynamics subject to the following restrictions:

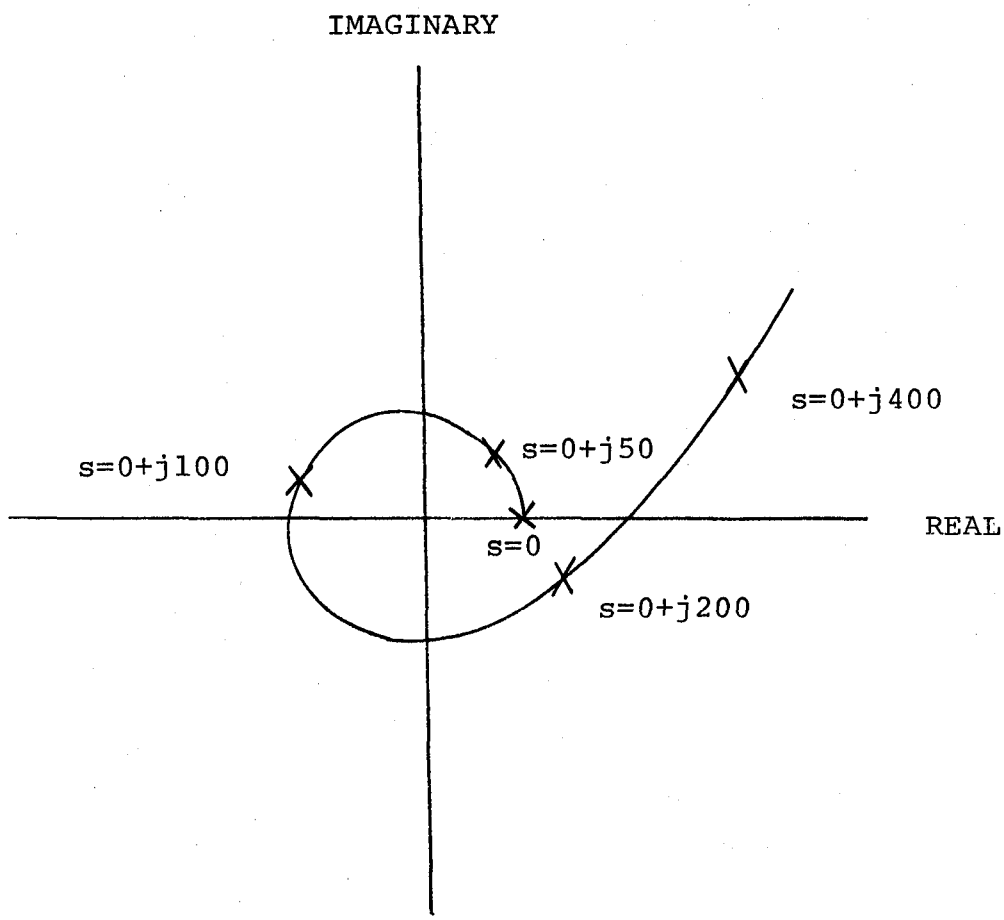

FIGURE 4.3 COMPLEX COEFFICIENTS AS A FUNCTION OF FREQUENCY

- It must have complex conjugate symmetry.
- It must have denominator roots in the left half-plane.
- It must approximate the value of the complex coefficient when $s = o + j\omega$, for those values of ω analyzed.

The approximating function for each element in the A_I matrix was determined after analysis at seven discrete frequencies. By substituting the approximating functions for the aerodynamic influence coefficients, the final form of the equations of motion results.

$$\left(s^2 [M] + s [Z] + [K]\right) \{q(s)\} \qquad (4.2)$$
$$+ \left(s^2 \rho [C_1] + \rho U_o s [C_2] + \rho U_o^2 [C_3] + \rho U_o^2 \sum_{i=1}^{4} [D_i] \frac{s}{s+U_o B_i}\right) \cdot$$
$$\{q(s)\} + \left(\rho U_o [R_o] + \rho U_o^2 \sum_{i=1}^{4} [R_i] \frac{s}{s+U_o G_i}\right) \{w_g(s)\} = \{0\}$$

The first line in equation (4.2) represents structural coefficients. The second line is aerodynamic coefficients and the third line is gust velocity coefficients.

With this equation, the air density, ρ, and velocity, U_o, can be varied so solutions can be found at all the flight conditions of interest. Solutions of equation (4.2) without control system augmentation yields the results in section 3.1.2.

4.1.2 Design Synethesis Techniques - The design criteria

established for the DAST ARW-1 FSS are:

- Extend flutter boundary by 20 percent.
- Design gust: 1.83 m/sec rms
- System stability at design speed (MIL-F-9490D)
  - Elastic Modes: GM = $\pm$6.0 DB; PM = $\pm$45 deg.
  - Maneuver Modes: GM = $\pm$4.5 DB; PM = $\pm$30 deg.
- No FSS redundancy
- No degration in structural mode damping (other than the flutter mode) below ζ = .01 except when the unagumented mode damping is less than ζ = .01.
- A single wing flutter suppression system will be analyzed but not implemented.

The synthesis started with a parametric evaluation to determine combinations of control surface locations and sensor type and location that would control the flutter mode and minimize the coupling with other wing structural modes. This parametric evaluation was achieved by using a zero locus to estimate modal stability and coupling as a function of sensor and control surface placement. If the sensor or control surface placed the zeros in the right half of the s-plane near the flutter mode it was eliminated. This would indicate the coupling was small. Other combinations were eliminated because their location in the right half of the s-plane indicated strong adverse coupling with other structural modes. Using this procedure, along with mode

shape information, candidate sensor and control surface locations were determined. Control laws were then synthesized and were evaluated using root locus methods.

The control surface size and location which was selected has the following characteristics:

- 23 percent chord hingeline
- .254 meter span
- Inboard edge is 1.71 meters (WBL 67.35) from the centerline.
- Outboard edge is 1.964 meters (WBL 77.35) from the centerline.

The sensor location is 2.007 meters (WBL 79) from the fuselage centerline and is attached to the rear spar.

This combination places the zeroes of the higher frequency modes very near their corresponding poles. The flutter mode zero is in the left half of the s-plane and influences the unstable flutter mode root into the left half of the s-plane when the control law in figure 4.4 is mechanized. This is the control law for the DAST FSS as of March, 1978. Some adjustments from the system shown in figure 4.4 are possible prior to delivery to NASA.

From figure 4.4 it can be seen that four accelerometers are utilized. One on each wing at the location specified before, one on the fuselage centerline at FS 265 and a roll angular accelerometer on the fuselage centerline at

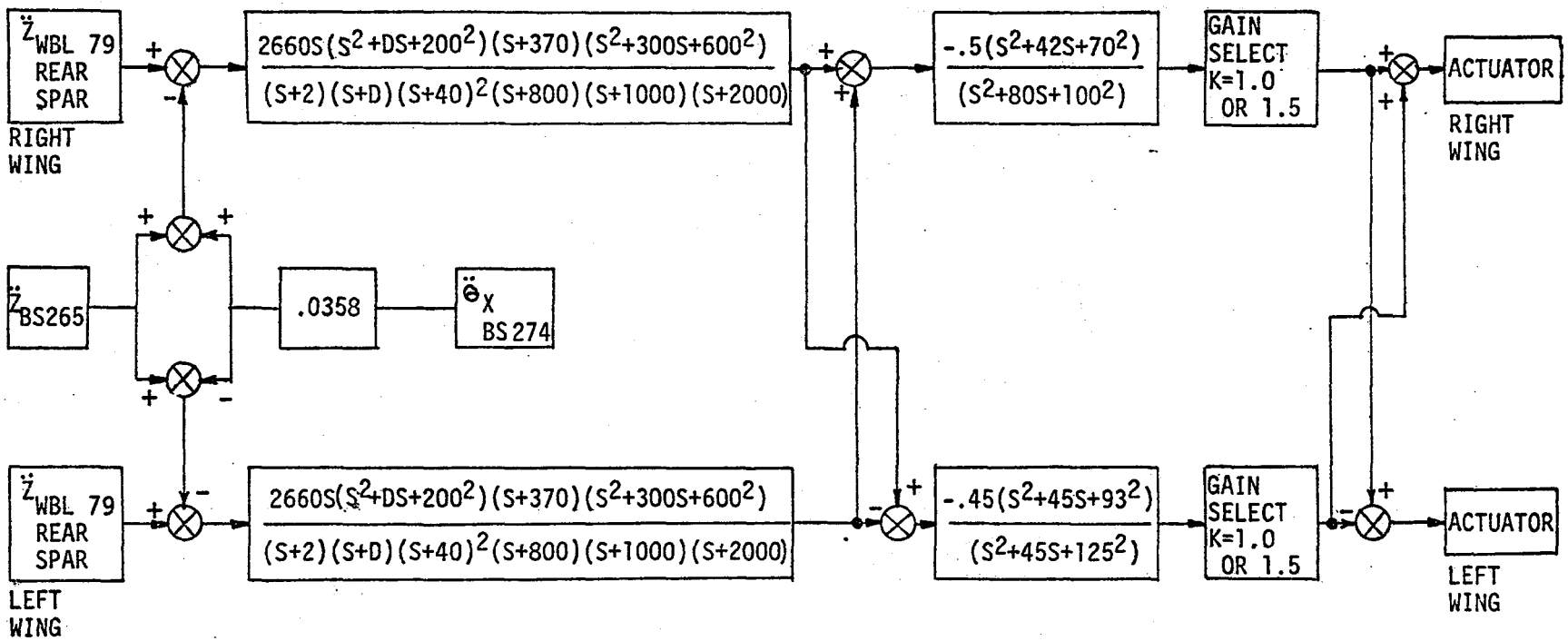

$D = f(M,h)$

$\ddot{Z} \sim$ +UP

$\theta_X \sim$ + RIGHT WING UP

$\delta_A \sim$ +TED

FIGURE 4.4 DAST I FSS BLOCK DIAGRAM

FS 274. The last two accelerometers on the fuselage centerline are used to subtract the rigid body vertical and roll accelerations from the wing sensors. The filter after the second summing junction has a parameter, D, in numerator and denominator terms which is gain scheduled with Mach number and altitude. Its purpose is to maintain adequate gain margins at both low and high dynamic pressure conditions. A washout filter (s/s + 2) eliminates the influence of the very low frequency rigid body modes. The numerator term, (s + 370), is compensation for an actuator pole. The second order lead term (s^2 + 300s + 600^2) is to achieve the proper high frequency phase and gain characteristic, as are the lag terms $(s + 40)^2$ and (s + 800). The lag terms (s + 1000) and (s + 2000) are for high frequency attenuation. Notch filters for both symmetrical and anti-symmetrical conditions are also seen in figure 4.4 and are to achieve the proper gain and phase at the corresponding flutter frequencies.

A root locus of this control law at the conditions of M = .9 and 3048 meters is shown in figure 4.5. Boeing's analysis showed that about 90 degrees of phase lag was required to damp the flutter mode. This amount of phase lag is typical of using an accelerometer for the feedback sensor giving a pseudo rate signal at the flutter mode frequency. It also provides attenuation of the higher fre-

SYMMETRIC

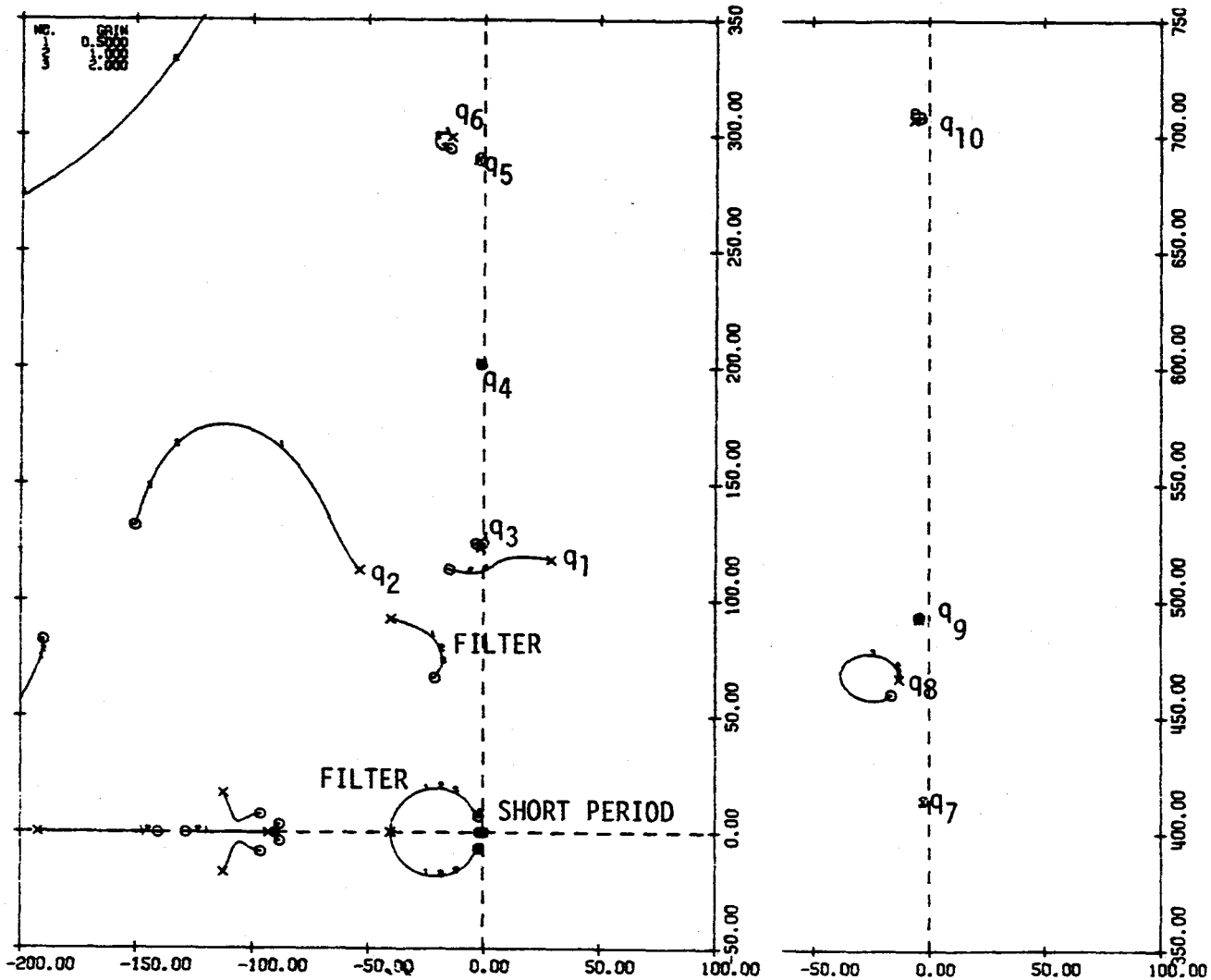

FIGURE 4.5 DAST I FSS ROOT LOCUS (PAGE 1 OF 2)

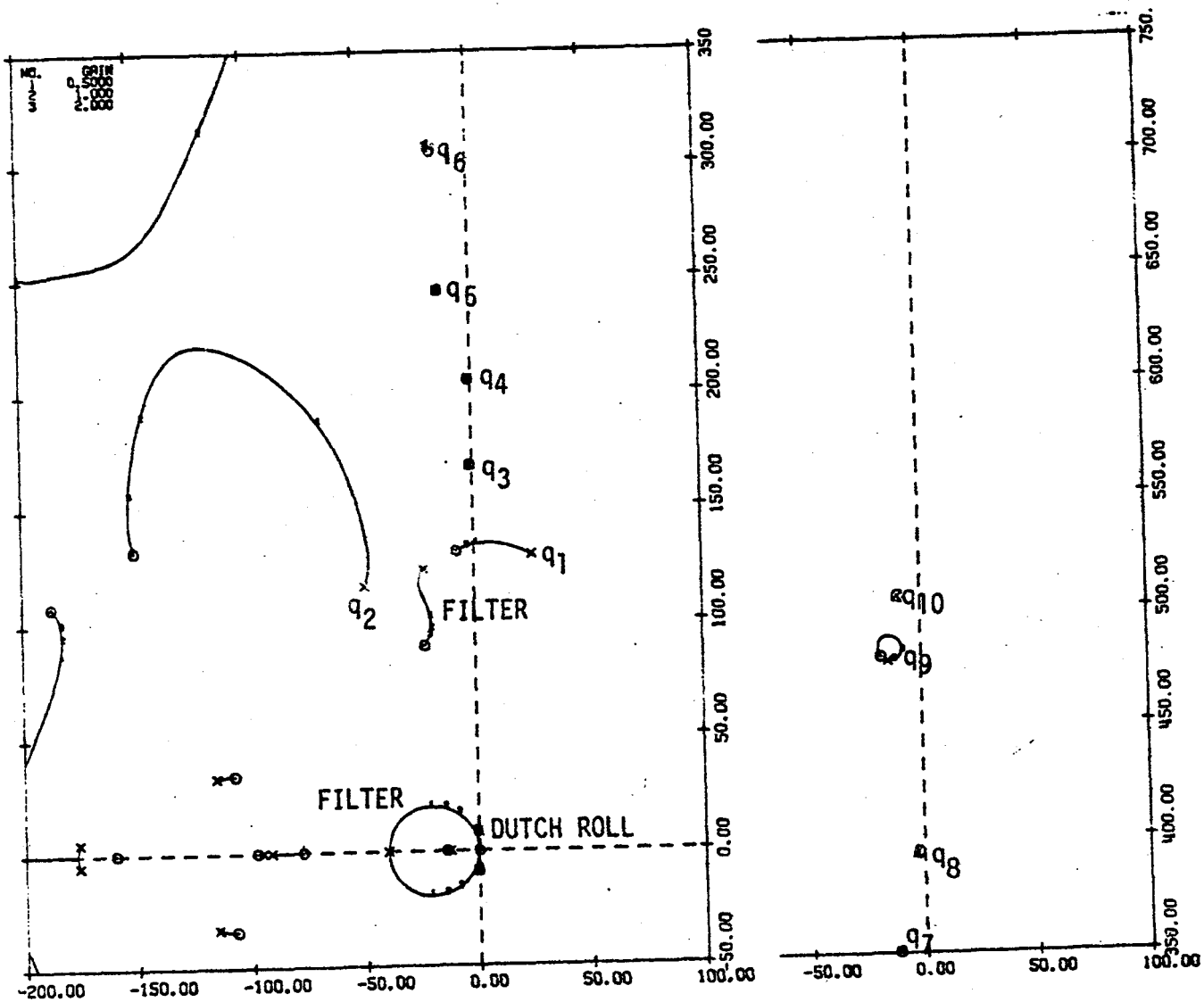

FIGURE 4.5 (CONCLUDED) (PAGE 2 OF 2)

quency modes thus helping to decouple them from the FSS.

The surface deflection limit for the wing FSS aileron is $\pm$ 12 degrees. The aileron surface displacement and rate requirements are shown in figure 4.6. The requirements for 3.67 m/sec peak gusts are a surface deflection of 18.135 degrees and a surface rate of 1460 deg/sec. Clearly with a 12-degree deflection limit, saturation of the control surface will occur. Increasing the surface size to eliminate this problem was not an option since increased hydraulic power requirements could not be met with the pump restrictions that existed for this vehicle.

4.1.3 Augmented Flutter Boundary - The improvement in the open loop flutter boundary which the FSS makes is shown in figure 4.7. If the jettisonable mass ballast at the trailing edge near the tips is removed, then the new open loop flutter boundary is shown. As long as the DAST vehicle is below this second boundary and encounters difficulty with the FSS, jettisoning the ballast will provide some improvement in safety. However, if the vehicle is flown above this boundary and difficulty is encountered, then even if the mass balance is jettisoned, flutter will occur.

To avoid exceeding M = .98 and still achieve the twenty percent increase in the flutter boundary, the DAST vehicle must fly at low altitudes. An altitude minimum for safety

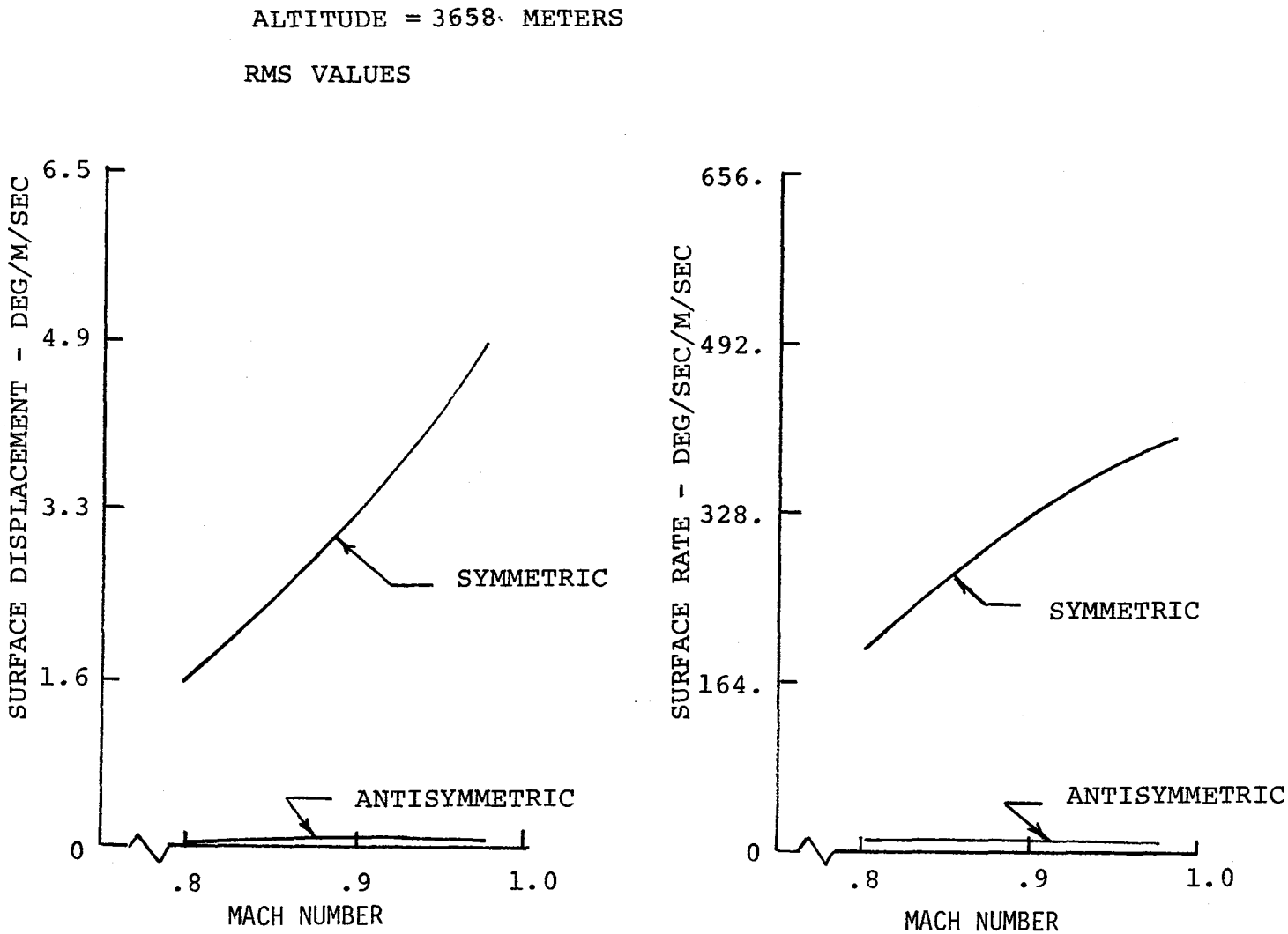

FIGURE 4.6 SURFACE DISPLACEMENT AND RATE REQUIREMENTS

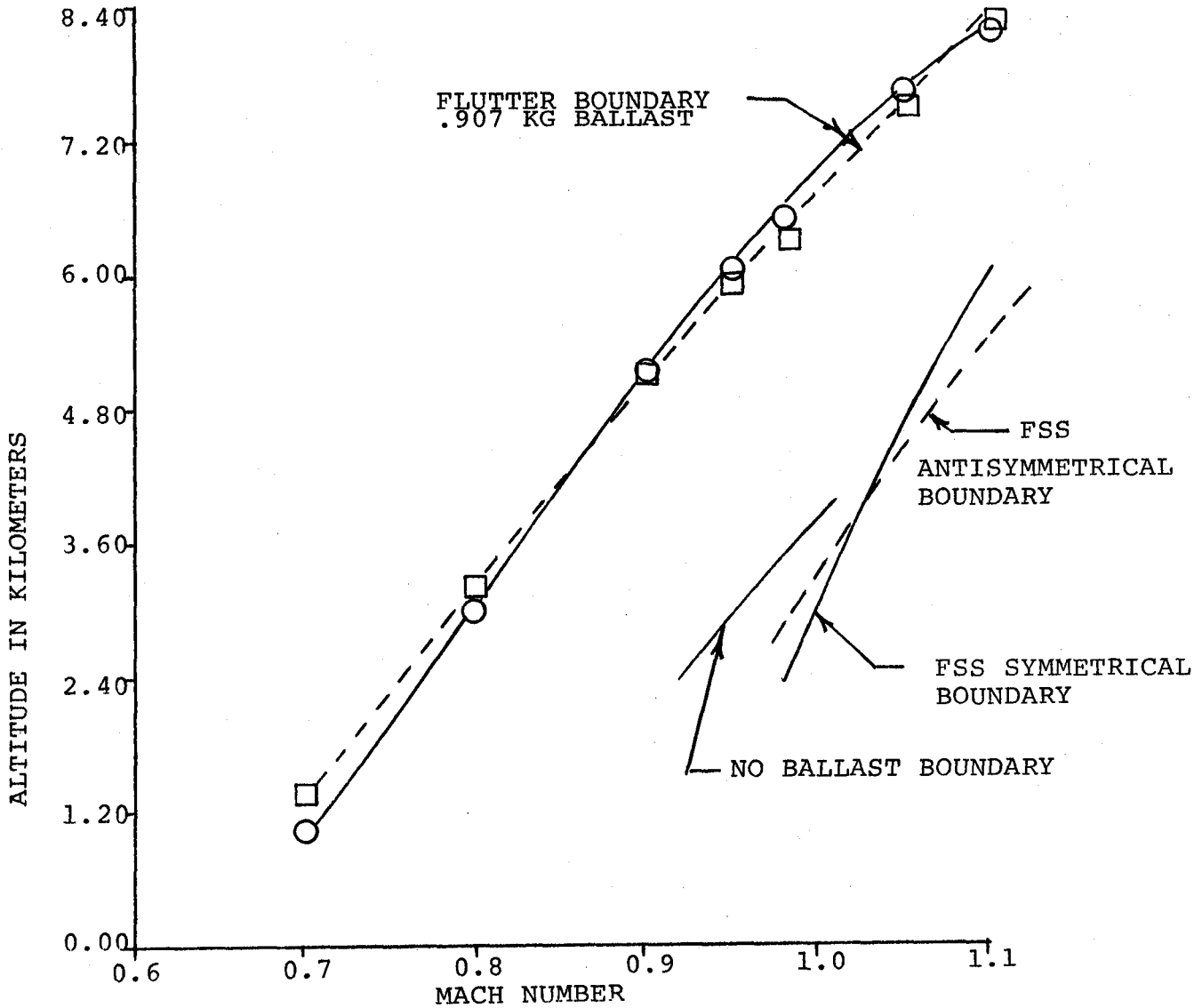

FIGURE 4.7 DAST I AUGMENTED FLUTTER BOUNDARY

reasons has been set at 3048 meters. The improvement in the flutter mode damping ratio with the FSS operating is illustrated in figures 4.8 and 4.9. It can be seen that the predicted inprovement in flutter mode damping exceeds the required twenty percent goal. The BWC plate-doublet aerodynamics were used through M = 1.1 in the analysis. The accuracy of a linear subsonic aerodynamic theory to this high a Mach number is questionable but BWC maintains that their prior experience in this area shows that although the theoretical results will be less accurate than at lower Mach number, they will be conservative. Thus their use in the analysis is considered appropriate.

4.2 RAV Primary Control System. - The remotely augmented control system will be the primary flight control system for the DAST RPRV. This system which was illustrated in figure 2.3 allows great flexibility in control system options. The DAST I will exercise a three mode RAV system. By this, it is meant that the pilot has the option of selecting three different control system configurations at his discretion. The three modes available for DAST are:

1. Computer Direct (CD)
2. Rate Damper (RD)
3. Command Augmentation (CAS)

The computer direct mode does utilize the RAV ground computer to determine pilot stick commands but does not augment the basic aircraft. The rate damper mode adds rate dampers to the pilot inputs. The damper gains are pilot

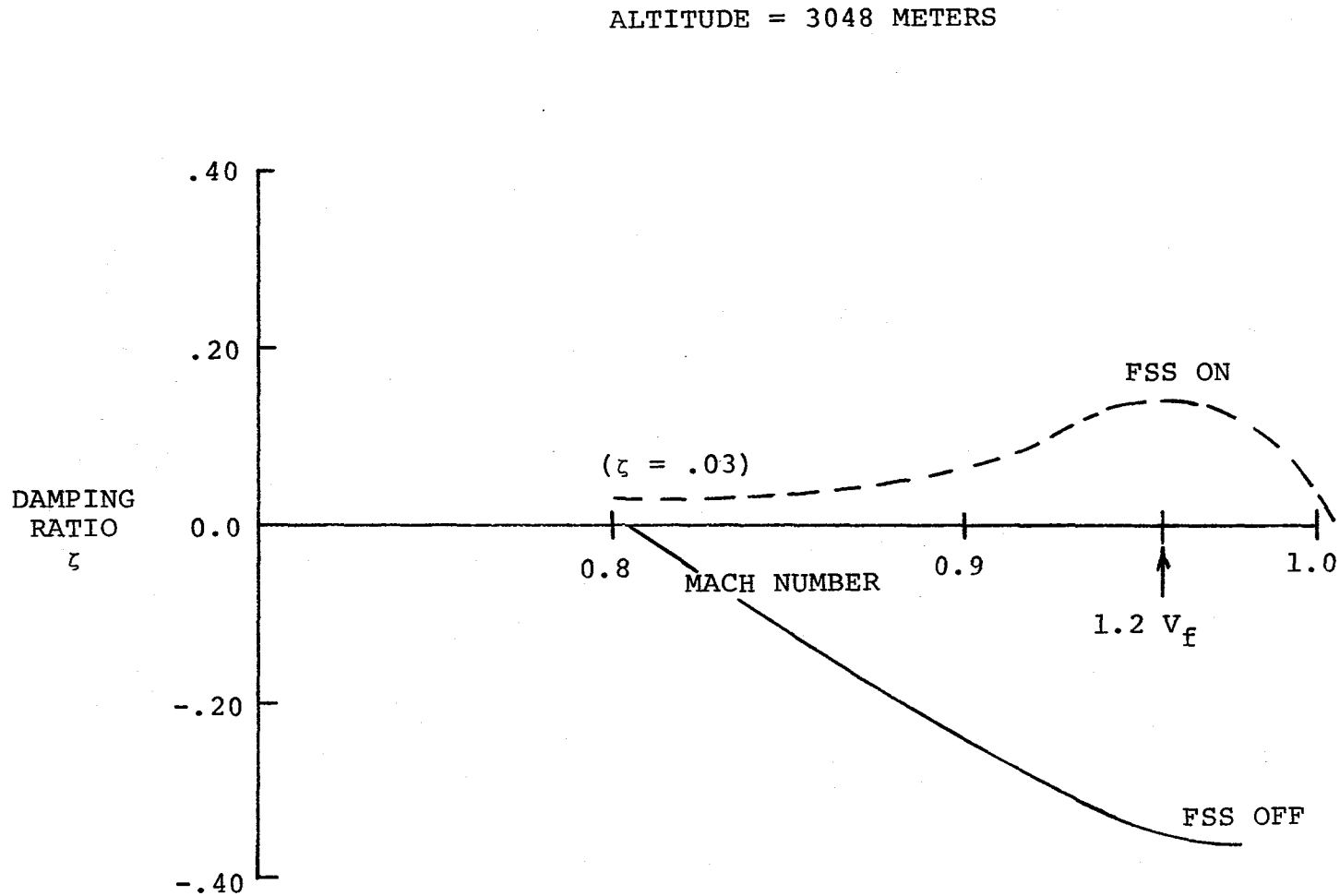

FIGURE 4.8 ARW-1 SYMMETRIC FLUTTER MODE DAMPING RATIO

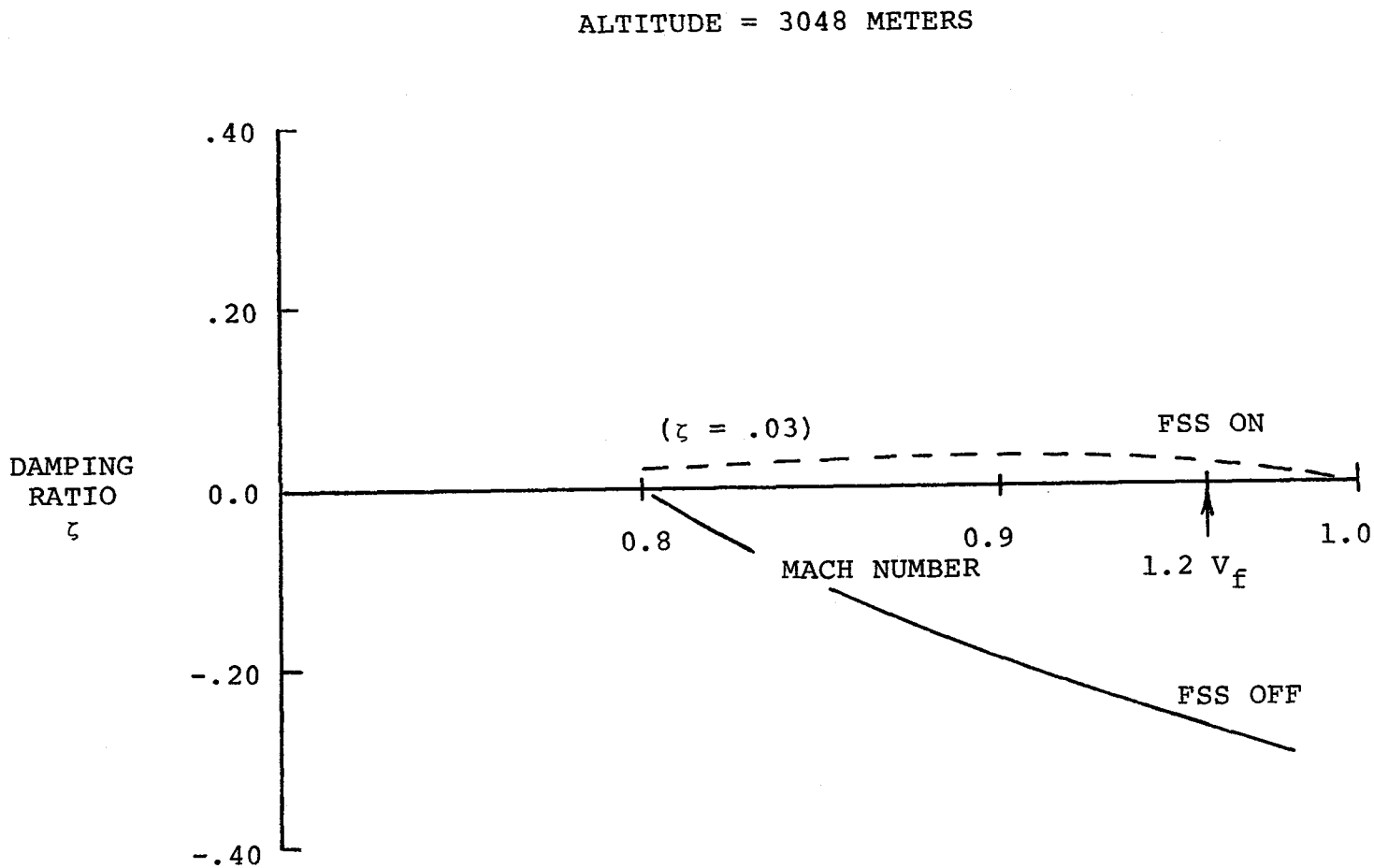

FIGURE 4.9 ARW-1 ANTISYMMETRIC FLUTTER MODE DAMPING RATIO

selectable. The command augmentation mode modifies the pilot inputs dependent upon flight conditions. The stick commands are input into an integrator, whose characteristics can be changed by certain flight conditions. In the CAS mode, the pilot does not have direct control of the control surfaces.

4.2.1 Design Considerations. - The RAV control system requirements were:

- Augment the DAST I to level 1 flying qualities (MIL-8785B) in all axes at all flight conditions.
- Control the unstable pitch-up characteristics of the unaugmented vehicle.
- Prevent the vehicle from exceeding the 2.5 g wing load limit.

The above requirements were established in order to reduce the pilot's workload during normal and emergency conditions. By offering load protection and controlling the vehicle's abrupt pitch-up tendency above approximately seven degrees angle of attack, the pilot can perform maximum performance pull-up maneuvers to reduce speed as fast as possible should an emergency arise in supercritical FSS testing.

The RPRV philosophy of no redundant systems was a factor in determining the type of augmentation supplied by the RAV ground computer. Recall that in section 2.2.2, the Air Force requirement for a secondary command capability was established. However, this backup system and the RAV system share many common and non-redundant systems. This consideration led to the establishment of the following design guidelines:

- Systems common to the RAV and on-board backup autopilot systems (servoes, hydraulic power supply, electrical power supply, etc.) have significantly better reliability than the mid-air recovery (MARS) technique, thus a single failure of common systems may result in the loss of the vehicle, but its occurence is much less likely than a MARS failure.
- The RAV and on-board control systems will have no sensors in common from the single sensor set in order to minimize the number of common systems.

Using these guidelines guarantees that no sensor failure can cause a degradiation in the performance of both control systems.

Due to the role which the autopilot performs, the attitude gyros and angle of attack sensor were reserved for its use. This is covered in detail in section 4.3. With the restriction from use of these sensors in the RAV system, the synthesis of the primary flight controls evolved into the system described in sections 4.2.2 and 4.2.3.

4.2.2 Longitudinal Modes. - A block diagram of the RAV system implemented in the pitch axis is shown in figure 4.10. As mentioned previously, the CAS mode will be the primary operating mode for the flight tests. It should be noted that the flight test experiment could be accomplished in the RD mode but the pitch-up and load limiting protection offered in the CAS mode would not exist. To fly the vehicle under these circumstances increases the risk and the pilot workload in-

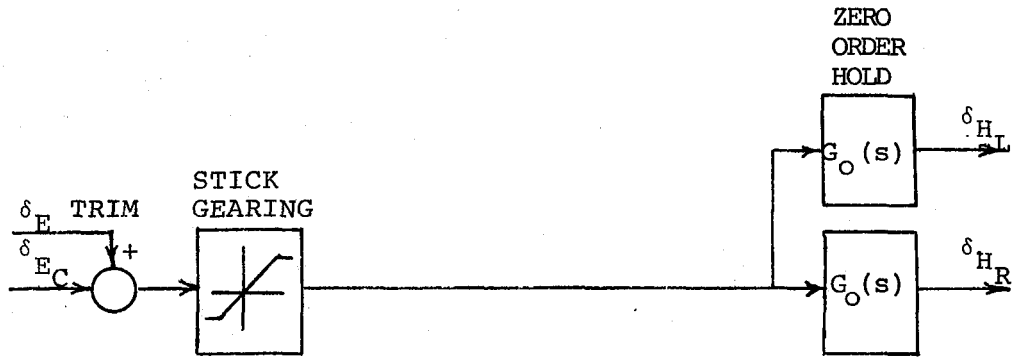

COMPUTER DIRECT (CD) MODE

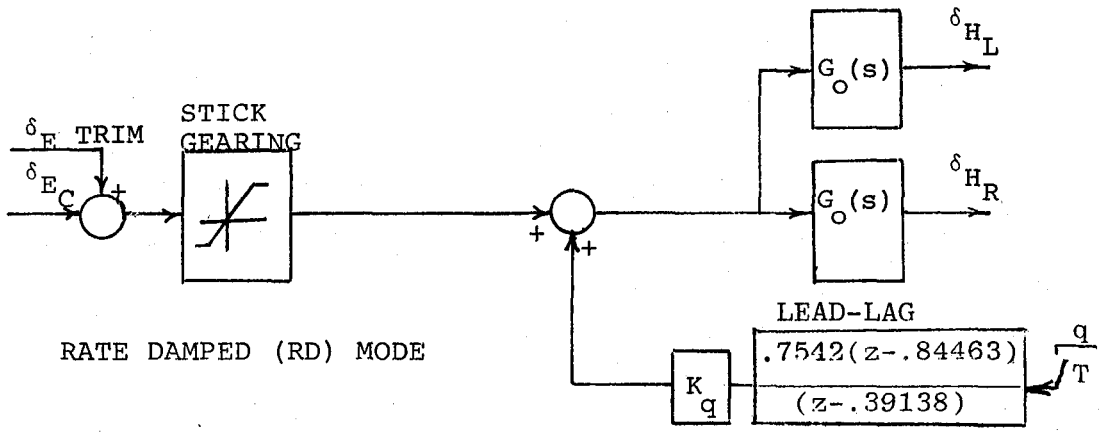

RATE DAMPED (RD) MODE

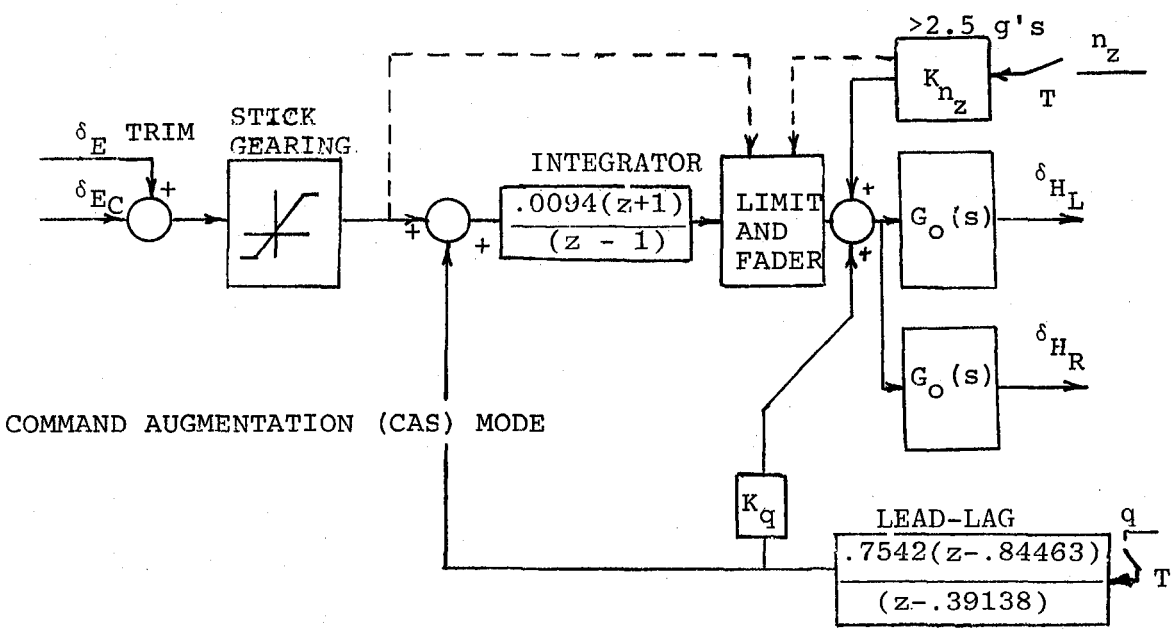

COMMAND AUGMENTATION (CAS) MODE

FIGURE 4.10 BLOCK DIAGRAM OF PITCH RAV AXIS

creases substantially. The philosophy behind the multi-mode option is twofold. First, if the pilot encounters flying characteristics significantly different from those predicted, the RD mode will be less sensitive to these changes and will give the pilot direct control of the vehicle's control surfaces, instead of operating through integrators as in the CAS mode. Second, the failure detection software described in section 5.5.4 can detect dangerous sensors failures and down-mode to the next lowest mode which does not require that sensor.

The limiter and fader block in figure 4.10 serves the purpose of putting the integrator in a hold status above the 2.5 g load limit. A trigger g level of 2.35 g's first activates the limiter and is required due to the fact that the aircraft's response lag's the pilot's inputs. The action of placing the integrator in hold prevent's the pilot from continuing the pull-up and over stressing the wing. The fader simply reduces the gain on the integrator between the 2.35 g trigger level and 2.5 g's so that continued pilot back pressure on the center stick allows the maximum 2.5 g maneuver without overshoot.

Normal acceleration feedback above 2.5 g's provides protection in turbulence when large g maneuvers are performed.

A lead-lag filter on the pitch rate signal was required to compensate for the one sample delay in the control law computation. The one sample delay is caused by the finite time interval required to make the control law computation.

This requires that past information must be used in the most current computations. Thus, introducing a time lag which is dependent on the age of the data used in the control laws. Without the lead, the additional delay in the pitch rate at high Mach number results in a signal similar to angle of attack (lagged pitch rate). Feeding this back only increases the short period frequency without improving the damping ratio.

Since the RAV system is a sampled data system, z-plane root locus methods were used in its design. The CONTROL program of reference 8 was used for the analysis. The flying qualities are defined in terms of the s-plane characteristics so the z-plane information can be related to the s-plane by the relationships:

$$\omega_d = \frac{\arctan \frac{\nu}{\mu}}{T} \tag{4.3}$$

$$\zeta = \cos\left\{ \arctan \left[\frac{-\arctan \frac{\nu}{\mu}}{\ell n \left[\frac{\mu}{\cos \arctan \frac{\nu}{\mu}} \right]} \right] \right\} \tag{4.4}$$

where ν is the imaginary part of the z-plane complex root, μ is the real part, and T is the sample period.

A z-plane root locus of the longitudinal RAV system is shown in figure 4.11. Lines of constant damping ratio appear as logarithmic spirals in the z-plane. These spirals are shown in figure 4.11. The flight condition corresponds to the worst case short period characteristics. Open loop ζ_{sp}

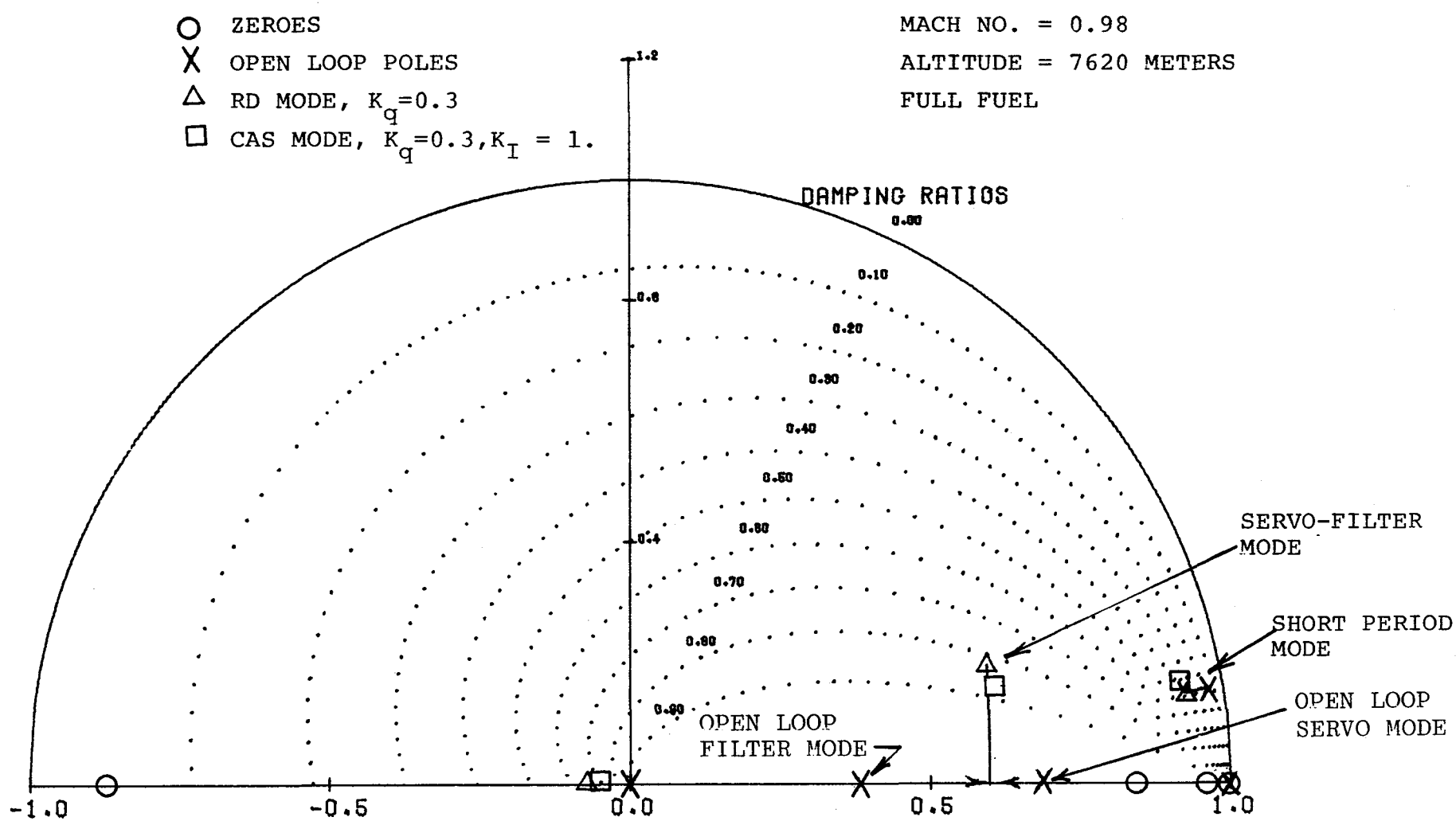

FIGURE 4.11 Z-PLANE ROOT LOCUS OF PITCH AXIS RAV (PAGE 1 OF 2)

EXPANDED AXIS Z-PLANE ROOT LOCUS

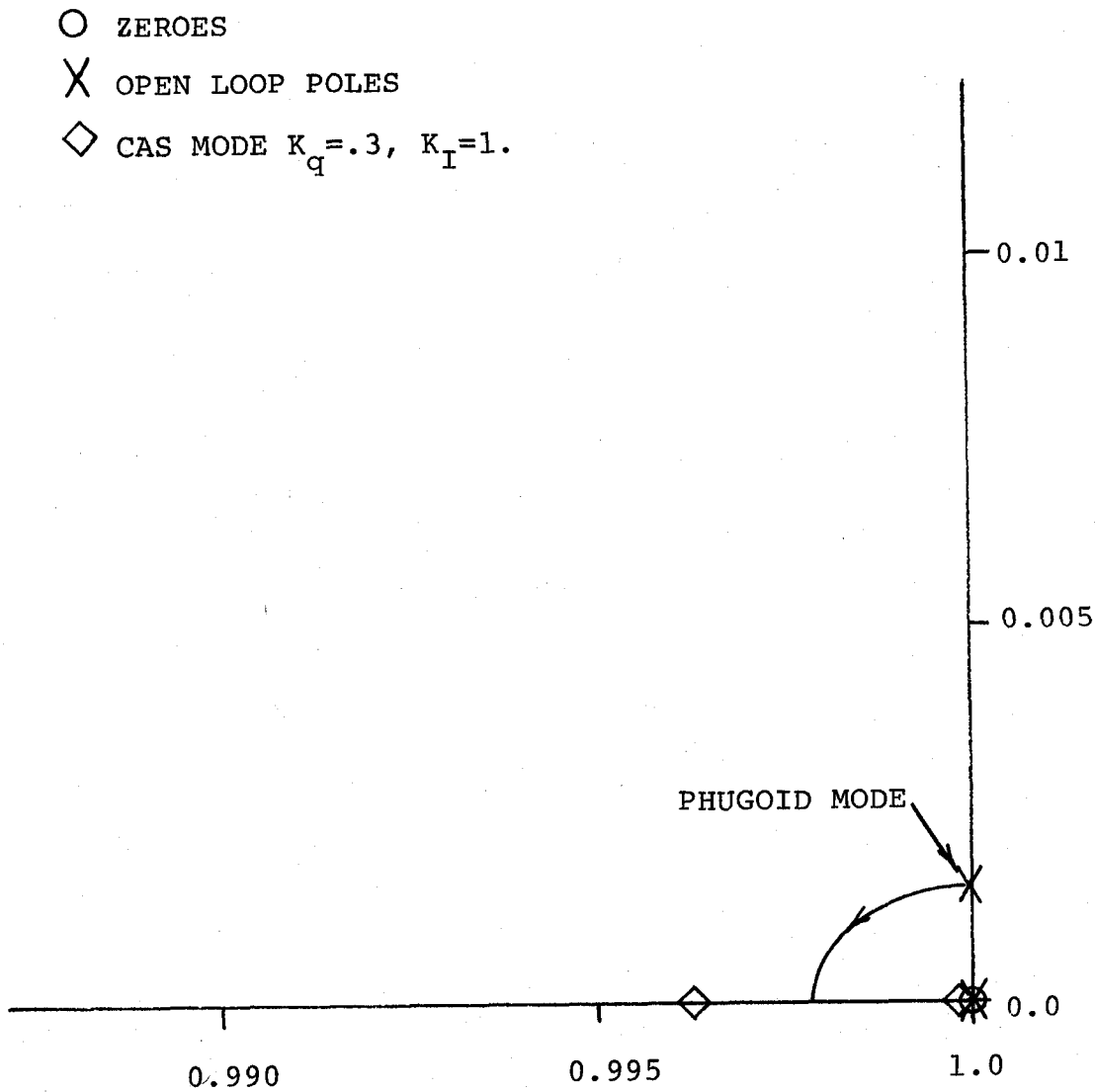

FIGURE 4.11 (CONCLUDED) (PAGE 2 OF 2)

= .15, while in the RD mode, ζ_{sp} is increased to .386. In the CAS mode the short period damping ratio is .356. This occurs at a feedback gain of .3 deg/deg/sec. The pitch CAS integrator is a pure integrator and therefore, its gain remains 1.0. The phugoid damping ratio, although not the worst case, is representative of how the CAS system augments it. Its open loop value in this case is 0.015, in RD ζ_{PH} =.016, and in the CAS mode with K_q = .3, ζ_{PH} is greater than one.

Under the best circumstances, that is h = 3048 meters and M = .90, and with the same gains, ζ_{sp} = .774. Since only transport-type maneuvers will be performed with DAST I, a washout filter in the pitch rate feedback path was deemed unnecessary. The phugoid damping ratio at this condition is greater than one in the CAS mode.

To show that the pitch RAV system is also adequate for unplanned emergency conditions, a pull-up maneuver was examined which is at the approximate condition where the pitch-up characteristic is evident. This might occur as the vehicle is in a maximum performance slow down and climb out following an FSS problem. As the vehicle slows to M = .7 going through h = 6096 meters, C_{m_α} begins to become positive since the vehicle is at approximately seven degrees angle of attack. For the open loop aircraft, its short period roots have migrated to the real axis, once the angle of attack approaches seven degrees. When C_{m_α} becomes positive, the short period mode has two real roots with one outside the unit circle. This situation is remedied with the pitch CAS system as can be

seen in figure 4.12. The short period frequency becomes 2.54 rad/sec with a damping ratio ζ_{sp} = .537. The z-plane locus in in figure 4.12 is of the normal acceleration feedback gain. The gain for normal acceleration feedback was found to have a significant effect on the short period frequency and damping. A gain of .2 deg/g proved to be the most satisfactory from simulation studies.

In order to compensate for any aeroelastic effects or other uncertainties the vehicle might exhibit in flight, a sensitivity analysis on the dominate longitudinal derivatives was conducted. A $\pm$ 20 percent variation in each derivative was examined for any adverse impact. For the short period mode the following effects were observed:

- Changes in C_{L_α}, C_{m_q}, and $C_{m_{\dot{\alpha}}}$ had little affect on the short period frequency
- Increasing C_{m_α} by 20 percent increased $\omega_{n_{sp}}$ at the worst case conditions by approximately 15 percent
- Short period damping was affected in the following manner at the worst case conditions:
  - ζ_{sp} is unchanged with a $\pm$20 percent change in $C_{m_{\dot{\alpha}}}$
  - ζ_{sp} decreases by 5.6 percent with a -20 percent change in C_{L_α}
  - ζ_{sp} decreases by 6 percent with a +20 percent change in C_{m_α}
  - ζ_{sp} decreases by 2.8 percent with a -20 percent change in C_{m_q}

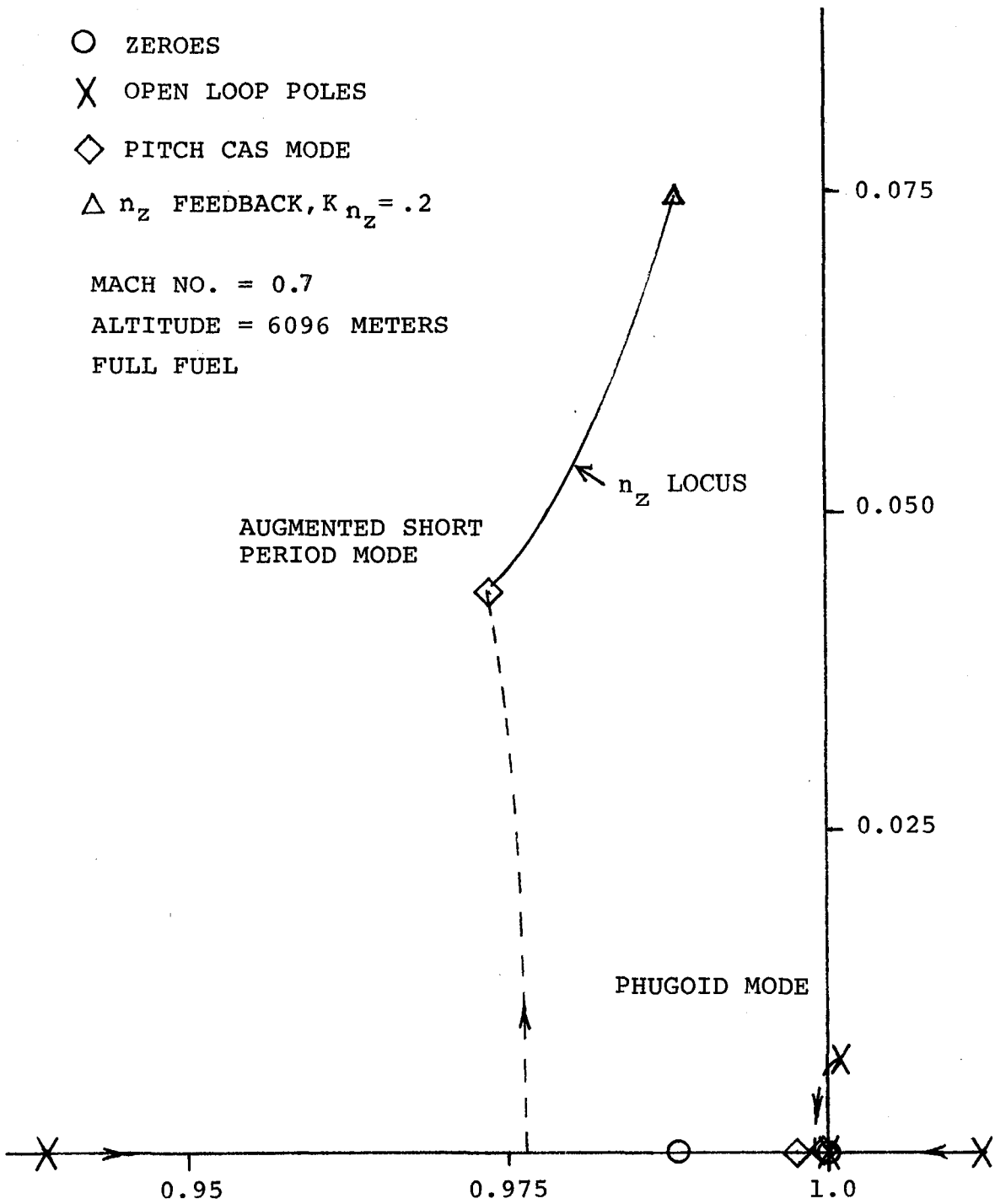

FIGURE 4.12 NORMAL ACCELERATION Z-PLANE ROOT LOCUS

With these worst case derivative changes added to the rigid body conditions existing at the worst case flight conditions (which is very unlikely to be encountered), the augmented short period characteristics become $\omega_{n_{sp}}$ = 10.55 rad/sec and ζ_{sp} = .305. These are still within level 1 flying quality ratings. The pitch CAS will satisfy its requirements for the short period mode at all flight conditions in the flutter testing region without the requirement for scheduling feedback gains with dynamic pressure.

In the case of the phugoid characteristics, which are not as critical, the speed derivatives were varied by the $\pm$20 percent margin. The effects are summarized below at the worst case conditions for the phugoid mode:

- Increasing C_{m_u} by 20 percent decreased $\omega_{n_{PH}}$ by six percent and ζ_{PH} by four percent
- Increasing C_{T_u} did not change $\omega_{n_{PH}}$ but did decrease ζ_{PH} by 2.5 percent
- Decreasing C_{D_u} did not effect $\omega_{n_{PH}}$ but did decrease ζ_{PH} by two percent
- Decreasing C_{L_u} decreased $\omega_{n_{PH}}$ by .8 percent but did not effect ζ_{PH}

Adding the worst case conditions listed above to the augmented values still results in a phugoid damping ratio orders of magnitude larger than MIL8785B Level 1 requirements.

4.2.3 Lateral-Directional Modes - The predicted open-loop lateral-directional characteristics for DAST I indicated that

the lateral-directional RAV system is less critical than the pitch axis. This is because in the flutter testing region, the open loop aircraft exhibits Level 1 flying qualities already. The dutch roll mode for the DAST is predominated by a rolling oscillation. Piloted simulation showed that because the roll inertia for this vehicle is so small, pilots preferred more dutch roll mode damping than the aircraft exhibited. Roll response was considered satisfactory.

The improvement in the dutch roll damping was achieved with the control system shown in figure 4.13. No augmentation was applied in the roll axis. Since the roll response was already adequate, a roll damper was not necessary nor desirable since it had a destabilizing effect on dutch roll damping.

The yaw axis utilizes washed-out yaw rate feedback in the RD mode. It was not necessary to add lead-lag to the yaw rate signal because the dutch roll mode frequency was not high enough to be affected by the .01875 second sample delay. Since the airplane has a relatively large diherdral effect, the yaw damper was found to be very effective in augmenting the dutch roll mode damping.

A z-plane root locus of the lateral-directional RAV control system is shown in figure 4.14. This flight condition corresponds to the worst case open loop characteristics of the dutch roll mode. The yaw damper increases the dutch roll natural frequency from 5.85 rad/sec to 6.89 rad/sec and augments the damping ratio from ζ_D= .181 to ζ_D = .449 at a

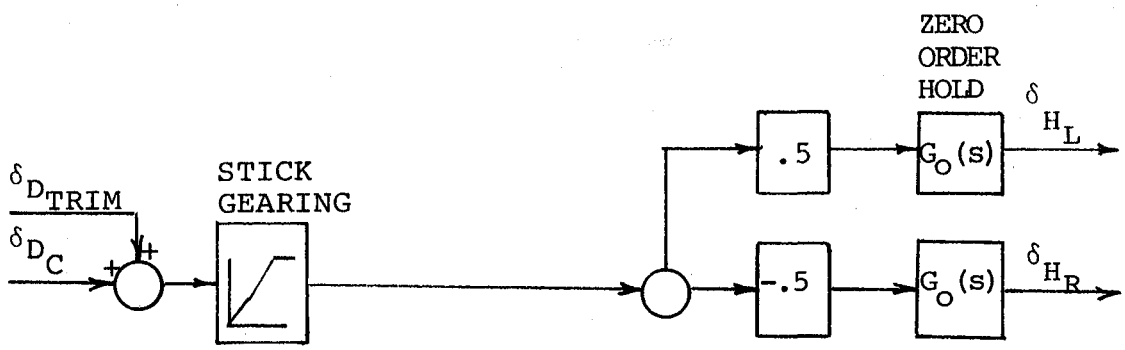

ROLL AXIS

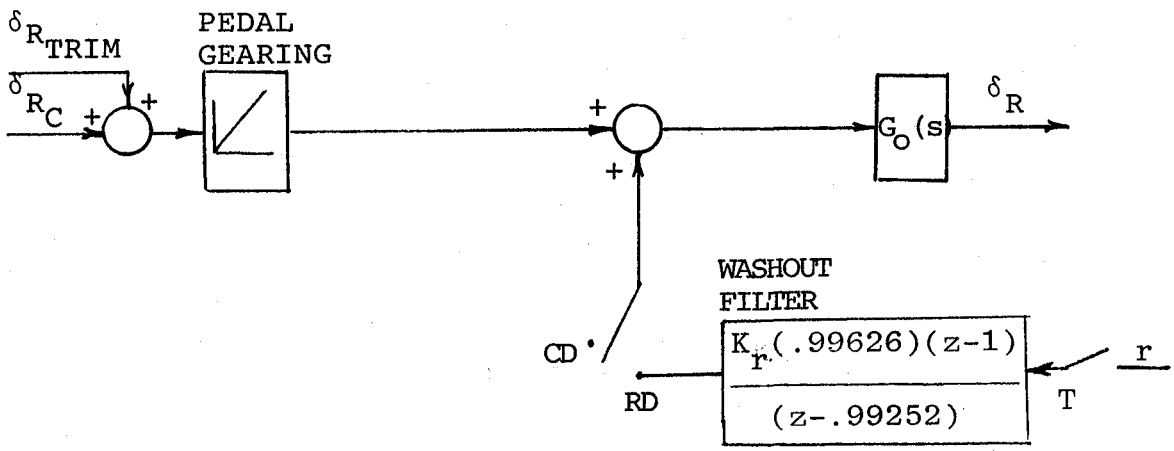

YAW AXIS

FIGURE 4.13 LATERAL-DIRECTIONAL RAV BLOCK DIAGRAM

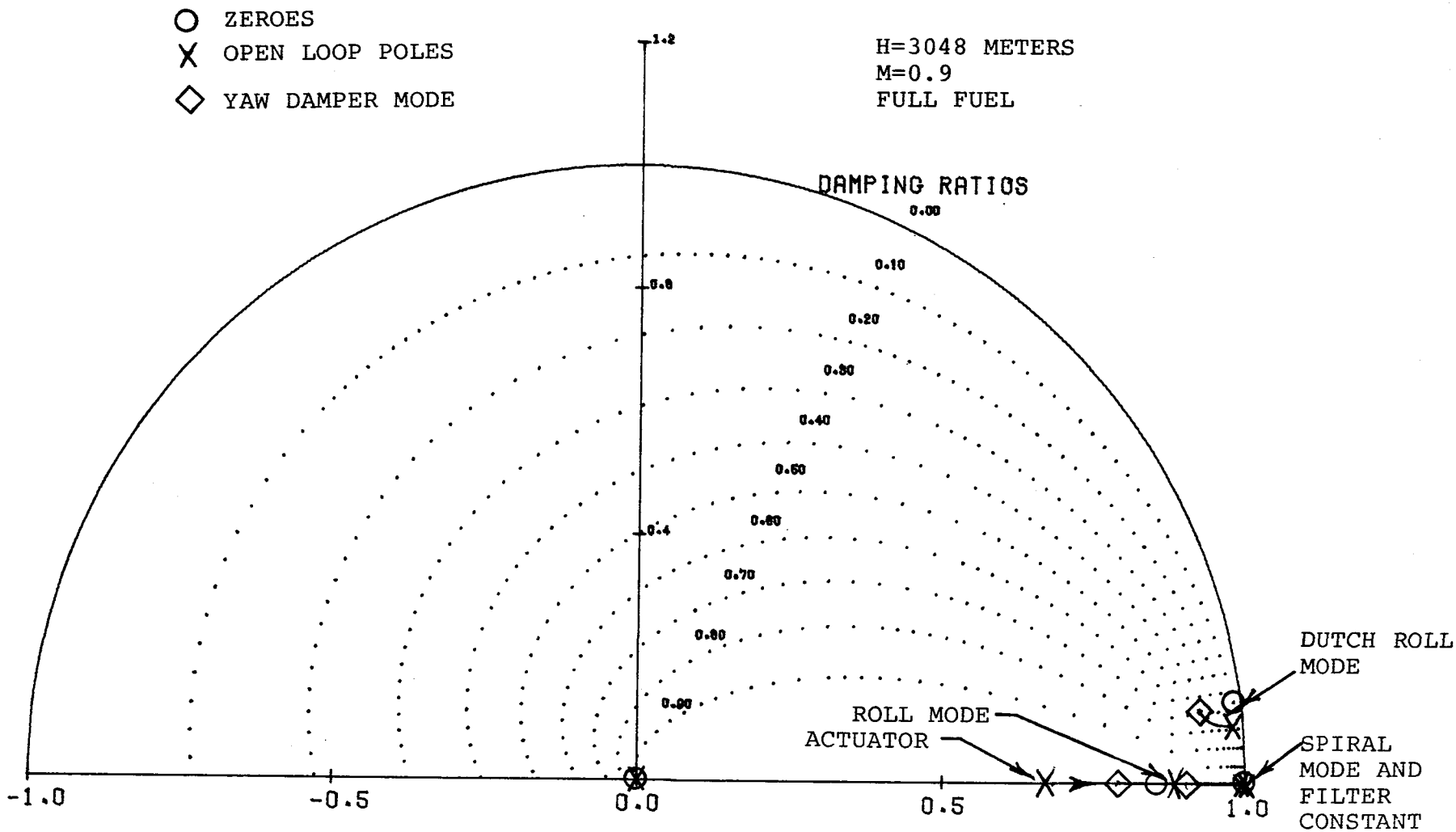

FIGURE 4.14 LATERAL-DIRECTIONAL RAV Z-PLANE ROOT LOCUS

gain of .3 deg/deg/sec. Under the best open loop circumstances, the yaw damper achieves a damping ratio of 0.596. The lateral-directional RAV system increases the roll time constant very slightly and the spiral is unaffected.

Due to the large amount of damping offered by the yaw damper, the sensitivity analysis of the dominate stability derivatives in the lateral directional equation was not of concern. The worst circumstances for the dutch roll mode damping showed a 13 percent reduction in ζ_D. At the worst flight conditions for the roll mode, the time constant is increased by approximately ten percent. Only the derivative C_{n_r} seemed to have an appreciable effect on the spiral mode. It increased the spiral mode time constant by only 6.5 percent. It should be recognized that the reason the $\pm$20 percent variation in the lateral-directional stability derivatives was not of great concern was that, even with the worst conditions, the RAV system implemented for the DAST I possesses damping and response characteristics substantially better than the MIL-8785B Level 1 minimums in the lateral-directional axes.

4.2.4 Control Law Functional Validation. - The RAV control laws were implemented in the DAST I real-time simulation. The z-plane transfer functions were coded in FORTRAN as difference equations. The RAV performance was tested in all areas of the flight envelope with a .3048 meter/second RMS gust in all axes.

Figure 4.15 shows time histories of the longitudinal parameters for the open loop (CD) and augmanted (CAS) at normal

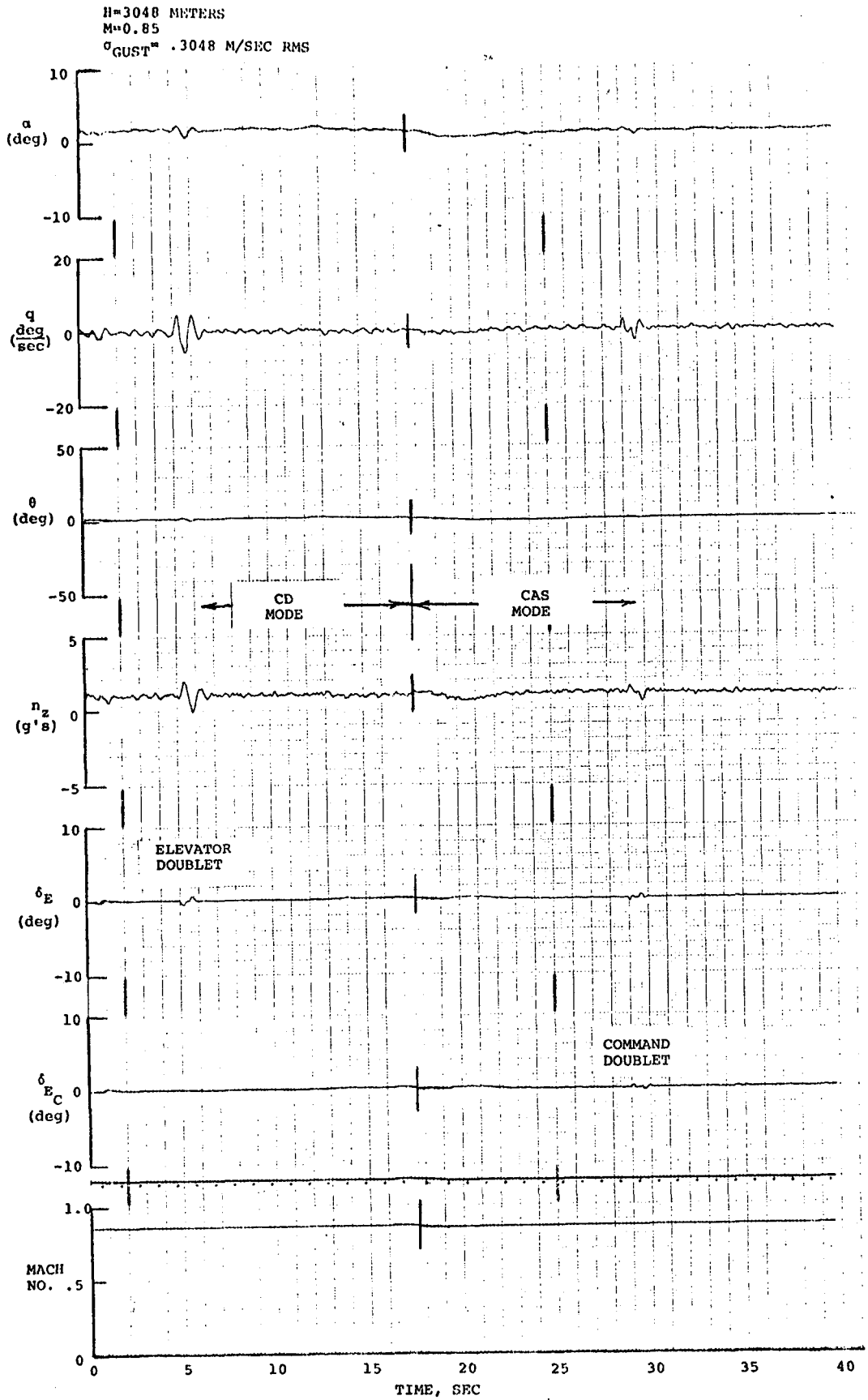

FIGURE 4.15 TIME HISTORY OF THE PITCH RAV OPERATION (PAGE 1 OF 2)

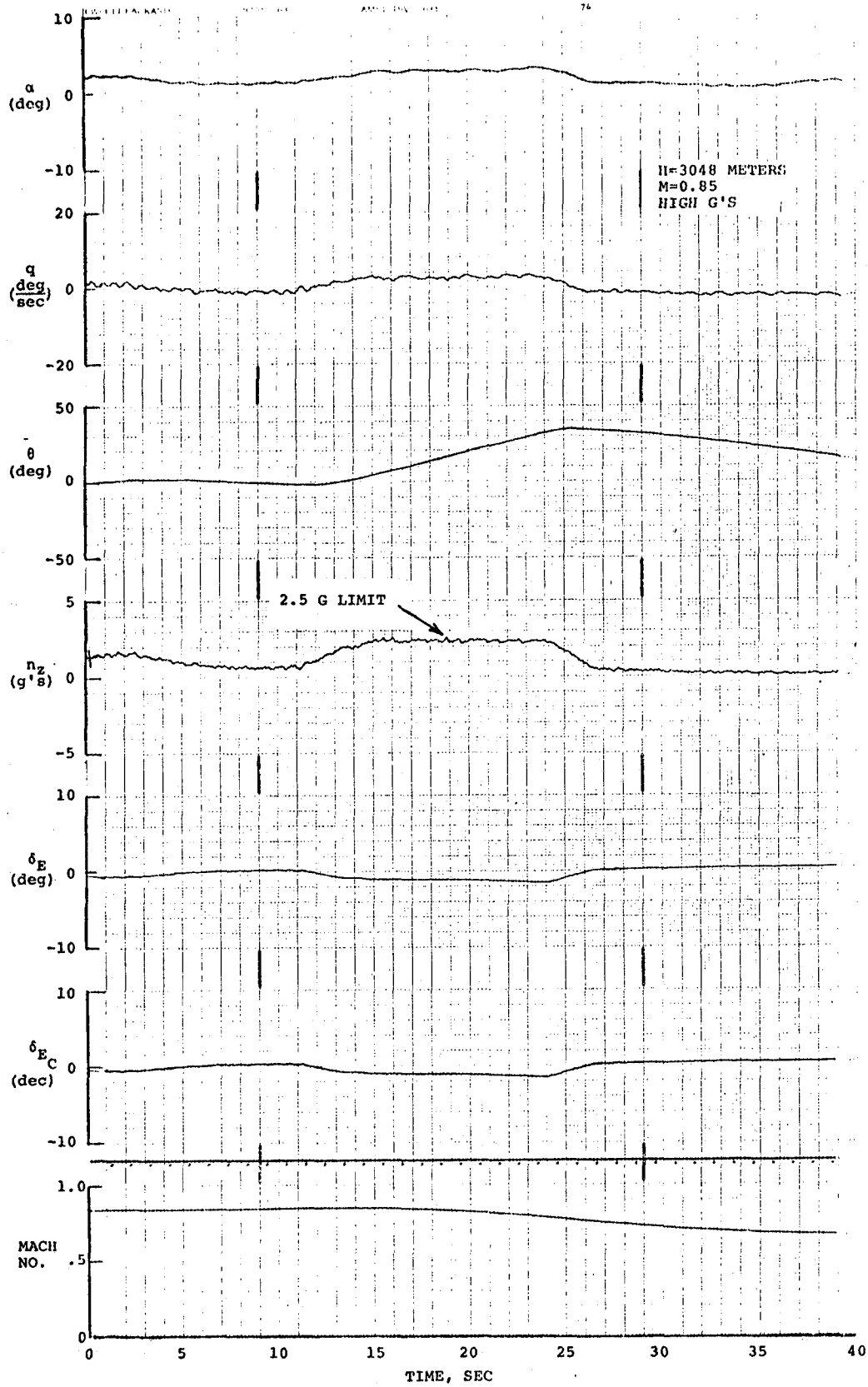

FIGURE 4.15 (CONCLUDED) (PAGE 2 OF 2)

one g flight and at the maximum 2.5 g condition. A smoothing of the angle of attack, pitch rate, and normal acceleration traces is evident when the augmented system is activated in the one g condition. Traces without the gust inputs verified the damping and frequency values resulting from the root locus analysis. Figure 4.15 includes the turbulence to illustrate the effect the RAV system will have in a more realistic environment. The high g condition, also shown in figure 4.15, represents a maximum performance pull-up maneuver which might be initiated if problems occur with the FSS. It basically illustrates the proper operation of the load limiting capability of the pitch CAS. The pilot pulls back on the stick and holds it against the 2.5 g limit. As his back pressure on the stick increases, the fader allows the pitch orientation integrator to slowly increase the surface deflection since the change in flight condition requires more deflection to maintain the maximum 2.5 g value. The fader's purpose, which is demonstrated here, is to reduce the gain on the integrator to a value (1/20 of normal) which keeps the vehicle at its maximum performance load limit without overshoot. The normal acceleration feedback above the 2.5 g limit is used to protect the vehicle from gust inputs at the limiter value.

Figure 4.16 shows the operation of the RAV lateral-directional system at the same one g flight condition used in the longitudinal case. The rudder and tail doublets during operation in the computer direct mode (CD) illustrates the following:

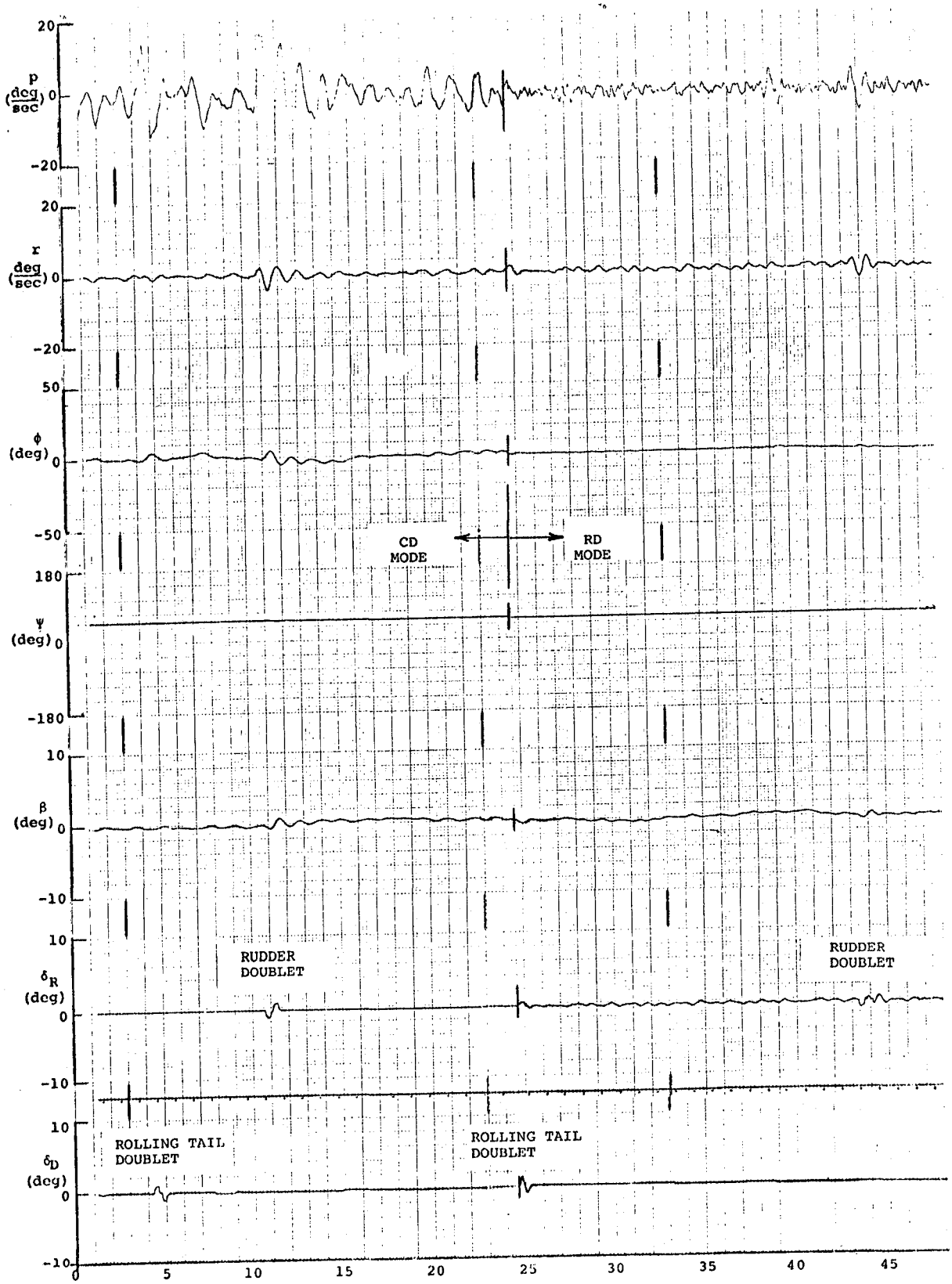

FIGURE 4.16 TIME HISTORY OF THE LATERAL-DIRECTIONAL RAV OPERATION

- The dutch roll mode involves much more rolling oscillation than yawing motion.
- The rolling tail has little effect in exciting the dutch mode.
- Rudder doublets are very effective in exciting the dutch roll mode.

This confirms the reasoning for augmenting the dutch roll mode damping with the yaw damper and not using a roll damper.

With the yaw damper operating, a significant reduction in the amplitude of the roll rate is evident. Doublets to the rolling tail and rudder illustrate the improvement in the dutch roll mode achieved with the lateral-directional RAV system in a gusty environment.

Pilot evaluations of this vehicle drew the following comments:

1. The pilots were surprised by the amount of improvement in flying qualities resulting from the ARW-1 wing.
2. All the control modes perform their desired tasks satisfactorily.
3. The pitch CAS mode reduces the pilot workload particularly in turns.

The third comment has significance in that the pilot felt that the pitch CAS mode allowed for time to concentrate on maintaining a constant airspeed which is critical in the flutter tests.

4.3 DAST I On-Board Autopilot. - The basic Firebee drone

had an on-board discrete command anlaog autopilot system. In order to interface this system properly with the digital proportional RAV system, a complicated interface box would have been required. For the requirement as an RPRV, only approximately 10 percent of the Firebee autopilot's functional capabilities were utilized. The other autopilot capabilities were associated with its role as a military target drone.

A new much simpler on-board autopilot system was developed for the following reasons:

1. The cumbersome Firebee autopilot and its interface equipment required a large portion of the room available in the DAST fuselage.
2. It was desirable to simplify the mechanization of the control systems by making the autopilot proportional like the RAV system.
3. Modifications to the Firebee autopilot to adapt it to the DAST flying characteristics would have been difficult since the Firebee autopilot construction was of multi-layer printed circuit boards.

4.3.1 Design Requirements. - The primary purpose of the DAST I autopilot is to take over command of the vehicle if the RAV control system malfunctions. It will be used only to fly the DAST safely to the MARS recovery area. With this in mind, the following requirements were established:

- Before F-104 chase captures command:
  - -wing leveling
  - -envelope limiting
    - * angle of attack containment

* limit velocity by α-control

-Have at least Level 3 flying qualities (with $\pm$20 percent uncertainty in aerodynamic derivatives).

- After F-104 chase captures command:

-bank angle control

-glide slope control with at lease Level 3 minimums

-Throttle control

If there is a loss of TM which causes RAV failure, the autopilot is to stabliize the vehicle at the last heading and altitude until the F-104 takes control or an automatic recovery is initiated. The throttle setting is automatically reduced to the 80 percent RPM setting when there is an RAV-to-AP transfer. Since the chase aircraft RPRV pilot cannot tell the magnitude of angle of attack at which the DAST is flying, the angle of attack must be limited to prevent inadvertant high angle of attack operation and pitch-up.

Priority in sensor selection was given to the autopilot, since the RAV computer gave the ground facility the capability to synthesize any parameter which it required.

4.3.2 Longitudinal Axis. - A block diagram of the complete autopilot is shown in figure 4.17. Pitch and roll commands are sent to the vehicle in the form of left and right horizontal stabilizer commands. These are symmetric for elevator inputs and differential for roll inputs. In this manner, the same digital word format used in the RAV uplink is used in the AP uplink. These digital commands are converted to

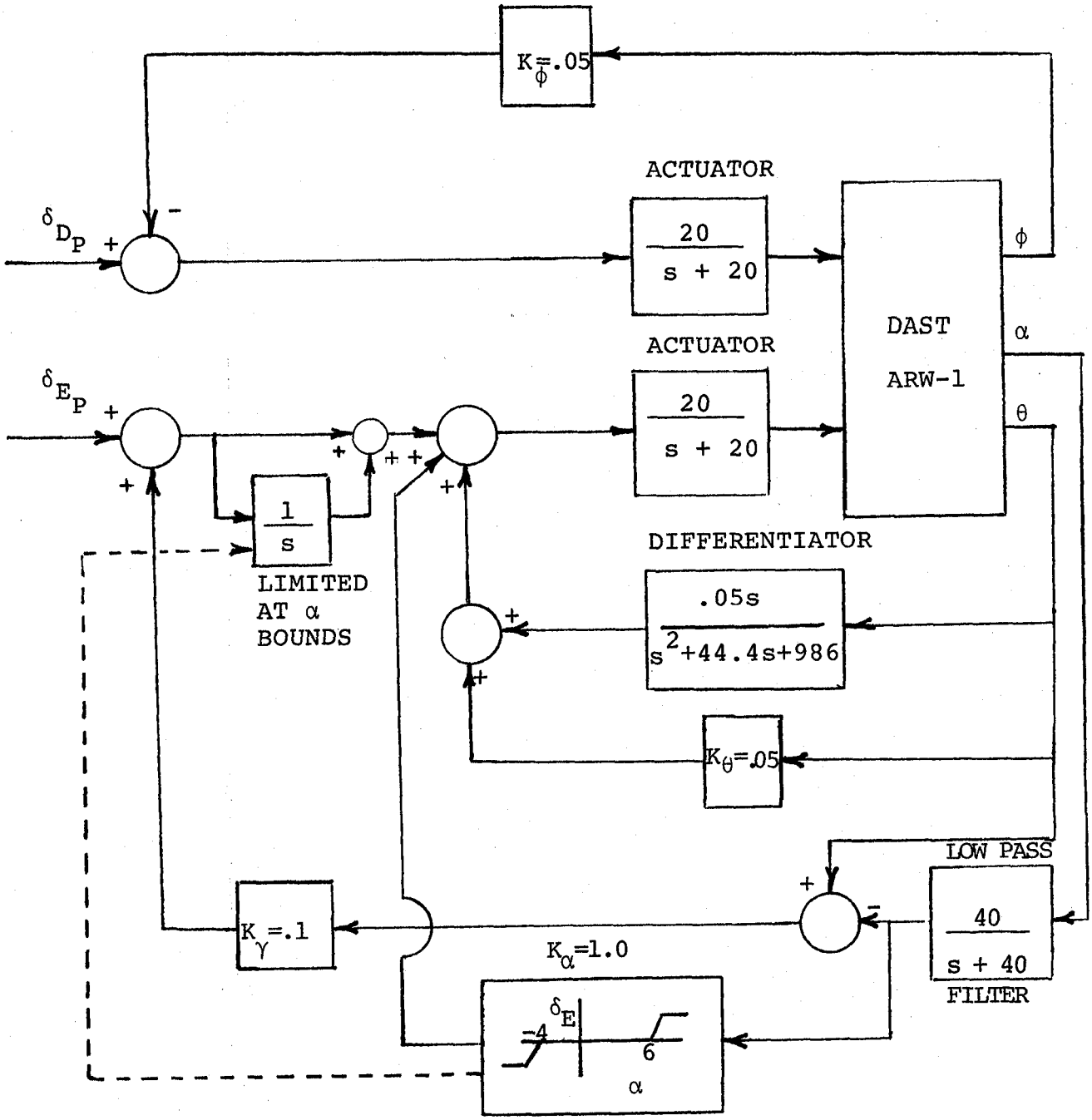

FIGURE 4.17 DAST I AUTOPILOT BLOCK DIAGRAM

analog signals on-board since the autopilot is an analog system.

The longitudinal functions in this system are:

- pitch damping
- pitch attitude hold
- angle of attack limiter
- glide slope hold

Pitch damping was achieved by differentiating the pitch attitude signal to produce an approximate pitch rate signal. Pitch attitude feedback augments the phugoid characteristics.

An s-plane root locus of the pitch damper and pitch attitude feedback loops is presented in figure 4.18. The flight condition corresponds to the worst case short period open loop characteristics in the flutter testing region. The short period frequency is increased to 9.56 rad/sec and the damping ratio increased to .208. The phugoid frequency jumps to 0.044 rad/sec while the damping ratio is increased from .015 to .79. The feedback loop gains are .05 deg/deg/sec for the damper and .05 deg/deg for the pitch attitude hold loop. The short period gain was chosen to provide sufficient margin so that when the $\pm$20 percent variation in the aerodynamic derivative values are included, at least Level 3 minimums exist. The high phugoid damping value was found to be desirable from simulation studies.

By controlling the vehicle's glide slope, both velocity and altitude excursions can be kept within safe limits. For the DAST autopilot, the glide slope signal, γ, was generated

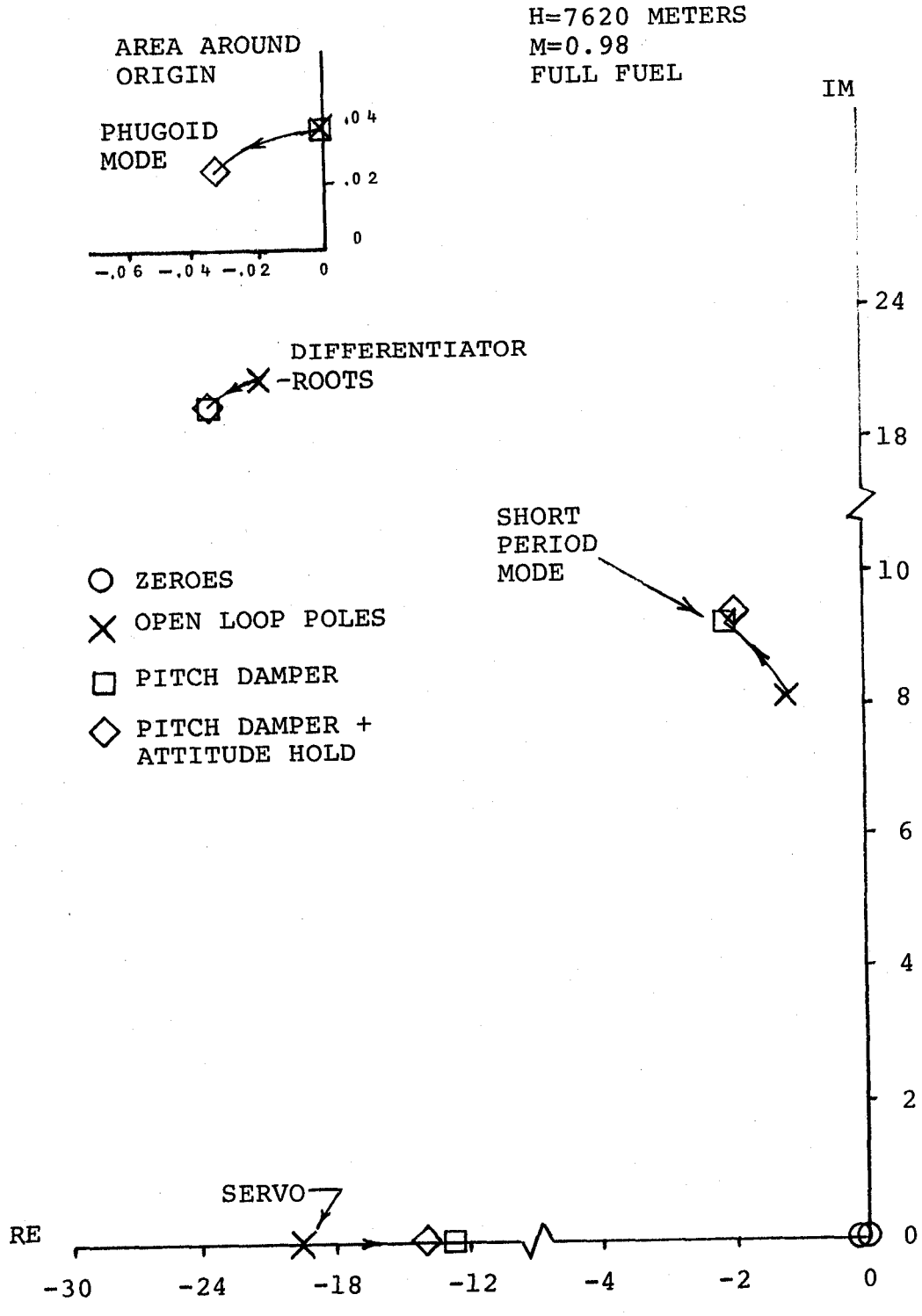

FIGURE 4.18 AUTOPILOT PITCH DAMPER AND PITCH ATTITUDE HOLD S-PLANE ROOT LOCUS

by subtracting angle of attack from pitch attitude. Since this signal is not bank angle compensated, the value for γ will only be accurate when the bank angle is not large. A root locus of the glide slope loop is shown in figure 4.19. The forward loop integrator is required to magnify, over a period of time, the error between the glide slope feedback path and the reference command so the steady state commanded γ can be achieved. The lag filter for the angle of attack signal was required to eliminate the nose boom structural dynamics from the signal. Due to the low frequency nature of flight path control, the glide slope hold has little effect on the vehicle's short period mode. With a pure integrator and a γ-loop gain of .1 deg/deg, the phugoid damping ratio becomes .767 at a frequency of .112 rad/sec.

At Mach numbers where the phugoid mode is unstable, the pole at the origin is attracted toward a zero in the right half of the s-plane near the origin. At the gains mentioned above , a pole-zero cancellation takes place in the γ/δ_e transfer function to effectively eliminate the divergence.

The zero which is in the right half of the s-plane can be approximated by:

$$\frac{1}{T_{\gamma 1}} \cong \frac{W}{g}\left[\frac{\partial D}{\partial U} - \frac{\partial T}{\partial U}\right] \qquad (4.5)$$

This equation is given to illustrate the source of this zero. Since the pitch attitude is tightly controlled by the inner loops, no divergence is evident in the pitch response.

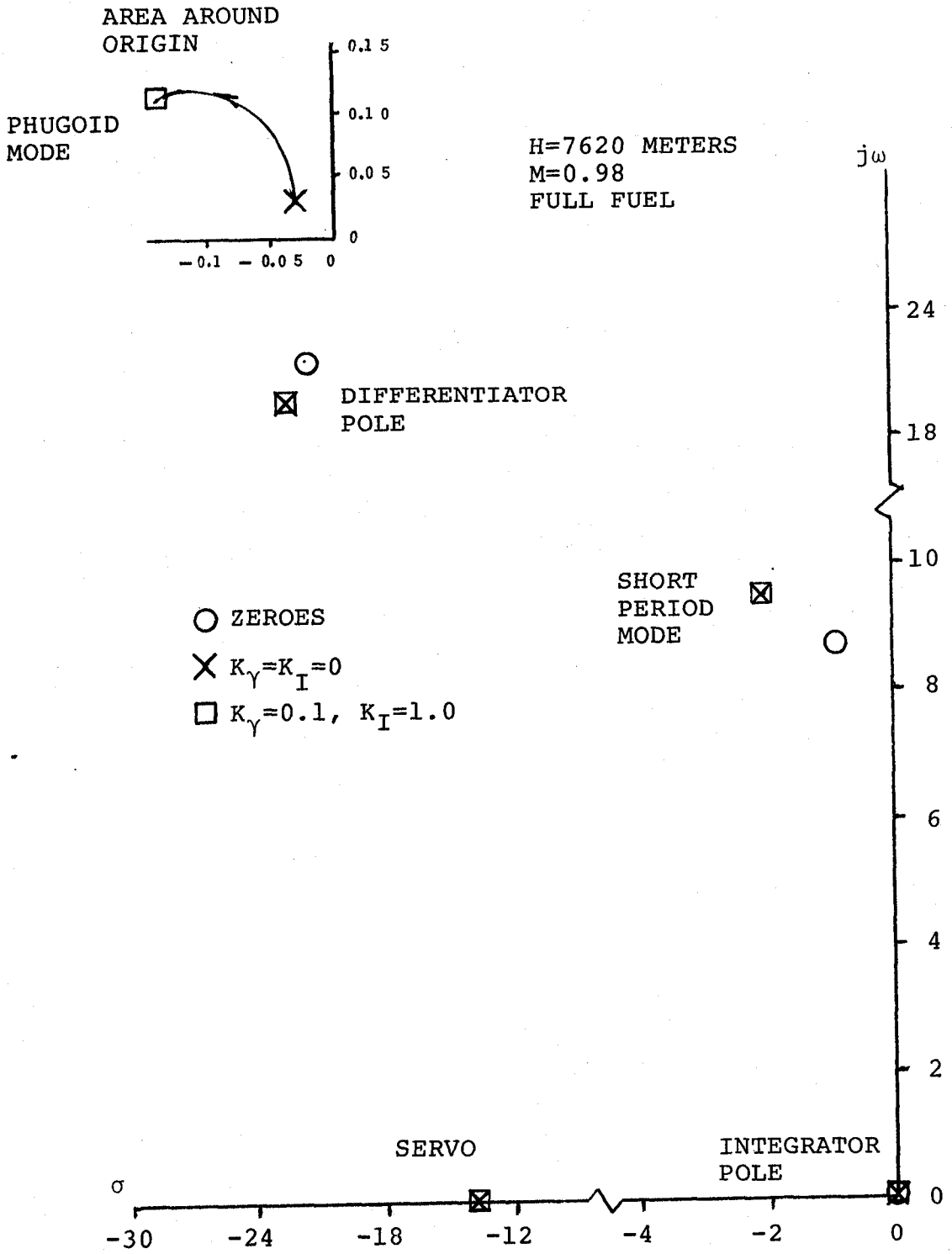

FIGURE 4.19 ROOT LOCUS OF AUTOPILOT GLIDE SLOPE HOLD

This zero does not exist in the u/δ_e transfer function, so no pole-zero cancellation occurs. The divergence shows up as a speed stability problem created by the fact that C_{D_u} is negative and C_{T_u} is positive in many regions of the flight testing envelope. It makes precise control of airspeed very difficult. In general, the conditions which possessed an unstable open loop phugoid mode also experienced this speed stability annoyance. Since speed brakes do not exist and throttle feedback is impractical due to very poor engine response characteristics, the $1/T_{\gamma_1}$ zero cannot be moved to solve this problem.

The alpha limiter in the longitudinal autopilot only works above 6 degrees angle of attack and below -4 degrees angle of attack. Between these limits no feedback occurs. The case which was set up to examine the limiter was:

$M = .8$

$h = 8680$ meters

load factor = 2.5 g's

$\alpha_{trim} = 7.25$ degrees

This might correspond to conditions in an emergency pull up maneuver to slow the vehicle down. With M = .8 at 7.25 degrees angle of attack, $C_{m_\alpha} = .241/\text{rad}$ which would represent a severe pitch-up tendency. The root locus of the alpha limiter is seen in figure 4.20. Because the glide slope hold is outer loop in nature, the forward loop integrator had to be disabled so that it would not overpower the angle of attack limits. With the rest of the autopilot augmentation operating,

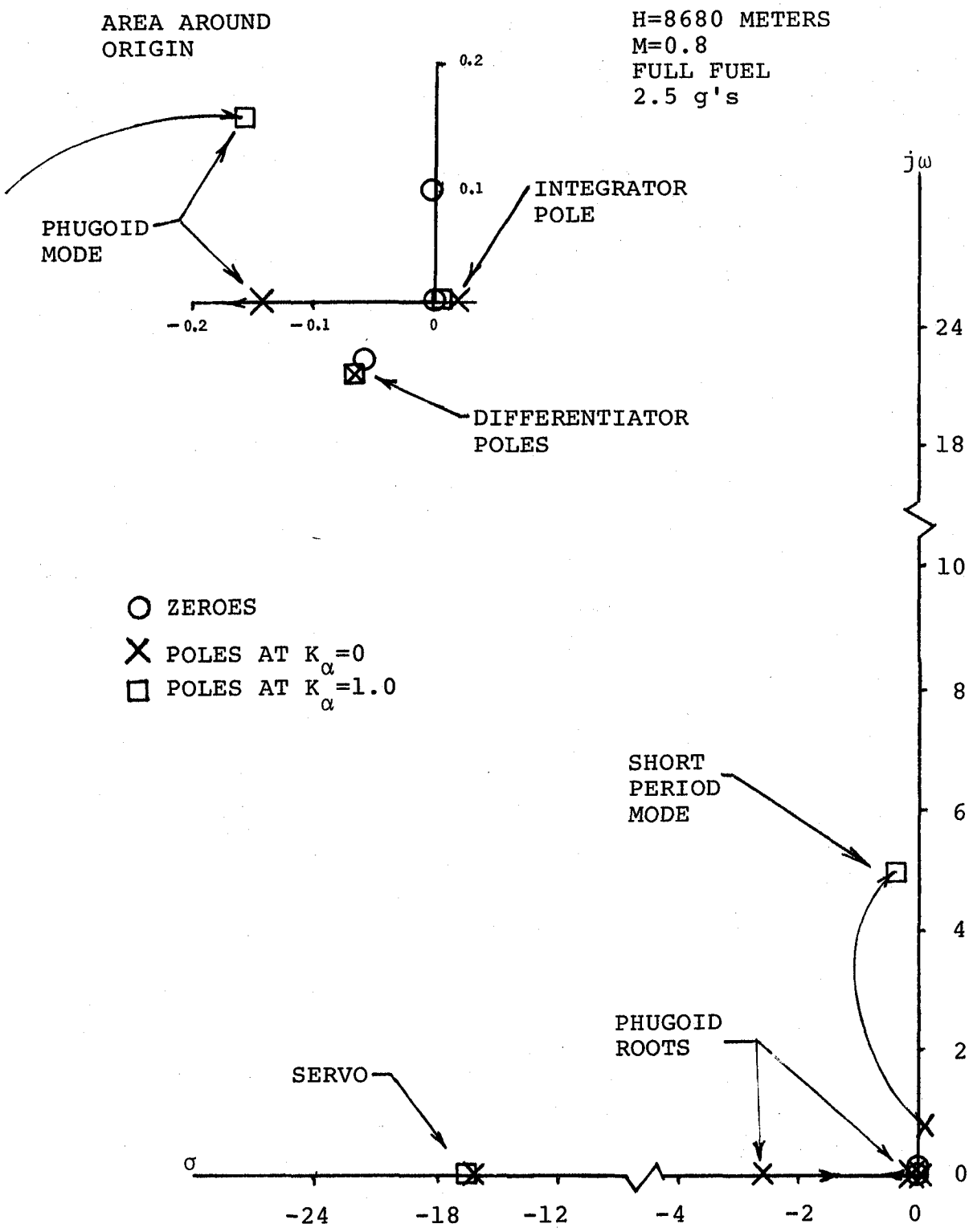

FIGURE 4.20 ROOT LOCUS OF AUTOPILOT ALPHA-LIMITER

the short period mode has a frequency of .775 rad/sec and a damping ratio of ζ_{sp} = -.127. The phugoid has become two real negative roots at this condition. With a gain of 1 deg/deg on the angle of attack feedback, ω_n = 5.02 rad/sec and ζ_{sp} = .08. Lower gains on the alpha limiter increased the damping ratio, ζ_{sp}, but simulator studies showed that lower gains were inadequate in dynamic tests. An authority limit on the alpha limiter of 1.5 degrees of elevator command gave it the characteristics of a soft limit which eliminated the limit cycle tendency this high gain produced across the alpha boundary.

4.3.3 Lateral-Directional Axes. - The inherent lateral-directional characteristics have been shown to be quite good for the DAST I vehicle. The autopilot design requirements specified only the need of a wing leveling capability. Upon examining a single wing leveler system using bank angle for feedback, it was found that no additional augmentation would be required to satisfy the design specifications. A root locus evaluation at the worst case conditions for the dutch roll mode is shown in figure 4.21. This mechanism increases the dutch roll frequency by only .16 rad/sec and increases ζ_D from .181 to .21. The roll mode time constant is increased by 15 percent. The spiral mode is stabilized with a time constant of 5.15 seconds.

4.3.4 Autopilot Control Law Functional Validation. - The F-104 RPRV control of the DAST autopilot in the pitch axis is demonstrated in figure 4.22. A climb maneuver followed by

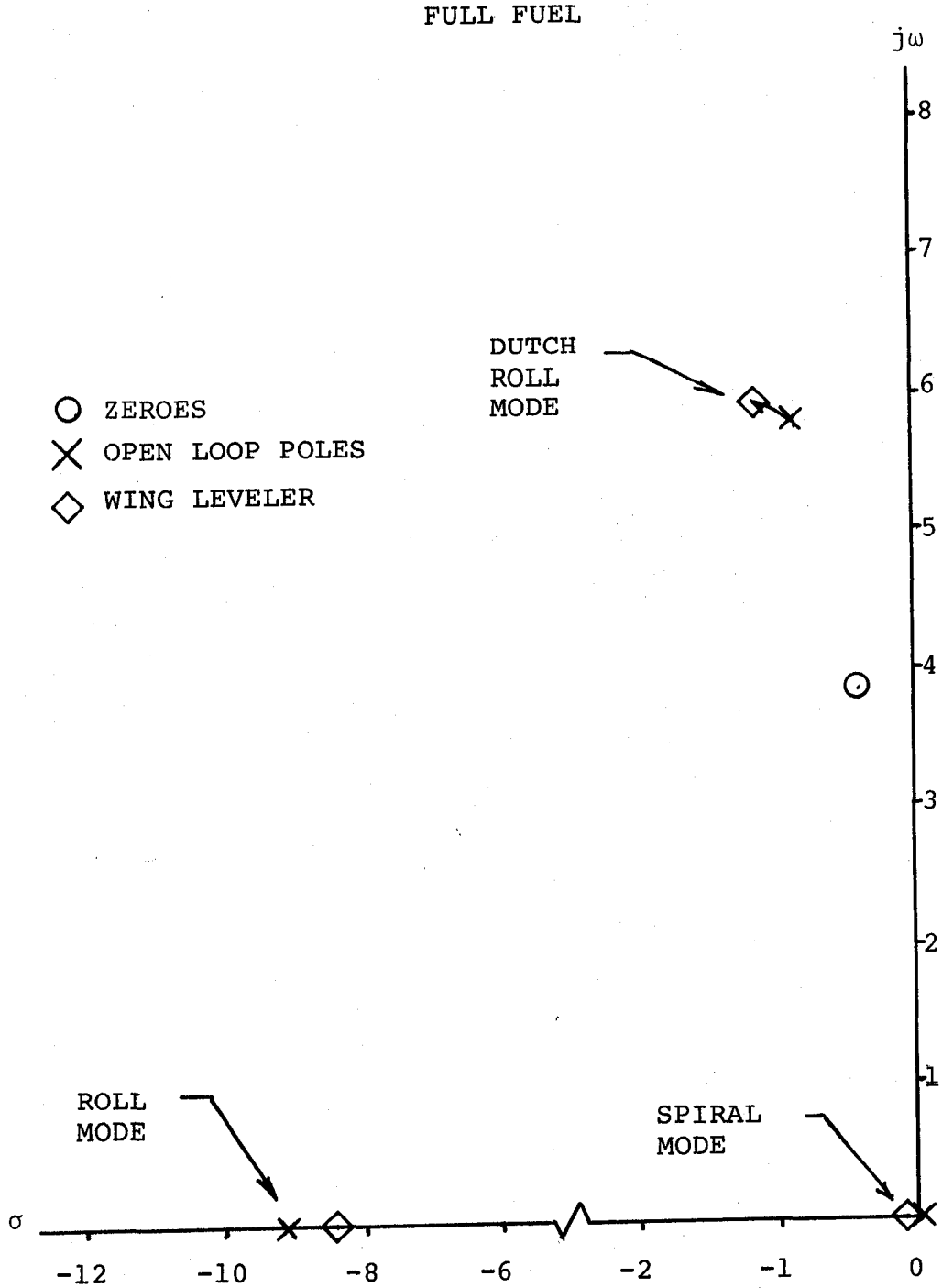

FIGURE 4.21 WING LEVELER ROOT LOCUS

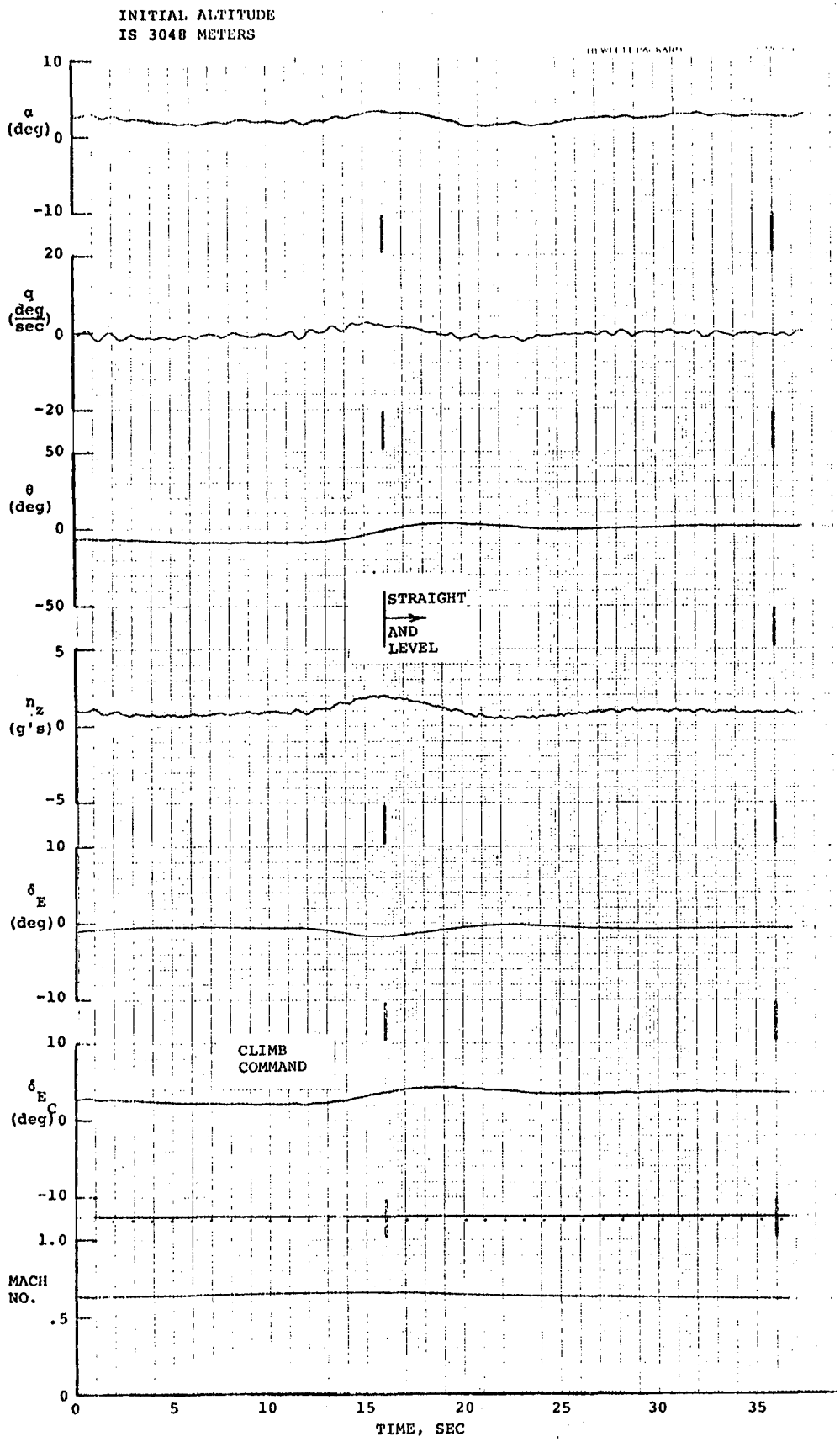

FIGURE 4.22 TIME HISTORY OF LONGITUDINAL AUTOPILOT OPERATION

a straight and level command is shown. The turbulence used in the RAV time histories is included as a disturbance. It is obvious from the trace of elevator deflection that only very gradual maneuvering is possible in the AP mode. If no inputs are made, the vehicle will maintain very precise control of altitude.

The function of the wing leveler is illustrated in figure 4.23. The roll rate trace shows very little difference from the open loop aircraft response indicating the dutch roll mode is influenced very little. The turn maneuver shows that the bank angle is held relatively constant in a turn and with wings level. The bank angle command was limited because the glide slope signal does not include the $\cos\phi$ term in the expression $\alpha = (\theta - \alpha)\cos\phi$. Without this compensation, large errors are created in the α values when ϕ becomes large. This error can drive the vehicle to the alpha limit creating high g's in the process.

Pilot evaluations of the autopilot in the real-time simulator produced the following comments:

1. The autopilot performs its task satisfactorily.
2. With the present trim rates on the F-104 DAST control stick, adequate turn capability exists and adequate climb and dive performance exists.
3. The slow response does provide the necessary load limiting protection.

4.3.5 Launch and Recovery Requirements. - At present, the launch requirements for the DAST I are to launch with the

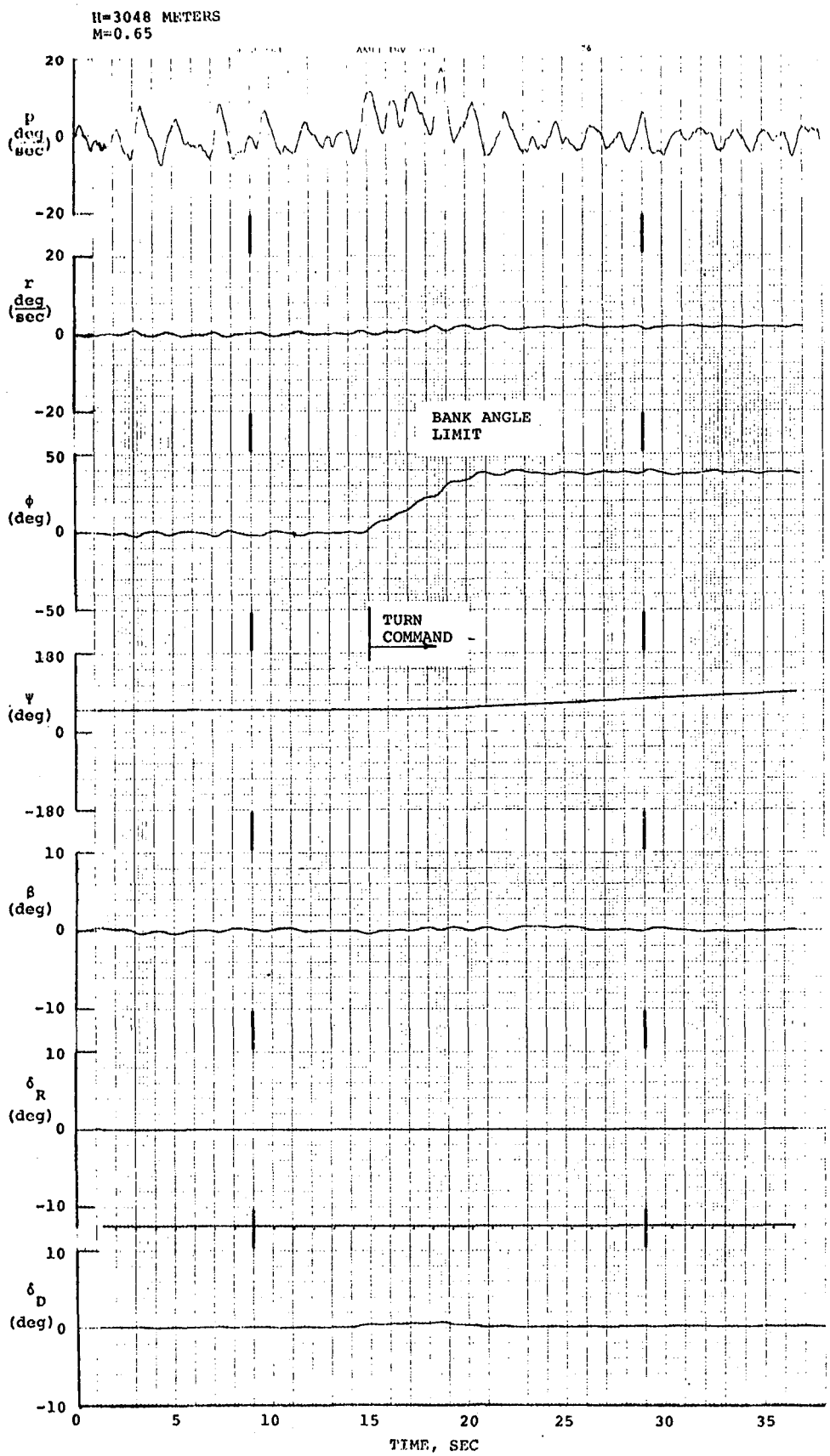

FIGURE 4.23 TIME HISTORY OF WING LEVELER OPERATION

control surface locked in a nose down command for three seconds before the control systems become active. To examine the reasonability of this requirement, the flowfield effects of the B-52 launch vehicle were added to the real time simulation. The flowfield model was developed for the 3/8 scale F-15 RPRV of reference 4. This same flowfield model was used in the basic Firebee simulation and compared reasonably well with flight results.

The DAST I vehicle is attached to the B-52 pylon with a -5 degrees angle of attack relative to the B-52 wing. The flowfield is estimated to add another -1.8 degrees to this value. The vehicle will sense a -2.7 degrees sideslip angle when attached to the pylon. Figure 4.24 shows a simulated launch from 4572 meters at M = .65. The B-52 wing angle-of-attack was estimated to be 5.8 degrees. The vehicle rolled to the right approximately 40 degrees before the RAV system was activated. No unsafe conditions were encountered.

In figure 4.25, a launch in the AP mode is shown. This would result if the DAST was launched active or the RAV failed to operate after launch. About 1.5 g's of normal acceleration is reached in the pull-up maneuver to achieve zero glide slope. The vehicle still rolls to about 40 degrees of bank angle and very little altitude is lost.

The recovery technique was investigated to see if the low g wing would encounter problems with the MARS recovery. Estimates for the drouge and main parachute drag characteristics were included in the equations of motion. The proper chute

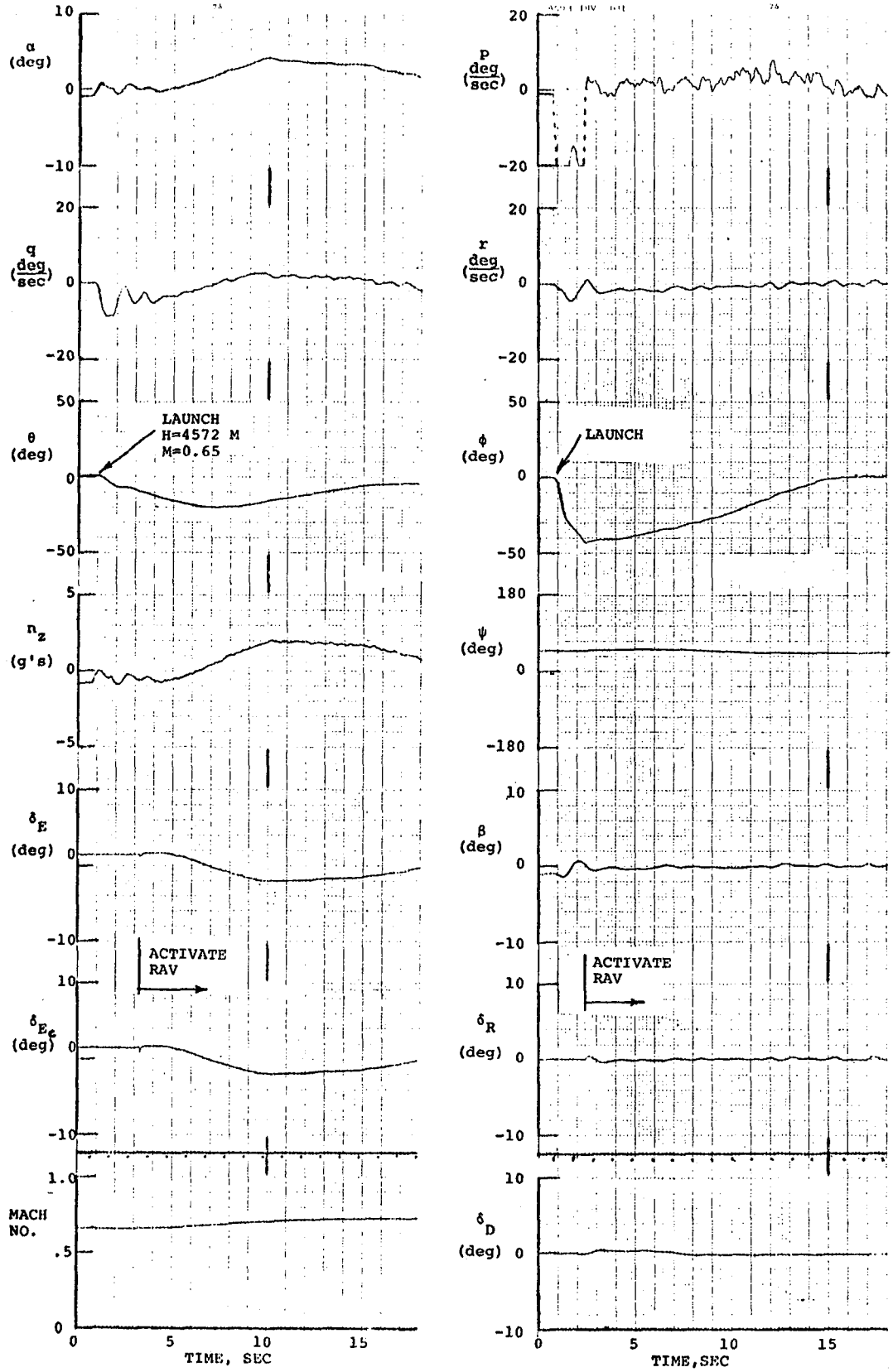

FIGURE 4.24 TIME HISTORY OF B-52 LAUNCH

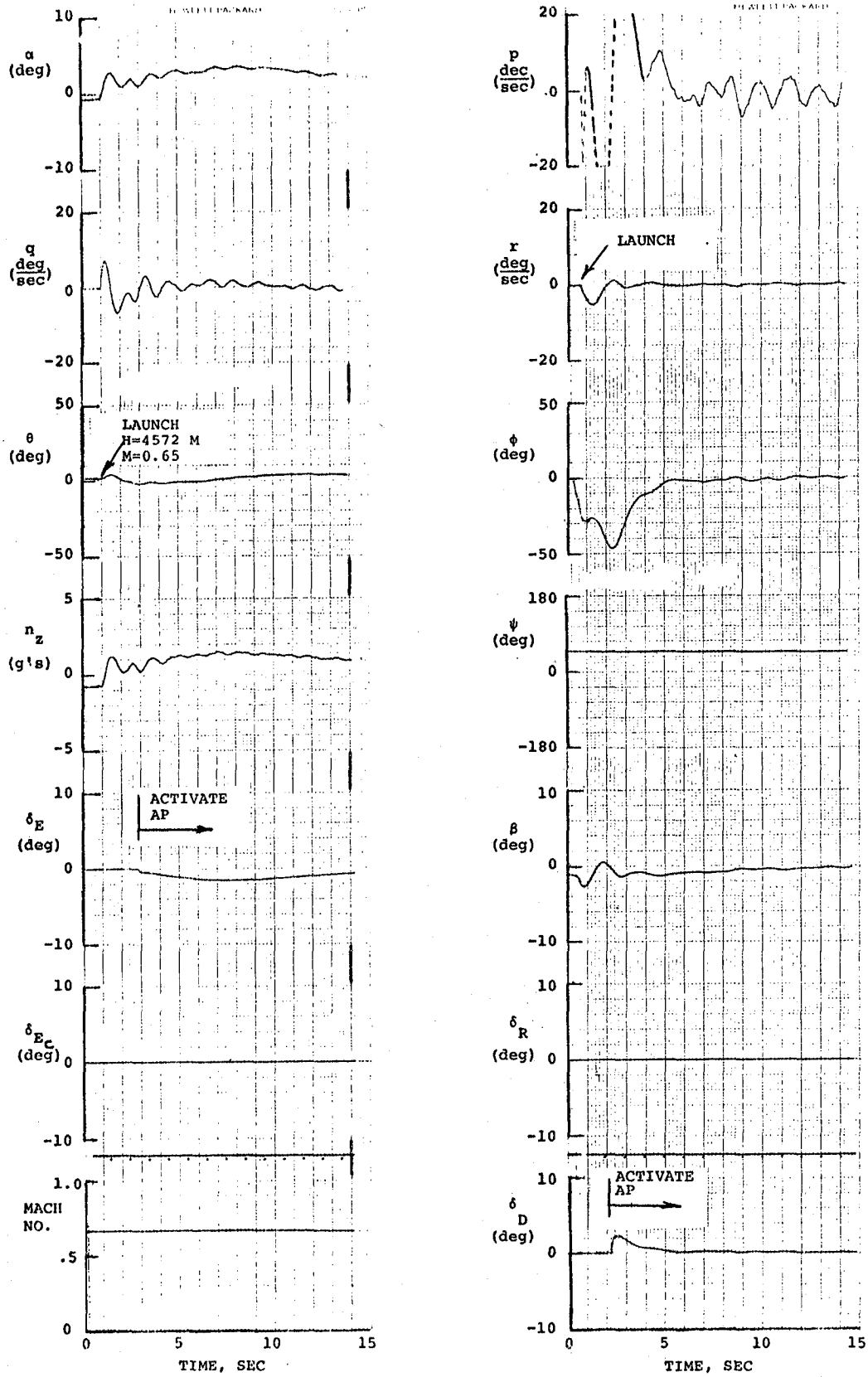

FIGURE 4.25 TIME HISTORY OF B-52 LAUNCH IN AP MODE

attachment points were included so some guess at the pitching moments caused by the parachute drag could be made. The drag created from the chutes was ramped into the equations to represent the time required to "unfurl" the chutes. The Firebee recovery logic was programmed into the simulation in the same fashion in which it interfaces on-board the vehicle. The vehicle has to be in the AP to recover. Time histories of the longitudinal parameters during a normal recovery initiated at M = .93 and h = 3658 meters are seen in figure 4.26. The aerodynamic data tables only go to 14 degrees angle of attack so the parameters are invalid above this value. The dynamic pressure is so low at this point that the main chute deployment creates no appreciable forces as the vehicle rotates to 90 degrees about the main chute attachment on the wing center section.

Two things were evident in the recovery study. First, if an emergency recovery is commanded at these same conditions, the wing would be overstressed when the main chute deployed. In an emergency recovery the main chute deploys 2.5 seconds after the drag chute which comes out immediately. This gives insufficient time to slow down before the vehicle rotates at main chute deployment. The resulting high dynamic pressures and high angles of attack would cause damage to the wing.

The second item resulted in a modification to the basic Firebee recovery logic. It was found that the DAST I would be hard against the alpha limiter with little control surface effectiveness below M = .4. The basic drone would not deploy

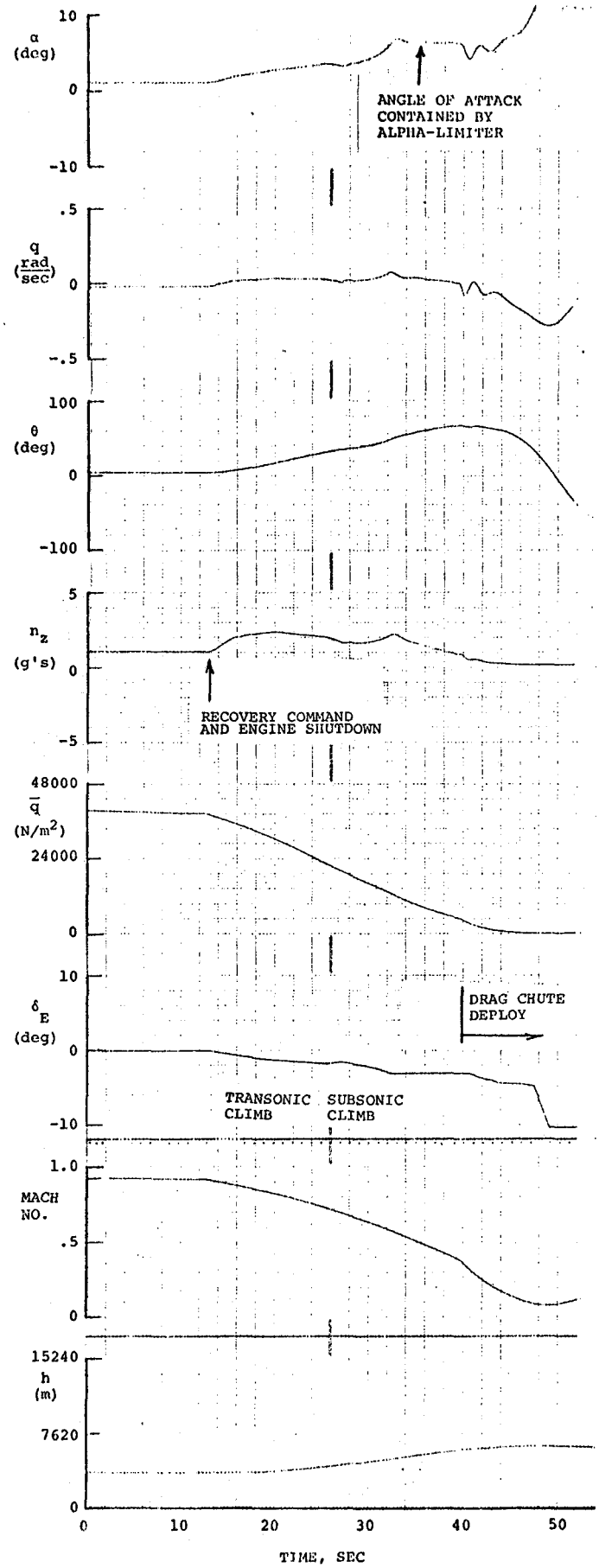

FIGURE 4.26 RECOVERY TIME HISTORY

the drag chute until it slowed to M = .3 in the normal recovery climb out (h > 4572 meters). Changing this Mach number deployment speed to M = .4 eliminated the controllability problems.

CHAPTER 5

IMPLEMENTATION

This chapter will describe the hardware and software mechanization of the DAST I systems. The construction of the wing is described with details on the jettisonable mass ballast mechanism provided. The vehicle instrumentation is covered and the mechanizations of the FSS and RAV control systems described previously are detailed.

5.1 ARW-1 Design and Construction. - The ARW-1 was designed by Teledyne Ryan Aeronautical of San Diego, California, under contract NAS1-13541 from NASA LaRC.

The above contract specified the following design requirements:

> The supercritical wing will be designed for cruise at a Mach number of 0.98 at 13,716 meters altitude and will have the following characteristics:
>
> | | |
> |---|---|
> | • Design lift coefficient | .36 |
> | • Reference Area, Square Meters | 2.787 |
> | • Thickness, Root, % chord | 11.0 |
> | • Thickness, Tip, % chord | 7.0 |
> | • Aspect Ratio | 6.8 |
> | • Span, Meters | 4.343 |
> | • Sweep at 25% chord, Degrees | 42.24 |
> | • Sweep at 50% chord, Degrees | 40.0 |
> | • Taper Ratio | .36 |
> | • Design Load Limit at 1041 kgs (with a 1.25 factor of safety) | +2.5
-1.5 |

The outboard sections of ARW-1 are a 3/8 scale model of

the F-8 supercritical wing (reference 2), but the wing-fuselage fairing, called the wing glove, is specifically adapted for the DAST. Access doors and spring loaded sway brace doors were designed for the glove section for equipment access and clearance for the forward sway braces on the wing pylon of the launch vehicle.

The wing glove was designed of laminated fiberglass because of the extreme contour changes. It is designed with aluminum formers and only minimal stresses are transferred to the glove/wing and glove/fuselage joint fasteners.

The wing center box is machined from thick aluminum plate and was not optimized for weight. The spar material is steel because of the subscale size restrictions of the vehicle. The ribs are formed aluminum except the tip rib, which is machined from solid stock. "Tee" clips for the wing rib/spar joints are located where shallowness of the spar will not permit an integral spar flange type of attachment. The leading and trailing edges are of laminated fiberglass construction to minimize torsional stiffness and for ease of manufacture. They are removeable for access to the wing instrumentation. The trailing edge is foam filled for skin panel support. The wing tip is a removable laminated foam filled fiberglass molding for instrumentation access. The laminated fiberglass skins between spars are attached permanently with rivets. All detachable portions of the wing and glove skins are attached by Voi-Sham screws. An illustration of the construction is shown in figure 5.1.

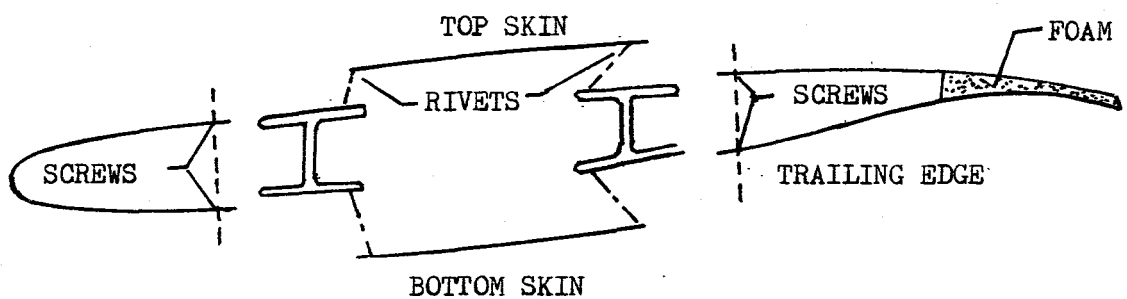

FIGURE 5.1 ILLUSTRATION OF WING CROSS-SECTION

The wing was constructed at the NASA LaRC Model Shop in Hampton, Virginia. A picture of the completed wing is seen in figure 5.2. The leading and trailing edges are removed from the left wing to show the rib arrangement.

The jettisonable mass ballast, which was added to lower the open loop flutter boundary when it was found that the fiberglass skin was stiffer than predicted, is shown in figure 5.3. The lead shot in this cylinder is ejected when the retaining cap is pushed back approximately 2.5 centimeters by a pyrotechnic activated bellows. The pyrotechnic charge is fired when an accelerometer signal exceeds a predetermined trigger level for a finite time interval. The electric circuit controlling the jettison mechanism integrates the accelerometer signal whenever it exceeds the trigger level of approximately 20 g's. When this integrated value reaches a preset level, the pyrotechnic bellows are fired. The integration scheme prevents spikes in the accelerometer signal from firing the charge and insures that the wing is indeed fluttering before jettisoning the shot. In tests on this system at NASA LaRC, the time required to fire the pyrotechnic charge once oscillations at the ARW-1 flutter frequency exceeded the trigger level was 0.4 of a second or approximately six cycles.

The GVT tests on ARW-1 and the DAST I vehicle arrangement, which was first mentioned in section 3.1.1, were conducted on the vehicle shown in figure 5.4. Only the forward wing glove/fuselage fairings are missing from what represents the DAST I that will be tested at NASA DFRC.

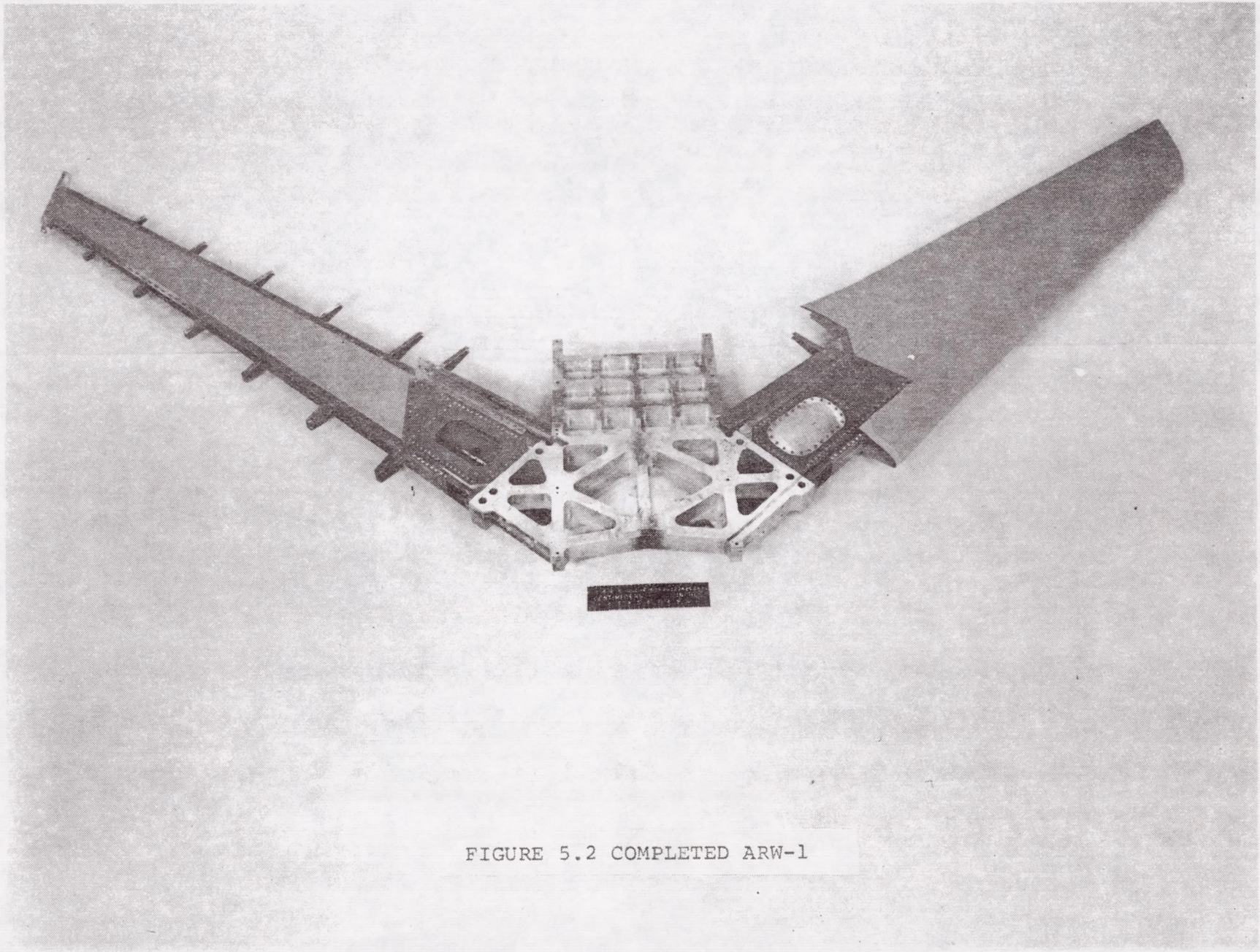

FIGURE 5.2 COMPLETED ARW-1

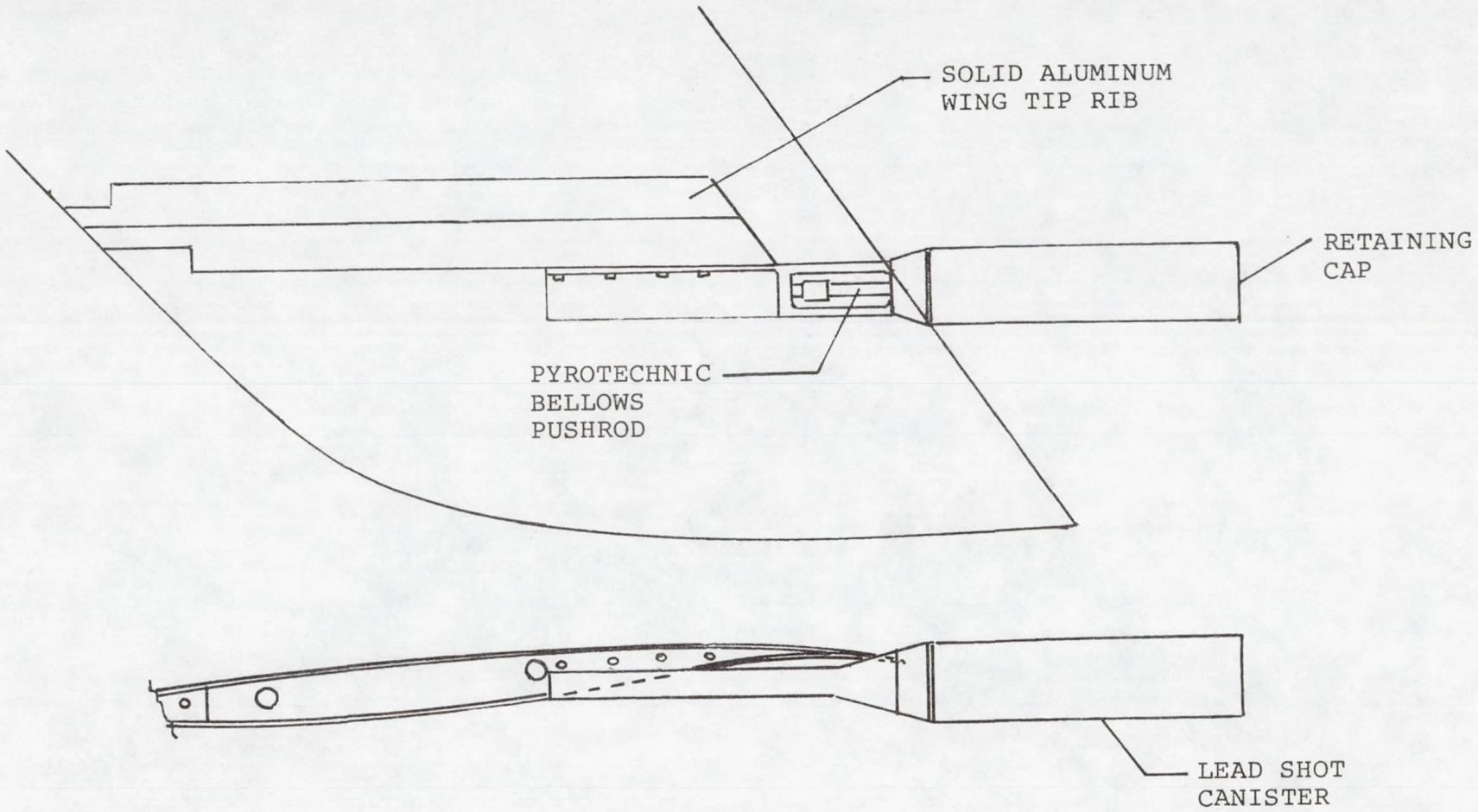

FIGURE 5.3 THE JETTISONABLE TIP MASS BALLAST ATTACHMENT

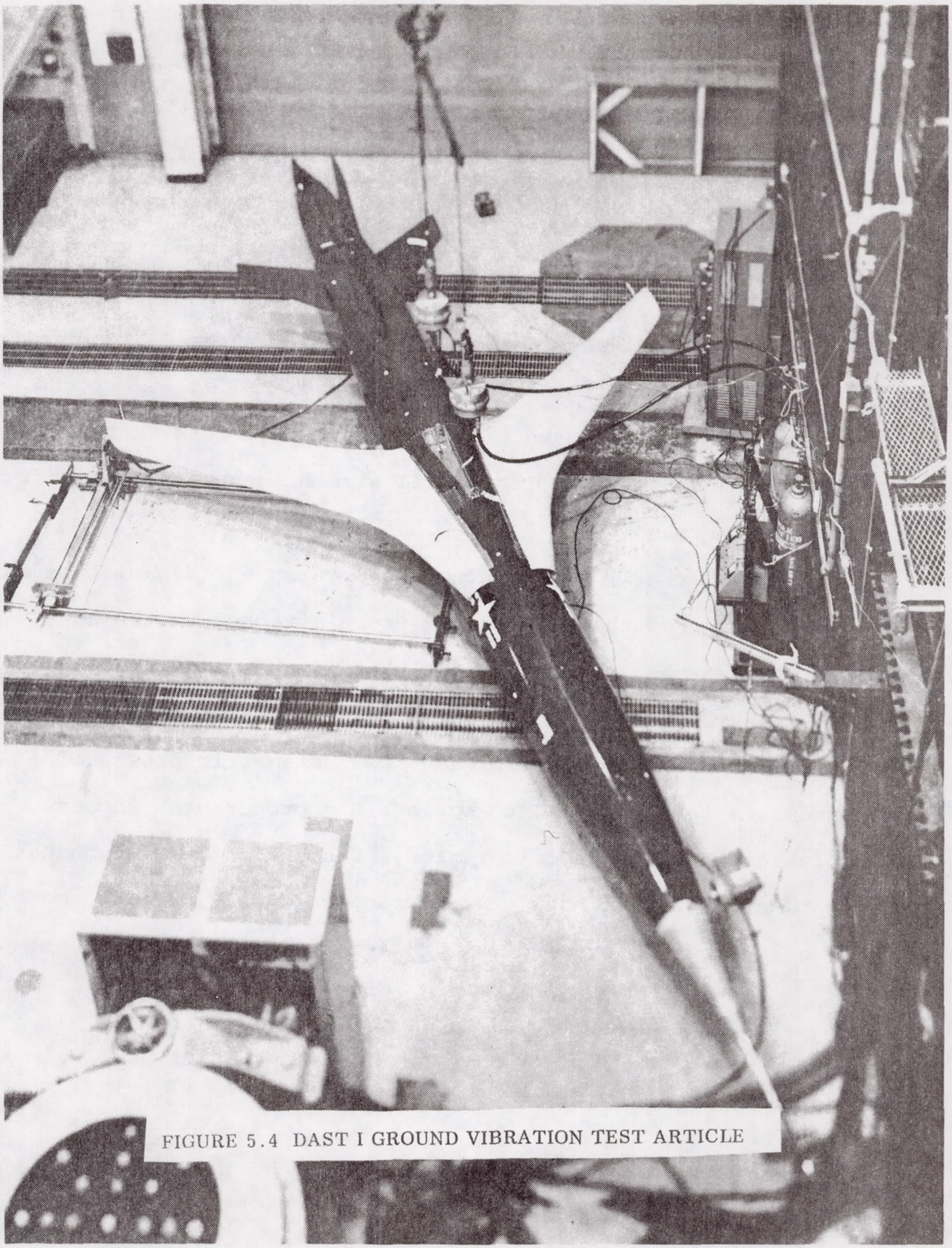

FIGURE 5.4 DAST I GROUND VIBRATION TEST ARTICLE

5.2 Instrumentation. - The primary telemetry information for the real-time flutter monitoring during the flight tests will be from accelerometers in the wings and potentiometers measuring FSS control surface movements. The PCM main frame rate is 500 samples per second. This high sample rate was deemed necessary for the adequate time domain reconstruction of the higher frequency modes in the response.

The rigid body sensor signals required for the RAV control system will be subcommutated at 100 and 50 samples per second. The data will be displayed on strip chart recorders in the DFRC control rooms. PCM tapes will also be generated for post flight analysis.

Mach number will be computed from static and dynamic pressure measurements from the compensated probe attached to the nose cone. This probe is the same one that was used on the F-8 SCW flight tests. The nose boom is position error compensated to account for the DAST I flowfield. Two Datametric pressure transducers were required to achieve the proper Mach number resolution in the transonic region. Resolution in Mach number will be at $\pm$.004 but absolute accuracy will only be achieved through dedicated airspeed calibration flights (which are not planned).

Ten accelerometers are involved in the FSS test. These are:

	Location
Left Wing FSS Accelerometer	WBL-76
Right Wing FSS Accelerometer	WBL-76
Left Wing Front Spar Accel.	WBL-79
Left Wing Rear Spar Accel.	WBL-79

	Location
Right Wing Front Spar Accel.	WBL-79
Right Wing Rear Spar Accel.	WBL-79
FSS Fuselage Normal Accel.	FS 265
FSS Fuselage Roll Angular Accel.	FS 274
Left Wing Tip Mass Accel.	WBL-79
Right Wing Tip Mass Accel.	WBL-79

The left and right wing aileron positions are measured by potentiometers attached to the actuator shafts.

The rigid body sensors are illustrated in the on-board equipment layout in Section 5.4.1 except for the boom mounted vanes measuring angle of attack and sideslip angle.

The pertinent instrumentation parameters and their accuracies are listed in Table 5.1.

5.3 FSS Mechanization. - An illustration of the FSS layout on board the vehicle is shown in figure 5.5. The hydraulic servovalves were placed in the fuselage due to size constraints in the wing. The relatively long hydraulic lines to the actuators near the wing tip were analyzed as part of the actuator math model and did not create a problem. The hydraulic pump, an electrically driven Sundstrand-Pesco Model 165-100, is rated at 3.558×10^{-3} cubic meters of fluid per minute at 1.034×10^{7} Newtons/meter^2. It was chosen because it met the FSS requirements and was the only "off the shelf" pump to do so that was compatable with the DAST I electrical power supply capabilities. This pump can supply 33.5% of the expected peak flow requirements. A 4.097×10^{-4} cubic meter capacity accumulator will supply the remainder of the peak flow demand.

The actuator location in the wing is shown in figure 5.6. This actuator is a single vane rotary design using an aluminum

TABLE 5.1

DAST I

TM PARAMETER LIST

SYSTEM I

(PAGE 1 OF 3)

PARMID	Name	Range	SPS	Filter
FSS Signals				
1. LWPOT	LW Aileron Pos	$\pm 12^{\circ}$	500	6P,70hz
2. RWPOT	RW Aileron Pos	$\pm 12^{\circ}$	500	6P,70hz
3. FSSEXC	FSS Excitation	$\pm 4^{\circ}$	500	6P,70hz
4. FSSLAC	LW FSS acc.	$\pm 10g$	500	3P,70hz
5. FSSRAC	RW FSS acc.	$\pm 10g$	500	3P,70hz
6. LWSERV	LW servo command	$\pm 12^{\circ}$	250	3P,70hz
7. RWSERV	RW servo command	$\pm 12^{\circ}$	250	3P,70hz
8. FSFUVAC	FSS Fuselage A_z	$\pm 5g$	250	3P,70hz
9. FSFURAC	FSS Roll ang. acc.	$\pm 4g$	250	3P,70hz
10. DPAR	FSS 'D' parameter	0-1000 units	50	1P,40hz
11. HYDSUP	FSS hyd supply press.	0-1500 psid	50	1P,40hz
12. HYDLOD	FSS hyd diff. load press.	± 1500 psid	50	1p,40hz
System II signals				
13. LFRACCL	LW front spar acc.	TBD	500	6P,70hz
14. LRRACCL	LW rear spar acc.	TBD	500	6P,70hz
15. RFRACCL	RW front spar acc.	TBD	500	6P,70hz
16. RRRACCL	RW rear spar acc.	TBD	500	6P,70hz
Tip mass signals				
17. LTMRAC	LW tip mass acc.	$\pm 50g$	250	3P,70hz

TABLE 5.1 (CONTINUED)
(PAGE 2 OF 3)

18.	RTMRAC	RW tip mass acc.	±50g	250	3P,70hz

Avionics signals

19.	X001	LH stab pos	8,-13°	50	1P,40hz
20.	X002	RH stab pos	8,-13°	50	1P,40hz
21.	X003	Rudder pos	±10°	50	1P,40hz
22.	X004	throttle pos	0-270°	50	1P,40hz
23.	X005	LH stab DAC	8,-13°	50	1P,40hz
24.	X006	RH stab DAC	8,-13°	50	1P,40hz
25.	X007	Rudder DAC	±10°	50	1P,40hz
26.	X008	Throttle DAC	0-270°	50	1P,40hz
27.	M001	Pitch angle	+80°	50	1P,40hz
28.	M002	Roll angle	±180°	50	1P,40hz
29.	M003	yaw angle	±180°	50	1P,40hz
30.	M004	RPM	0-110%	50	1P,40hz
31.	M005	Fuel flow rate	0.5/8 gpm	50	1P,40hz
32.	M006	Fuel remaining	0-305 lbs.	50	1P,40hz
33.	T001	EGT	700-850°C	50	1P,40hz
34.	M007	AGC	0/-110db	50	1P,40hz
35.	M008	Alpha	+30,-12°	100	1P,40hz
36.	M010	Beta	±20°	100	1P,40hz
37.	M011	±12 VDC monitor	0-25VDC	50	1P,40hz

Instrumentation Signals

38.	A001	Pitch rate	+60 °/s	100	1P,40hz
39.	A002	roll rate	±100 °/s	100	1P,40hz
40.	A003	yaw rate	±40 °/s	100	1P,40hz
41.	M012	+28 VDC monitor	0-30 VDC	50	1P,40hz
42.	M013	26 VAC monitor	0-28 VAC	50	1P,40hz
43.	A004	Az,cg	+6,-3g	100	1P,40hz
44.	A005	Az,cg fine	+3,-0.5g	100	1P,40hz
45.	A006	Ay,cg	±1 g	100	1P,40hz
46.	A007	Ax,cg	±1 g	100	1P,40hz
47.	M009	Alpha, fine	±6,-2°	100	1P,40hz
48.	D001	Airspeed diff. press.	0-1500 psfd	50	1P,40hz

49.	STADIF	Ps-Pref, ΔP	$\pm$2.5 psid	50	1P,40hz

Digital Signals - Avionics

1.	M014	Recovery	DW-1	50
2.	M015	AP	DW-1	50
3.	PHOCOM	Camera on-off	DW-1	50
4.	FSSON	FSS on-off	DW-1	50
5.	PULCOM	FSS pulse excitation	DW-1	50
6.	M016	Emergency Recovery	DW-1	50
7.	TMRCOM	Tip Mass eject.	DW-1	50
8.	M017	Smoke	DW-1	50
9.	AMPCOM	FSS excitation amp.	DW-1	50
10.	SWECOM	FSS sweep excitation	DW-1	50

Digital Signals - Avionics

1.	FSGAIN	FSS gain	DW-2 hi-low	50
2.	SYMCOM	FSS excitation	DW-2 sym-anti	50
3.	LEREL	LW Pyro verify	DW-2	50
4.	RIREL	RW Pyro verify	DW-2	50
5.	HRESLV	Hyd pump Res. status	DW-2	50
6.	M018	90° roll switch	DW-2	50
7.	PMPON	Hyd pump on-off	DW-2	50

Digital Signals - Inst.

1.	P002C	altitude, course (6 kits)	DW 3	50
2.	P002F	altitude, fine (6 kits)	DW 4	50

PCM Frame Status - Channels

	Available	Used	
500 SPS	9	9	
250 SPS	6	6	
100 SPS	10	10	
50 SPS	30	28	(24 analog, 4 digital)

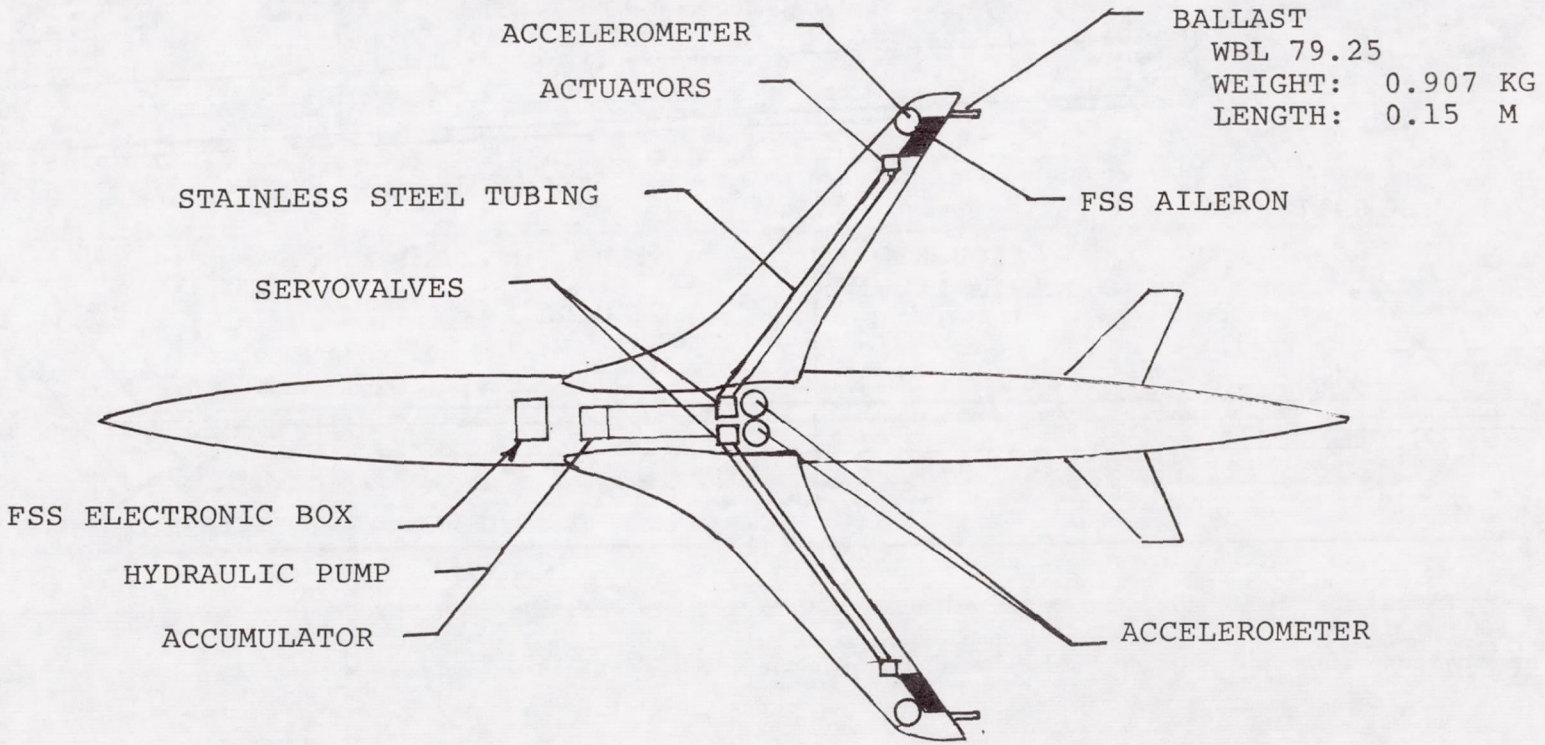

FIGURE 5.5 FSS ON-BOARD LAYOUT

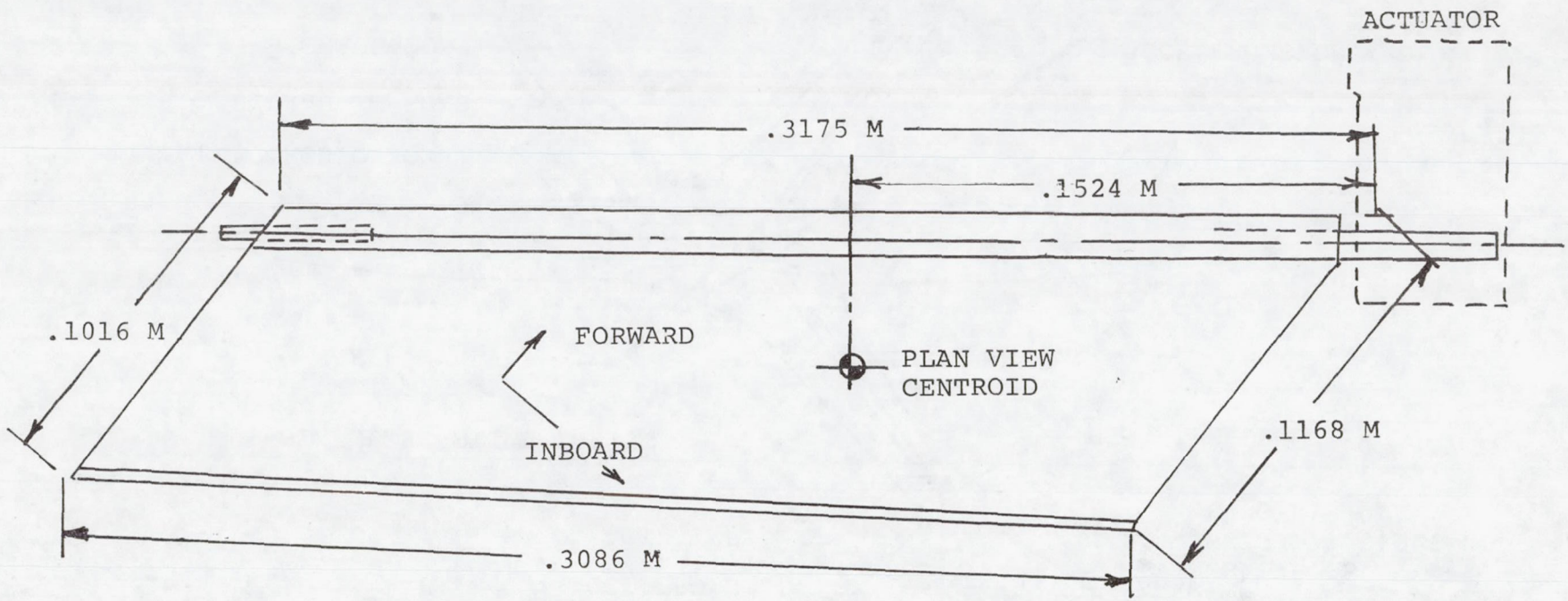

FIGURE 5.6 CONTROL SURFACE AND ACTUATOR ILLUSTRATION

body with a stainless steel shaft and vane. The control surface is directly coupled to the shaft. This system was sized so that the stall torque equals the maximum expected hinge moment. The actuator has a 5.03 meter/sec peak velocity at 1460 deg/sec. The servoactuator block diagram, shown in figure 5.7, shows the closed loop transfer function which was used in the analysis in Chapter 6.

The functional interface requirements of the FSS with the rest of the DAST I systems is illustrated in figure 5.8. Dual potentiometers are utilized on the actuator shaft so that a spare would exist. A possible major disassembly of the system is prevented by incorporating the spare into the actuator at the initial buildup. The two pressure tranducers are utilized with the servovalves so that absolute and differential pressure can be monitored.

5.4 Flight Control Mechanization. - The flight test philosophy for the FSS experiment is based on the vehicle operating under RAV control. If the telemetry link required by the RAV control system is broken, automatic reversion to the on-board autopilot occurs. This interface is critical to safe operation of the DAST RPRV.

5.4.1 DAST I On-Board Systems. - One of the critical systems in the operation of the DAST as an RPRV is the wrap-around nose cone antenna. The basic Firebee drone had a receiving and transmitting antenna on the lower surface of each wing tip. The single nose cone antenna for the DAST I serves as both the point of transmission and receiving. The nose cone antenna was fabricated

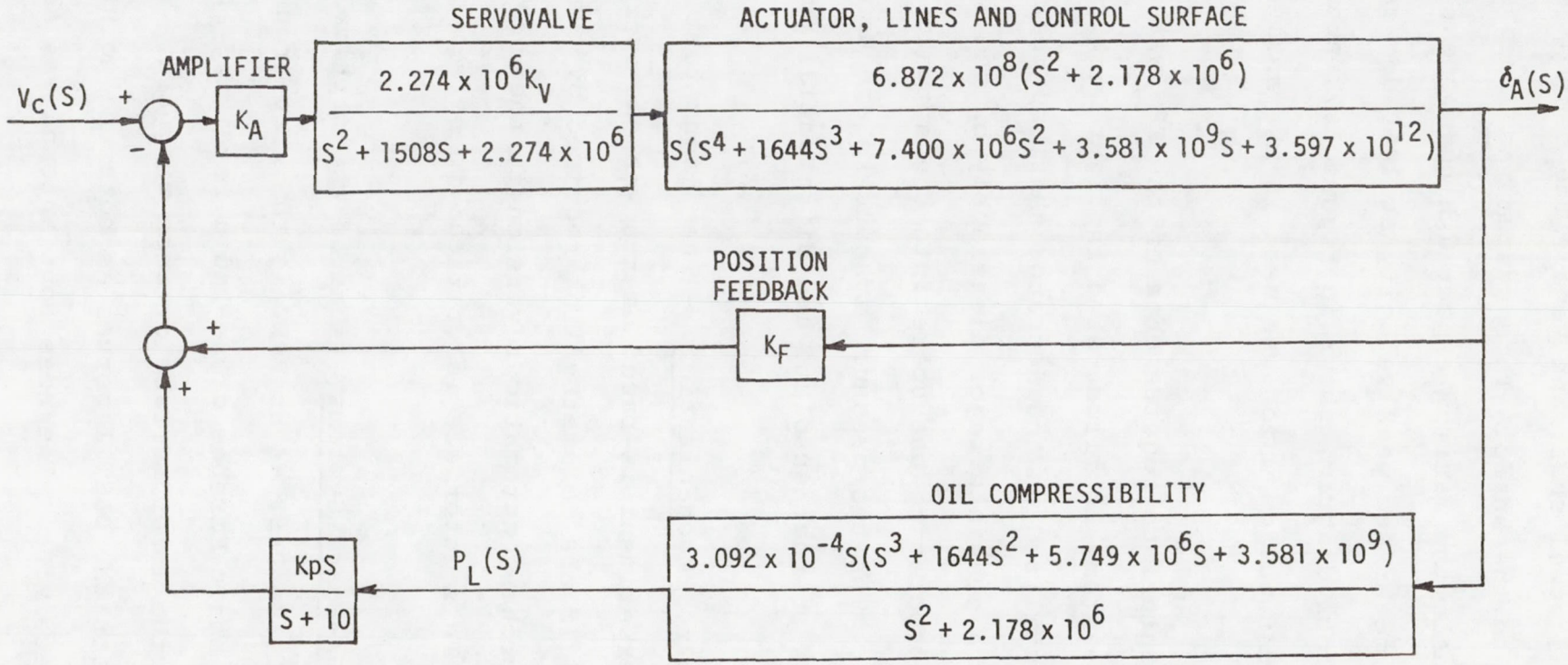

CLOSED LOOP NO-LOAD TRANSFER FUNCTION

$$\frac{\delta_S}{\delta_C} = \frac{2.721 \times 10^{21}(S + 10) \quad \text{DEG/DEG}}{(S + 10.14)(S + 375.4)(S^2 + 758.0S + 7.158 \times 10^5)(S^2 + 852.9S + 1.591 \times 10^6)(S^2 + 1164S + 6.277 \times 10^6)}$$

FIGURE 5.7 FSS SERVOACTUATOR BLOCK DIAGRAM

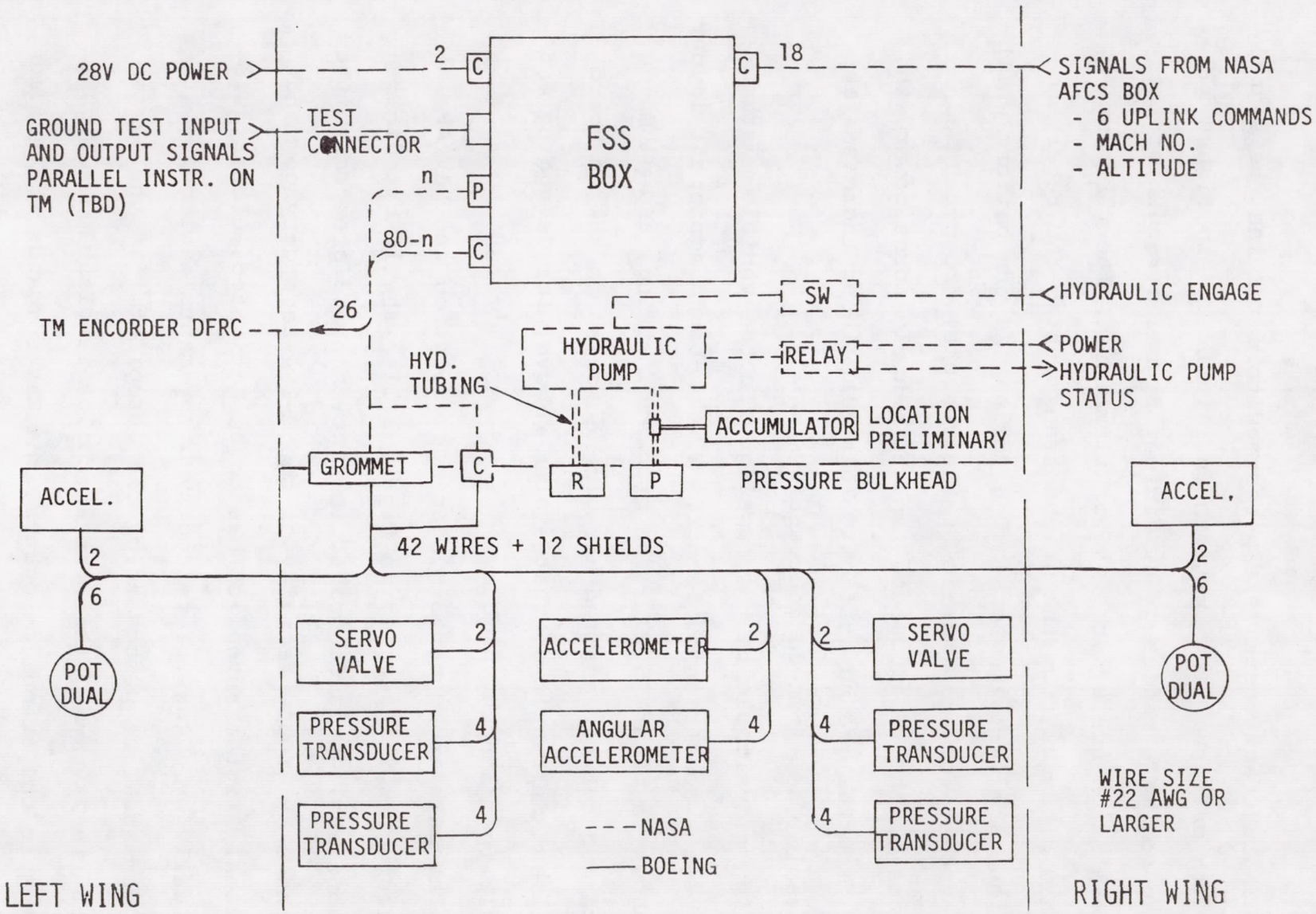

FIGURE 5.8 ARW-1 FSS INTERFACES

at NASA LaRC and tests were performed to determine its signal strength pattern. This pattern is illustrated in figure 5.9. The approximate radius of sufficient signal strength of the pattern is on the order of 96.5 kilometers. The furthest planned distance from the ground transmitting and receiving station is 72.4 kilometers. The "holes" in the pattern which are evident forward and aft of the vehicle, are potential sources of the TM "dropouts" as the vehicle turns toward and away from the ground station. This likelihood increases as the vehicle's altitude decreases.

Space available in the fuselage for the vehicle systems has been a constraining factor. The on-board equipment layout is shown in figure 5.10. The brackets, wiring, and plumping, which are not represented here, make access to the on-board equipment difficult so that system removal for debugging and repair is a lengthy process.

The on-board control system mechanization and RAV/AP interfacing is illustrated in figure 5.11. The 10-bit digital proportional words described in section 5.5.3 are transmitted by the RPRV ground facility or the F-104 secondary command station. If the autopilot has to be activated, either automatically by a loss of telemetry or by manual switching, then the commands are processed by the autopilot. If the system is in the RAV mode, then the autopilot is disabled. When a switch to the autopilot occurs, the RAV commands are ramped out over a three second interval to minimize the transients in the pitch axis. Recall that after the RAV/AP switch, the

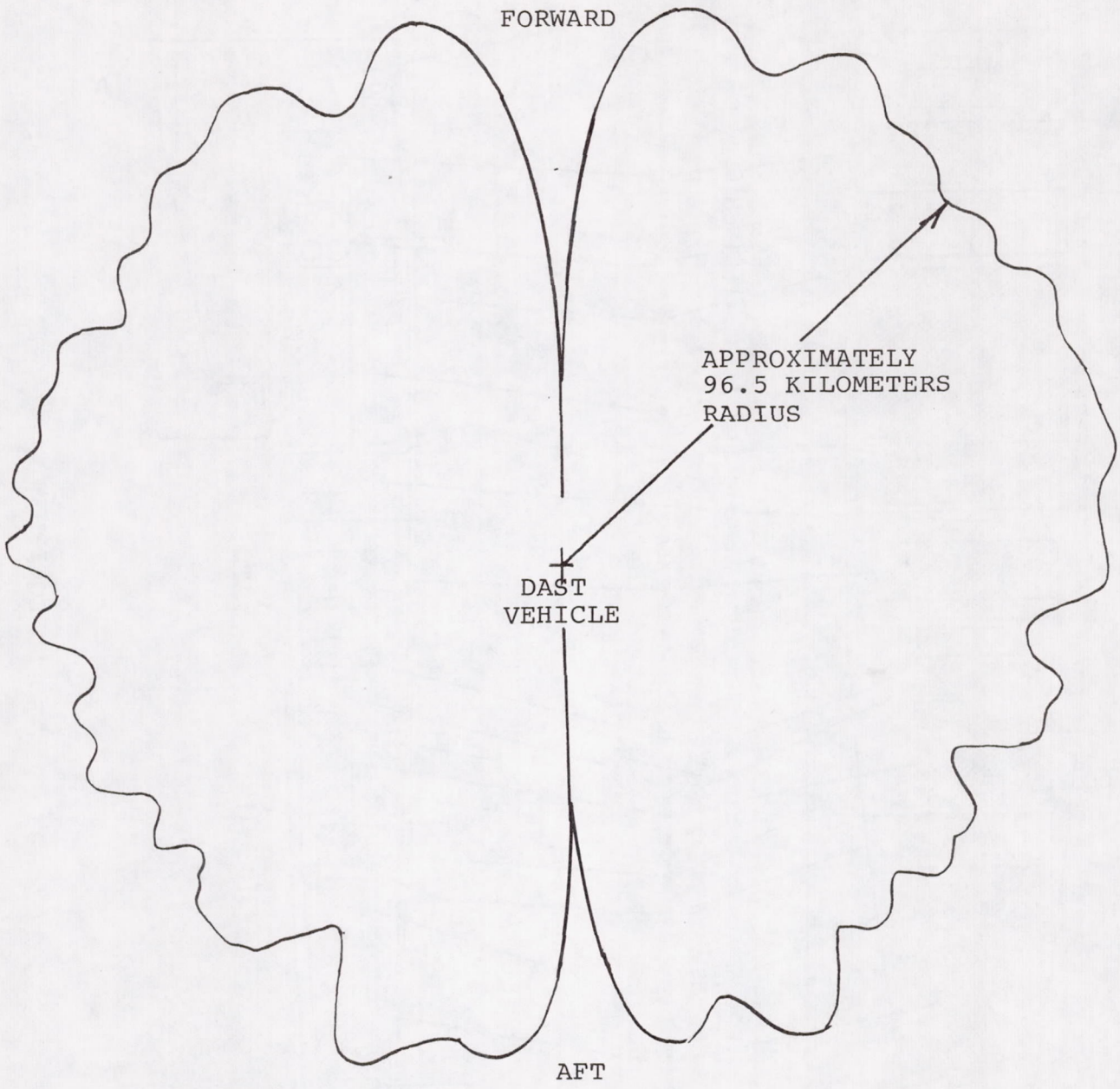

FIGURE 5.9 DAST I NOSE CONE ANTENNA PATTERN

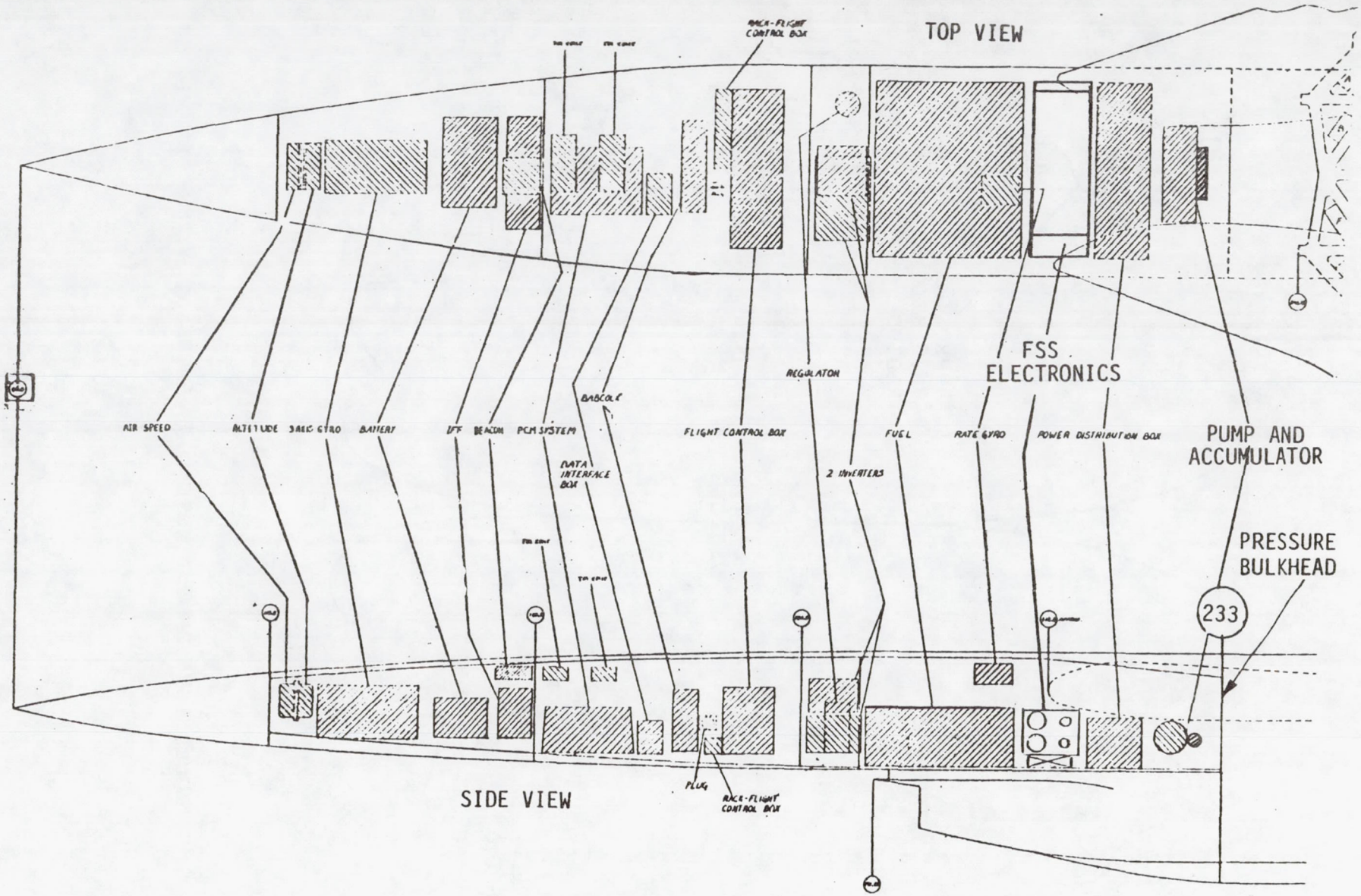

FIGURE 5.10 ON-BOARD EQUIPMENT LAYOUT

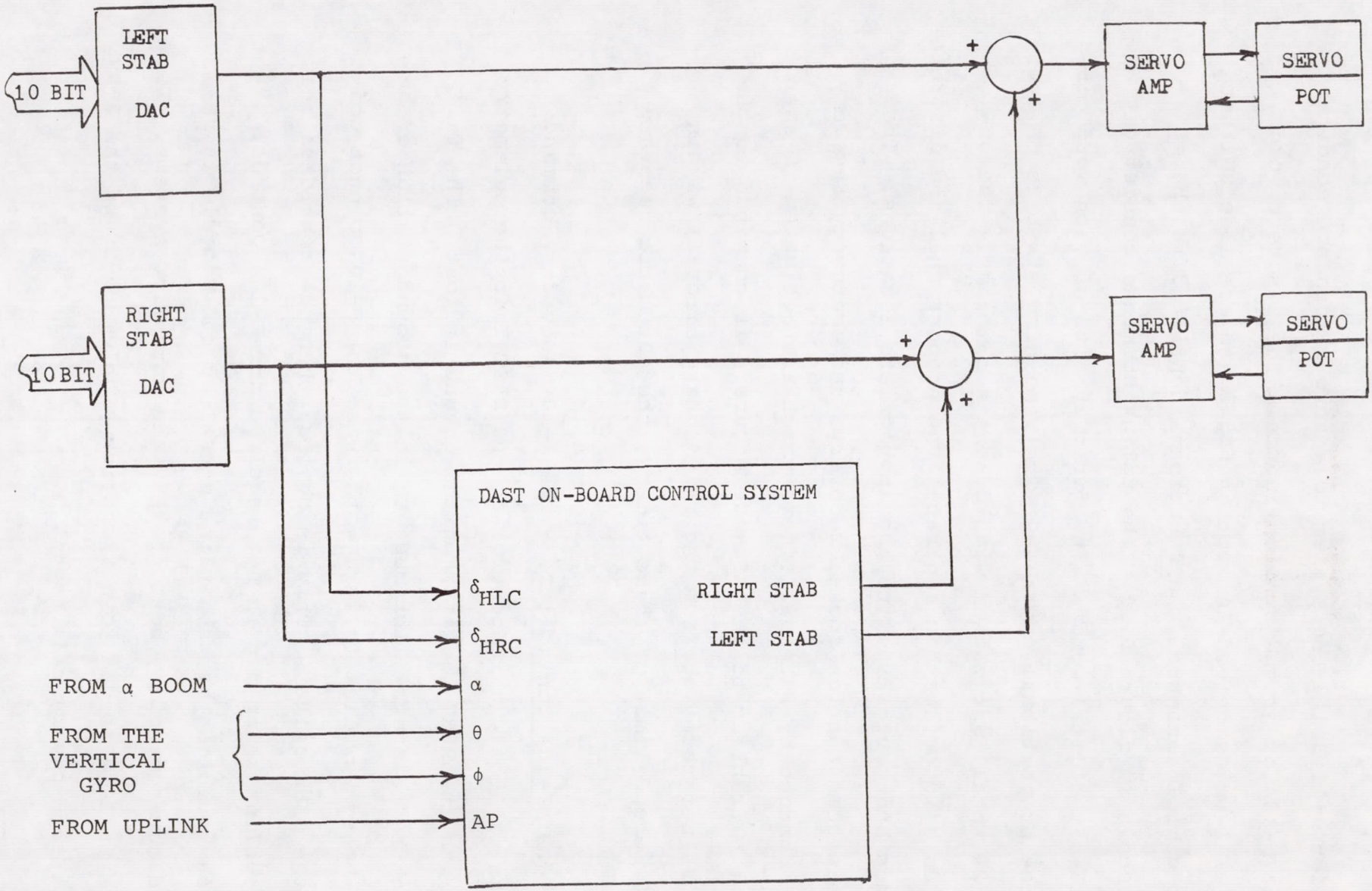

FIGURE 5.11 DAST ON-BOARD CONTROL SYSTEM INTERFACE

autopilot will drive the system to a zero glideslope condition without F-104 or ground station inputs. The discrete words, which will be described in section 5.5.3 and are also uplinked to the vehicle, control the functions identified in the schematic shown in figure 5.12. The uplink commands consist of four 16-bit digital words. The first 10 bits of each word contain the proportional commands. The remaining six bits on each word (24 total) are packed with discrete commands. The on-board data interface box separates the proportional and discrete commands and routes them to the appropriate locations. The discrete commands for smoke, recovery, and emergency recovery can be changed by internal timers which are activated if an automatic transfer to the AP mode occurs. If commands to the DAST are not received from the F-104 chase aircraft within the 20 second limit of these timers, the automatic recovery begins.

5.4.2 F-104 Controller. - The F-104 secondary command station will only take control of the DAST I if the telemetry link with the RPRV facility on the ground is lost. The failure in the telemetry link must be in the ground station or be an on-board downlink failure, otherwise the F-104 cannot control the DAST either. This is obvious when one considers that the downlink telemetry is not required for F-104 control, whereas reception of the uplink signal by the vehicle is required for control by both the RAV and autopilot systems. If the TM failure is due to a reception problem on-board the RPRV, automatic recovery will result.

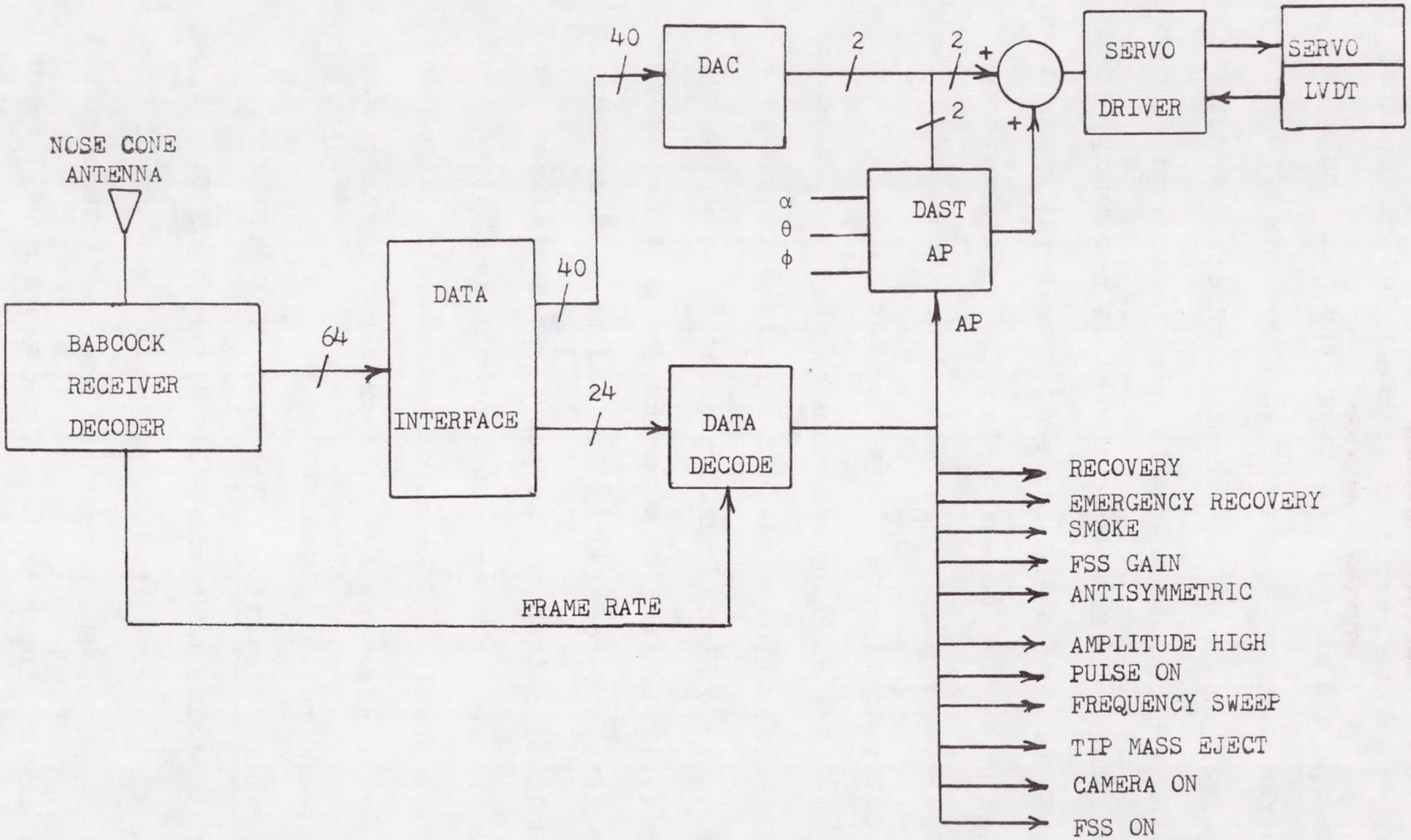

FIGURE 5.12 ON-BOARD TM PROCESSING AND DISCRETE COMMANDS

The RPRV pilot in the rear seat of the F-104 can control the DAST engine rpm and make climb, dive, and bank angle command inputs to the vehicle. Figure 5.13 shows the RPRV control-panel in the F-104. There is an automatic throttle reduction to the 80% rpm setting whenever the AP mode is activated. If the RPRV pilot determines that more thrust is necessary, the dial on the panel is lifted and rotated. The F-104 chase aircraft RPRV pilot can only judge the throttle requirement relative to the F-104 airspeed since he will have no indication of the magnitude of engine rpm changes he makes.

Turns and altitude changes are made by the trim switch on the panel. The integration rates and authority limits on this stick are such that no high g maneuvers can be made and the vertical velocity is limited to a maximum of $\pm$ 30 meters per second. The bank angle command is limited to $\pm$ 40 degrees. A straight and level switch on the panel, when utilized, will zero the pitch and roll commands and let the autopilot maintain altitude and heading. Extensive piloted simulation was performed to verify adequate and safe values for the trim rates and limits throughout the flight envelope.

5.5 RPRV Ground Facility. - The NASA DFRC RPRV facility was developed to enable high risk flight testing. Due to the nature of some flight experiments, subscale remotely piloted aircraft were chosen as the safest and most efficient method of performing some of these tests. This section will describe this facility and how it operates.

5.5.1 Ground Cockpit. - The ground cockpit used for the

LEFT-HAND F-104 RPRV PANEL

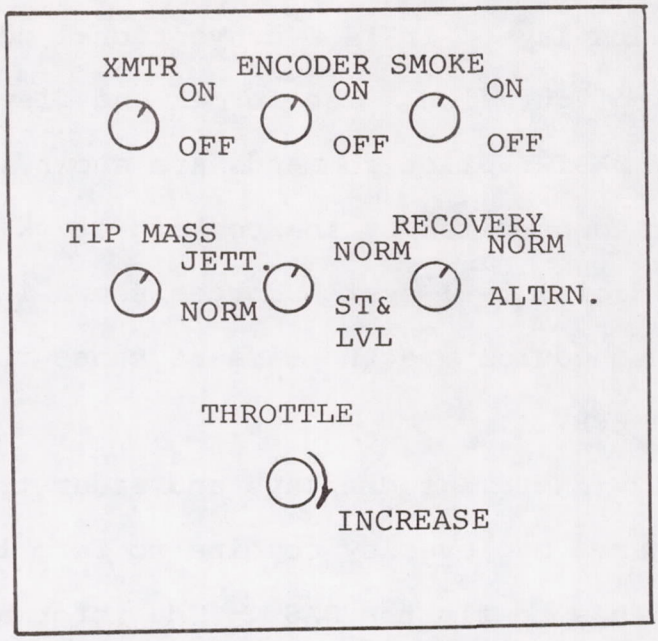

RIGHT-HAND F-104 RPRV PANEL

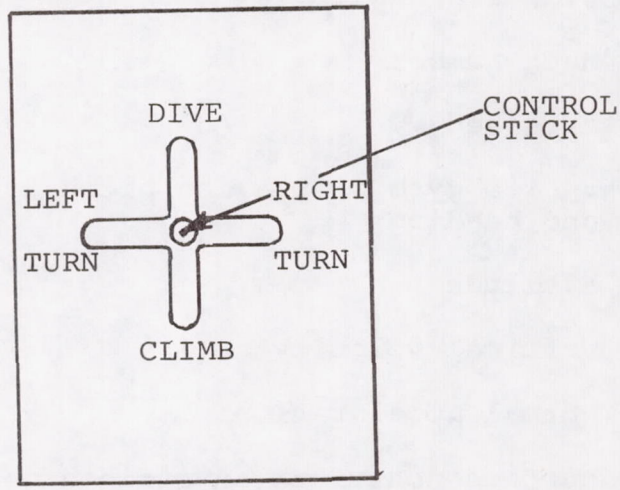

FIGURE 5.13 F-104 RPRV CONTROL PANEL

the basic Firebee RPRV is shown in figure 5.14. This is the cockpit which will be used with the DAST I with some changes in instrument displays. It is a conventional center stick and rudder pedal configuration. The forces and displacements chosen for the DAST I pilot commands are shown in figure 5.15. Electric motors controlled by the cockpit stick computer, generate the artificial feel system forces shown in figure 5.15. These gearing schedules are the same as those that were utilized on the Firebee RPRV.

The cockpit instrument displays and radar tracking plot board with an area map overlay combine to form the information the pilot will use to fly the DAST. The information displayed to the pilot from the cockpit instruments are:

1. angle of attack
2. sideslip angle
3. Mach number
4. airspeed
5. 3-axis gyro displaying pitch attitude, roll attitude and heading
6. altitude
7. vertical velocity
8. normal acceleration
9. surface positions on strip gages
10. surface commands
11. engine rpm in percent
12. commanded engine rpm
13. fuel flow rate
14. fuel quantity in weight
15. engine exhaust temperature

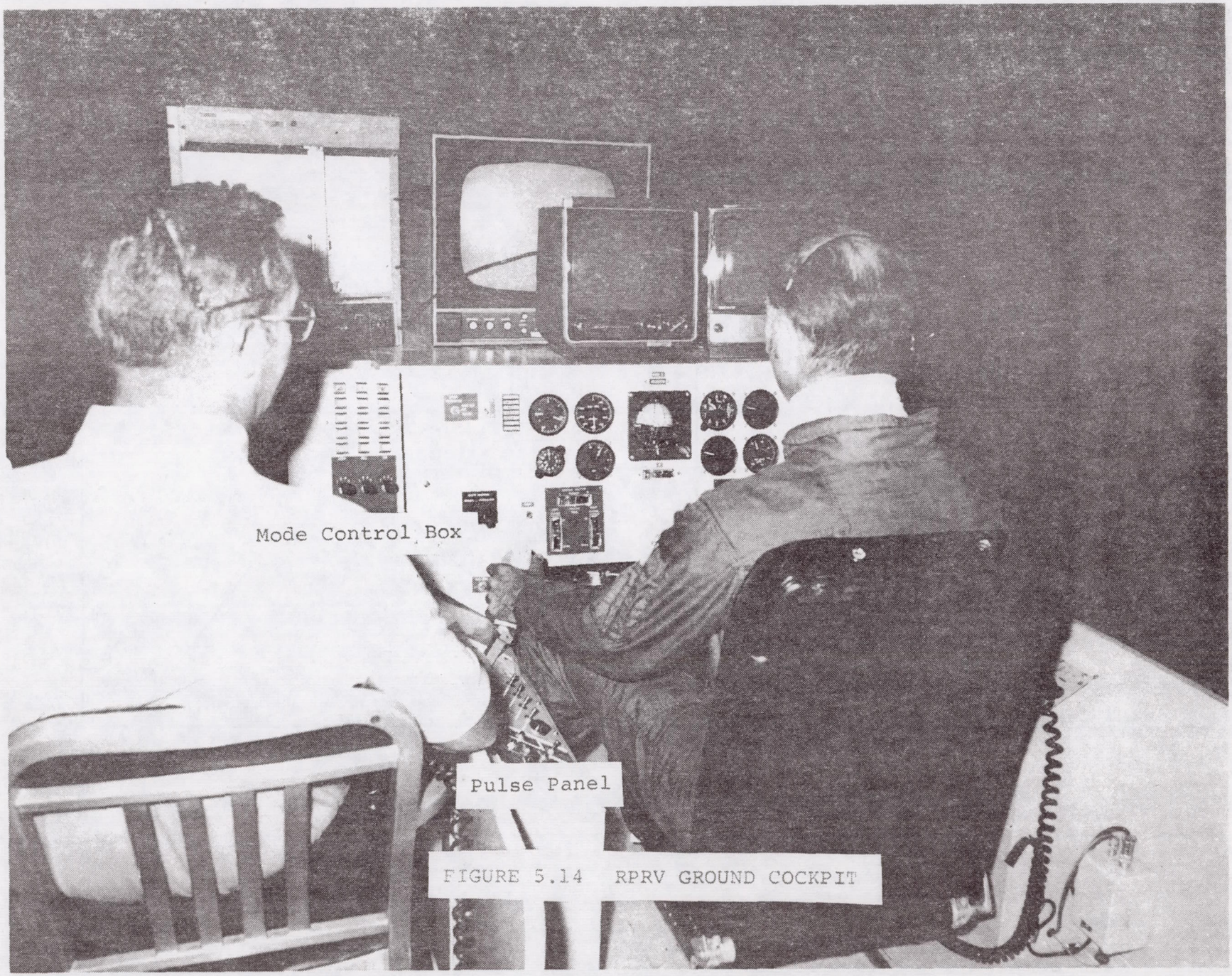

FIGURE 5.14 RPRV GROUND COCKPIT

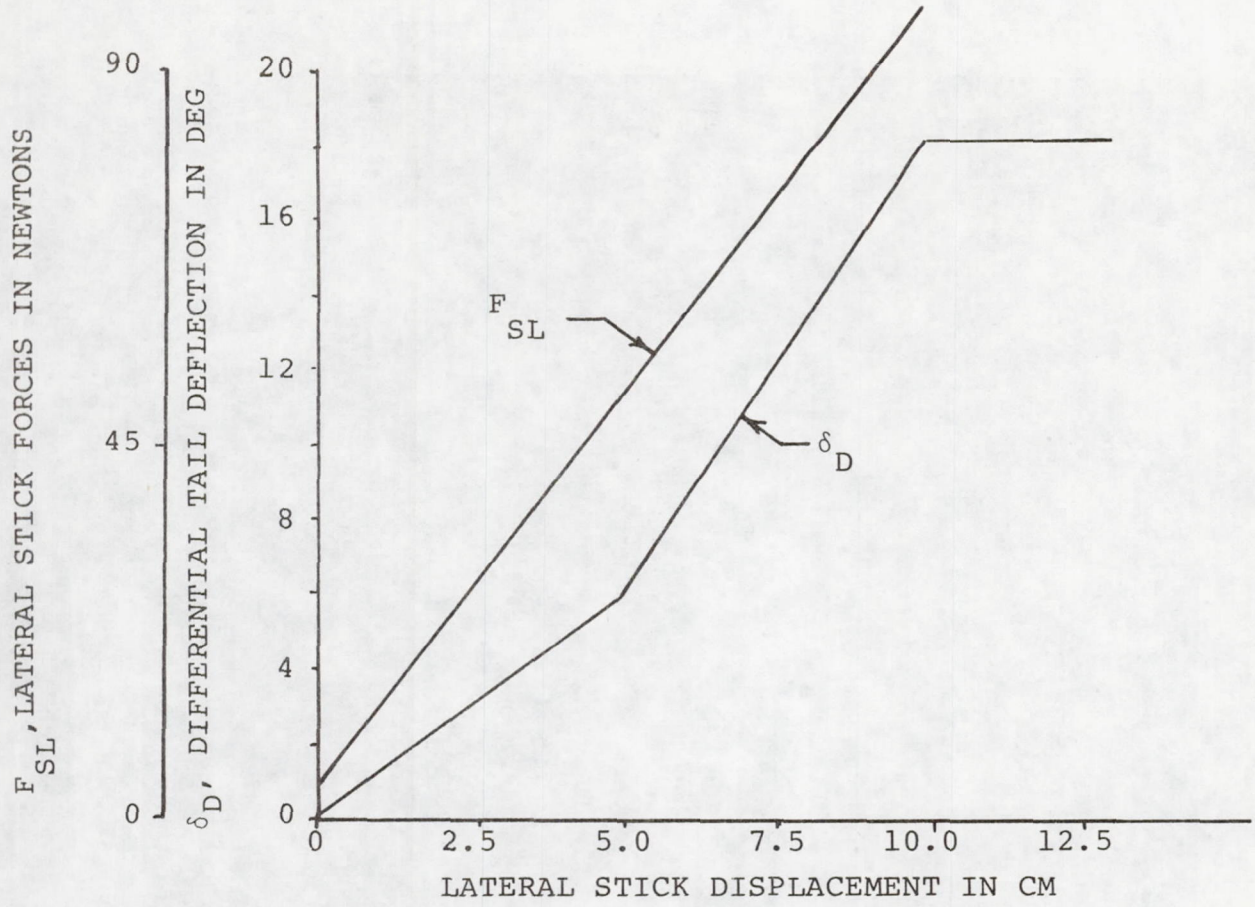

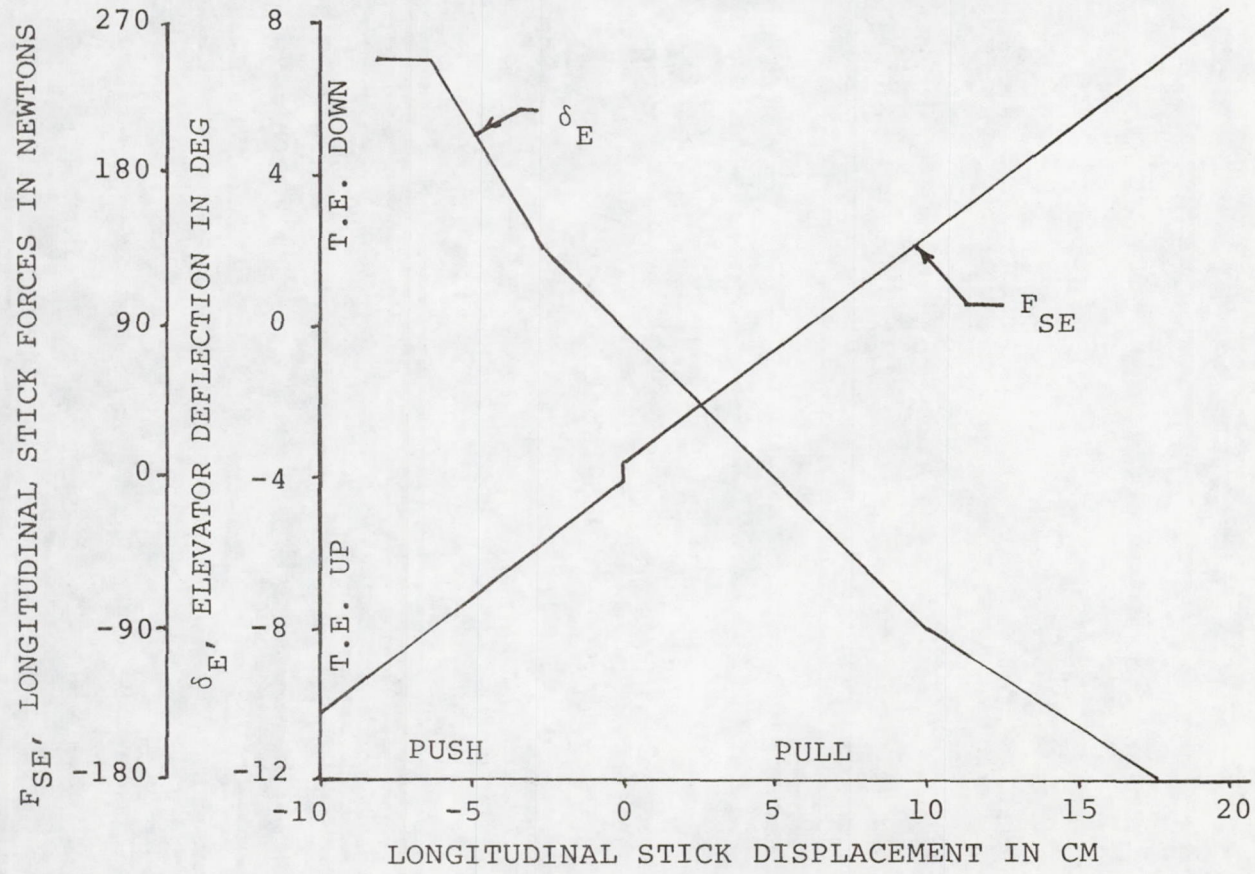

FIGURE 5.15 COCKPIT STICK FORCES (PAGE 1 OF 2)

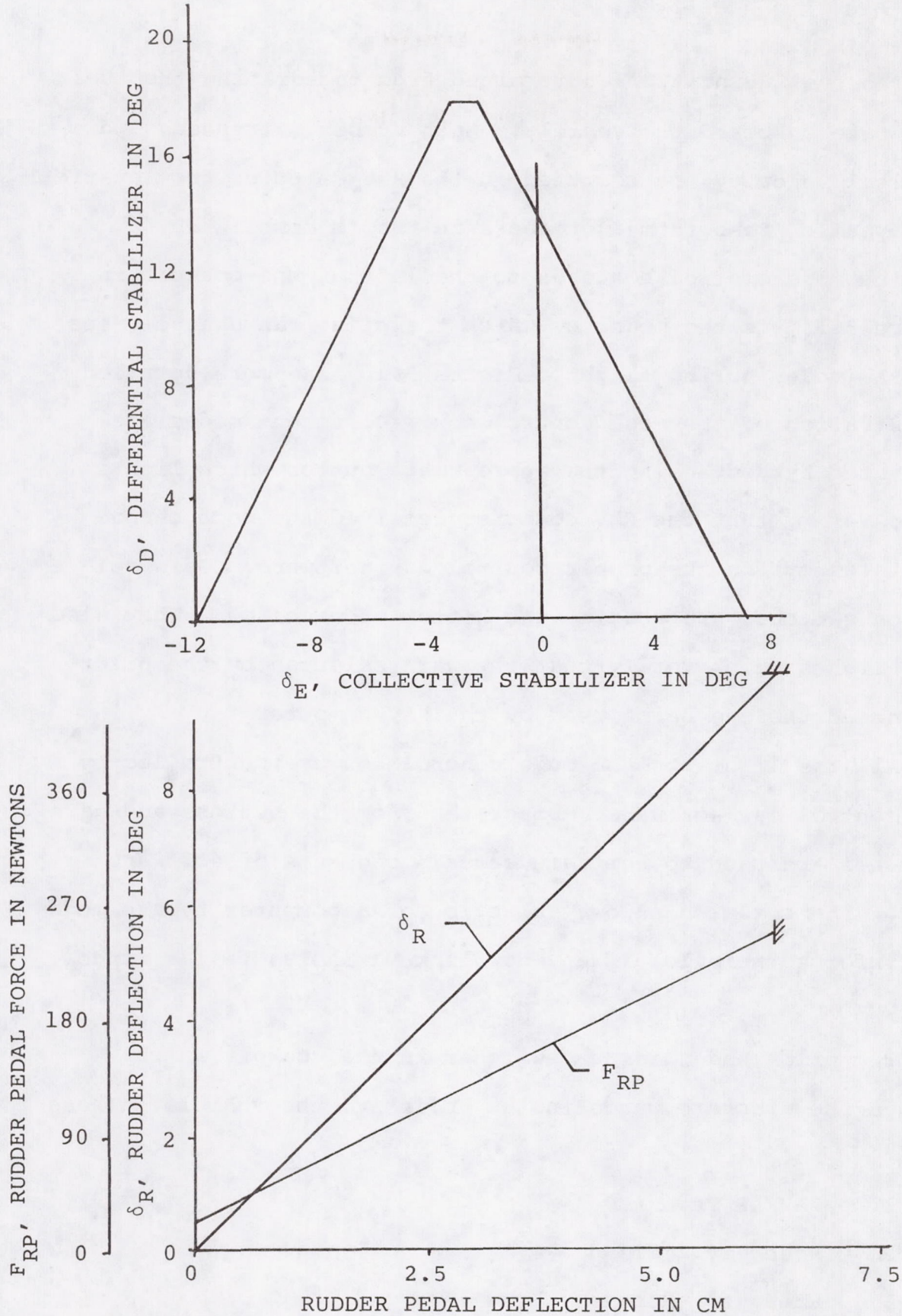

FIGURE 5.15 (CONCLUDED) (PAGE 2 OF 2)

The fuel quantity is determined from integrating the fuel flow rate on board the vehicle. Mach number, airspeed, and vertical velocity are computed in the RAV computer from static and dynamic pressure measurements in the TM downlink.

The mode control box seen to the left of the cockpit in figure 5.14, is the means by which the pilot can change gains and RAV modes during flight. Figure 5.16 is a more detailed illustration of the mode control box. Different modes are activated by depressing the appropriate button which lights up to verify that the RAV computer received the mode change and is executing the proper control law software. Gain selection switches are seen at the bottom of each row. They also have lights which verify that the gain selected by the pilot is indeed the one being used by the RAV computer.

All the lights on the mode control box are controlled by the control law software. Discretes from the buttons and gain switches are used to activate certain segments of software code. The box also allows selection of a computer bypass mode and informs the pilot if any downlink variables fail a window check.

The pilot has numerous switches in the cockpit which change the discrete words in the uplink to the vehicle. These are:

1. RAV/AP Transfer
2. Recovery command
3. Emergency Recovery
4. Ground Transmitter On/Off
5. Smoke Generation

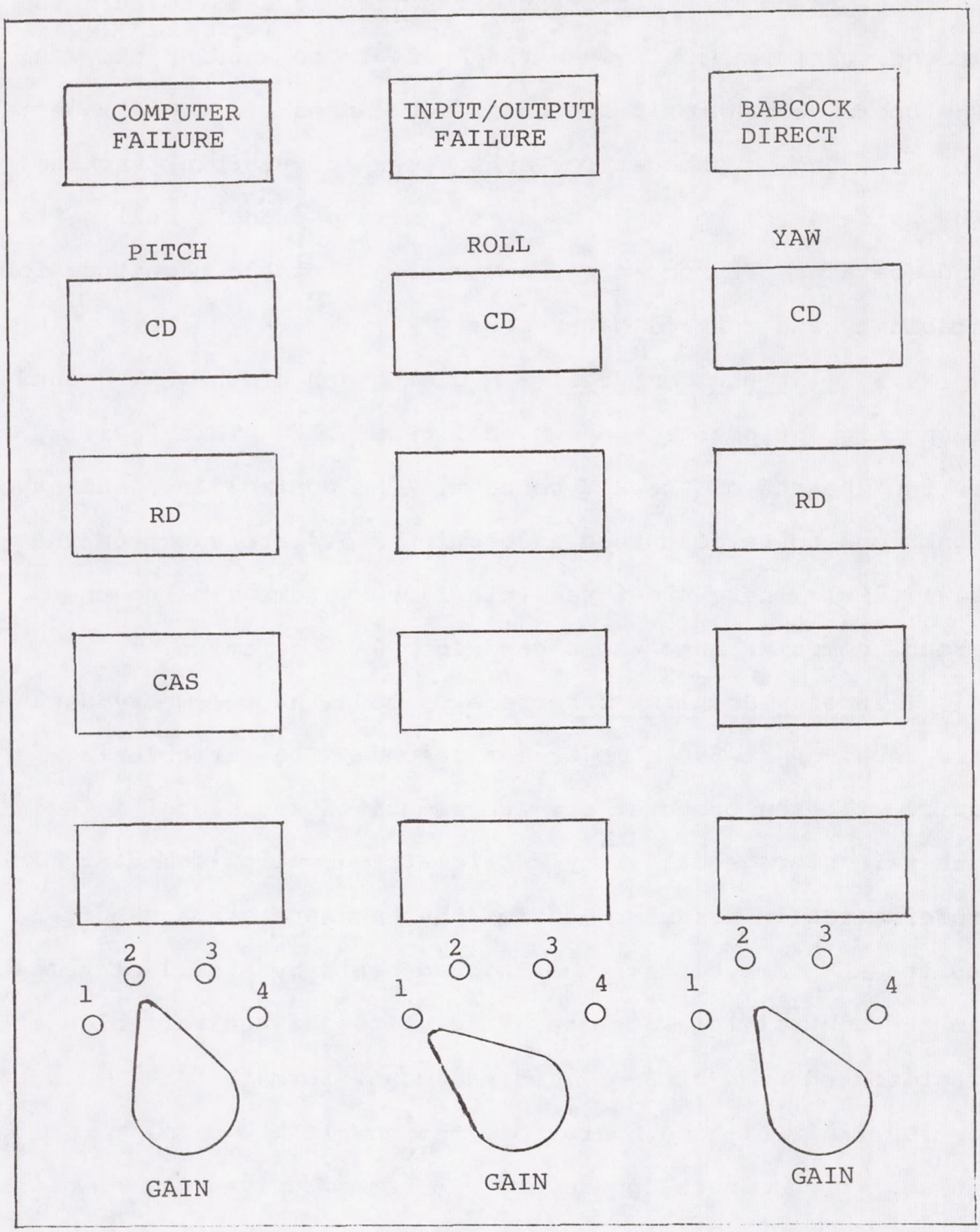

FIGURE 5.16 RAV MODE CONTROL BOX

6. Control Surface Pulses and Doublets

The ground transmitter on/off switch is used to turn the ground transmitter off when the F-104 is commanding the vehicle. The smoke generation function switch causes oil to be injected into the engine exhaust for enhancement of visible tracking. The pulse panel would be used to generate rudder, rolling tail, and elevator preprogrammed inputs of selectable magnitude for stability and control maneuvers.

5.5.2 Ground Computer. - A photograph of the RAV ground computing equipment is shown in figure 5.17. This facility is the "heart" of the RAV concept. The control laws and other functions to be described in section 5.5.4 are executed in real-time. There are three interface systems linking the ground computer into the closed loop RAV operation.

Telemetry Downlink Interface. - Downlink telemetry data are received at 500 samples per second. The variables required for the computer are subcommutated and placed in a hardware storage buffer by a telemetry downlink computer. This information is transferred from the hardware storage buffer to the RAV computer on an as needed basis by a call statement in the control law software. The values of the variables are represented by a 0 to 511 decimal count format.

During real-time operation, the downlink interrupt sync pulse, which occurs once every PCM frame, drives the downlink computer service routines to continuously update the downlink storage buffer so that the most recent data will always be available to the control laws computation. This minimizes the time delay in the closed loop cycle.

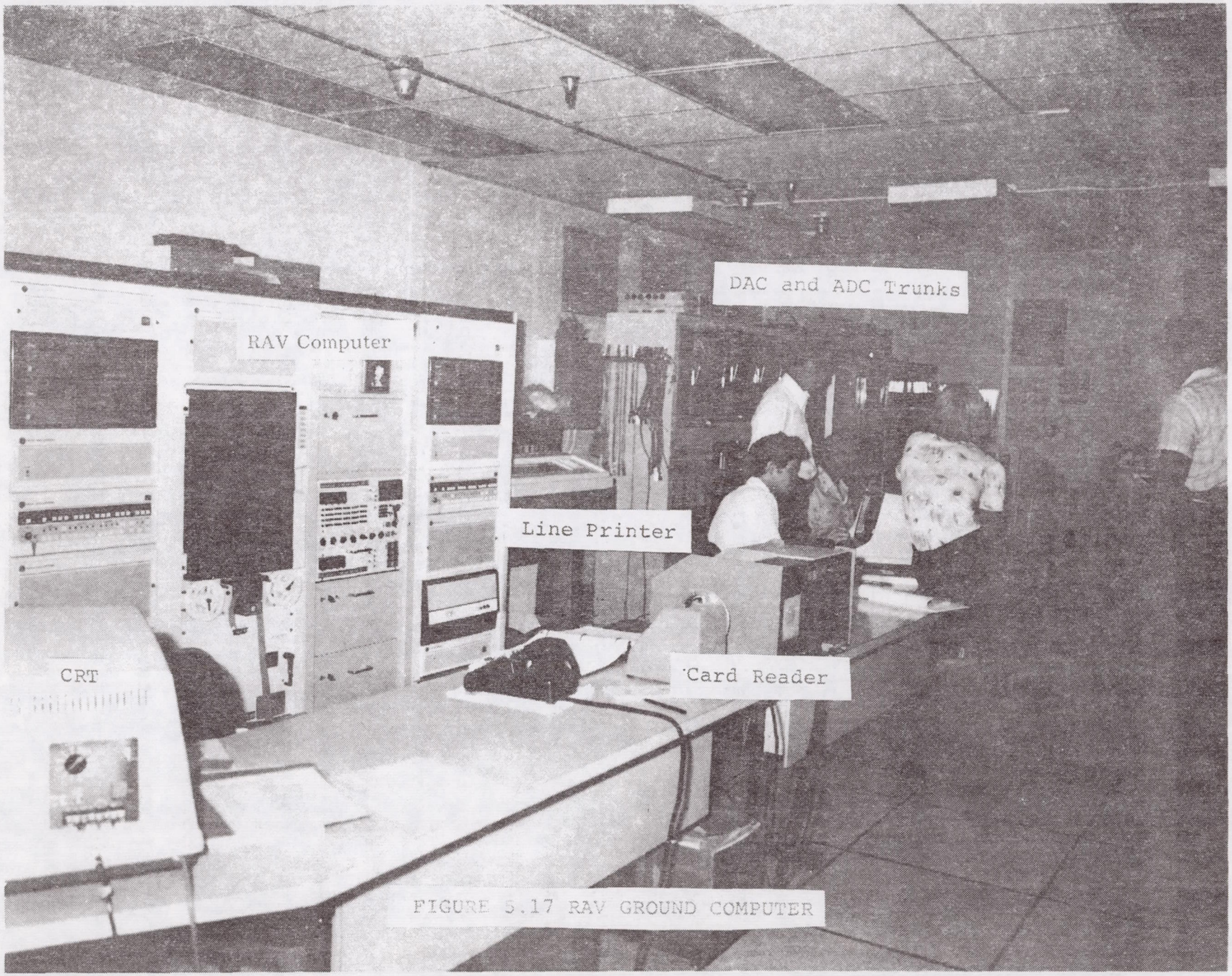

FIGURE 5.17 RAV GROUND COMPUTER

Telemetry Uplink Interface. - The computer encoder uplink interrupts the computer every 3.75 milliseconds to request one of four 16-bit data command words or a 16-bit synchronization word. If the computer program and uplink encoder get out of synchronization, the computer sends the variable that the encoder requested. The uplink mainframe rate is 53.33 samples per second.

Ground Cockpit Interface. - The pilot's proportional command signals, mode control box, and cockpit switches status are sampled once each cycle at the 53.33 samples per second rate. The RAV software main FORTRAN program determines if any mode or gain changes are being commanded by the pilot. The cockpit data is transferred to the RAV computer during the synchronization word computation mentioned above.

The computer used in the RPRV system is a general purpose rack-mounted mini-computer with a 32K memory of 16-bit words and with a 330-nanosecond cycle time. Peripheral equipment includes a CRT, card reader, line printer, magnetic tape unit, disc unit, and peripheral floating point processor. The software is composed of an assembler, a FORTRAN compiler, and a mathematical subroutine support library. The open-loop and closed-loop control law computations are implemented in floating point FORTRAN. This allows the FORTRAN compiler to be used in debugging and checking out programs, and the floating point feature eliminates the need for variable scaling. The FORTRAN feature is ideally suited for research programs because of the ease with which programs can be written and changed.

5.5.3 RAV Software Structure. - Because of the experience gained at NASA DFRC in the operation of RAV and other flight programs requiring flight software (F-8-DFBW aircraft), rather stringent and extensive software control requirements have been established. For safety of flight considerations, extensive verification testing and documentation procedures are required and reviewed by a designated program Software Control Board.

This section is intended to provide a description of the required software structure which makes the RAV concept workable while sections 5.5.4 and 5.5.5 will describe some of the safety features and possible failure areas which can occur from RPRV operations.

The RAV program executive software structure is illustrated in figure 5.18. The background displays and program initializations are executed only in the non-real time mode of the program.

The CRT background displays will be used for:

- Internal program monitoring
- Software and hardware debugging
- Program status and timing information

These diagnoistic and informational displays will be one of the primary tools used in the software verification tests. Line printer copies of these displays are available for documentation. All the information required for proper RPRV facility checkout and software functional checks will be available on these CRT displays.

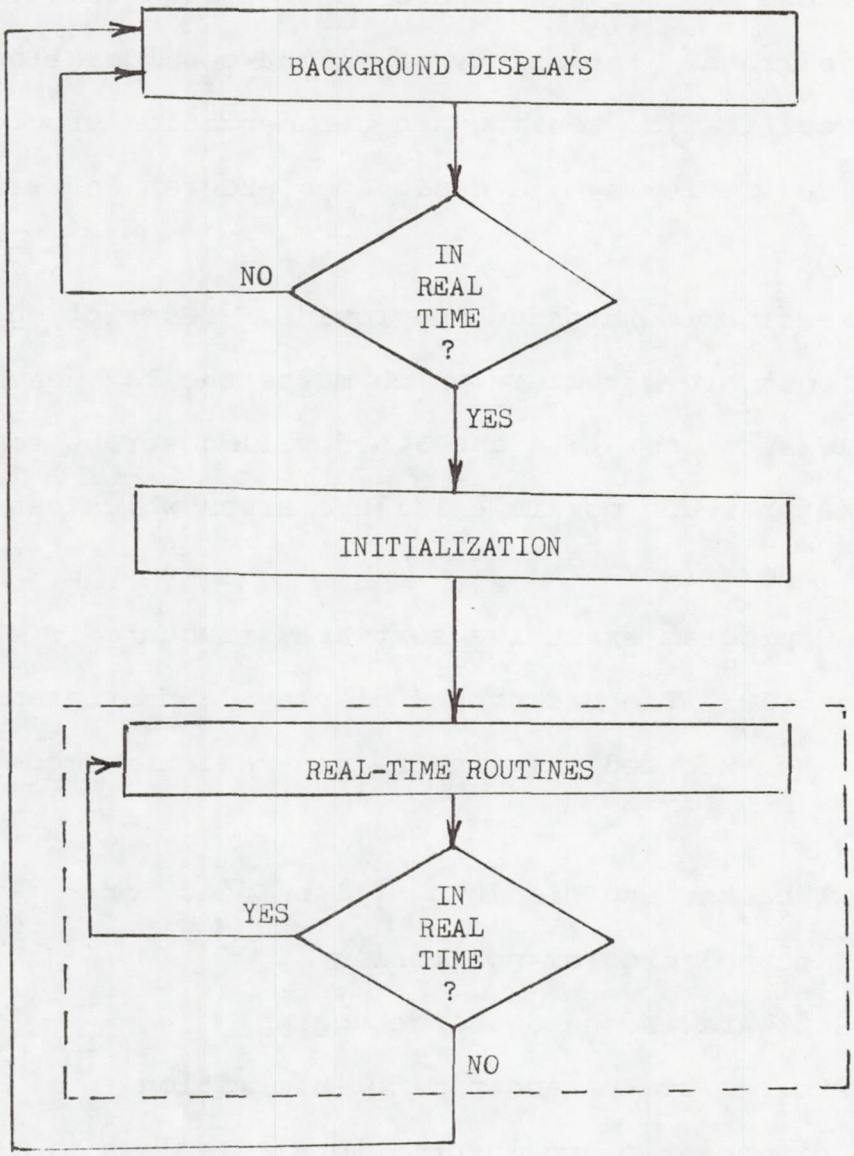

FIGURE 5.18 RAV PROGRAM EXECUTIVE STRUCTURE (SIMPLIFIED)

The program initiation will be performed prior to activation of real-time operations. Its purpose is to ensure that no program variable or hardware element is left undefined prior to entering the real-time software code. Software variables which require initialization include limits, gains, constants, calibrations, and the fault thresholds, tolerances, and documentation of fault occurrences which will be discussed in section 5.5.4. The hardware elements which require initialization are digital-to-analog converters, analog-to-digital converters, and the uplink controller.

The real-time functions of the RAV software are the real time loop structure, the system input/output interfaces, and the control laws. The Babcock uplink encoder external interrupt drives the real-time loop structure of the DAST computer program. This interrupt is on an 18.75 millisecond frame rate. During the uplink interrupt loop, the control law algorithms, some elements of the system input and output interfaces, and the fault detection algorithms are executed. The downlink operation requires no program external interrupts, although a fault detection algorithm will utilize the PCM sync word arriving every 2 milliseconds.

The downlink interface described in section 5.5.2 between the RAV computer and the downlink servicing computer transfers the variables required in the computations in decimal counts, then converts them to engineering units using linear slope/

intercept formulas before they are used in the uplink interrupt cycle.

The downlink proportional inputs required in the computations are:

1. Pitch rate
2. Yaw rate
3. Normal acceleration
4. Free stream static pressure
5. Free stream differential pressure

Several downlink discrete inputs are required by the ground computer to provide status information to the pilot. These are:

1. Carrier loss discrete
2. FSS hydraulic pump reserve status
3. Left wing pyrotechnic verify (fired)
4. Right wing pyrotechnic verify (fired)
5. FSS gain verify
6. Recovery commanded
7. FSS on/off verify
8. Emergency recovery

The four uplink data words generated are shown in figure 5.19. The first ten bits of each uplink word are under computer control and the last six bits are hardwired to the uplink encoder. It can be seen from figure 5.19 that the discrete words are complimented on every other digital word. It

	BITS 0 THRU 9	BIT 10	BIT 11	BIT 12	BIT 13	BIT 14	BIT 15
WORD 1	LEFT HAND STAB	RECOVERY 1 (OFF)	AP CMD 0 (OFF)	ANTI-SYMMETRIC 1 (OFF)	CAMERA ON 0 (OFF)	FSS ON 1 (OFF)	PULSE ON 0 (OFF)
WORD 2	RIGHT HAND STAB	EMER RECOVERY 1 (OFF)	TIP MASS EJECTION 0 (OFF)	1 (OFF)	SMOKE 0 (OFF)	AMPLITUDE HI 1 (OFF)	FREQ ON 0 (OFF)
WORD 3	YAW	RECOVERY 0 (OFF)	AP CMD 1 (OFF)	ANTI-SYMMETRIC 0 (OFF)	CAMERA ON 1 (OFF)	FSS ON 0 (OFF)	PULSE ON 1 (OFF)
WORD 4	THROTTLE	EMER RECOVERY 0 (OFF)	TIP MASS EJECTION 1 (OFF)	0 (OFF)	SMOKE 1 (OFF)	AMPLITUDE HI 0 (OFF)	FREQ ON 1 (OFF)

FIGURE 5.19 UPLINK WORD STRUCTURE

has been found that this scheme minimizes the changes of a spike in the uplink generating an unwanted command.

The control law computation structure within the uplink interrupt cycle is illustrated in figure 5.20. Since the RAV control laws were not complicated, the computation time for the control laws is only requiring approximately 42 per cent of the 18.75 milliseconds available. The computations for driving the Mach meter, airspeed indicator, vertical velocity indicator and fault detection algorithms therefore, do not tax the system. These calculations are divided up so that their software call statements are evenly distributed with respect to the control surface computations of the control laws.

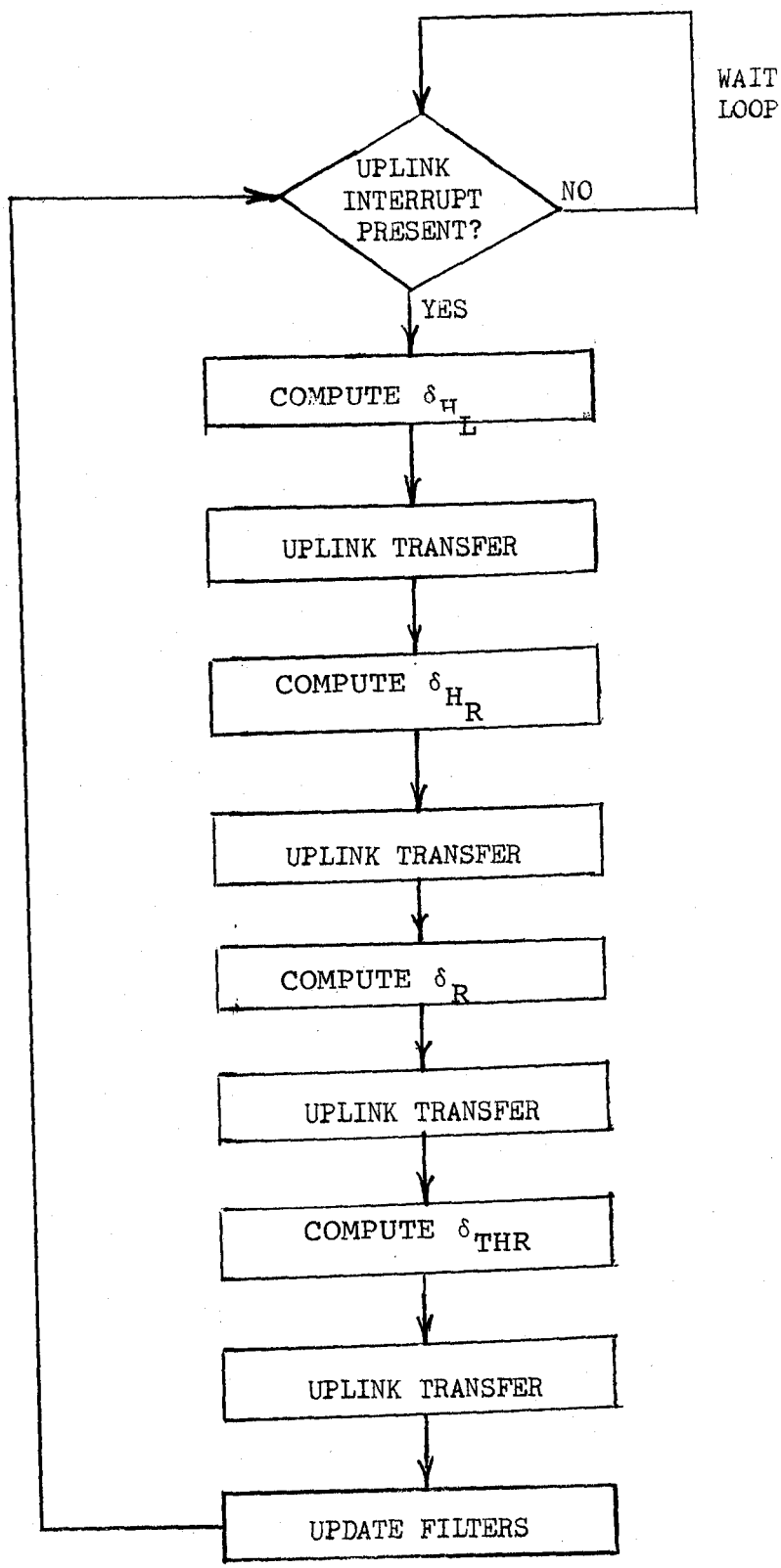

FIGURE 5.20 CONTROL SYSTEM EXECUTE STRUCTURE (SIMPLIFIED)

5.5.4 Failure Detection Methods. - Although the RPRV concept has proven to be an excellent method of performing high risk flight experiments, the concept itself introduces additional mechanisms from which a failure in flight can occur. Fortunately, the computational capability which is available in the ground facility can reduce the chances of endangering the vehicle from some failures which can occur with the RPRV technique.

The mechanisms which have been employed in past and present RAV programs at NASA DFRC and which will be used in the DAST program are summarized in Table 5.2. The time-out counter concept is illustrated in figure 5.21. The purpose of the time-out counters are to prevent asynchronous operation of the uplink and downlink during closed-loop operation. Asynchronous operation would allow unacceptable time delays in the control laws and other possible dangerous operations.

The rate checks on the uplink commands prevents "hard over" commands, that could result from something like a short circuit in the cockpit stick sensors, from being sent to the vehicle. Downlink rate checks protect against possible sensor "hard-over" failures from being used in the feedback computations. Automatic mode changes and AP transfer are ways of preventing dangerous and unintentional RAV commands resulting from the types of failures described above from being sent to the vehicle.

5.5.5 Failure Modes Assessment - Part of the policy of qualifying software for flight is to perform a failure modes

TABLE 5.2

RAV Fault Detection Mechanisms

Mechanisms	Detects
Downlink Software Time-Out Counter	Hang Up in Downlink Process
Uplink Software Time-Out Counter	Hang Up in Uplink Process
Uplink Command Rate Check	Unreasonable Changes in RAV Commands
Uplink Command Authority Limit	Out of Range Commands
Downlink Variable Rate Check	Unreasonable Changes in Downlink Parameters
Stick-Trim Opposition Logic	Trim Discrete Failure
Computer Heartbeat Monitor	Ground Computer Hardware Malfunction
Pilot	Unexpected, Uncommanded Vehicle Motion

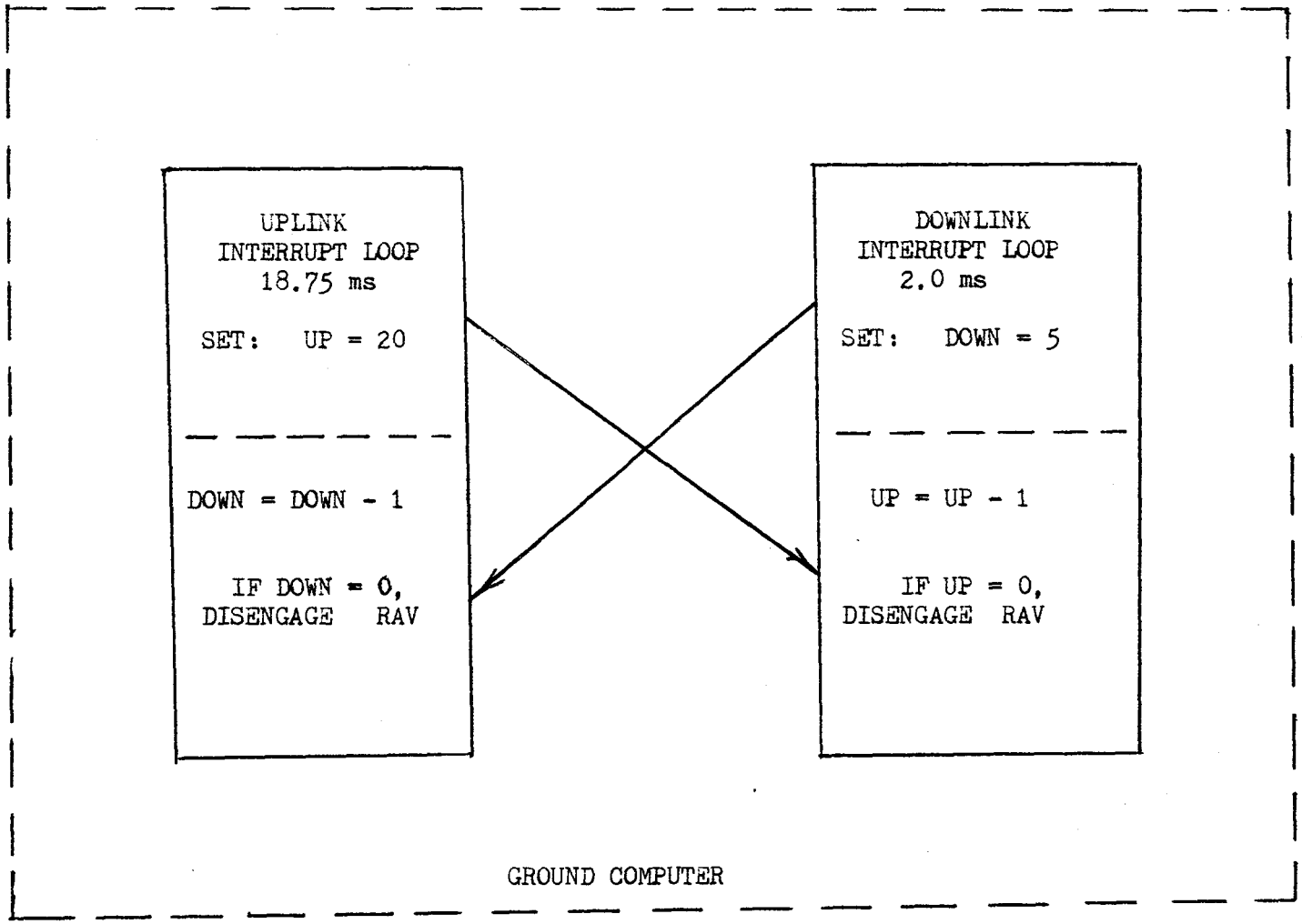

FIGURE 5.21 TIME-OUT COUNTER CONCEPT

and effects analysis (FMEA) on the system. Prior to beginning a FMEA, the software must have successfully completed static, dynamic, and closed-loop real-time simulation testing. Static checks are accomplished by holding all inputs constant and checking the output of each control system element for proper values. In dynamic verification testing, all dynamic control system elements, such as filters, rate checks, and faders, are checked individually input to output. Closed loop operation is verified in the real-time simulation. When the software has been verified to this level and documented, an FMEA is the next step. The proper operation of the failure detection schemes are verified in the types of test shown in Table 5.3.

An on-board receiver failure, autopilot sensor failure, or horizontal stabilizer servo failure all place the vehicle in potentially disasterous circumstances. The automatic recovery resulting from an on-board receiver failure is considered potentially disasterous because it will probably mean the recovery parachutes will deploy outside the recovery area. This would mean that the MARS helicopter could not reach the DAST before it impacted the ground. This is also true if a horizontal tail servo fails and the vehicle survives any uncontrollable maneuvers before the recovery chutes deploy. With an autopilot sensor failure the vehicle would probably encounter uncontrollable maneuvers when the vehicle recovery is commanded, thus jepardizing the success of the recovery.

TABLE 5.3

Failure Modes and Effects Analysis

Simulation	RPRV Facility/DAST
Downlink Faults • opens • hardovers • ramps • dropout • frozen value Uplink Faults • open • hardovers • ramps • frozen value Software Faults • hardover • ramps • frozen value • runaway integrator Ground Computer • power loss • halt	Downlink Faults • opens • hardovers • ramps • frozen value • TM station • power loss • TM station sync loss Uplink Faults • opens • hardovers • ramps • frozen value • signal loss • parity fail • power loss • Babcock encoder failure • TM transmitter failure

CHAPTER 6

ASSESSMENT OF FLUTTER TESTING METHODS

This chapter examines some of the unique aspects of the FSS flight testing requirements. A testing philosophy is discussed which addresses the new aspects of flutter testing this research experiment creates. An evaluation of candidate testing techniques is accomplished by using DAST ARW-1 simulated flutter data. The development of the DAST ARW-1 flutter simulation is also described.

6.1 Flight Testing Philosophy and Limitations. - The FSS flutter testing experiment is a new regime of flutter testing. The flutter characteristics are explosive and of high frequency. Demonstrating an increase in the flutter speed of this magnitude has never been attempted before in flight testing. For DAST I, the testing philosophy is to rely on the tip mass ejection system to prevent the wing from fluttering if problems arise in the supercritical testing region. A test engineer on the ground will monitor the accelerometer signals but since he will not be able to identify a flutter problem on this wing in sufficient time to manually jettison the tip ballast, the automatic system will be relied upon to catch any problems. Only closed loop testing of DAST I will occur near the flutter boundary. The risk, because of the explosive flutter, makes precise determination of the unaugmented boundary very dangerous. It will be determined "as well as possible" so that some gage of the FSS

performance can be made. A preliminary first flight test point grid is shown in figure 6.1. The lowest altitude test points will be completed first so the vehicle can decelerate while climbing to the next test altitude.

A possible second flight test grid is seen in figure 6.2. The flight plan calls for the FSS to be on at all times. The unaugmented flutter boundary will be exceeded on the second flight. Consideration is being given to demonstrating the 20 per cent increase in the flutter boundary on the third flight. The test program is scheduled for six flights at a one flight per month rate.

The difficulty of conducting the DAST I FSS experiment is increased slightly by limitations introduced by the vehicle's performance characteristics. These are:

1. Limited flight time
2. Limited antenna range
3. Lack of precise speed control
4. Limited FSS hydraulic capacity
5. The relatively low MARS reliability

In examining the first three items listed above, their effects on the flight tests can be minimized by adopting flutter testing techniques which require short record lengths of data.

The limited flight time, caused by a small fuel capacity and a large fuel consumption rate, is still of concern but the amount of data per flight is greater with these new testing methods. With the limited antenna range and high vehicle

- FSS ON AND OFF
- SYMMETRIC AND ANTISYMMETRIC EXCITATION
- SWEEPS AND PULSES
- STAY 0.1 M AWAY FROM PREDICTED BOUNDARY

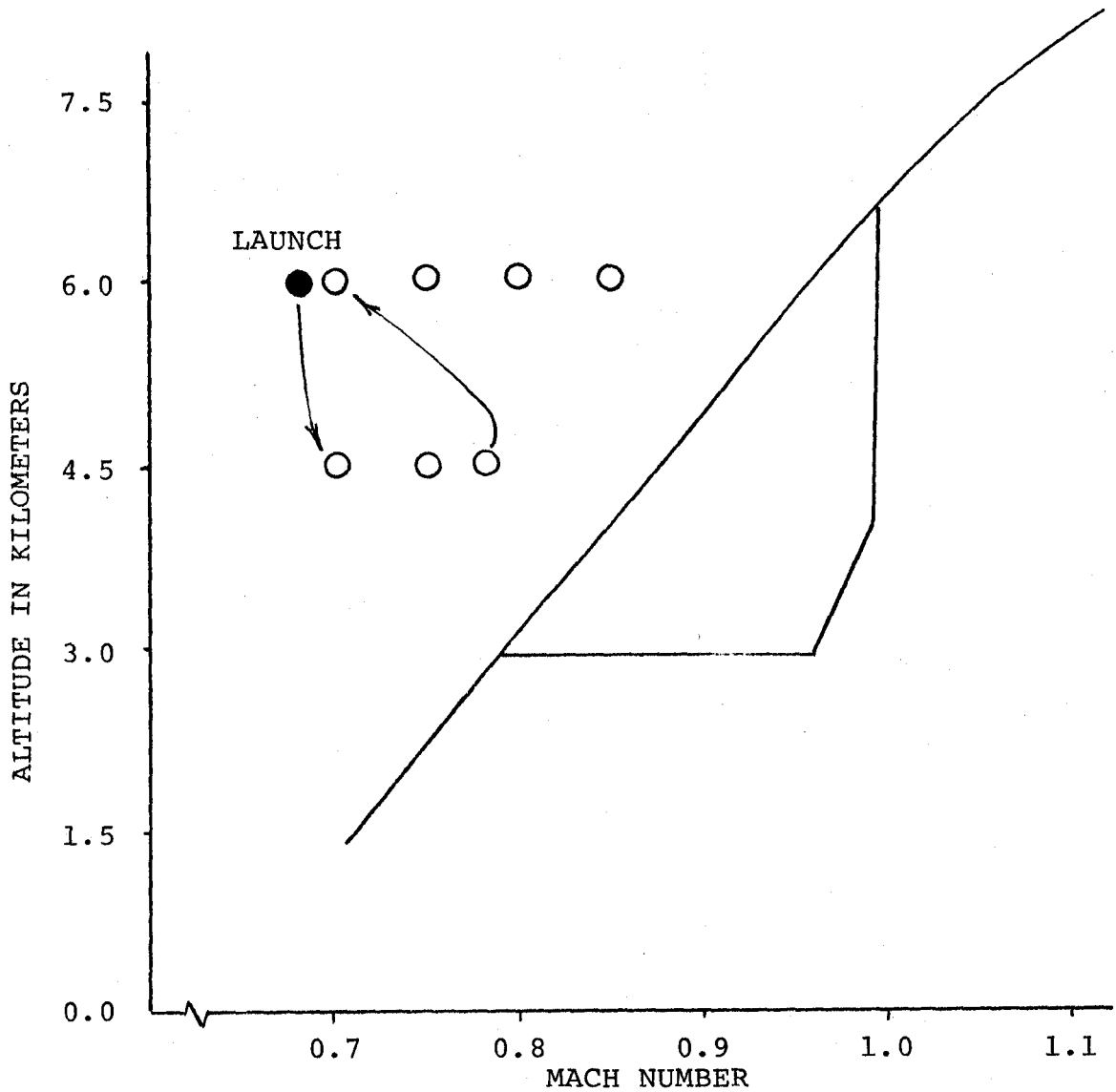

FIGURE 6.1 FIRST FLIGHT TEST POINT GRID

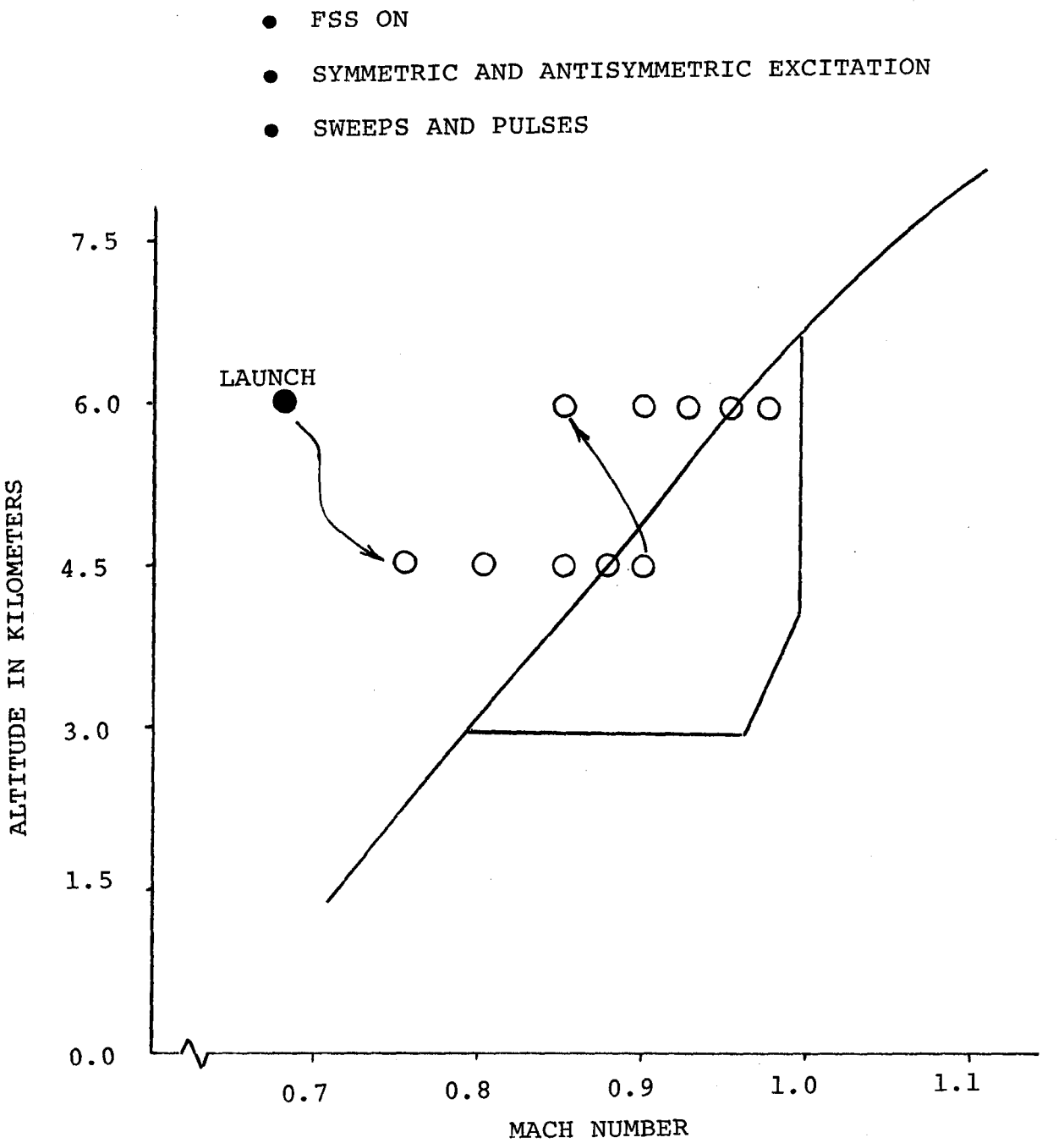

FIGURE 6.2 SECOND SUPERCRITICAL FLIGHT TEST POINT GRID

speeds, the DAST can fly only three or four minutes before a turn must be made. Since the data record length requirements are short, the constant flight condition requirements during data collection are easily achieved. The precise speed control problem is resolved somewhat because the testing methods require data records on the order of only ten seconds. Very little change in Mach number will occur in this short time interval even if the vehicle has not been totally speed stabilized by the pilot. Of course, this is only true if the RPRV pilot is trying to establish nonaccelerating conditions. The point is that the flutter testing methods don't require the vehicle to be totally speed stabilized during the tests. Trying to establish a totally constant Mach number condition with DAST I is difficult because of the poor engine response and the rate of change in flight parameters due to the rapid fuel burnoff.

The concern of limited FSS hydraulic capacity is created by the fact that 80 per cent of the FSS hydraulic capacity is required just to maintain the control surface in the faired position. Aft loading from the trailing edge camber of the SCW is the cause. If turbulence is encountered and excitation inputs are also added, the hydraulic system could be overpowered and surface saturation could result. Flying in reasonably calm flight conditions reduces the risk of this happening. Another concern is that the load on the control surface in the faired position requires nonlinear actuator loop gain. This is illustrated in figure 6.3. This type of non-

LOOP GAIN VARIATIONS DURING SYSTEM OPERATION

- SERVOVALVE FLOW GAIN IS A FUNCTION OF LOAD PRESSURE OR CONTROL SURFACE HINGE MOMENT-

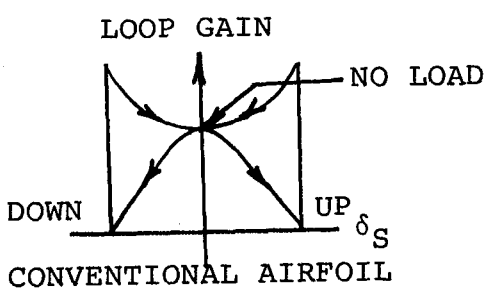

CONVENTIONAL AIRFOIL

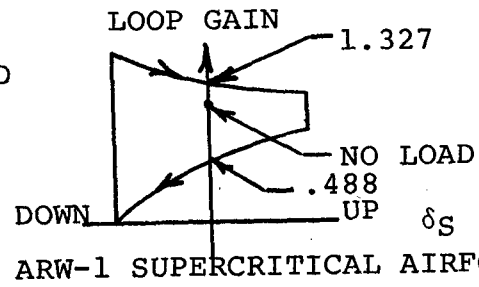

ARW-1 SUPERCRITICAL AIRFOIL

$$K_V = \frac{Q}{i} = \frac{Q_{MAX}}{i_{MAX}} \sqrt{1 - \frac{P_{LOAD}}{P_{SYSTEM}}} \quad \text{WHERE } P_{LOAD} \text{ CAN BE } \lesseqgtr 0$$

- IF SERVOVALVE GAIN IS UNBALANCED, THE NO LOAD LOOP GAIN NONLINEARITY CAN BE MINIMIZED-

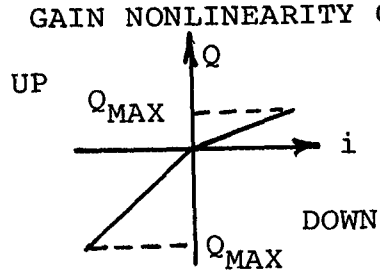

SERVOVALVE FLOW CHARACTERISTICS

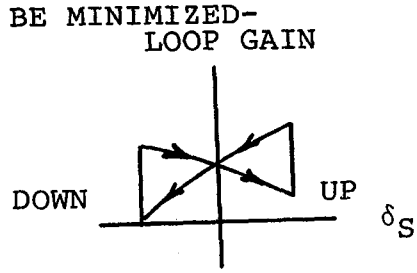

ARW-1 SUPERCRITICAL AIRFOIL (WITH UNBALANCED SERVOVALVE)

FIGURE 6.3 FSS NONLINEAR ACTUATOR LOOP GAIN

linearity introduces the possibility of a limit cycle in the FSS system.

Air Force experience with MARS recoveries of Firebee II's shows an approximately 80 per cent success rate. This justifies the rather bold approach to the flight testing. By having a success oriented approach, the amount of data on the FSS performance characteristics is maximized. If, on the other hand, a more conservative and cautious philosophy were adopted, the chances diminish of completing the tests successfully before a MARS failure. By using some of the relatively new flutter testing techniques described in the next section, a large amount of information on the FSS system can be attained quickly. Thus, the risks involved in rapid expansion of the DAST flutter envelop are reduced.

6.2 Near Real-Time Testing Methods. - The requirement for flutter testing methods which can make estimates of structural frequency and damping from short record lengths of data has been established. An evaluation of some of the relatively new methods was done in reference 11. Their performance was measured by testing the accuracy of frequency and damping extimates in a two-dimensional flutter model. This section concerns itself with describing those techniques which are suited to the requirements of the DAST experiment.

Most flutter test frequency and damping estimation methods operate in the frequency domain. The frequency response transfer function, H_2, of an accelerometer signal is determined by

taking the Fast Fourier Transform (FFT) of the time domain acceleration response.

Those methods considered as candidates for the DAST near real-time requirement are:

1. PSD's
2. Co-Quad
3. Amplitude-Phase
4. Modulus of the Transfer Function
5. Impulse Response Function

The Power Spectral Density (PSD) technique is illustrated in figure 6.4. Very short data record lengths can be used with this method. The Spectrum of H_2, which assumes white noise input, shows the modal frequencies by peaks in the power spectrum. The damping estimate is made by determining the width of the frequency peak at its half power point and dividing by twice the peak frequency. The white noise input is usually approximated by pulses and doublets of the control surfaces which create broad band width excitation.

The Co-Quad method generally uses a frequency sweep of the control surfaces to excite the different modes. As the sweep frequency coincides with a modal frequency, energy is input into that mode and its response increases. The transfer function, H_2 is determined for this input and its real (coincidence) and imaginary (quadrature) components are plotted as in figure 6.5. When a structural mode is excited by the input, the amplitude of the transfer function increases. Then the damping estimate is determined from the changes in the

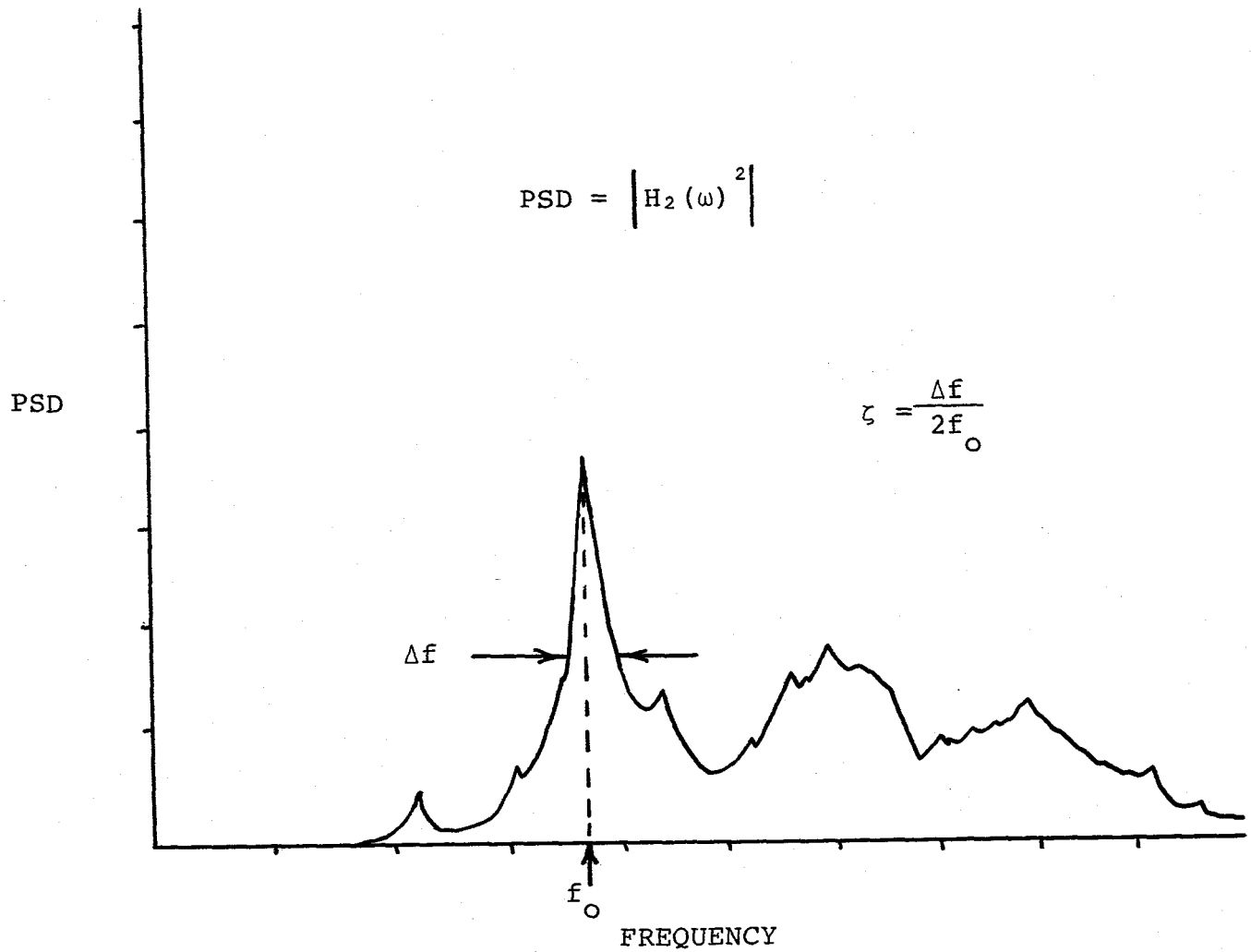

FIGURE 6.4 ILLUSTRATION OF PSD FLUTTER TESTING METHOD

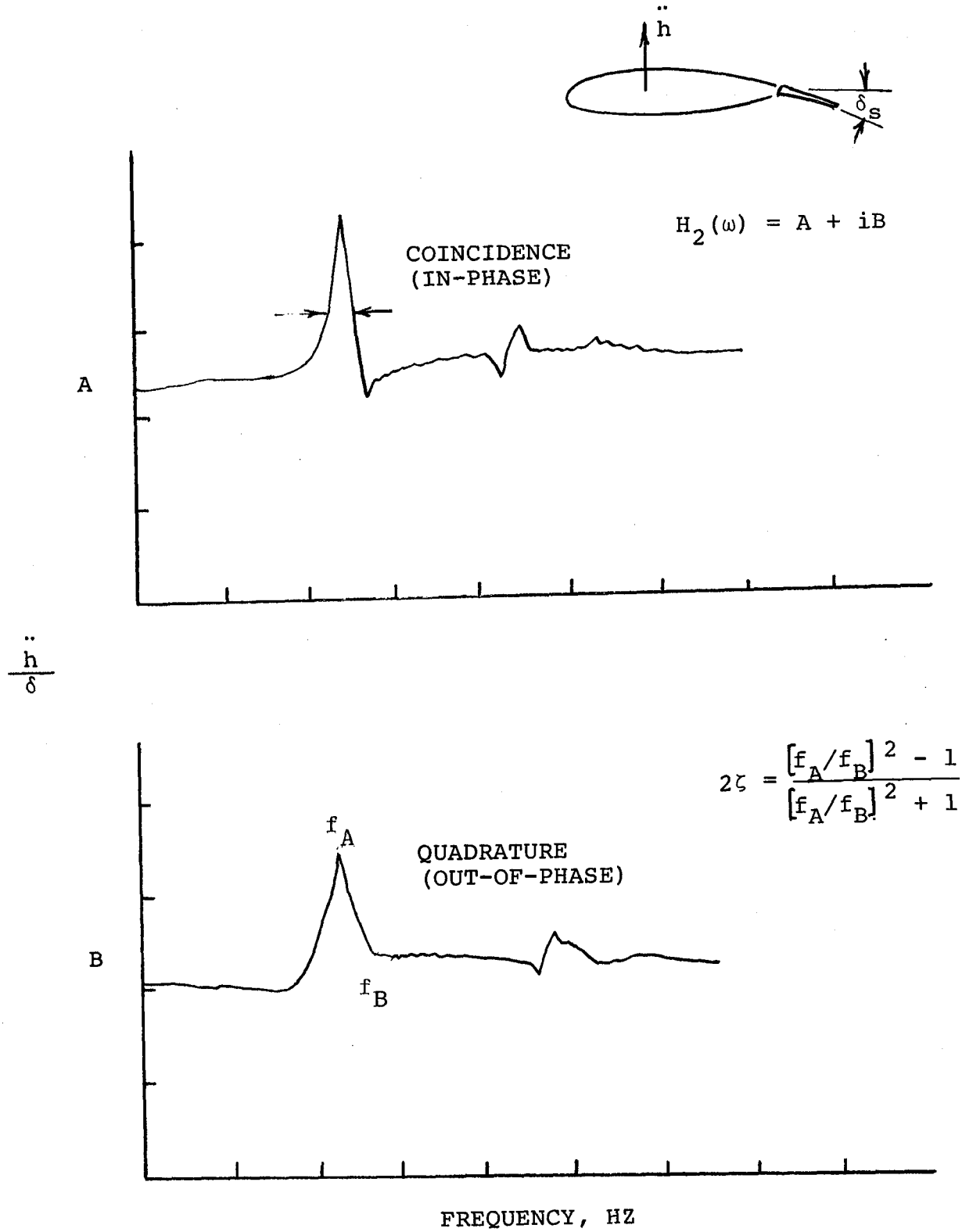

FIGURE 6.5 ILLUSTRATION OF THE CO-QUAD METHOD

imaginary part at the half power frequencies.

The PSD and Co-Quad methods assume that the form of the damping is structural. This means that the damping is proportional to the square of the amplitude of displacement of the structure. If viscous damping is present, the damping estimates produced from the PSD plot and Co-Quad plot will not be truly representative of damping within the system.

The Amplitude-Phase method is not dependent upon the structural damping assumption. Figure 6.6 illustrates this method. The frequency response transfer function is used in its polar coordinate form. The amplitude ratio indicates the modal frequency and the damping is determined from the slope of the phase angle at that frequency.

The modulus of the frequency response function, e.i., the square of the transfer function, will generate PSD's from system inputs such as surface frequency sweeps. Frequency and damping are then determined in the same manner as the PSD method. Its advantage over the PSD method is its noise reduction capability which is discussed later in this section.

The impulse response function is the inverse Fourier transform of the frequency response function:

$$\ddot{h}(t) = \frac{1}{2\pi} \int_{-\infty}^{\infty} H_2(\omega) e^{i\omega t} d\omega \qquad (6.1)$$

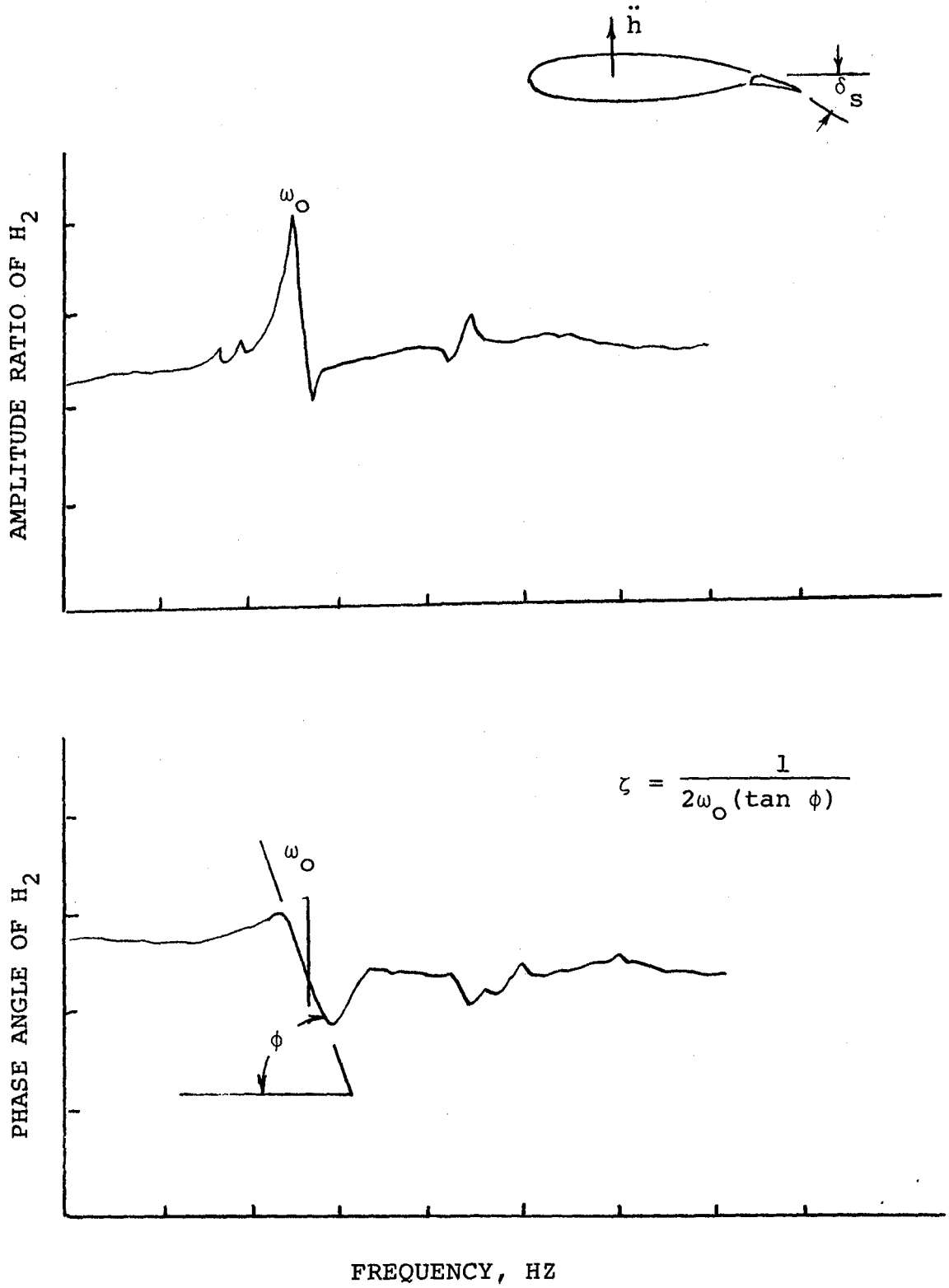

FIGURE 6.6 ILLUSTRATION OF THE AMPLITUDE-PHASE METHOD

Frequency and damping measurements from the impulse response are illustrated in figure 6.7. Frequency is measured by the period of oscillation and damping is determined from the log-decrement of the oscillation.

Aside from the PSD method, all the methods deal with the noise problem by the following mechanism. The response due to an applied excitation and due to a noise environment may be written as:

$$\ddot{Y} = \ddot{Y}_f + \ddot{Y}_n = \int (f + f_n)\, \ddot{h}\,(t-\tau)\,d\tau \qquad (6.2)$$

where f_n is the unknown input noise and $\ddot{Y}_n$ is the associated noise in the response. The Fourier transform of $\ddot{Y}$ is:

$$F_{\ddot{Y}} = F_{\ddot{Y}_f} + F_{\ddot{Y}_n} = (F_f + F_{f_n})\, H_2 \qquad (6.3)$$

If F_f is multiplied by the complex conjugate $\bar{F}_f$, then the following spectrum equation results:

$$\phi_{F_{\ddot{Y}_f}} + \phi_{F_{\ddot{Y}_n}} = (\phi_f + \phi_{ff_n})H_2 \qquad (6.4)$$

Since f and f_n are uncorrelated, the cross spectra, $\phi_{F_{\ddot{Y}_n}}$ and ϕ_{ff_n}, should vanish. This yeilds:

$$H_2 = \frac{\phi_{F_{\ddot{Y}_f}}}{\phi_f} \qquad (6.5)$$

which should appear as a noise-free result.

For the analysis performed in Section 6.3, the frequency

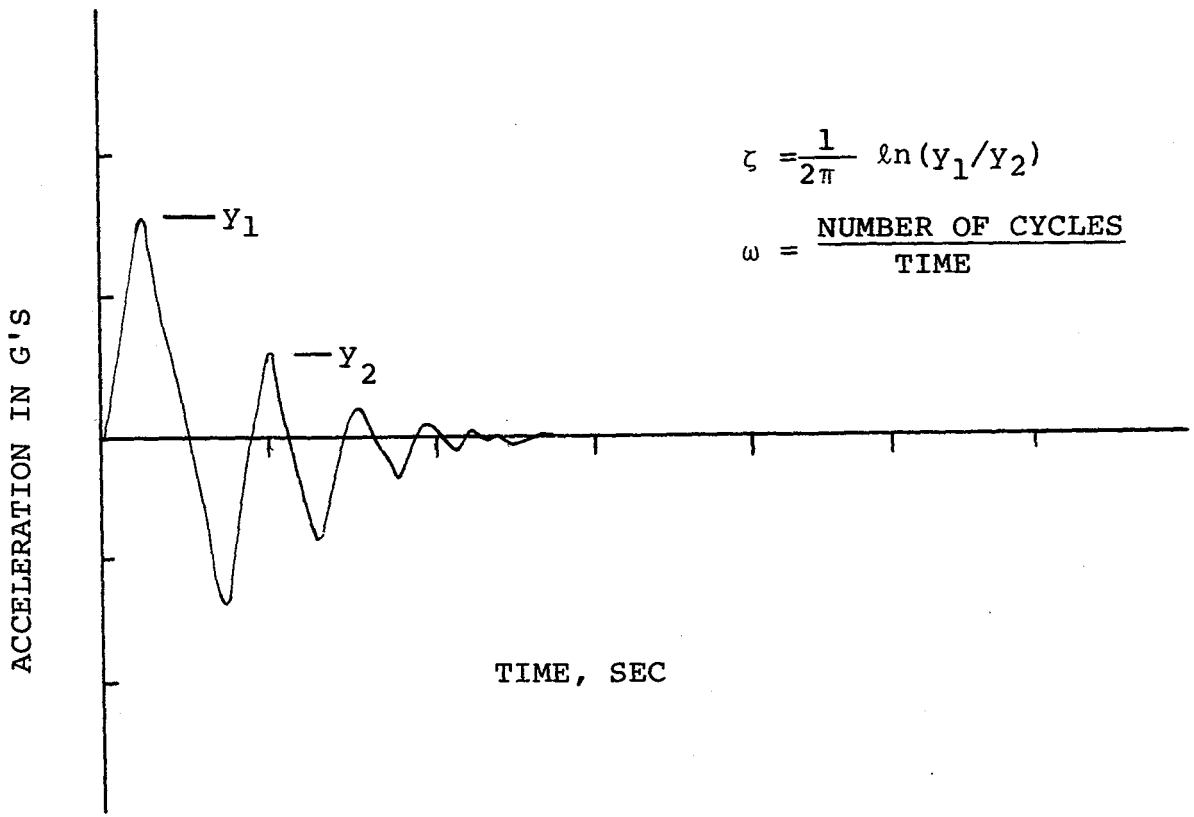

FIGURE 6.7 ILLUSTRATION OF THE IMPULSE RESPONE FUNCTION

response function, H_2, was generated in this manner. The impulse response function was determined from the inverse Fourier transfer of H_2. The PSD's determined in the next section, are from simulated accelerometer responses only.

For the DAST I flight tests, a modal analysis computing facility will be used to calculate the frequency response function and will be able to produce plots of any one of the methods described previously in about 10 seconds. Strip chart readouts of accelerometer signals will be used to watch for "ballooning" in the response. The communication link between the modal analysis facility, the control room, and the pilot in the RPRV facility is critical. The individuals in all three locations must be well coordinated in their activities.

Flutter margins, which all three groups must be conscious of, will be displayed on a plot board showing ω and ζ versus attitude and Mach number. Frequency coalesence will be evident in this type of display and projections of the damping, ζ, to the zero crossing can indicate the altitude and Mach number that the flutter boundary might first be encountered.

6.3 Simulated Responses. - In an attempt to evaluate the flutter testing methods to determine which are best suited for the DAST experiment, a simulation of the DAST ARW-1 structural and rigid body motions was developed. The math model of the DAST ARW-1 developed for the FFS analysis was transformed into a state space representation and implemented in a modified version of the CONTROL computer

program. The transformation equations required to make this conversion are presented in Appendix C.

Many of the data characteristics which the DAST will possess were duplicated in the model. These are:

- 500 samples per second instrumentation
- Identical control inputs
- Record lengths not exceeding 4096 points
- Noise (Dryden Turbulence)

The unaugmented equations of motion were of 54th order. They include:

- 1 rigid body mode
- 6 wing and fuselage structural modes
- 36 artifical states representing the unsteady aerodynamics
- Gust effects
- Control surface mode

The augmented equations which include a simplified FSS control law, supplied by BWC, are of 60th order. The simplified FSS control law has characteristics very close to the complete FSS system up to 400 radians in frequency.

The rigid body pitch mode was included to see if there was any appreciable coupling of the rigid body modes and the flexible modes.

The data generated for the doublet and sweep inputs of the control surface are of the same record length as planned in the flight tests. The modal analysis system can only store and use a maximum of 4096 data points per

calculation. The record length of data points for the doublets is 904 to allow complete decay. The maximum 4096 points were used for the frequency sweep inputs. This required a time history of 5000 data points or seconds.

The control surface inputs planned for the flight tests and used in the flutter simulation are a 25-hertz square wave doublet and a logarithmic frequency sweep from 10 to 40 hertz in 6 seconds. The sweep is ramped in and out over a .3 second time interval. These inputs are shown in figure 6.8. This is a time history plot of control surface commands and movements during a simulation run. PSD's of the surface movements in figure 6.8 show the frequency content of the inputs. The 25-hertz doublet creates a broad bandwith input about the doublet frequency. The PSD of the control surface sweep shows the effect of the ramping in and out of the sweep. The power spectrum indicates that ramping in and out reduces the bandwith of the original input. If this were not done, however and the commands were inserted abruptly and removed abruptly, the spectrum characteristics at the beginning and end of the sweep would appear as large bandwidth peaks since the abrupt changes are similar to pulses.

With the simulated responses created by the methods described above, a preliminary investigation of the candidate flutter testing techniques was made. The analysis presented in Sections 6.3.1 through 6.3.3 is based on no external disturbance, that is, the only input is through the control surface excitation. Responses with turbulence as a noise source

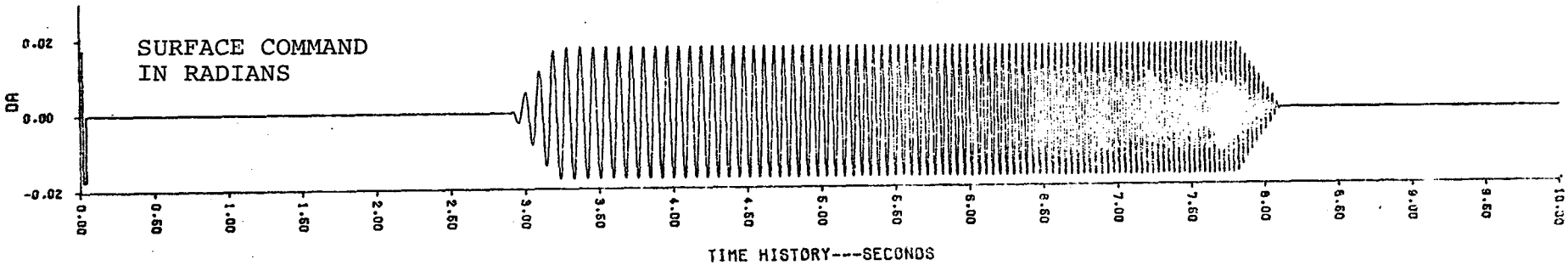

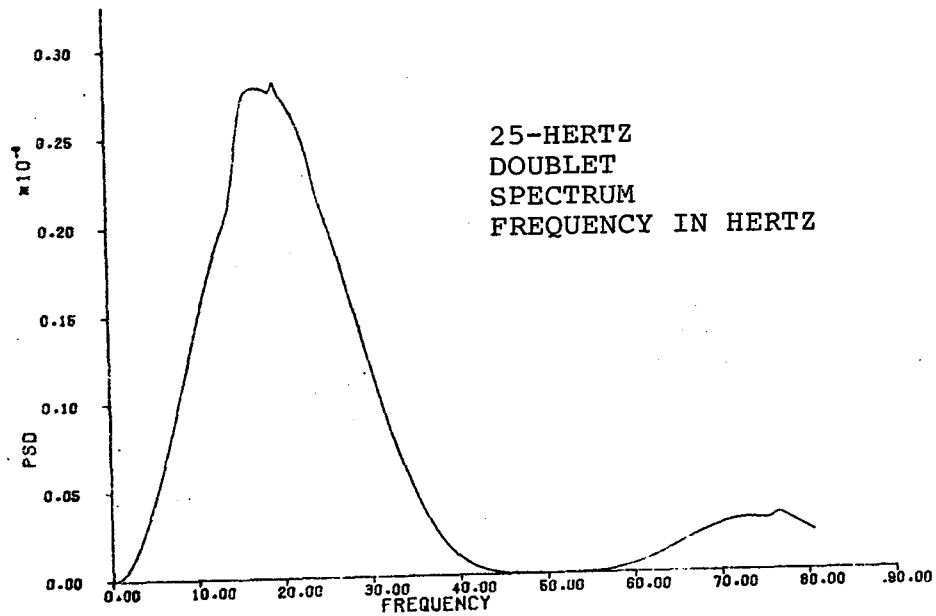

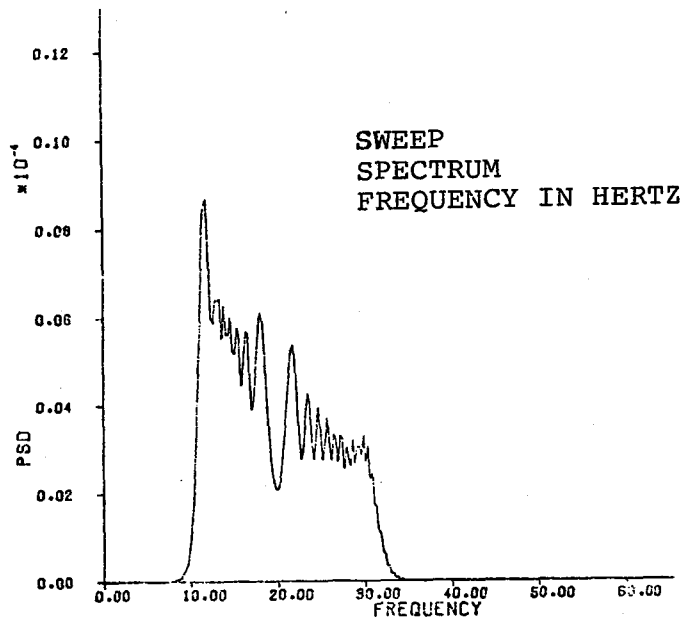

FIGURE 6.8 FLUTTER TESTING CONTROL SURFACE INPUTS

are examined in Section 6.3.4 in order to evaluate the performance of the FSS in a noise contaminated environment.

One concept in particular which was evaluated was the determination of the unaugmented characteristics of the wing from the closed loop response. Using the clean (noise free) data, the ideal circumstances necessary to test the feasibility of the concept are created. The interest in this concept stems from the fact that if it proves feasible, the open loop flutter boundary can be determined accurately with the FSS operating. The danger associated with flying with the system off while close to the unaugmented boundary could be avoided.

An unpublished spectral analysis computer program, developed under NASA DFRC sponsorship, was modified to include all the flutter methods mentioned in Section 6.1. This program, called SPA, created the plots for the analysis used in the next sections.

6.3.1 Subcritical Open-Loop. - The subcritical unaugmented simulated accelerometer response at wing station WBL 79 (rear spar, 2.01 meters from the fuselage centerline) is shown in figure 6.9. The flight condition is M = 0.9 and h = 6096 meters. The control surface movement and command are also shown. The gust input is zero. Individual modal responses from this case and subsequent cases are presented in Appendix C.2. The increased response as the surface sweeps through the first wing bending frequency is evident.

Figure 6.10 presents the results of the various flutter testing methods. The exact values are the eigenvalues of the

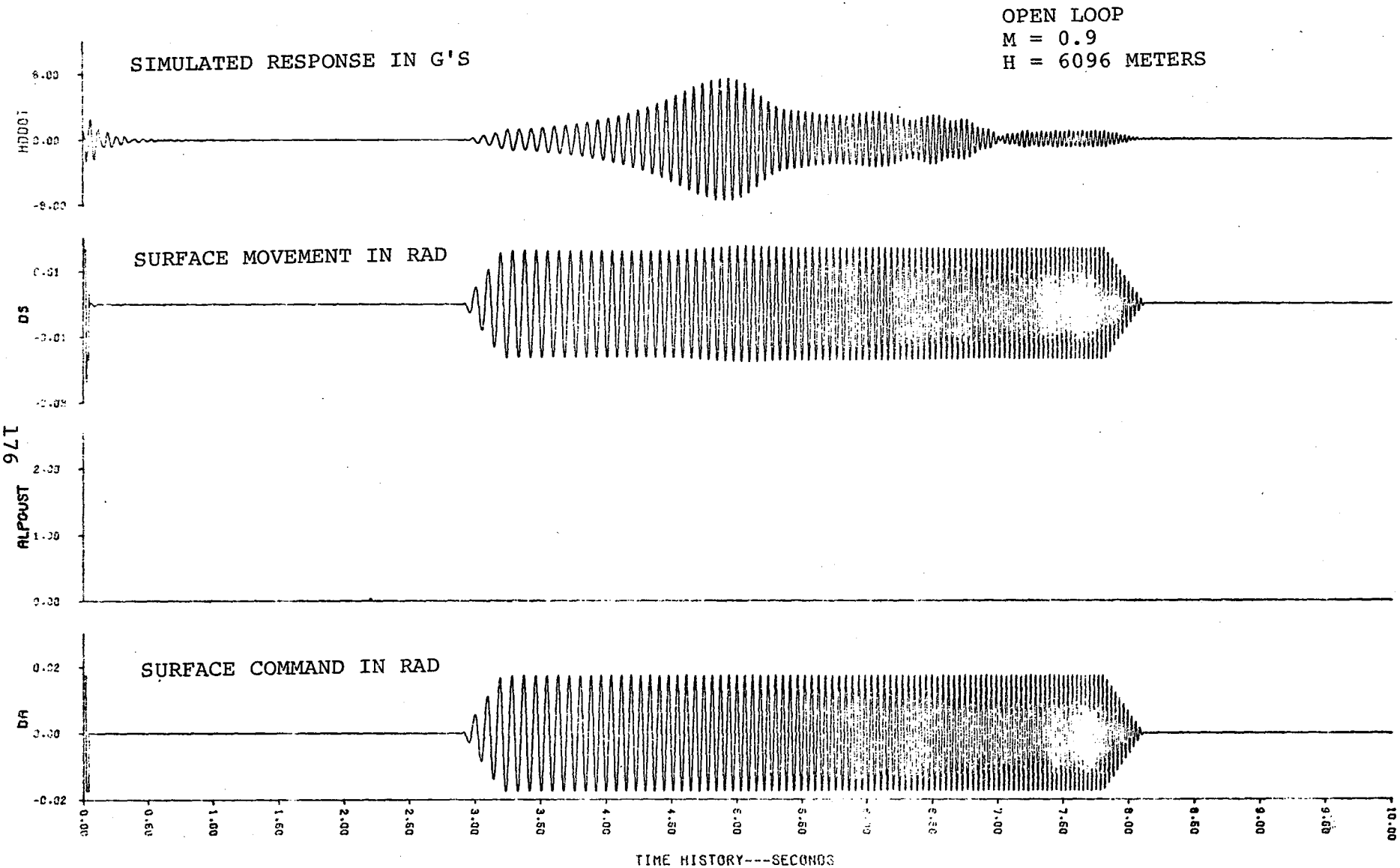

FIGURE 6.9 UNAUGMENTED SUBCRITICAL RESPONSE

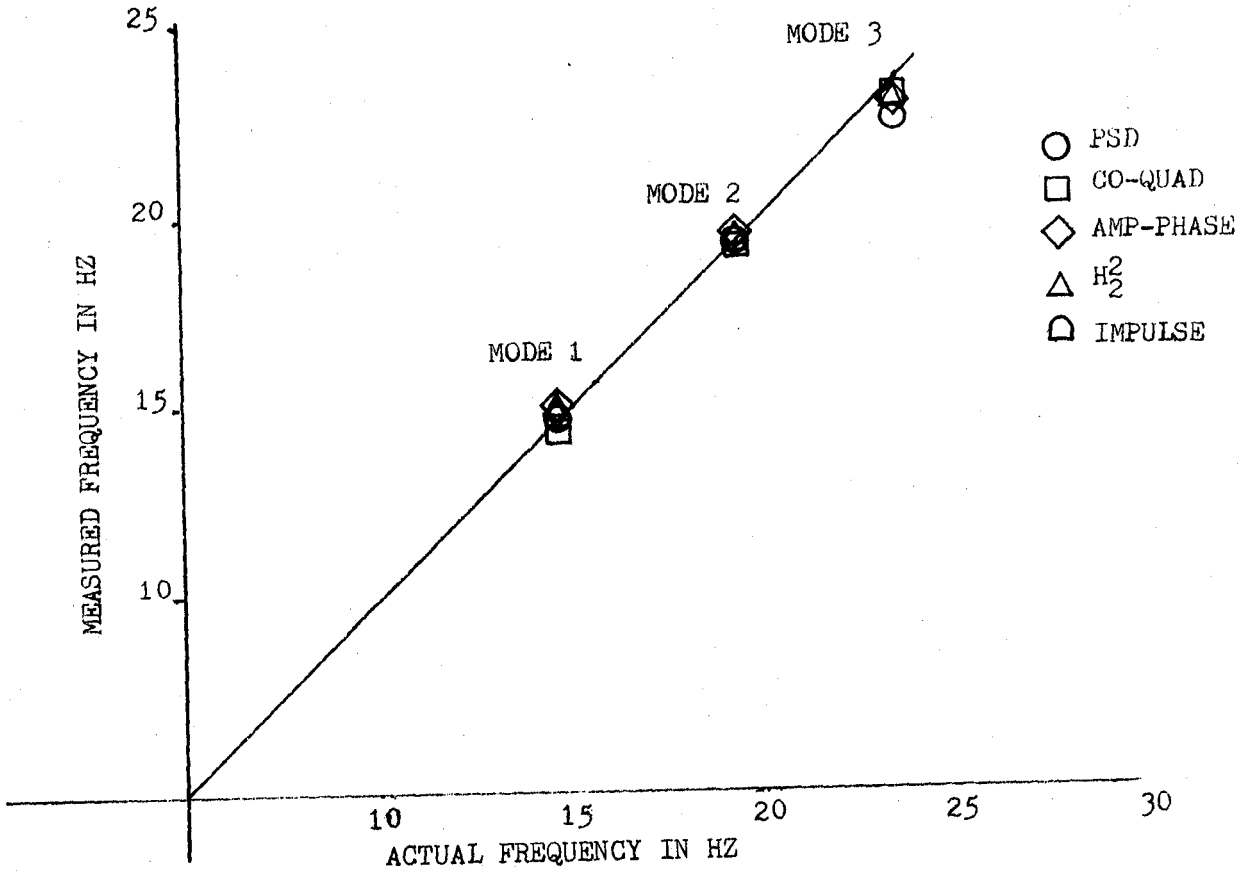

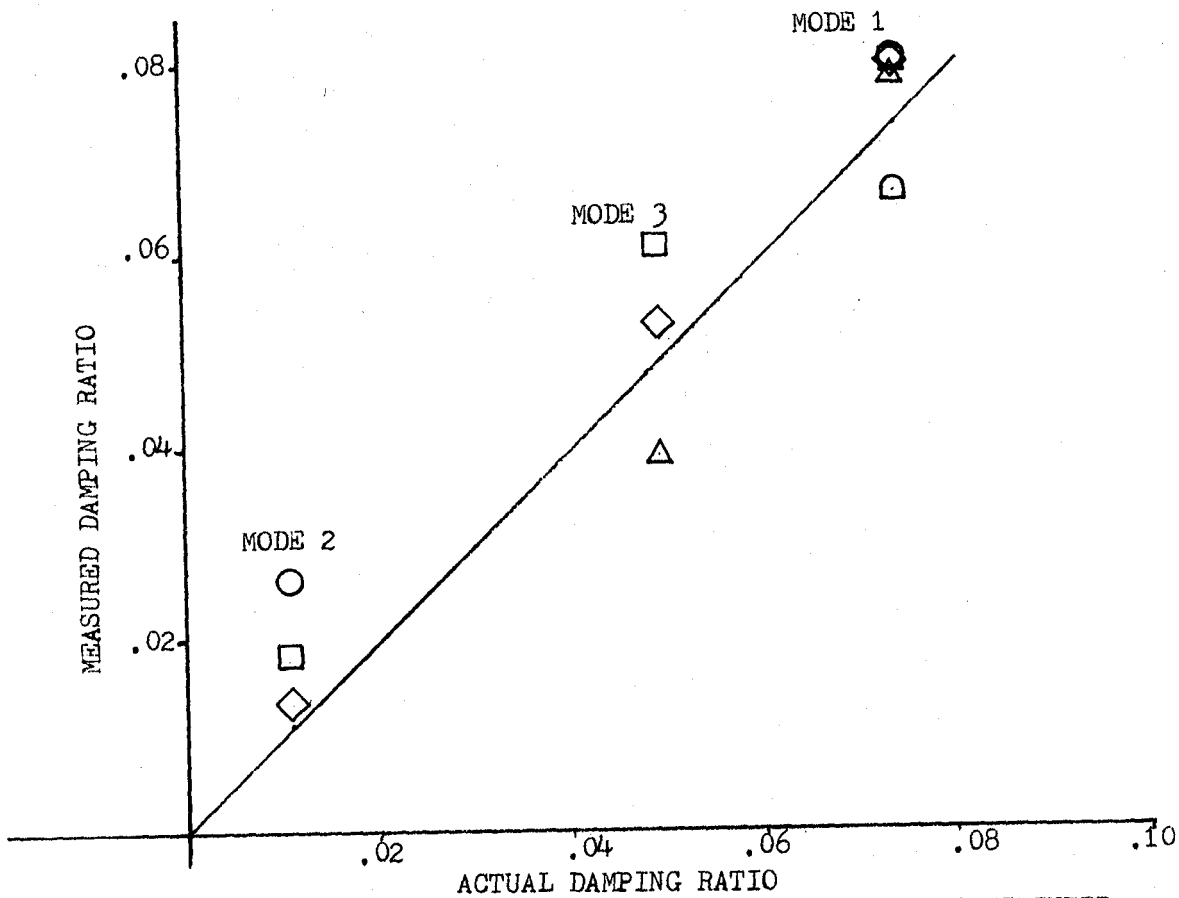

FIGURE 6.10 COMPARISON OF FLUTTER TESTING METHODS ON THE UNAUGMENTED SUBCRITICAL RESPONSE

system of equations representing DAST I. The PSD of the response due to the doublet is seen in figure 6.11. The first and second mode (q_1 and q_2) are well defined. Damping for mode q_3 cannot be estimated because of the lack of a well defined frequency peak. The estimate for damping in the second wing mode is accomplished by projecting the peak shape downward to estimate the half-power frequencies.(reference 12)

Figure 6.12 is a plot of the real and imaginary parts of the H_2 transfer function. Only the 10-30 hertz frequency range is plotted because the lack of excitation outside this range creates erroneous or very little response in the low and high frequencies. Much more information is evident in the expanded frequency scale so better frequency and damping estimates can be extracted.

The Amplitude-Phase plots shown in figure 6.13 indicate the three modes near the flutter frequency very distinctly. The square of H_2 is shown in figure 6.14. The third mode is much better defined in this plot than in the PSD plot of figure 6.11. Too little information is present in the 19.2 hertz mode to make a proper damping estimation.

The inverse Fourier transform of H_2 results in the impulse response function shown in figure 6.15. The determination of the damping estimate from the logarithmic decrement of the consecutive peaks assumes only one mode is present in the response. Recall from the previous plots that the first wing bending mode has much more response evident than the other two modes so it should dominate the initial part of the impulse response. This creates in essence the appearance of

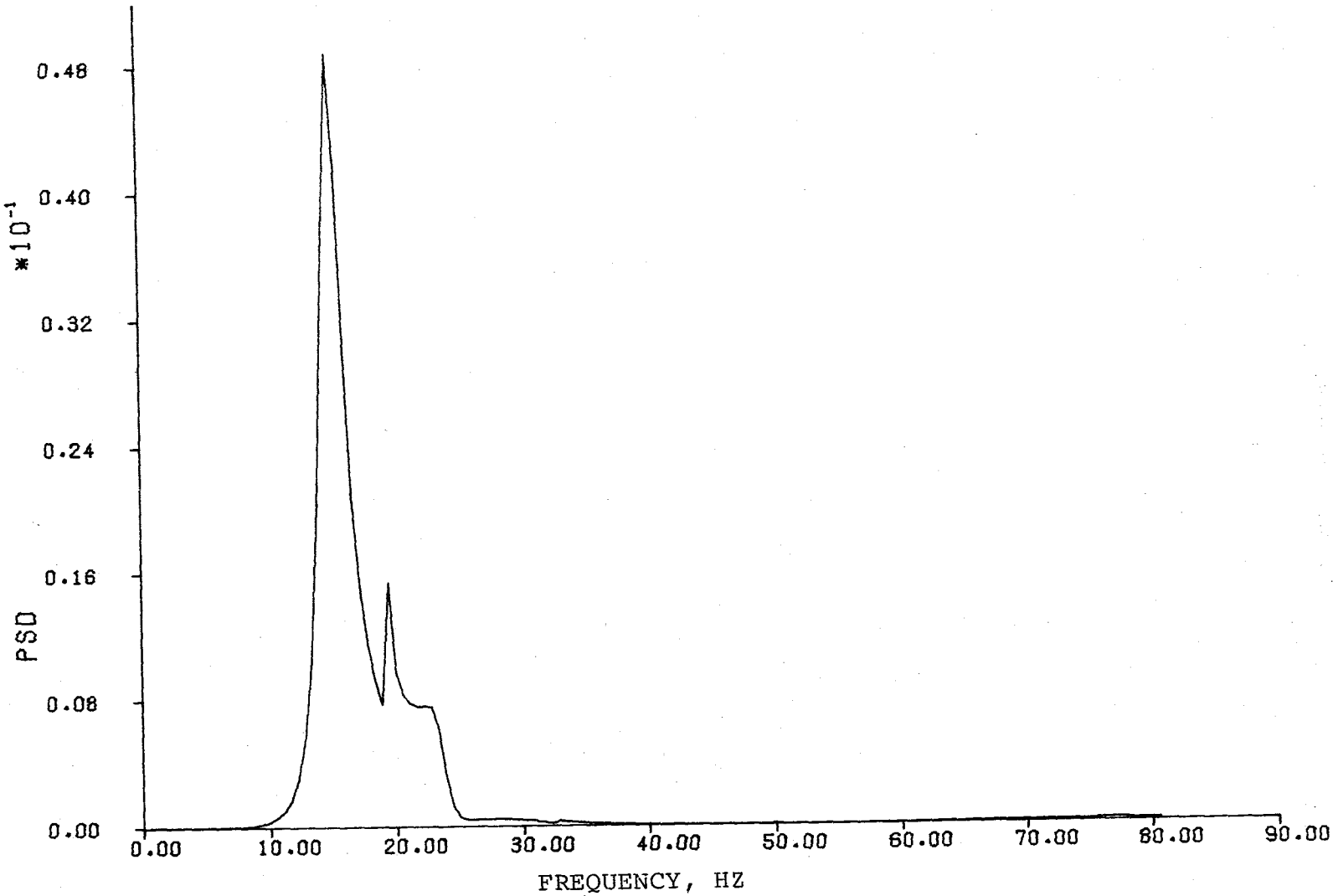

FIGURE 6.11 PSD PLOT OF THE OPEN LOOP RESPONSE TO A DOUBLET

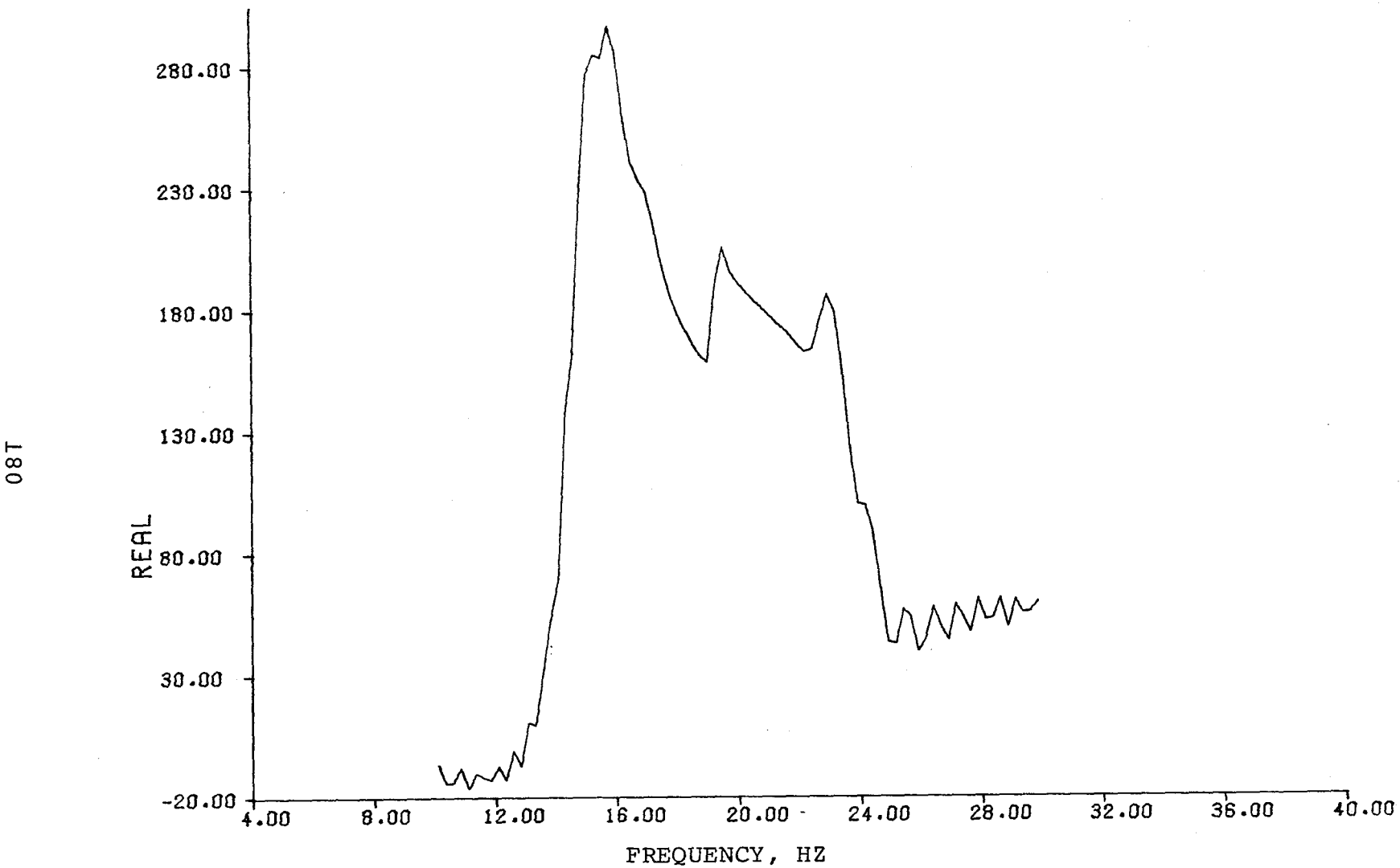

FIGURE 6.12 OPEN LOOP CO-QUAD PLOT (PAGE 1 OF 2)

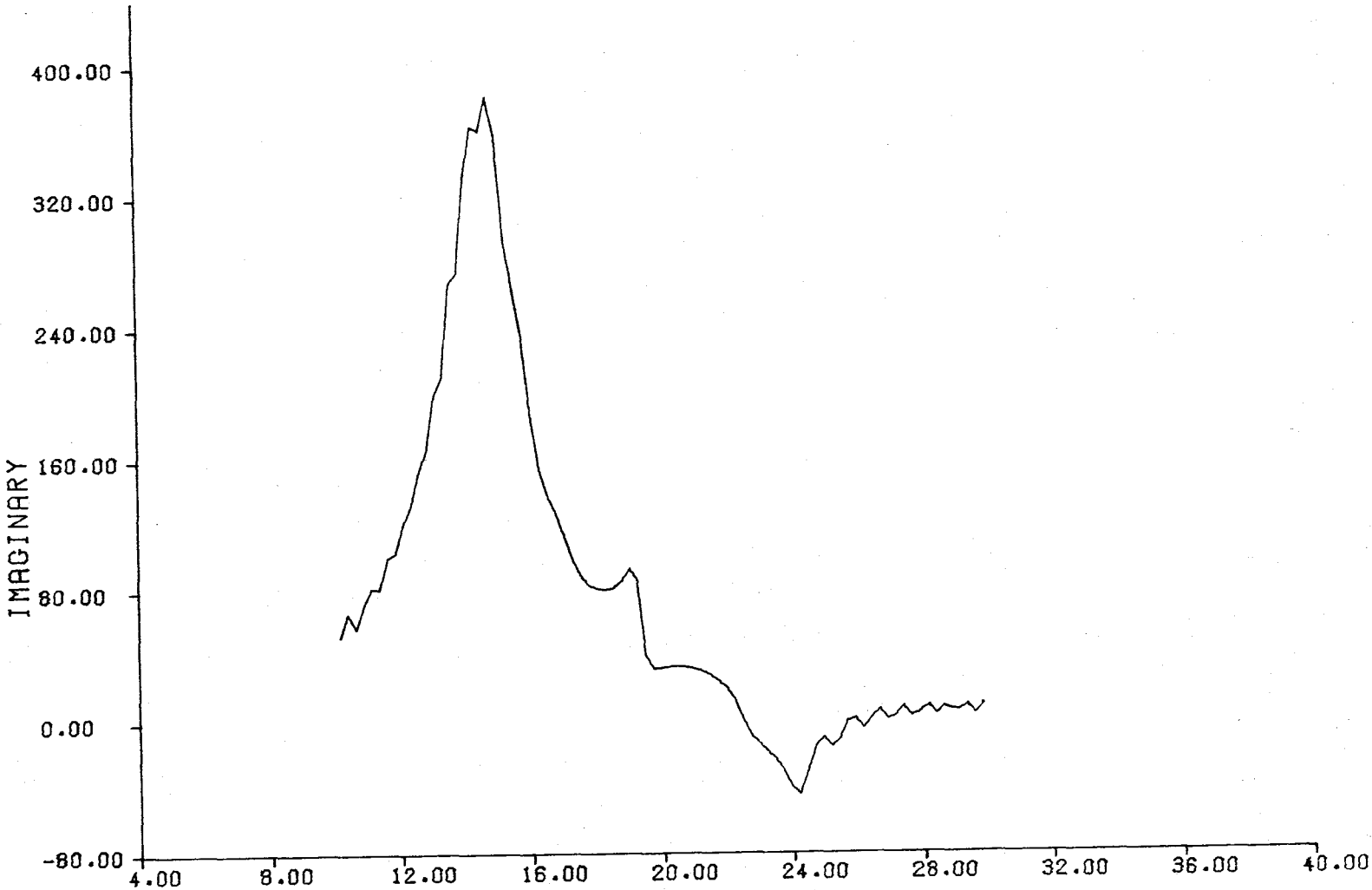

FIGURE 6.12 (CONCLUDED) (PAGE 2 OF 2)

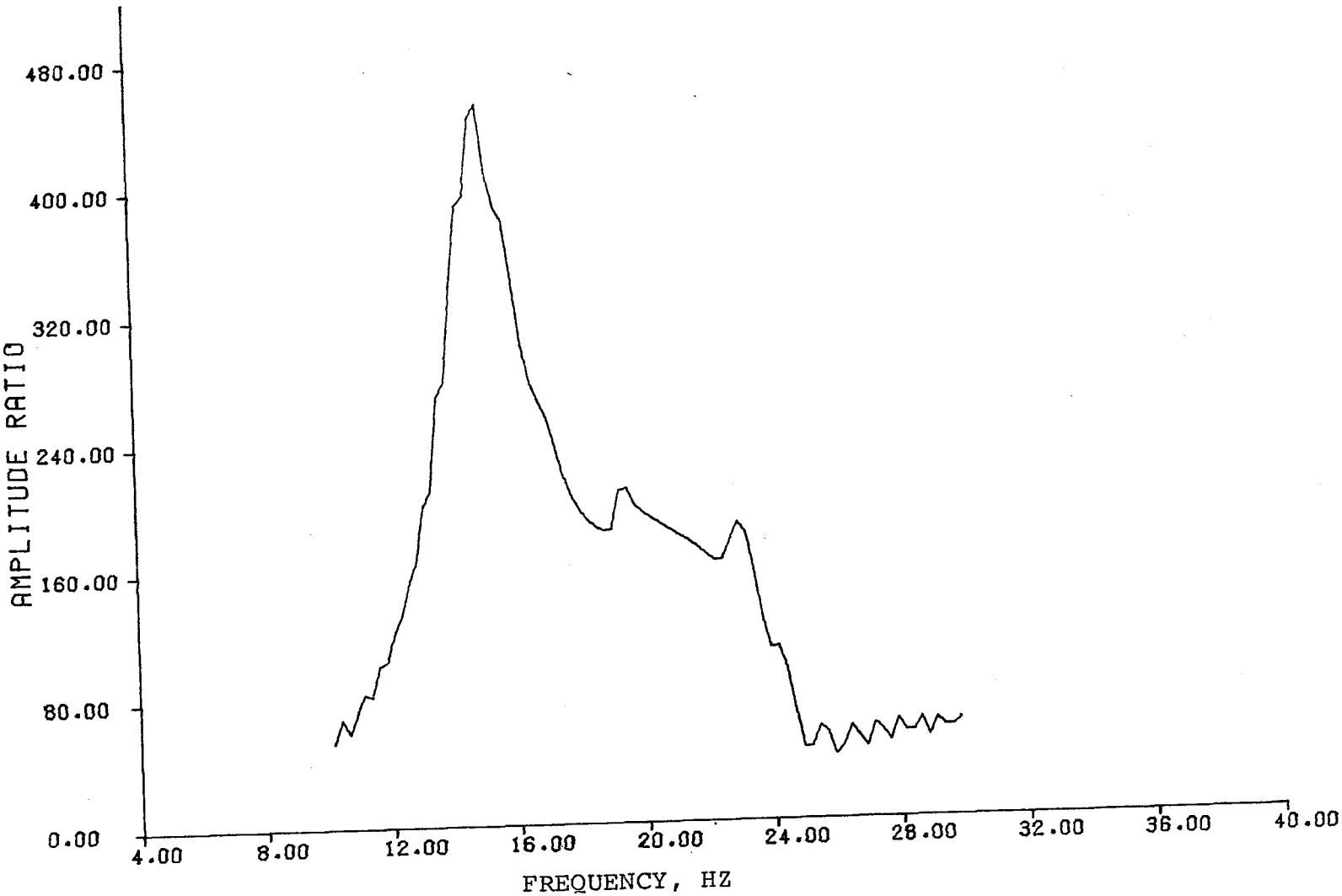

FIGURE 6.13 OPEN LOOP AMPLITUDE-PHASE PLOT (PAGE 1 OF 2)

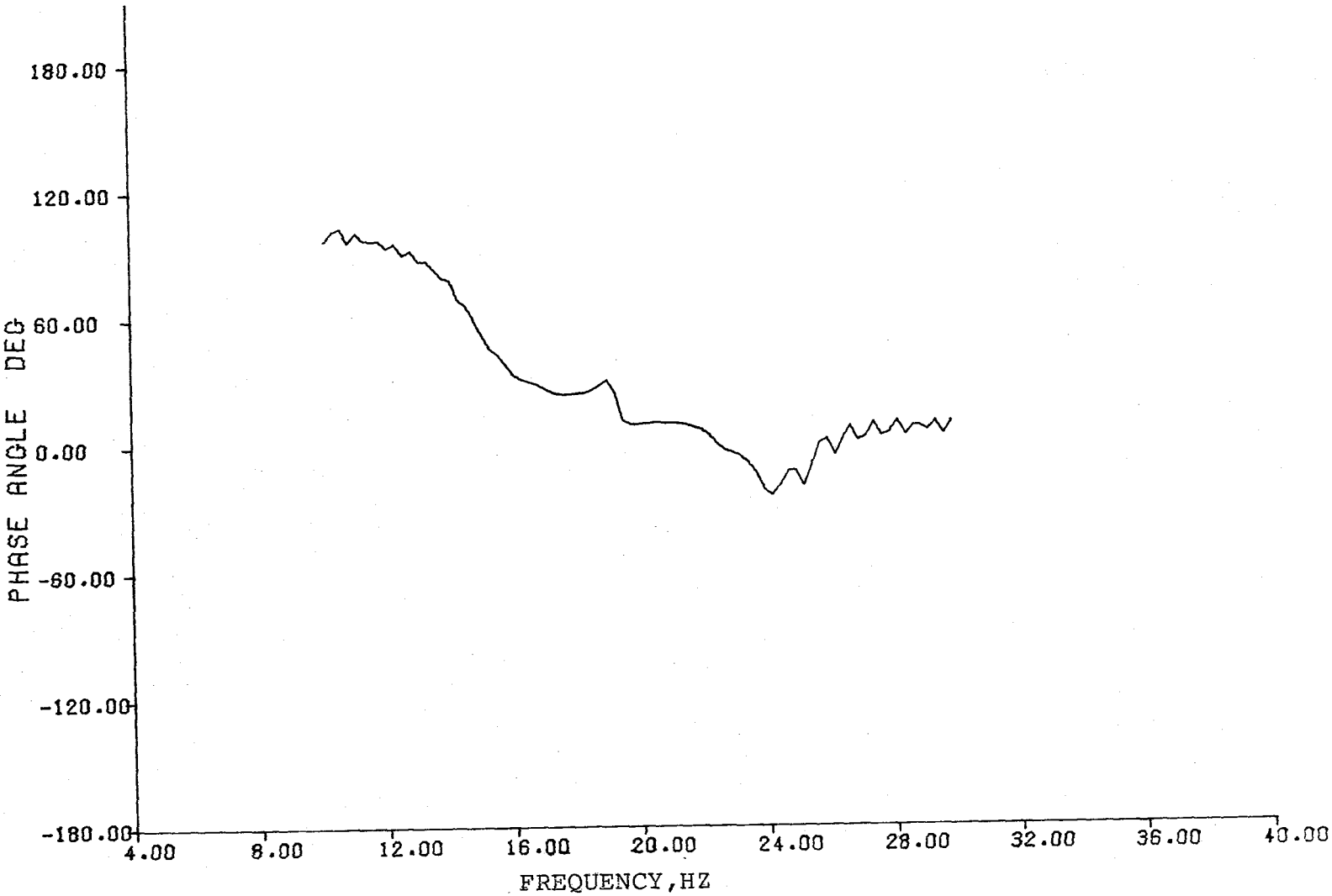

FIGURE 6.13 (CONCLUDED) (PAGE 2 OF 2)

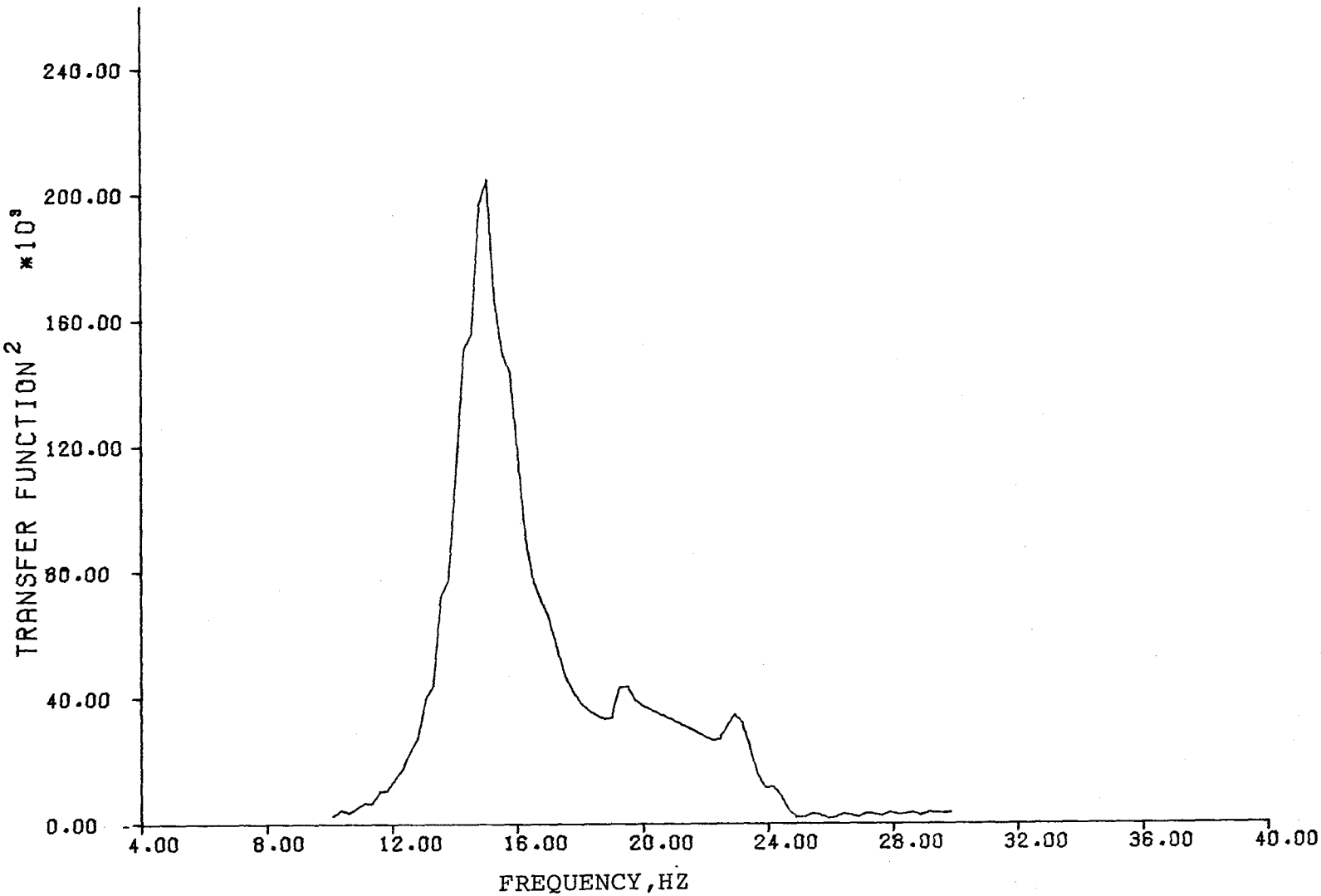

FIGURE 6.14 OPEN LOOP TRANSFER FUNCTION MODULUS

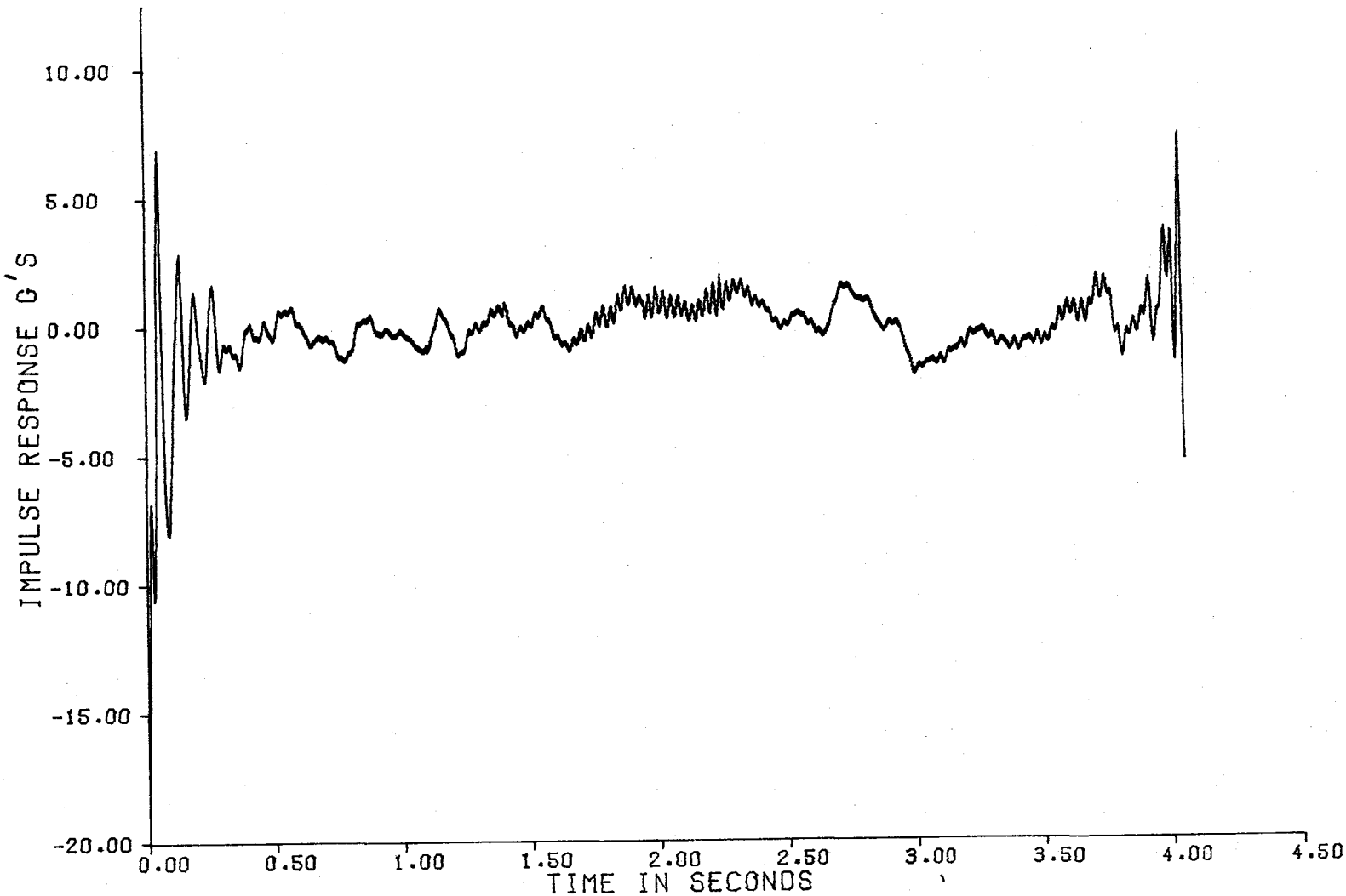

FIGURE 6.15 OPEN LOOP IMPULSE RESPONSE FUNCTION

the q_1 mode as the only mode present in the initial response. After approximately 0.3 seconds, the impulse response represents essentially useless information.

6.3.2 Subcritical Closed-Loop

The subcritical augmented response is shown in figure 6.16. The flight condition is the same as in the open loop case (h=6096 meters and M=0.9). The affect of comparing this augmented response with the open loop response is the same as turning the FSS on and off in flight. The closed loop operation obviously has a large affect on the surface deflection during the doublet and sweep commands as can be seen by comparing figures 6.9 and 6.16.

The results of the application of the flutter testing methods on the augmented subcritical response is summarized in figure 6.17. Again three modes were identifiable but one is different than in the open loop case. The fuselage mode, q_2 , at 19 hertz did not appear but the third wing mode, q_4, at 32 hertz was evident.

The closed loop input spectrum of the surface movement due to the command sweep is shown in figure 6.18. The control surface is responding to the excitation of the first three wing modes. The first wing bending mode, q_1 , has been moved to a lower frequency than was evident in the open loop case. The mode q_3, the first wing torsion, is basically at the same frequency, however, it now is the mode that dominates the power spectrum. This implies that much more response should be evident in the mode q_3 than at either the q_2 or q_4 wing mode frequencies.

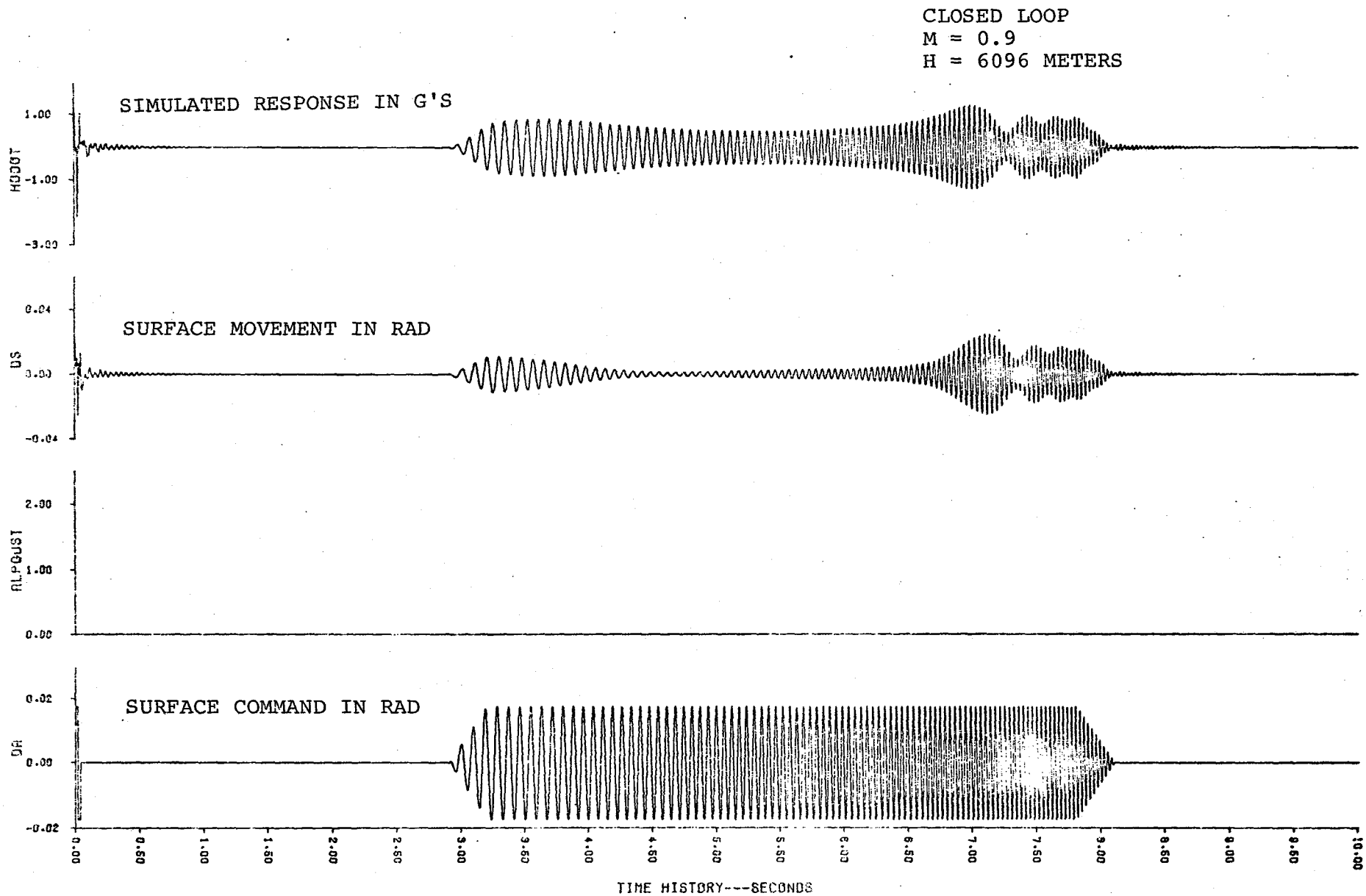

FIGURE 6.16 SUBCRITICAL CLOSED LOOP RESPONSE

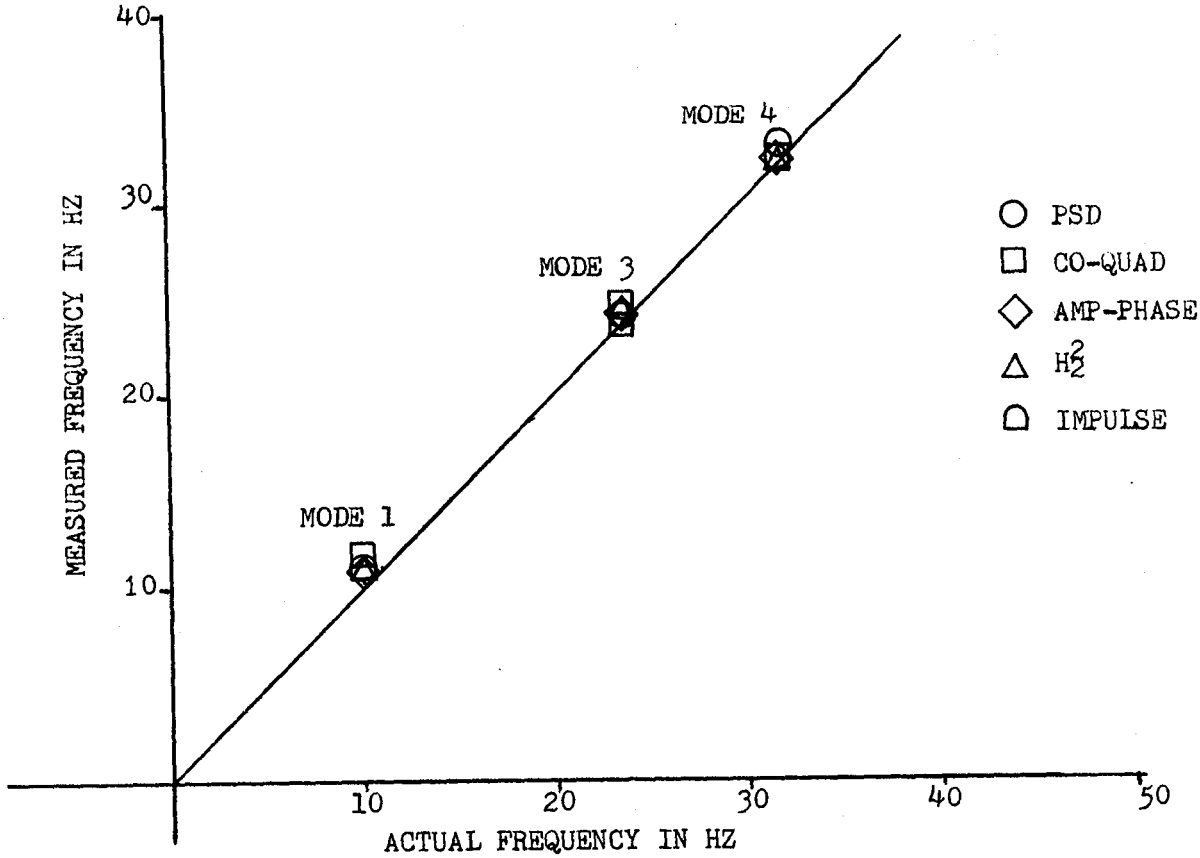

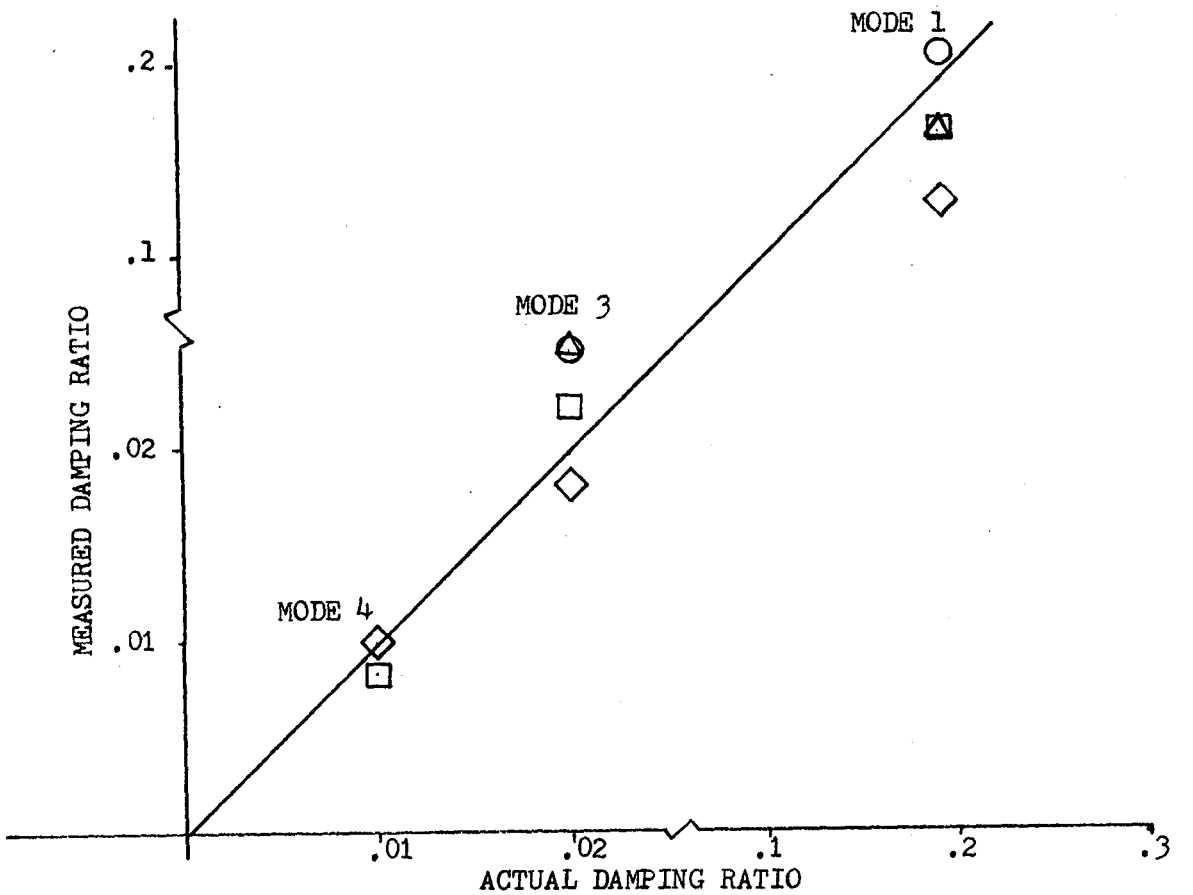

FIGURE 6.17 COMPARISON OF FLUTTER TESTING METHODS ON THE AUGMENTED SUBCRITICAL RESPONSE

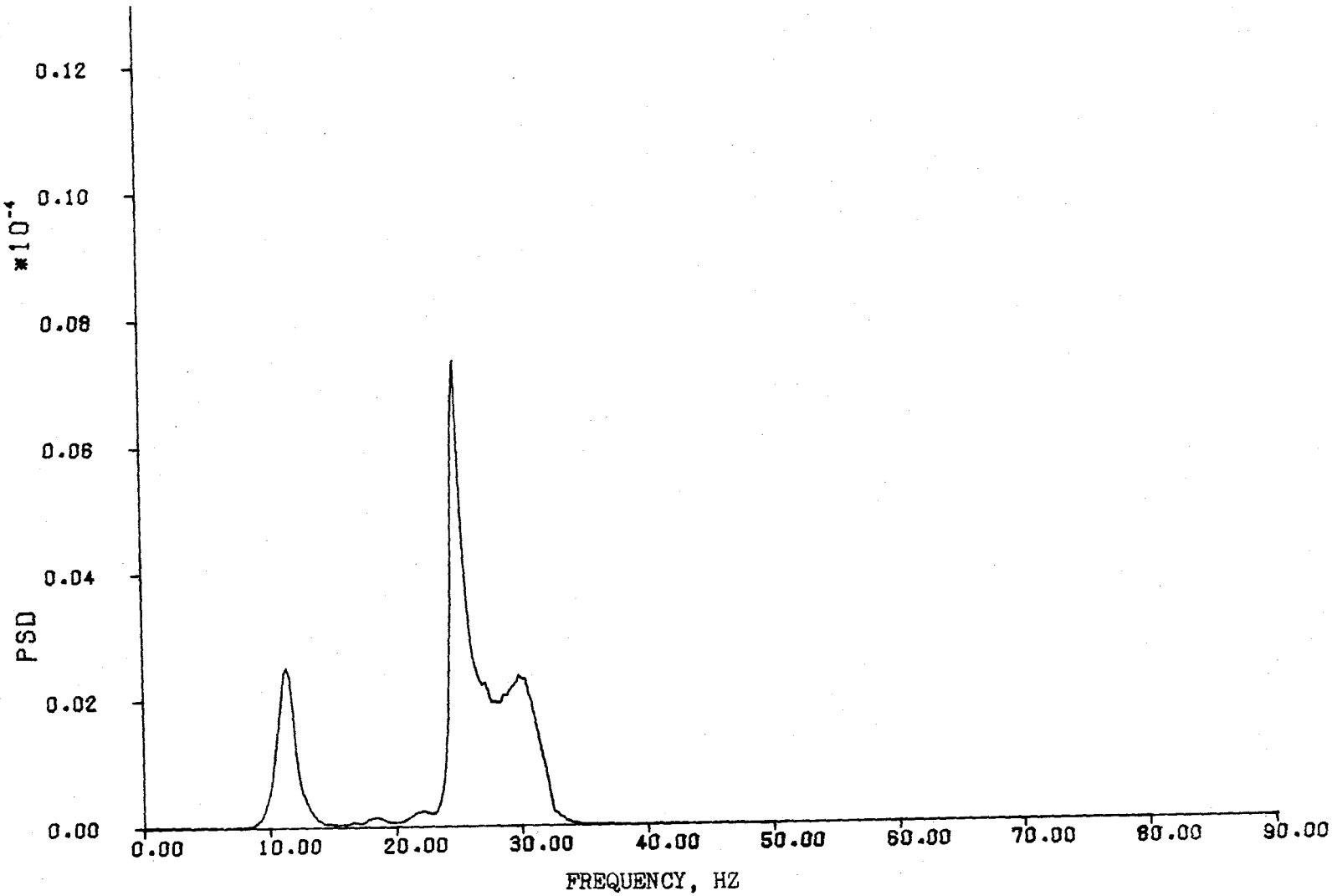

FIGURE 6.18 CLOSED LOOP INPUT SPECTRUM FROM A FREQUENCY SWEEP

The fuselage mode, q_2, is totally suppressed.

The PSD plot of the wing response to a command doublet is shown in figure 6.19. The figure indicates the 8th structural mode at 77 hertz besides the first three wing modes. The fuselage mode is not excited by the commands in these subcritical closed loop tests. Although the command is for a 25-hertz doublet, the PSD of the surface movement in figure 6.20 does not show the same characteristics as found for the open loop case of figure 6.11. It is simply responding to the wing motions.

Figure 6.21 is a Co-Quad plot of the closed loop transfer function. The estimate of the frequency and damping of q_4 was made from this plot, whereas the lower frequency modes were estimated from figure 6.22 which is an expanded scale plot of figure 6.21. No modes above q_4 appear.

The Amplitude-Phase plots of figure 6.23 were used to estimate the characteristic of q_4 while the lower modes were estimated from figure 6.24. The "flatness" of the phase angle plot makes estimates of q_1 difficult. This flattening effect has appeared in wind tunnel testing of FSS models. It is an indication of a highly damped system.

The modulus of the transfer function did indicate the presence of the q_4 mode, but the peak was not usable as an estimator for damping. Figure 6.25 shows an expanded scale plot of $\left|H_2^2\right|$. The first wing torsion mode, q_3, is very well represented and indicates much more response in the third mode than the first.

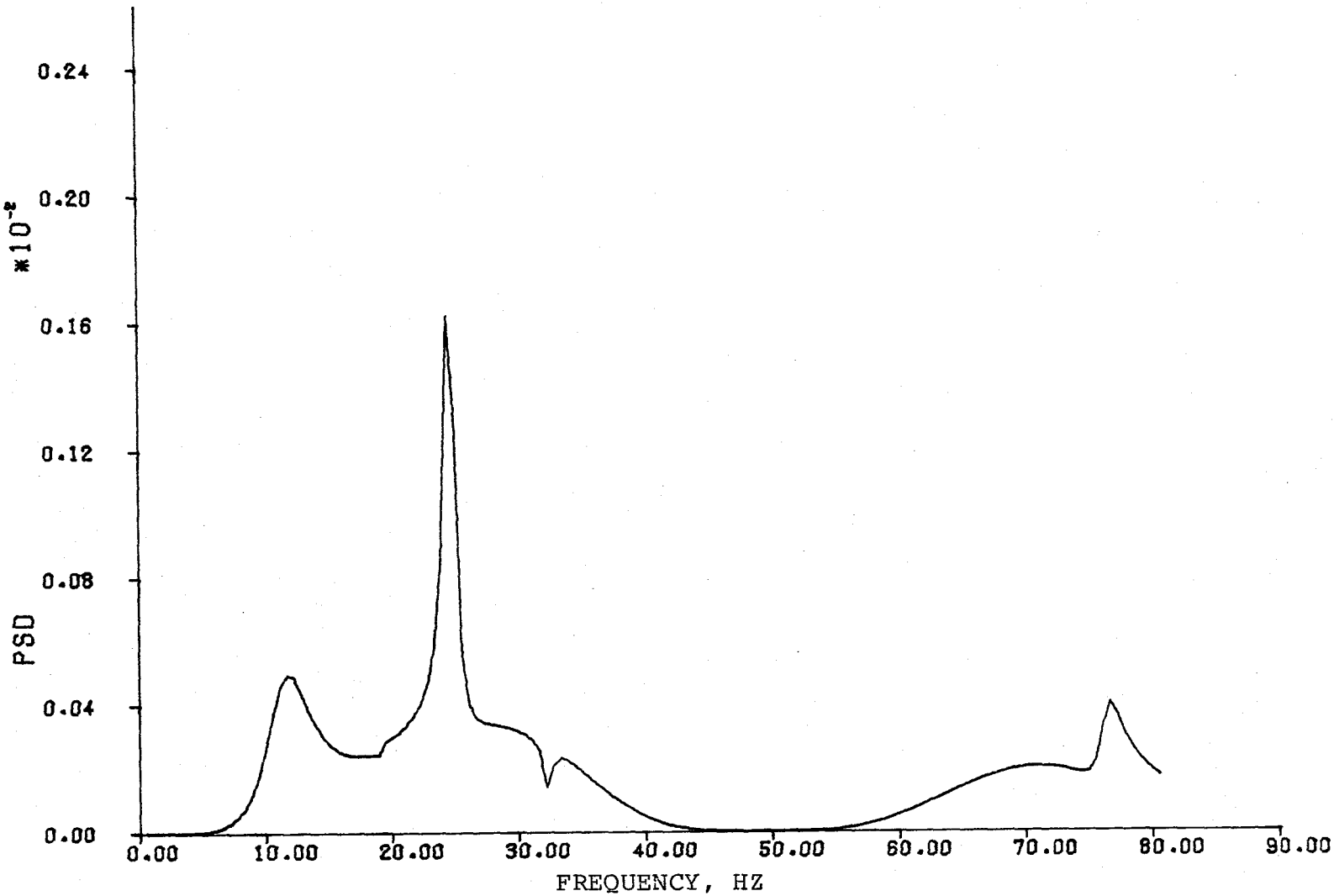

FIGURE 6.19 PSD PLOT OF CLOSED LOOP RESPONSE DUE TO A COMMAND DOUBLET

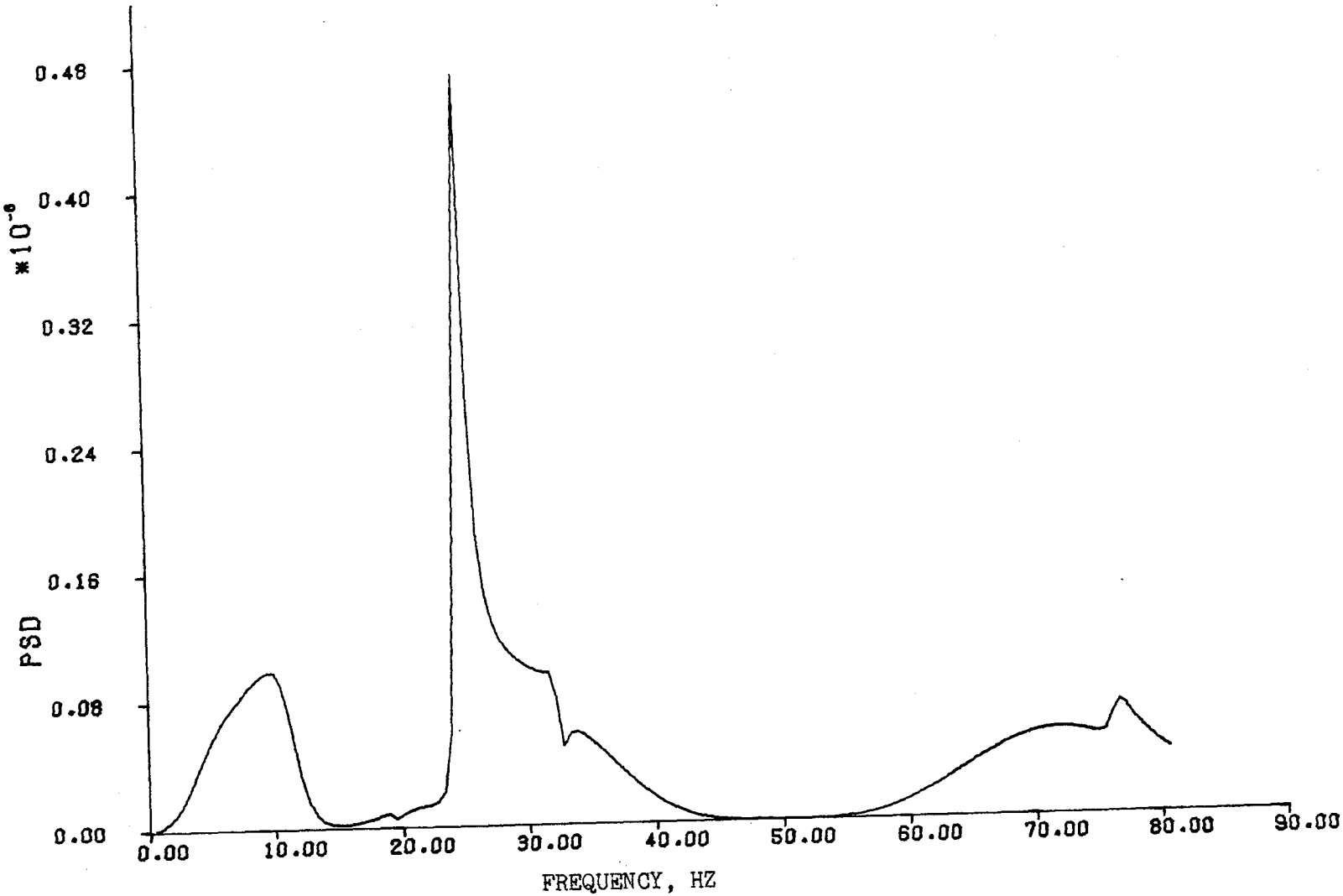

FIGURE 6.20 PSD PLOT OF SURFACE MOVEMENT TO A CLOSED LOOP DOUBLET COMMAND

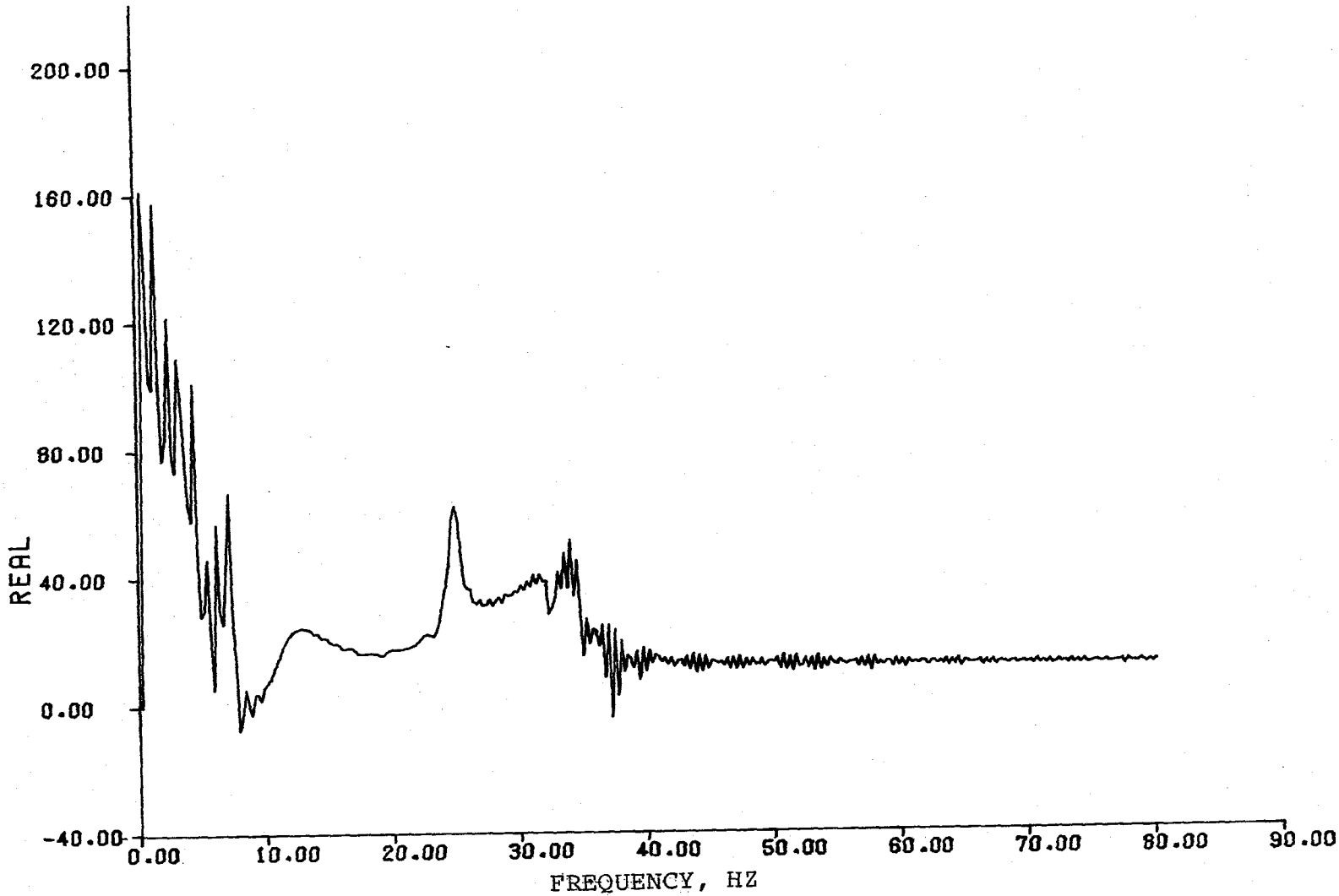

FIGURE 6.21 CLOSED LOOP SUBCRITICAL CO QUAD PLOT (PAGE 1 OF 2)

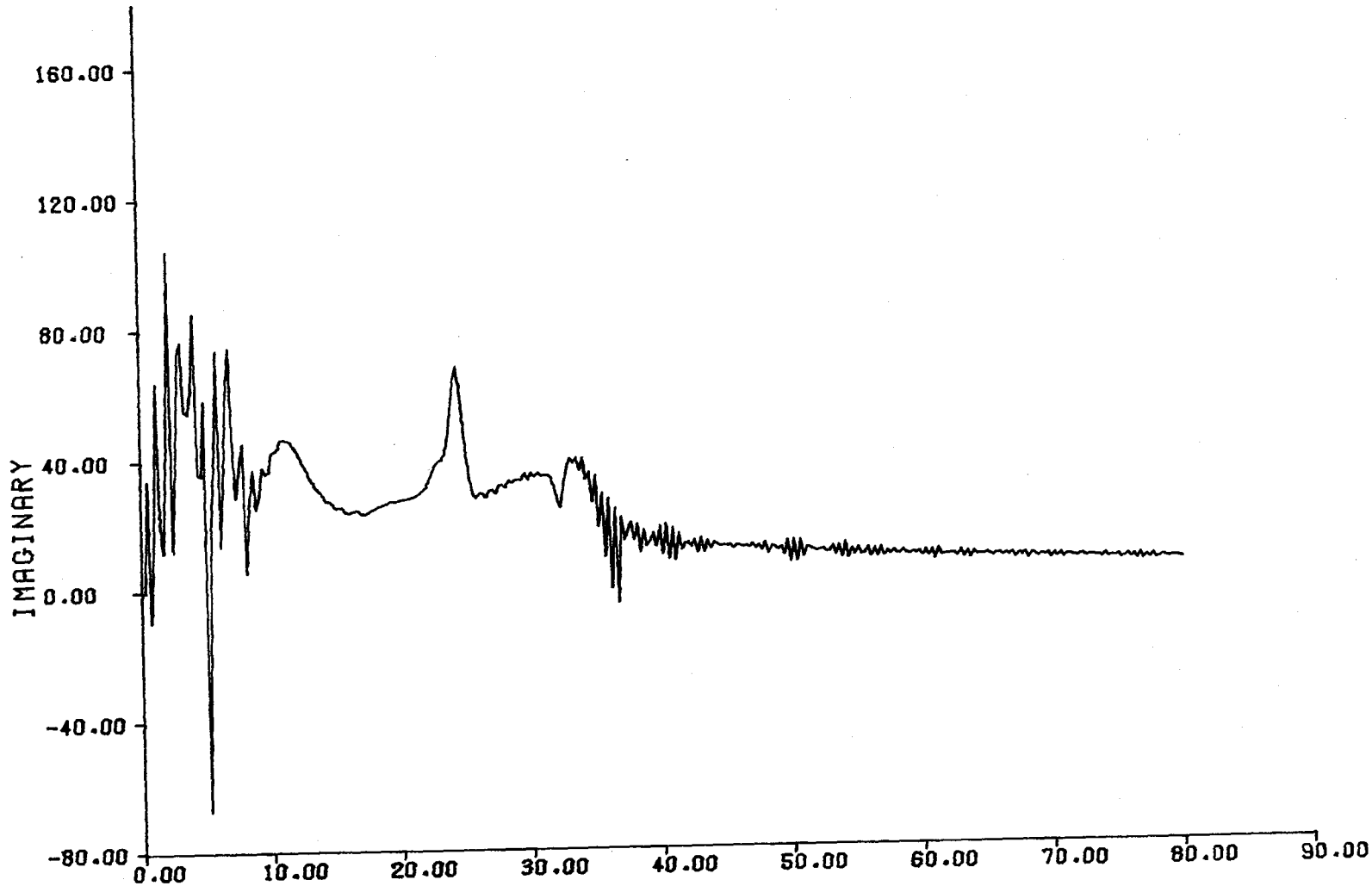

FIGURE 6.21 (CONCLUDED) (PAGE 2 OF 2)

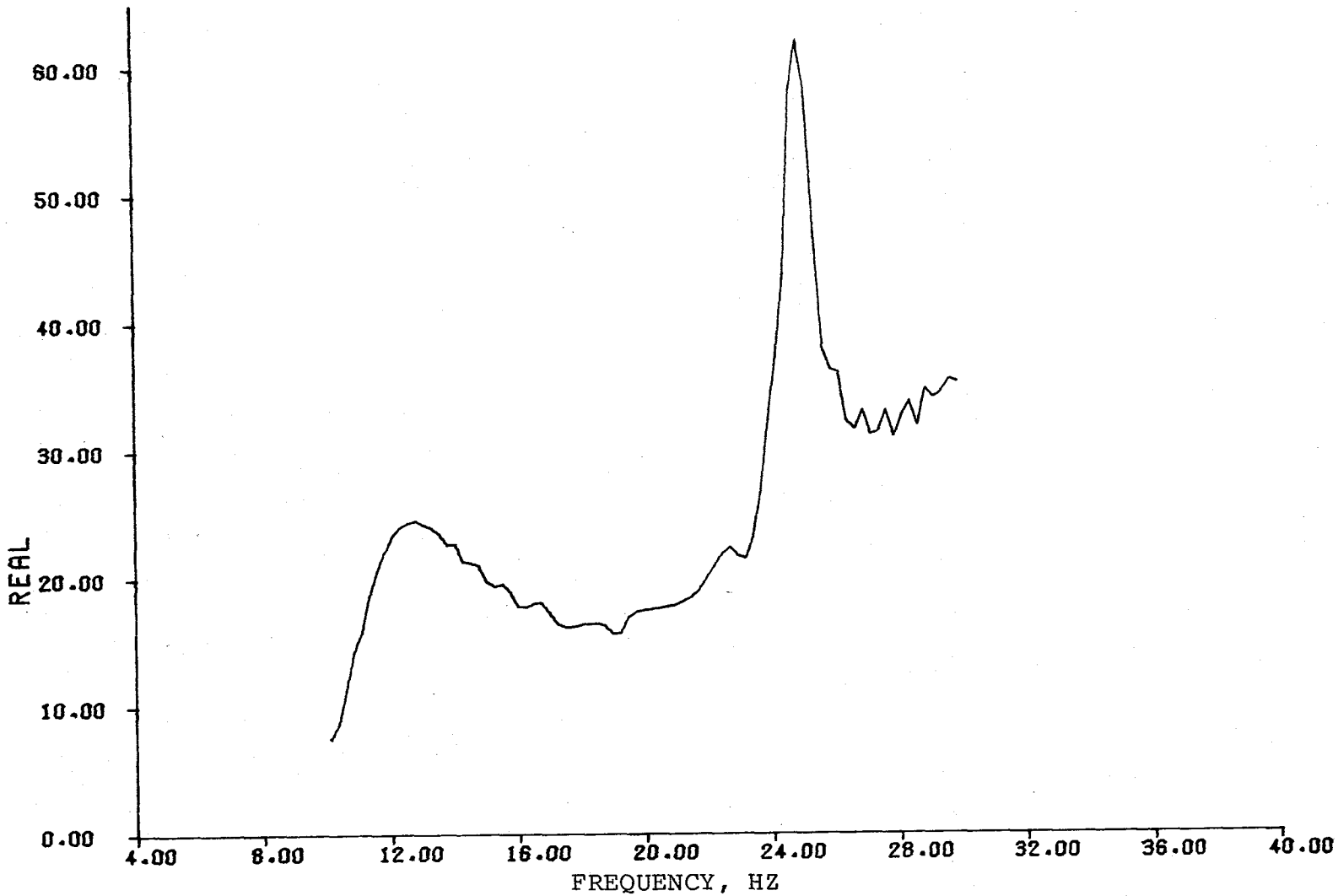

FIGURE 6.22 CLOSED LOOP SUBCRITICAL EXPANDED AXIS CO-QUAD PLOT (PAGE 1 OF 2)

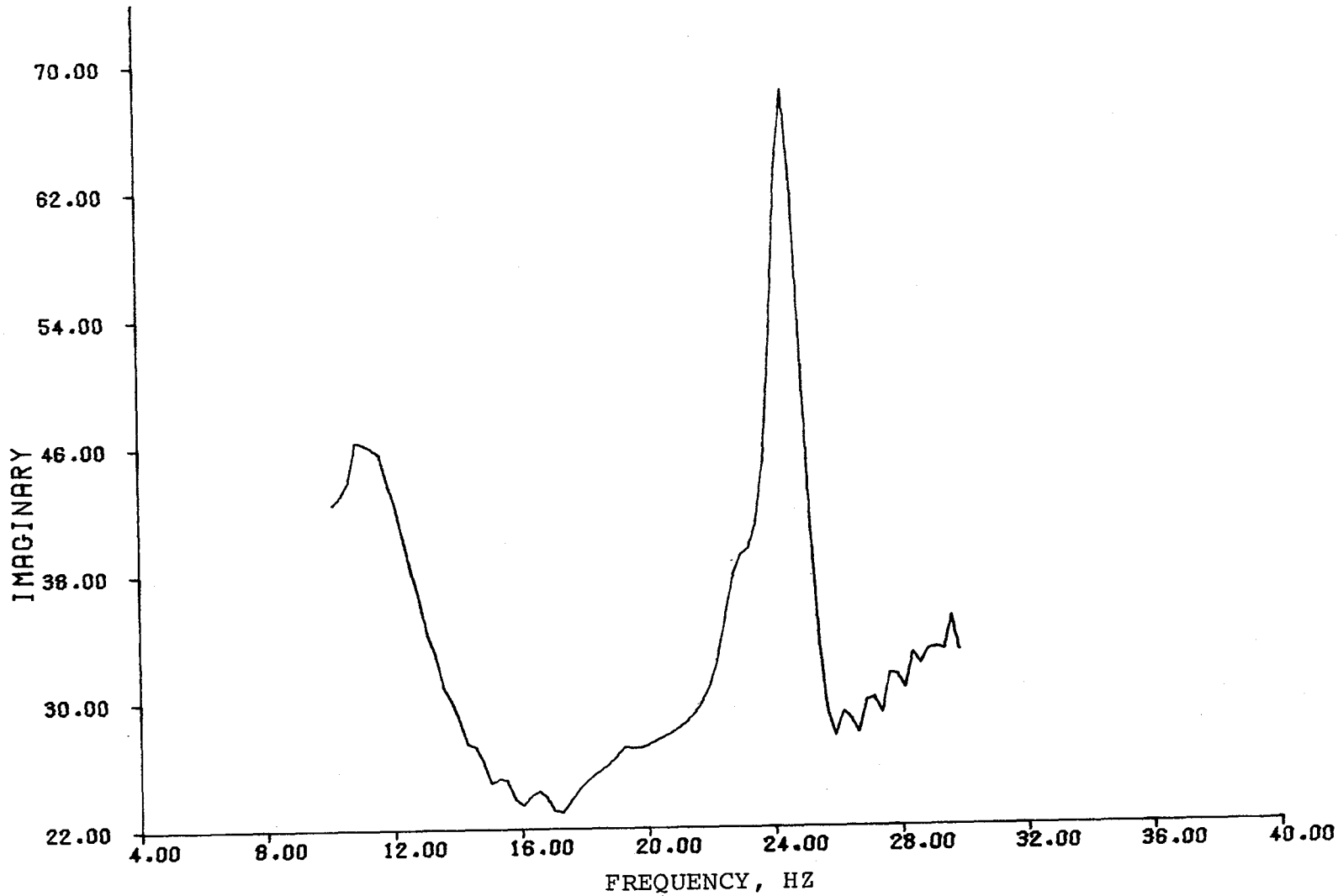

FIGURE 6.22 (CONCLUDED) (PAGE 2 OF 2)

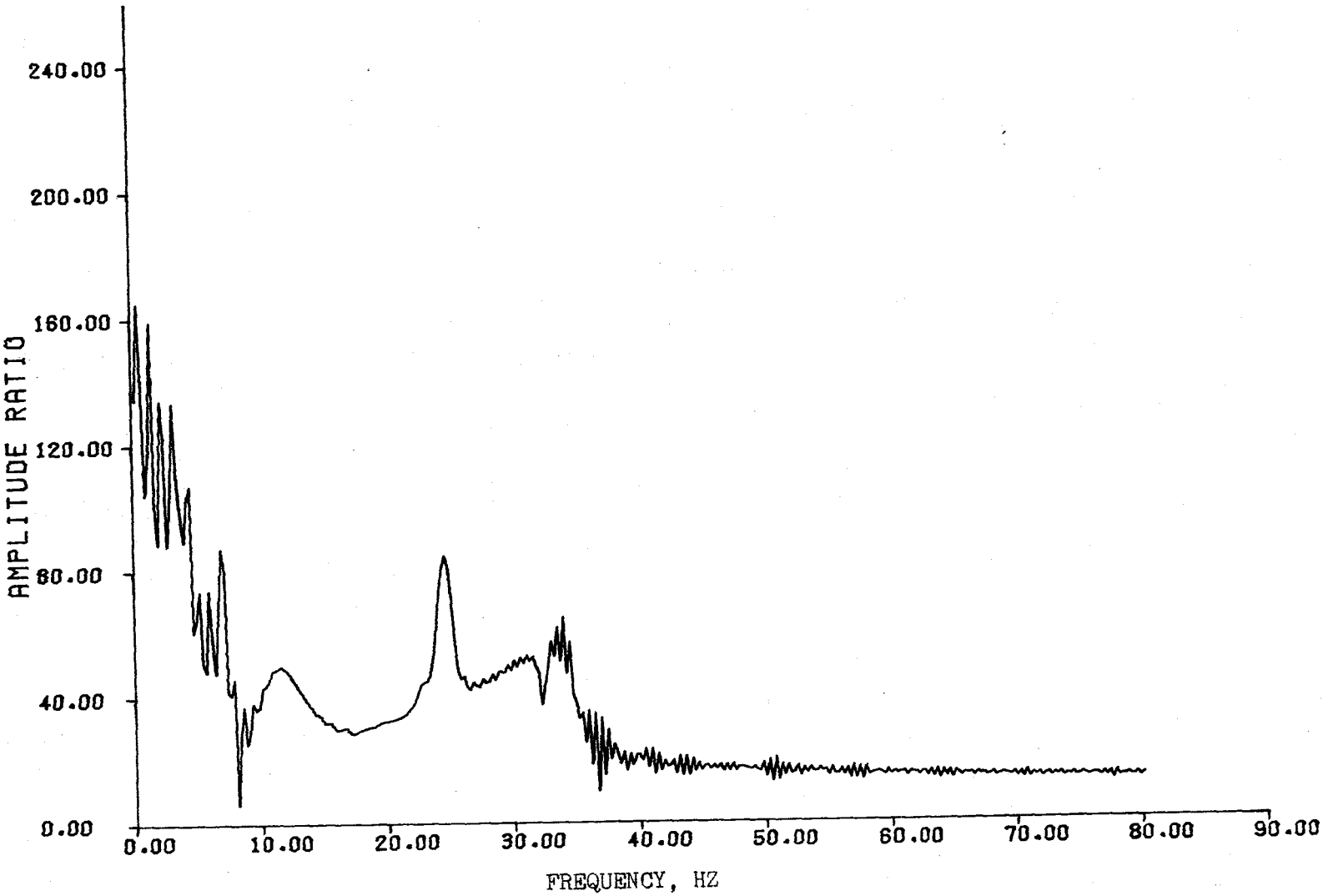

FIGURE 6.23 CLOSED LOOP SUBCRITICAL AMPLITUED-PHASE PLOT (PAGE 1 OF 2)

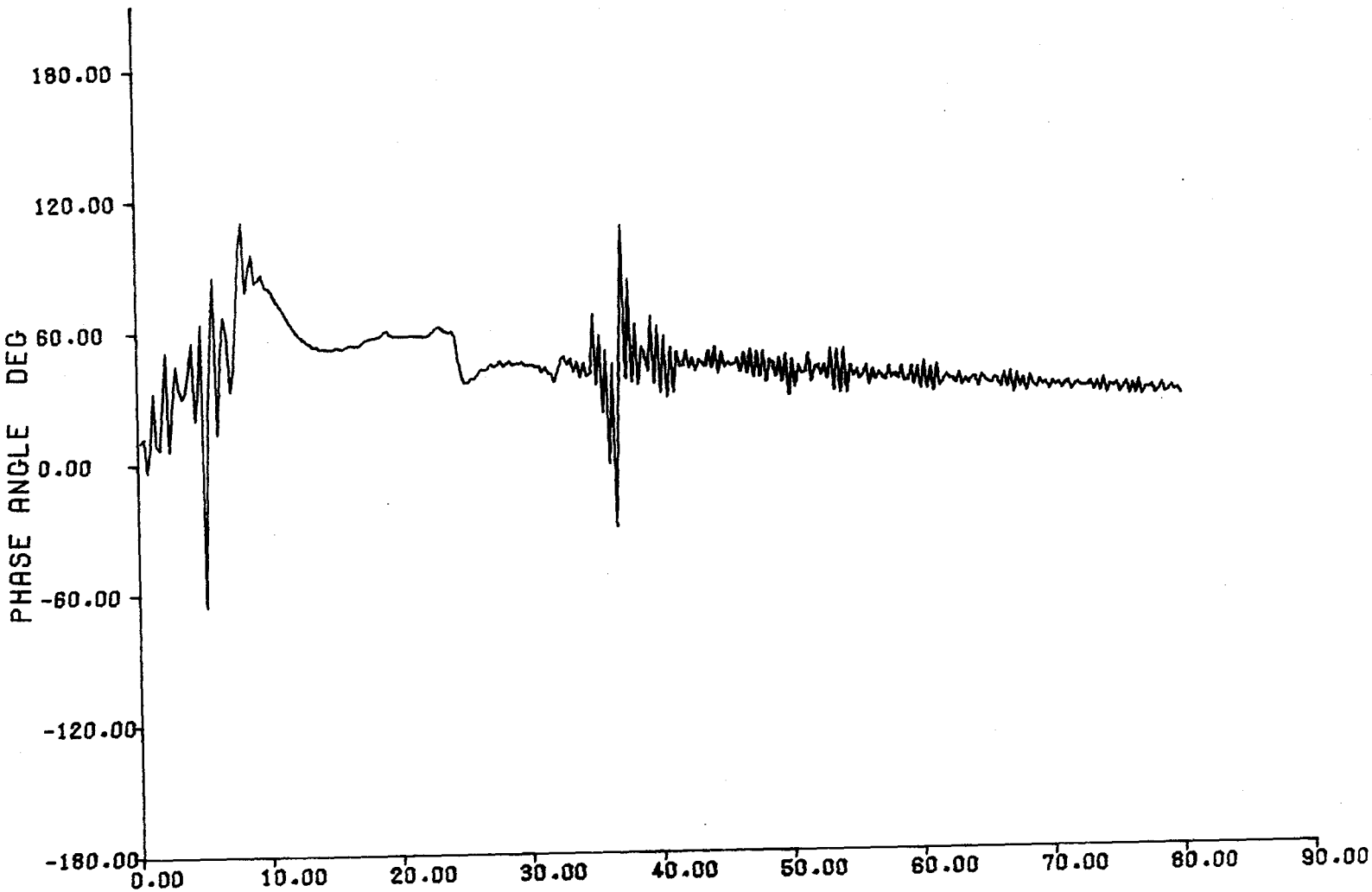

FIGURE 6.23 (CONCLUDED) (PAGE 2 OF 2)

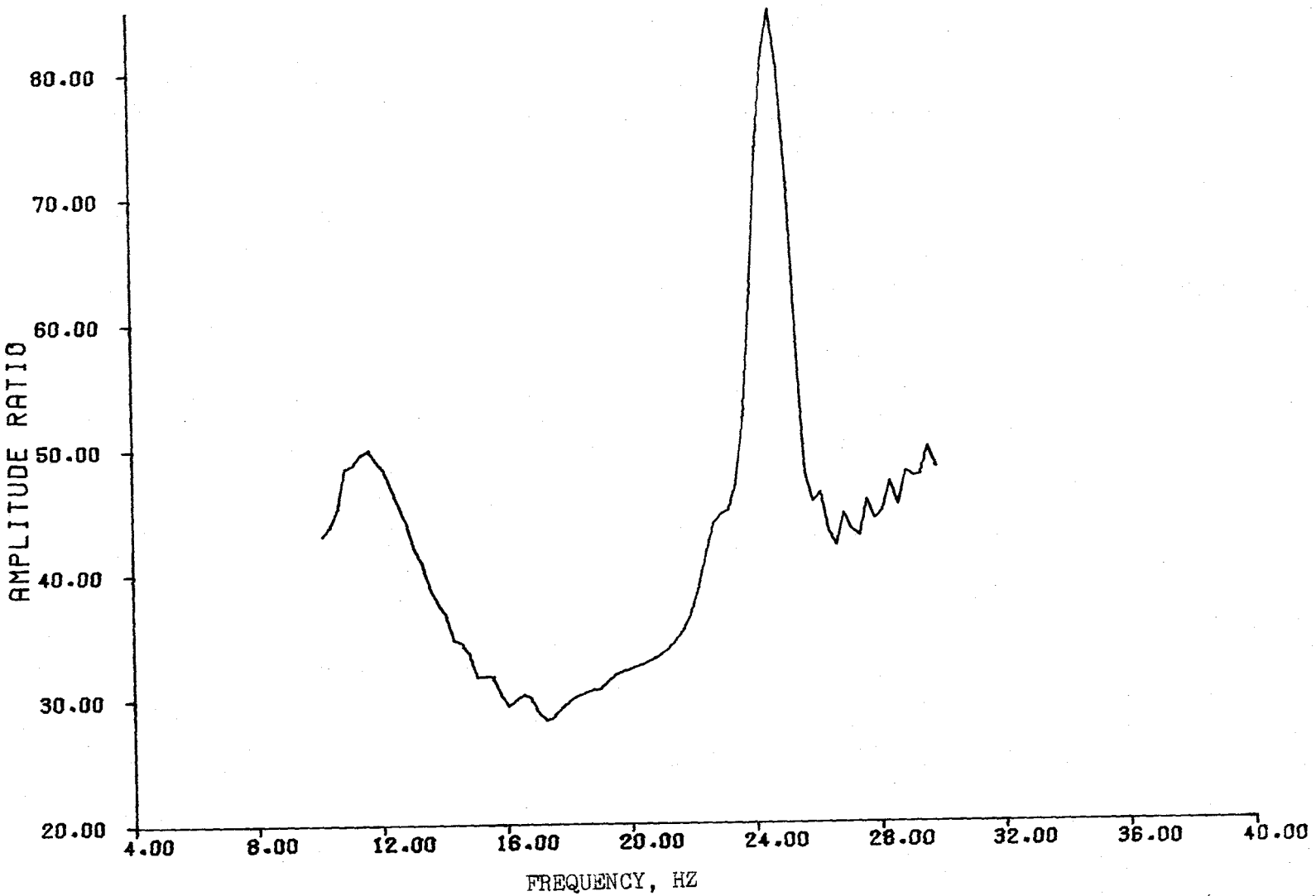

FIGURE 6.24 CLOSED LOOP SUBCRITICAL EXPANDED AXIS AMPLITUDE PHASE PLOT (PAGE 1 OF 2)

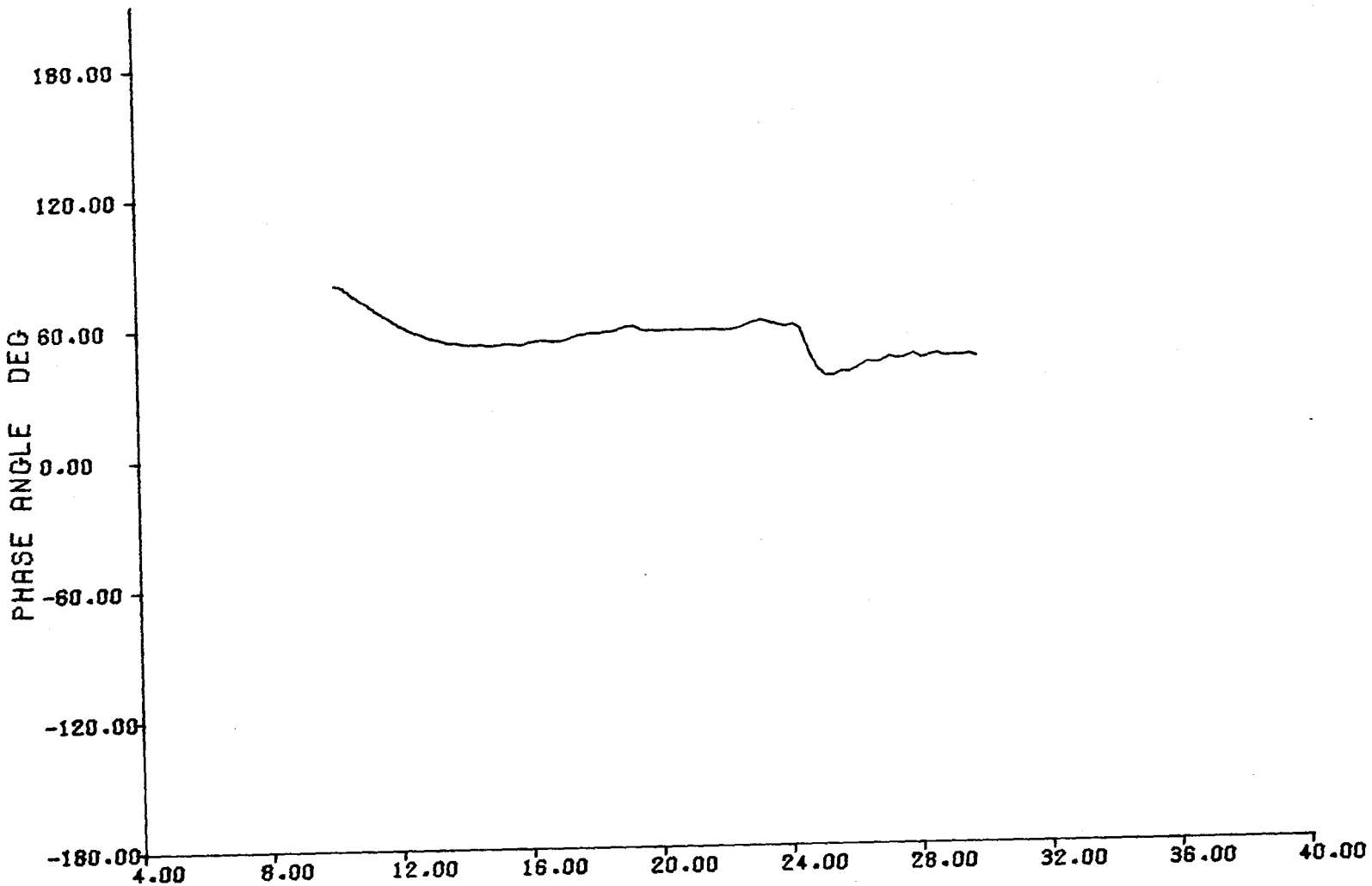

FIGURE 6.24 (CONCLUDED) (PAGE 2 OF 2)

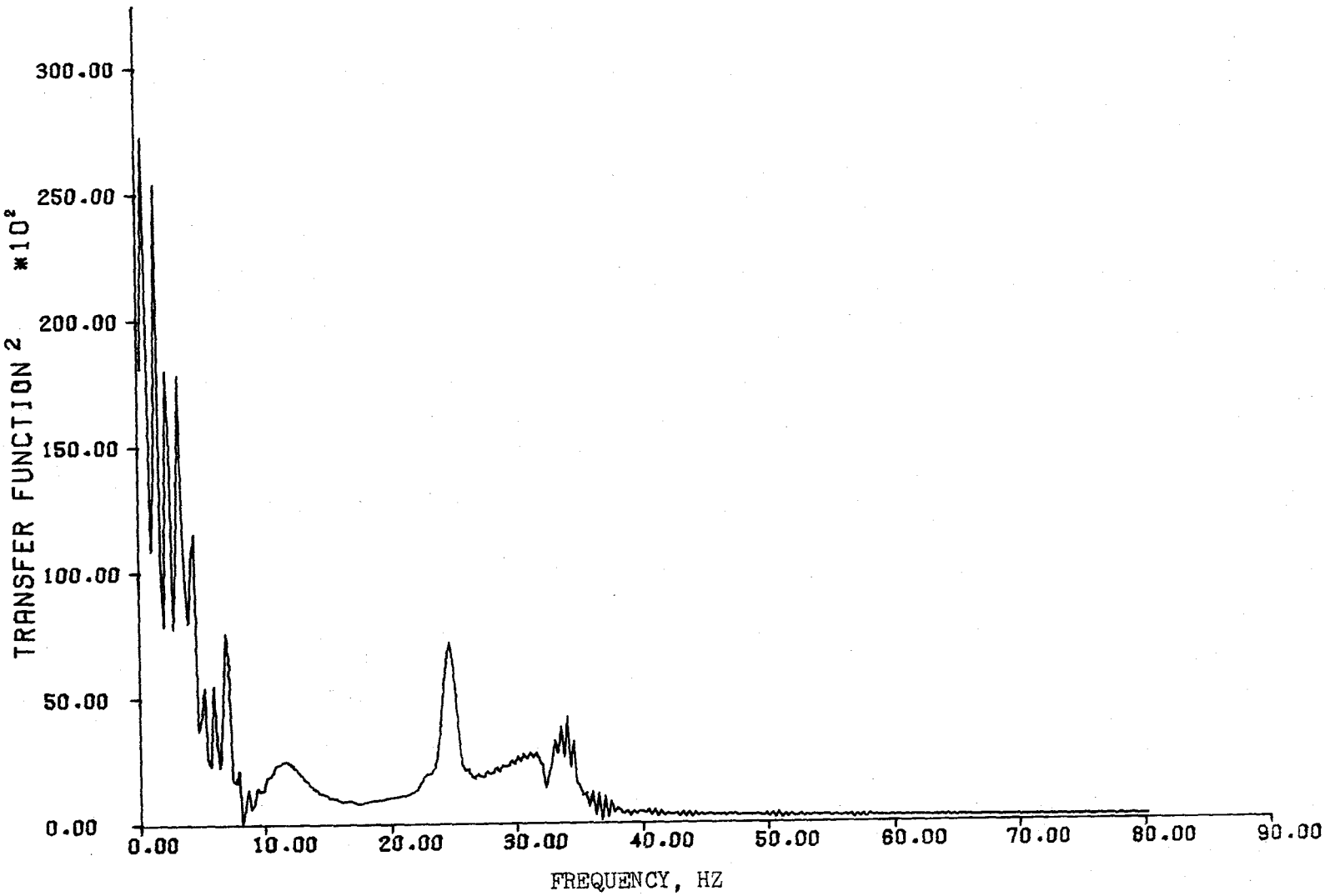

FIGURE 6.25 CLOSED LOOP SUBCRITICAL TRANSFER FUNCTION MODULUS (PAGE 1 OF 2)

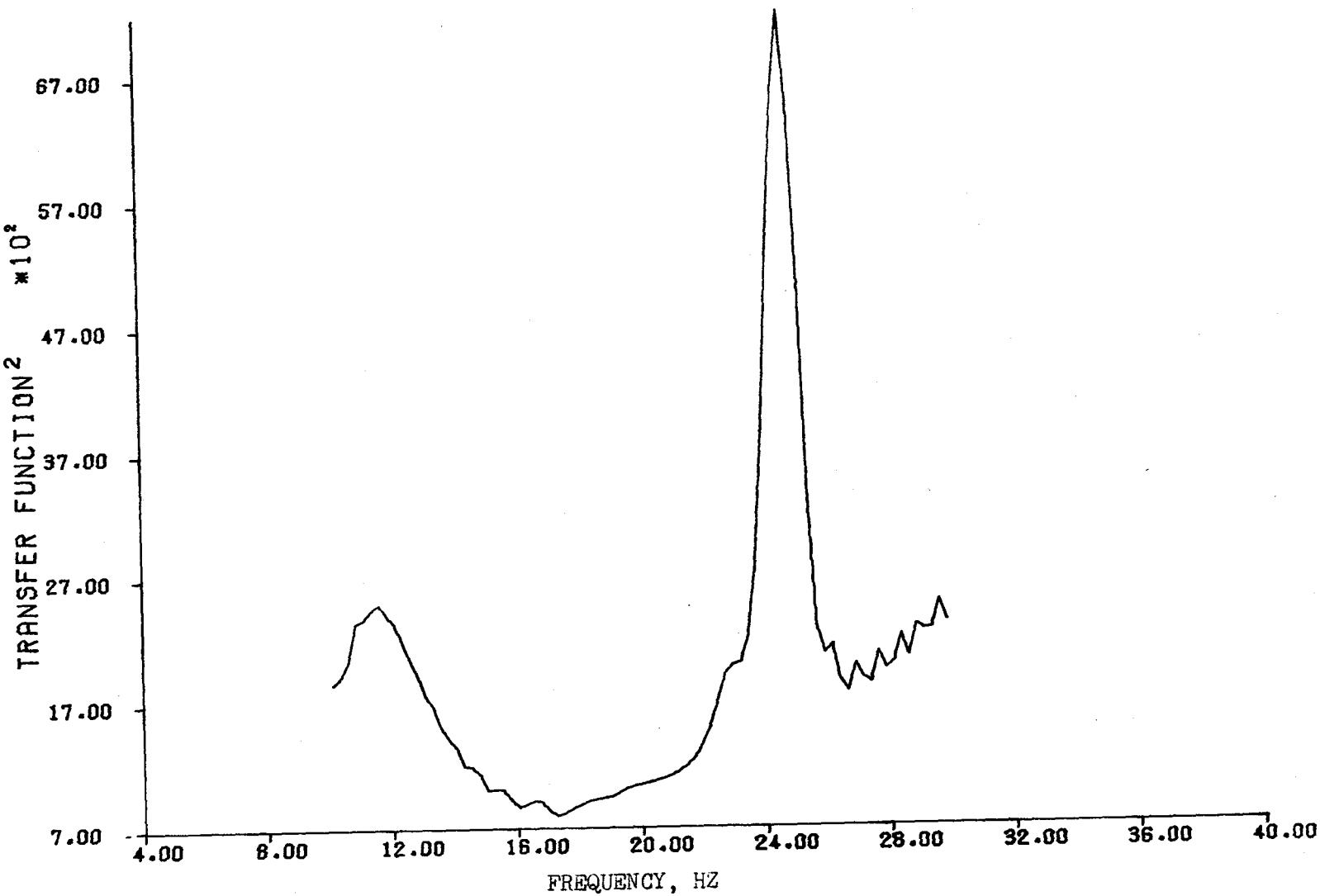

FIGURE 6.25 (CONCLUDED) (PAGE 2 OF 2)

As indicated from $|H_2^2|$ we would expect to see the q_3 mode dominate the initial part of the impulse response. Figure 6.26 verifies this fact. This response is not well enough defined to estimate damping.

It has been seen that the FSS subcritical affects at 6096 meters is to reduce the frequency of the wing bending mode, q_1, and increase its damping ratio. The fuselage mode appears totally suppressed and the first wing torsion mode, q_3, has had its damping reduced, although it is still sufficient. There is some coupling of the FSS system to the fourth mode as evidenced by an increased response to the commanded sweep.

The same testing methods were applied to try to determine the open loop vehicle characteristics from the closed loop response. Surface movement is used as the input instead of surface commands. The results are summarized in figure 6.27. No PSD plot is available because with the PSD method only the response is evaluated. The input is assumed to be white noise. Figure 6.28 shows the Co-Quad plots of the open loop transfer function. The three modes which appeared in Section 6.3.1 are evident. The q_1 mode peak is slightly noisy but a single peak is easily assumed. Comparing this plot to figure 6.12 demonstrates that the open loop characteristics have been reproduced. It should be noted that the q_4 mode was indicated much better by determining the open loop characteristics from the closed loop response than from the basic open loop response. This was evident in both the

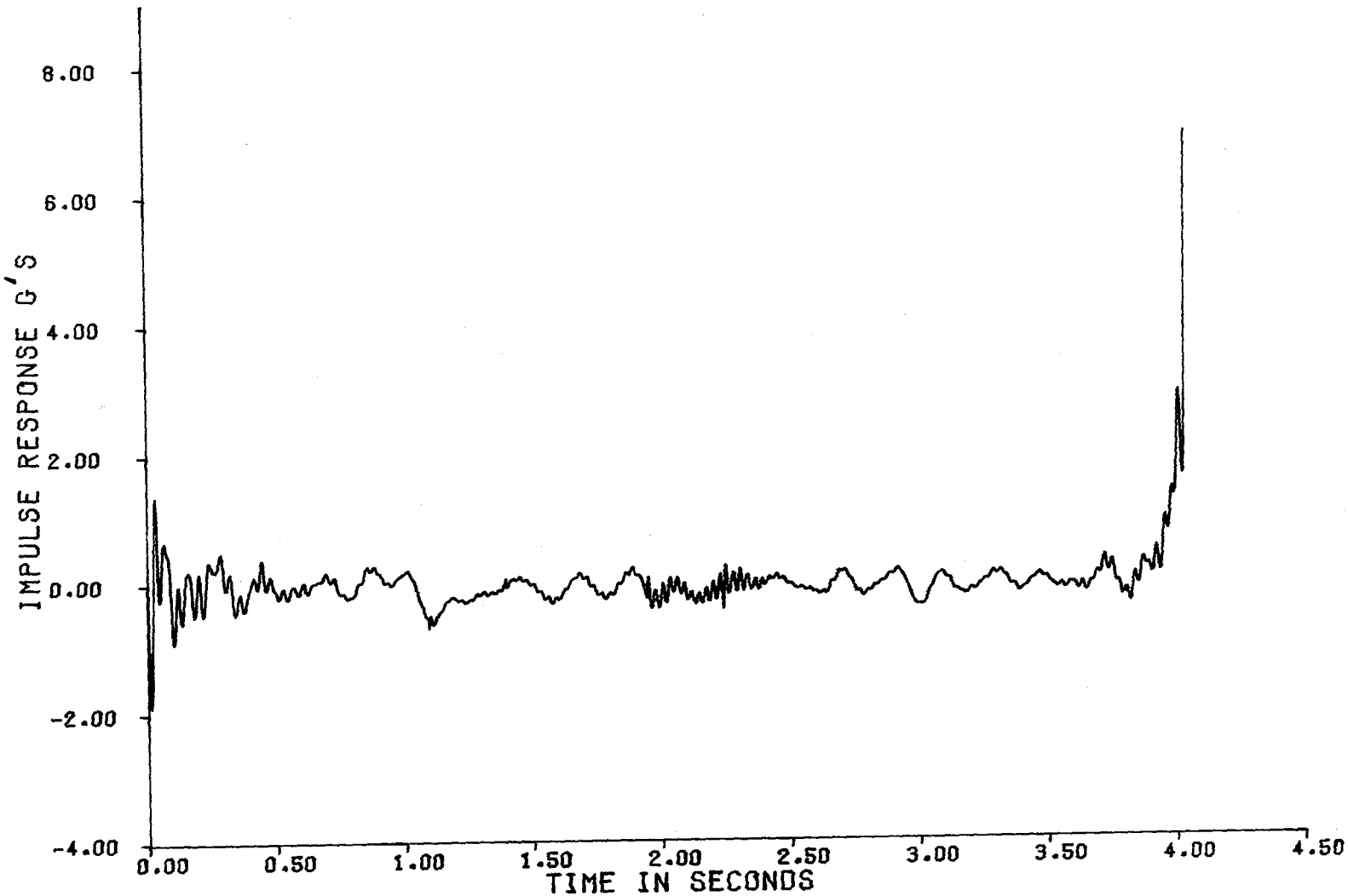

FIGURE 6.26 SUBCRITICAL CLOSED LOOP IMPULSE RESPONSE FUNCTION

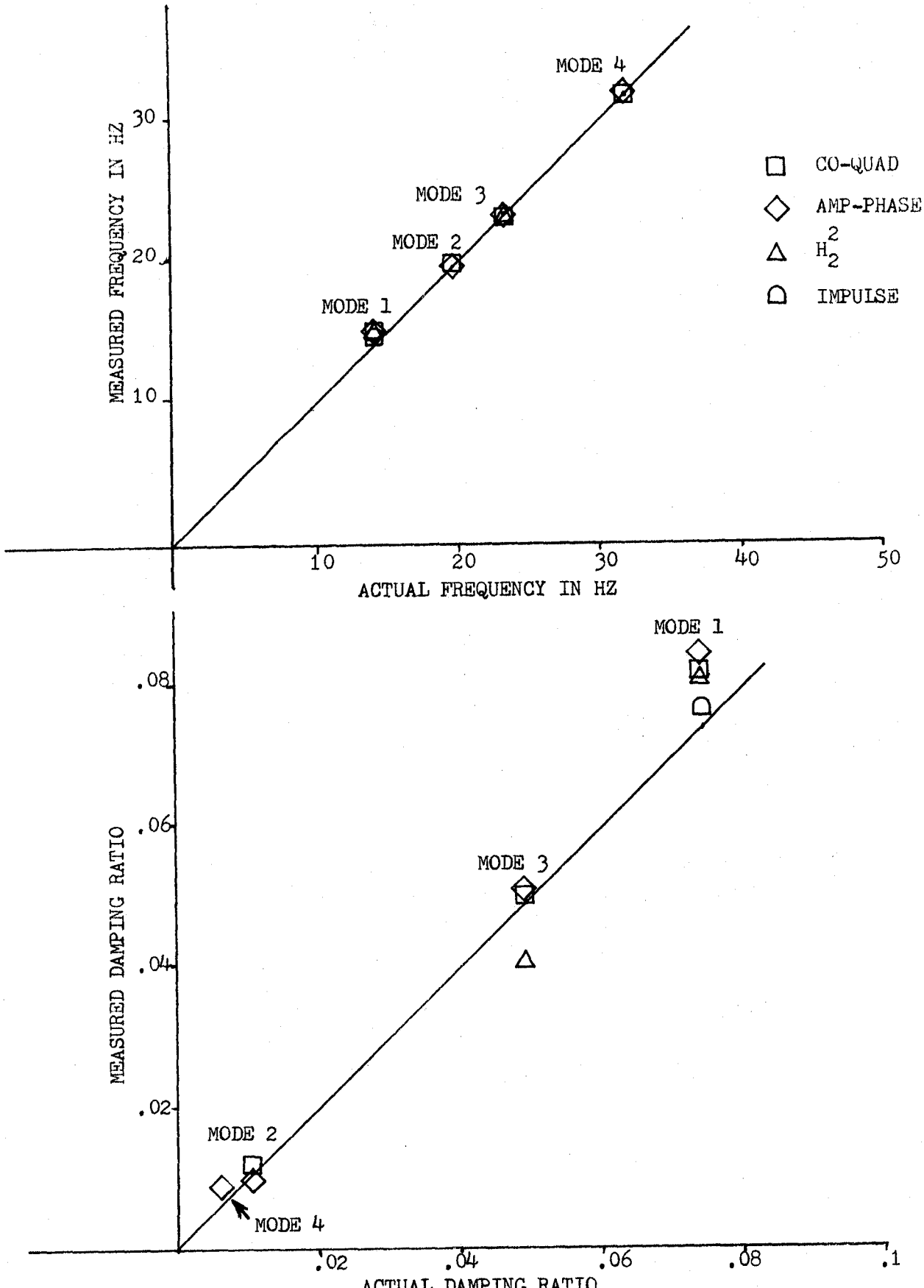

FIGURE 6.27 COMPARISON OF FLUTTER TESTING METHODS FOR DETERMINING OPEN LOOP CHARACTERISTICS FROM THE SUBCRITICAL CLOSED LOOP RESPONSE

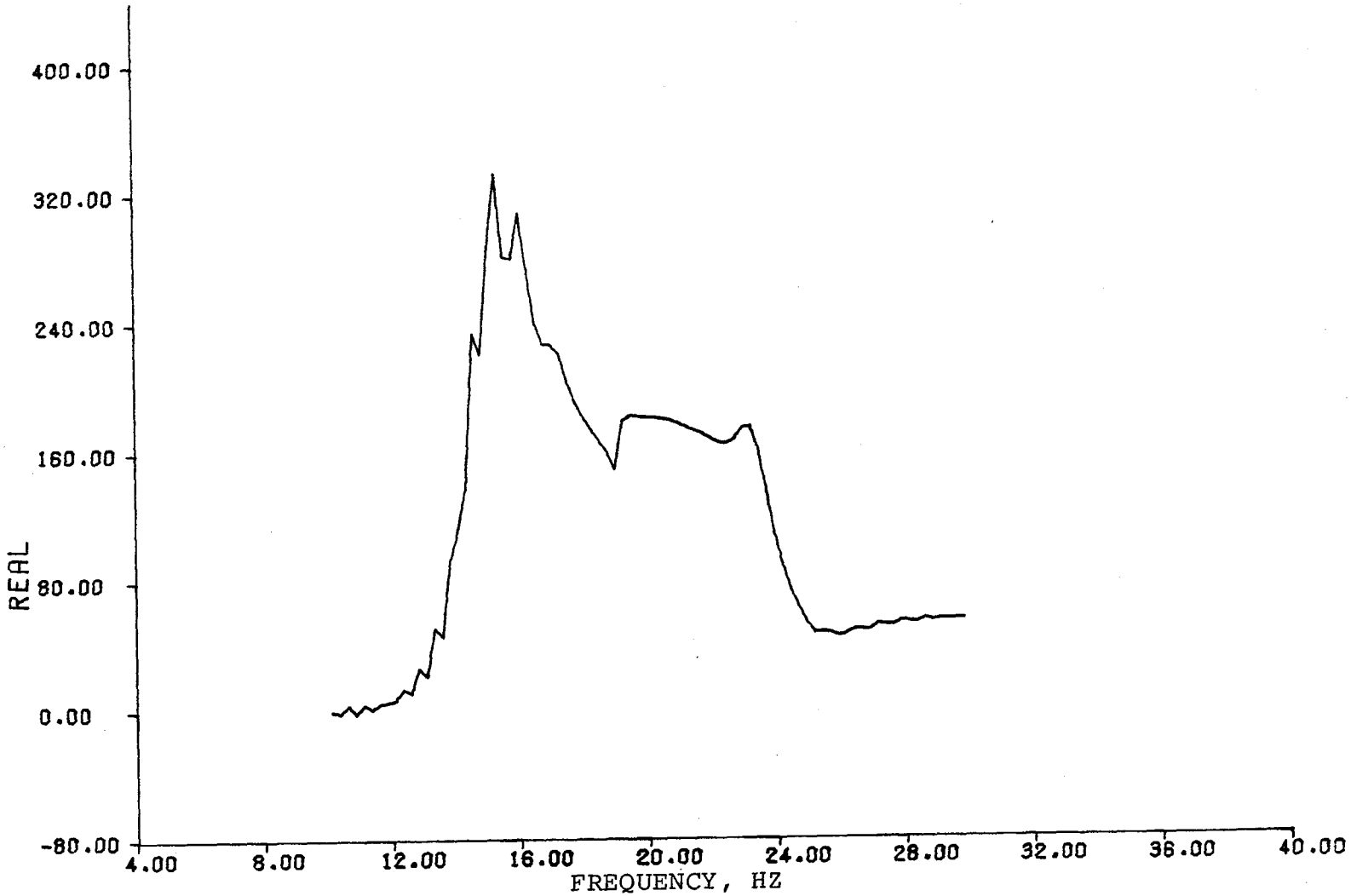

FIGURE 6.28 OPEN LOOP RESPONSE OFF OF SUBCRITICAL CLOSED LOOP CO-QUAD PLOTS
(PAGE 1 OF 2)

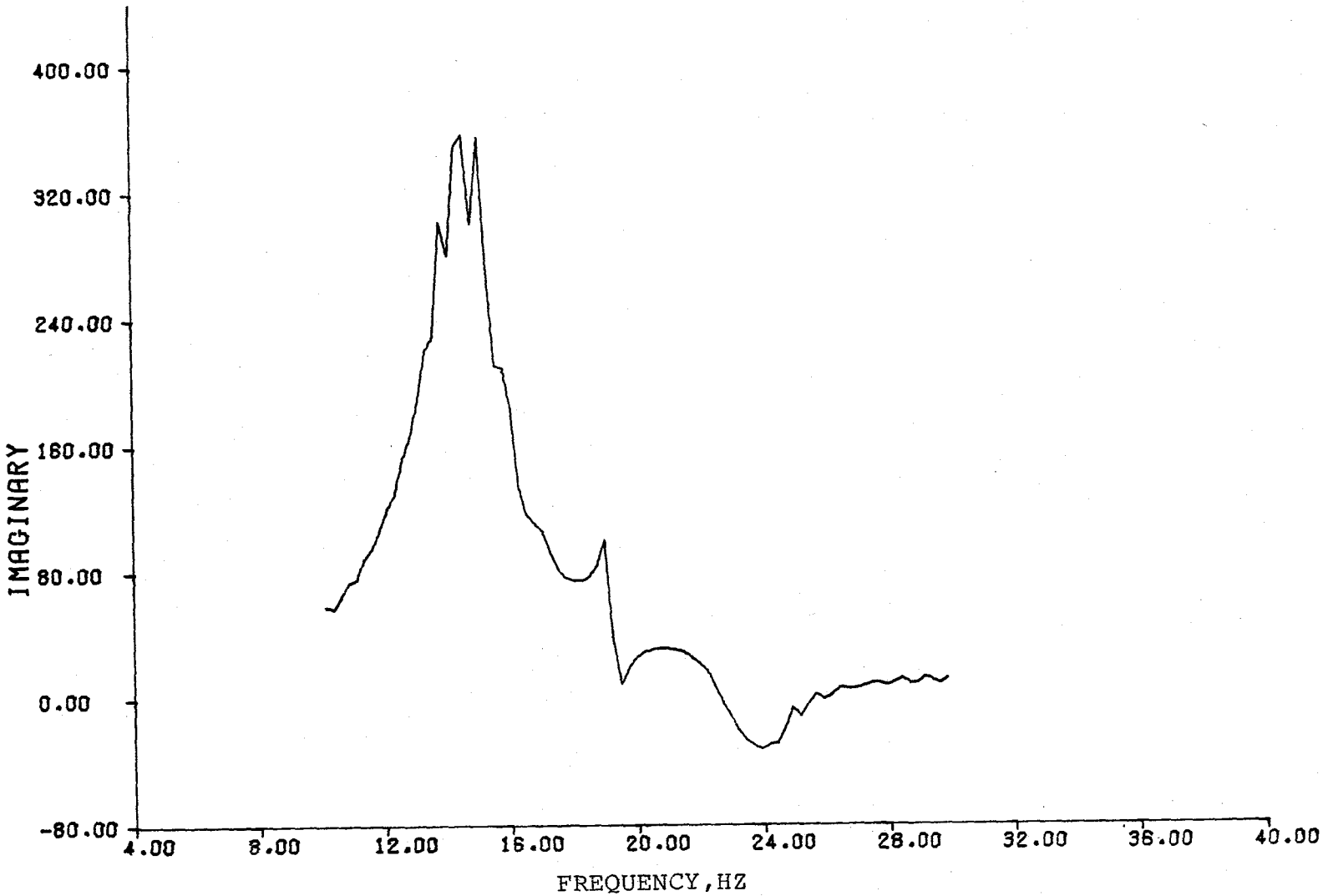

FIGURE 6.28 (CONCLUDED) (PAGE 2 OF 2)

Co-Quad and Amplitude Phase methods. It is best illustrated by examining the broad spectrum plots of Amplitude-Phase of the open loop from the closed loop response seen in figure 6.29a and the open loop analysis seen in figure 6.29b. The 32 hertz mode, q_4, is represented much better in figure 6.29a than in figure 6.29b.

The Amplitude-Phase plots for the open loop identification from the closed loop response is shown in figure 6.30 for an expanded scale. The fuselage mode is faintly evident from this plot.

The transfer function modulus shown in figure 6.31 only indicates q_1 and q_3. Only the first mode is sufficiently indicated to estimate damping. Figure 6.32 is the impulse response function of the open loop system determined from the closed loop response. This, as much as any other plot, indicates that the subcritical open loop system is represented in a closed loop response. Comparing figure 6.32 to the impulse response function generated from the open loop response in figure 6.15 shows that the initial response is duplicated.

6.3.3 Supercritical Closed-Loop. - The supercritical flutter test region conditions for this section are M = 0.9 at h = 3048 meters. The time history of the simulated response is seen in figure 6.33. The first wing torsion mode q_3 is the one which flutters first in this region. The time history traces show that the accelerometer traces do not indicate as much response in q_1 as it does in q_3 during the

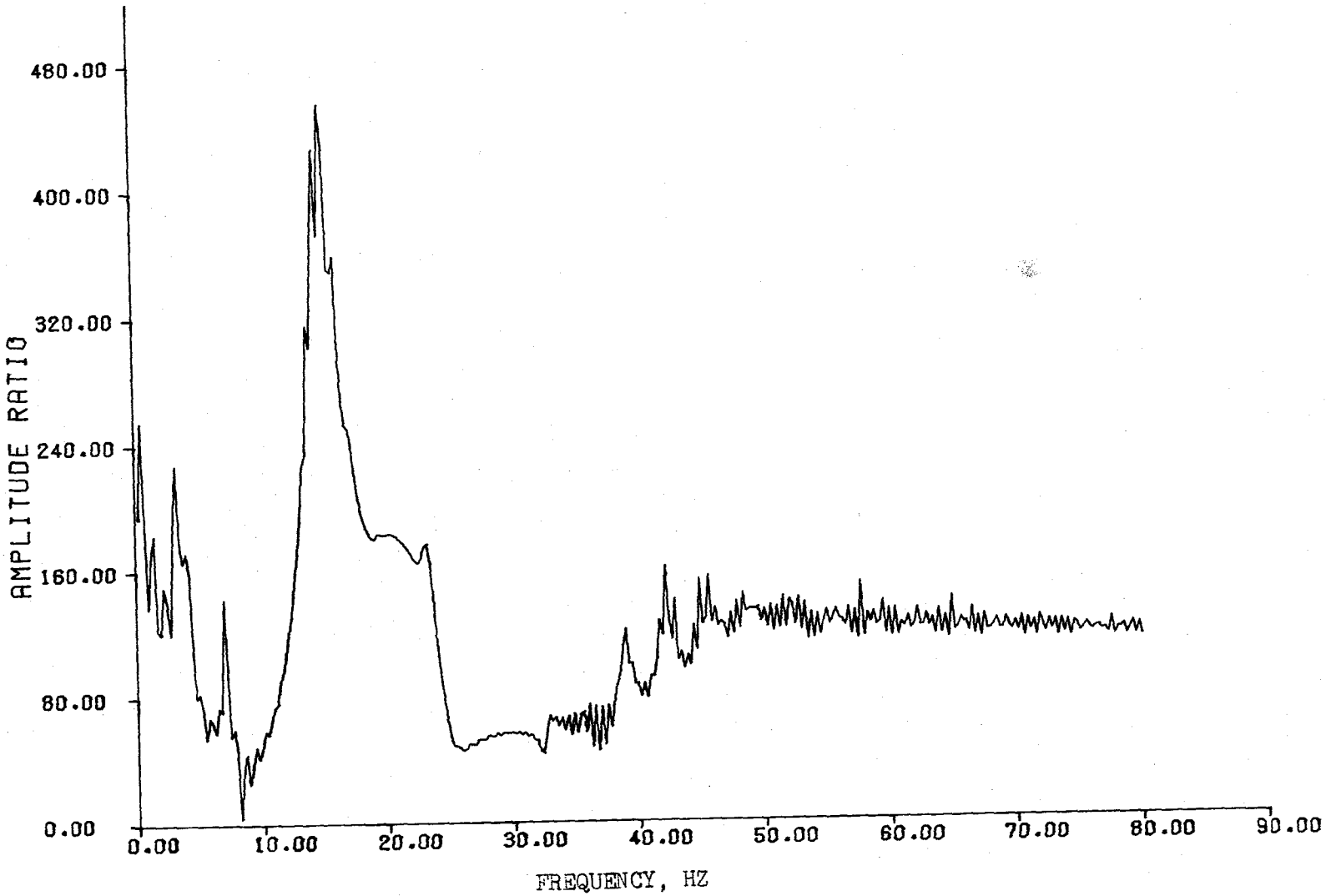

FIGURE 6.29a BROAD SPECTRUM AMPLITUDE - PHASE PLOTS OF THE OPEN LOOP CHARACTERISTICS FROM THE CLOSED LOOP SUBCRITICAL RESPONSE
(PAGE 1 OF 2)

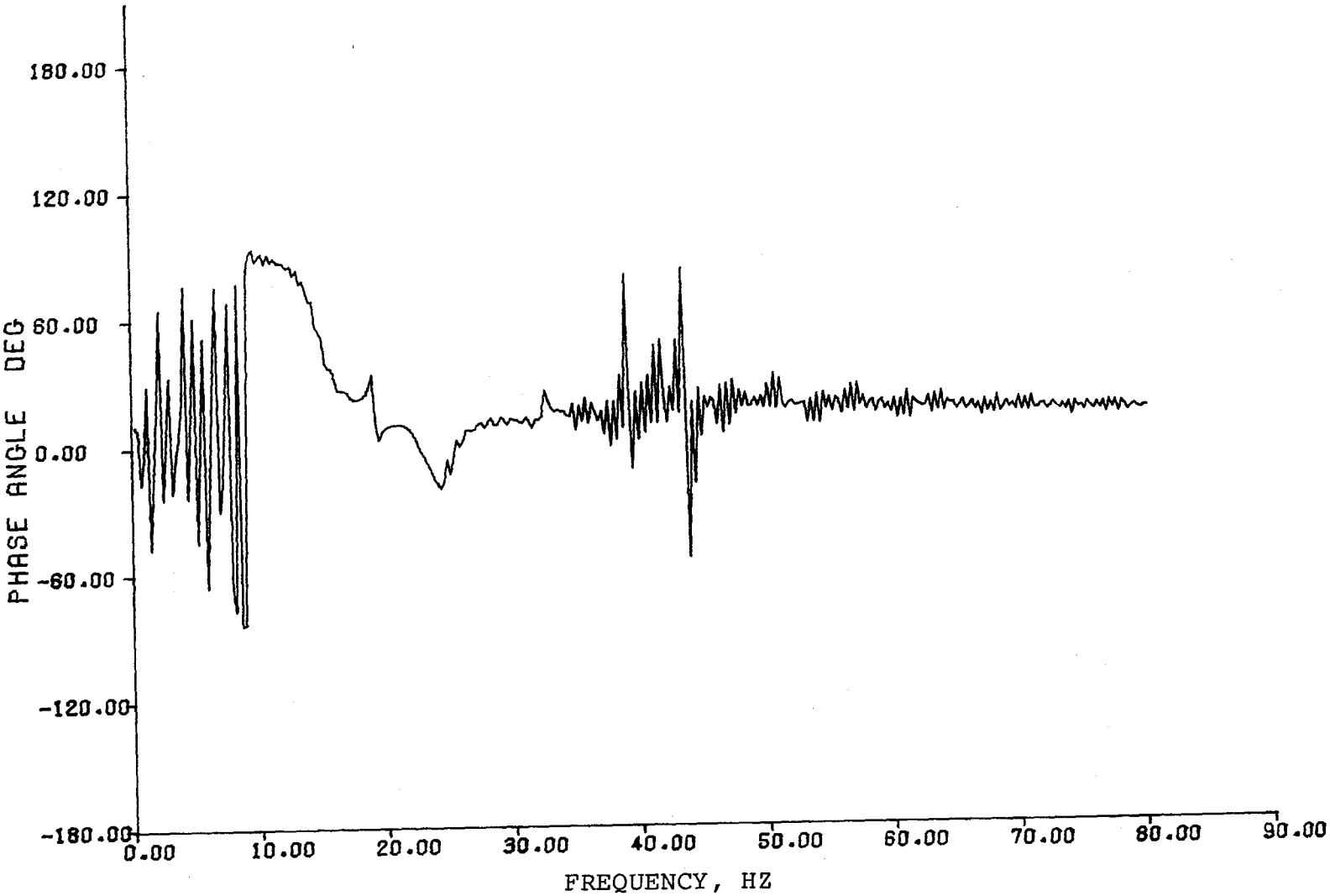

FIGURE 6.29a (CONCLUDED) (PAGE 2 OF 2)

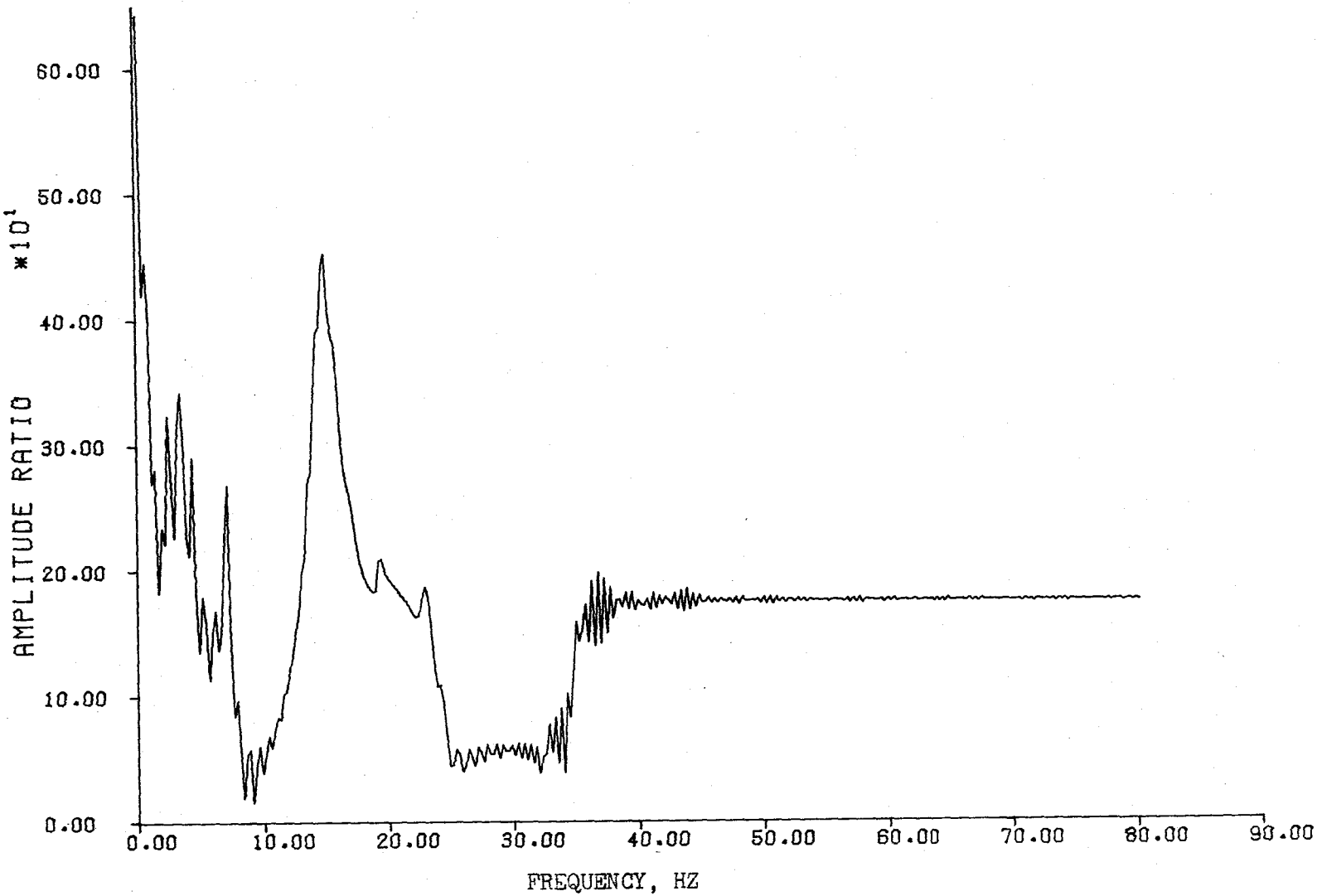

FIGURE 6.29b BROAD SPECTRUM AMPLITUDE - PHASE PLOTS OF THE OPEN LOOP SUBCRITICAL RESPONSE (PAGE 1 OF 2)

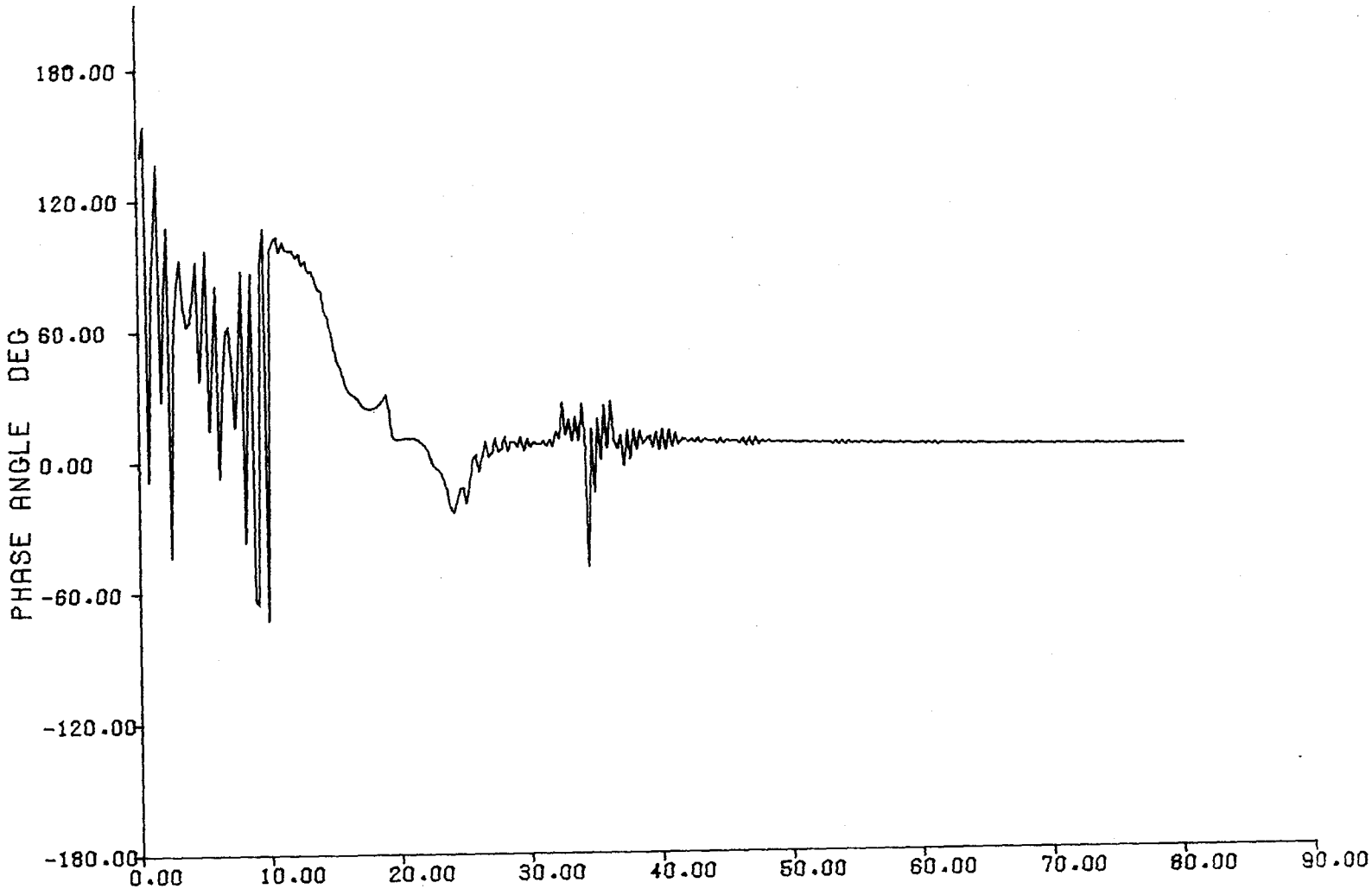

FIGURE 6.29b (CONCLUDED) (PAGE 1 OF 2)

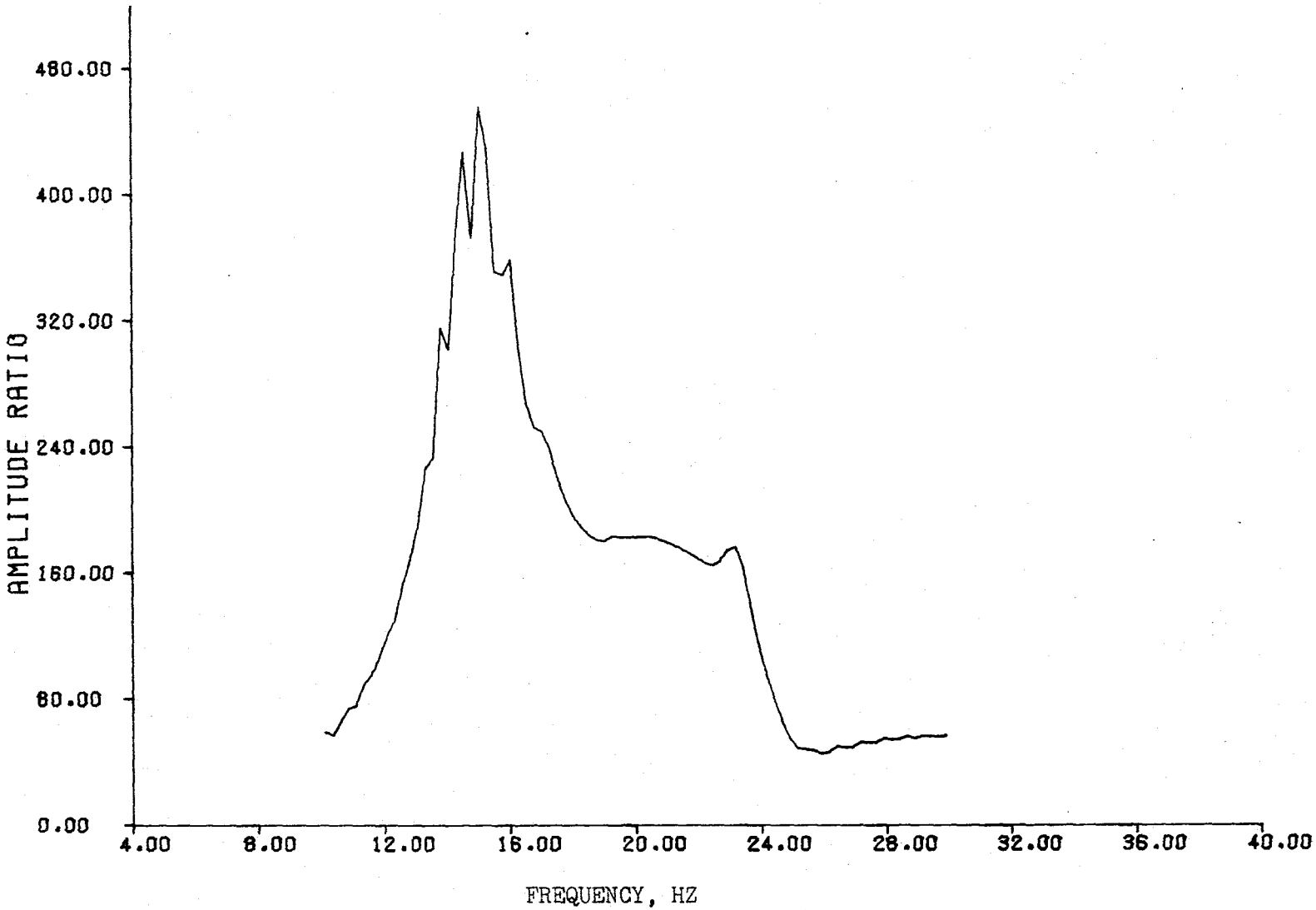

FIGURE 6.30 OPEN LOOP RESPONSE OFF THE SUBCRITICAL CLOSED LOOP AMPLITUDE-PHASE PLOTS

(PAGE 1 OF 2)

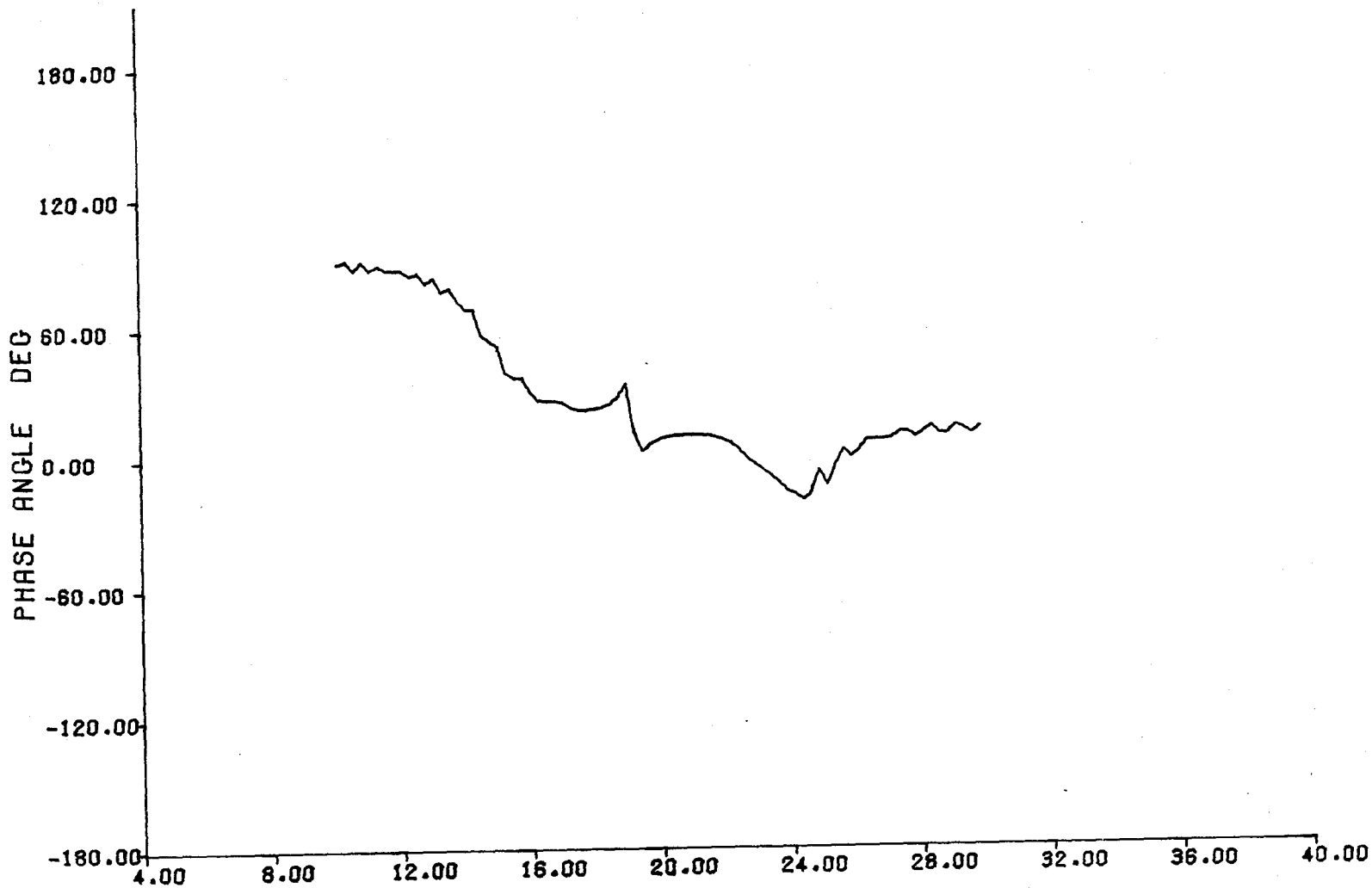

FIGURE 6.30 (CONCLUDED) (PAGE 2 OF 2)

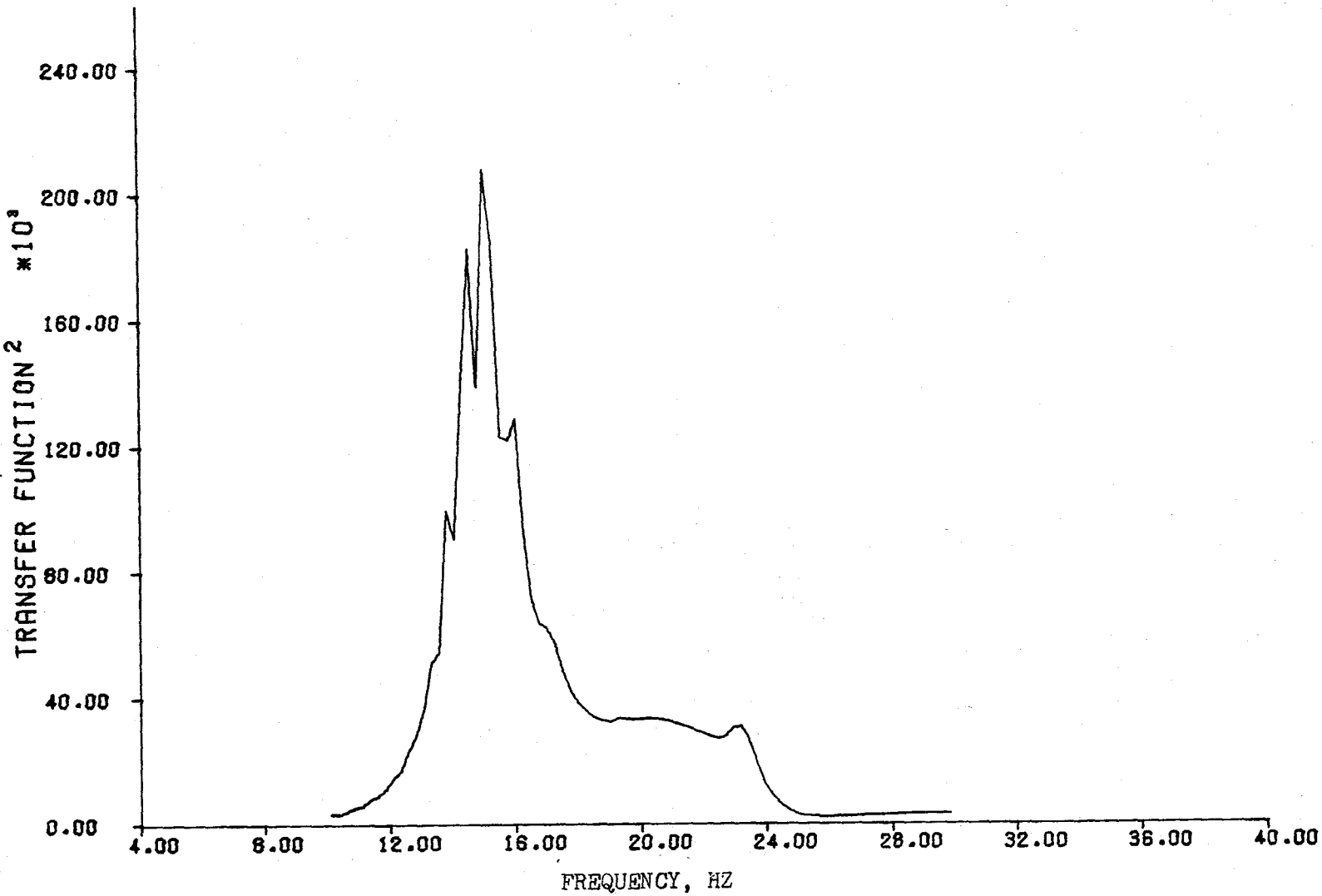

FIGURE 6.31 TRANSFER FUNCTION MODULUS OF THE OPEN LOOP RESPONSE OFF THE SUBCRITICAL CLOSED LOOP RESPONSE

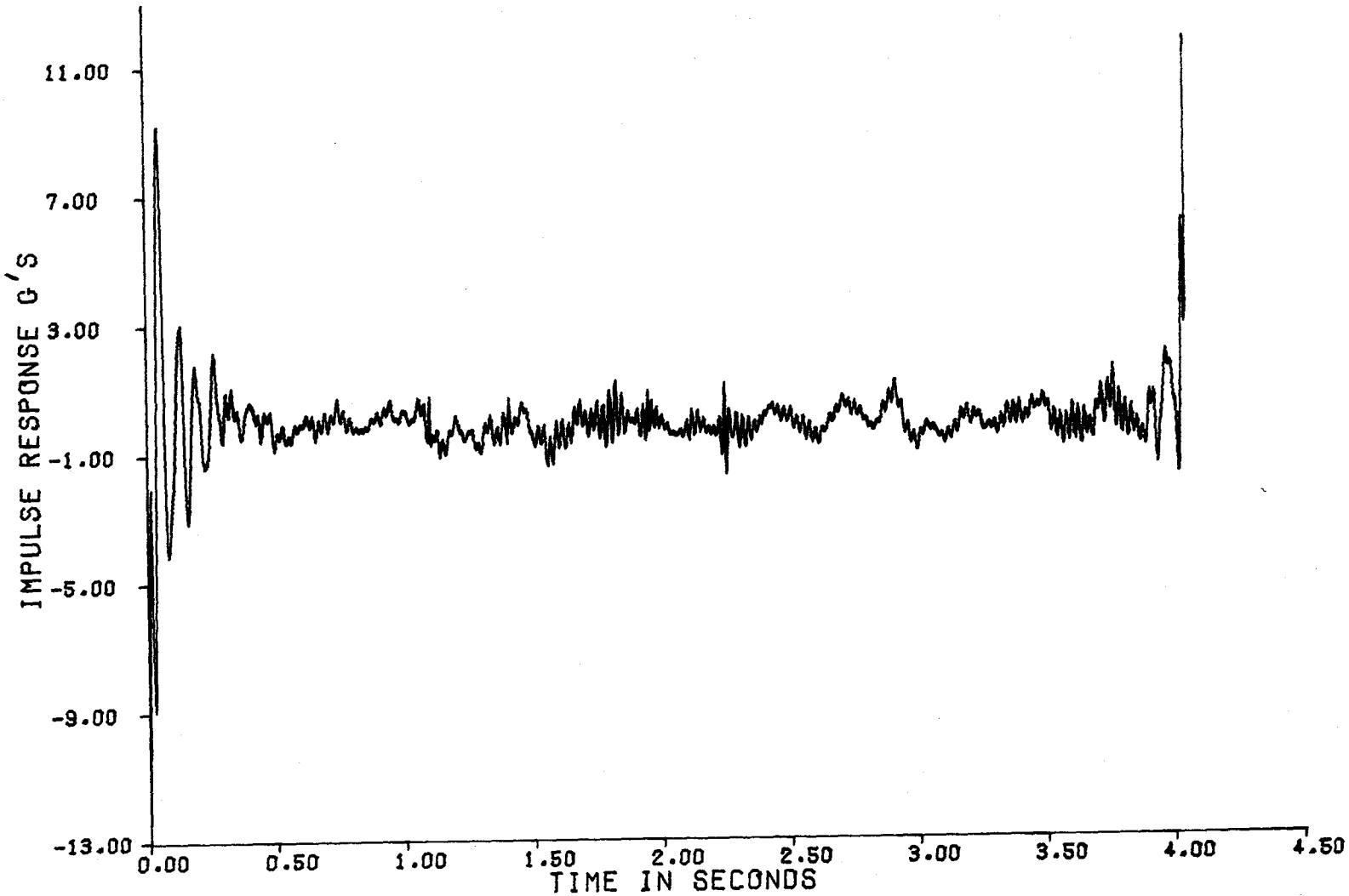

FIGURE 6.32 OPEN LOOP RESPONSE OFF OF THE SUBCRITICAL CLOSED LOOP IMPULSE RESPONSE FUNCTION

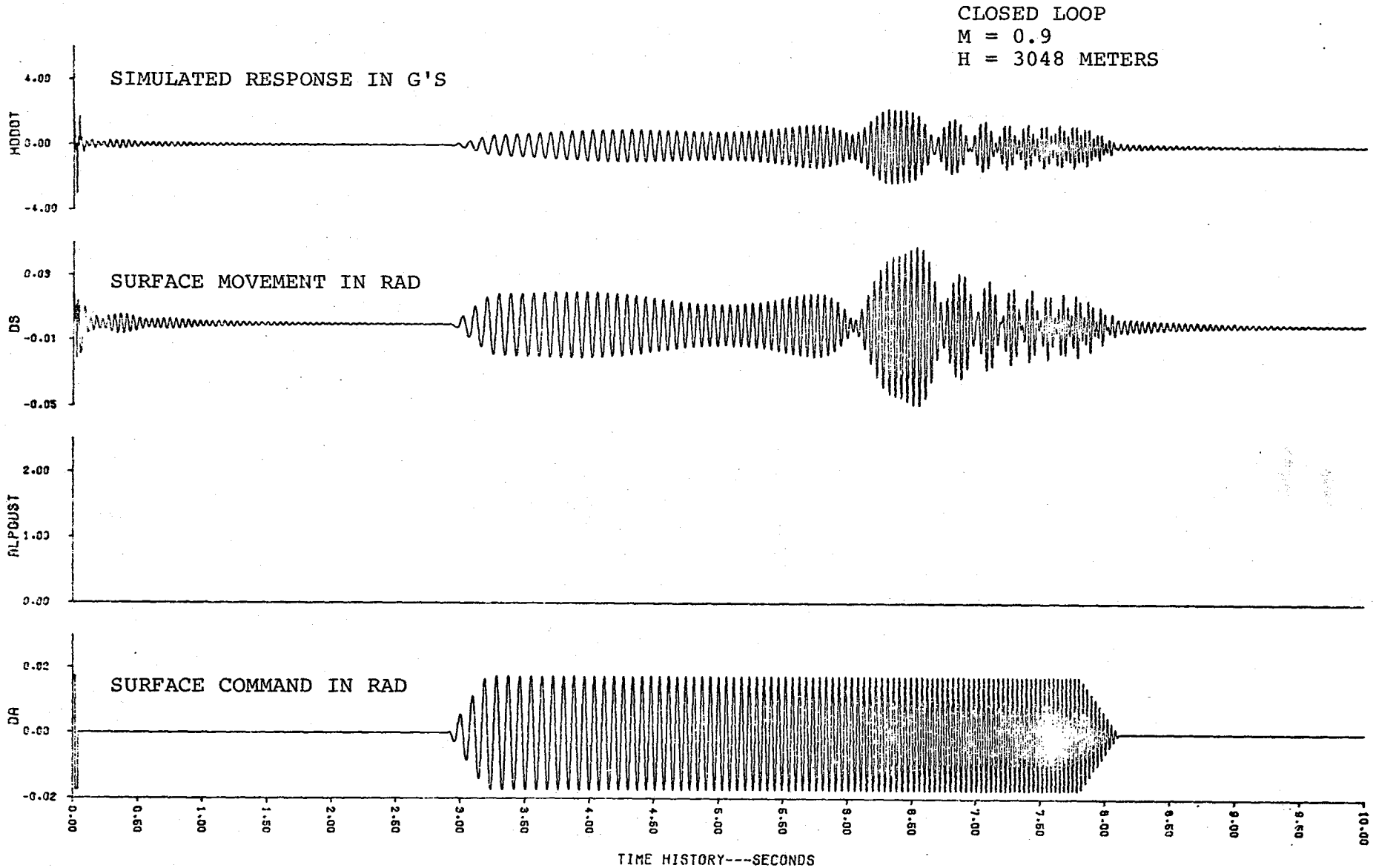

FIGURE 6.33 SUPERCRITICAL AUGMENTED RESPONSE

frequency sweep.

The estimates of the closed loop frequencies and damping by the various methods are shown in figure 6.34. Figure 6.35 shows the altered spectrum of surface movement to command input for the frequency sweep. The wing mode at approximately 32 hertz is the flutter mode but its damping ratio with the FSS operating based on analysis is .92. So this mode was never present in the data. Only the q_1 and q_2 modes are evident as can be seen by the PSD plot of the response to a command doublet in figure 6.36. The 18.5 hertz q_1 wing mode and the fuselage mode q_2 are evident with a slight indication of the 77 hertz wing mode, q_8, appearing. The PSD of the surface movement to the doublet command is almost identical to the response PSD.

Both the Co-Quad and Amplitude-Phase plots shown in figures 6.37 and 6.38 respectively, are almost representative of classical examples of the methods. For the two modes excited, the information for the frequency and damping estimates is well defined.

The transfer function modulus seen in figure 6.39 would indicate that the impulse response function should be dominated by the 21 hertz fuselage mode q_2. Figure 6.40 shows this to be true although a damping estimate cannot be made from the impulse response.

The FSS completely suppresses the known flutter mode q_3 and good damping is indicated in the wing bending mode q_1. The response in the fuselage mode has increased sub-

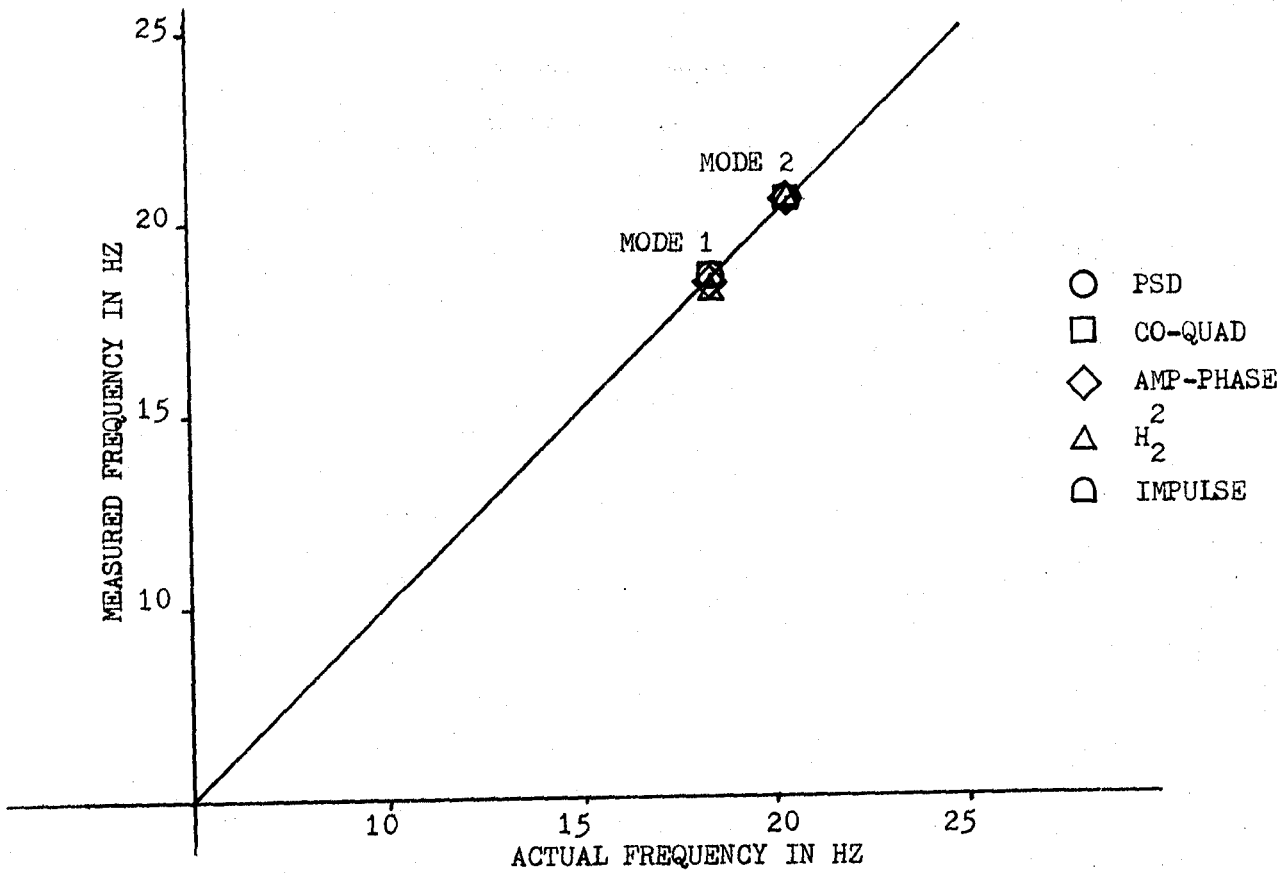

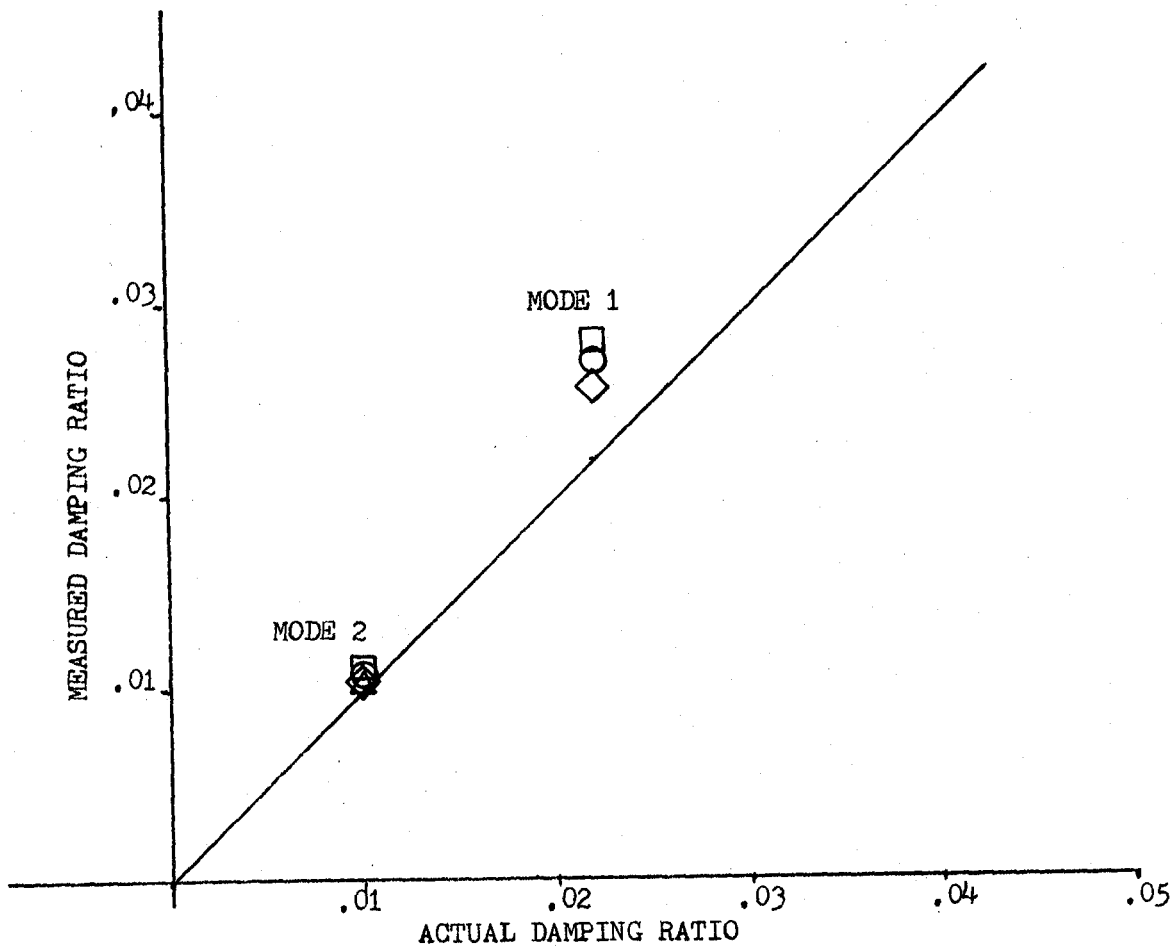

FIGURE 6.34 COMPARISON OF FLUTTER TESTING METHODS ON THE AUGMENTED SUPERCRITICAL RESPONSE

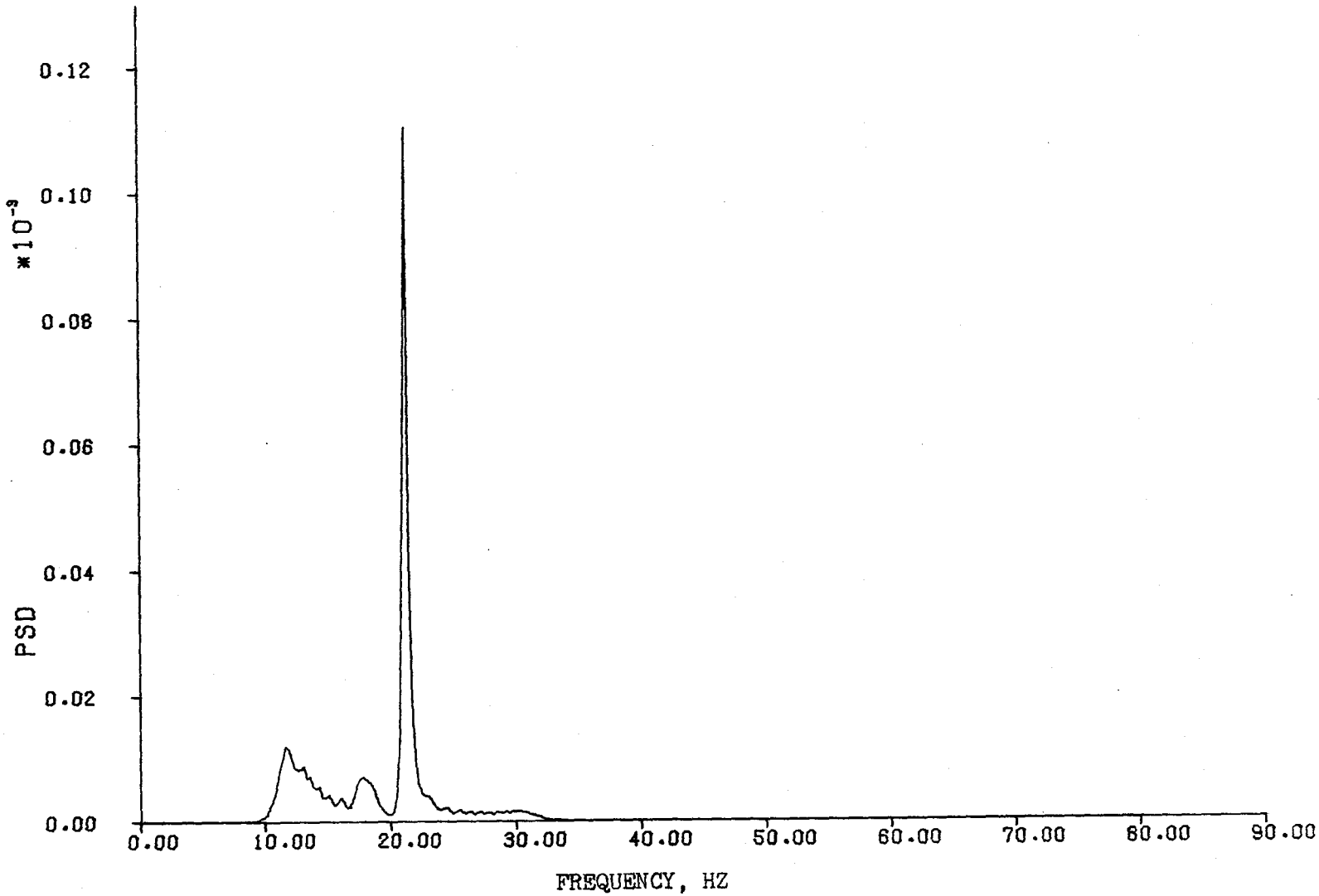

FIGURE 6.35 SPECTRUM OF SUPERCRITICAL SWEEP INPUT

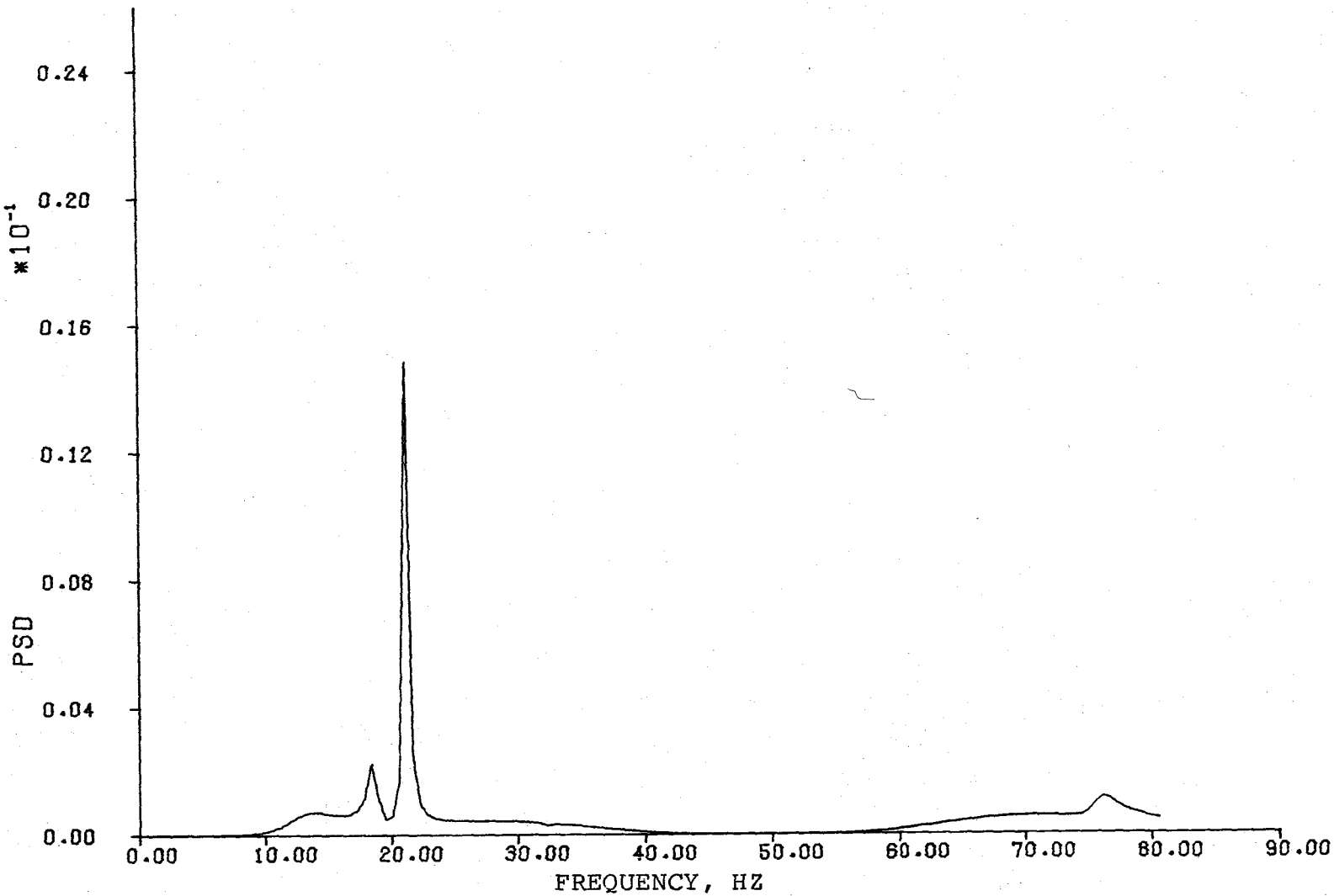

FIGURE 6.36 PSD PLOT OF THE SUPERCRITICAL CLOSED LOOP RESPONSE TO A COMMAND DOUBLET

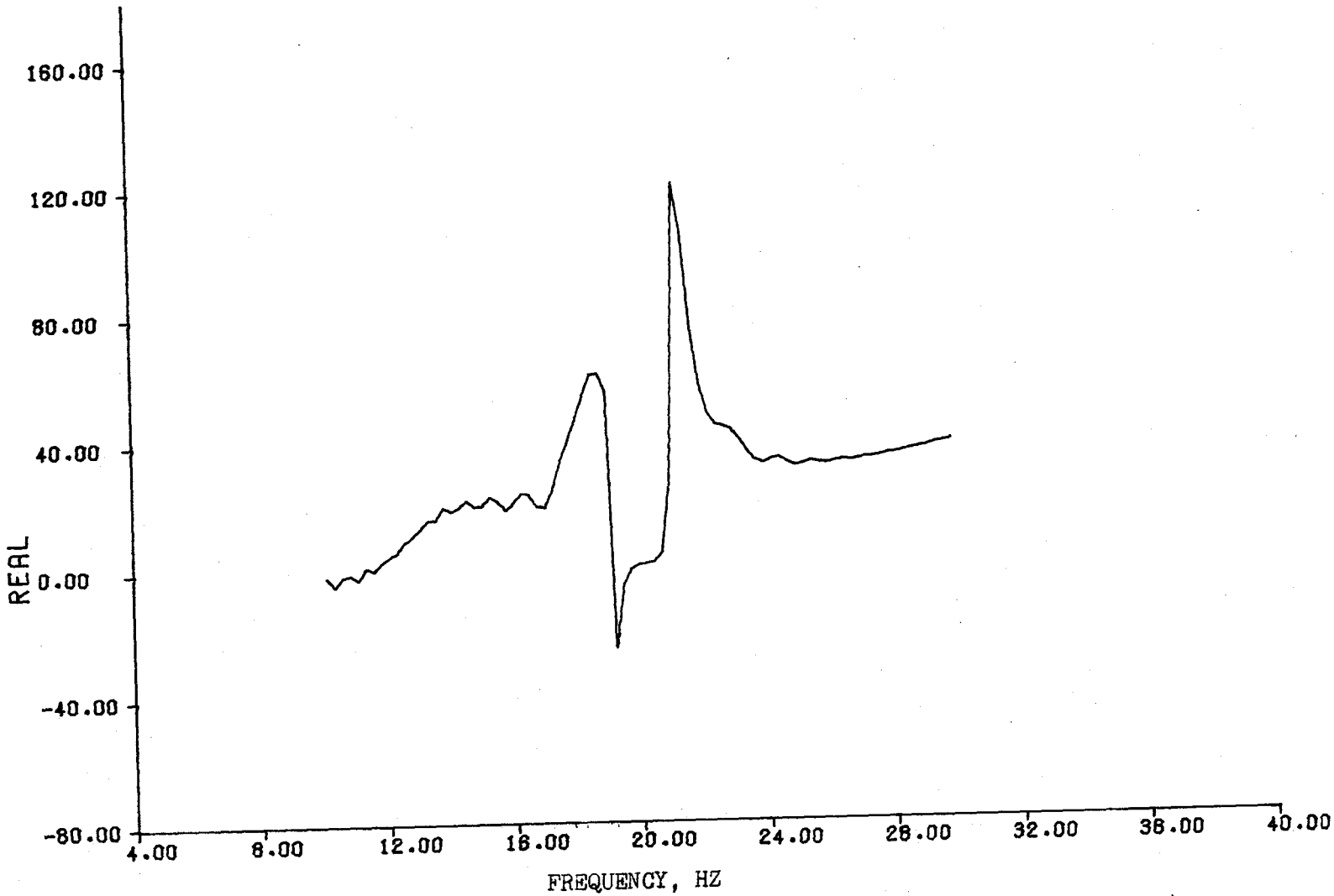

FIGURE 6.37 CLOSED LOOP SUPERCRITICAL CO-QUAD PLOT (PAGE 1 OF 2)

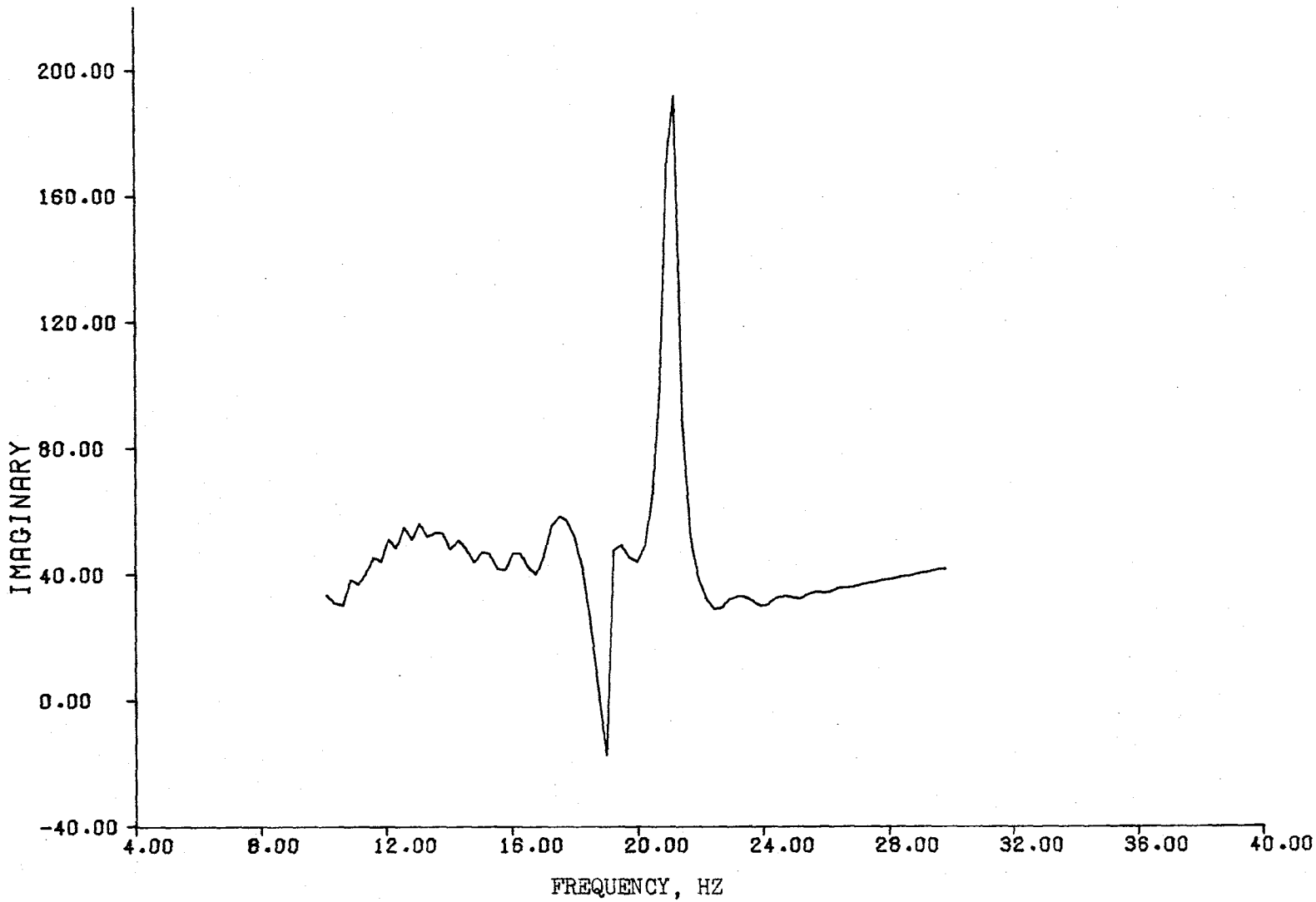

FIGURE 6.37 CONCLUDED (PAGE 2 OF 2)

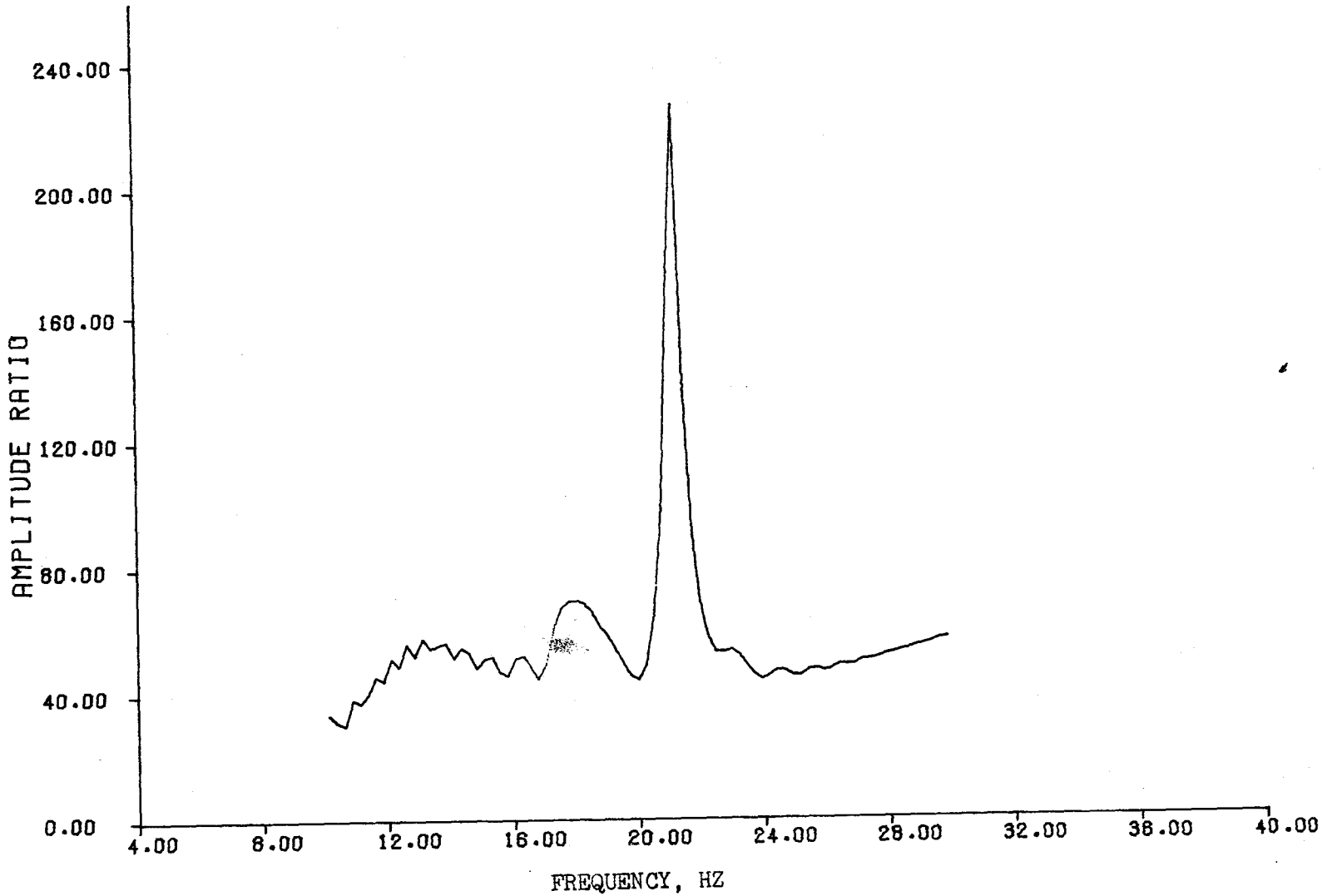

FIGURE 6.38 CLOSED LOOP SUPERCRITICAL AMPLITUDE-PHASE PLOT (PAGE 1 OF 2)

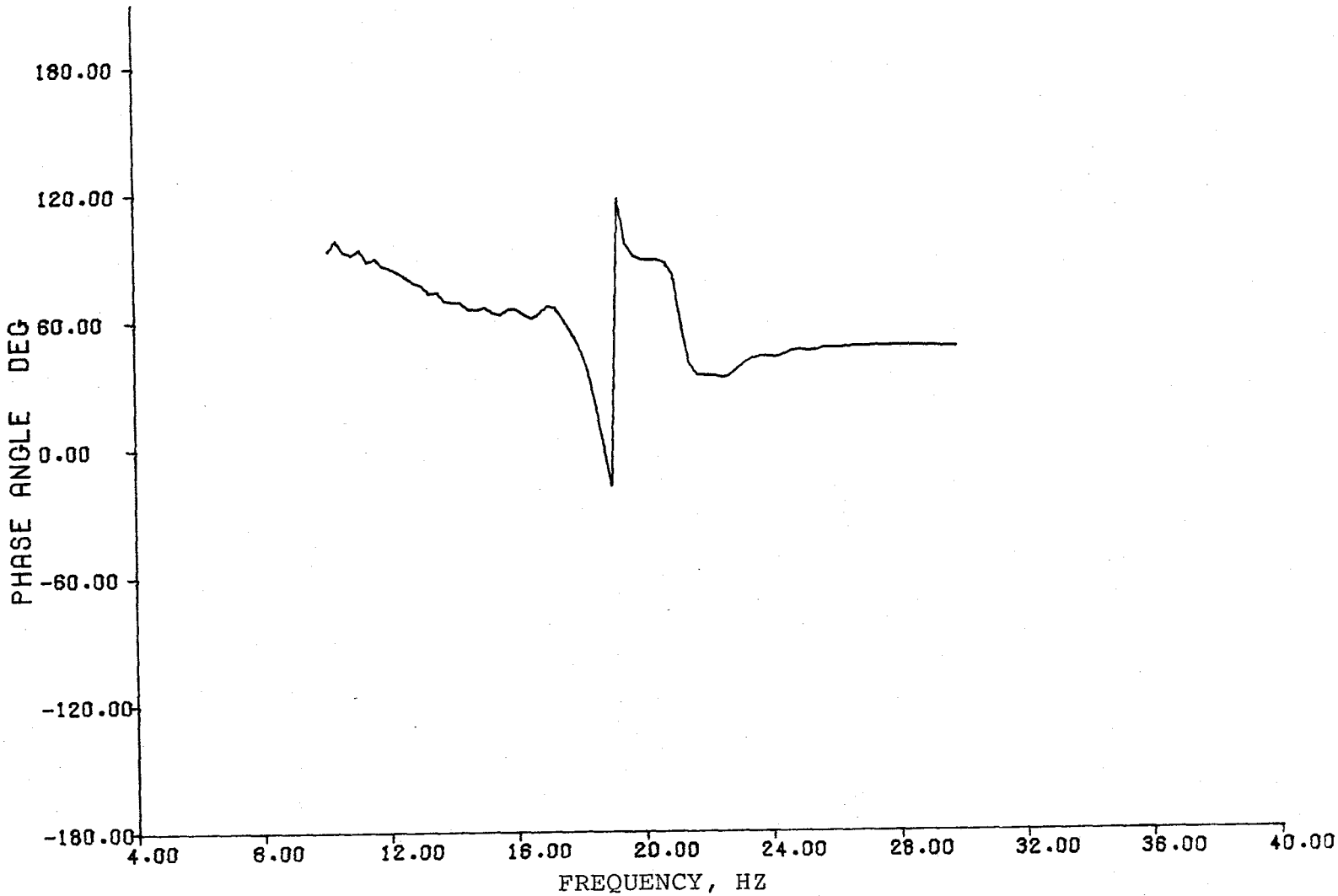

FIGURE 6.38 CONCLUDED (PAGE 2 OF 2)

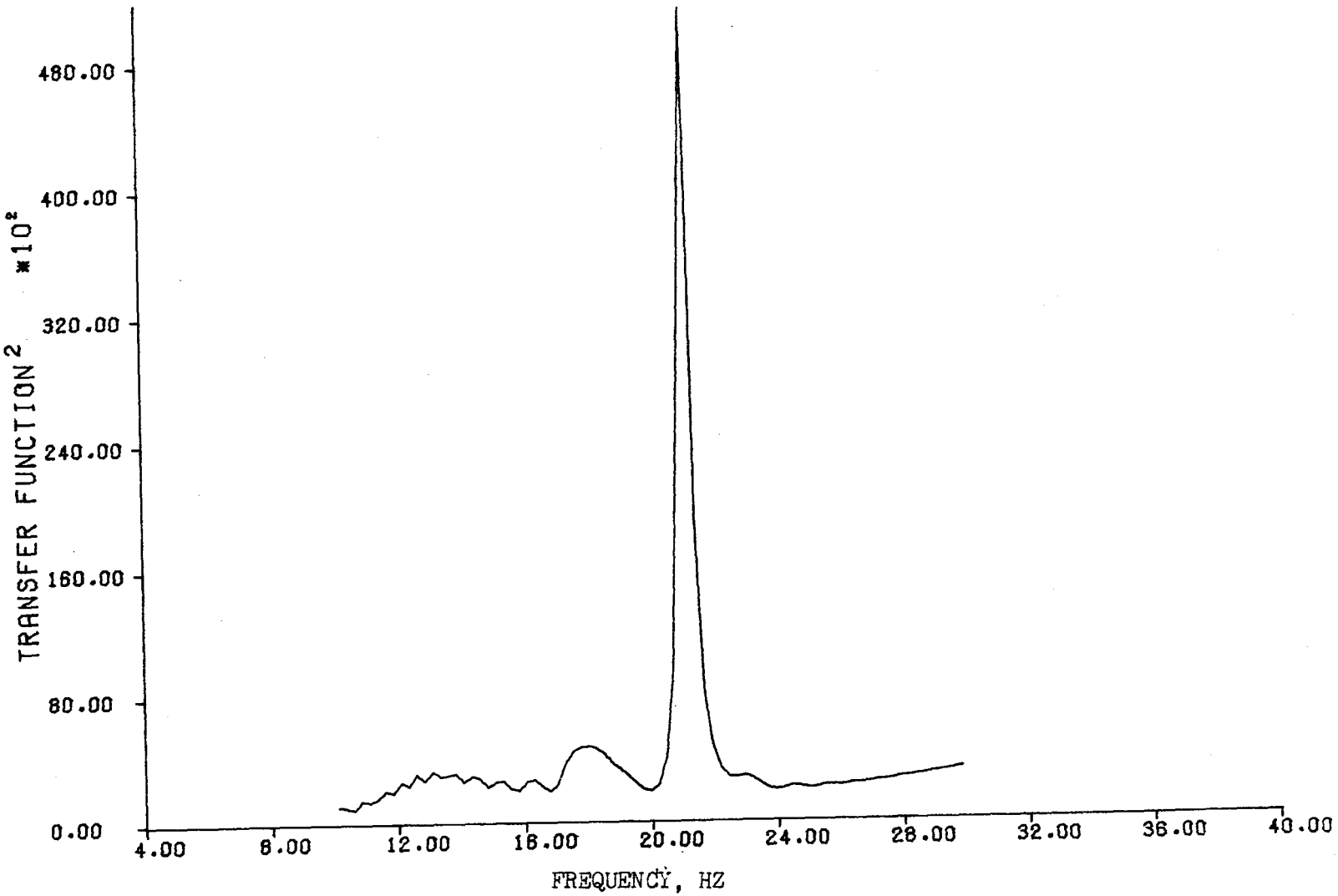

FIGURE 6.39 CLOSED LOOP SUPERCRITICAL TRANSFER FUNCTION MODULUS

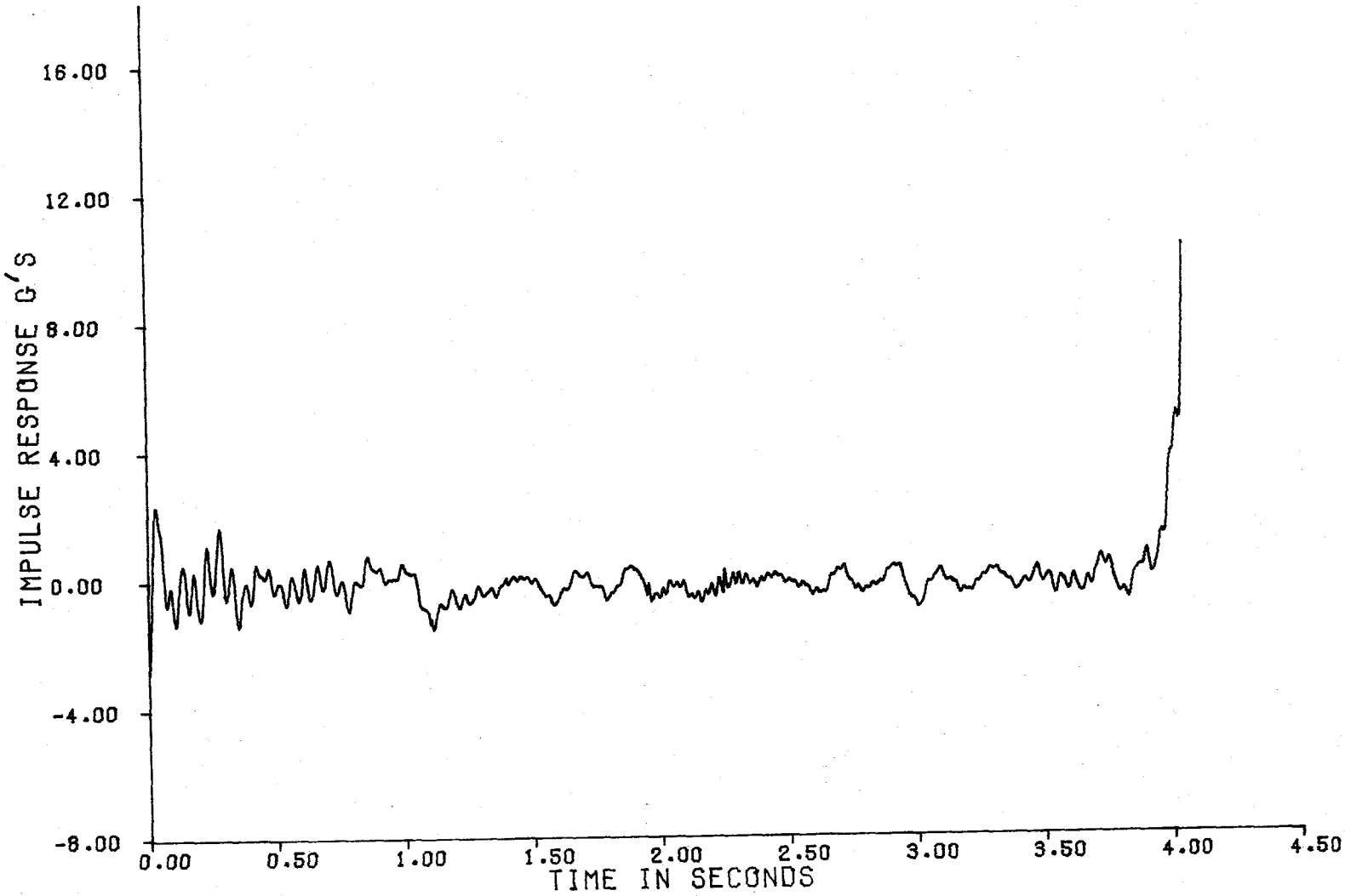

FIGURE 6.40 CLOSED LOOP SUPERCRITICAL IMPULSE RESPONSE FUNCTION

stantially however.

The attempt at extracting the open loop characteristics of the wing from the closed loop supercritical response is summarized in figure 6.41. The open loop roots for the first three modes range from 19.3 to 19.7 hertz. The Co-Quad plots in figure 6.42 indicate a lightly damped mode at about 19.6 hertz. This is probably the fuselage mode q_2 since q_3 is highly damped and q_1 is unstable for the open loop case. The source of the peaks below 14 hertz are unknown since very little input excitation exists at these frequencies it is probably just noise due to an extremely small denominator term. The Amplitude-Phase plot of figure 6.43 indicates very little information. The Phase plot does indicate the q_2 mode but little else. The transfer function modulus presents inconclusive results as is evident in figure 6.44. From figure 6.44 one would expect the impulse response function, shown in figure 6.45, also to be inconclusive. The plot is representative of a highly damp system of indeterminate frequency.

Although some of the open loop modes are present in the supercritical response, the modes involved in flutter cannot be reliably identified.

6.3.4 FSS Performance In Turbulence.- The preliminary analysis on flutter testing methods performed in the previous section was done on a noise-free data. This allowed the evaluation of the concept of determining open loop flutter characteristics from the closed loop responses. In a flight test environment noise sources from turbulence,

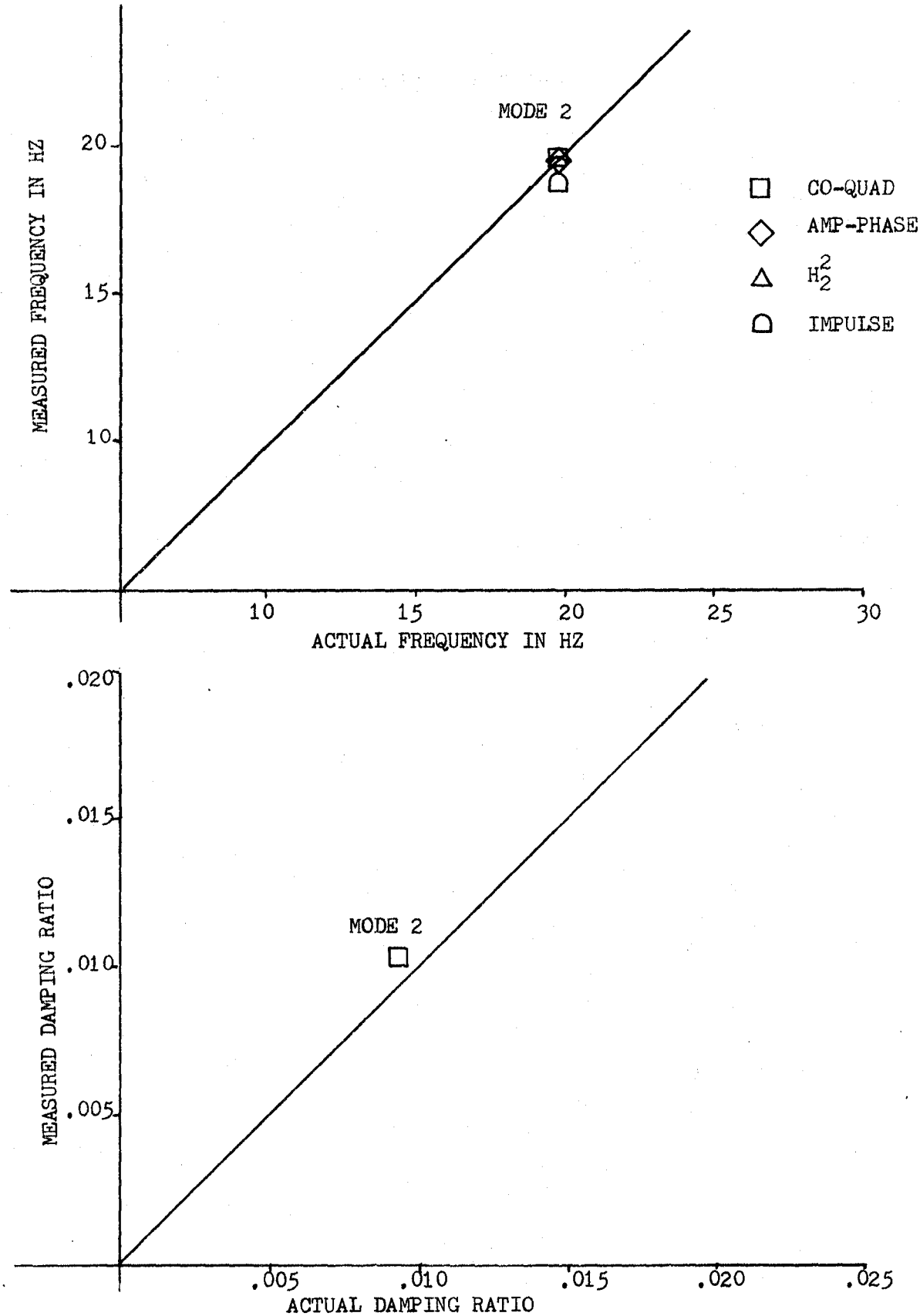

FIGURE 6.41 COMPARISON OF FLUTTER TESTING METHODS FOR DETERMINING OPEN LOOP CHARACTERISTICS FROM THE SUPERCRITICAL CLOSED LOOP RESPONSE

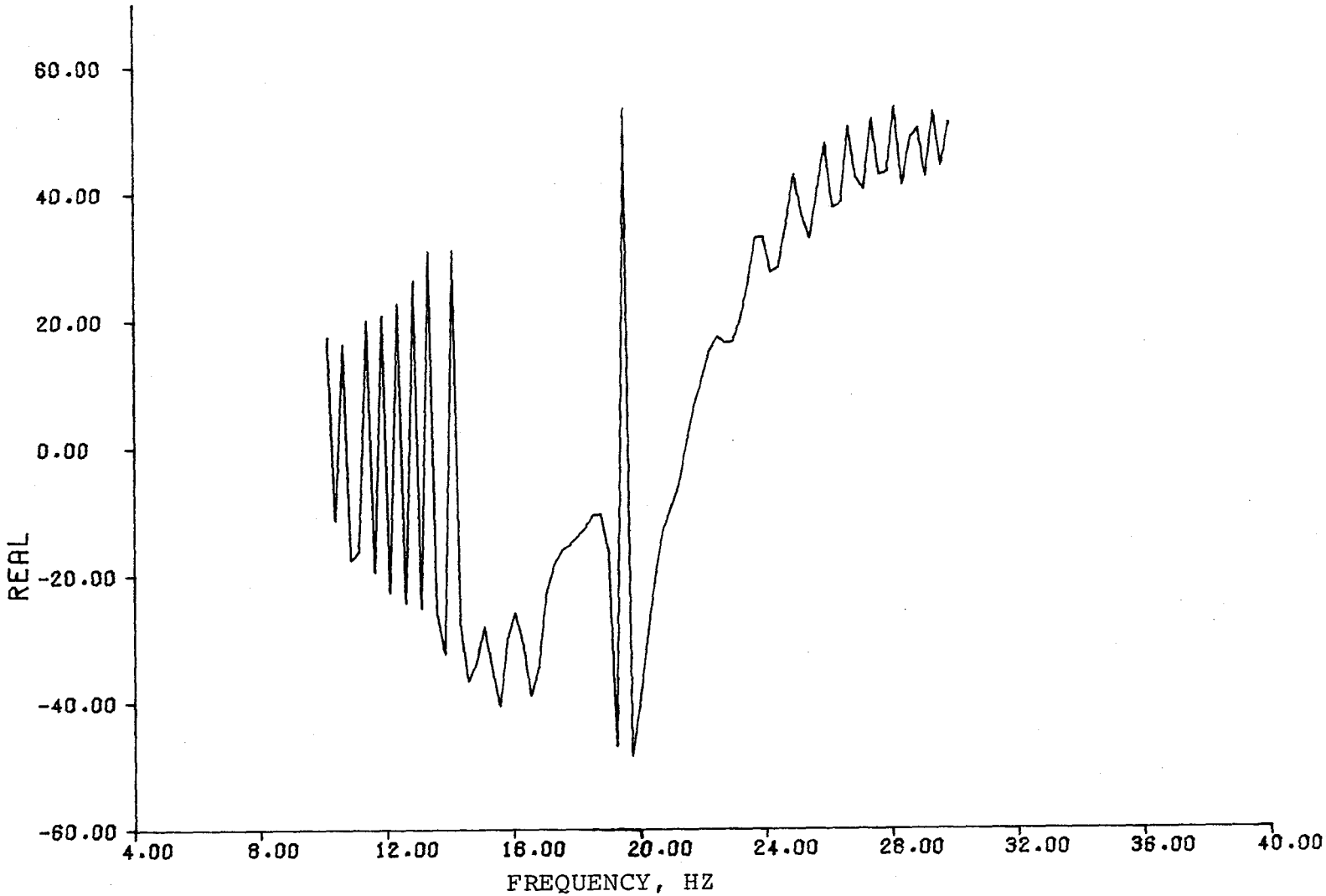

FIGURE 6.42 OPEN LOOP RESPONSE OFF OF CLOSED LOOP CO-QUAD PLOT OF OF SUPERCRITICAL RESPONSE (PAGE 1 OF 2)

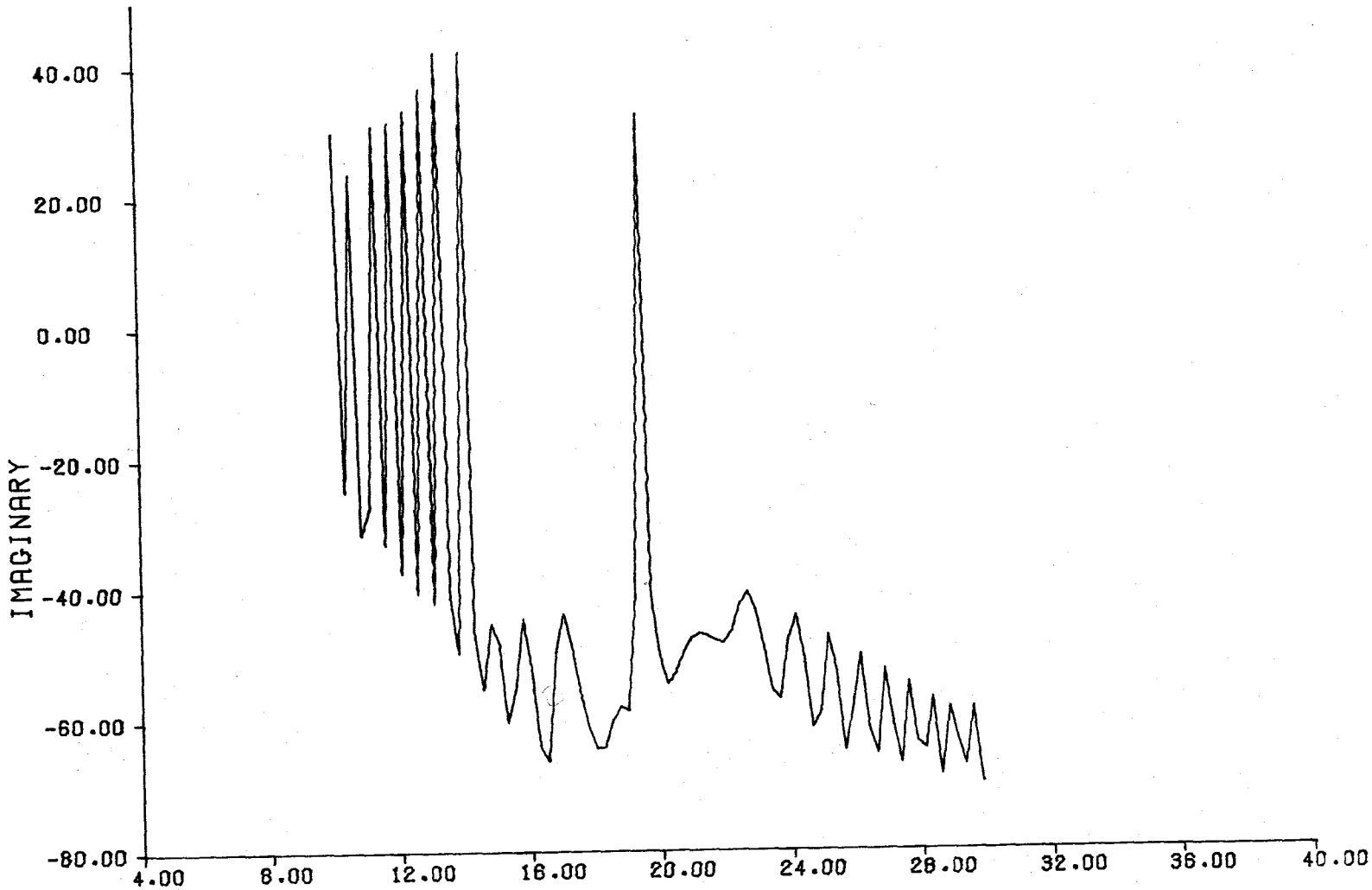

FIGURE 6.42 CONCLUDED (PAGE 2 OF 2)

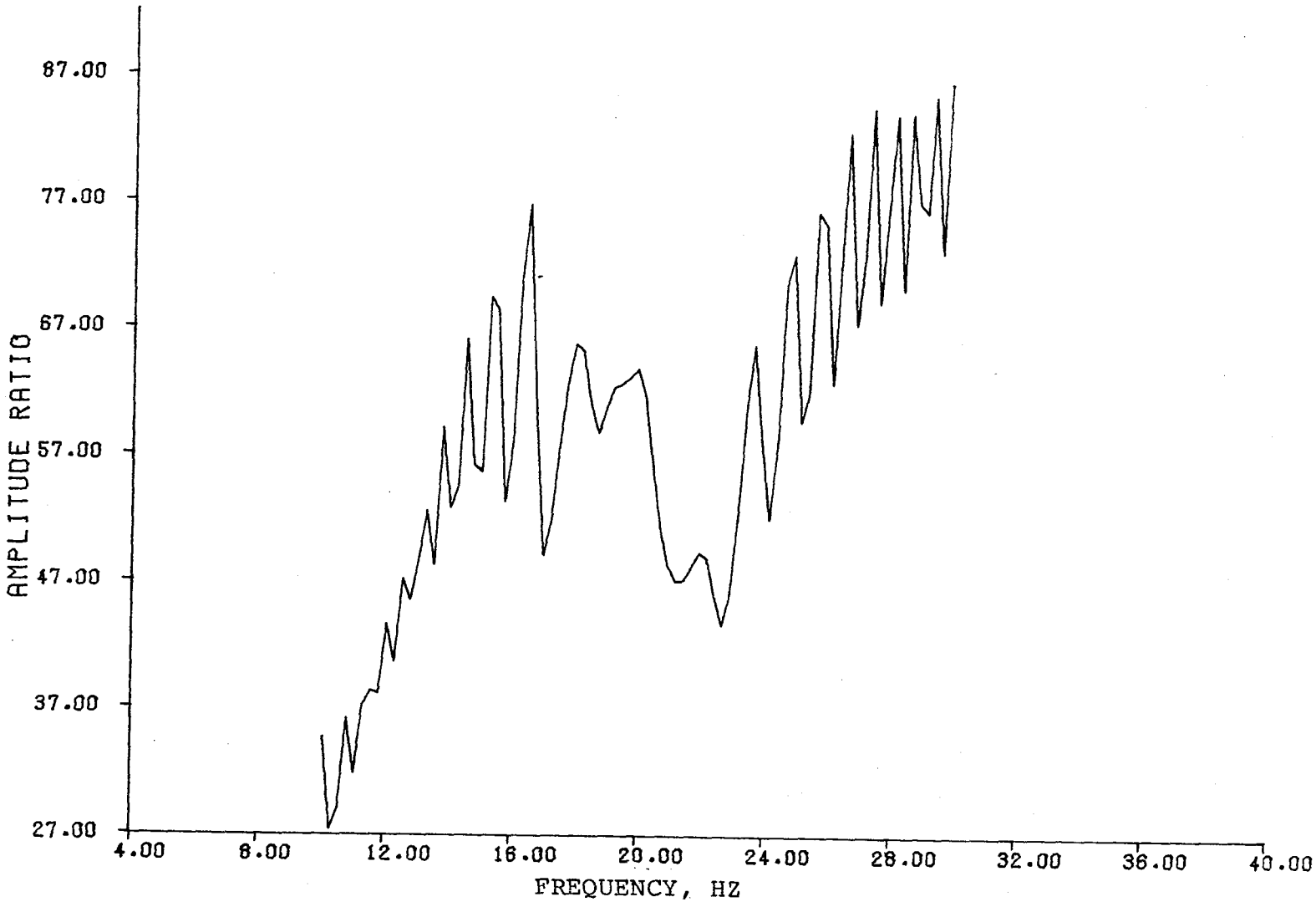

FIGURE 6.43 OPEN LOOP RESPONSE OFF OF CLOSED LOOP AMPLITUDE PHASE PLOT OF THE SUPERCRITICAL RESPONSE
(PAGE 1 OF 2)

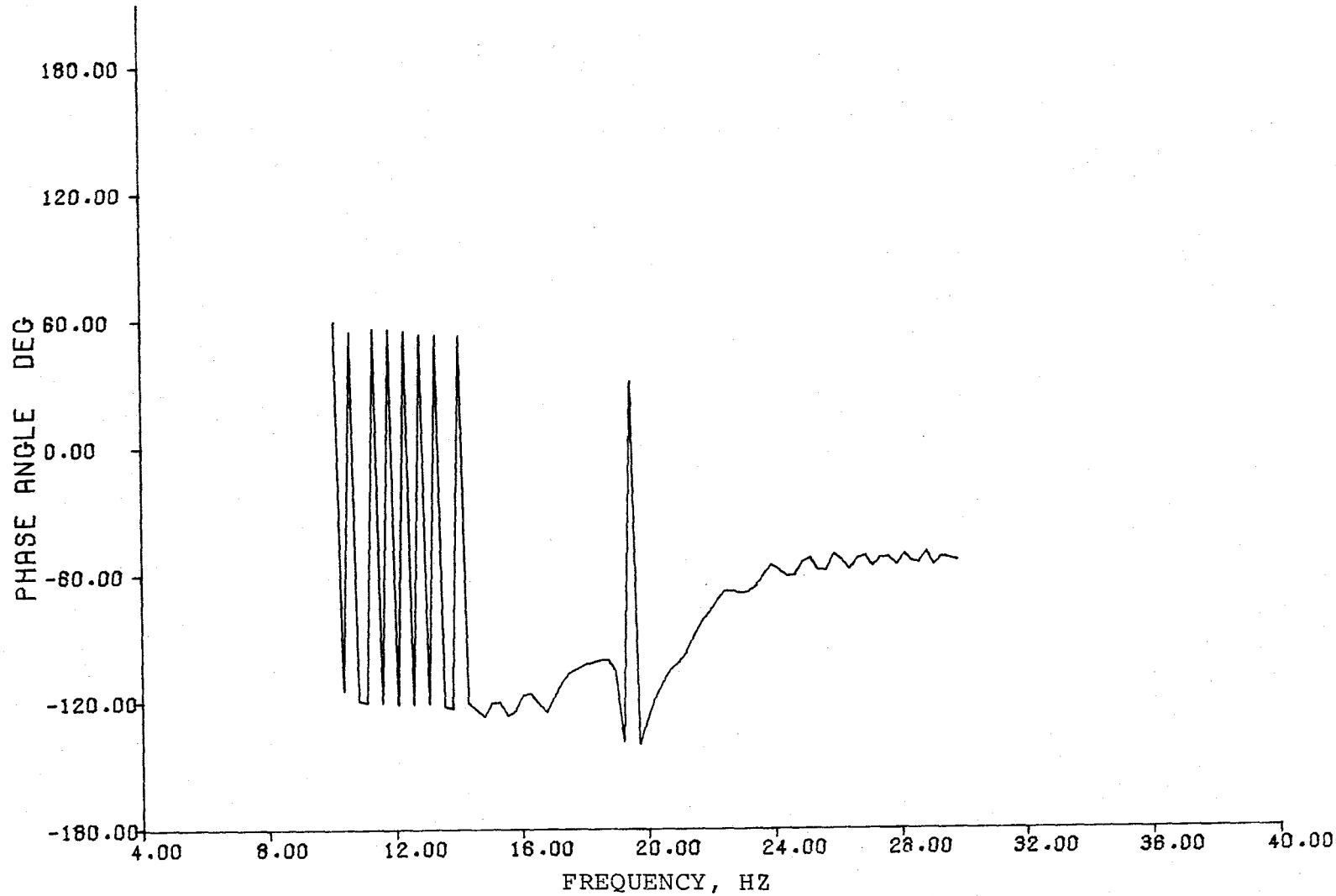

FIGURE 6.43 CONCLUDED (PAGE 2 OF 2)

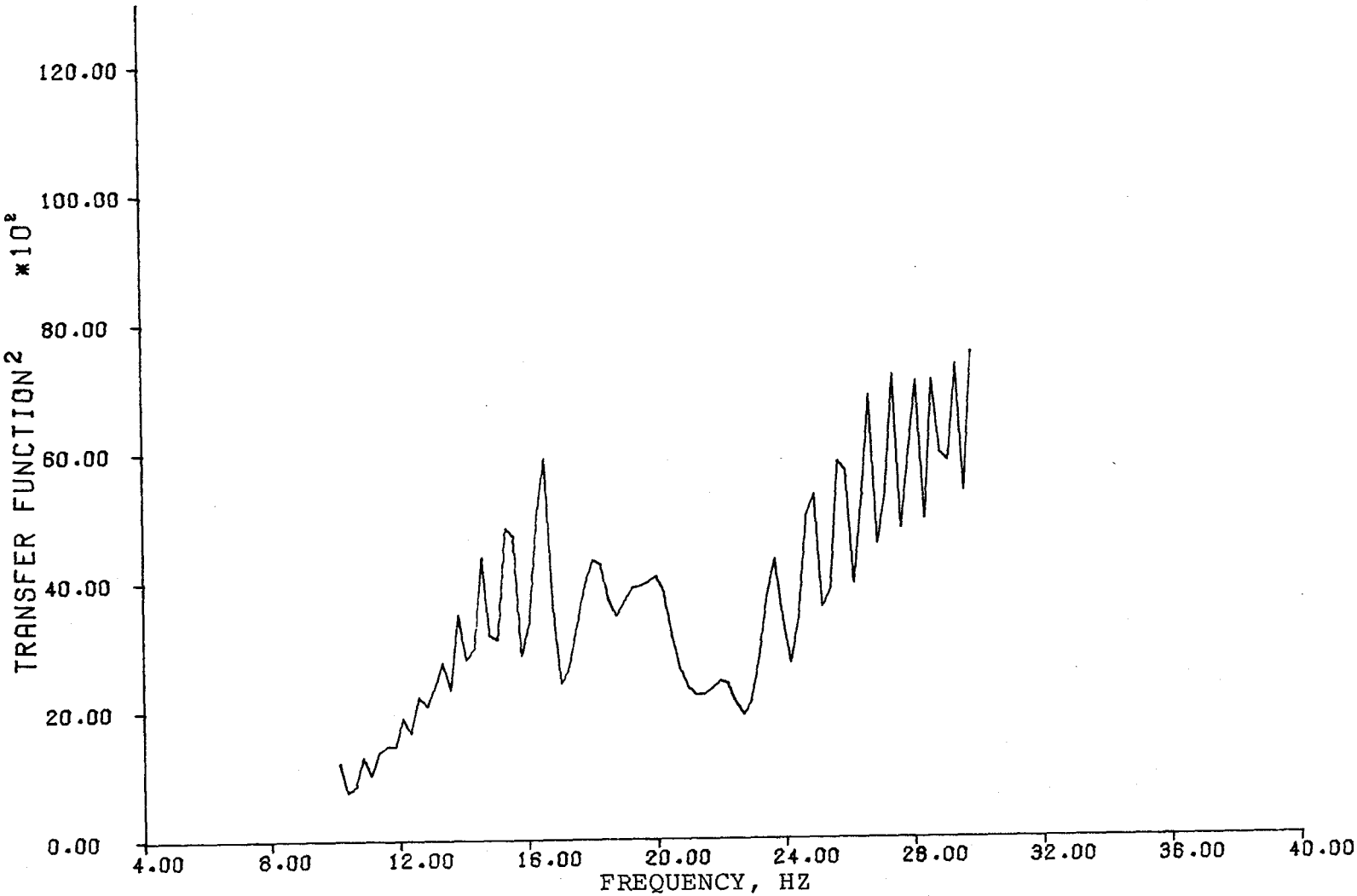

FIGURE 6.44 OPEN LOOP RESPONSE OFF OF CLOSED LOOP TRANSFER FUNCTION MODULUS OF THE SUPERCRITICAL RESPONSE

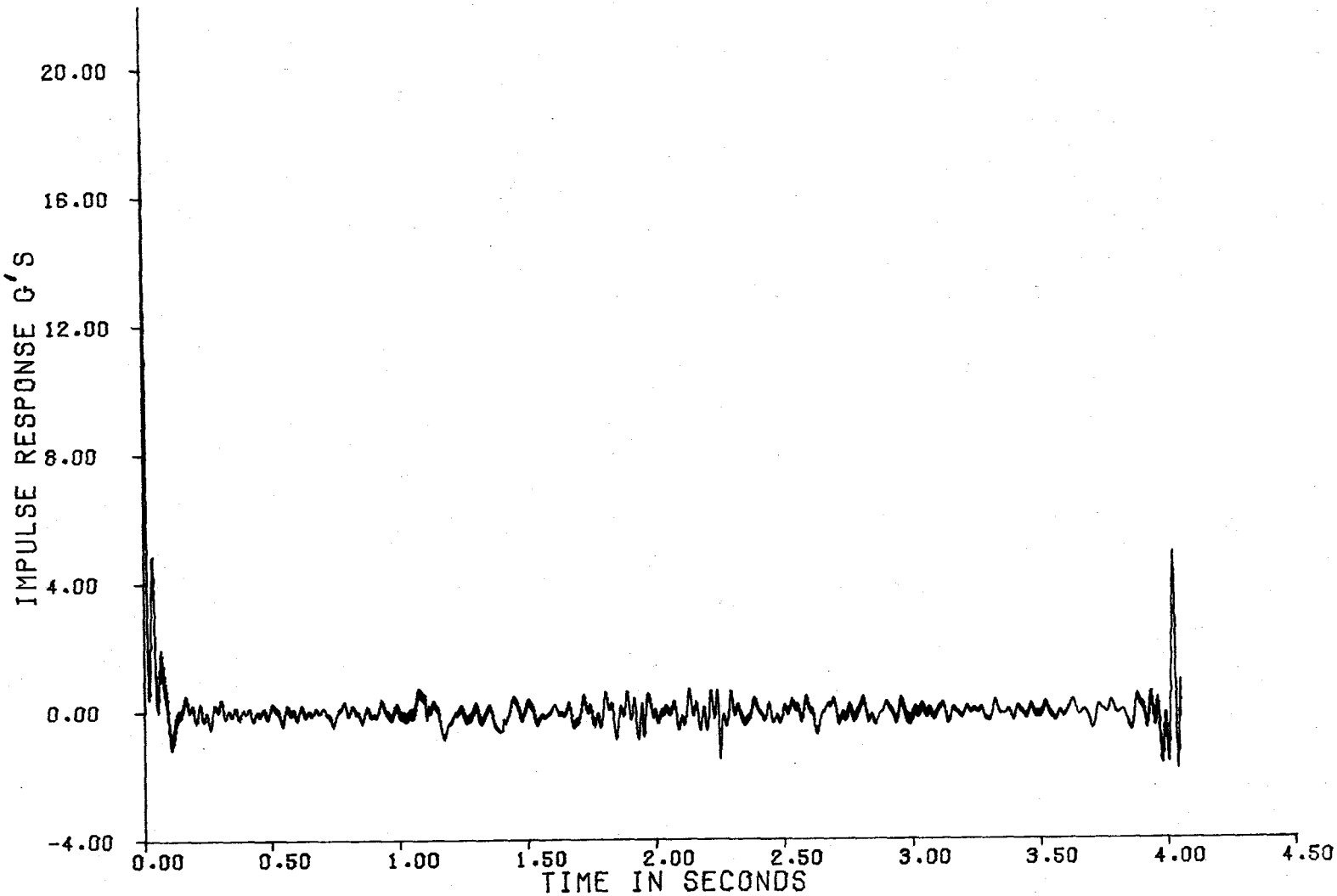

FIGURE 6.45 OPEN LOOP RESPONSE OFF OF CLOSED LOOP IMPULSE RESPONSE FUNCTION

engine noise, and separated flow will cause contamination of the data. The methods described previously all determined the frequency response transfer function in a way which will eliminate noise in the data. This is only true if the response due to the command excitation is a large portion of the total response. If on the other hand the majority of the response is due to the noise inputs the determination of the transfer function becomes an extremely difficult task (if not impossible).

Figure 6.46 shows the transient response of the ARW-1 FSS at M = 0.9, h = 3048 meters, and with a .3048 meters/sec rms gust level in the vertical axis. Peak accelerations are approximately 6 g's. The peak surface deflections are approximately 5.5 degrees. Since the amplitude of the command inputs are only 1 degree, it should be expected that with this input magnitude a reasonable H_2 estimate would be difficult to achieve. The "bursting" in the accelerometer trace is considered representative of the traces from wind tunnel and flight test results.

A determination of the rms level of the surface deflection, δ_s, in figure 6.46 has not been completed to date. Therefore no comparison in surface deflection requirements to BWC's predictions were made.

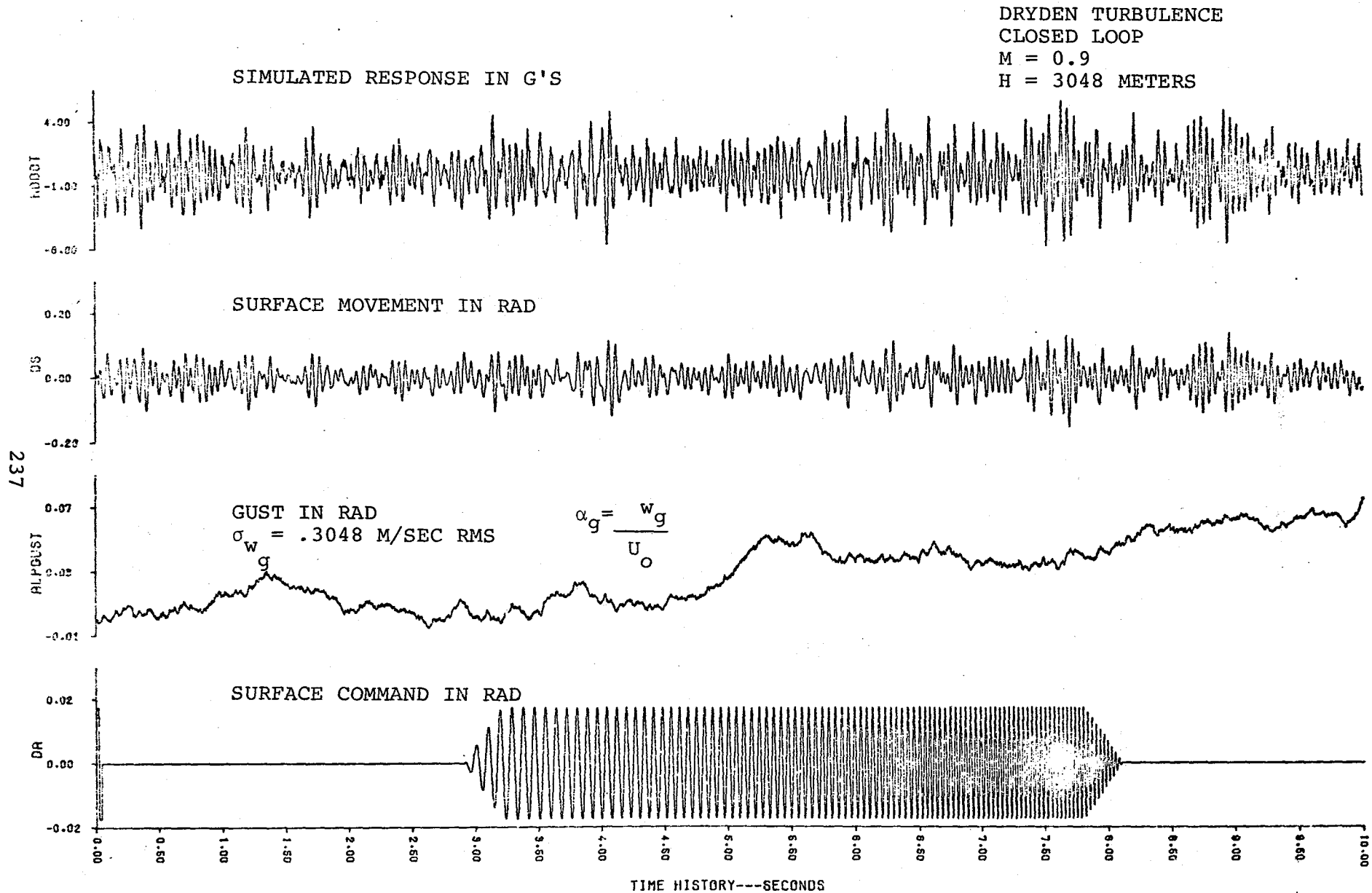

FIGURE 6.46 SUPERCRITICAL RESPONSE IN TURBULENCE

CHAPTER 7

CONCLUDING REMARKS AND RECOMMENDATIONS

7.1 Concluding Remarks

7.1.1 Vehicle Development

1. Based on analysis, the Boeing FSS design is predicted to stabilize the ARW-1 flutter mode the required 20 percent margin past the open loop boundary.
2. A digital remotely augmented rigid body control system which provides attitude and load limiting protection was designed and evaluated for the DAST I. Based on wind tunnel and DATCOM estimated rigid body aerodynamic characteristics, this RAV system meets the design specifications and has performed satisfactorily during real-time piloted simulations.
3. An on-board backup autopilot control system was designed to provide an envelop limiting command capability from an F-104 chase aircraft. The design has flight path control and wing leveling as automatic functions. Linear analysis and real-time simulations show this system to be satisfactory.

7.1.2 Evaluation of Flutter Methods

Simulated data was generated from a state variable representation of the DAST ARW-1 equations of motion. This data was used to evaluate candidate flutter

testing methods. The following conclusions can be drawn from the evaluation:

1. The five candidate methods all predicted modal frequencies accurately.
2. The damping estimates for noise free data are good for all the methods. However the PSD and transfer function modulus are more optimistic than the others.
3. If one mode dominates the accelerometer response the impulse response function can identify that one mode well.
4. Open loop and closed loop characteristics are both identifiable from their respective responses.
5. The concept of determining open loop characteristics from the closed loop responses with the flutter testing methods works very well for subcritical data. Although some modes are present in determining the open loop characteristic from the supercritical responses using Co-Quad and Amplitude-Phase methods, the open loop flutter mode was not readily identifiable with any of the methods examined.

7.2 Recommendations

1. Further investigation of determining unaugmented modal characteristics from closed loop responses should be investigated. The degradiation in the frequency and damping estimates by this method with noise input needs to be examined.

2. The effect noise has on the five techniques examined for near real-time testing needs examination. The results obtained from "noise free" data could be quite different if the same study were conducted with noisy inputs.
3. The non-linear loaded transfer function of the FSS actuator should be included in the simulation to make an accurate assessment of the surface rms displacement and rate requirements in turbulence and check for possible limit cycle tendencies.

REFERENCES AND BIBLIOGRAPHY

1. Roger,K. L. ; Hodges, G. E.; and Felt, L. : Active Flutter Suppression--A Flight Test Demonstration, J. of Aircraft, June 1975, pp. 551-556.

2. Matheny, N. W.; and Gatlin, D. H.: Flight Evaluation of the Transonic Stability and Control Characteristics of an Airplane Incorporating a Supercritical Wing, NASA TP 1167, February 1978.

3. Lake, A. A.: Basic Data Report for BQM-34F Supersonic Aerial Target, Teledyne Ryan Aeronautical Report TRA 16620-6, 5 October, 1973.

4. Edwards, J., W.; and Deets, D. A.: Development of a Remote Digital Augmentation System and Application to a Remotely Piloted Research Vehicle, NASA TND-7941, April 1975.

5. et. al.:Design Analysis of a Supercritical Wing for Test with a BQM-34F Drone Aircraft, Volume 1, Teledyne Ryan Aeronautical Report TRA 16669-11, 10 April, 1975.

6. Hoak, D. E.; and Ellison, D. E.; and et. al.: USAF Stability and Control Datcom. Flight Control Divison, Air Force Flight Dynamics Laboratory, Wright-Patterson Air Force Base, Ohio 45433,1974.

7. Heffhey, R. K.; and Jewell, W. F.: Aircraft Handling Qualities Data, Systems Technology Inc. Technical Report 1004-1, Hawthowne, Cal., May 1972.

8. Edwards, J. W.: A FORTRAN Program for the Analysis of Linear Continuous and Sampled-Data Systems, NASA TM X-56038, January 1976.

9. Roskam, J. : Flight Dynamics of Rigid and Elastic Airplanes, Published by Author,(1973).

10. Visor, O. E.; and Sevart, F. D. : Preliminary Design Study of a Flutter Suppression Control System for the BQM-34E/F Drone Aircraft with a Supercritical Wing, NASA CR-132480, 1977.

11. Houbolt, J. C. : Subcritical Flutter Testing and System Identification, NASA CR-132480, August 1974.

12. Flight Flutter Testing: Proceedings of the 1975 Symposium at NASA DFRC, NASA SP-415, October 1975.

13. Roskam, J.: Methods for Estimating Stability and Control Derivatives of Conventional Subsonic Airplanes, Published by Author, (1973).

14. Flight Flutter Testing: Proceedings of the 1958 Symposium at Washington, D. C., NASA SP-385, 1958.

15. Cheng, Y. : Applications of Active Controls Technology to Gust Alleviation Systems for Tilt Rotor Aircraft, NASA CR-137958, November 1976.

16. Dynamics of the Airframe, Basic Volume, Northrop Aircraft, Inc. Report AE=61-4 II, September 1952.

17. Parks, W. C. ; and Riley, T. V.: Stability and Control Report for the BQM-34E/F Supersonic Aerial Target, Teledyne Ryan Aeronautical Report TRA -166654-10, 1971.

18. Petersen, K. L. : Evaluation of an Envelope Limiting Device Using Simulation and Flight Test of a Remotely Piloted Research Vehicle, NASA TN D-8216, April 1976.

19. Painter, G. H. : Ground Vibration and Compliance Data Report for BQM-34E/F Supersonic Aerial Targets, Teledyne Ryan Aeronautical Report TRA 16651-10B, 1 October, 1975.

20. Rickard, N. D. : Flutter and Vibration Basic Data Report ofr BQM-34E/F Supersonic Aerial Target, Teledyne Ryan Aeronautical Report TRA 16651-26, 21 November, 1972.

21. Zoldos, A. J. : Preliminary Flutter and Vibration Report for BQM-34E/F Supersonic Aerial Target, Teledyne Ryan Aeronautical Report TRA 16651-3B, 7 January, 1972.

22. Bisplinchoff, R. L.; Ashley, H.; and Halfman, R. L.: Aeroelasticity. Addison-Weslsey Publishing Company, Inc., Reading, Mass., (1957).

23. Hoy, W. : Structural Description Report for BQM-34E/F Supersonic Aerial Target, Teledyne Ryan Aeronautical Report TRA 16642-26, 7 January, 1972.

24. Edwards, J. W. : Unsteady Aerodynamic Modeling and Active Aeroelastic Control, Stanford University Report SUDAAR 504, February 1977.

25. Aircraft Load Alleviation and Mode Stabilization, AFFDL-TR-68-158, Air Force Flight Dynamics Lab., Wright-Patterson Air Force Base, Ohio, December 1968.

26. Jones, R. T. : The Unsteady Lift of a Wing of Finite Aspect Ratio, NACA Report No. 681, 1940.

27. Theodorsen, T.: General Theory of Aerodynamic Instability and the Mechanism of Flutter, NACA Report No. 496, 1935.

28. Theodorsen, T.; and Garrick, I. E. : Mechanism of Flutter, a Theoretical and Experimental Investigation of the Flutter Problem, NACA Report No. 685, 1940.

29. Vepa, R. : Finite State Modeling of Aeroelastic Systems, Ph. D. Dissertation, Dept. of Applied Mechanics, Stanford University, Stanford, Ca., 94305, June 1975.

30. Edwards, J. W. : Active Flutter Control Using Generalized Unsteady Aerodynamic Theory,Paper presented at AIAA Atmospheric Flight Mechanics Conference, Hollywood, Florida, August 1977.

APPENDIX A

DAST ARW-1 AERODYNAMIC CHARACTERISTICS

This appendix presents the rigid body aerodynamic data developed for the DAST I flight simulator and control systems analysis. The derivatives for the DAST are given as functions of Mach number and angle of attack to make them compatable with the NASA DFRC simulation. The lateral-directional derivatives are in the body axis coordinate system while the longitudinal derivatives, C_L, C_D, and C_m are in the stability axis system.

A.1 Static Aerodynamic Characteristics

A.1.1 Longitudinal Coefficients - Lift, drag and pitching moment coefficients for the Mach number conditions tested in the NASA LaRC 8-foot Transonic Dynamic Tunnel are shown in figure A.1. The angle of attack of the wind tunnel tests varied from approximately -4 degrees to 12 degrees. The pitch-up characteristics of the DAST I is evident in these figures. When M = .90, the change in lift curve slope and pitching moment coefficient becomes very pronounced at about seven degrees angle of attack. This behavior was present on the F-8 SCW aircraft and is attributed to spanwise separation of airflow near the wing tip.

In order to obtain the angle of attack derivatives

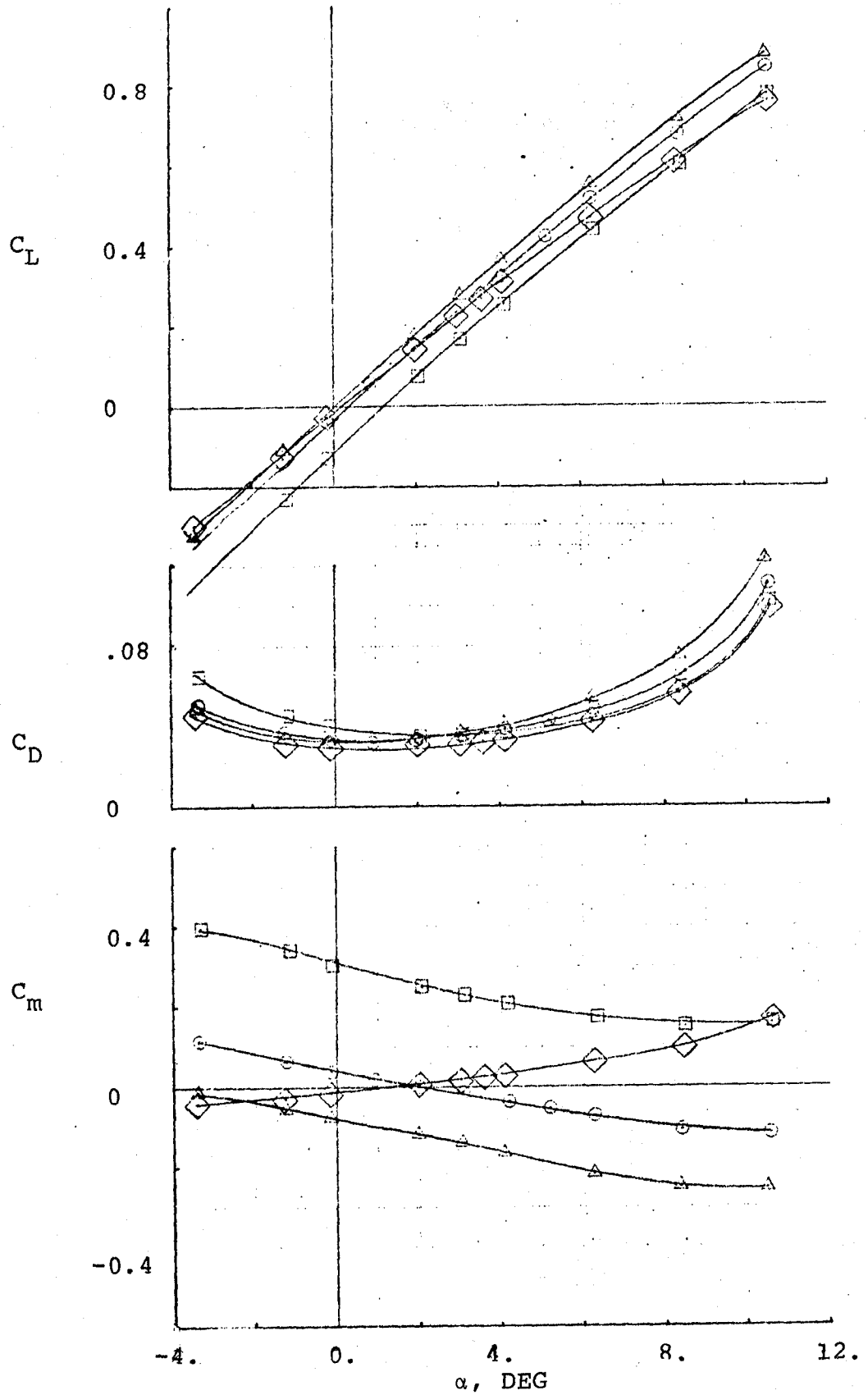

FIGURE A.1 LIFT, DRAG AND PITCHING MOMENT COEFFICIENT VARIATION WITH ANGLE OF ATTACK (PAGE 1 OF 6)

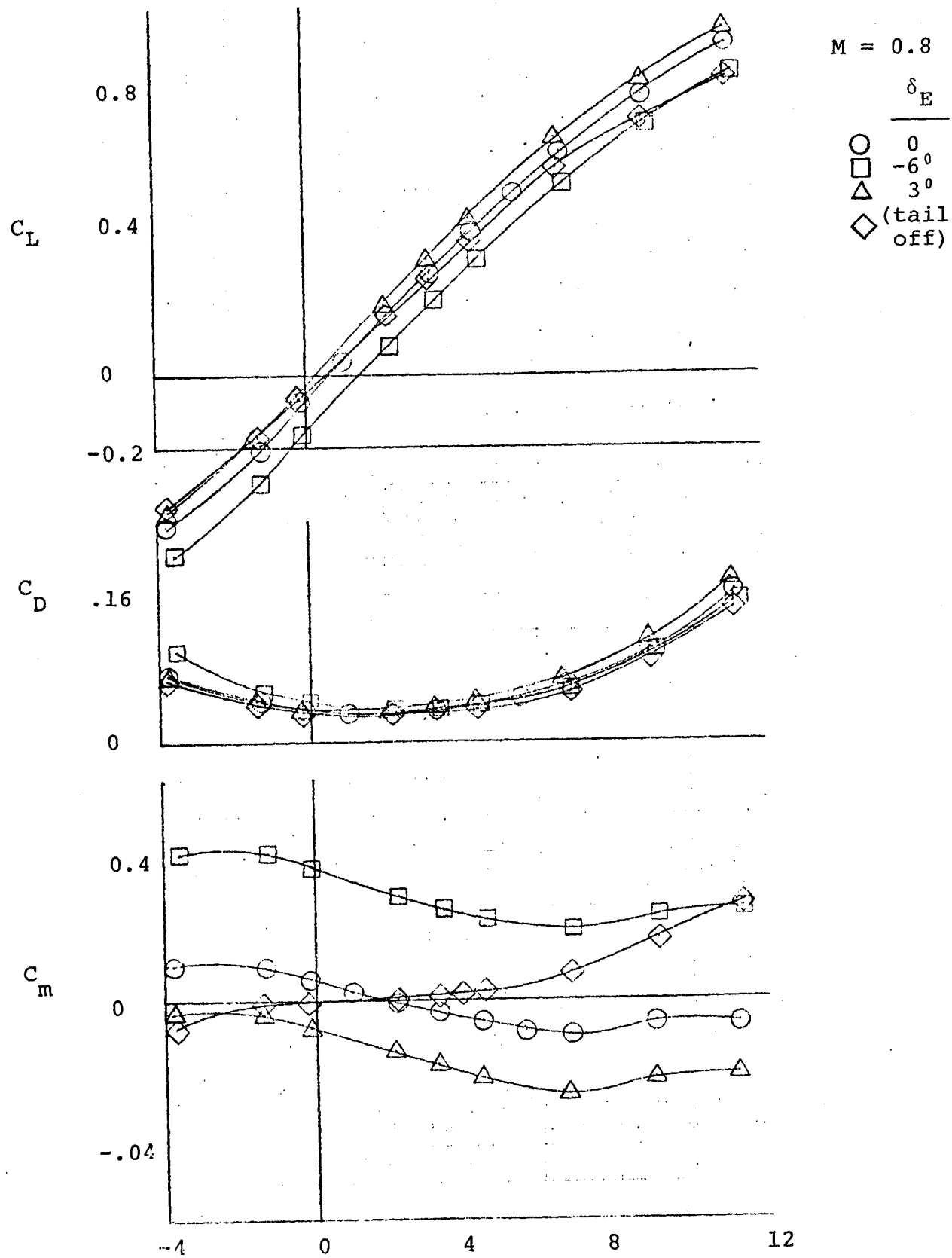

FIGURE A.1 (CONTINUED) (PAGE 2 OF 6)

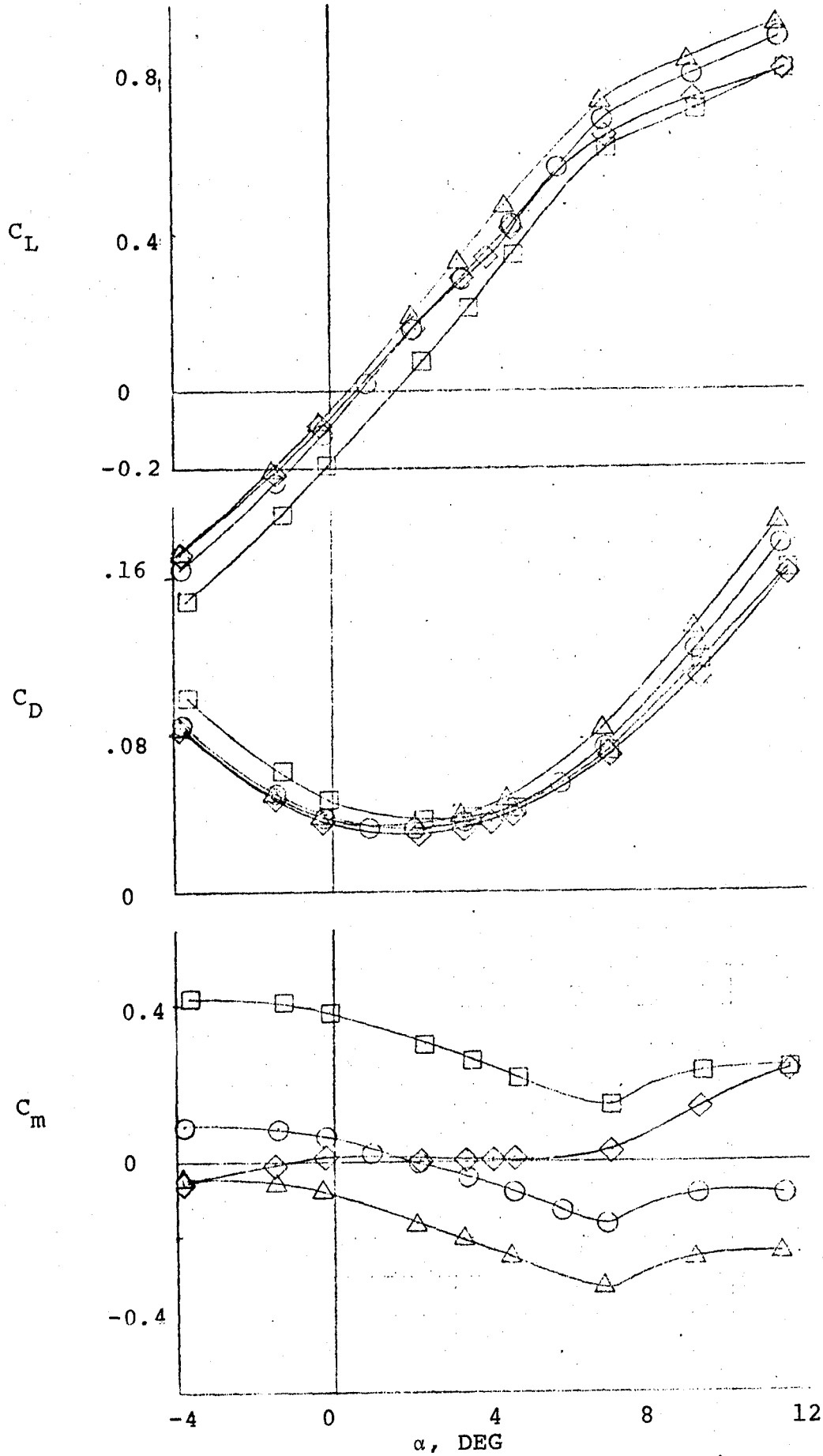

FIGURE A.1 (CONTINUED) (PAGE 3 OF 6)

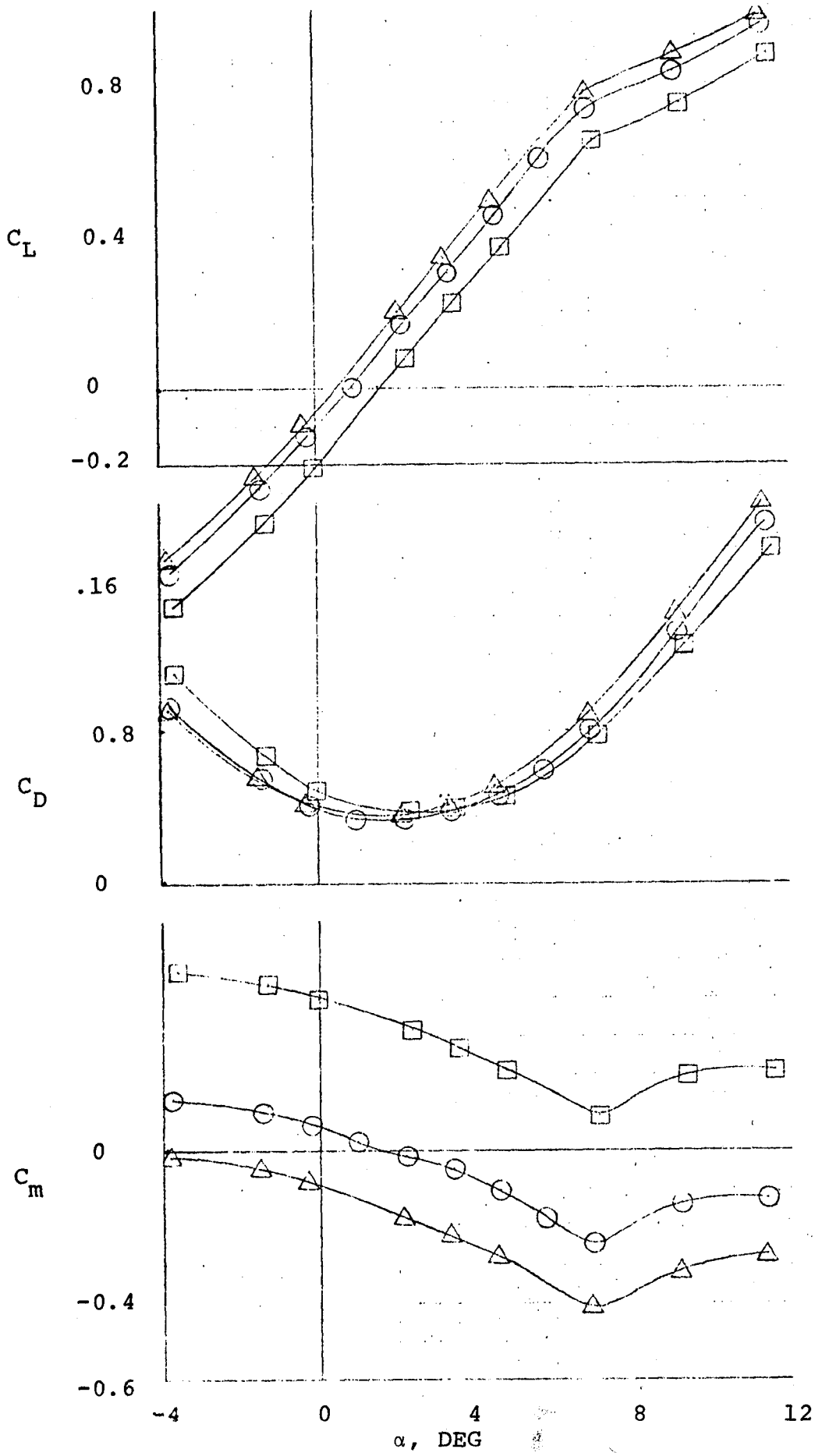

FIGURE A.1 (CONTINUED) (PAGE 4 OF 6)

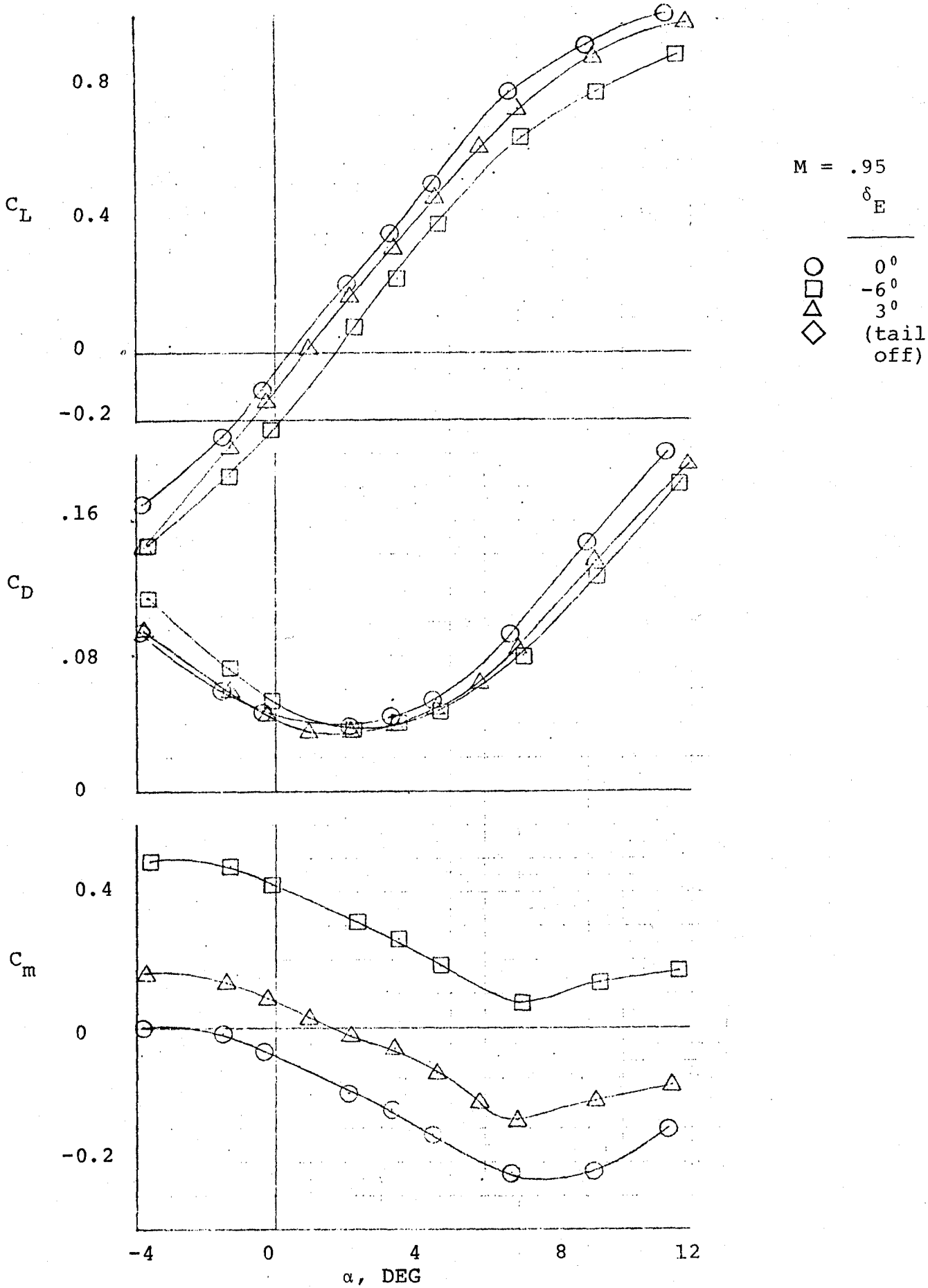

FIGURE A.1 (CONTINUED) (PAGE 5 OF 6)

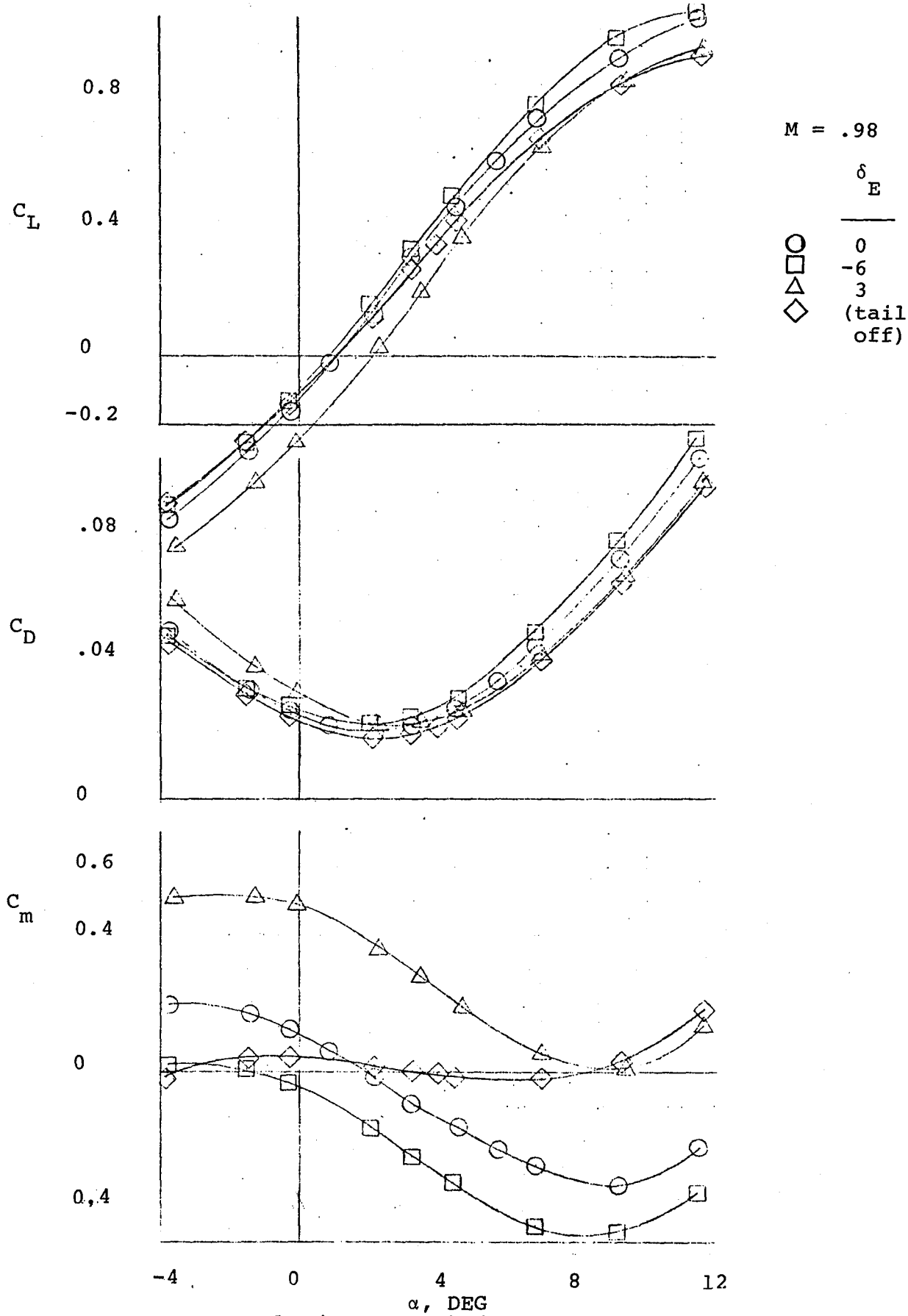

FIGURE A.1 (CONTINUED) (PAGE 6 OF 6)

C_{D_α} and C_{m_α} in the next section, trim points from the C_L versus C_m curves in figure A. 2 were found. This allows a determination of the trim C_L and C_D from the drag polars also presented in figure A. 2, referring these conditions back to figure A. 1. The slope of the drag and pitching moment curves can then be established at trim conditions.

A.1.2 Angle of Attack Derivatives - The plot of C_{L_α} at various Mach numbers and angles of attack is shown in figure A. 3 along with the effective intercept coefficient C_{L_O}. The maximum value of C_{L_α} is 7.74 per radian (.135 per degree) and occurs at M=.98 and two degrees angle of attack. The dashed lines after M=.98 represent the extrapolated data. By using an effective slope intercept coefficient C_{L_O}, non-linear lift curves can be represented. Observing C_{L_α} for six degrees and eight degrees angle of attack in figure A.3, the large change in C_{L_α} associated with the tip separation can be seen.

The power-off rate of change of drag coefficient with angle of attack is shown in figure A.4. Here C_{D_O} is also the effective intercept coefficient. These derivatives are determined at trim conditions. It is interesting to note that C_{D_α} is still negative at almost two degrees angle of attack. A great amount of testing will be done below two degrees angle of attack in the FSS flight experiment. The dip in C_{D_α} and C_{D_O} corresponds to the dip in C_{L_α}

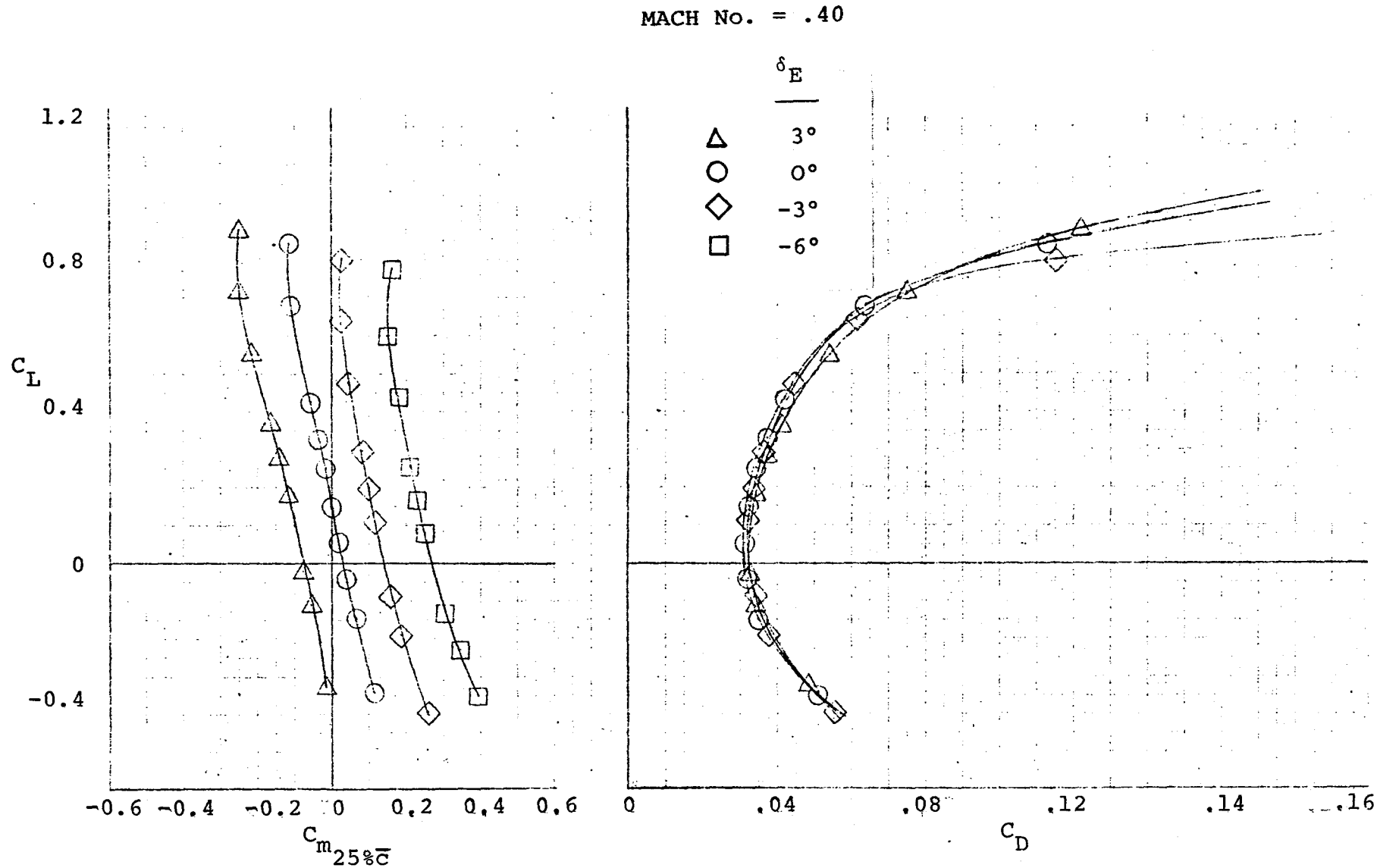

FIGURE A.2 STATIC STABILITY DATA AND FIREBEE DAST DRAG POLARS

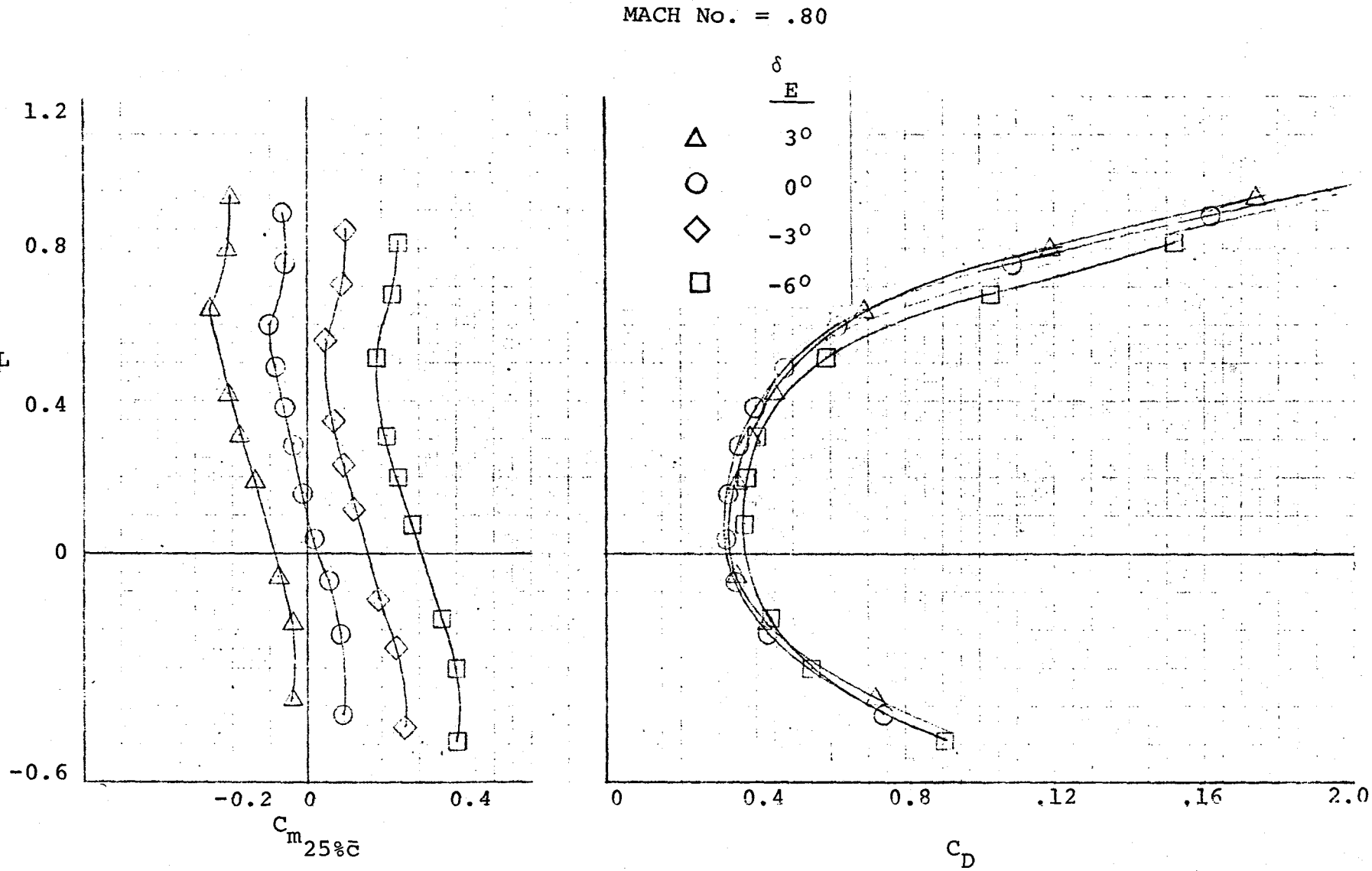

FIGURE A.2 (CONTINUED) (PAGE 2 OF 6)

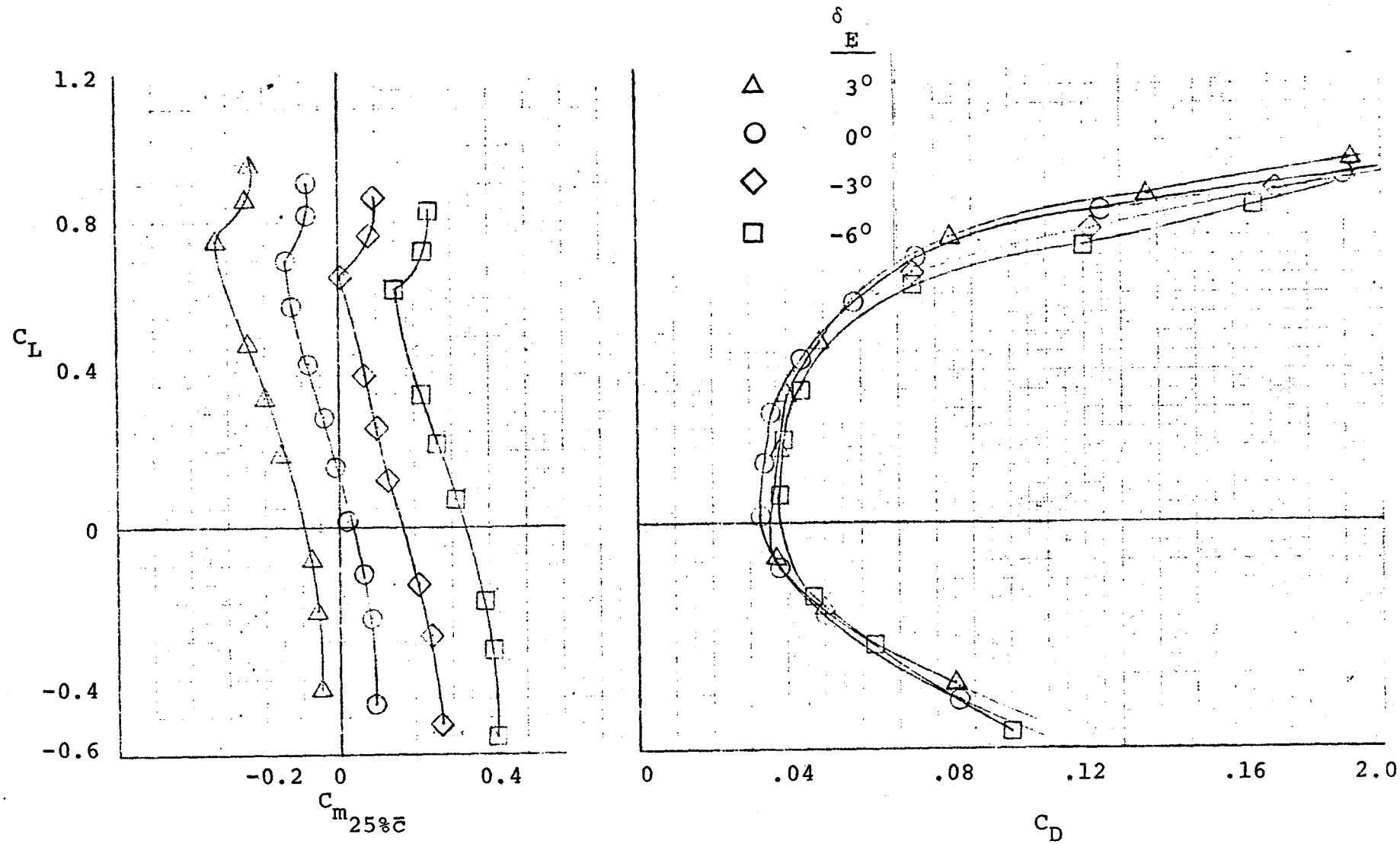

FIGURE A.2 (CONTINUED) (PAGE 3 OF 6)

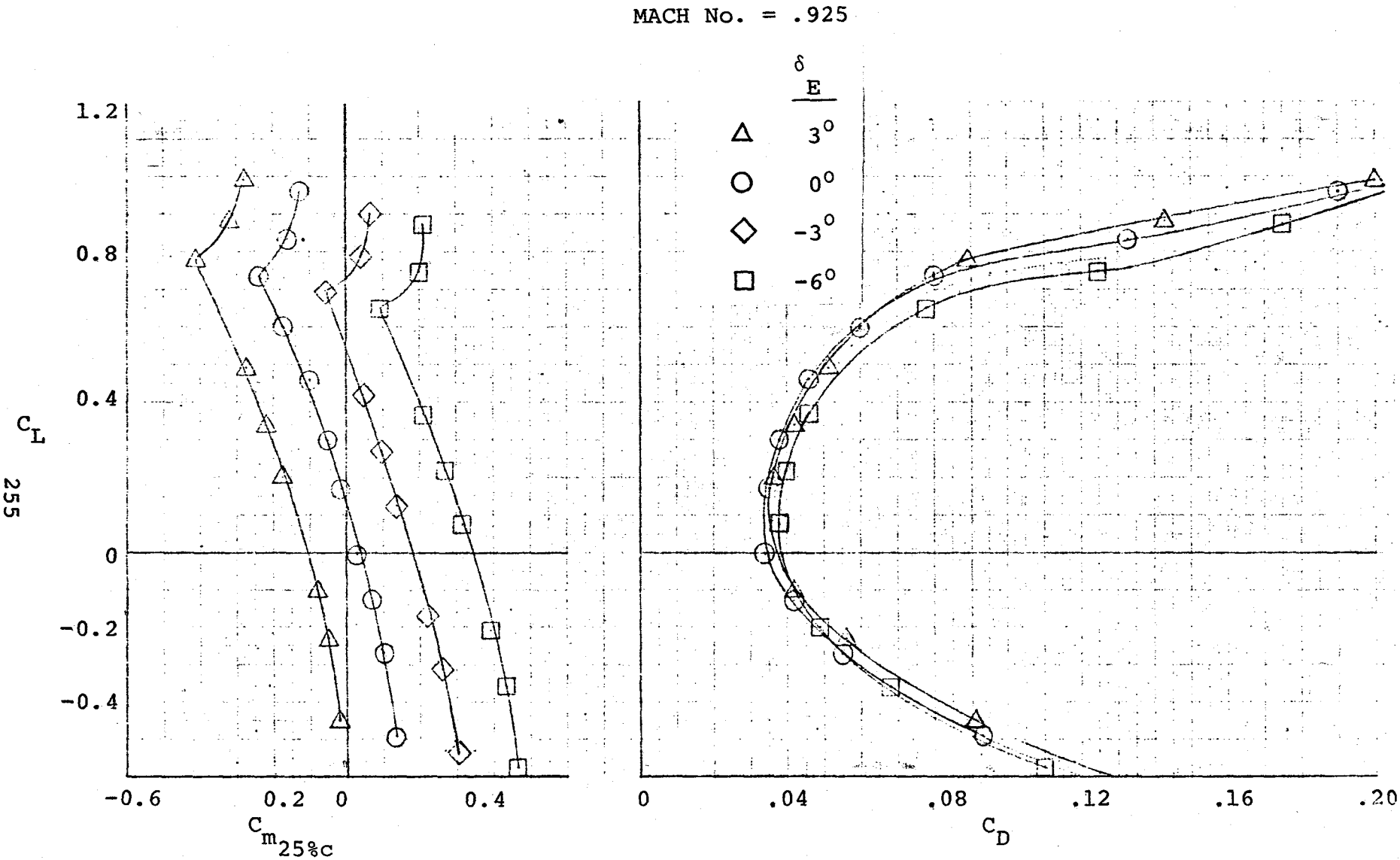

FIGURE A.2 (CONTINUED) (PAGE 4 OF 6)

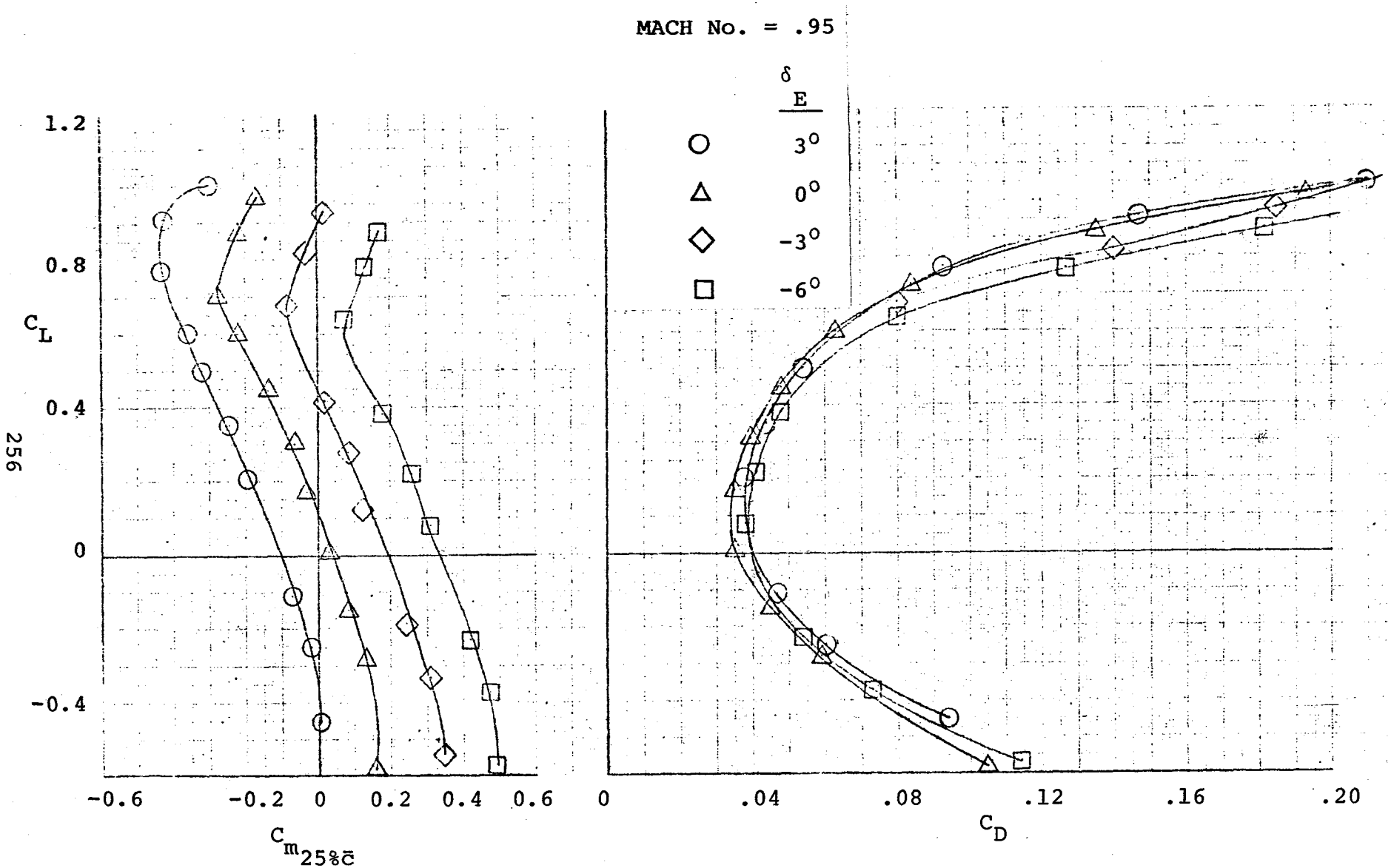

FIGURE A.2 (CONTINUED) (PAGE 5 OF 6)

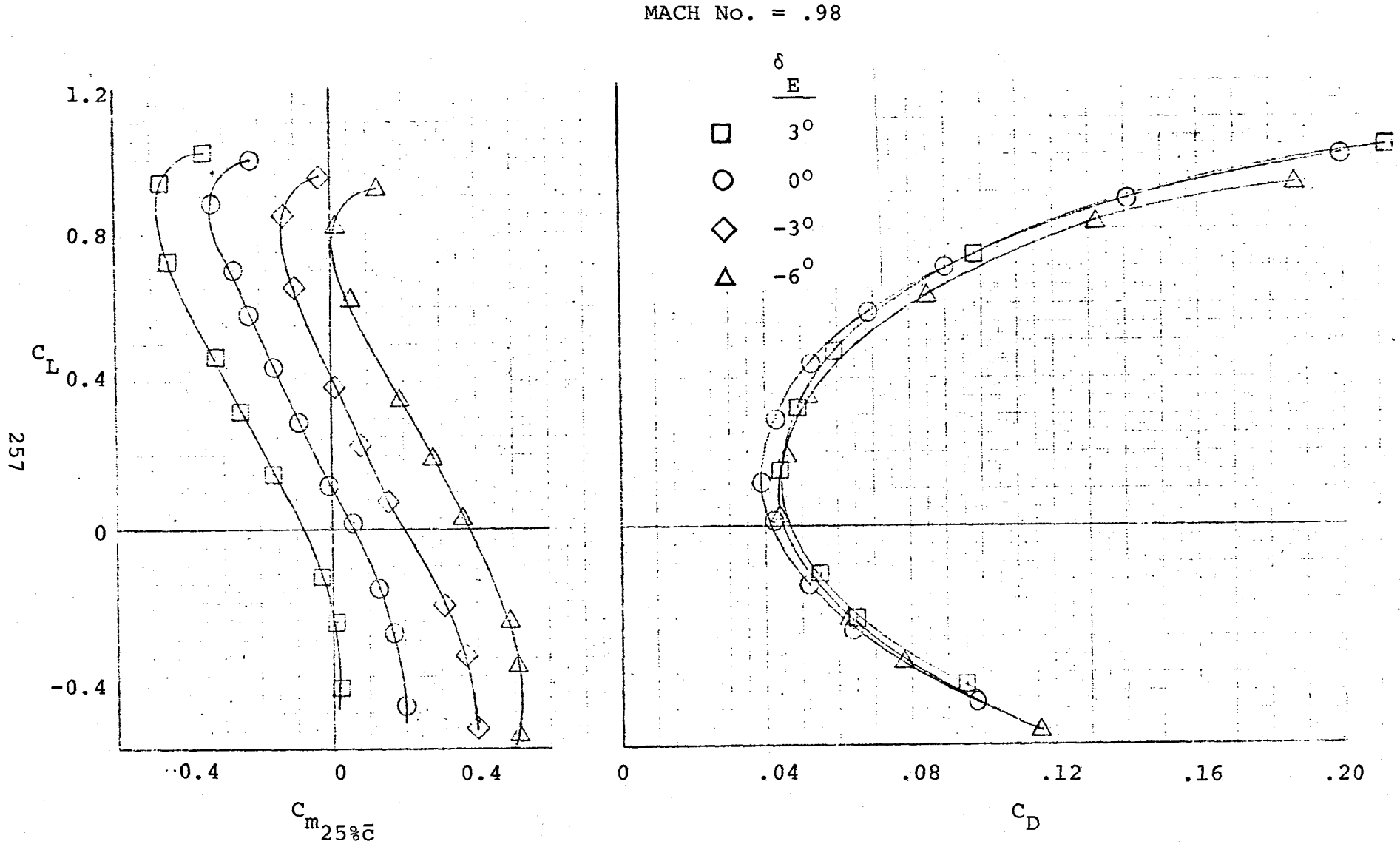

FIGURE A.2 (CONTINUED) (PAGE 6 OF 6)

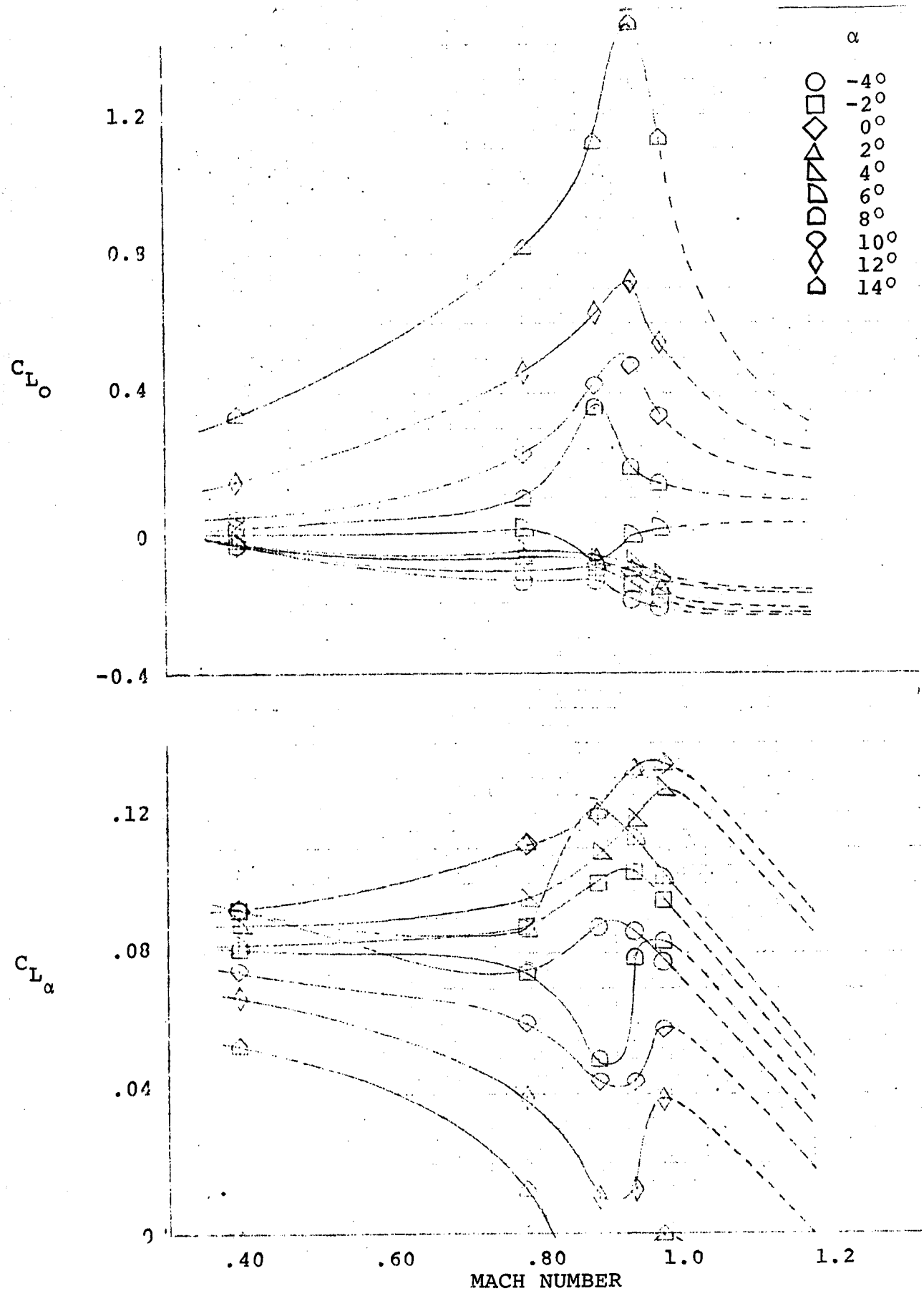

FIGURE A.3 VARIATION IN LIFT CURVE SLOPE AND EFFECTIVE INTERCEPT WITH MACH NUMBER AT VARIOUS ANGLES OF ATTACK

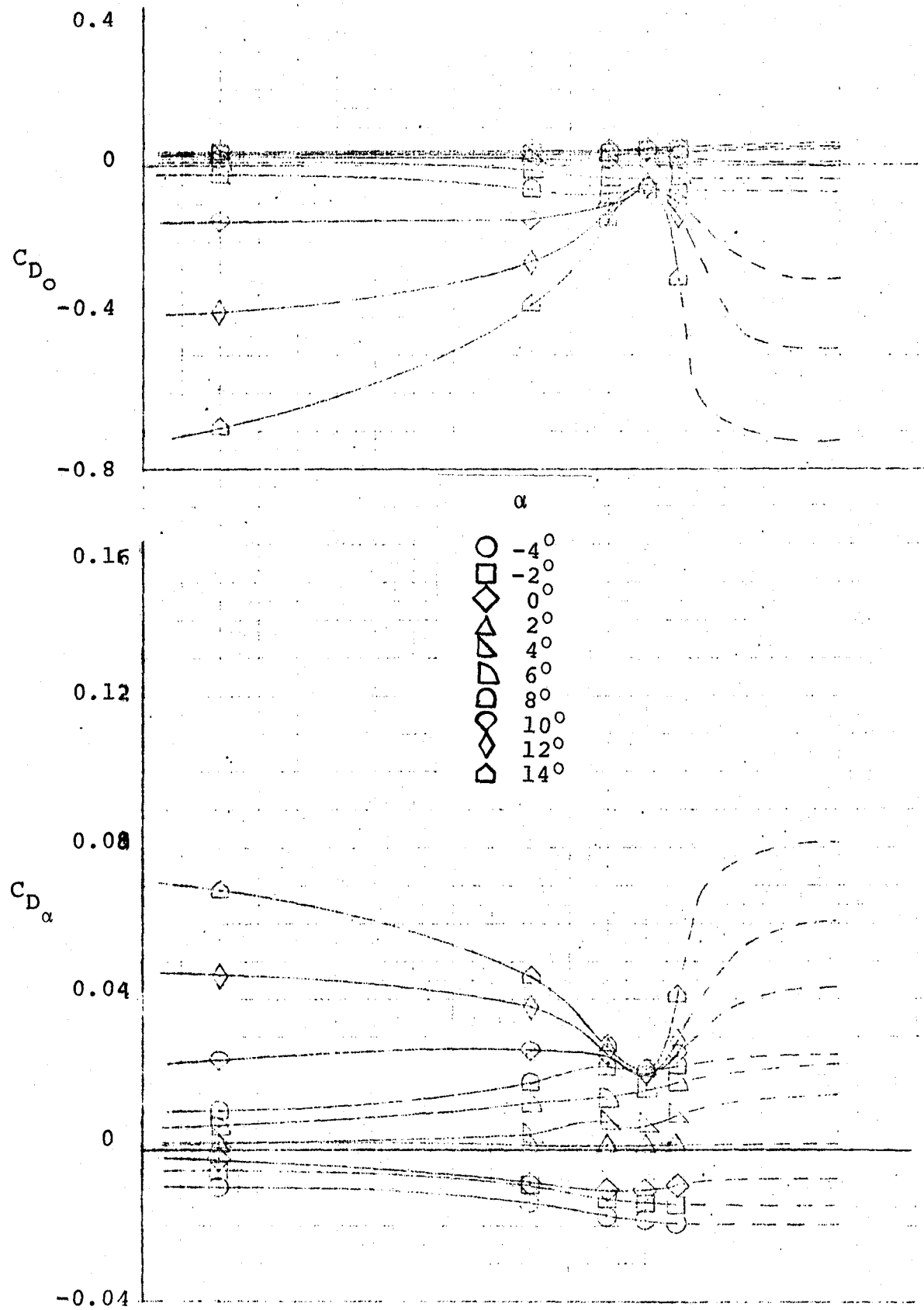

FIGURE A.4 VARIATION IN RATE OF CHANGE OF DRAG COEFFICIENT AND EFFECTIVE INTERCEPT WITH MACH NUMBER AT VARIOUS ANGLES OF ATTACK

and C_{L_o} associated with the tip separation problem discussed earlier.

The rate of change of pitching moment coefficient with angle of attack is shown in figure A.5. The large positive values of C_{m_α} due to pitch-up are very apparent. It can be seen that the change in sign of C_{m_α} occurs very abruptly. The slope intercept coefficient C_{m_o} is also shown in figure A.5.

A.1.3 Longitudinal Control Derivatives - Values of the rate of change in lift coefficient with horizontal tail deflection are shown in figure A.6. Control surface effectiveness increases substantially between M = .9 and M = .98. In comparison with the basic Firebee drone, $C_{L_{\delta_E}}$ for DAST is approximately 27 percent greater although the ratio of Firebee reference areas to DAST reference area is 1.07.

The rate of change of drag coefficient with horizontal tail deflection is presented in figure A.7. Trim points were found from the C_L versus C_m curves of figure A.2 and the increase in drag coefficient at that horizontal tail deflection is determined from the corresponding drag polars also in figure A.2 The increment in drag coefficient is then divided by the amount of tail deflection to trim the aircraft and the result is $C_{D_{\delta_E}}$. A "hump" in the $C_{D_{\delta_E}}$ curve in figure A.7 is evident around

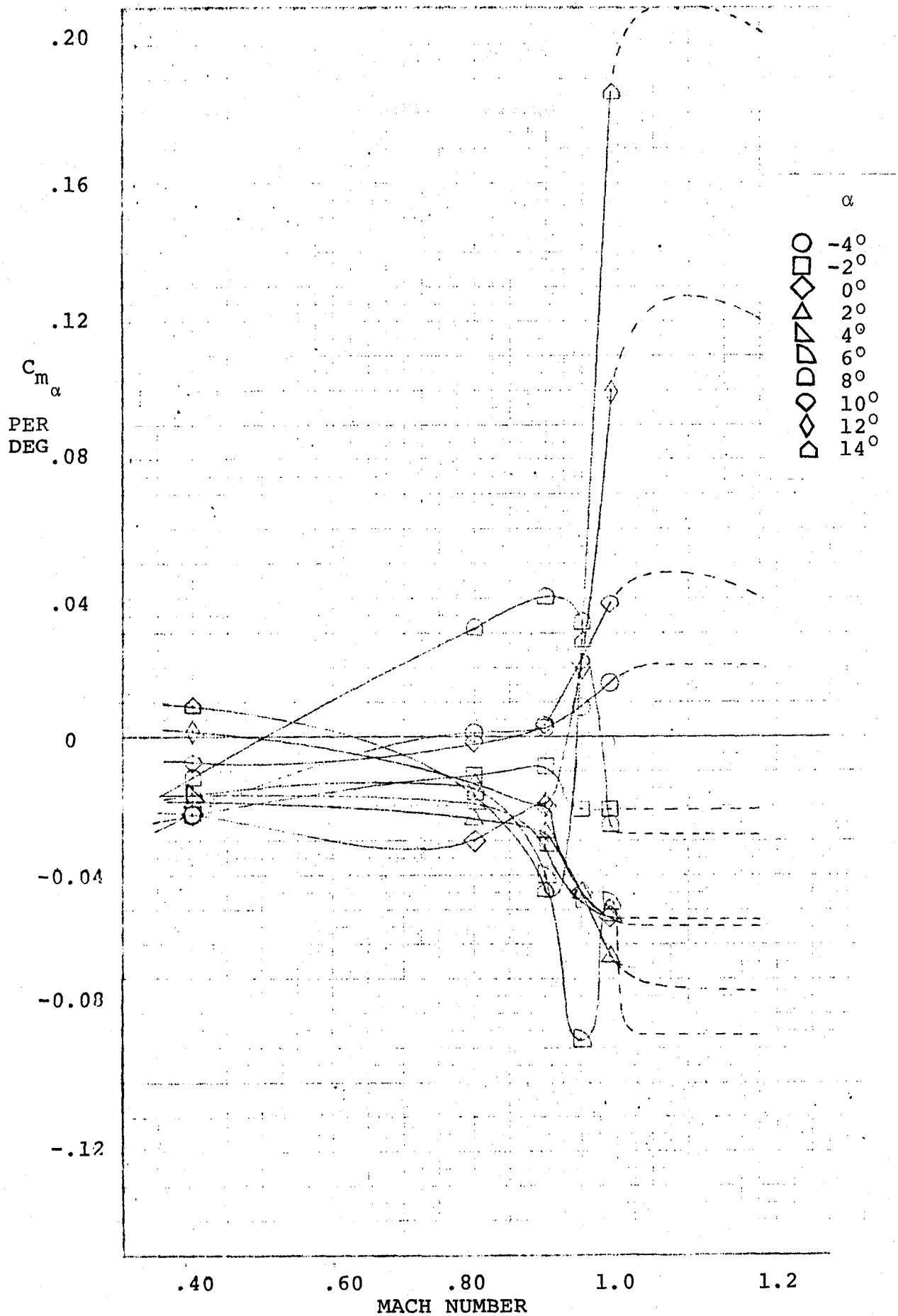

FIGURE A.5 VARIATION IN RATE OF CHANGE OF PITCHING MOMENT WITH MACH NUMBER AT VARIOUS ANGLES OF ATTACK

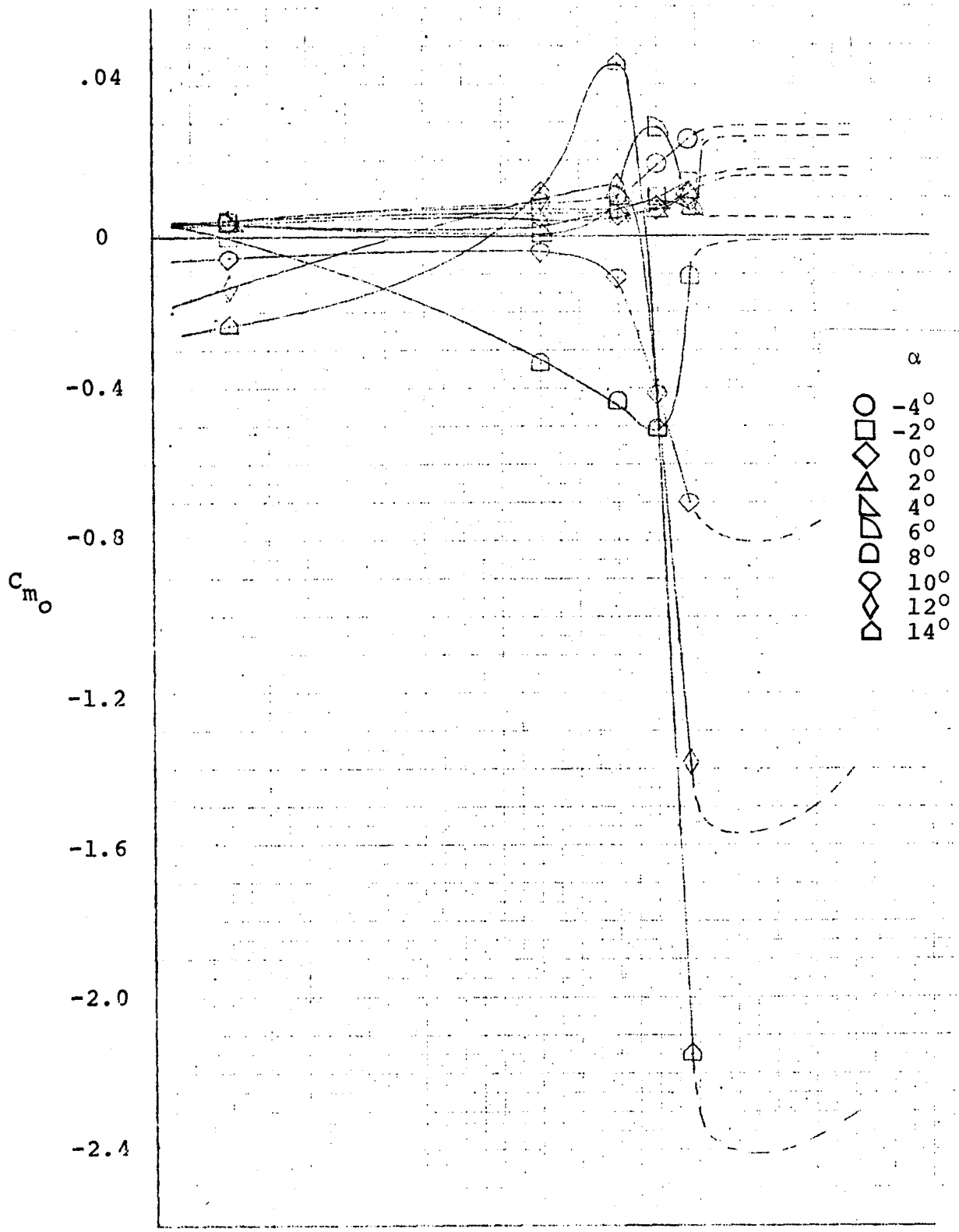

FIGURE A.5 (CONCLUDED)

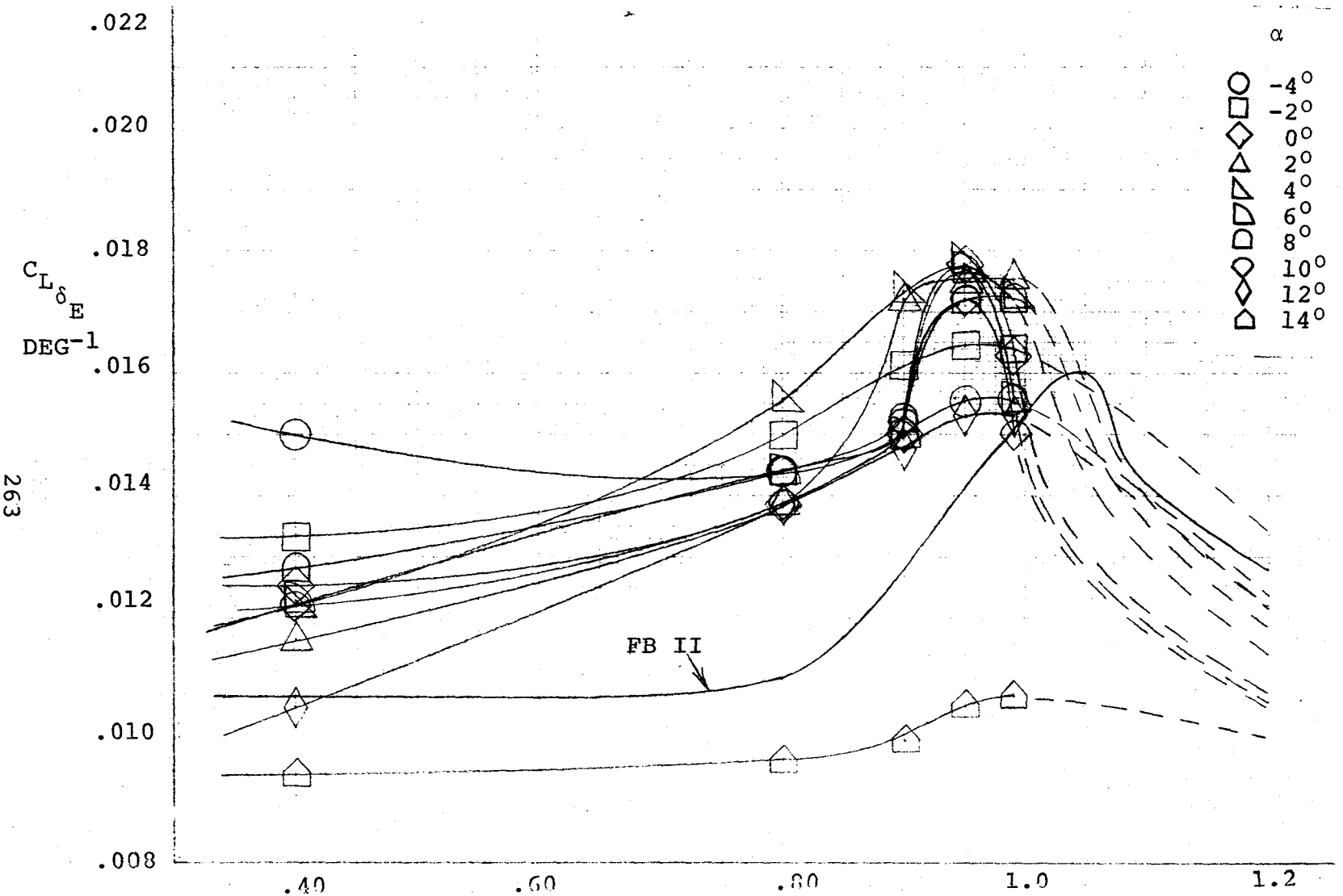

FIGURE A.6 VARIATION IN RATE OF CHANGE IN LIFT COEFFICIENT WITH HORIZONTAL TAIL DEFLECTION WITH MACH NUMBER AT VARIOUS ANGLES OF ATTACK

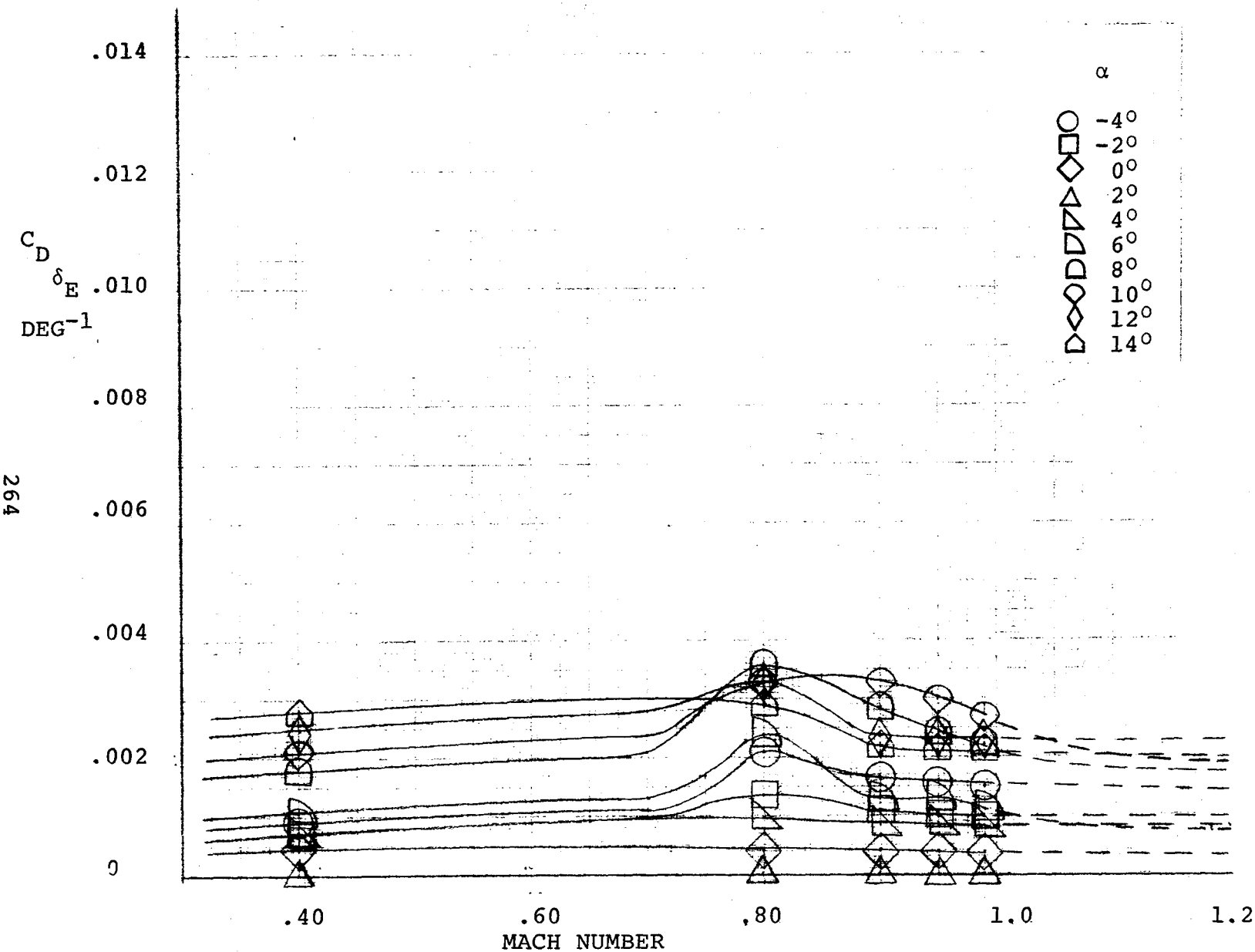

FIGURE A.7 VARIATION IN RATE OF CHANGE OF DRAG COEFFICIENT WITH HORIZONTAL TAIL DEFLECTION WITH MACH NUMBER AT VARIOUS ANGLES OF ATTACK FOR THE DAST

M = .80. The initial rise in $C_{D_{\delta_E}}$ is attributed to a rearward shift in the aircraft aerodynamic center. The decrease is associated with less trim deflection required because of the separation at the wing tip.

The derivative $C_{m_{\delta_E}}$ is presented in figure A.8. All wind tunnel data were referenced to 25 percent MAC of the wing. The magnitude of $C_{m_{\delta_E}}$ for DAST is approximately twice that of the basic Firebee drone.

A.1.4 Lateral-Directional Coefficients - Wind tunnel data for the DAST I showed that the lateral-directional coefficients, C_ℓ, C_n, and C_Y were mildly non-linear with respect to sideslip angle. No provisions exist in the simulation equations to include this effect. Since the effect worsened with larger sideslip angles the assumption was made to use the values which exist at small ($\pm 3^\circ$) sideslip. The validity of this assumption rests in the fact that the sideslip angle, β, will be nearly zero in flight. Large rudder inputs are required to increase it substantially.

The variations in C_ℓ, C_n, and C_Y with angle of attack and Mach number is shown in figure A.9. Only at M = .95 does there appear any change in C_Y with angle of attack. Since C_Y versus angle of attack at $\beta = 2^\circ$ and M = .95 does not show this effect, it is assumed that C_Y was independent of angle of attack. However,

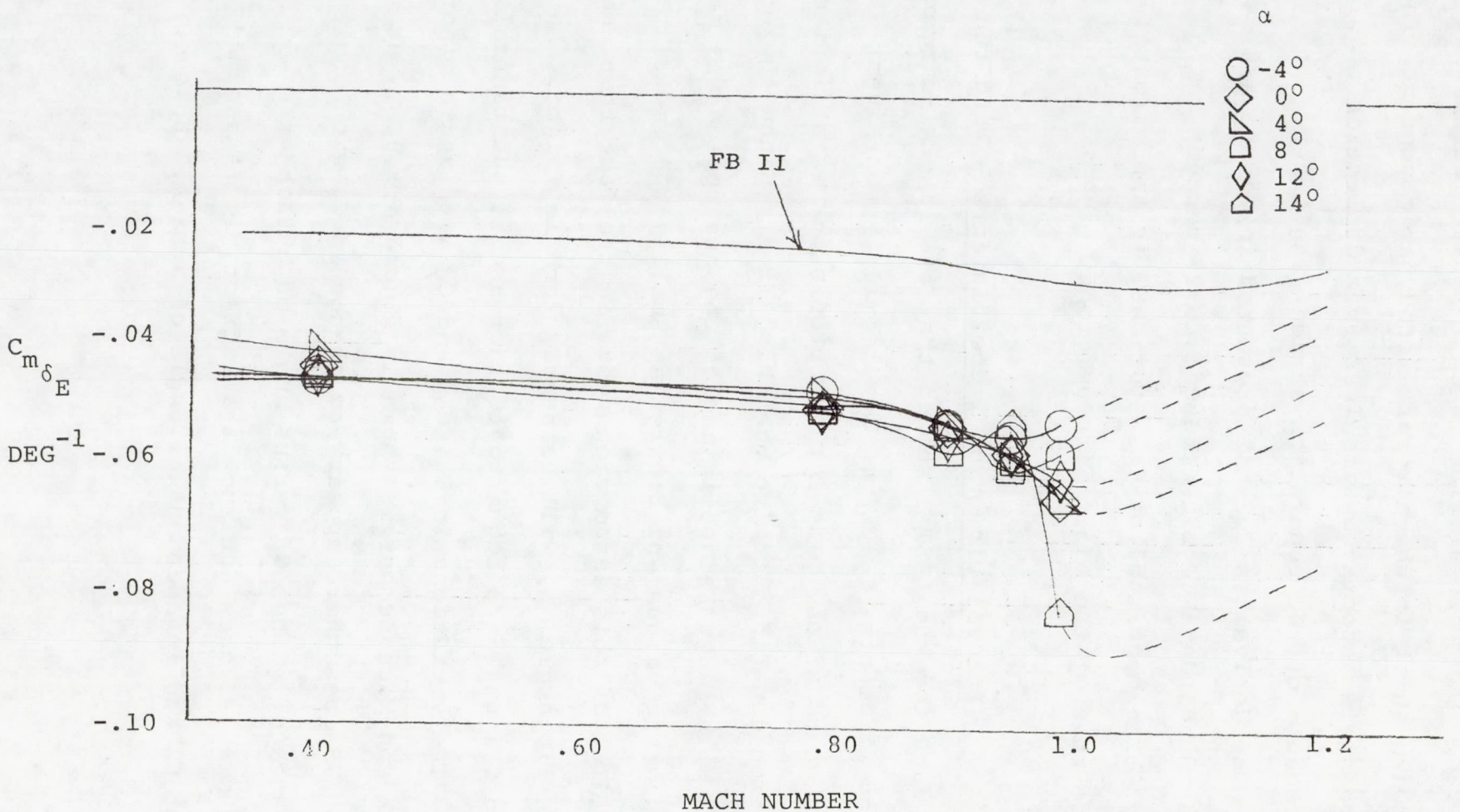

FIGURE A.8 VARIATION IN RATE OF CHANGE OF PITCHING MOMENT COEFFICIENT WITH HORIZONTAL TAIL DEFLECTION AT VARIOUS MACH NUMBERS AND ANGLES OF ATTACK

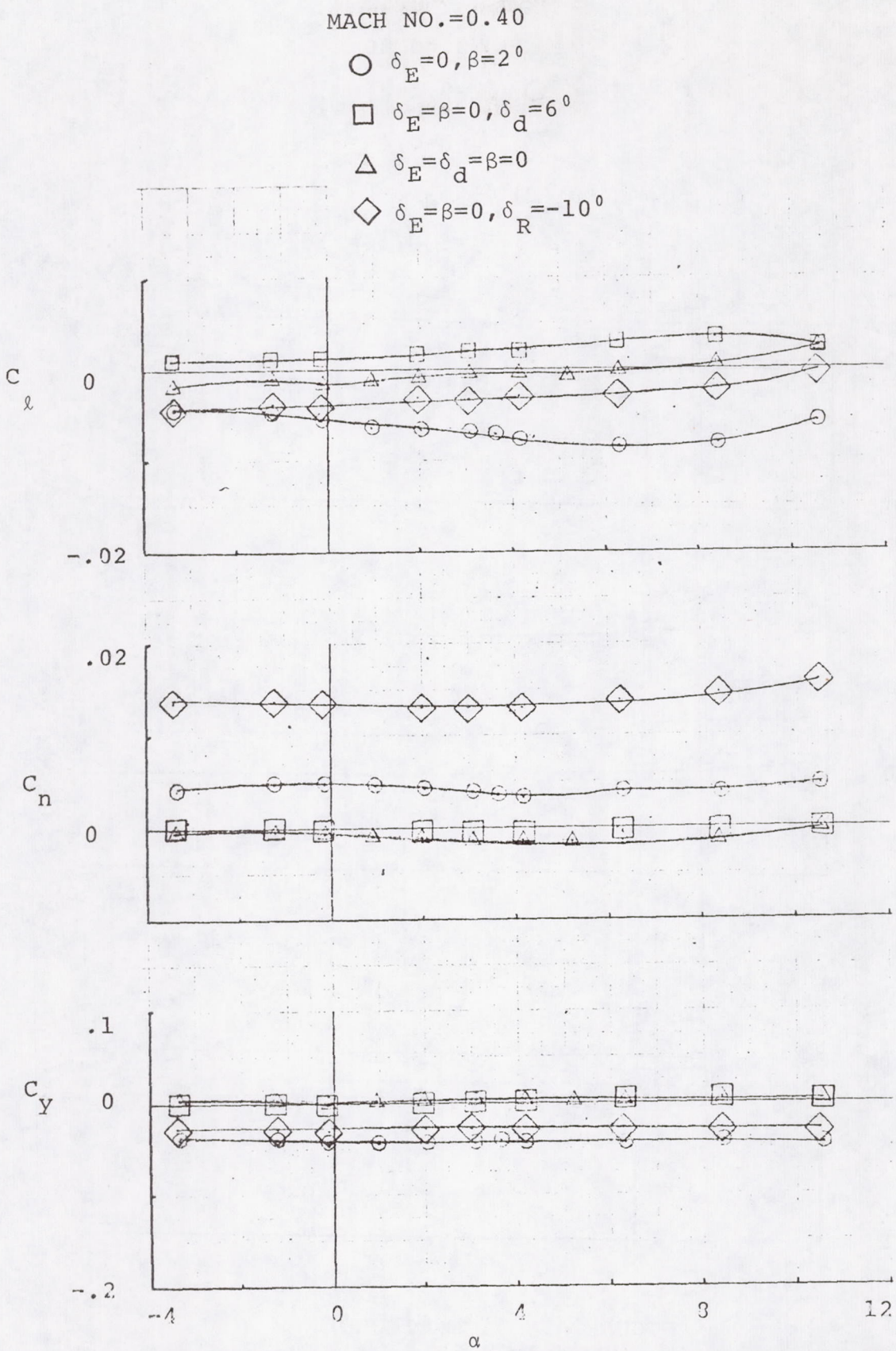

FIGURE A.9 VARIATION IN ROLLING MOMENT, YAWING MOMENT, AND SIDEFORCE COEFFICIENTS WITH ANGLE OF ATTACK AT VARIOUS MACH NUMBERS AND SIDESLIP ANGLES

(PAGE 1 OF 6)

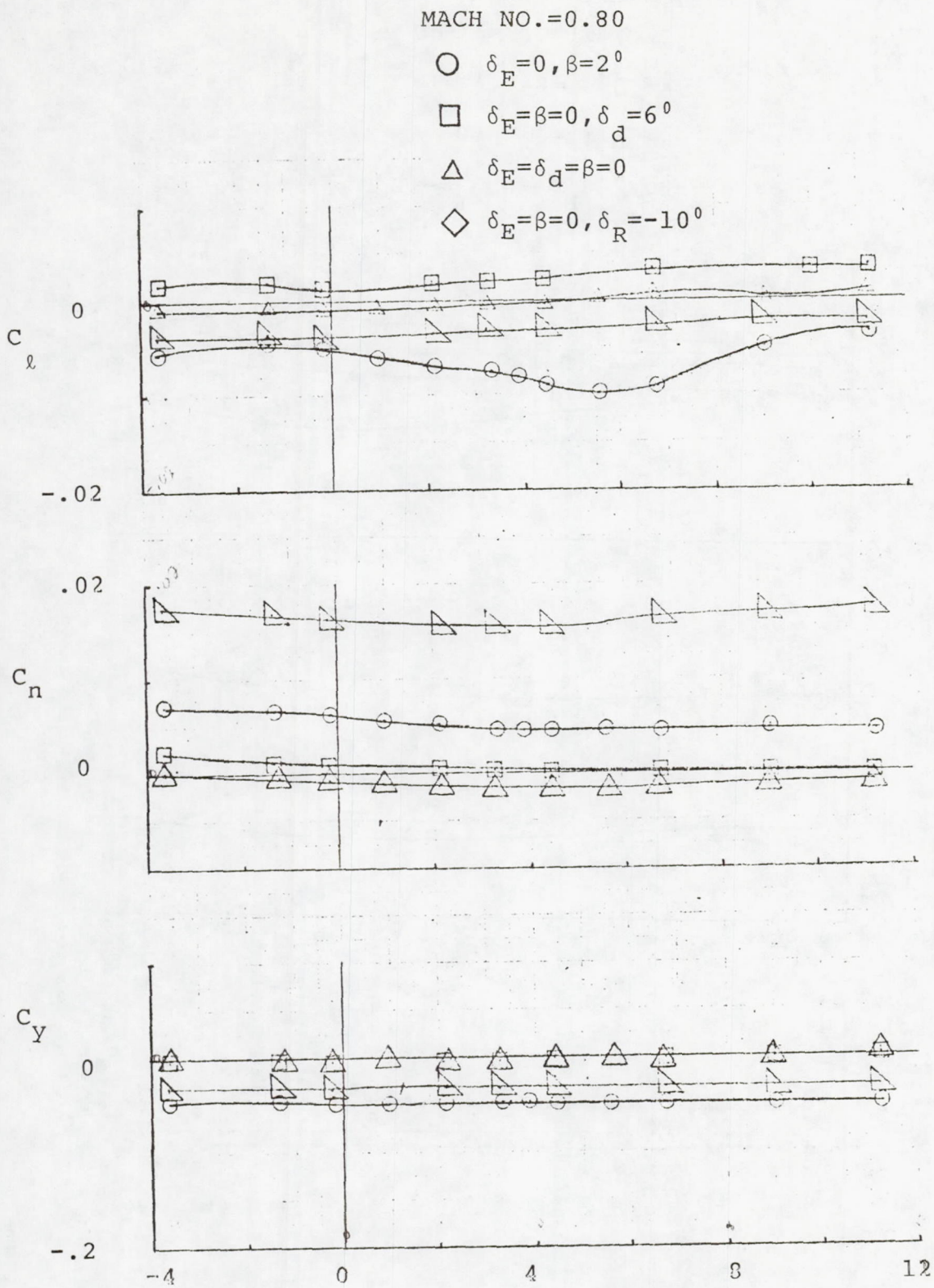

FIGURE A.9 (CONTINUED)
(PAGE 2 OF 6)

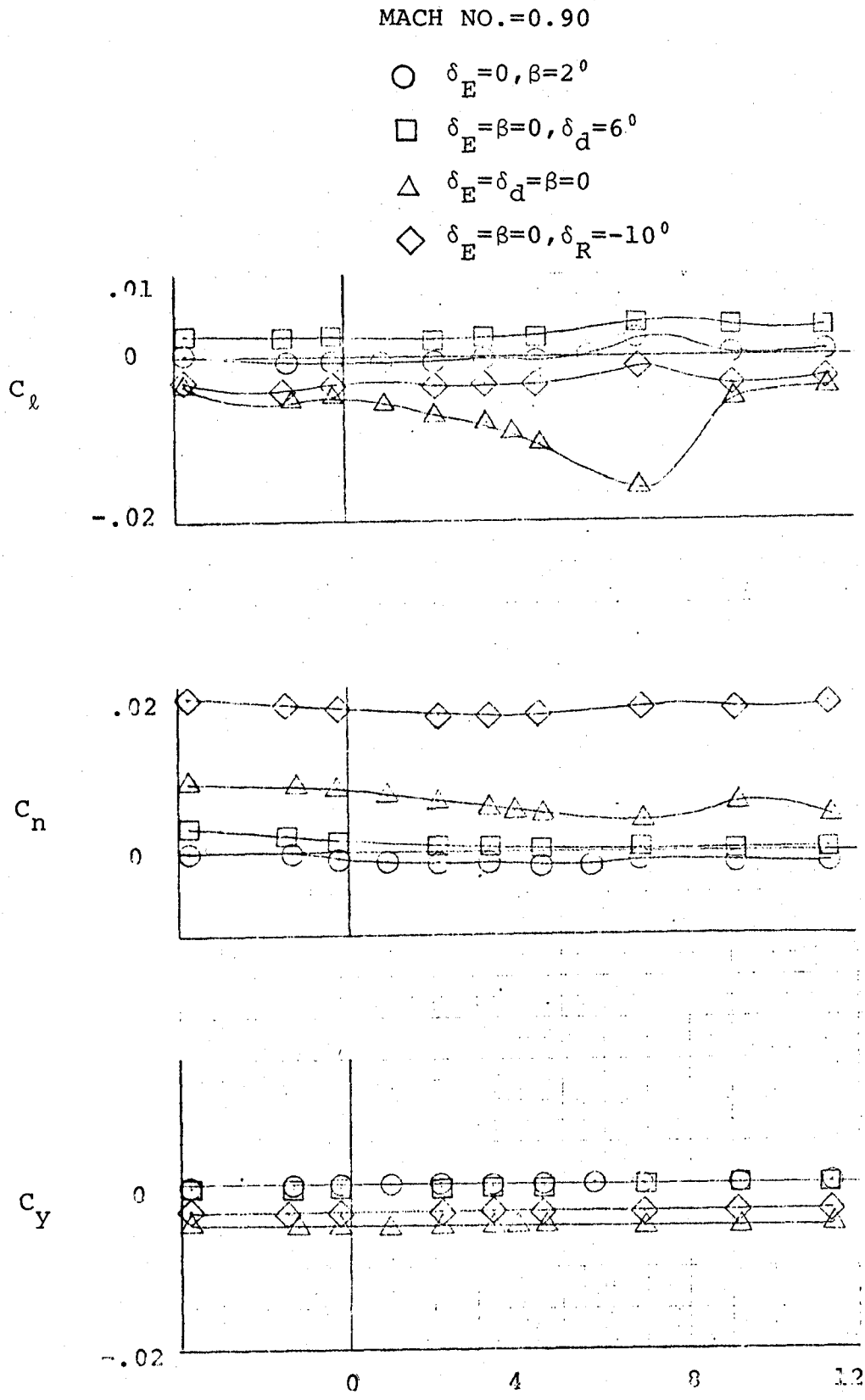

FIGURE A.9 (CONTINUED)

(PAGE 3 OF 6)

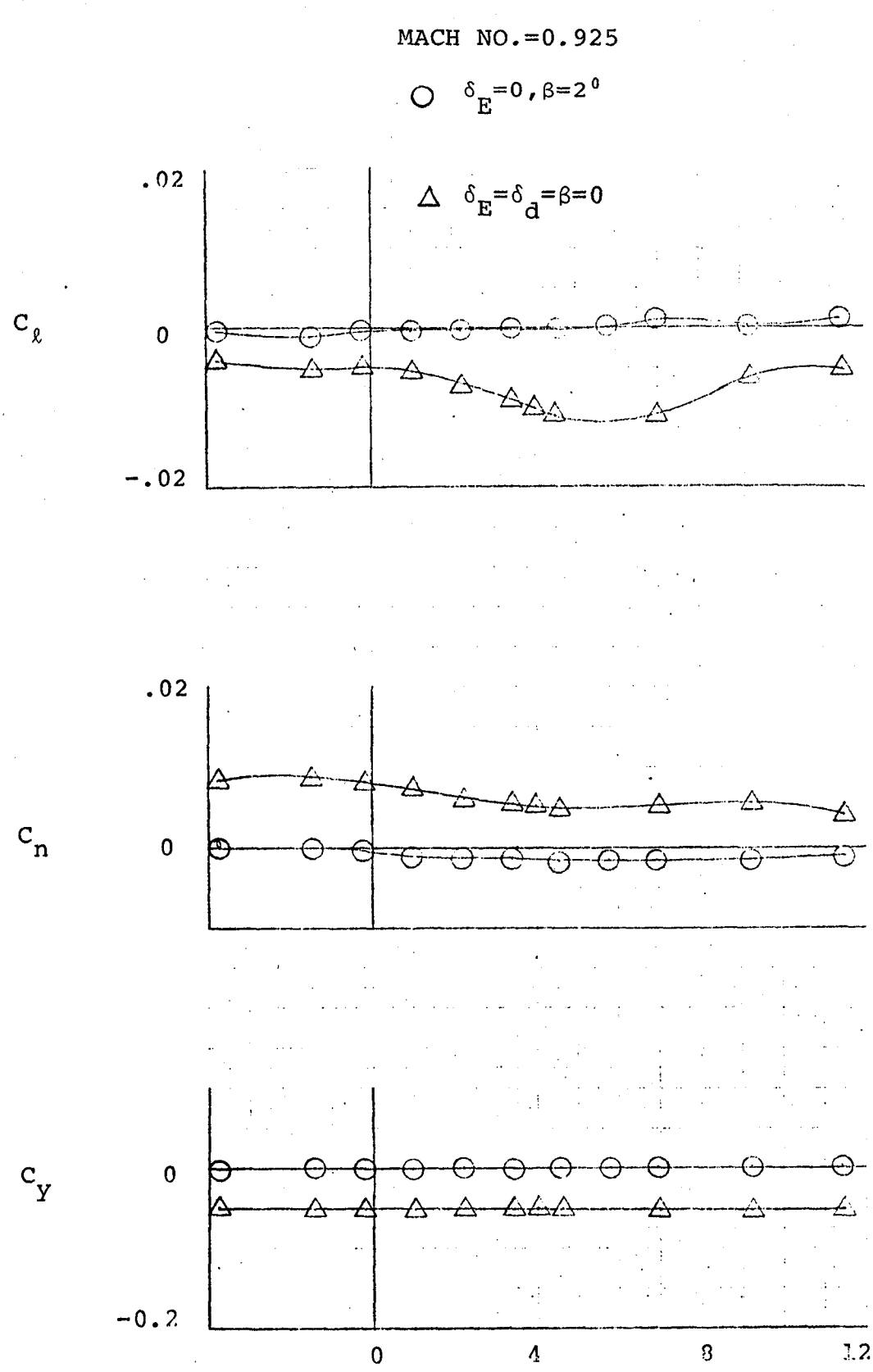

FIGURE A.9 (CONTINUED) (PAGE 4 OF 6)

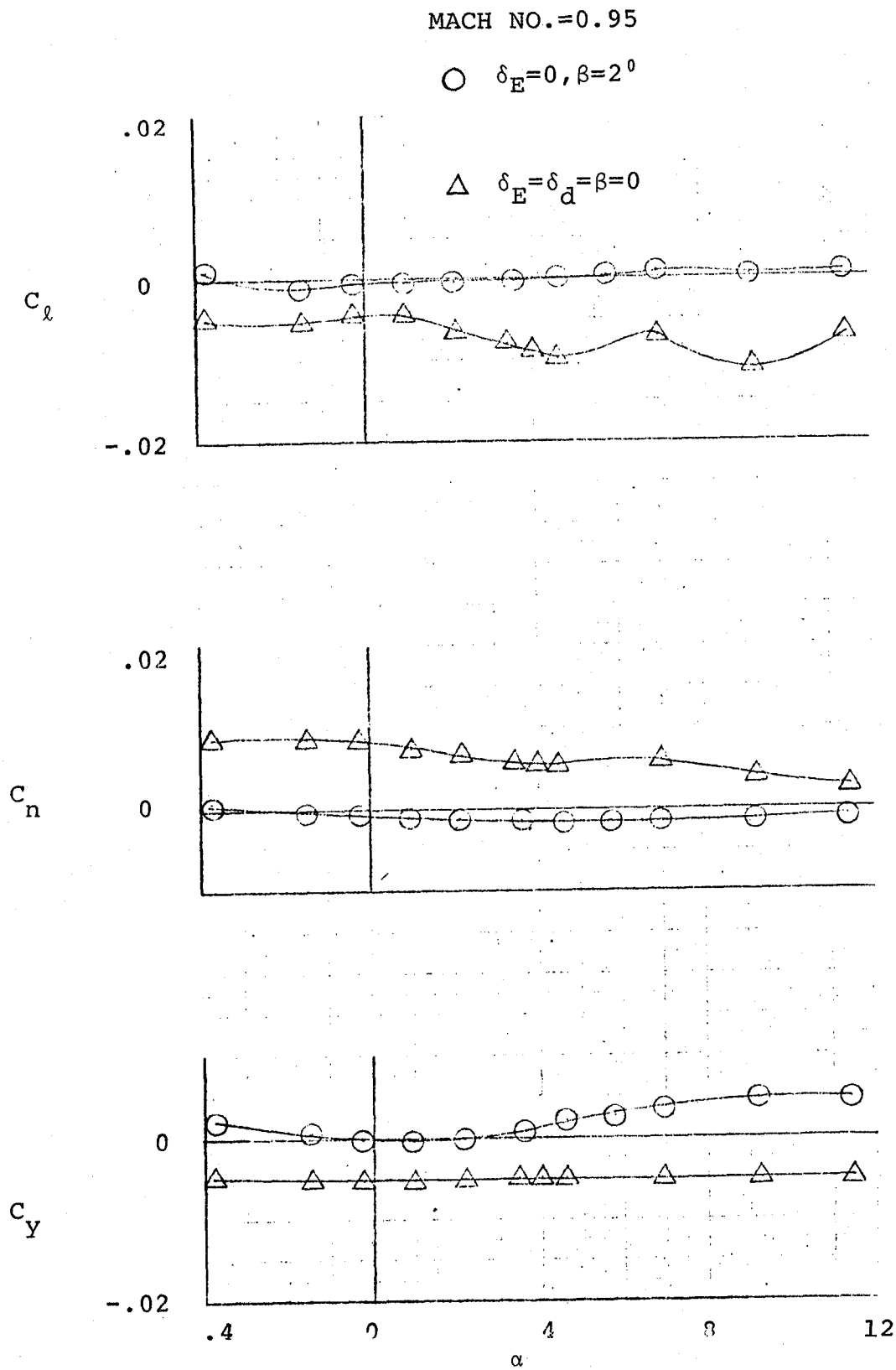

FIGURE A.9 (CONTINUED) (PAGE 5 OF 6)

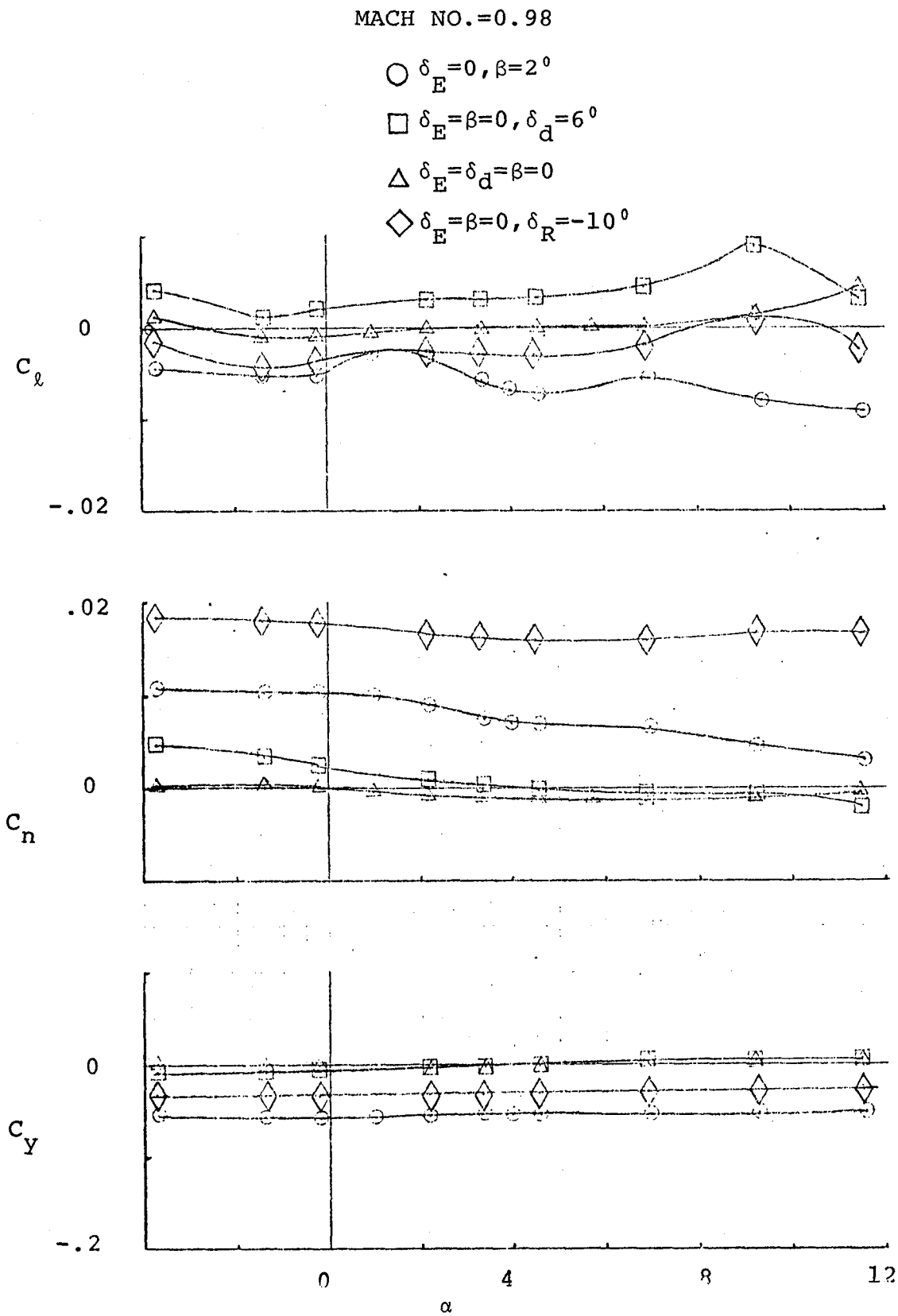

FIGURE A.9 (CONCLUDED) (PAGE 6 OF 6)

C_ℓ and C_n do show a dependency on angle of attack at all Mach numbers. Rolling moment coefficient, C_ℓ, seems particularly affected in the region where the pitch-up characteristic is observed.

A.1.5 Sideslip Derivatives - The rate of change in side force coefficient with sideslip angle, Cy_β, is presented in figure A.10. The vertical tail component is shown because of its importance in estimating some of the dynamic derivatives in Section A.2.2. The side force produced by the vertical tail is assumed to be the same on both the DAST and basic Firebee vehicles. The differences in Cy_{β_v} seen in figure A.10 is due to the different reference areas of the two aircraft.

Figure A.11 presents the directional stability derivative, C_{n_β}. Values for the DAST are approximately 60 percent of the Firebee's magnitude. The differences are attributed to the wing-body interference affects at low angles of attack and wing tip separation at high angles of attack.

The rate of change of the rolling moment coefficient, C_{ℓ_β}, due to sideslip angle is shown in figure A. 12. The large jump in C_{ℓ_β} which occurs around eight degrees angle of attack above M = .80 is caused by the increased spanwise separation of the downstream wing tip. This results in an effective dihedral of very large proportions.

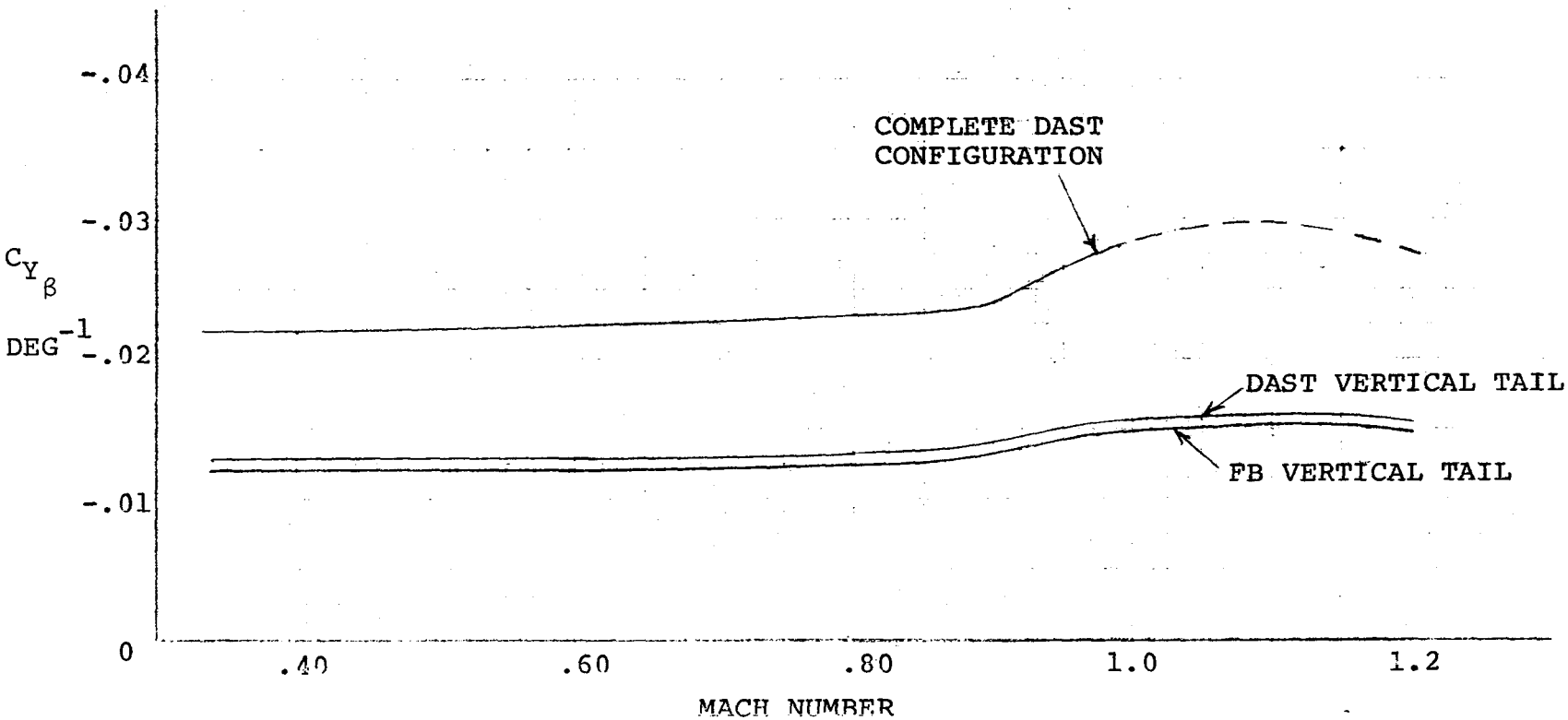

FIGURE A.10 VARIATION IN RATE OF CHANGE IN SIDEFORCE COEFFICIENT DUE TO SIDESLIP ANGLE WITH MACH NUMBER

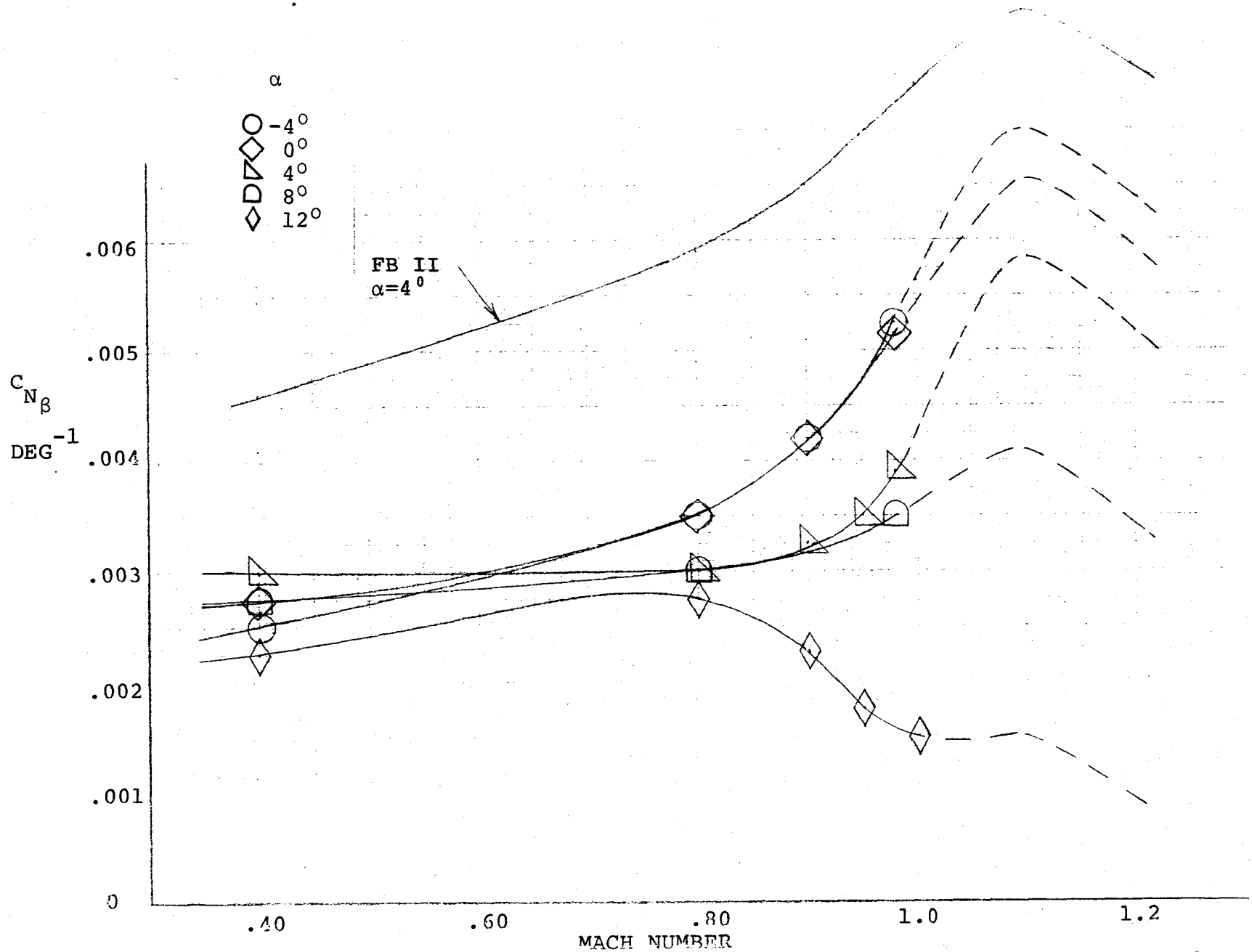

FIGURE A.11 VARIATION IN RATE OF CHANGE OF YAWING MOMENT COEFFICIENT DUE TO SIDESLIP ANGLE WITH MACH NUMBER AT VARIOUS ANGLES OF ATTACK

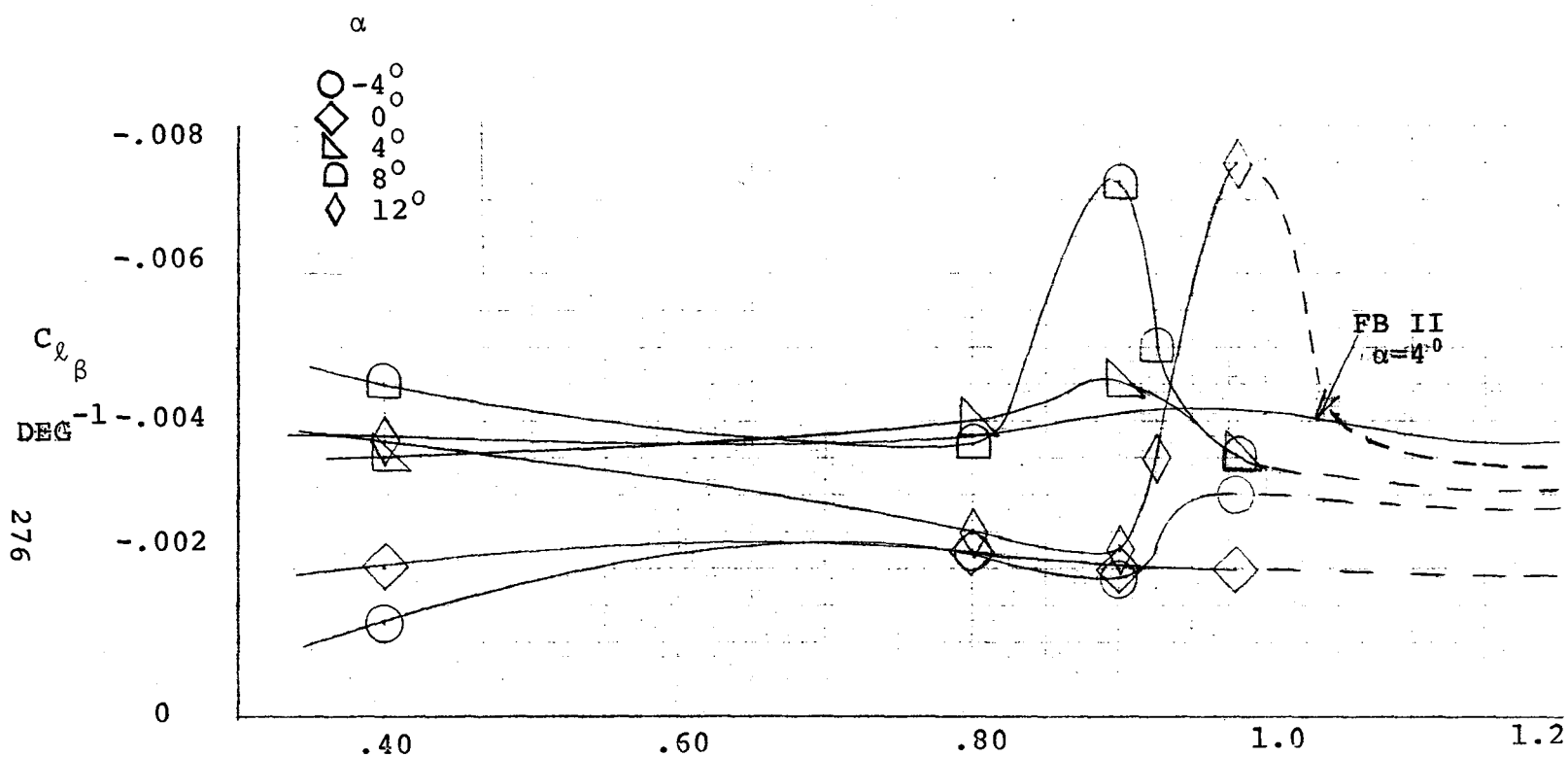

FIGURE A.12 VARIATION IN RATE OF CHANGE OF ROLLING MOMENT COEFFICIENT DUE TO SIDESLIP ANGLE WITH MACH NUMBER AT VARIOUS ANGLES OF ATTACK

The low angle of attack values of C_{ℓ_β} for DAST are close to the values of the Firebee. The magnitude of C_{ℓ_β} at low angles of attack are also close to those experienced on lifting bodies.

A.1.6 Lateral-Directional Control Derivatives - The rate of change in sideforce coefficient with rudder deflection is presented in figure A. 13. These values were calculated from wind tunnel data using rudder deflections from zero degrees to -10 degrees. From this data it was observed that $C_{y_{\delta_R}}$ did not vary with angle of attack and was close to the Firebee values as one would expect.

Figure A.14 shows the variation in yawing moment coefficient due to rudder deflection. The values for $C_{n_{\delta_R}}$ in this figure are approximately 60 percent of the Firebee's values. This change can be attributed to the large reference span of ARW-1.

The variation of rolling moment due to rudder deflection, $C_{\ell_{\delta_R}}$, is shown in figure A. 15. It is apparent that at large angles of attack the value of $C_{\ell_{\delta_R}}$ is reduced substantially. Otherwise, the magnitude is representative of those experienced on the basic Firebee drone.

The rate of change in sideforce coefficient due to differential tail deflection, $C_{y_{\delta_d}}$, is presented in figure A. 16. The magnitude of $C_{y_{\delta_d}}$ for DAST is five times that of the standard drone. This large difference is

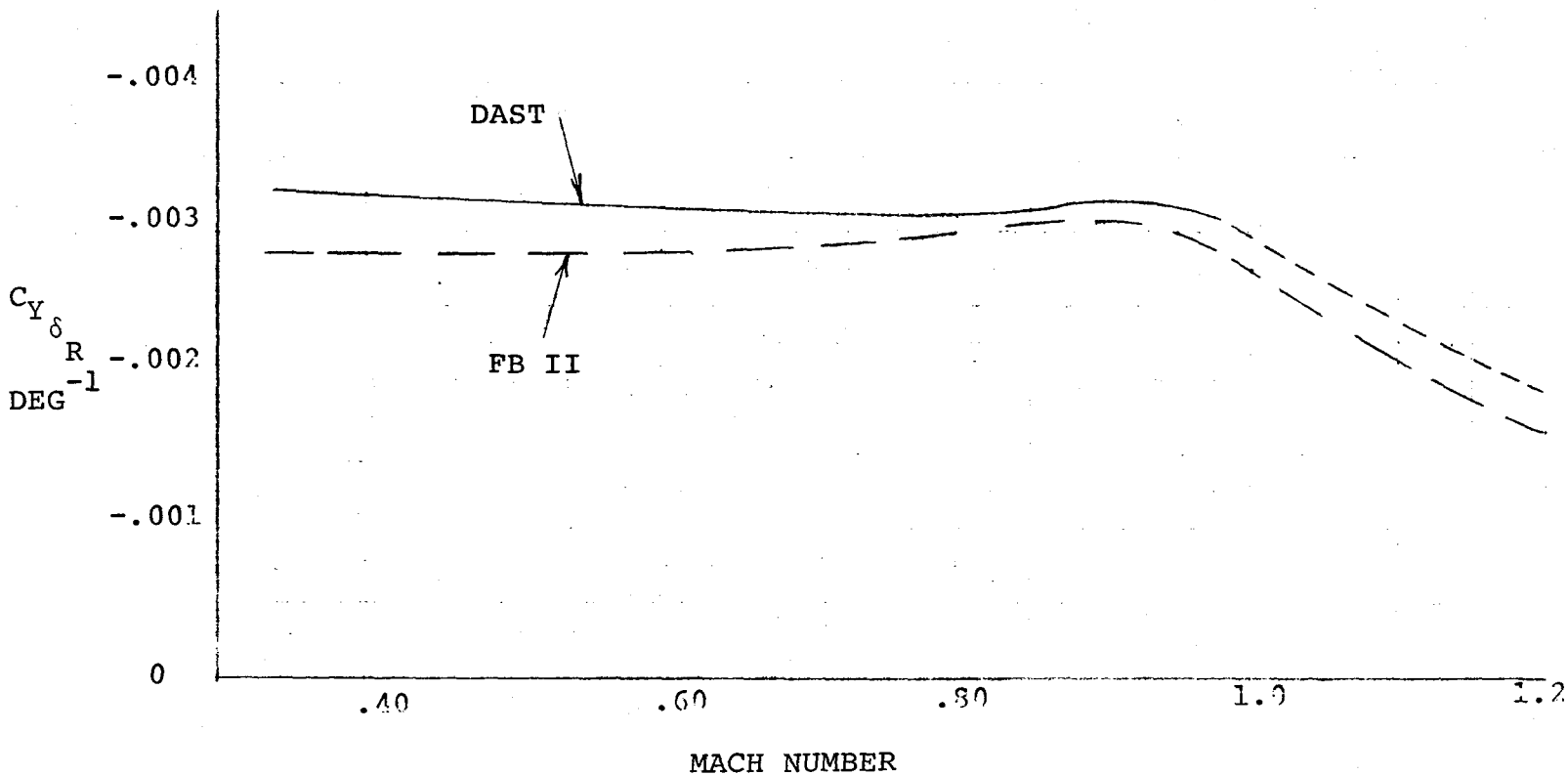

FIGURE A.13 VARIATION IN SIDEFORCE COEFFICIENT DUE TO RUDDER DEFLECTION WITH MACH NUMBER

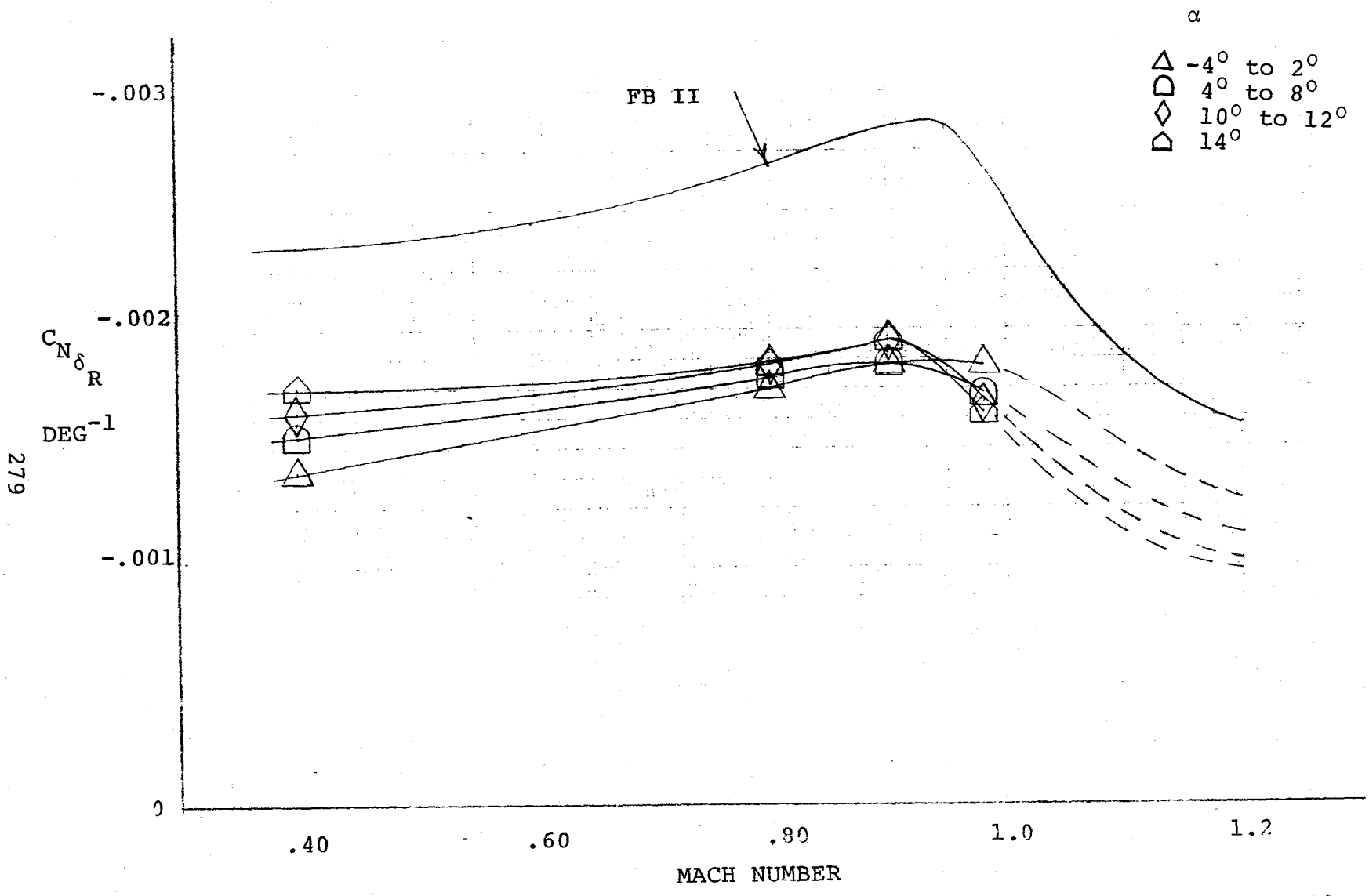

FIGURE A.14 VARIATION IN YAWING MOMENT COEFFICIENT DUE TO RUDDER DEFLECTION WITH MACH NUMBER AT VARIOUS ANGLES OF ATTACK

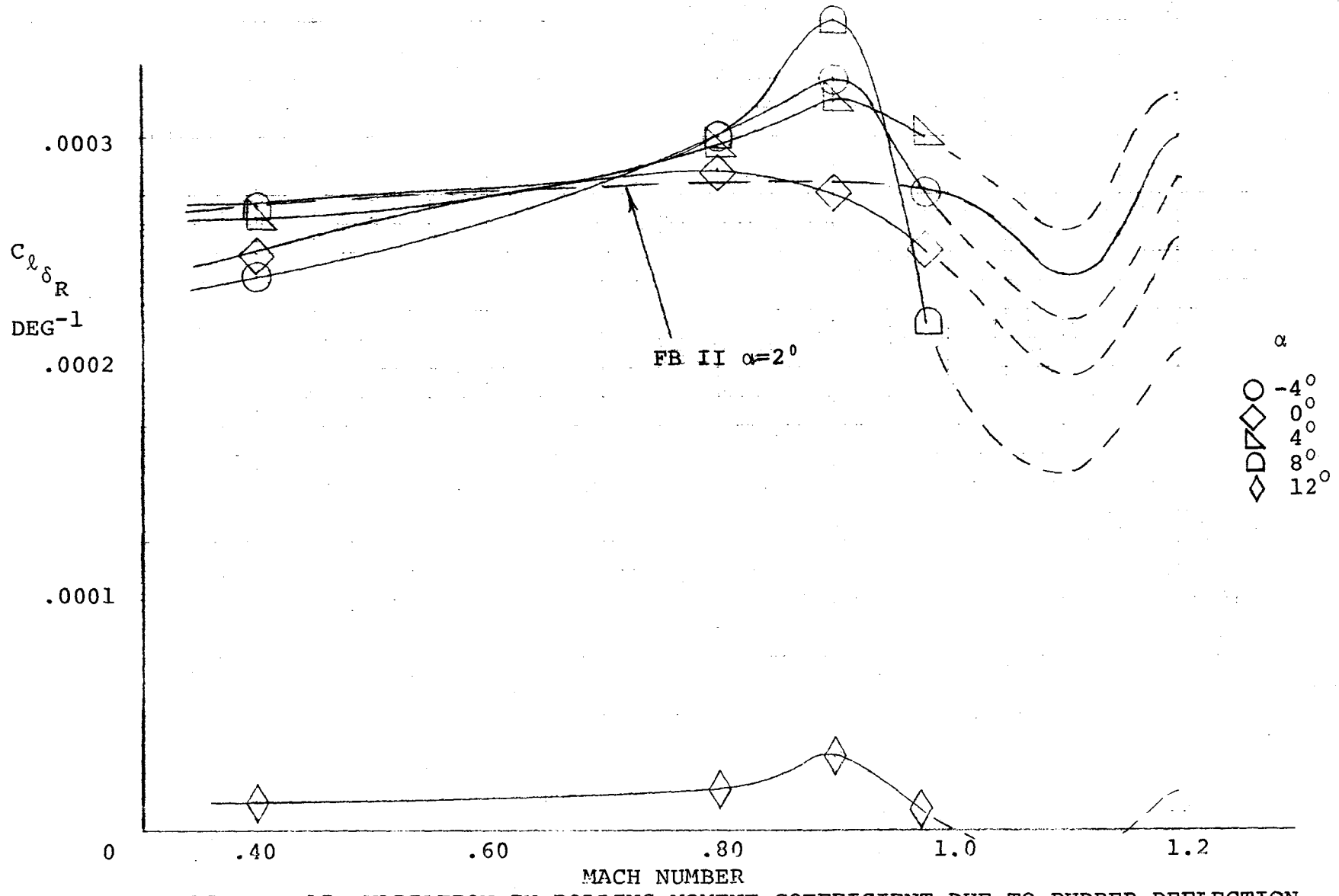

FIGURE A.15 VARIATION IN ROLLING MOMENT COEFFICIENT DUE TO RUDDER DEFLECTION WITH MACH NUMBER AT VARIOUS ANGLES OF ATTACK

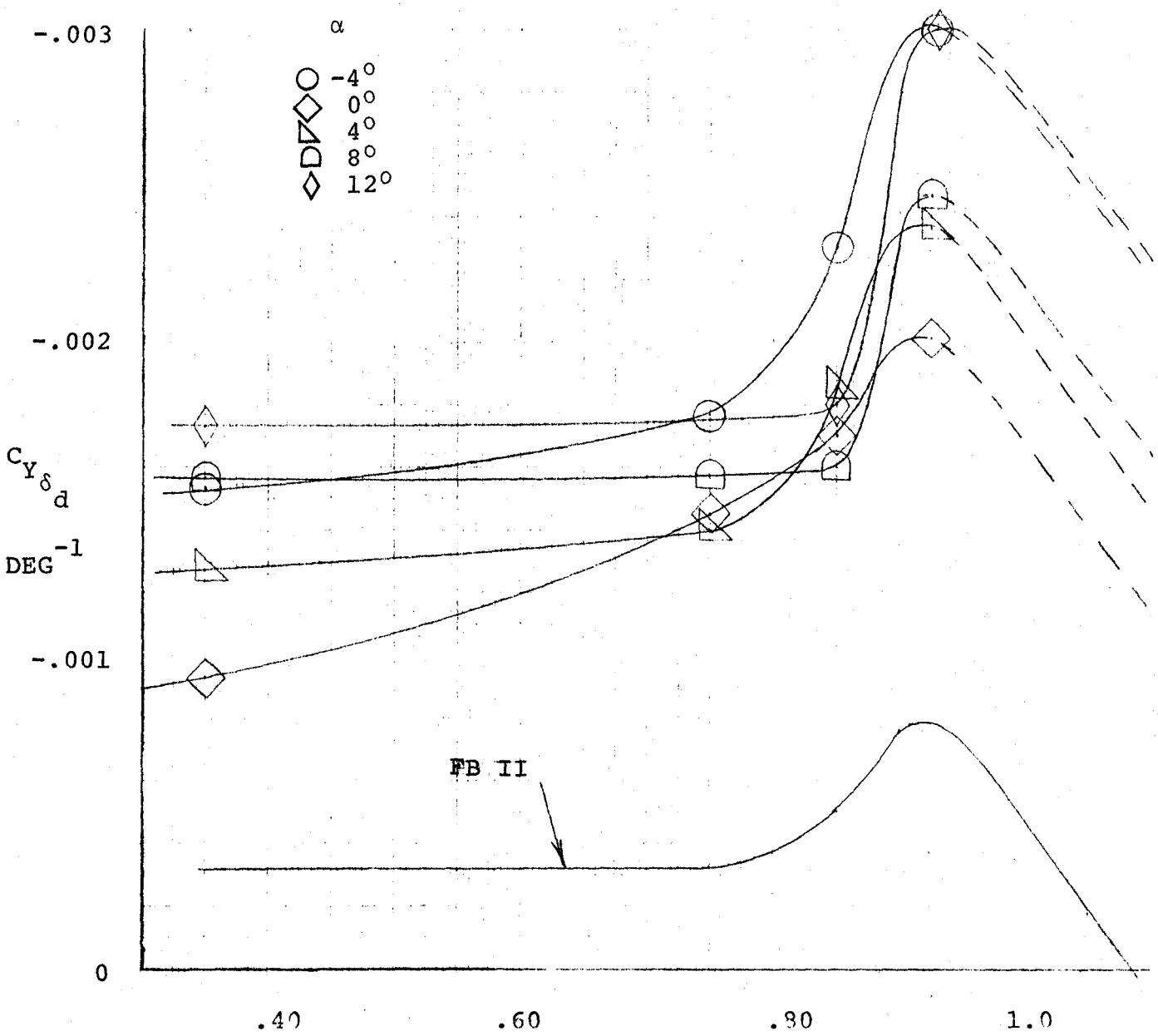

FIGURE A. 16 VARIATION IN SIDEFORCE COEFFICIENT DUE TO DIFFERENTIAL HORIZONTAL TAIL DEFLECTION WITH MACH NUMBER AT VARIOUS ANGLES OF ATTACK

considered to be due to the different downwash effects behind the thin uncambered supersonic wing of the Firebee and the much thicker ARW-1. Differences in reference span also contribute.

Figure A. 17 shows the variation in yawing moment coefficient due to differential tail deflection, $C_{n_{\delta_d}}$. The Firebee values for $C_{n_{\delta_d}}$ are approximately sixty percent of the DAST values at higher Mach numbers. Flight test results of the basic Firebee II drone indicate values of the same magnitude but of opposite sign of the wind tunnel values compared here.

The rate of change in rolling moment coefficient due to differential tail deflection, $C_{\ell_{\delta_d}}$, is shown in figure A. 18. The high angle of attack region appears to influence this control derivative. The wind tunnel data indicated that the variations in $C_{\ell_{\delta_d}}$ due to collective differential tail deflection and elevator deflection are insignificant. The magnitude of $C_{\ell_{\delta_d}}$ on DAST is about forty percent higher at low angles of attack than that experienced with the Firebee.

A.2 Dynamic Derivative Estimates

All derivatives in this section were determined by the latest USAF DATCOM (reference 6) methods and those of reference 13. Static wind tunnel data were used as input information to the empirical expressions whenever appropriate.

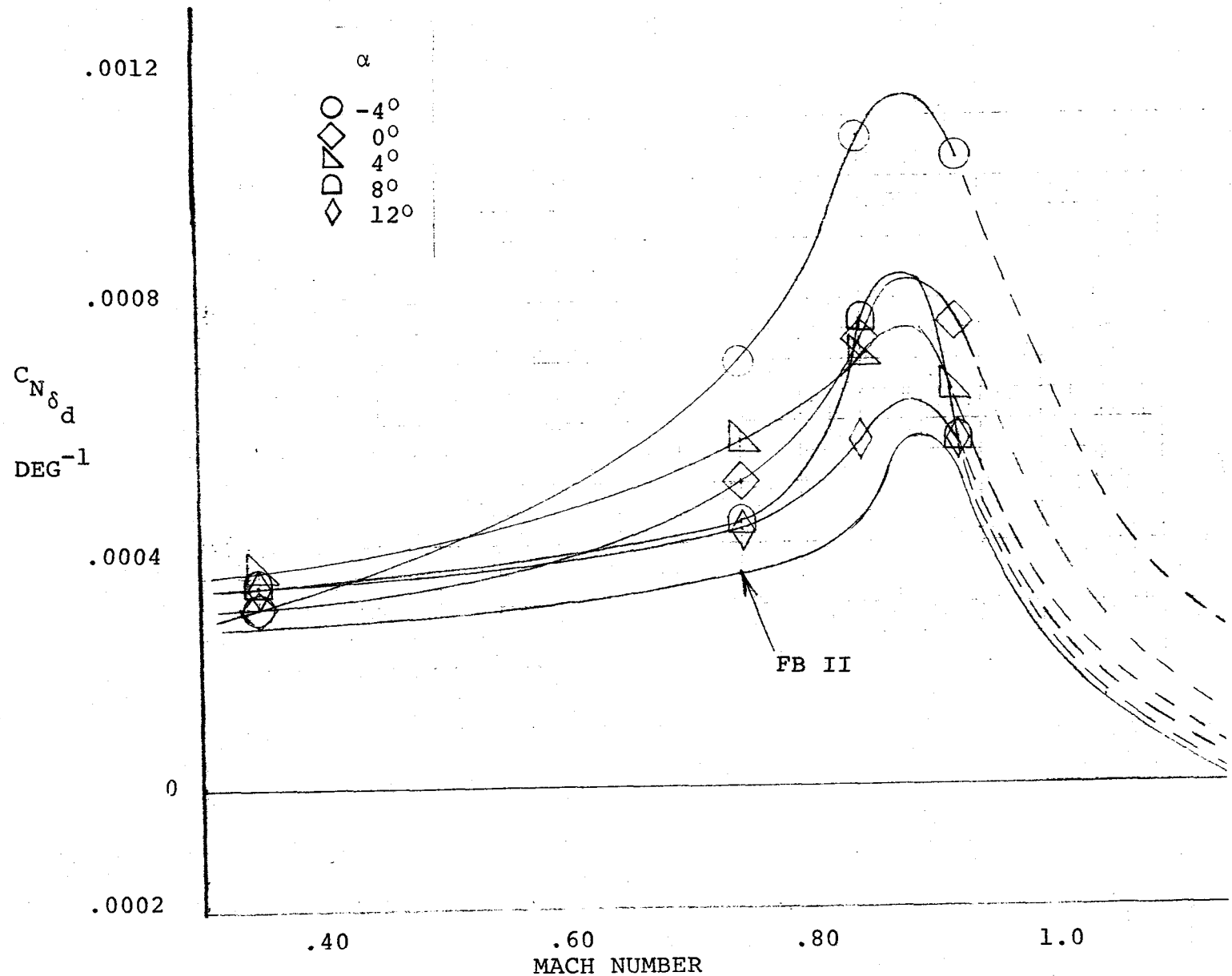

FIGURE A.17 VARIATION IN YAWING MOMENT COEFFICIENT DUE TO DIFFERENTIAL HORIZONTAL TAIL DEFLECTION WITH MACH NUMBER AT VARIOUS ANGLES OF ATTACK

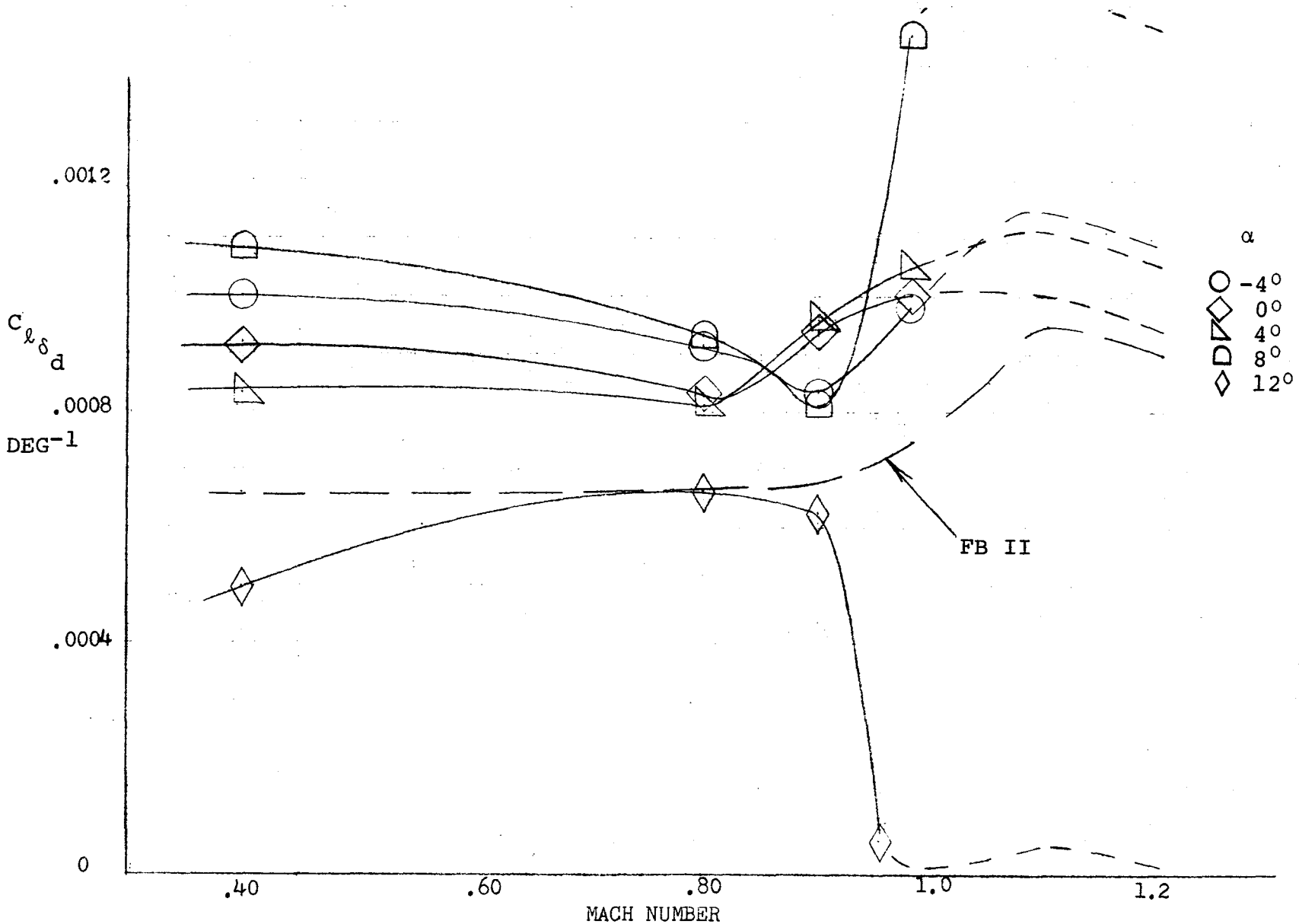

FIGURE A.18 VARIATION IN ROLLING MOMENT COEFFICIENT DUE TO DIFFERENTIAL HORIZONTAL TAIL DEFLECTION WITH MACH NUMBER AT VARIOUS ANGLES OF ATTACK

A.2.1 Longitudinal Dynamic Characteristics - The estimated values for lift coefficient due to rate of change of angle of attack are presented in figure A.19. It is assumed that the horizontal tail increment was the only significant contribution to the derivative. For the horizontal tail contribution, $C_{L_{\dot{\alpha}_H}}$, is calculated by the expression:

$$C_{L_{\dot{\alpha}_H}} = 2\, C_{L_{\alpha_H}}\, \eta_H\, \bar{V}_H\, \frac{de}{d\alpha} \qquad (A.1)$$

The lift curve slope for the horizontal tail was obtained from reference 3, page 29. The term $\bar{V}_H$ is the horizontal tail volume coefficient defined as:

$$\bar{V}_H = \frac{X_H}{\bar{c}}\,\frac{S_H}{S} \qquad (A.2)$$

Where X_H is the distance from the airplane cg to the horizontal tail aerodynamic center, S_H and S are the tail and wing areas respectively, and $\bar{c}$ is the mean aerodynamic chord of the wing.

The rate of change of downwash angle with angle of attack, $d\varepsilon/d\alpha$, is shown in figure A. 20. It was determined by the following equations:

$$\left.\frac{d\varepsilon}{d\alpha}\right|_M = \left.\frac{d\varepsilon}{d\alpha}\right|_{M=o} \cdot \frac{C_{L_{\alpha_{wb}}}|_M}{C_{L_{\alpha_{wb}}}|_{M=o}} \qquad (A.3)$$

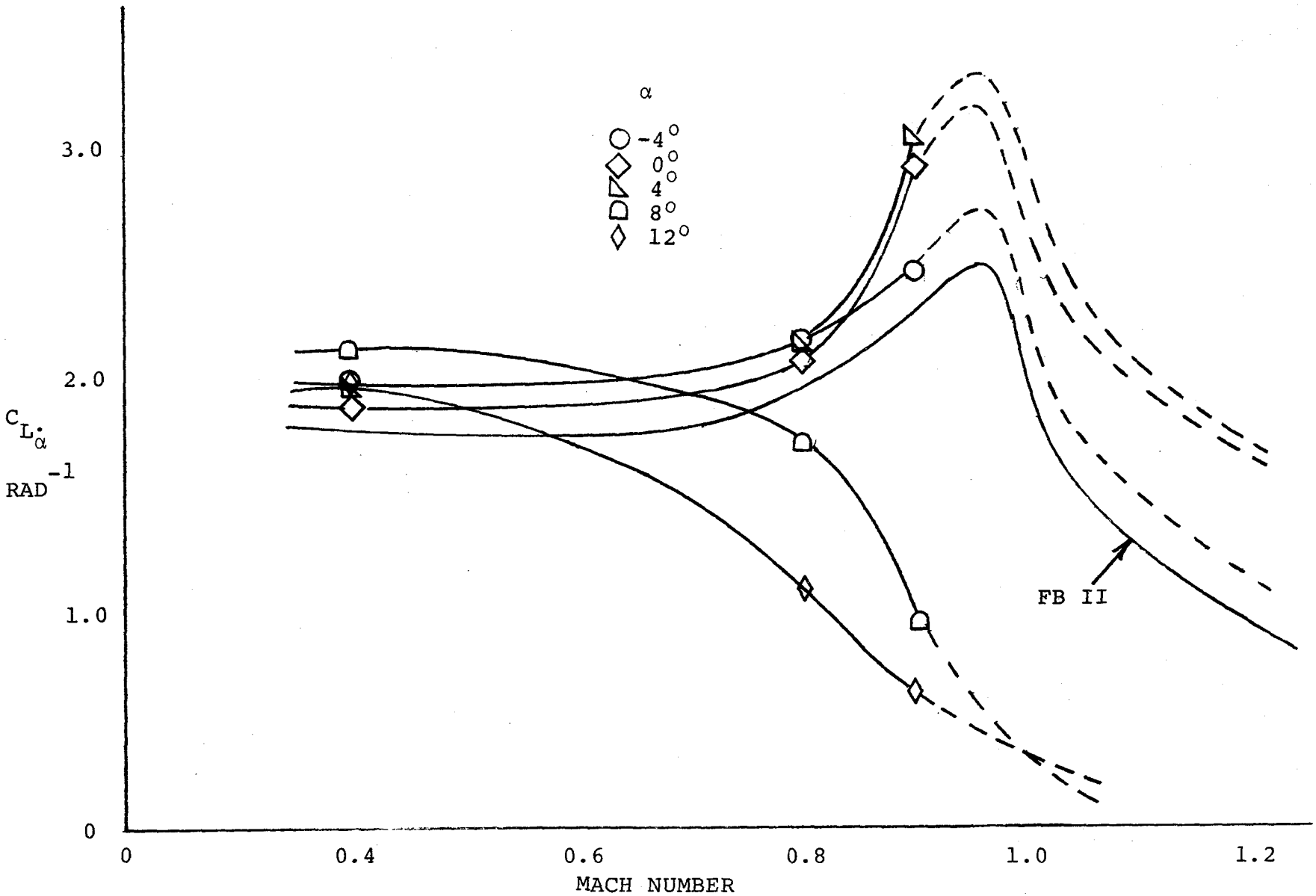

FIGURE A.19 VARIATION IN LIFT COEFFICIENT WITH RATE OF CHANGE IN ANGLE OF ATTACK

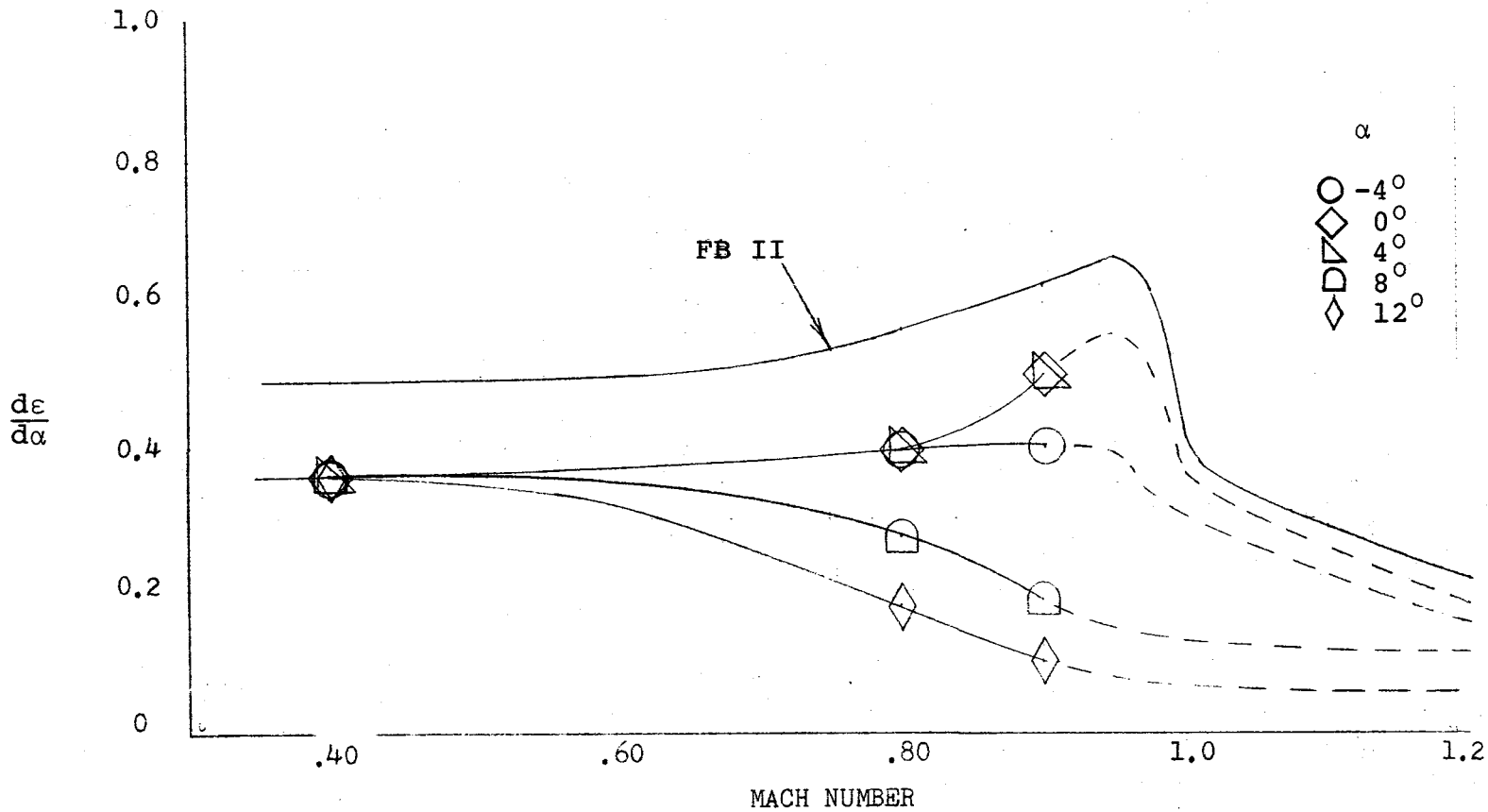

FIGURE A.20 VARIATION IN THE RATE OF CHANGE OF DOWNWASH ANGLE WITH ANGLE OF ATTACK WITH MACH NUMBER AT VARIOUS ANGLES OF ATTACK

$$\left.\frac{de}{d\alpha}\right|_{M=0} = 4.44\left[\left(\frac{1}{AR} - \frac{1}{1+AR^{1.7}}\right)\left(\frac{10-3\lambda}{7}\right)\left(\frac{1-\frac{h_H}{b}}{\sqrt[3]{\frac{2\ell_H}{b}}}\right)\sqrt{\cos \Lambda_{c/4}}\right] \quad (A.4)$$

where

λ = taper ratio

AR = aspect ratio

b = wing span

$\Lambda_{c/4}$ = quarter chord angle

ℓ_H = distance from 25% $\bar{c}$ of the wind to 25% $\bar{c}$ of the horizontal tail

h_H = vertical distance of the horizontal tail from the root chord plane of the wing

The ratio of lift curve slopes used in equation (A.3) was determined from the wind tunnel data. Since the transonic force-break Mach number for the DAST I was approximately M = .9 (reference 6, figure 4.1.3.2-53b), the wing-body lift curve slope for M = .40 was used in the denominator of equation (A.3).

The dynamic pressure ratio at the horizontal tail, η_H, used in equation (A.1) is shown in figure A.21. This ratio was estimated by :

$$\eta_H = 1 - \frac{\Delta q}{q} \quad (A.5)$$

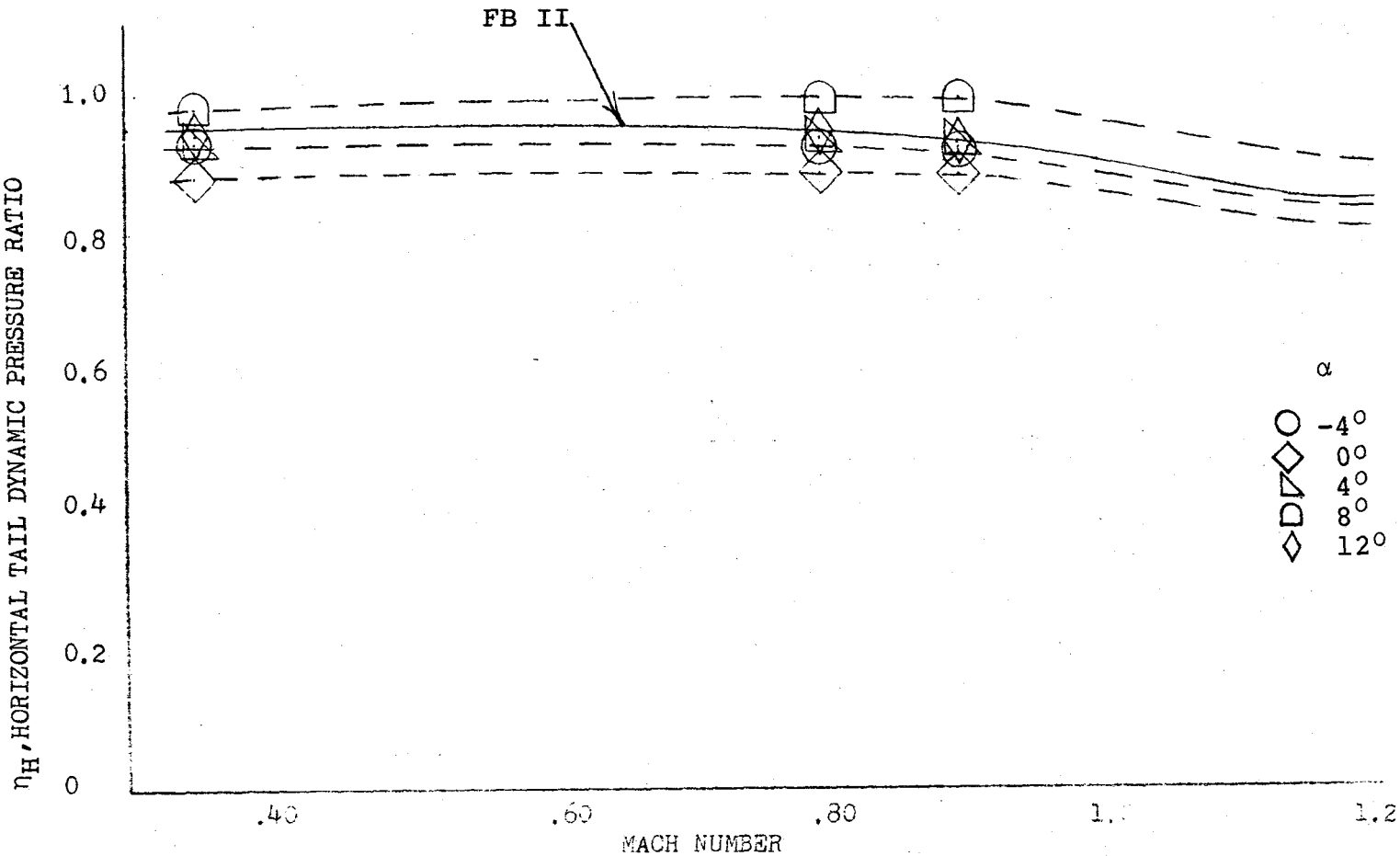

FIGURE A. 21 VARIATION IN HORIZONTAL TAIL DYNAMIC PRESSURE RATIO WITH MACH NUMBER AT VARIOUS ANGLES OF ATTACK

$$\frac{\Delta q}{q} = \left(\frac{\Delta q}{q_o}\right) \cos^2 \left(\Pi/2 \cdot Z/Z_w\right) \tag{A.6}$$

$$\left(\frac{\Delta q}{q_o}\right) = \frac{2.42 \left(C_{D_o}\right)^{\frac{1}{2}}}{\frac{X_H}{\bar{c}} + .30} \tag{A.7}$$

$$Z = X_H \tan (\varepsilon - \alpha) \tag{A.8}$$

$$\varepsilon = \frac{1.62\ C_L}{\Pi\ AR} \tag{A.9}$$

$$Z_w = 0.68\ \bar{c} \sqrt{C_{D_o}\left(\frac{X_H}{\bar{c}} + .15\right)} \tag{A.10}$$

The term C_{D_o} in equations (A.7) and (A.10) does represent the conventional drag coefficient at zero angle of attack, and C_L is the total lift coefficient at the particular flight condition of interest. Both C_{D_o} and C_L were determined from the wind tunnel data.

The values for C_{L_α} in Figure A. 19 are not significantly different than that of the Firebee at low angles of attack but degrade at high Mach numbers at high angles of attack.

The derivative C_{L_q} is composed of a wing contribution and horizontal tail contribution. The wing contribution is estimated by:

$$C_{L_{q_{wb}}}\Big|_M = \left[\frac{AR + 2 \cos \Lambda_{c/4}}{AR\ B + 2 \cos \Lambda_{c/4}}\right] \cdot C_{L_{q_{wb}}}\Big|_{M=o} \tag{A.11}$$

$$B = \sqrt{1 - M^2 \cos^2 \Lambda_{c/4}} \tag{A.12}$$

$$C_{L_{q_{wb}}}\Big|_{M=o} = \left(1/2 + \frac{2X_w}{\bar{c}}\right) \quad C_{L_{\alpha_{wb}}}\Big|_{M=o} \tag{A.13}$$

where X_w is the distance from the airplane cg to the wing aerodynamic center.

The tail contribution was found from :

$$C_{L_{q_H}}\Big|_M = 2\, C_{L_{\alpha_H}}\Big|_M \eta_H \bar{V}_H \tag{A.14}$$

Summing equations (A.11) and (A.14) yields the values plotted in Figure A.22. Values of C_{L_q} for the DAST and Firebee are comparable.

No explicit methods exist to calculate the wing contribution to the derivative $C_{m_{\dot{\alpha}}}$ except for triangular wings. For most conventional airplane configurations its contribution is small. For the horizontal tail contribution the estimate is:

$$C_{m_{\dot{\alpha}}} \approx C_{m_{\dot{\alpha}_H}} = -2\, C_{L_{\alpha_H}} \eta_H \bar{V}_H \frac{X_H}{\bar{c}} \frac{d\varepsilon}{d\alpha} \tag{A.15}$$

The derivative $C_{m_{\dot{\alpha}}}$ is plotted in Figure A.23 as a function of Mach number and angle of attack. At low angles of attack $C_{m_{\dot{\alpha}}}$ for DAST I is about twice that of the basic vehicle. Above M = .8 and at high angles of attack $C_{m_{\dot{\alpha}}}$ decreases sharply. Improved methods were used in the DAST calculation.

The variation in pitching moment coefficient with

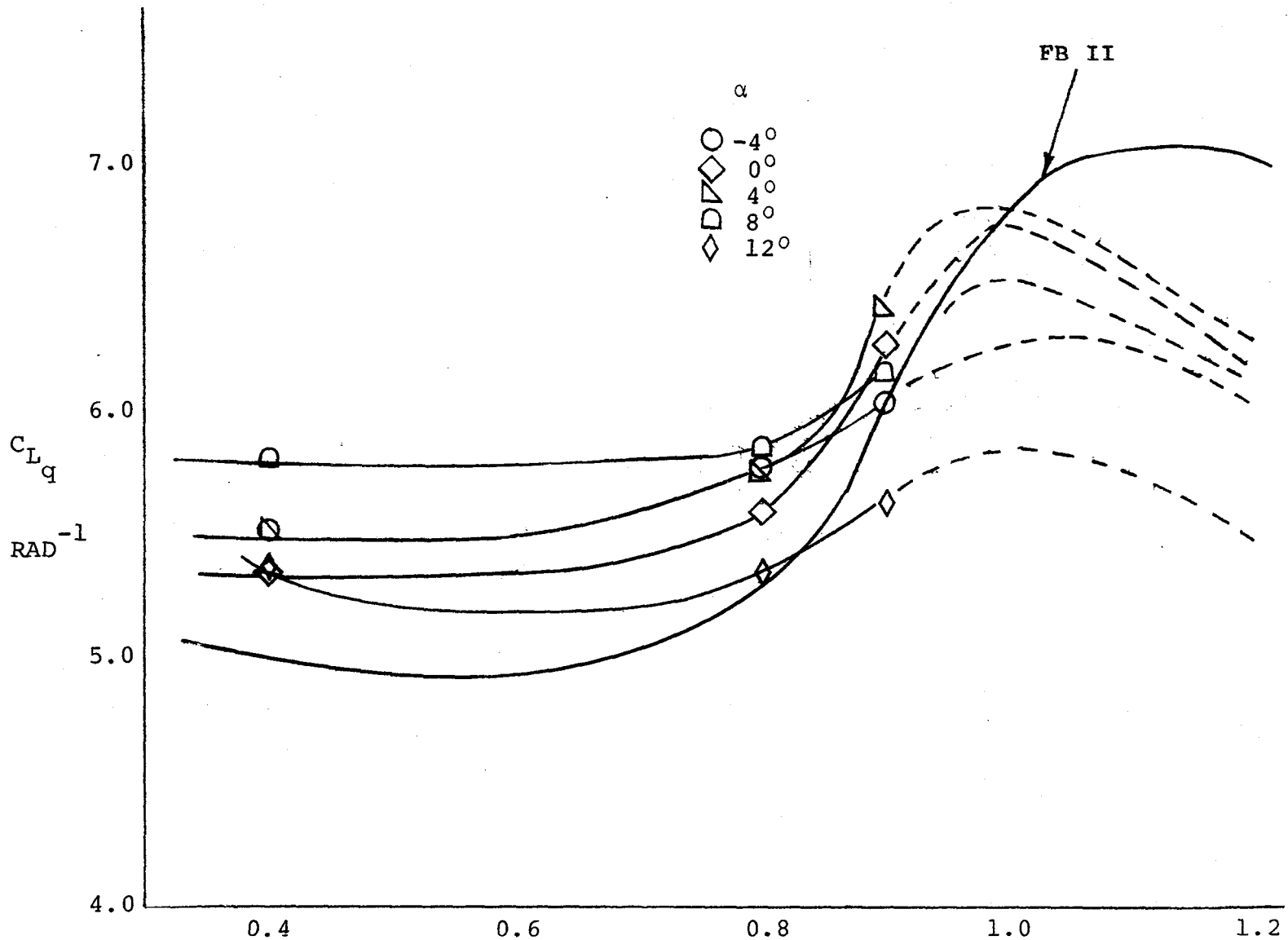

FIGURE A.22 VARIATION IN LIFT COEFFICIENT WITH PITCH RATE

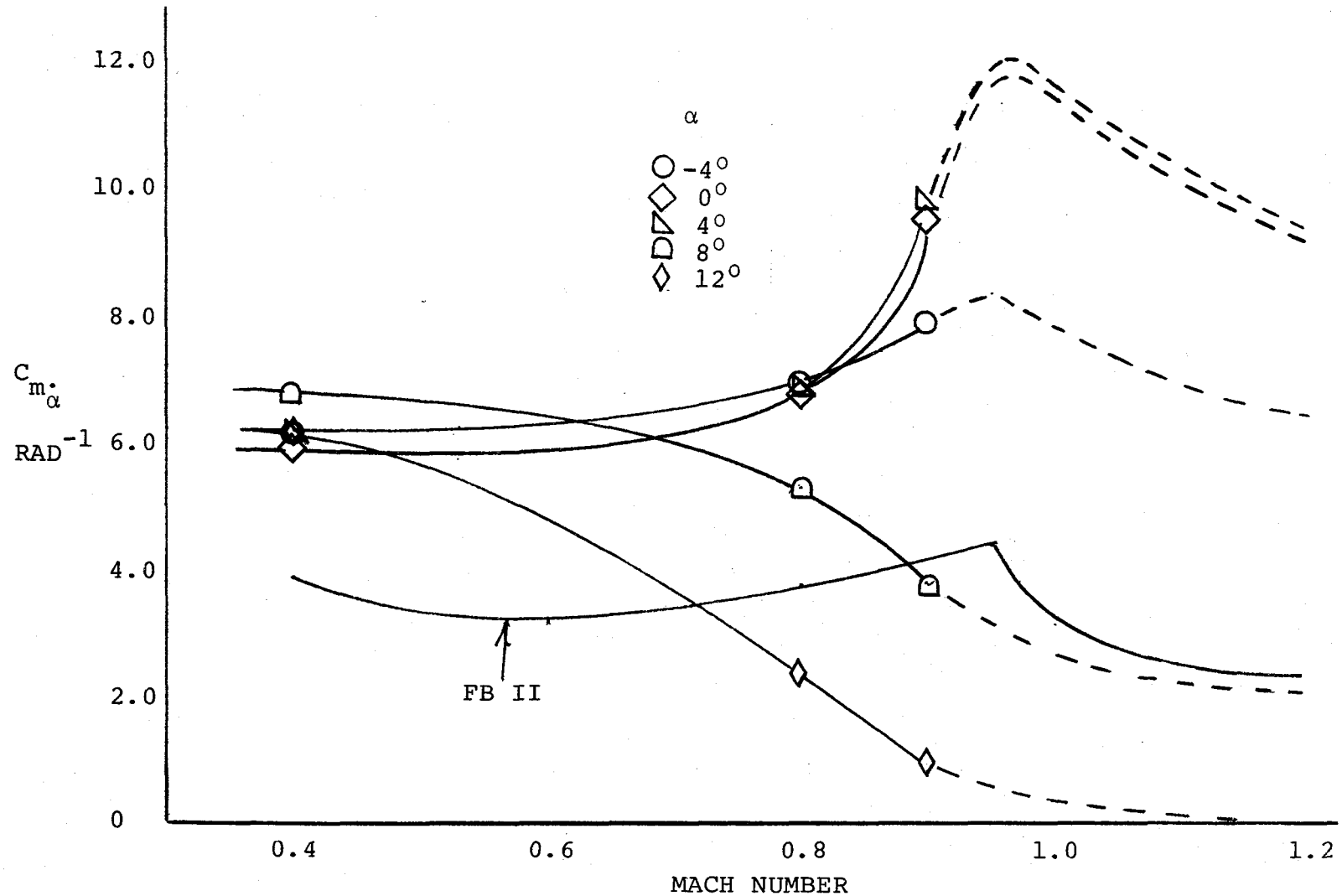

FIGURE A.23 VARIATION IN PITCHING MOMENT COEFFICIENT WITH RATE OF CHANGE ANGLE OF ATTACK

change in pitch rate is considered the sum of the wing and tail contributions. The wing contribution is found by:

$$C_{m_{q_{wb}}}\Big|_M = C_{m_{q_{wb}}}\Big|_{M=o} \left[\frac{\frac{AR^3 \tan^2 \Lambda_{c/4}}{AR \cdot B + 6 \cos \Lambda_{c/4}} + \frac{3}{B}}{\frac{AR^3 \tan^2 \Lambda_{c/4}}{AR + 6 \cos \Lambda_{c/4}} + 3} \right] \qquad (A.16)$$

$$C_{m_{q_{wb}}}\Big|_{M=o} = .71\, C_{\ell_{\alpha_w}} \cos \Lambda_{c/4} \left[\frac{AR\left[2\left(\frac{X_w}{\bar{c}}\right)^2 + 1/2\left(\frac{X_w}{\bar{c}}\right)\right]}{AR + 2 \cos \Lambda_{c/4}} + \frac{1}{24} \frac{AR^3 \tan^2 \Lambda_{c/4}}{AR + 6 \cos \Lambda_{c/4}} + \frac{1}{8} \right] \qquad (A.17)$$

In equation (A.17), $C_{\ell_{\alpha_w}}$ is the spanwise average value of the wing section lift curve slope.

The tail contribution to C_{m_q} is estimated from:

$$C_{m_{q_H}} = -2\, C_{L_{\alpha_H}} \eta_H \bar{V}_H \frac{X_H}{\bar{c}} \qquad (A.18)$$

The derivative C_{m_q} is presented in Figure A.24. The DAST values for C_{m_q} are about 13 per cent higher than those of the Firebee at the same angle of attack. The increased aspect ratio for the DAST works to its benefit.

A.2.2 Lateral-Directional Dynamic Characteristics -

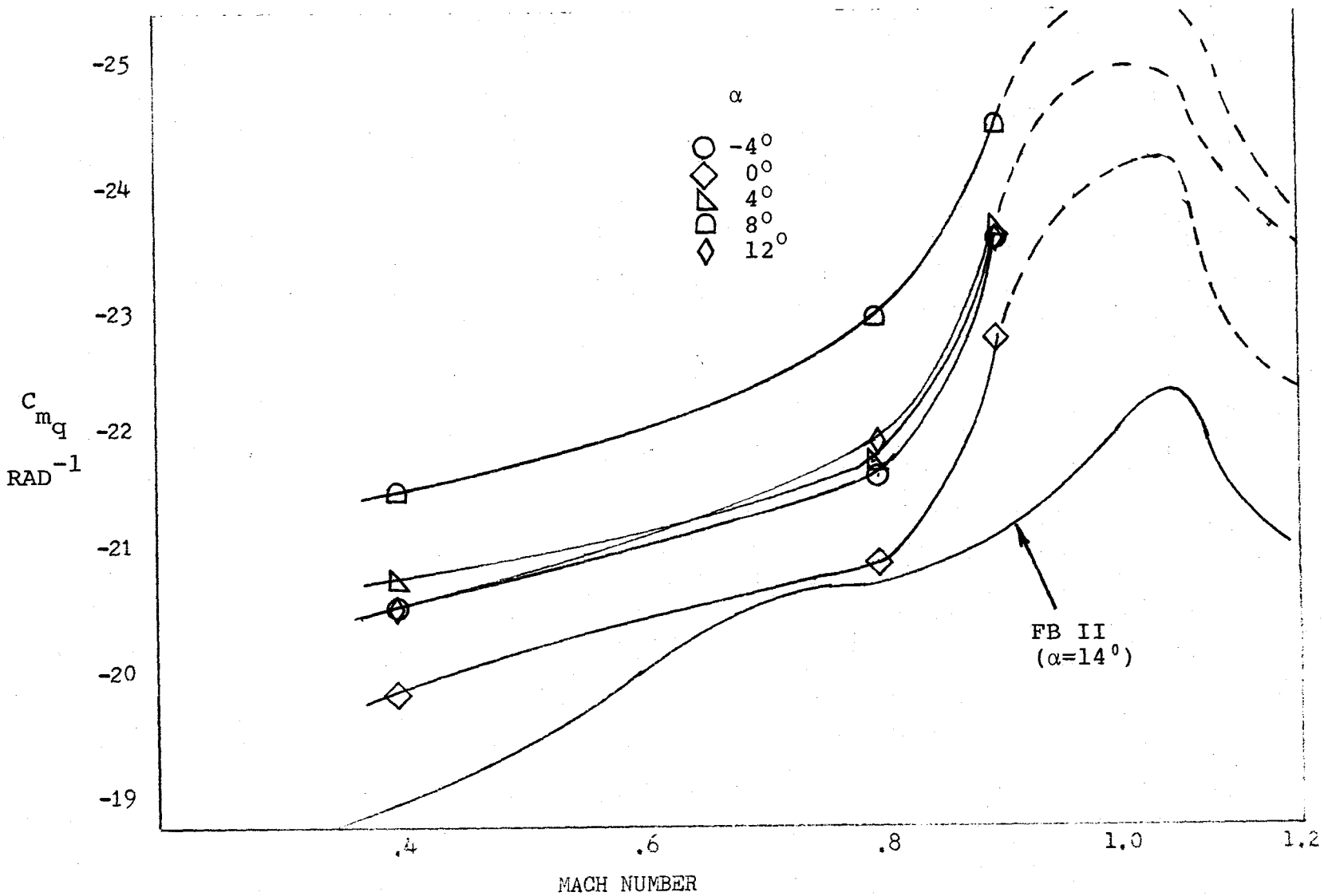

FIGURE A.24 VARIATION IN PITCHING MOMENT COEFFICIENT WITH PITCH RATE.

The sideforce coefficient due to angular roll velocity is plotted in figure A.25. This derivative is composed of two components, one for the vertical tail and one for the wing. At low angles of attack the vertical tail is the main contributor while at high angles of attack the wing component is the larger of the two.

The vertical tail component is estimated from:

$$C_{y_{p_v}} = 2 \frac{Z_v \cos \alpha - \ell_v \sin \alpha}{b} C_{y_{\beta_v}} \qquad (A.19)$$

where Z_v is the distance from the vertical tail aerodynamic center to the body x-axis and ℓ_v is the distance from the vertical tail aerodynamic center to the aircraft center of gravity.

The wing-body component is estimated from:

$$\left(\frac{C_{y_{p_{wb}}}}{C_L}\right)_M = \left(\frac{C_{y_{p_{wb}}}}{C_L}\right)_{M=o} \cdot \left[\frac{AR + 4 \cos \Lambda_{c/4}}{AR \cdot B + 4 \cos \Lambda_{c/4}}\right]\left[\frac{AR \cdot B + \cos \Lambda_{c/4}}{AR + \cos \Lambda_{c/4}}\right] \qquad (A.20)$$

the value of $\left(C_{y_{p_{wb}}} / C_L \right)_{M=o}$ is found from figure 7.1.2.1-3a of reference 6.

The variation in yawing moment coefficient with roll rate is estimated from its wing and vertical tail components. For a wing with no twist or flaps its contribution is estimated from:

$$C_{n_p} = -C_{\ell_{p_{wb}}} \tan \alpha - \left[-C_{\ell_p} \tan \alpha - \left(\frac{C_{n_p}}{C_L}\right)_{\substack{C_{L=o} \\ M}} C_L \right] \qquad (A.21)$$

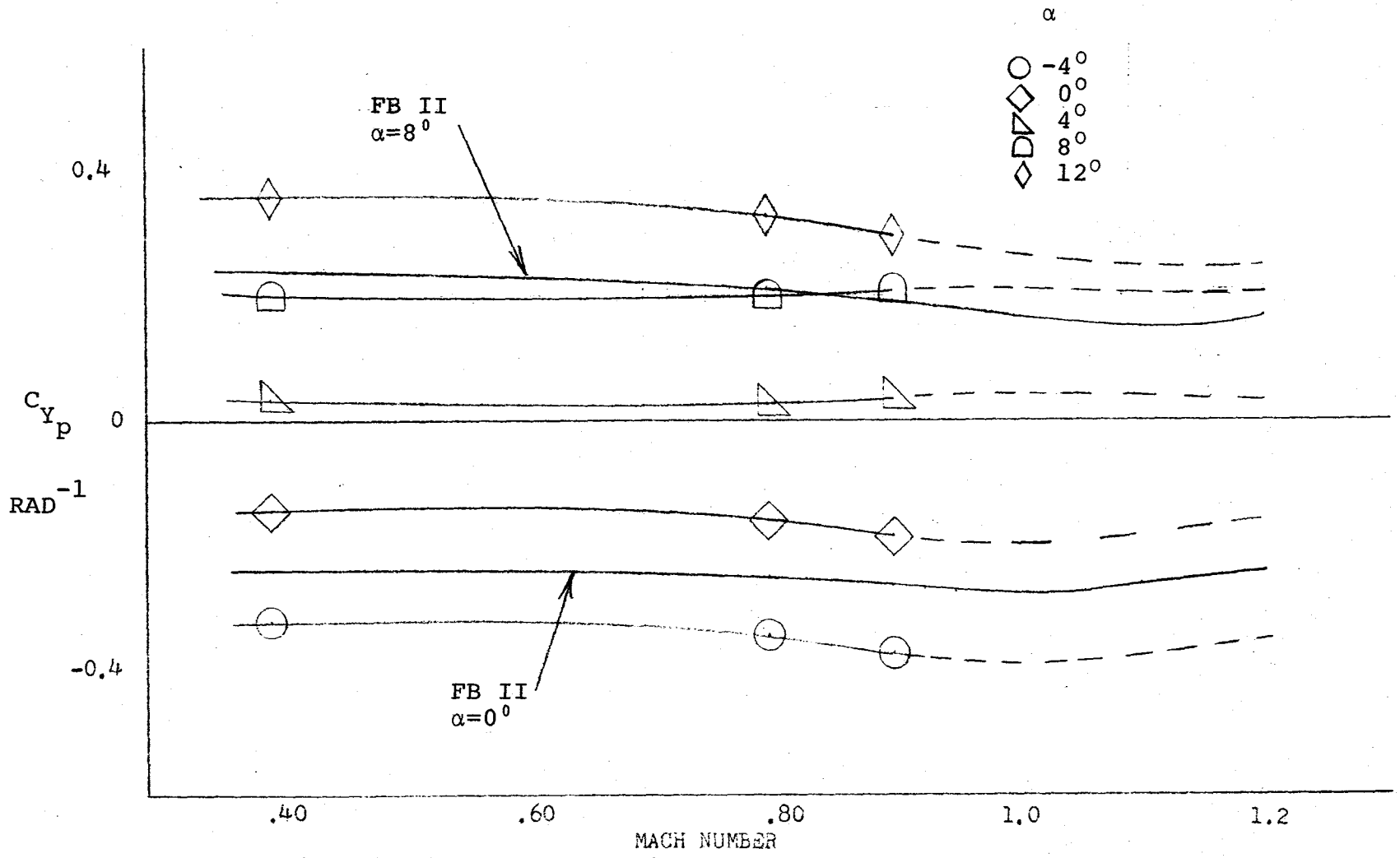

FIGURE A. 25 VARIATION IN SIDEFORCE COEFFICIENT DUE TO ROLL RATE WITH MACH NUMBER AT VARIOUS ANGLES OF ATTACK

where :

$$C_{\ell_p} = \left(\frac{\beta C_{\ell_p}}{K}\right) K/\beta \qquad (A.22)$$

and $(\beta C_{\ell_p}/K)$ is found from figure 8.1 of reference 13. The term K is the ratio of average wing section lift curve slope, $C_{\ell_{\alpha_w}}$, to 2π, and $\beta = \sqrt{1-M^2}$.

The roll damping derivative, C_{ℓ_p}, in equation (A.21) is determined later in this section. The term $(C_{n_p}/C_L)_{\substack{C_L=o \\ M}}$ was determined by :

$$\left(\frac{C_{n_p}}{C_L}\right)_{\substack{C_L=o \\ M}} = \left[\frac{AR + 4\cos\Lambda_{c/4}}{AR\cdot B + 4\cos\Lambda_{c/4}}\right]\left[\frac{AR\cdot B + \frac{1}{2}(AR\cdot B + \cos\Lambda_{c/4})\tan^2\Lambda_{c/4}}{AR + \frac{1}{2}(AR + \cos\Lambda_{c/4})\tan^2\Lambda_{c/4}}\right] \left(\frac{C_{n_p}}{C_L}\right)_{\substack{C_L=o \\ M=o}} \qquad (A.23)$$

where :

$$\left(\frac{C_{n_p}}{C_L}\right)_{\substack{C_L=o \\ M=o}} = 1/6\left[\frac{AR + 6(AR + \cos\Lambda_{c/4})\left(\frac{\bar{X}}{\bar{c}}\frac{\tan\Lambda_{c/4}}{AR} + \frac{\tan^2\Lambda_{c/4}}{12}\right)}{AR + 4\cos\Lambda_{c/4}}\right] \qquad (A.24)$$

The vertical tail contribution can be found from :

$$C_{n_{p_v}} = -2/b\ (\ell_v\cos\alpha + Z_v\sin\alpha)\left(\frac{Z_v\cos\alpha - \ell_v\sin\alpha}{b}\right) C_{Y_{\beta_v}} \qquad (A.25)$$

The summation of equations (A.21) and (A.25) is presented in figure A.26.

This estimated derivative differs significantly from the basic drone. This variance is attributed to the

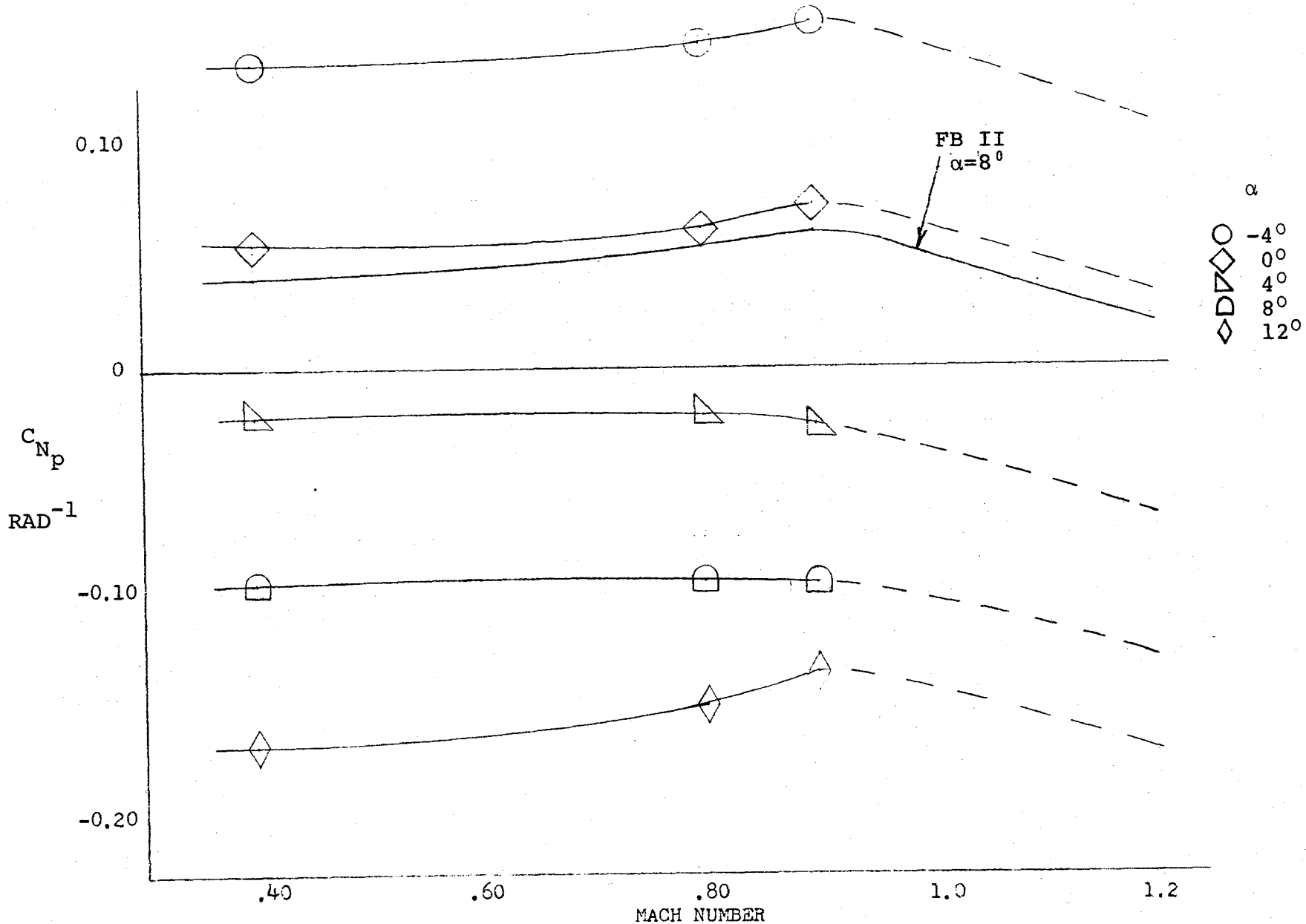

FIGURE A. 26 VARIATION IN YAWING MOMENT COEFFICIENT DUE TO ROLL RATE WITH MACH NUMBER AT VARIOUS ANGLES OF ATTACK

very different wing geometries of the two vehicles.

The roll damping derivative is derived from contributions of wing, horizontal tail, and vertical tail. The wing contribution at zero lift was estimated from equation (A.22). When C_L is greater than zero, the additional wing component is estimated by:

$$\Delta C_{\ell_{p_w}} = -\frac{1}{8}\left[\frac{C_L^2}{\pi\ AR\ \cos^2\ \Lambda_{c/4}}\left(1 + 2\ \sin^2\ \Lambda_{c/4}\left[\frac{AR + 2\ \cos\ \Lambda_{c/4}}{AR + 4\ \cos\ \Lambda_{c/4}}\right]\right) + C_{D_o}\right] \qquad \text{(A. 26)}$$

where C_{D_o} is the drag coefficient at zero angle of attack.

The horizontal tail component is approximated by:

$$C_{\ell_{p_H}} = .5\left(C_{\ell_p}\right)_H \frac{S_H}{S_{REF}}\left(\frac{b_H}{b}\right)^2 \qquad \text{(A. 27)}$$

where $\left(C_{\ell_p}\right)_H$ is the tail contribution based on its own geometry and found from equation (A. 22).

The vertical tail contribution is estimated from:

$$C_{\ell_{p_V}} = 2\left(\frac{Z_V}{b}\right)^2 C_{Y_{\beta_V}} \qquad \text{(A. 28)}$$

Figure A. 27 shows C_{ℓ_p} for the total aircraft. The higher aspect ratio of DAST I causes C_{ℓ_p} to be about twice that observed on the Firebee.

The sideforce coefficient due to angular yaw velocity is estimated from a vertical tail component only. The wing contribution is considered negligible. This derivative may be

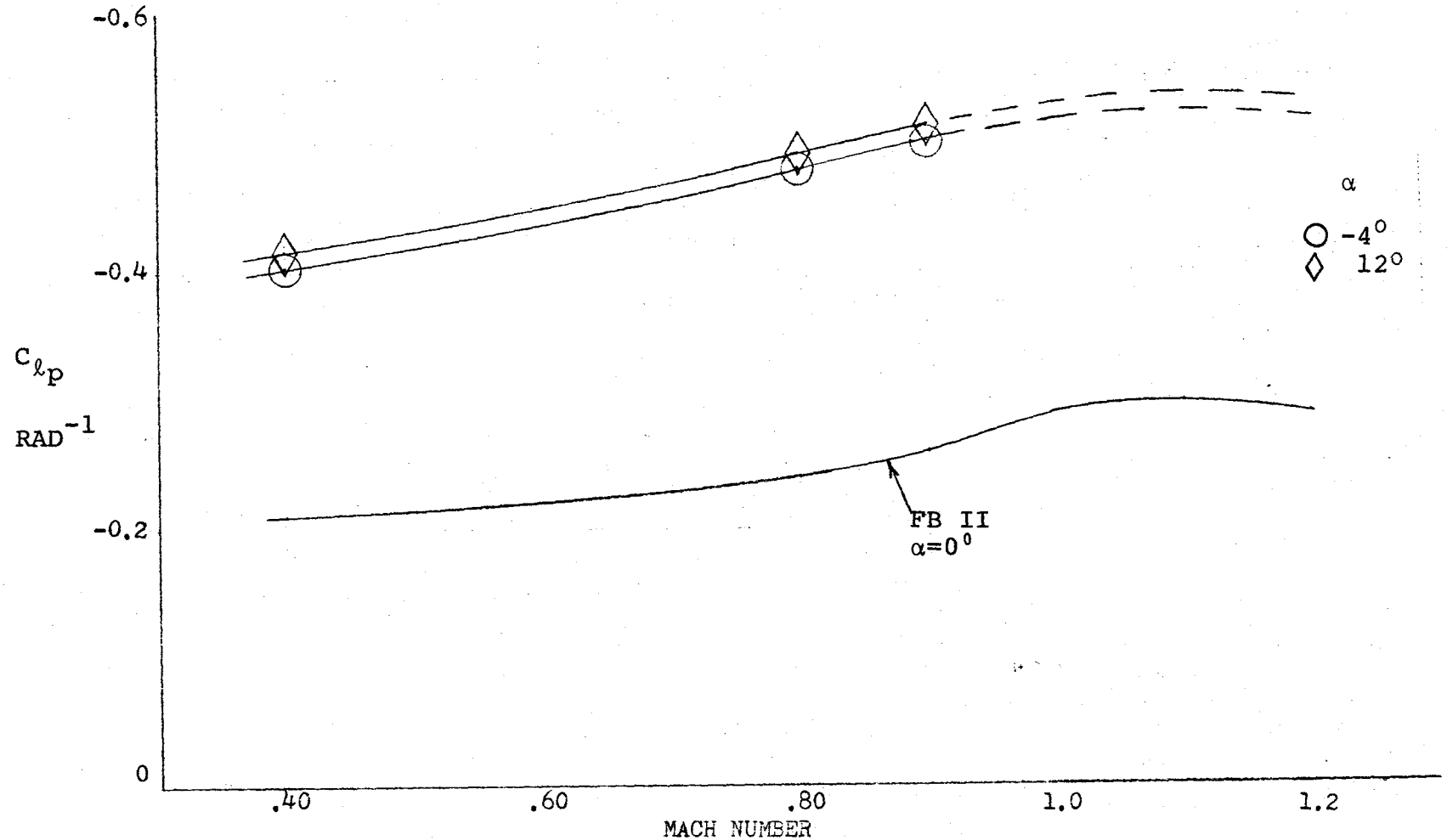

FIGURE A.27 VARIATION IN ROLLING MOMENT COEFFICIENT DUE TO ROLL RATE WITH MACH NUMBER AT VARIOUS ANGLES OF ATTACK

found from:

$$C_{y_r} \approx C_{y_{r_V}} = -\frac{2}{b}\left(\ell_V \cos\alpha + Z_V \sin\alpha\right) C_{y_{\beta_V}} \qquad \text{(A. 29)}$$

It is shown in figure A. 28. The much larger reference span of ARW-1 causes C_{y_r} to be only sixty percent of the Firebee values.

The yaw damping derivative, C_{n_r}, is estimated from consideration of two components, that due to the vertical tail and that due to the wing.

The wing contribution can be estimated by:

$$C_{n_{r_w}} = \left(\frac{C_{n_r}}{C_L{}^2}\right) C_L{}^2 + \left(\frac{C_{n_r}}{\bar{C}_{D_o}}\right) \bar{C}_{D_o} \qquad \text{(A. 30)}$$

where the ratio $(C_{n_r}/C_L{}^2)$ is found in figure 9.4 of reference 13, and the ratio $(C_{n_r}/\bar{C}_{D_o})$ can be found from figure 9.5 of reference 13. The term $\bar{C}_{D_o}$ is the drag coefficient at zero angle of attack and zero control surface settings.

The vertical tail component is found from:

$$C_{n_{r_V}} = \frac{2}{b^2}\left(\ell_V \cos\alpha + Z_V \sin\alpha\right)^2 C_{y_{\beta_V}} \qquad \text{(A. 31)}$$

The larger values for C_{n_r}, seen in figure A. 29, for the DAST I vehicle are due to the larger span.

The rolling moment coefficient due to yaw rate is presented in figure A. 30. This derivative can be estimated from a wing and vertical tail component.

The wing component of the derivative for a zero-twist,

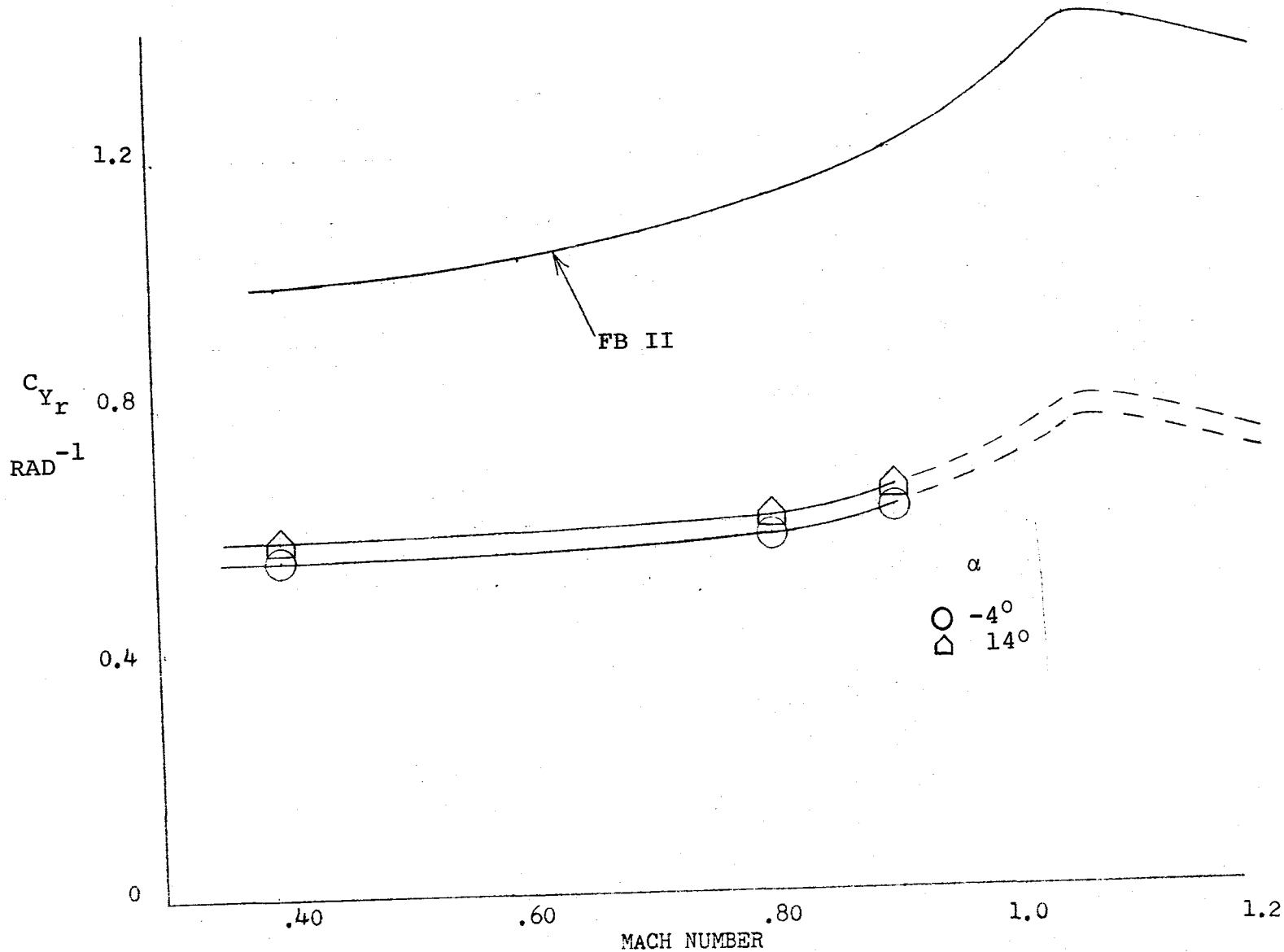

FIGURE A.28 VARIATION IN SIDEFORCE COEFFICIENT DUE TO YAW RATE WITH MACH NUMBER AT DIFFERENT ANGLES OF ATTACK

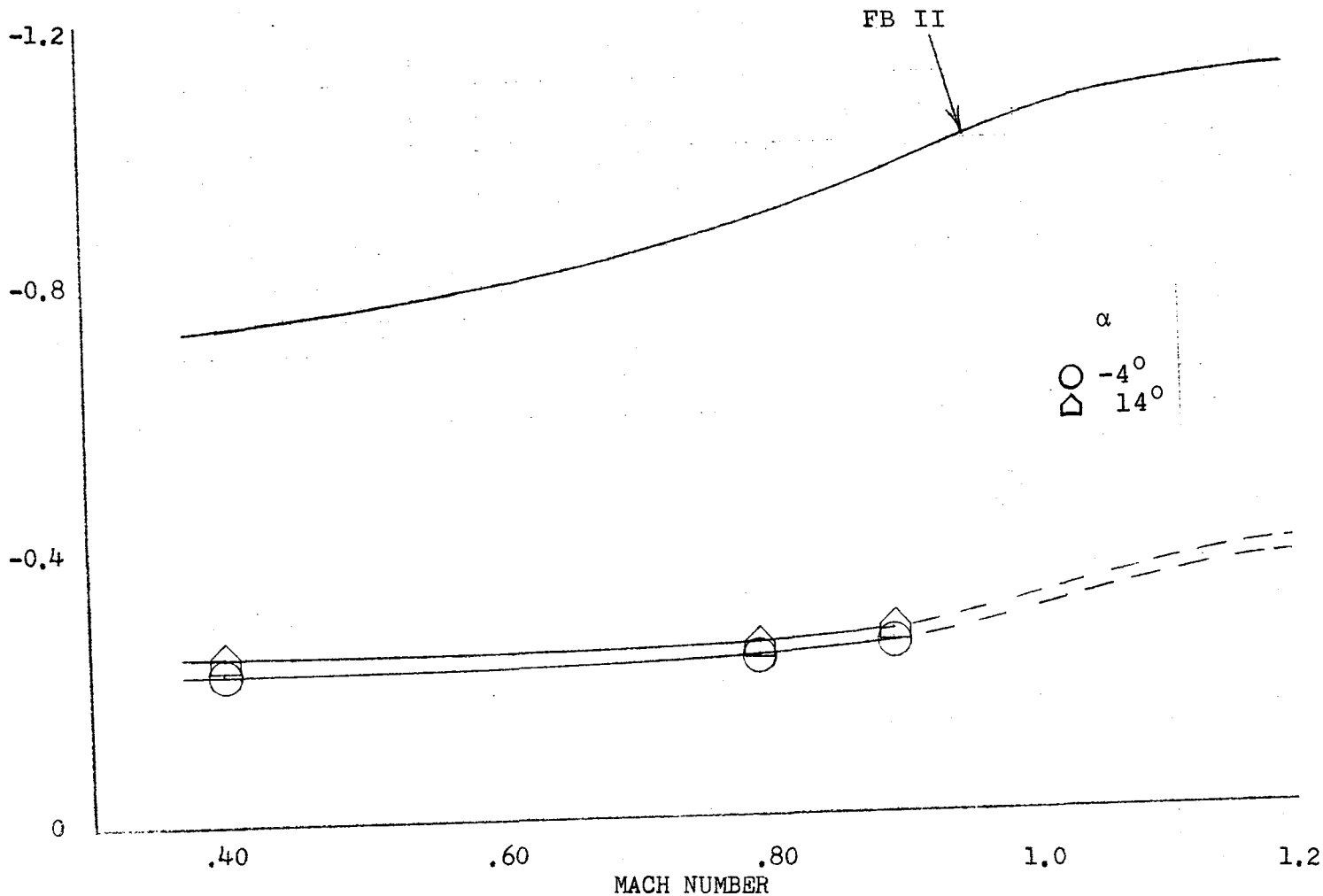

FIGURE A. 29 VARIATION IN YAWING MOMENT COEFFICIENT DUE TO YAW RATE WITH MACH NUMBER AT DIFFERENT ANGLES OF ATTACK

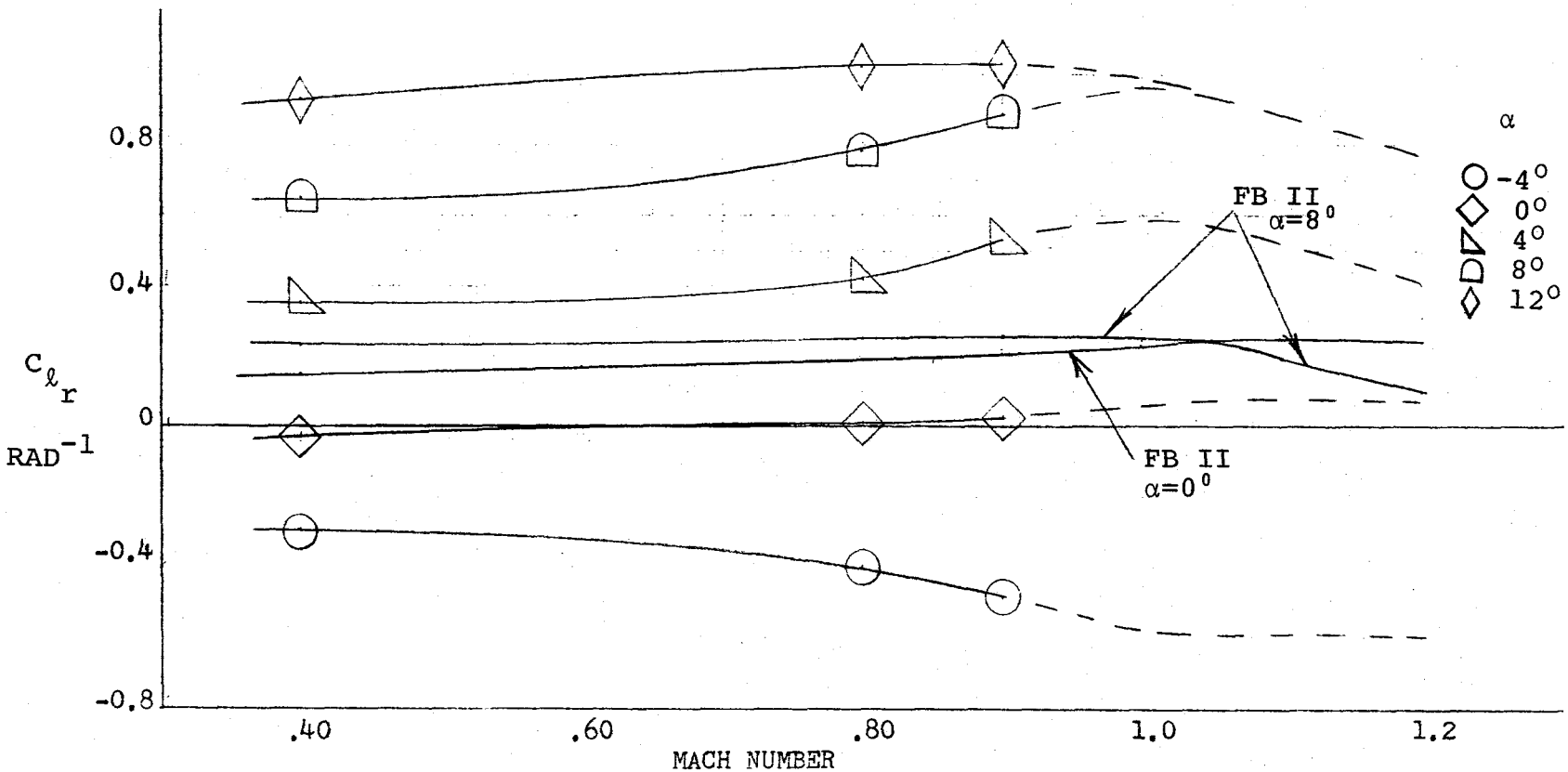

FIGURE A. 30 VARIATION IN ROLLING MOMENT COEFFICIENT DUE TO YAW RATE WITH MACH NUMBER AT VARIOUS ANGLES OF ATTACK

un-flapped, and no dihedral wing is estimated by:

$$C_{\ell_{r_w}} = C_L \left(\frac{C_{\ell_r}}{C_L}\right)_{\substack{C_L=0 \\ M}} \qquad \text{(A. 32)}$$

where the slope of the rolling moment due to yaw rate at zero lift is given by:

$$\left(\frac{C_{\ell_r}}{C_L}\right)_{\substack{C_L=0 \\ M}} = \left[\frac{1 + \frac{AR(1-B^2)}{2B(AR\cdot B + 2\cos \Lambda_{c/4})} + \frac{AR + 2\cos \Lambda_{c/4}}{AR\cdot B + 4\cos \Lambda_{c/4}} \cdot \frac{\tan^2 \Lambda_{c/4}}{8}}{1 + \frac{AR + 2 \cos \Lambda_{c/4}}{AR + 4 \cos \Lambda_{c/4}} \cdot \frac{\tan^2 \Lambda_{c/4}}{8}}\right] \cdot \left(\frac{C_{\ell_r}}{C_L}\right)_{\substack{C_L=0 \\ m=0}} \qquad \text{(A. 33)}$$

and $\left(\frac{C_{\ell_r}}{C_L}\right)_{\substack{C_L=0 \\ M=0}}$ is obtained from figure 9.1 in reference 13 as a function of quarter chord sweep angle, taper ratio, and aspect ratio.

The contribution of vertical tail was found from:

$$C_{\ell_{r_V}} = -\frac{2}{b^2} (\ell_V \cos\alpha + Z_V \sin\alpha)(Z_V \cos\alpha - \ell_V \sin\alpha) C_{Y_{\beta_V}} \qquad \text{(A.34)}$$

APPENDIX B

PROJECT RESPONSIBILITIES AND TIMETABLE

This appendix will identify the project responsibilities of the three participating organizations in the DAST I program. A milestone chart indicating the relative state of progress toward the first flight is also shown.

B.1 Project Responsibilities

The NASA Langely Research Center is the lead center in the DAST program. The NASA Dryden Flight Research Center has the responsibility for flight operations. The Boeing Wichita Company has the responsibility for design and fabrication of the flutter suppression system. Within these guidelines, the specific project responsibilities are identified in Table B.1. During flight testing BWC will participate as a consultant, but the principal investigators from DFRC and LaRC will be responsible for the conduct of the flight experiments.

B.2 Project Timetable

The DAST I project milestones are listed in Table B.2 The program began in July, 1974, and will continue through late 1979. First flight is planned for March, 1979, and the flight activity rate is expected to be one flight per month for the six scheduled flights. A system check flight (milestone number 26) with a standard wing is planned for late 1978.

TABLE B.1 PROJECT RESPONSIBILITIES

Tasks	LaRC	DFRC	BWC
Project Funding and Procurement	X		
Define Goals and Objectives	X	X	
Flutter Experiment Requirements	X	X	
Wing Design and Construction	X		
FSS Design			X
FSS Fabrication			X
Wing Instrumentation	X		
Flutter Instrumentation (PCM)	X	X	
Wind Tunnel Tests	X		X
DAST Avionic Systems		X	
DAST Simulation		X	
DAST Flight Controls		X	
Flutter Testing Methods	X	X	X
Flight Planning		X	
Flight Operations		X	
Flight Safety		X	
Data Collection		X	
Data Reduction	X	X	
Flight Testing	X	X	X
Reporting	X	X	X

TABLE B.2 - DAST I PROJECT MILESTONES (PAGE 1 OF 2)

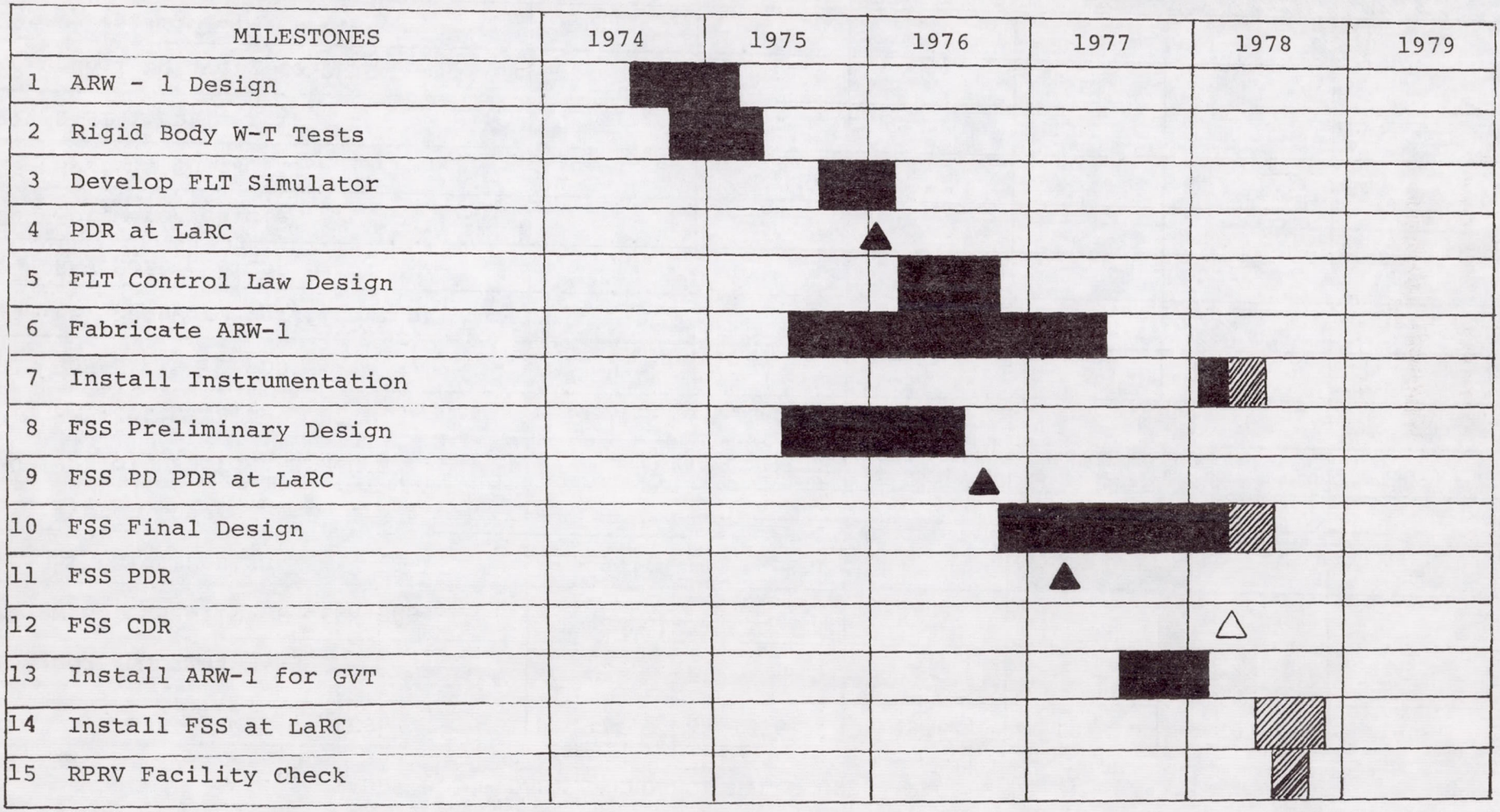

TABLE B.2 - DAST I PROJECT MILESTONES (PAGE 2 OF 2)

MILESTONES	1974	1975	1976	1977	1978	1979
16 B52 and F104 Mods						
17 Wind Tunnel Test with FSS						
18 Avionics Design						
19 System Checks						
20 Vehicle Buildup DFRC						
21 RAV Software Dev.						
22 RAV Software PDR						
23 RAV Software Verification						
24 RAV Software CDR						
25 Software/Vehicle FRR						
26 Systems Check FLT						
27 DAST I FRR						
28 ARW-1 Delivery to DFRC						
29 Install ARW-1						
30 Evaluate Flutter Testing Methods						
31 DAST I FLT Activity						

APPENDIX C

ARW-1 FLUTTER SIMULATION

This appendix describes the development of the state variable representation of the ARW-1 equations of motion used in the FSS analysis. Transient responses at the accelerometer location at WBL(79) were generated using a modified version of the CONTROL program (reference 8). This system of equations includes inputs from the control surface and turbulence from a Dryden gust model.

C.1 State Variable Formulation

The Laplace representation of the ARW-1 equations of motion was given in equation (4.2) of section 4.1.1. To generate time histories of this system using CONTROL the equations were transformed to the form:

$$\{\dot{X}\} = [A]\{X\} + [B]\{U\} \qquad (C.1)$$

This transformation was accomplished in the following manner:

$$\{X^i_1\} = \{q_i(t)\} \qquad (C.2)$$

$$\{X^i_2\} = \{\dot{X}^i_1\} = \{\dot{q}_i(t)\} \qquad (C.3)$$

The augmented states which represent the lag in buildup of circulation are:

$$\{X^i_3\} = \frac{S}{S + U_o b_1} \{q_i(s)\} \qquad (C.4)$$

$$\left\{X_4^i\right\} = \frac{s}{s + U_o b_2} \left\{q_i(s)\right\} \tag{C.5}$$

$$\left\{X_5^i\right\} = \frac{s}{s + U_o b_3} \left\{q_i(s)\right\} \tag{C.6}$$

$$\left\{X_6^i\right\} = \frac{s}{s + U_o b_4} \left\{q_i(s)\right\} \tag{C.7}$$

In time domain the equations (C.4) through (C.7) become:

$$\left\{\dot{X}_3^i\right\} = -U_o b_1 \left\{X_3^i\right\} + \left\{\dot{q}_i\right\} = -U_o b_1 \left\{X_3^i\right\} + \left\{X_2^i\right\} \tag{C.8}$$

$$\left\{\dot{X}_4^i\right\} = -U_o b_2 \left\{X_4^i\right\} + \left\{X_2^i\right\} \tag{C.9}$$

$$\left\{\dot{X}_5^i\right\} = -U_o b_3 \left\{X_5^i\right\} + \left\{X_2^i\right\} \tag{C.10}$$

$$\left\{\dot{X}_6^i\right\} = -U_o b_4 \left\{X_6^i\right\} + \left\{X_2^i\right\} \tag{C.11}$$

If the higher wing modes are truncated and seven modes are kept , the number of states generated is 42. This truncation causes no problems since the accuracy in the higher modes is dubious due to the 400 rad/sec limitation on the aerodynamic approximations and the higher modes were shown to have no effect on the flutter characteristics. The x-translation and z-translation rigid body modes were also dropped to reduce computer core memory requirements. They also were shown to be irrelavant to the flutter problem. The rigid body pitch mode was kept.

The wing's response due to gust inputs also requires augmented states to represent the lag in buildup of circulation.

These terms are:

$$X_{43} = \frac{S}{S + U_o g_1} \quad w_g(s) \tag{C.12}$$

$$X_{44} = \frac{S}{S + U_o g_2} \quad w_g(s) \tag{C.13}$$

$$X_{45} = \frac{S}{S + U_o g_3} \quad w_g(s) \tag{C.14}$$

$$X_{46} = \frac{S}{S + U_o g_4} \quad w_g(s) \tag{C.15}$$

or:

$$\dot{X}_{43} = -U_o g_1 \; X_{43} + \dot{w}_g \tag{C.16}$$

$$\dot{X}_{44} = -U_o g_2 \; X_{44} + \dot{w}_g \tag{C.17}$$

$$\dot{X}_{45} = -U_o g_3 \; X_{45} + \dot{w}_g \tag{C.18}$$

$$\dot{X}_{46} = -U_o g_4 \; X_{46} + \dot{w}_g \tag{C.19}$$

The Dryden form of the spectra for the turbulence velocity (MIL - F8785B ASG) for a vertical gust is:

$$\Phi_{w_g}(\Omega) = \sigma_w^2 \frac{L_w}{\pi} \frac{1 + 3\left(L_w\Omega\right)^2}{\left[1 + \left(L_w\Omega\right)^2\right]^2} \tag{C.20}$$

In converting from spatial frequency, equation (C.20) becomes:

$$\Omega = \frac{\omega}{U_o}$$

$$\phi_{w_g}(\omega) = \sigma_w^2 \frac{L_w}{\pi U_o} \frac{1 + 3\left(L_w \frac{\omega}{U_o}\right)^2}{\left[1 + \left(L_w \frac{\omega}{U_o}\right)^2\right]^2} \qquad (C.21)$$

The frequency, ω, is related to the Laplace variable by $\omega = s/j$ so equation (C.21) reduces to :

$$\left|\frac{w_g(s)}{\eta(s)}\right|^2 = \sigma_w^2 \frac{L_w}{\pi U_o} \frac{1 + 3\left(\frac{L_w}{U_o} s/j\right)^2}{\left[1 + \left(\frac{L_w}{U_o} s/j\right)^2\right]^2} \qquad (C.22)$$

$$= \sigma_w^2 \frac{L_w}{\pi U_o} \frac{1 - 3\left(\frac{L_w}{U_o} s\right)^2}{\left[1 - \left(\frac{L_w}{U_o} s\right)^2\right]^2}$$

$$= \left[\sigma_w \sqrt{\frac{L_w}{\pi U_o}} \frac{\left(1 + \sqrt{3}\frac{L_w}{U_o} s\right)}{\left(1 + \frac{L_w}{U_o} s\right)^2}\right]\left[\sigma_w \sqrt{\frac{L_w}{\pi U_o}} \frac{\left(1 - \sqrt{3}\frac{L_w}{U_o} s\right)}{\left(1 - \frac{L_w}{U_o} s\right)^2}\right]$$

$$= \left|\frac{w_g(s)}{\eta(s)} \cdot \frac{\overline{w_g(s)}}{\eta(s)}\right| \qquad (C.23)$$

From equation (C.23) the expression describing the vertical gust is:

$$\frac{w_g(s)}{\eta(s)} = \sigma_w \sqrt{\frac{L_w}{\pi U_o}} \frac{\left(1 + \sqrt{3}\frac{L_w}{U_o} s\right)}{\left(1 + \frac{L_w}{U_o} s\right)^2} \qquad (C.24)$$

After equation (C.24) is placed in a standard transfer function form the state variable representation of the vertical becomes:

$$\dot{X}_{47} = X_{48} \tag{C.25}$$

$$\dot{X}_{48} = \frac{-2U_o}{L_w} X_{48} - \frac{U_o^2}{L_w^2} X_{47} + \sigma_w \sqrt{\frac{3U_o}{\pi L_w}}\ \eta \tag{C.26}$$

$$w_g = \frac{U_o}{\sqrt{3}\, L_w} X_{47} + X_{48} \tag{C.27}$$

$$\begin{aligned} \dot{w}_g &= \frac{U_o}{\sqrt{3}\, L_w} \dot{X}_{47} + \dot{X}_{48} \\ &= \frac{U_o}{L_w} \left(\frac{1}{\sqrt{3}} - 2 \right) X_{48} - \frac{U_o^2}{L_w^2} X_{47} + \sigma_w \sqrt{\frac{3U_o}{\pi L_w}}\ \eta \end{aligned} \tag{C.28}$$

The input variable, η_t, represents Gaussian white noise of unity variance.

Although the control surface is considered one of the ARW-1 modes, it was considered separately so that actuator dynamics could be included in the equations.

$$X_{49} = \delta_s \tag{C.29}$$

$$X_{50} = \dot{\delta}_s \tag{C.30}$$

$$\dot{X}_{51} = X_{50} - U_o b_1 X_{51} \tag{C.31}$$

$$\dot{X}_{52} = X_{50} - U_o b_2 X_{52} \tag{C.32}$$

$$\dot{X}_{53} = X_{50} - U_o b_3 X_{53} \tag{C.33}$$

$$\dot{X}_{54} = X_{50} - U_o b_4 X_{54} \tag{C.34}$$

Equations (C.31) through (C.34) represent the lag in buildup of circulation due to control surface movement.

The transfer function representing the actuator is:

$$\frac{\delta_s}{\delta_c} = \frac{(846)^2}{s^2 + 758s + (846)^2} \qquad (C.35)$$

This is a simplification of the closed loop no-load transfer function described in the first critical design review at BWC held in October of 1977. The complete transfer function is presented in Section 5.3. The poles at 10.14 radians and 375.4 radians were neglected because of pole-zero cancellation. The pole at 10.14 radians is cancelled by a zero in the actuator transfer function and the pole at 375.4 radians is essentially cancelled by the pole in the compensation filter shown in figure 4.5. The higher frequency second order poles in the complete actuator transfer function are neglected due to their frequencies being much higher than the frequency range of the wing modes.

The equations of motion now become: (C.36)

$$\left[M\right]\left\{\dot{X}^i_2\right\} + \left(\left[Z\right] + \rho U_o\left[C_2\right]\right)\left\{X^i_2\right\} + \left(\left[K\right] + \rho U_o^2\left[C_3\right]\right)\left\{X^i_1\right\}$$

$$+ \rho U_o^2 \sum_{j=1}^{4}\left[D_j\right]\left\{X^i_{j+2}\right\} + \left(\rho U_o^2\left[C_{3_{i\delta s}}\right] + (846)^2\left[M_{i\delta s}\right]\right)X_{49}$$

$$+ \left(\rho U_o\left[C_{2i\delta_s}\right] + 758\left[M_{i\delta_s}\right]\right)X_{50} + \rho U_o^2 \sum_{j=1}^{4}\left[D_{ji\delta_s}\right]X_{j+50}$$

$$+ \frac{\rho U_o^2}{\sqrt{3}\,L_w}\left[R_o\right]_i X_{47} + \rho U_o\left[R_o\right]_i X_{48} + \rho U_o \sum_{j=1}^{4}\left[R_j\right]_i X_{j+42} = 0$$

Moving all the terms in equation (C.36) to the right hand side and multiplying by the inverse of the mass matrix ($[M]^{-1}$) the vector $\left\{\dot{X}_2^i\right\}$ is defined. This only leaves $\dot{X}_{50}$ undefined in order to use equation (C.1).

Acceleration of the control surface is

$$\dot{X}_{50} = -\left[M_{\delta_s i}\right]^{-1}\left[\left(\rho U_o^2\left[C_{3_{i\delta_s}}\right] + (846)^2\left[M_{i\delta_s}\right]\right)X_{49}\right.$$
$$+\left(\rho U_o\left[C_{z_{i\delta_s}}\right] + 758\left[M_{i\delta_s}\right]\right)X_{50} \qquad (C.37)$$
$$+\rho U_o^2\sum_{j=1}^{4}\left[D_{j_{i\delta_s}}\right]X_{50+j} + \rho U_o\left[R_o\right]_{\delta_s}X_{48}$$
$$\left.+\frac{\rho U_o^2}{\sqrt{3}L_w}\left[R_o\right]_{\delta_s}X_{47} + \rho U_o\sum_{j=1}^{4}\left[R_j\right]_{\delta_s}X_{42+j}\right]$$
$$+\delta_c\,(846)^2$$

Equation (C.37) differs from the control surface terms in equation (C.36) in that they represent the coupling of the control surface to the wing modes in equation (C.36) while in equation (C.37) the coupling of the wing modes to the control surface are represented. The coupling of the wing modes to the control surface were necessary to prevent a destabilization of the sixth wing mode in closed loop FSS operation.

The inputs into the system are illustrated in figure C.1. The noise input to the gust is uncorrelated Guassian white noise of unity variance.

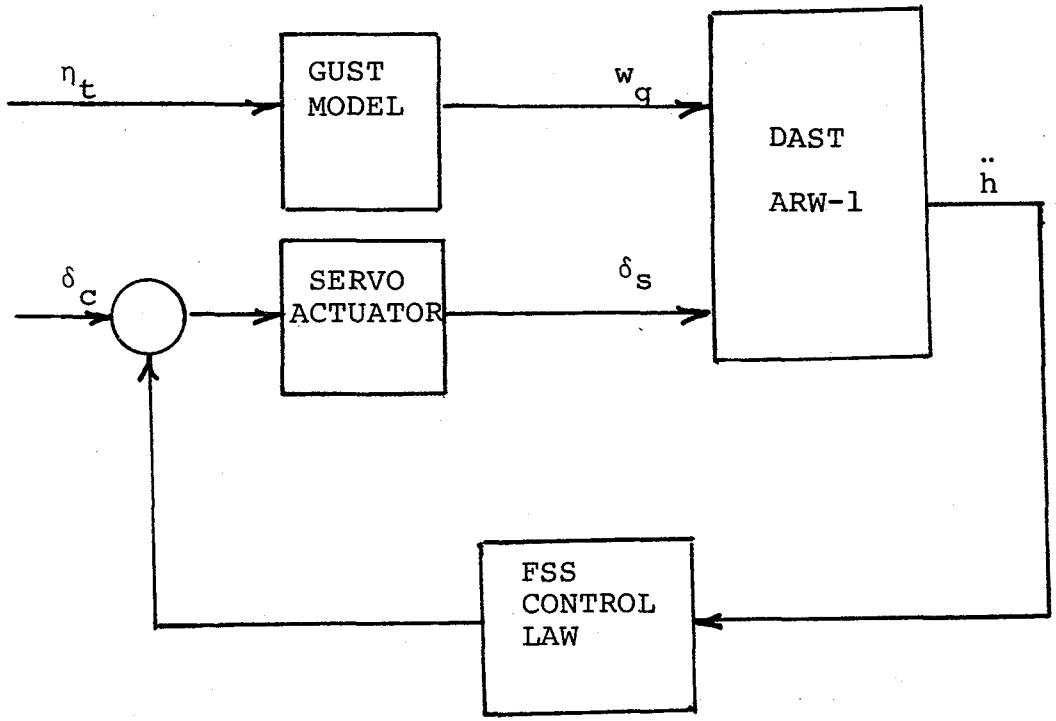

FIGURE C.1 DAST FLUTTER SIMULATION INPUTS

The input vector is:

$$\{u\} = \begin{Bmatrix} \delta_c \\ \eta_t \end{Bmatrix} \qquad (C.38)$$

The first term, δ_c, is input to $\dot{X}_{50}$ (equation (C.37) after being multiplied by the gain $(846)^2$ in the [B] matrix. The noise input, η_t, into the gust terms $\dot{X}_{43}$ through $\dot{X}_{46}$ and $\dot{X}_{48}$ is multiplied by the constant $\sigma_w\sqrt{\frac{3U_o}{\pi L_w}}$ in [B].

The output equation is:

$$\{h\} = [H]\{X\} + [G]\{\dot{X}\} \qquad (C.39)$$

The matrices [H] and [G] contain the modal response information:

$$h = \sum_{i=1}^{m} \phi_i(x,y)\, q_i(t) \qquad (C.40)$$

$$\dot{h} = \sum_{i=1}^{m} \phi_i(x,y)\, \dot{q}_i(t) \qquad (C.41)$$

$$\ddot{h} = \sum_{i=1}^{m} \phi_i(x,y)\, \ddot{q}_i(t) \qquad (C.42)$$

If the wing coordinates for the accelerometer location are used then equation (C.42) gives the simulated accelerometer signal. The vertical gust and surface movement were also output for analysis purposes.

C.2 Solution Methods - The transient responses for the DAST ARW-1 were generated by a modified version of CONTROL. In this computer program the transition matrix and its integral are used. These are:

$$\phi(t) = e^{[A]t} = I + [A]t + \frac{1}{2!}[A]^2 t^2 + \frac{1}{3!}[A]^3 t^3 + \frac{1}{n!}[A]^n t^n \quad (C.43)$$

$$\int_o^t e^{[A](t-\tau)} d\tau = It + \frac{1}{2!}[A] t^2 + \frac{1}{3!}[A]^2 t^3 + \frac{1}{n!} \cdot [A]^{(n-1)} t^n \quad (C.44)$$

The solution of the state equations becomes:

$$\{X(t)\} = \phi(t) \{X_o\} + \int_o^t \phi(t-\tau)\, u^*(\tau) d\tau \quad (C.45)$$

where $u^*(\tau) = [B] \{u(\tau)\}$

The eigenvalues of the system were in good agreement with BWC's results.

The closed loop responses were generated using a simplified FSS control law supplied by BWC. This simplified control law matches the complete FSS control law very well up to about 400 rad/sec. A block diagram of this symmetric control law is shown in figure C.2.

The accelerations in the individual modes for the cases examined in this report are presented in the following:

Figure C.3 Subcritical Open Loop Responses

Figure C.4 Subcritical Closed Loop Responses

Figure C.5 Supercritical Closed Loop Responses

Figure C.6 Supercritical Closed Loop with Turbulence

For purposes of comparison to the simulated accelerometer signal and control surface movements shown in figure 6.46, the following responses are also included:

Figure C.7 Subcritical Open Loop with Turbulence

Figure C.8 Subcritical Closed Loop with Turbulence

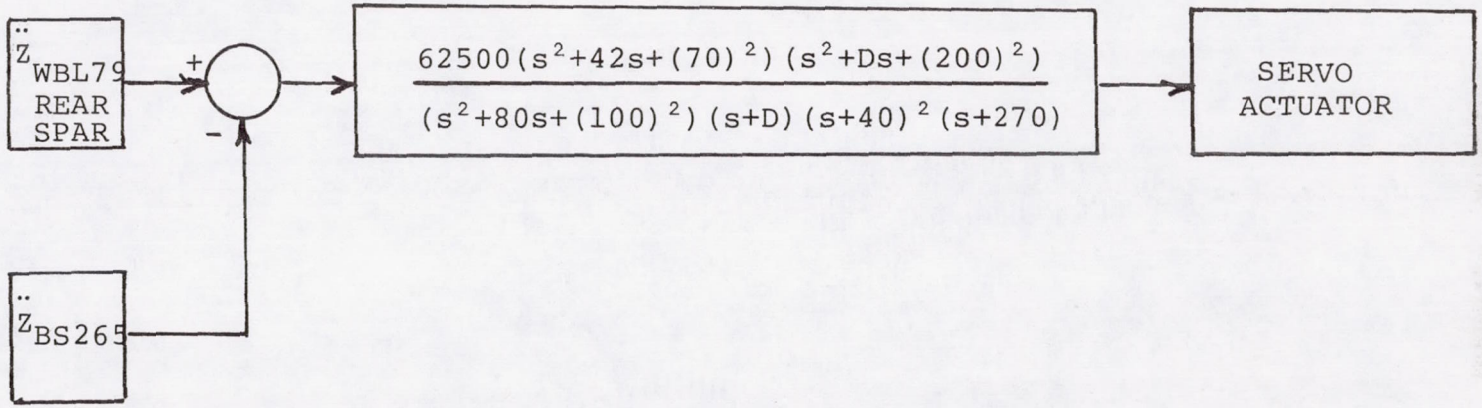

FIGURE C.2 DAST I FSS SIMPLIFIED CONTROL LAW

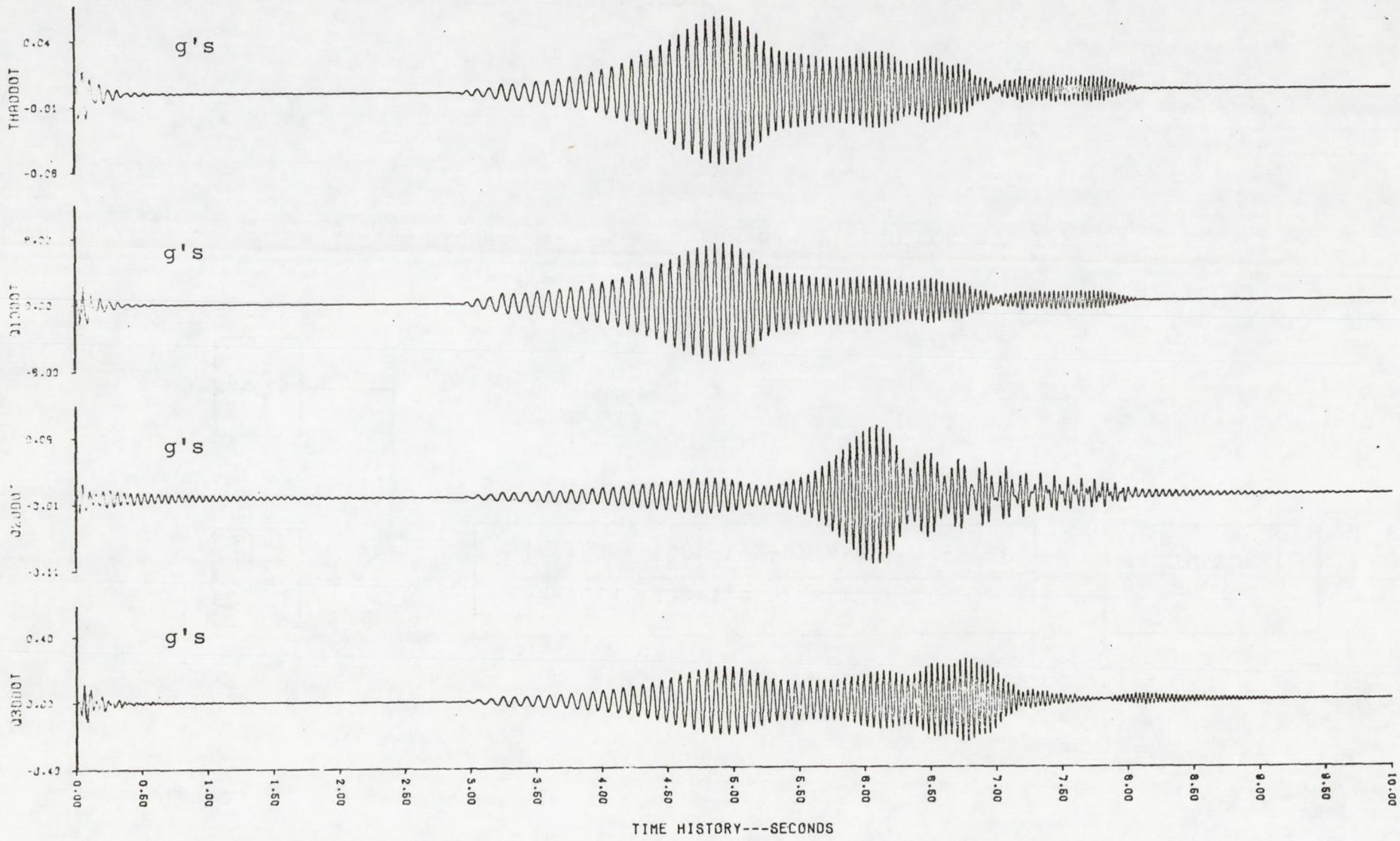

FIGURE C.3 SUBCRITICAL OPEN LOOP RESPONSES (PAGE 1 OF 2)

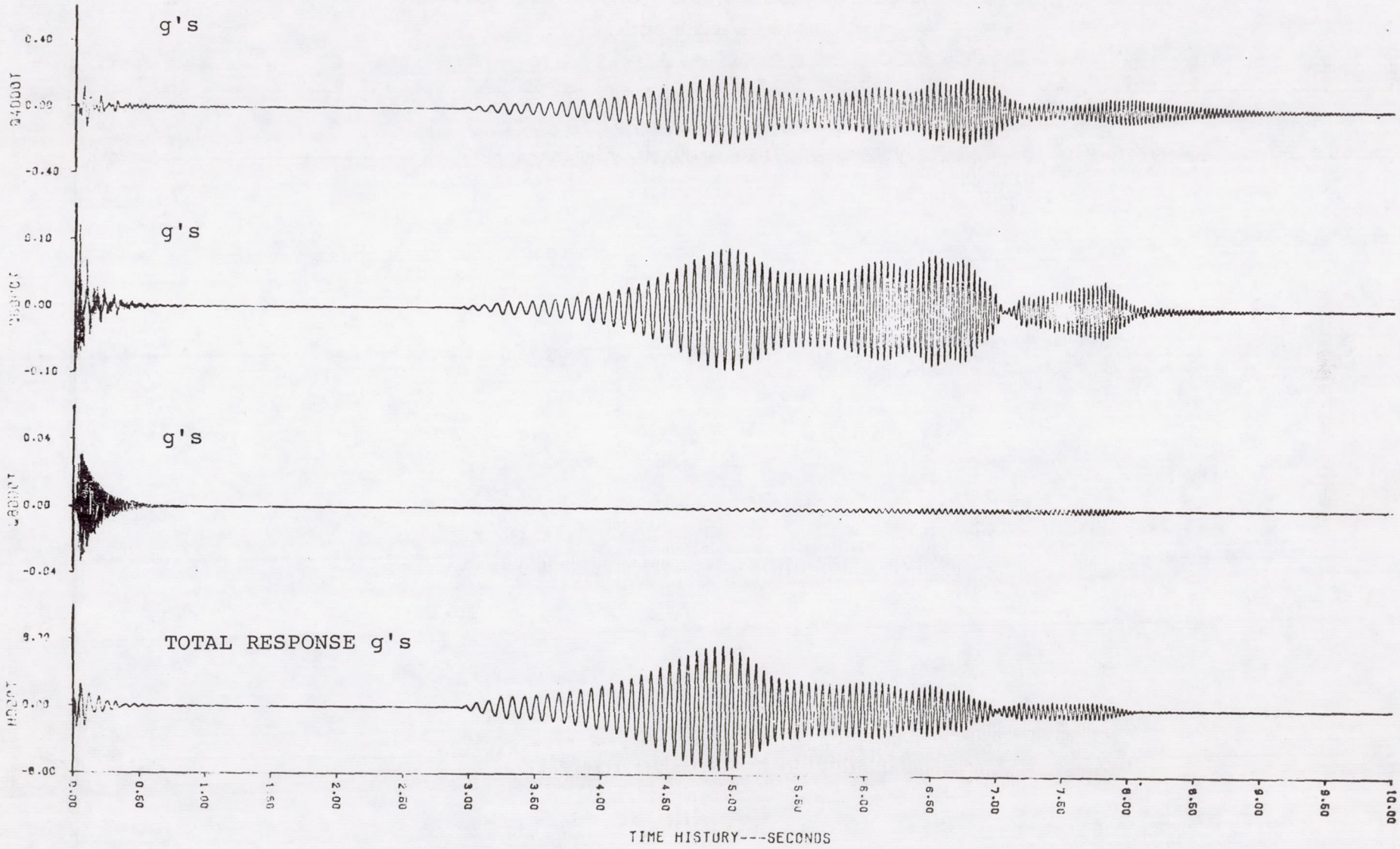

FIGURE C.3 (CONCLUDED) (PAGE 2 OF 2)

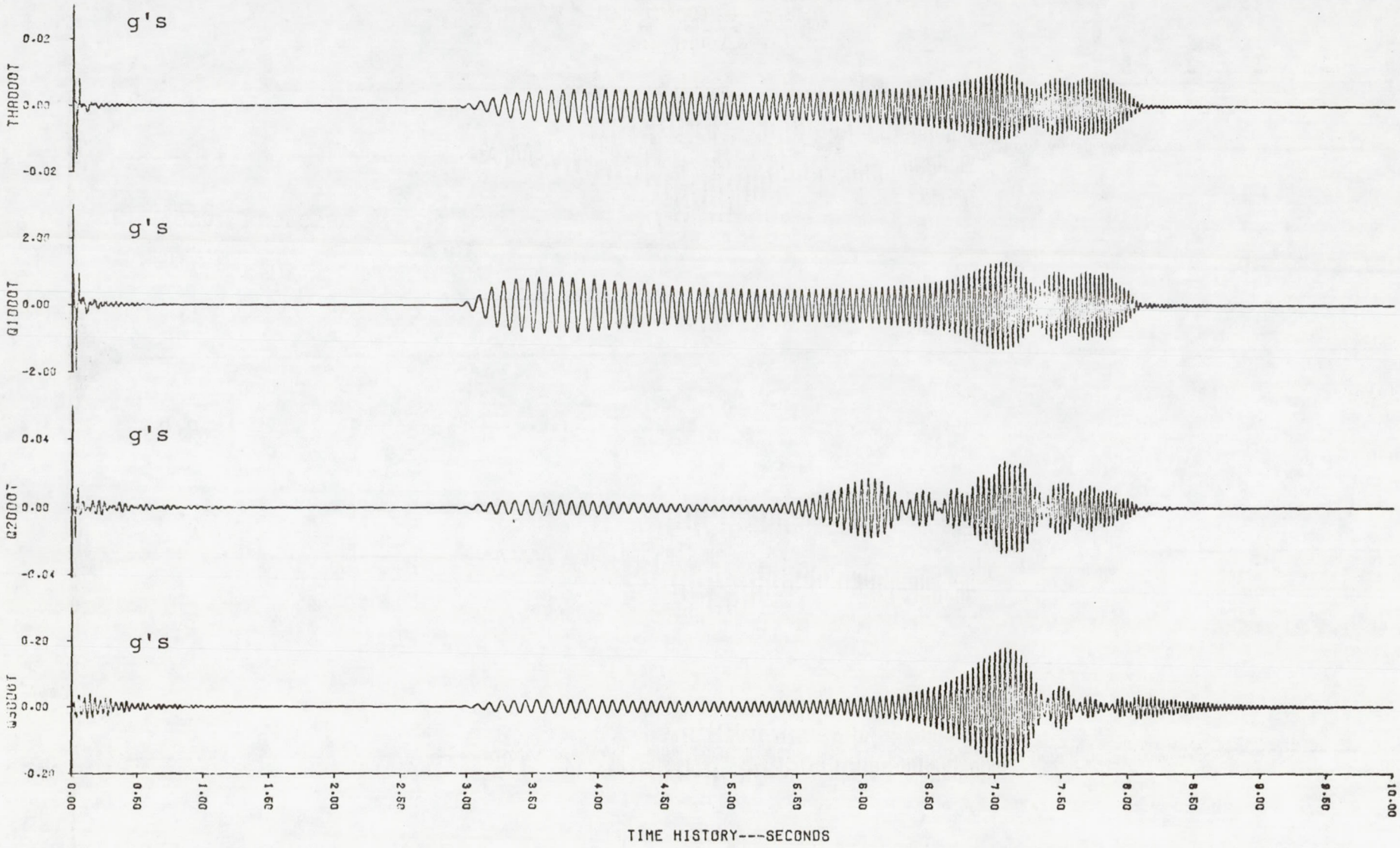

FIGURE C.4 SUBCRITICAL CLOSED LOOP RESPONSES (PAGE 1 OF 2)

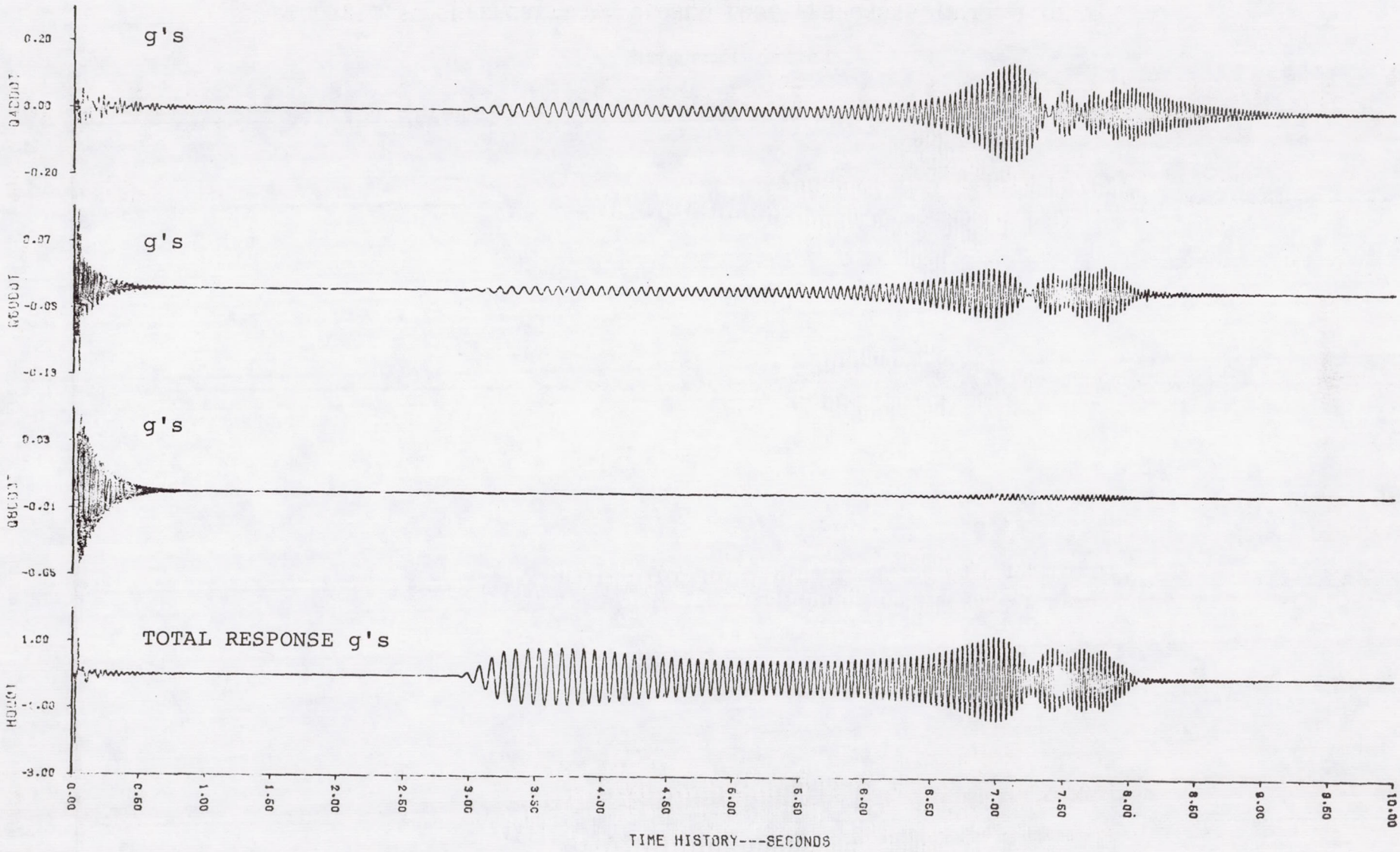

FIGURE C.4 (CONCLUDED) (PAGE 2 OF 2)

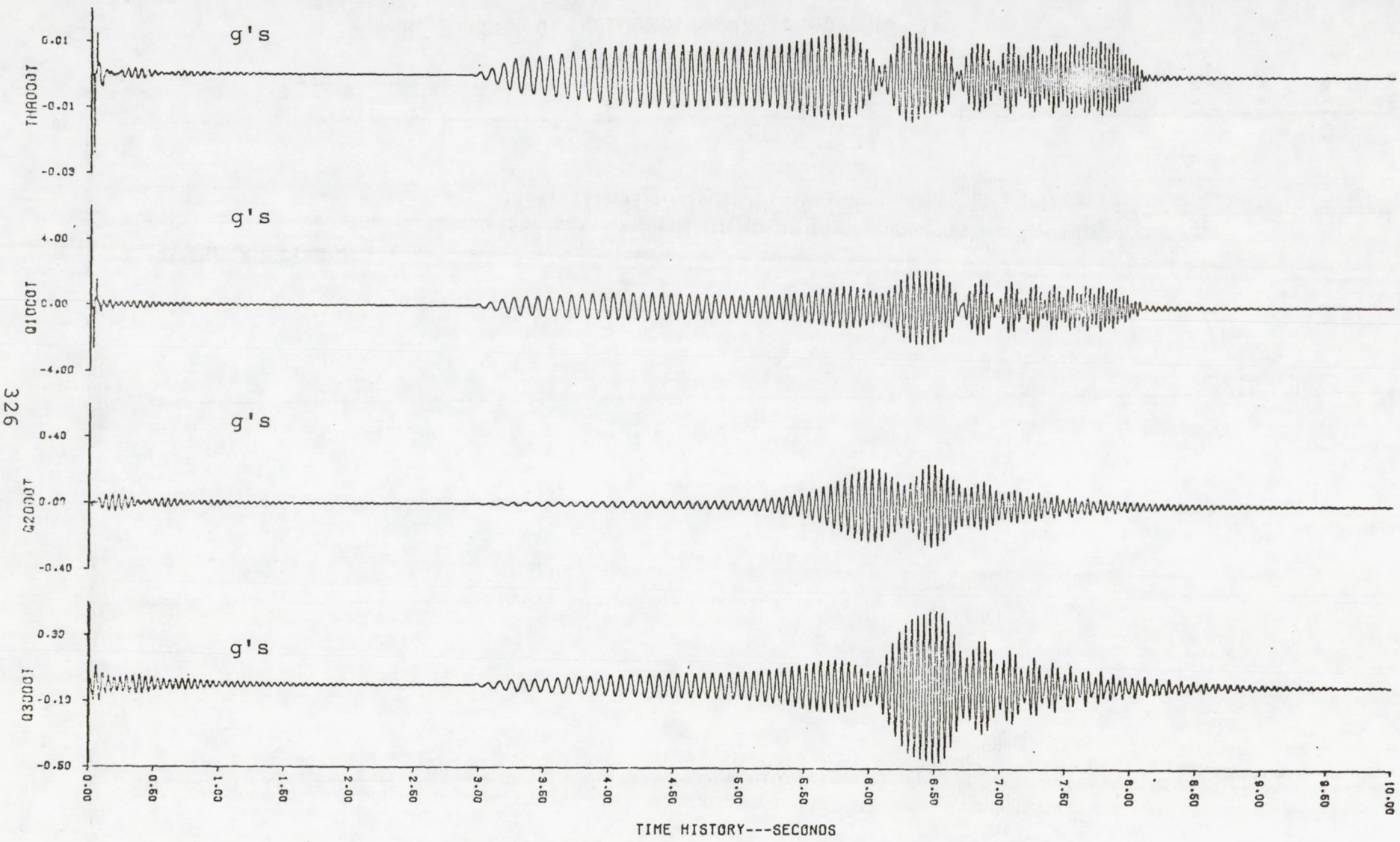

FIGURE C.5 SUPERCRITICAL CLOSED LOOP RESPONSES (PAGE 1 OF 2)

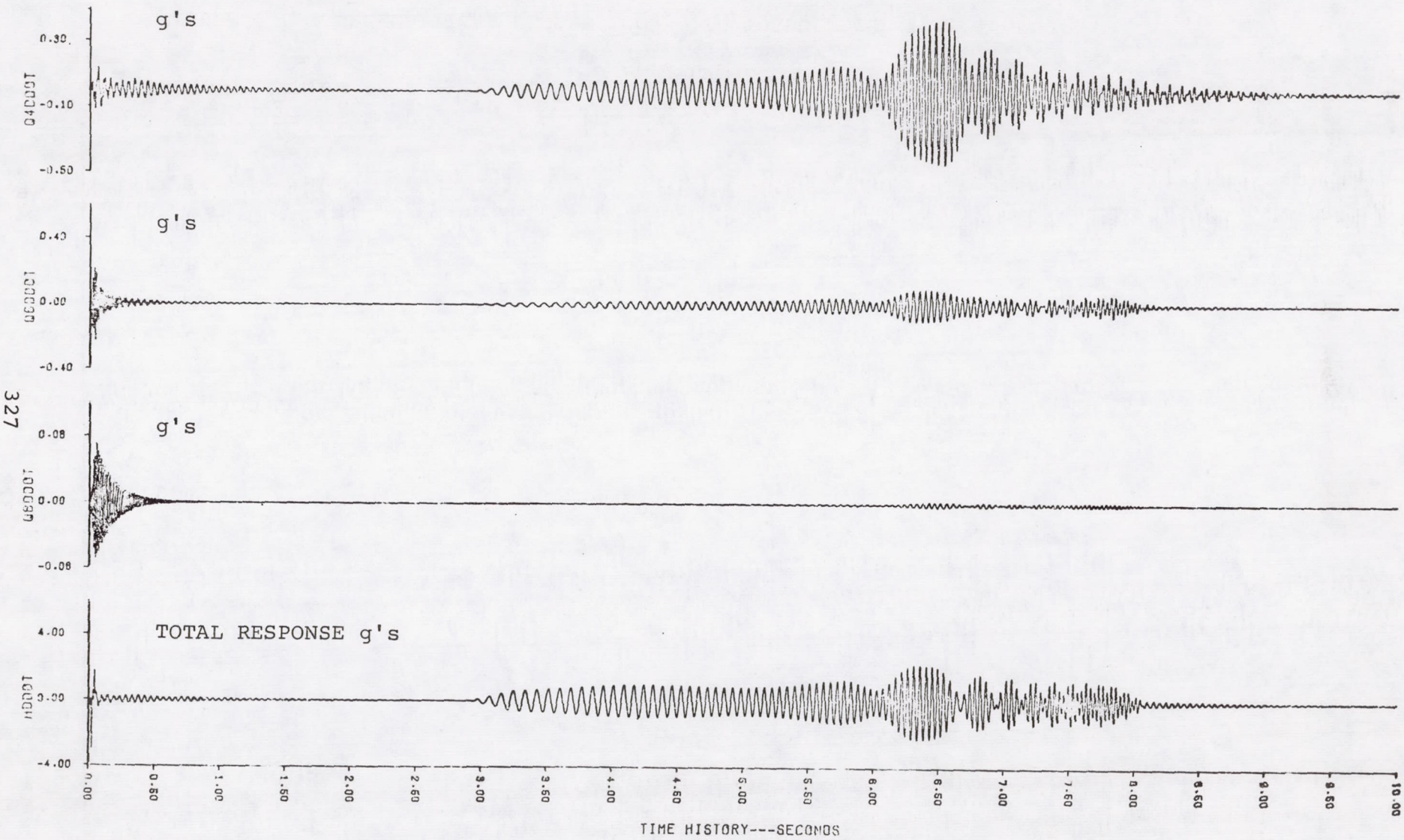

FIGURE C.5 (CONCLUDED) (PAGE 2 OF 2)

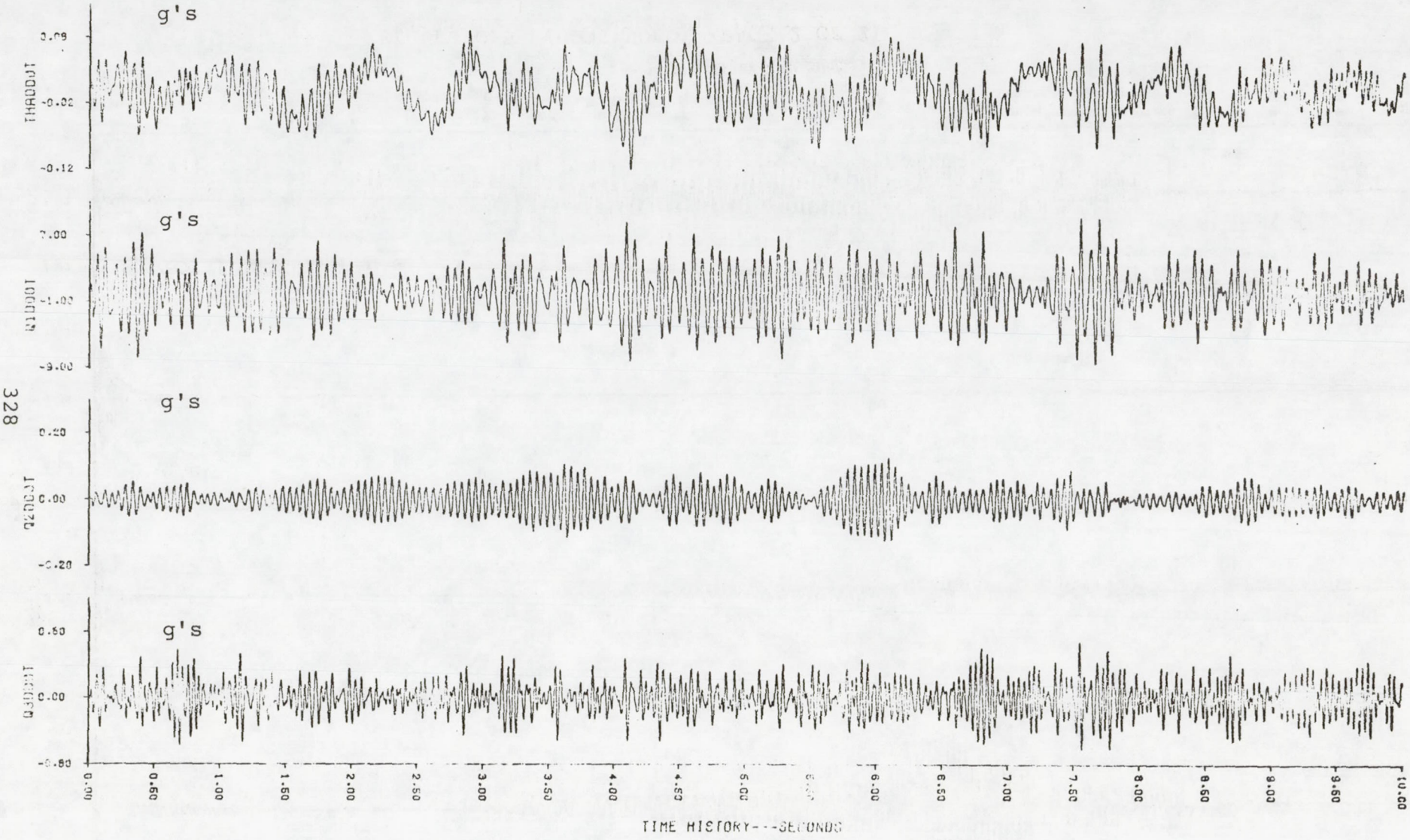

FIGURE C.6 SUPERCRITICAL CLOSED LOOP WITH TURBULENCE (PAGE 1 OF 2)

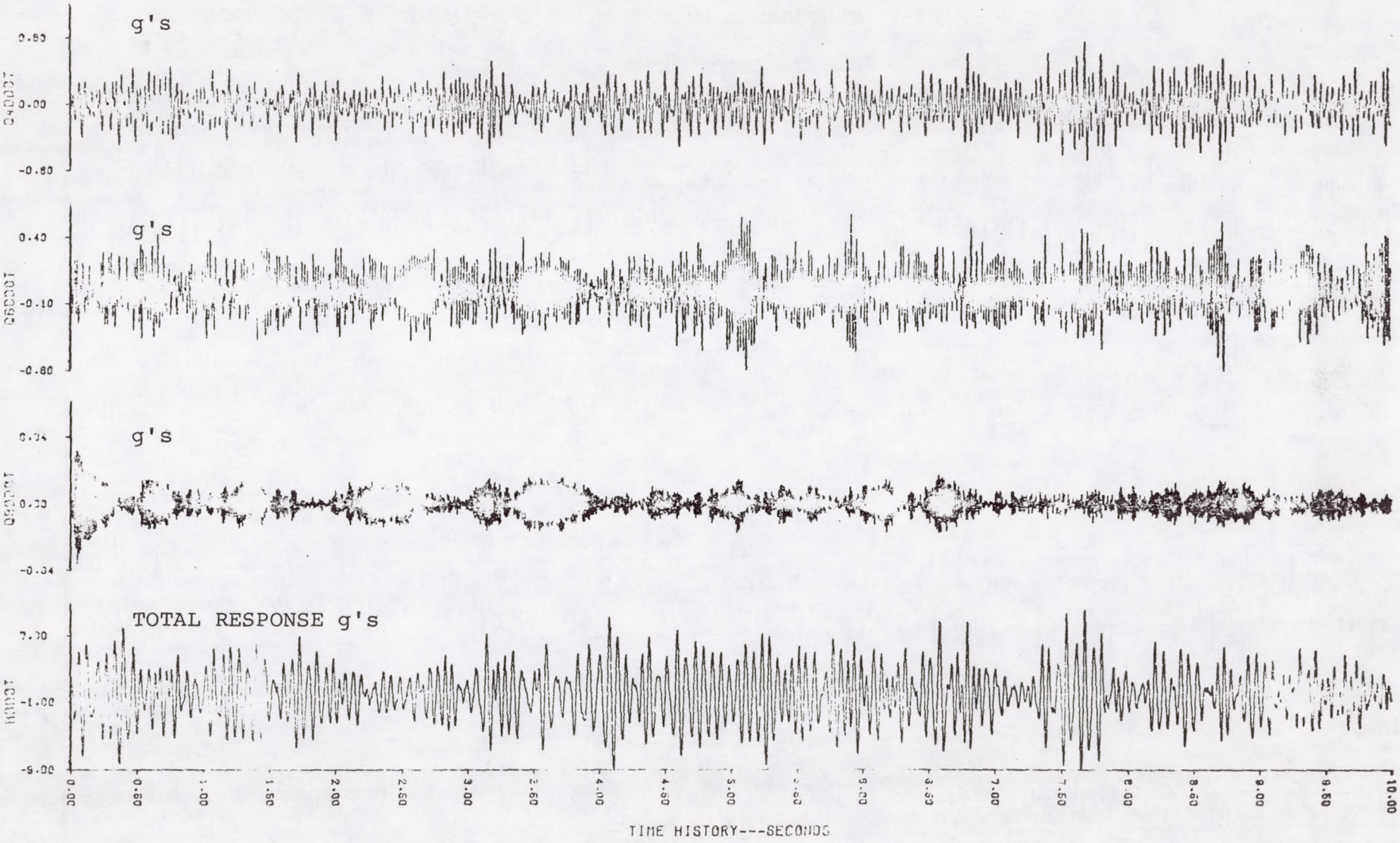

FIGURE C.6 (CONCLUDED) (PAGE 2 OF 2)

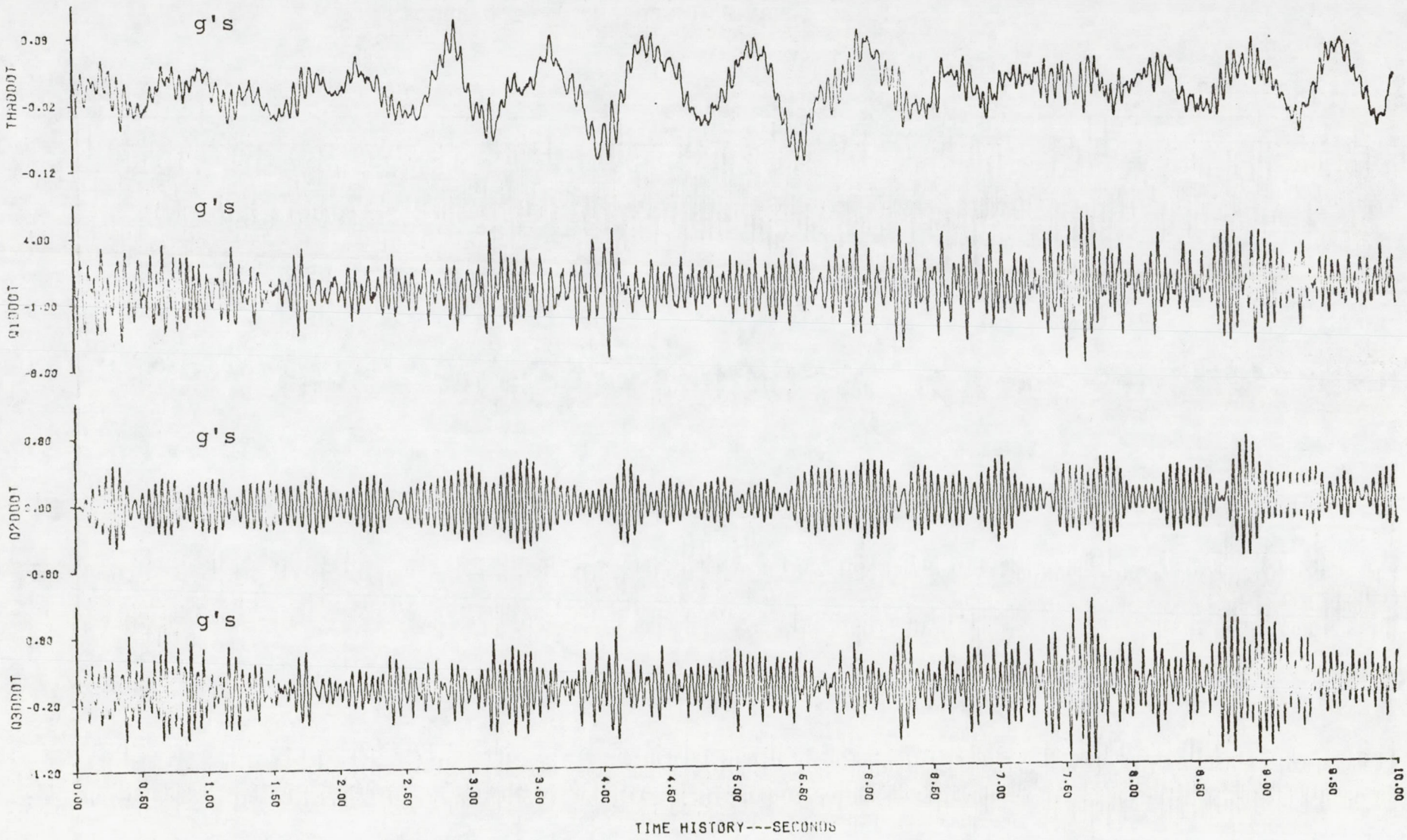

FIGURE C.7 SUBCRITICAL OPEN LOOP WITH TURBULENCE (PAGE 1 OF 3)

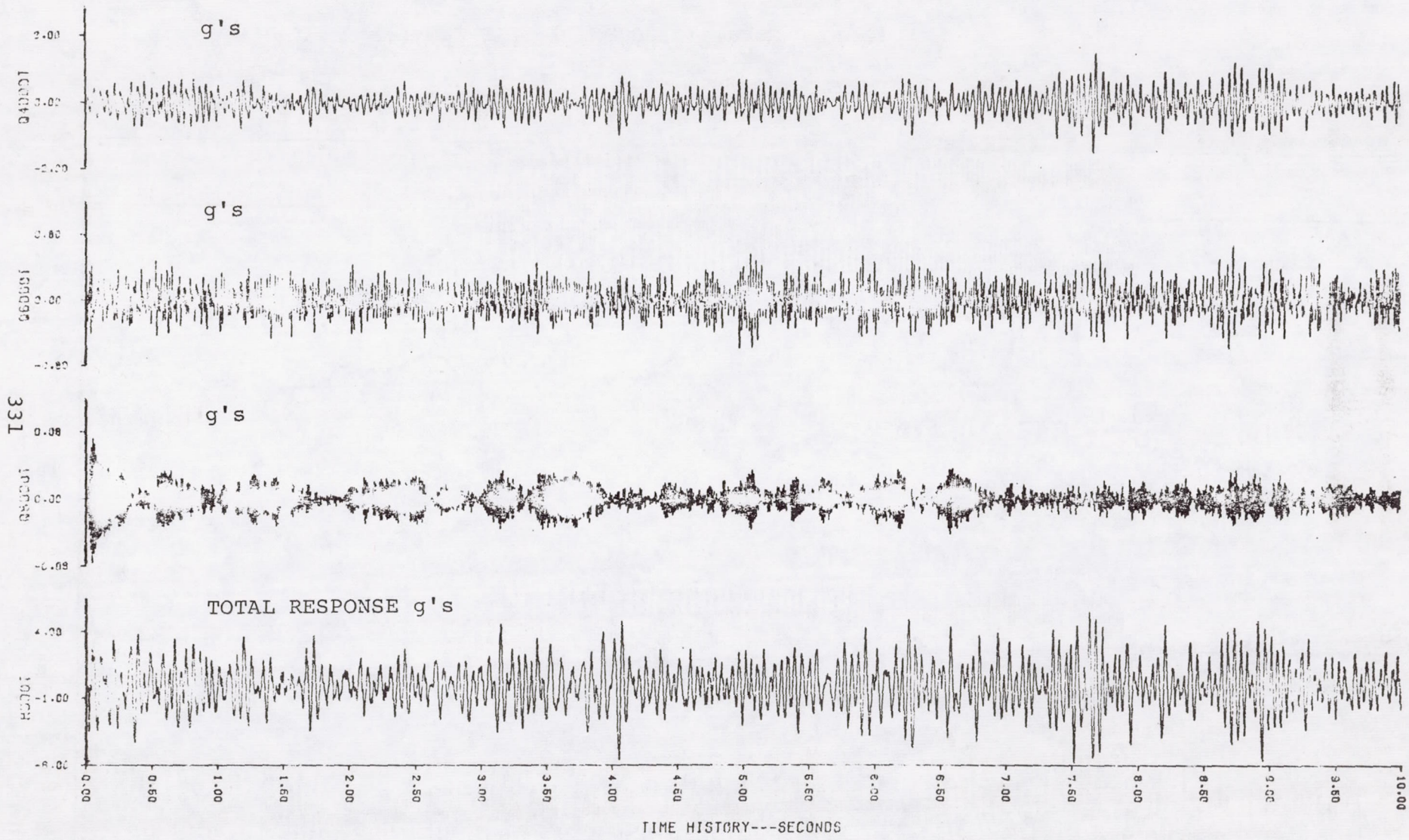

FIGURE C.7 (CONTINUED) (PAGE 2 OF 3)

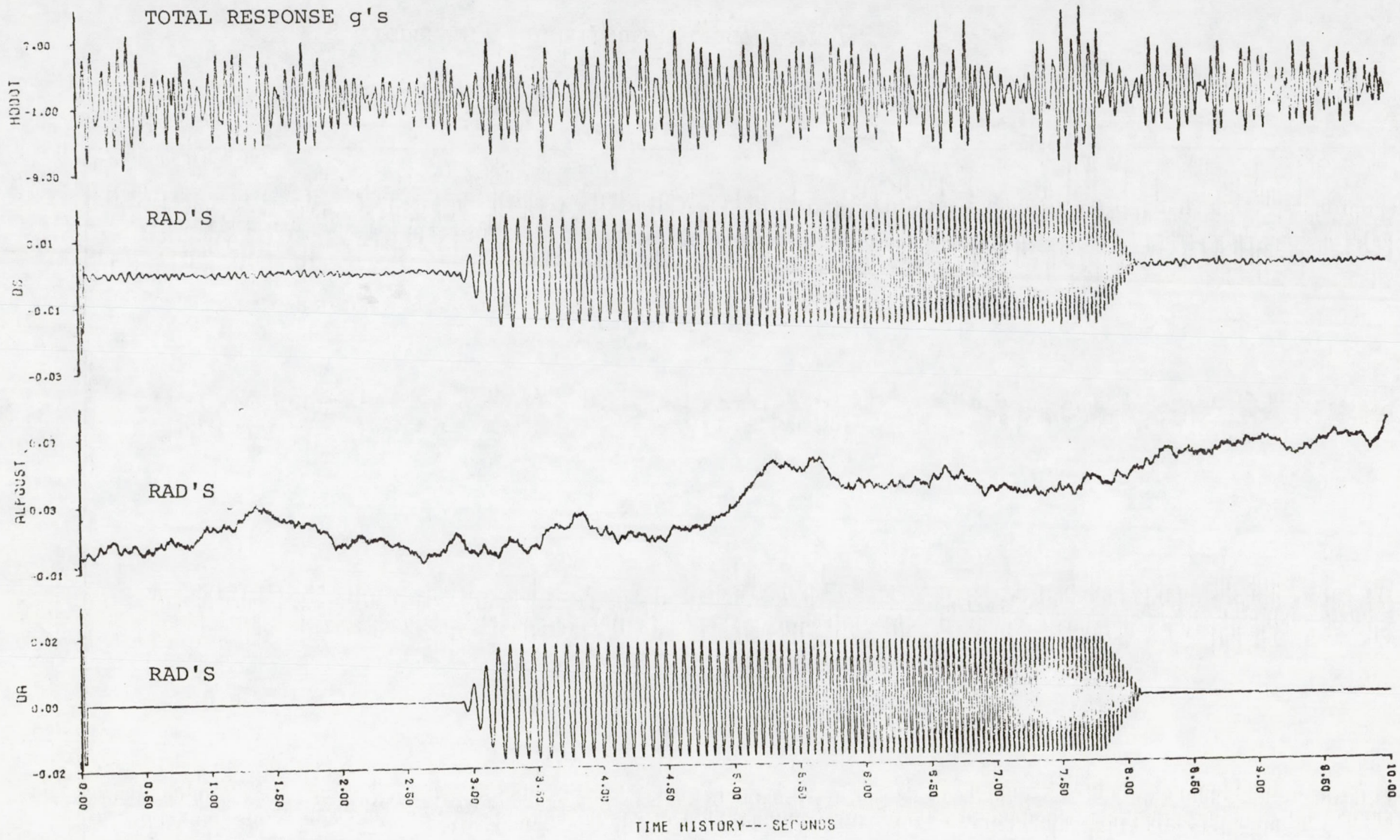

FIGURE C.7 (CONCLUDED) (PAGE 3 OF 3)

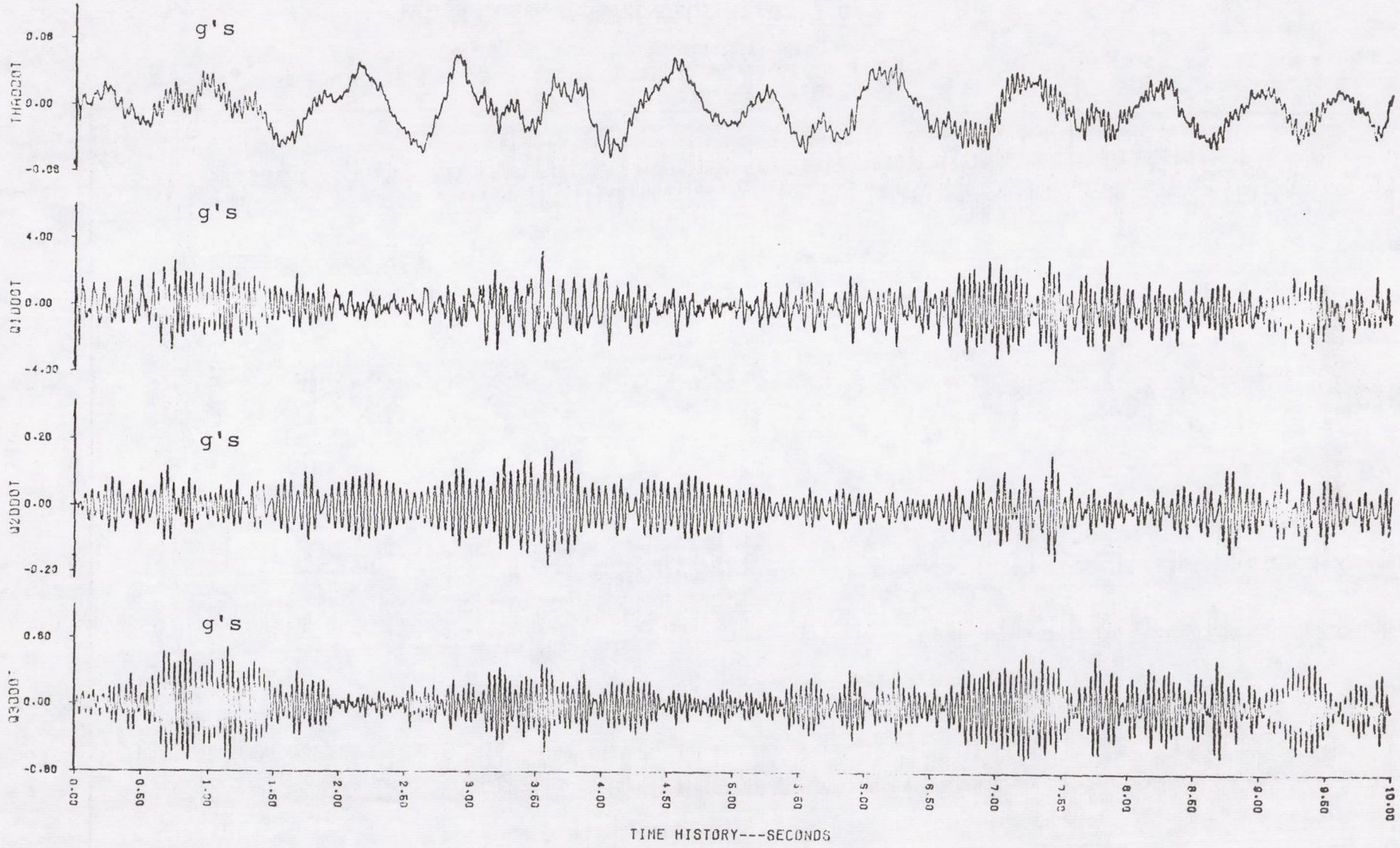

FIGURE C.8 SUBCRITICAL CLOSED LOOP WITH TURBULENCE (PAGE 1 OF 3)

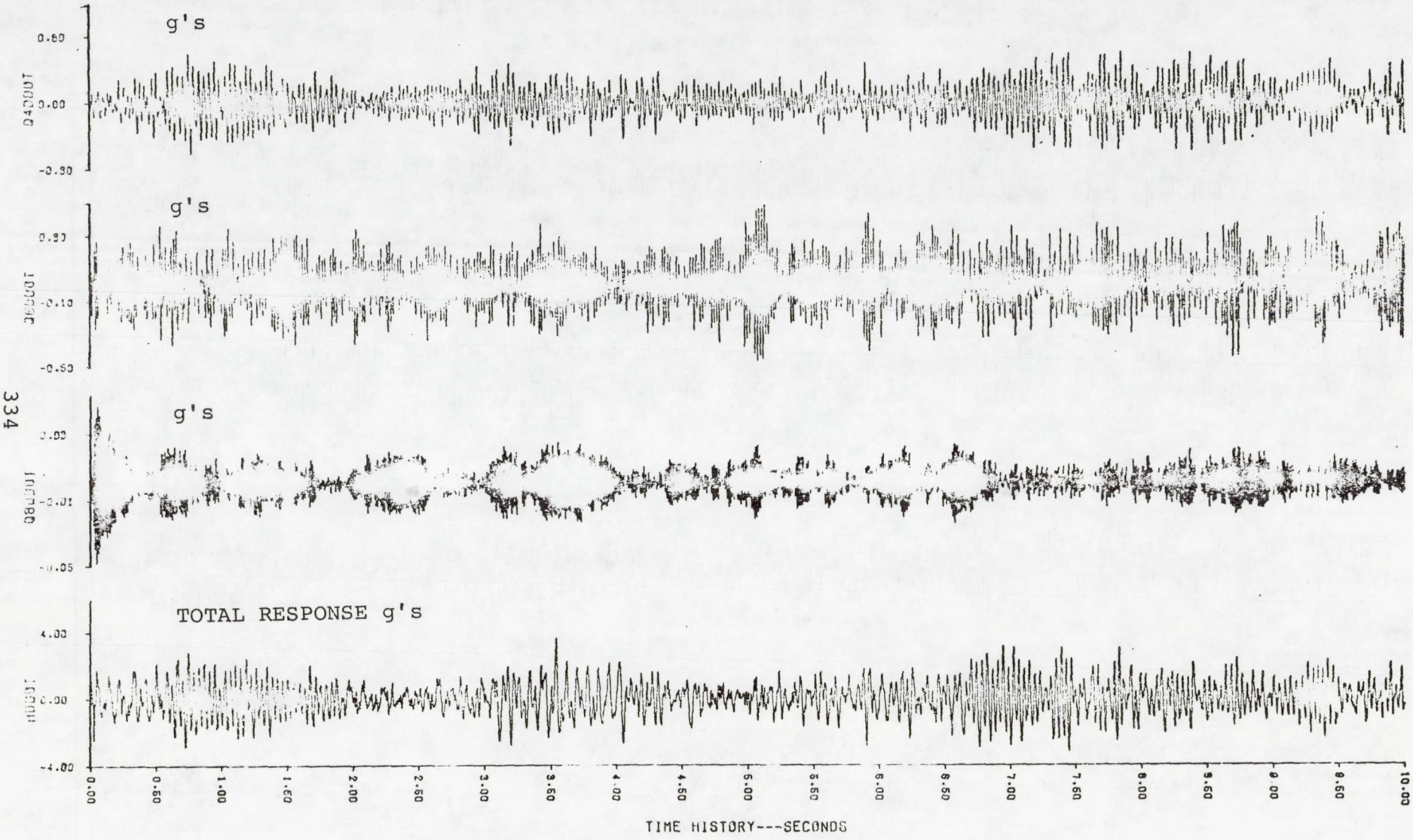

FIGURE C.8 (CONTINUED) (PAGE 2 OF 3)

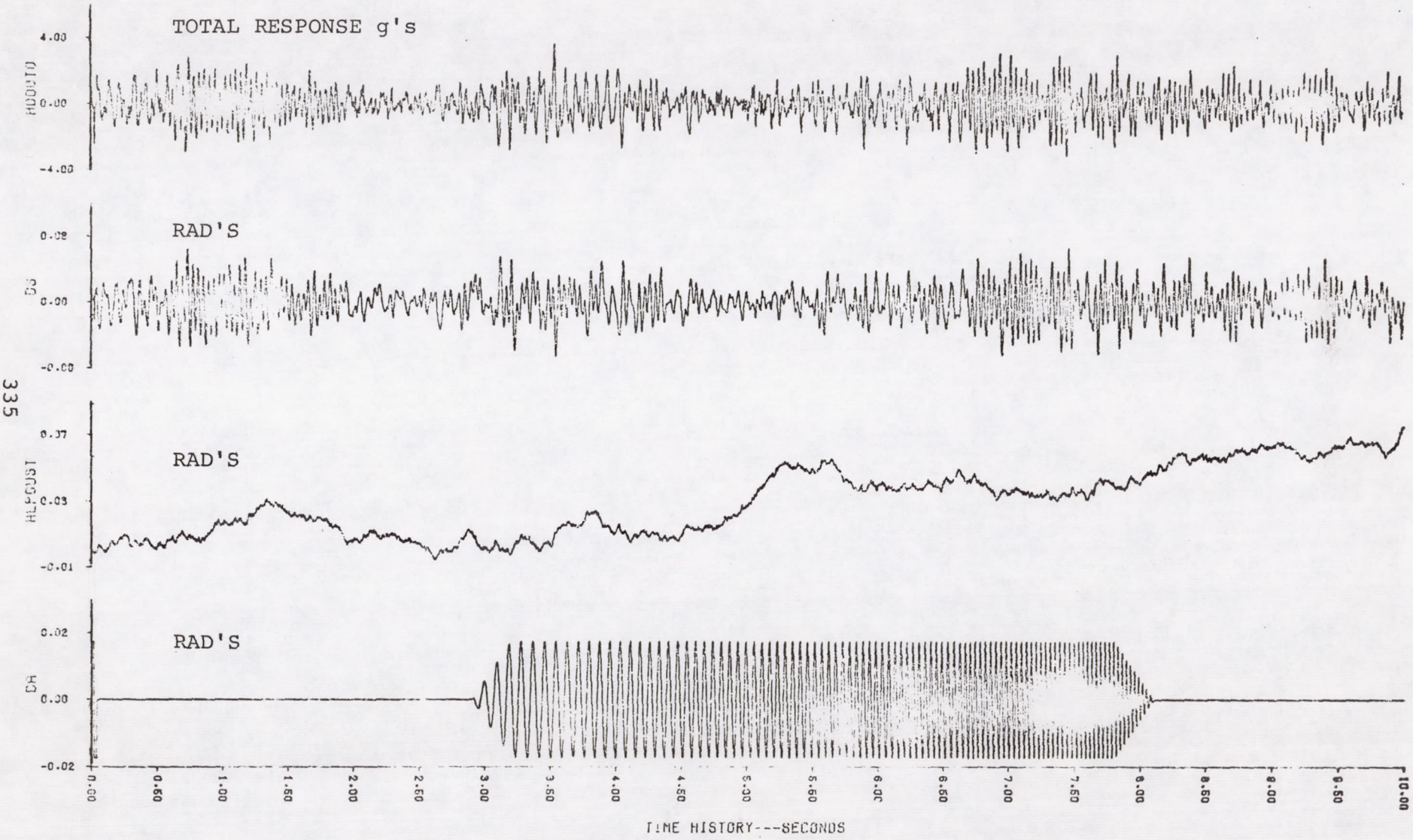

FIGURE C.8 (CONCLUDED) (PAGE 3 OF 3)